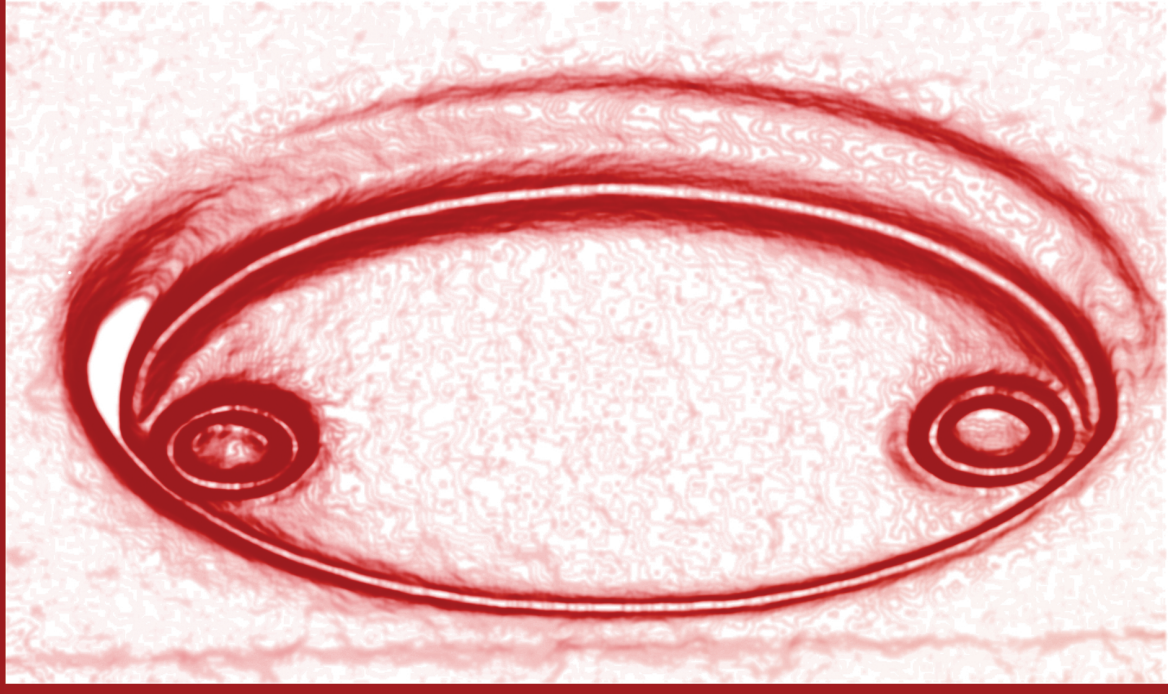

Matthias Hensen

Concentrating Light:

Nano-devices for spectroscopy, ultra-fast current injection and coherent energy transport

Dissertation

University of Bielefeld

Concentrating Light: Nano-devices for spectroscopy, ultra-fast current injection and coherent energy transport

---

Matthias Hensen

A Dissertation Submitted in Partial Fulfilment
of the Requirements for the Degree of

Doktor der Naturwissenschaften
(Dr. rer. nat.)

at the
Lehrstuhl für Molekül- und Oberflächenphysik
Fakultät für Physik
Universität Bielefeld
March, 2016

Supervisor: Prof. Dr. Walter Pfeiffer
2^{nd} Referee: Prof. Dr. Thomas Huser

"Physics is not the most important thing. Love is."

Richard P. Feynman [1]
(Nobel Prize in Physics 1965)

Publications

First author publications

- M. Hensen, D. Differt, I. Heesemann, F. Becker, A. Godt, D. Diesing, and W. Pfeiffer (2015) Few-cycle laser pulse induced plasmon assisted thermionic injection in metal-insulator-metal junctions, *Ultrafast Phenomena XIX (Springer Proceedings in Physics)*, 698-701, Springer Berlin

Co-author publications

- M. Aeschlimann, T. Brixner, A. Fischer, M. Hensen, B. Huber, D. Kilbane, C. Kramer, W. Pfeiffer, M. Piecuch, and P. Thielen (2016) Determination of local optical response functions of nanostructures with increasing complexity by using single and coupled Lorentzian oscillator models, *Applied Physics B: Lasers and Optics*, submitted

- D. Differt, M. Hensen, and W. Pfeiffer (2016) Time reversal versus adaptive optimization for spatiotemporal nanolocalization in a random nanoantenna, *Applied Physics B: Lasers and Optics*, submitted

- M. Aeschlimann, T. Brixner, D. Differt, U. Heinzmann, M. Hensen, C. Kramer, F. Lükermann, P. Melchior, M. Piecuch, C. Schneider, H. Stiebig, C. Strüber, and P. Thielen (2015) Perfect absorption in nanotextured thin films via Anderson localized photon modes, *Nature Photonics* **9**, 663-668

- F. Merschjohann, S. Neb, P. Bartz, M. Hensen, C. Strüber, S. Fiechter, N. Müller, W. Pfeiffer, and U. Heinzmann (2015) Delayed core-level photoemission from the van der Waals crystal WSe_2, *Ultrafast Phenomena XIX (Springer Proceedings in Physics)*, 68-71, Springer Berlin

First author publications in preparation

- M. Hensen, M. Aeschlimann, T. Brixner, B. Frisch, B. Hecht, B. Huber, C. Kramer, E. Krauss, T. Löber, W. Pfeiffer, M. Piecuch, and P. Thielen, Coherent energy transfer between widely separated nanoantennas coupled via an all-plasmonic cavity
- M. Hensen, F. Becker, D. Differt, I. Heesemann, A. Godt, D. Diesing, and W. Pfeiffer, Nanoantenna-supported ultrafast thermionic current injection in metal-insulator-metal-junctions
- M. Hensen, I. Heesemann, E. Oberländer, A. Godt, T. Huser, and W. Pfeiffer, Nanoparticle dimer induced resonant Raman enhancement in Au-nanoparticle aggregates formed with rod-like alkyne-rich dithiol as linker and Raman reporter

Co-author publications in preparation

- M. Aeschlimann, T. Brixner, M. Cinchetti, N. Haag, M. Hensen, B. Huber, C. Kramer, W. Pfeiffer, M. Piecuch, C. Schneider, B. Stadtmüller, and P. Thielen, Long-lived coherence in the metal-organic-hybrid cobalt/Alq_3

Conference contributions as a presenting author

- M. Hensen, M. Aeschlimann, T. Brixner, B. Frisch, B. Hecht, B. Huber, C. Kramer, E. Krauss, T. Löber, W. Pfeiffer, M. Piecuch, and P. Thielen, *Coherent and periodic energy transfer between widely separated and cavity-coupled nanoantennas*, DPG Spring Meeting 2016, Regensburg, Germany (2016)

- M. Hensen, M. Aeschlimann, T. Brixner, B. Frisch, B. Hecht, B. Huber, C. Kramer, E. Krauss, T. Löber, W. Pfeiffer, M. Piecuch, and P. Thielen, *Coherent and long-range plasmon-assisted energy transfer between two plasmonic nanoantennas*, 4^{th} International Workshop on Ultrafast Nanooptics, Bad Dürkheim, Germany (2015)

- M. Hensen, *Nanophotonic structures for light harvesting and coherent energy transfer*, FOM Institute for Atomic and Molecular Physics, Amsterdam, The Netherlands (2015)

- M. Hensen, F. Becker, D. Diesing, D. Differt, W. Pfeiffer, and C. Strüber, *Resonance enhanced local thermionic emission*, Annual SPP Meeting 2014, Bad Dürkheim, Germany, (2014)

- M. Hensen, I. Heesemann, E. Oberländer, A. Godt, T. Huser, and W. Pfeiffer, *Wavelength-specific response of surface-enhanced Raman scattering in nanoparticle dimer structures*, DPG Spring Meeting 2014, Dresden, Germany (2014)

- M. Hensen, D. Differt, I. Heesemann, A. Godt, D. Diesing, W. Pfeiffer, and C. Strüber, *Single nanoparticle assisted few-cycle laser pulse induced local multiphoton internal photoemission in MIM junctions*, 8^{th} International Symposium on Ultrafast Surface Dynamics, Estes Park, Colorado, USA (2013)

- M. Hensen, M. Aeschlimann, M. Birlo, T. Brixner, D. Differt, C. Kramer, P. Melchior, W. Pfeiffer, M. Piecuch, H. Stiebig, C. Strüber, and P. Thielen, *Light trapping in nanotextured thin-film silicon solar cells*, 8^{th} International Symposium on Ultrafast Surface Dynamics, Estes Park, Colorado, USA (2013)

- M. Hensen, D. Akemeier, D. Diesing, D. Differt, A. Godt, I. Heesemann , A. Hütten, W. Pfeiffer, and C. Strüber, *Nanoantenna supported internal photoemission in metal-insulator-metal (MIM) junctions*, DPG Spring Meeting 2013, Regensburg, Germany (2013)

- M. Hensen, D. Differt, M. Aeschlimann, D. Akemeier, M. Birlo, T. Brixner, D. Diesing, A.Fischer, A. Godt, I. Heesemann, A. Hütten, C. Kramer, P. Melchior, W. Pfeiffer, M. Piecuch, C. Schneider, H. Stiebig, C. Strüber, and P. Thielen, *Nanophotonic phenomena in thin-layer systems: Light localization and highly nonlinear charge carrier transport*, 1^{st} Bielefeld Workshop on Nanolayers and Artificial Membranes, Bielefeld, Germany (2013)

- M. Hensen, M. Aeschlimann, M. Birlo, T. Brixner, D. Differt, A. Fischer, C. Kramer, P. Melchior, W. Pfeiffer, M. Piecuch, C. Schneider, H. Stiebig, C. Strüber, and P. Thielen, *Light trapping in thin-film silicon solar cells investigated by spectral interference and time-resolved PEEM*, 17^{th} International Workshop on Microchip Plasmonics, Erlangen, Germany (2012)

- M. Hensen, D. Diesing, D. Differt, W. Pfeiffer, and C. Strüber, *Nanoantenna induced internal photoemission in metal-isolator-metal junctions, 2nd SPP 1391 student seminar*, 2^{nd} Student Seminar of the SPP 1391, Lauterbad, Germany (2012)

- M. Hensen, W. Pfeiffer, and C. Strüber, *Frequency comb stabilization with zero phase slip frequency for high repetition rate carrier envelope sensitive experiments*, DPG Spring Meeting 2011, Dresden, Germany (2011)

Contents

List of Figures

Introduction

The electromagnetic force is one of the four fundamental forces of nature and its interaction is mediated by quantised force carriers called photons. For human beings the most obvious impact of electromagnetic radiation on every day life is visual perception: It allows to process information of the surrounding environment which is encoded by photons of the visible part of the electromagnetic spectrum. The significance of electromagnetic radiation for life, technology and knowledge in general was recently honoured by the United Nations with the *International Year of Light 2015* in which most parts of the present thesis have been written [2].

Anniversaries of some important milestones coincided in that year: For instance, 150 years ago James Clerk Maxwell formulated a field theory for describing all phenomena associated with classical electrodynamics [208]. 40 years later Albert Einstein, inspired by the idea of Max Planck about quantised exchange of energy, explained the photoelectric effect with the concept of photons [96] and thus opened the door to a quantised field theory. The emission and detection of electromagnetic radiation, i.e. photons, delivered knowledge on different spatial scales: While atomic physics in the laboratory is an example for smallest scales [178], the detection of the cosmic microwave background by Penzias and Wilson 50 years ago is an example for enormously large scales [235]. At an intermediate level photons are exchanged in ever-growing global communication networks. Besides these technological and academic aspects, light has a fundamental impact on life itself: In photosynthesis, light is captured in molecular antenna systems, so called *light-harvesting complexes*, and its excitation energy is directed towards reaction centres where it fuels the organisms' activities [36]. Actually, the photosynthesis process is the fundamental example for all the aforementioned technological aspects: Capturing signals or energy efficiently and transporting them from one form and location to another is a universal theme in all areas of physics [72].

Light harvesting is associated with the concentration of excitation energy, so that the chance for the desired interaction or process is enhanced. Due to the

diffraction limit in far-field optics, the confinement of freely propagating electromagnetic waves is limited to regions as small as the light wavelength. This fact could be perceived as a limit for the miniaturisation of photonic devices. However, the progress in the field of nano-technology facilitated to design so-called *plasmonic* antennas, which capture light due to resonant interaction cross-sections and convert optical radiation into intense and deep-sub-wavelength electromagnetic near-field distributions [33, 34]. The corresponding excitations, which are coupled to metal-dielectric interfaces, are called *surface plasmons*. They can be described as collective oscillations of charge carriers, near a metal-dielectric interface, coupled to an evanescent, i.e. exponentially decaying, electric field on both sides of the interface [197]. Surface plasmons can be localised at nano-scale structures like nano-particles and nano-rods, or they can propagate along a surface or a waveguide to which they are bound.

Concentrating electromagnetic energy to the size of state-of-the-art electronic devices while maintaining a propagation speed close to that of photons in free-space, make surface plasmons an interesting candidate for on-chip routing of information and energy on ultra-fast time-scales [338, 175]. Furthermore, the broad tunability of surface plasmon resonances is exploited for harvesting photons of the solar spectrum in photovoltaic devices [23], to build nano-scale light detectors [162], and to drive chemical reactions with hot-electrons generated by photons of the plasmonic excitation [50] which recently culminated in an autonomous plasmon-assisted photosynthetic device [219]. Moreover, concentrated light near nanostructures can be used for the observation of the temporal dynamics of vibrational wave packets in single molecules [323], or to manipulate and engineer light emission of quantum systems positioned in strongly confined electromagnetic fields [18].

The present thesis describes the author's contribution to the research field of light concentration in plasmonics. Different devices will be presented which utilise light concentration to enable e.g. a coherent energy transfer between widely separated plasmonic nano-antennas for the first time ever. In a theoretical approach it will be assessed if these systems are suited to prepare entanglement between quantum systems exposed to the concentrated electromagnetic near-field of the incorporated nano-antennas. Another device, a nanoparticle-decorated metal-insulator-metal junction, facilitates to generate yet unexplored states in non-equilibrium

dynamics through intense light concentration: Thermionic emission, supported by instantaneous thermalisation of the excited electron gas, is identified as the dominating current injection mechanism although ultra-short laser pulses are used for excitation. In a third device the near-field enhancement, i.e. light concentration, of nano-structures is exploited to transfer spectroscopic information of molecules located in a nano-scale volume to the far-field. In the following the four different chapters are shortly introduced in more detail and a sketch of the respective topics is shown in Fig. 0.1.

Thesis outline

Chapter 1. The research of recent years revealed that molecules in light harvesting complexes are strongly coupled to their nearest neighbours so that they can interact in a coherent fashion [47, 262]. Plasmonic systems can also couple to one another when their electromagnetic modes exhibit a spatial and spectral overlap [244]. The stronger light is concentrated, the stronger surface charges are accumulated and associated electric fields act, in addition to the external stimulus, as an enhanced local driving force. Here, it will be demonstrated for the first time in theory and experiment that the localised plasmon resonances of two widely separated nano-antennas can be strongly coupled (hybridised) via a surface plasmon mode that is confined to an elliptical shaped cavity. The antennas are separated by a distance of $2\lambda_0$, in which λ_0 is the vacuum wavelength of the antenna resonance. A strong interaction between the single antennas alone, i.e. without the cavity structure, via intense electromagnetic near-fields is usually not feasible at these large distances. However, interaction is greatly enhanced by placing the nano-antennas in the focal spots of the elliptic cavity where the electromagnetic energy of the cavity mode is concentrated, therefore supporting hybridisation. Energy is then periodically exchanged between the sub-systems whereupon the temporal dynamics can be described by three coupled oscillators. Since the nano-antennas are coupled via the cavity mode, the overall system represents an all-plasmonic analogue of the quantum mechanical Tavis-Cummings model, in which several atoms are coupled via a cavity mode [290]. This device might serve as a plasmonic

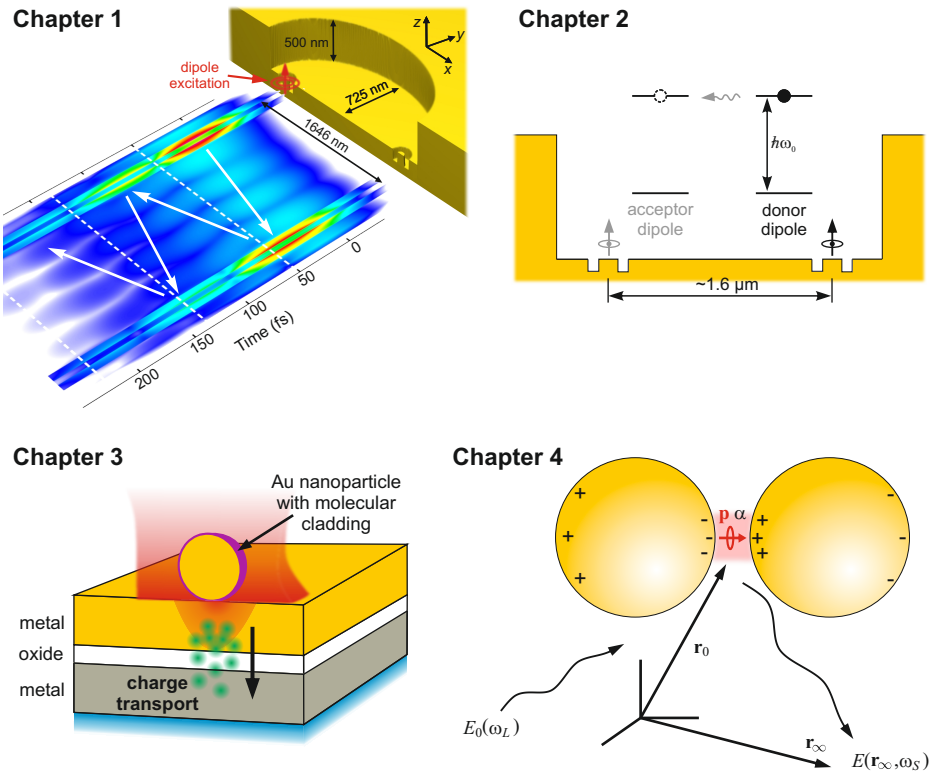

Fig. 0.1: Chapter 1: Two nano-antennas positioned in the focal spots of an elliptical cavity mode enable the coherent transfer of energy between the single constituents. Chapter 2: Investigation of mutual interaction between quantum systems positioned on top of the nano-antennas in the hybridised cavity system of Chapter 1. Chapter 3: Nano-antenna enhanced current injection in metal-insulator-metal junctions. Chapter 4: Light concentration in the gap between two adjacent nano-particles to overcome the rather low cross-section of Raman scattering. Plus and minus signs indicate surface charges of the symmetric plasmon mode which corresponds to a hybridised system.

bus which enables to coherently route plasmonic excitations between emitting and receiving elements, i.e. nano-antennas.

Chapter 2. The coupled cavity-antenna system presented in Chapter 1 is not only suited for distributing plasmonic energy between the widely separated nano-antennas but also for enhancing the energy transfer between donor and acceptor systems like molecules or quantum dots which are exposed to the concentrated electromagnetic energy of the localised antenna modes. Since the early works of

Edward Mills Purcell [245] and Karl-Heinz Drexhage [90], it is known that quantum emitters can experience self-interaction when coupled to electromagnetic modes resulting in enhanced or suppressed spontaneous decay rates. Moreover, light-concentrating structures can increase the probability for photon absorption in nearby quantum system, i.e. the chance of finding a photon near the quantum emitter is increased [269]. By combining both aspects, it will be shown in this chapter, by means of finite-difference time-domain simulations, that the normalised energy transfer rate of the incoherent dipole-dipole interaction is increased up to seven orders of magnitude compared to the donor-acceptor pair at equal distance in free-space. Then realistic quantum dot parameters are utilised to asses the chance of a coherent interaction, i.e. the transfer between both quantum emitters could be so fast that it is not possible to distinguish between donor and acceptor. Such an entangled (strongly coupled) system is highly desired for realising on-chip quantum information applications. Additionally, finite-difference time-domain simulations will be utilised to demonstrate *Dicke superradiance* [84] of quantum emitters inside the elliptical cavity. The corresponding mutual interaction between the emitters can enhance or suppress the emitter decay rates and this phenomenon has not been experimentally demonstrated in plasmonics, yet. Once realised, it is a promising candidate to generate an entangled state of widely separated systems in the absence of strong coupling [205].

Chapter 3. One of the most prominent technological implementations of light harvesting is the generation of electrical currents by electron-hole pair separation in semiconductors. The availability of optical nano-antennas led to a growing interest in exploiting the strong near-field enhancement of resonant metallic structures to improve the efficiency of solar cells [23]. In the last years especially metal-insulator-metal (MIM) junctions have become an interesting candidate for generating light-induced electric currents [308, 22, 61]. In these devices electrons are excited by surface plasmon decay in one electrode and they travel across the tunnel-barrier, i.e. through the conduction band of the insulator, to the back-electrode. In this chapter a device is presented which utilises pre-arranged nanoparticles as light concentrators on top of MIM junctions. In contrast to previous works [88, 293, 308, 89, 22, 61], the research presented here is based on rather extreme excitation conditions with respect to the overall setup: Intense few-cycle Ti:sapphire laser pulses are utilised to experimentally demonstrate nanoparticle-

supported charge carrier injection. The experimental results, in combination with numerical simulations, imply that the concentration of energy underneath the nanoparticle is so intense that a recently proposed regime in non-equilibrium dynamics [220] is reached: The excited electron gas instantaneously thermalises and it can be represented by a Fermi-distribution of temperatures > 1000 K. Heat diffusion simulations suggest that the ultra-short character of the laser pulse is imprinted on the injected current pulse.

Chapter 4. Surface-enhanced Raman scattering (SERS) exploits the enhanced near-field of metallic nanostructures to overcome the low scattering cross-section in Raman scattering experiments so that the unique spectroscopic fingerprints of molecular vibrations are appreciably amplified [283]. In this chapter the strongly concentrated light in the gap of plasmonically coupled and laser-excited nanoparticle aggregates, preferably nanoparticle dimers, is utilised to increase the acquired Raman signals from associated molecules. The work is distinguishes itself from similar approaches by using a newly synthesised alkyne-rich molecule for nanoparticle aggregation: The corresponding carbon triple bonds provide a Raman feature in a spectral region that is not affected by the signature of solvents or living cells, while its rigid character is promising for obtaining well-defined structures. Furthermore, all experiments in this chapter, like wavelength-resolved Raman scattering and UV-Vis extinction measurements, are performed with as-prepared solutions. Hence, the number molecules bound to the nanoparticles will not change since equilibrium in the sample is not affected. This allows to assign reliable enhancement factors for the SERS process since the number of participating molecules can be estimated from experimental data.

Annotation

The results in this thesis have been obtained in a collaborative effort with colleagues and other working groups. The only exception is the content of Chapter 2 which was motivated and handled by the thesis author himself. In the specific introduction of all other chapters the contribution to the presented results is explicitly itemised with respect to the involved people.

1 Cavity-mediated coupling of widely separated nano-antennas

1.1 Coupling of bright and dark plasmonic resonances

Hybridisation, i.e. the coupling, of plasmonic systems [244] is a phenomenon widely utilised in photonics. The coupled gold nanoparticles used for surface-enhanced Raman scattering in Chapter 4 are only one of the most prominent structures (see Fig. 0.1 for a sketch). Another simple and similar example are end-to-end aligned nanorods which also facilitate enhanced optical near-fields inside the inter-rod gap [145, 8].

Coupling in more complex systems has been demonstrated with concentric nanoshells [244], self-assembled nanoparticles [99], non-concentric ring-disc nanocavities [276] and dolmen structures [331, 193]. These complex structures are of special interest since they facilitate the coupling of so-called *bright modes* (low-Q resonances) and *dark modes* (high-Q resonances). The terms *bright* and *dark* usually refer to the fact that only one constituent of the hybridised system is efficiently excited by far-field illumination, e.g. an electric dipole resonance, while the other constituent requires the excitation of an electric quadrupole (magnetic dipole) for instance. The latter resonance can be represented by two anti-phased electric dipoles. Radiation damping is appreciably reduced in this case because the radiated electric fields interfere destructively, leading to narrow spectral features and hence long-lived excitations. In analogy to atomic physics the interference of broad and narrow spectral features in plasmonic systems is called a *Fano resonance* [154].

These plasmonic Fano resonances are very sensitive to modifications of the sample environment [196] and therefore they are suited for chemical or biological sensing applications [194]. Moreover, if the coupled bright and dark modes are tuned to resonance and if the associated life-times differ considerably, the absorption of the bright mode is suppressed by destructive interference with the coupled

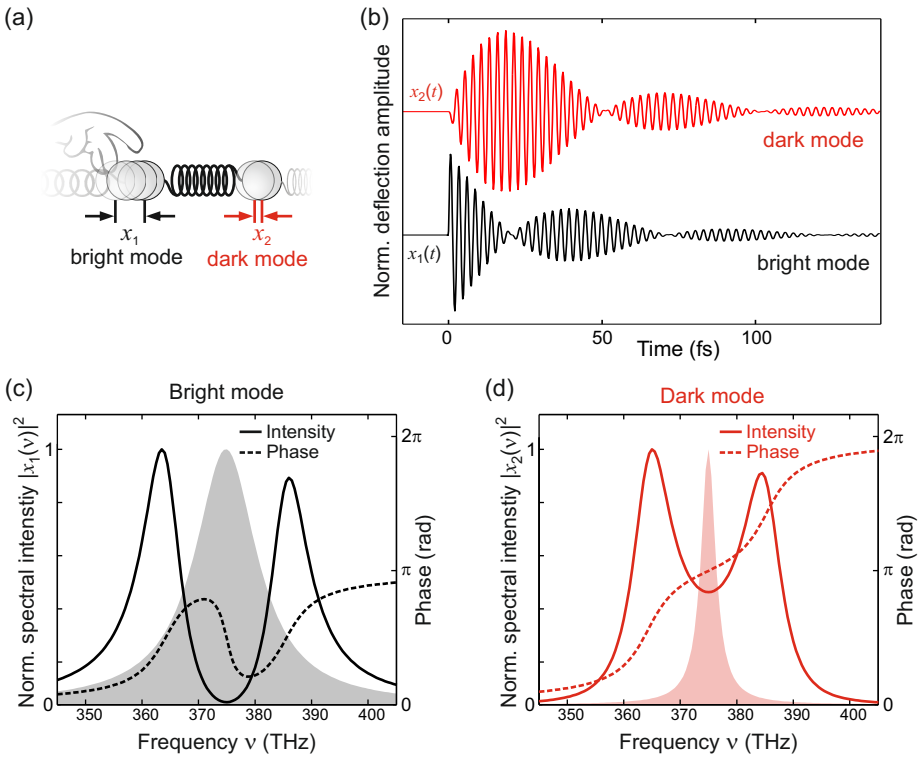

Fig. 1.1: Hybridisation of a low-Q and a high-Q resonance. (a) Hybridisation of the different modes sketched as coupled pendulums with deflections $x_{1,2}$. Only the bright resonance is initially excited. (b) Temporal evolution of the deflections $x_{1,2}$ after a δ-pulse excitation of the bright mode. Amplitudes are normalised to the maximum deflection of each curve, respectively. (c) and (d): Spectral intensity and phase of the single constituents of the coupled system. The spectral intensity of the uncoupled system is shown for comparison as grey and red shaded areas for the bright and dark mode, respectively.

dark mode. As a consequence of this, the material gets transparent in a narrow spectral window near the dark mode. This effect is known from atomic physics as *electromagnetically induced transparency* (EIT) [39] and it was proposed [331] and demonstrated [193] in plasmonics via the above mentioned dolmen structures. Furthermore, the abrupt change of optical properties in the spectral vicinity of the transparency window leads to a substantial slow-down of light propagation [54]. Hence, in plasmonics these coupled systems might be utilised as metamaterials [196] while in atomic systems EIT has been exploited for storing coherent information of light pulses in cold atom clouds for durations of up to 1 ms [192].

The research presented in this chapter was motivated by an additional aspect: As a consequence of hybridisation the unique feature of one sub-system is imprinted onto the other sub-system [271]. For example, intense electric fields of bright nano-antenna resonances (low-Q) can be combined with the longevity of dark modes (high-Q) to give an elongated and therefore enhanced interaction of optical near-fields with nearby quantum systems. Moreover, as in the case of coupled pendulums, energy can be coherently exchanged between the plasmonic sub-systems.

These statements are depicted in Fig 1.1: The bright and dark plasmonic modes are represented by pendulums, i.e. Lorentzian oscillators, which are coupled via an additional spring between them. The deflection amplitudes are labelled x_1 and x_2 for the bright and dark mode, respectively. Since only the bright mode couples to a far-field stimulus, it is initially excited as sketched in Fig. 1.1(a). The temporal evolution of the deflection amplitudes upon a δ-pulse excitation is shown in Fig. 1.1(b): A beating behaviour occurs so that energy, which is proportional to the squared envelope of the temporal dynamics, is transferred back and forth between both modes. The important point to note is that the decay constants of both oscillating deflections appear to be similar although the Q-factors, and hence the amount of dissipation, in the individual sub-systems should be clearly different. This is further investigated by looking at the spectral signature of the hybridised sub-systems in Fig. 1.1(c) and (d) of the bright and dark mode respectively. The spectral intensity of the uncoupled resonances with considerably different widths are represented by shaded areas. When coupling is switched on, the single peaks of both resonances split into two distinct peaks representing symmetric and anti-symmetric modes. The spectral intensity of the bright mode is vanishingly small between these two new modes. This is the above mentioned transparency window of EIT in which the motion of the bright mode oscillator is quenched by the dark mode oscillator and the bright mode phase shows a characteristic Fano dip [154]. Besides this effect, it is pointed out that the widths of split-up peaks are similar in the local coordinates of both sub-systems: The symmetric and anti-symmetric peak width of the bright mode is narrower than the peak width of the isolated resonance (grey-shaded area), while in the case of the dark mode both new peaks are broader than the respective uncoupled resonance (red-shaded area). Consequently, both time signals in Fig. 1.1(b) decay with comparable time

constants and the feature of one mode is imprinted onto the other.

With respect to these findings, it would be highly desirable to find a narrowband and hence long-living plasmonic system that can be strongly coupled to an intense localised surface plasmon resonance (LSP) to greatly enhance the interaction of optical near-fields with incorporated quantum systems. Such structures could be utilised to enhance the energy transfer between different quantum systems like molecules or quantum dots [92, 206]. Moreover, it could be possible to reach the so-called *strong coupling regime* of light-matter interaction in which particular peaks of the hybridised modes again split up due to *vacuum Rabi splitting*, i.e. modes of the plasmonic and molecular system get hybridised [295]. In this case quantum emitters coupled to the plasmonic mode can interact coherently which will pave the way for quantum information theory [198] on a chip. Although the strong coupling of single emitters and single plasmons has been proposed [148, 263, 297, 272, 62, 77] an experimental realisation has not been demonstrated so far [295]. However, this topic will be extensively discussed in Chapter 2 of this thesis. Here, the focus lies on the realisation of the fundamental plasmonic properties of such a system. The task is to find a combination of plasmonic nano-antennas and long-living plasmonic excitations so that the coherent and periodic transfer of optical near-fields, as sketched in Fig. 1.1(b), can be demonstrated in theory and experiment. This task includes the ambitious goal to couple more than one nano-antenna to the dark plasmonic mode in order to realise a coherent exchange of energy between selectively addressable ports of a plasmonic hub (see Fig. 0.1, Chapter 1).

Coupling of localised and propagation surface plasmons

Extended surface plasmon polaritons (SPPs) [171, 197] are interesting candidates for excitation of long-living surface-bound electromagnetic waves. SPPs have generally rather long coherence life-times since they do not couple directly to the far-field and they exhibit only a small overlap with bulk electronic states [6]. At typical Ti:sapphire operation wavelengths of 800 nm the propagation length δ_{SPP}, i.e. the e^{-1}-decay of intensity, of SPPs on atomically flat and single-crystalline Au surfaces amounts to $\approx 50\ \mu$m according to Section A.1. Since in the NIR spectral region the SPP group velocity $v_{g,SPP}$ is similar to the vacuum speed of light

c, i.e. $v_{g,SPP}(800\,\mathrm{nm}) = \partial\omega/\partial k \approx 0.92c$ (retrieved from Fig. A.1(a)), the e^{-1} life-time of near-field intensity is about 180 fs. This duration is considerably long compared to typical coherence life-times of LSPs of about 10 fs [131, 222, 277]. However, coupling of a textbook SPP with a single LSP turns out to be difficult due to the following reason: It has been shown that hybridisation of plasmonic modes can be described in a similar fashion compared to how molecular orbitals are constructed from interacting atomic orbitals in electron structure theory [281]. In short, the interaction of the electric charges and associated fields of the distinct constituents leads to a redistribution of charges forming the new (symmetric and anti-symmetric) eigenmodes [281]. This has been verified experimentally [244] and with density functional theory [243]. Hence a considerable mode overlap is required which is unlikely to occur by considering the quasi-infinite spatial extension of a textbook SPP and the nano-localisation of a single LSP.

To date a prearranged strong coupling of SPP and LSP was only achieved by using a large number of nano-antennas interacting with a propagating SPP. This approach is similar to the strong coupling of plasmons and quantum emitters which is facilitated due to the vast amount of e.g. J-aggregate molecules interacting with the plasmonic excitation [31]. In the case of SPP-LSP coupling, Holland and Hall showed in 1983 that in the presence of an SPP excitation the resonance wavelength of a light scattering Ag nanoparticle film shifts. Later, in 1998, Hall and Stuart could furthermore demonstrate that Ag island films exchange energy with optical waveguide modes of a silicon layer or with SPPs from a non-contact Ag layer. They attributed modifications in particle scattering spectra to the surface-mode-modified dipole-dipole interaction [287]. The first experimental evidence for mode-splitting and hence a strong coupling of LSPs with SPPs was reported by Cesario and co-workers [60]. They used an array of Au nano-discs for both, LSP excitation and grating coupling of SPPs into an ITO-coated Au layer. By varying the grating period the SPP resonance was tuned into the LSP resonance, resulting in a slightly observable mode splitting. A clear mode splitting of 35 THz was observed in 2009 by Chu and Croizer who also utilised Au nano-disc arrays: They varied both, the grating period as well as disc diameters and hence the LSP resonance [66]. The coupling of nanoparticle arrays with SPPs was numerically studied by Papanikolaou [233] and by Ghoshal and Kik [115]. In the latter paper the charge distribution in nanoparticles and the metal layer had also

been shown for the new emerging modes, clearly indicating the symmetric and anti-symmetric character. Furthermore, Ghoshal and Kik demonstrated explicitly that the numerical results, obtained with the finite integration technique [315], could be perfectly described by a coupled oscillator model similar to the sketch in Fig. 1.1(a). In 2014 Yun and co-workers also observed a strong coupling of SPPs and LSPs of a nano-cube array by using the Kretschmann excitation geometry [171], in contrast to all previous works which utilised nano-antenna-supported grating coupling of SPPs [330].

So far, the only experimental demonstration of a single LSP resonance coupled quite strongly to a delocalised surface plasmon excitation occurred by chance: Aeschlimann and co-workers observed an unexpected long phase memory of localised plasmon resonances of about 90 fs on a corrugated Ag surface [6]. They explained the long coherence life-time by coupling of the LSP to a delocalised surface plasmon which is confined between the ridges of the corrugated Ag films on length scales of some micrometers. Some important aspects are shown in Fig. 1.2:

A scanning electron microscopy image of the corrugated Ag surface shows that the topography is dominated by ridges and valleys (Fig. 1.2(a)). The ridges exhibit heights of about $\sim 1\ \mu$m according to atomic force microscopy (Fig. 1.2(b)). These ridge heights facilitate reflection of excited SPPs since the e^{-1} penetration depth into air at energies of 1.55 eV is about 600 nm (see Fig. A.1(d)). By chance the ridges can form random micro-resonators and only a small part of the broadband SPP wave packet, injected by laser pulses, is allowed to exist inside this system by forming a standing SPP pattern. Due to the momentum mismatch of far-field photons and SPPs of the same frequency (see Fig. A.1(a)), surface corrugations like the particle-like protrusions in Fig. 1.2(a) are required to act as broadband optical nano-antennas and to transform energy from the far-field into the aforementioned SPP wave packets. Additionally, strong electric field enhancement occurs at the particle-like corrugations due to the simultaneously excited localised plasmon modes. The strong fields facilitate multi-photon photoelectron emission at the random nano-antennas whereupon two of these hot-spots are systematically investigated with two-pulse-correlation measurements (Fig. 1.2(c)). Two laser pulses of 50 fs duration are delayed by a time T to probe the phase memory of plasmonic excitations of two adjacent hot-spots (see inset of Fig. 1.2(d)).

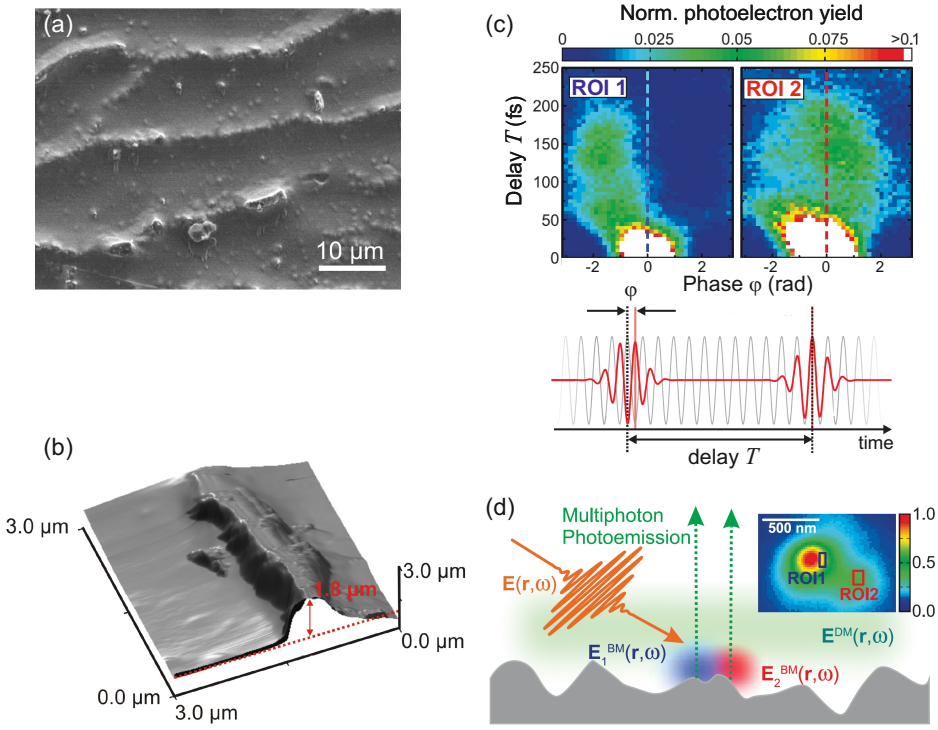

Fig. 1.2: Hybridisation of SPPs with single LSPs in random resonators. (a) Scanning electron microscopy image of the sample: A corrugated Ag surface showing a ridge and valley topography. (b) Atomic force microscopy reveals typical ridge heights of 1 μm. (c) Two-pulse-correlation measurements at adjacent hot-spots, ROI 1 and ROI 2 (region of interest), separated by less than 500 nm (see inset part (d)). The signal, i.e. ejected photoelectrons from a multi-photon photoelectron emission process, is normalised to $T = 0$ and $\varphi = 0$. (d) Interpretation of results: An incident laser pulse $\mathbf{E}(\mathbf{r},\omega)$ ($\sim$ 50 fs duration) excites bright LSPs $\mathbf{E}_1^{\mathrm{BM}}(\mathbf{r},\omega)$ and $\mathbf{E}_2^{\mathrm{BM}}(\mathbf{r},\omega)$ which couple to a delocalised dark mode $\mathbf{E}^{\mathrm{DM}}(\mathbf{r},\omega)$. Inset: Photoemission pattern of investigated hot-spots. (a) and (b) are reproduced from [286] while (c) and (d) are reproduced from [6].

The measured and integrated photoelectron yield in both regions of interest (ROI1 and ROI2) is a measure of the local electric field intensity. Due to the short life-time of LSPs and the non-linearity of the photoelectron emission process, the yield is expected to diminish quickly for non-overlapping pulses ($T > 50$ fs). However, the yield in both ROIs does not monotonically decrease but it increases again after 100 fs and then finally decreases to the signal baseline not until 200 fs. Aeschlimann and co-workers ascribe this unusual behaviour by coupling of

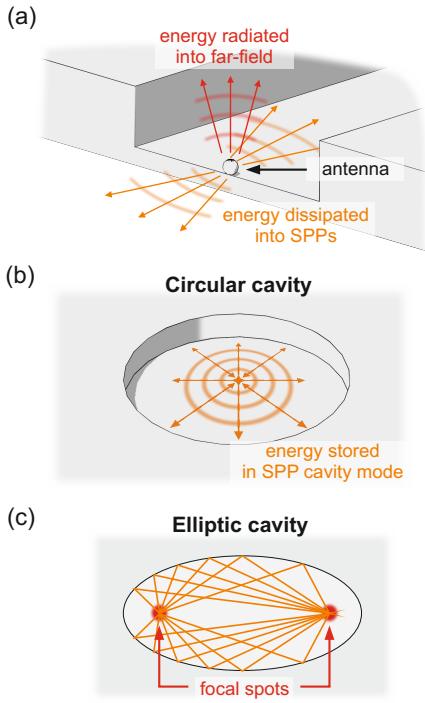

Fig. 1.3: Sketched cavity schemes for coupling of extended surface plasmon polaritons (SPPs) with single localised surface plasmon (LSP) resonances. (a) Examples for an inappropriate design of cavities and nano-antennas: Since SPPs are bound at the interface of two media they should be confined in all lateral directions which is not possible in a simple 1D Fabry-Pérot cavity. In this case electromagnetic energy is transferred into SPPs that will never return to the interaction region. Also very bright nano-antennas should be avoided since they efficiently radiate energy into the far-field instead of exchanging energy with SPPs. (b) A circular cavity: SPPs injected with radial symmetry by a nano-antenna in the cavity centre are simply reflected by encasing metallic walls and are subsequently refocused. (c) A cavity with elliptic metallic walls allows for an enhanced interaction of two nano-antennas: If placed in the focal spots emitted SPPs are refocused at the opposite antenna so that LSPs can interact via a cavity mode.

dark SPP modes confined between the ridges in a random micro-resonator to a random LSP of a particle-like bump of the corrugated Ag surface (Fig. 1.2(d)). Hence, according to Fig. 1.1(b), random LSP nano-antennas inject energy into a dark SPP mode which recurs at the antenna due to hybridisation so that a coherent superposition of local electric fields and the probe pulse leads to an increased photoelectron emission yield at later times. The coherence of this process and therefore the unusual long phase memory of LSPs is demonstrated by the fact that the measured electron yield at $T > 100$ fs depends on the relative phase between the pump and probe laser pulse (see the abscissa in Fig. 1.2(c)).

Chapter aim and outline

In this chapter a device is presented, in theory and experiment, that allows for the first time a prearranged strong coupling of extended surface plasmon polari-

tons with localised plasmonic resonances of well-defined nano-antennas. Inspired by the first results of Aeschlimann and co-workers in random micro-resonators, the extended SPP modes will be confined in designed plasmonic cavities. Confinement is achieved by SPP reflection at upright metallic (Au) walls which exhibit a height of some hundred nanometres to account for the SPP penetration depth into the vacuum half-space. The cavity floor, to which the SPPs are bound, will be an atomically flat Au surface in both, theory and experiment. Ultimately, the strong coupling of two nano-antennas to the same cavity mode will result in a device that facilitates a coherent and periodic energy transfer between antennas with a resonance wavelength of 800 nm, which are separated by more than one micrometre. Without such a cavity structure a strong interaction between the antennas would not be possible since the intense near-fields usually do not overlap at these large distances. The chapter is structured as follows:

Section 1.2 is dedicated to the introduction of the nano-antenna that will be utilised inside the cavities. According to the considerations depicted in Fig. 1.3(a), it should be avoided that the antenna couples strongly to the far-field since the energy dissipated in this loss channel is no longer available for SPP injection. On the other hand the antenna still needs to be addressable by laser pulse excitation. It will be shown via finite-difference time-domain (FDTD) simulations that a specific and often neglected operation mode of so-called *whispering gallery mode resonators* (WGMs), which have been previously investigated by Vesseur and co-workers [305, 306], is perfectly suited to interact with extended SPPs. For this purpose electric near-field distributions, far-field projections, absorption cross-sections and Q-factors for the specific antenna geometry will be extracted from simulation data. With view to later sections some technical aspects will be addressed which deal with the effect of different excitation geometries of electromagnetic field sources.

In Section 1.3 it will be shown via FDTD simulations that a WGM antenna placed in the centre of a cavity of circular shape (Fig. 1.3(b)) indeed leads to strong coupling of a single LSP with an extended SPP. First the performance of the pure cavity is evaluated by retrieving e.g. Q-factors from simulation data. Then the hybridised system will be investigated with view to its temporal and spectral signatures. It will turn out that the perceivable altered response functions of single constituents can be perfectly described by a model of two coupled harmonic oscillators as sketched in Fig. 1.1. To further proof hybridisation the charge

distribution of emerging symmetric and anti-symmetric modes will be calculated from FDTD simulations and associated near-field distributions will also be shown.

In Section 1.4 a cavity of elliptic shape will be introduced (Fig. 1.3(c)). Such a design allows the incorporation of two identical WGM antennas at the positions of the focal spots of the corresponding cavity eigenmode. First, it will be demonstrated by FDTD simulations that the electric field distribution in the spots is perfectly suited for the present antenna operation mode. Then it will be shown with FDTD simulations and an analytical model of three coupled oscillators that the incorporated WGM antennas are coupled over a large distance of $\sim 2\lambda_0$ via the extended SPP cavity mode. Thereby it will be emphasised that one oscillator is the cavity mode itself and hence the system depicts an all-plasmonic analogue of the quantum mechanical Tavis-Cummings model [290], which describes the interaction of N atoms with a common light field.

Furthermore, the impact of different cavity wall heights, i.e. the degree of reflectivity, on the temporal dynamics of energy transfer between the three subsystems will be investigated. By using the analytical model of coupled oscillators it will be shown that the hybridised system obeys the phenomenon of *impedance matching*. It will be shown that the relative amount of cavity and antenna loss determines how energy is distributed between the sub-systems.

Finally, Section 1.5 is dedicated to the experimental realisation of a device which facilitates the coupling of two widely separated WGM antennas via an extended SPP mode inside the elliptic cavity. First, single crystalline gold plates with atomically flat surfaces [127, 143, 319] will be introduced as building blocks for the fabricated structures. Then, WGM antenna patterns with different size parameters will be investigated by laser irradiation and photoelectron emission microscopy (PEEM) to demonstrate the desired antenna operation mode. Last, the fabricated systems are mainly studied in the temporal domain by PEEM-based two-pulse-correlation measurements which reveal the coherent back-and-forth energy transfer between the opposite WGM antennas.

In Section 1.6 results will be reviewed in short and an outlook for future projects is given.

The idea and design of devices that allow a prearranged strong coupling of

single LSPs and extended SPPs for the first time ever is ascribed to the author of the thesis. All FDTD simulations and the corresponding evaluation, as well as the implementation of the coupled oscillator model, were also done by the author. Single-crystalline gold plates with the pure elliptic cavities have been fabricated by Enno Krauss from the *Nano-Optics and Bio-Photonics Group* of Bert Hecht (University of Würzburg). WGM antennas have been incorporated via focused ion beam milling with support of Thomas Löber (*Nano Structuring Center*, TU Kaiserslautern). PEEM measurements and preliminaries were performed at the TU Kaiserslautern by Benjamin Frisch, Martin Piecuch and Philip Thielen from the working group of Martin Aeschlimann (TU Kaiserslautern), Bernhard Huber and Christian Kramer from the working group of Tobias Brixner (University of Würzburg) and the thesis author (Walter Pfeiffer group - University of Bielefeld).

1.2 SPP injection with whispering gallery mode resonators

To foster hybridisation, hence a persistent interaction of localised plasmon resonances with extended SPP modes, the appropriate nano-antenna should exhibit several properties: While still being addressable from the far-field it, should inject most of its electromagnetic near-field energy into propagating SPP modes. This requires an appreciable mode overlap. Since SPPs are bound to a surface, the near-field intensity of the nano-antenna should also be mainly localised at the cavity floor. Moreover, since hybridisation results in a redistribution of surface charges, it would be beneficial if the nano-antenna is directly incorporated into the cavity floor so that LSP and SPP dynamics is governed by a common electron gas. Additionally, by considering the proposed cavity shapes (Fig. 1.3 (b) and (c)) the resonant mode of the nano-antenna should posses a radial symmetry and the antenna itself should be equal or smaller in size compared to spatial features of the supported cavity mode. In the case of circular cavity walls a radial symmetric field would match the cavity curvature radius and the electromagnetic energy would be imaged back to the source point in the centre. In the case of elliptic cavity walls, a rather small size renders the antennas as point sources in the focal spots and a coupling to other cavity modes of different symmetry is averted.

1.2.1 Introduction to nanoscale whispering gallery mode resonators

All of the above goals are to a certain extent fulfilled by a particular operation mode of an all-metallic *whispering gallery mode* (WGM) resonator which has been introduced by Vesseur and co-workers [305, 304, 306]. Whispering gallery waves are acoustical or optical excitations that are usually guided along concave surfaces. Compared to excitations spread into all spatial dimensions these waves exhibit reduced decay rates. Whispering gallery modes were first mentioned in acoustics by Lord Rayleigh [248] in 1878 and had been later introduced in optics where they, for instance, enable to store light for 36 μs by successive total internal reflection in dielectric cavities of macroscopic size [126]. Microscopic whispering gallery cavities for surface plasmon polaritons have been demonstrated by Min and co-workers by using hybrid metal-dielectric toroidal discs [214]. The above mentioned all-metallic WGM resonators, which were investigated by Vesseur and co-workers, can in principal be fabricated on scales below the diffraction limit and they are therefore suited to be used as nano-antennas in the proposed SPP cavities presented here.

An example of such WGM antennas is shown in Fig. 1.4(a): The antennas consist of annular grooves which are milled into a single-crystalline Au microplate by focused ion beam (FIB) technique. The scanning electron microscopy (SEM) image was taken during a preparation process with the support of Thomas Löber (NSC, TU Kaiserslautern). Note that the SEM column is tilted by 52° with respect to the surface normal. This allows to cut through the entire Au substrate which reveals a cross-section of the V-shaped grooves of the antenna in the foreground. These grooves support the existence of electromagnetic surface waves which are confined between the groove boundaries and which exhibit a real-valued wave vector k perpendicular to the groove cross-section. Hence, these near-field excitations propagate along the channel and they are therefore known as *channel plasmon polariton* (CPP) modes, as introduced by Novikov and co-workers [227]. These confined plasmon modes have been demonstrated [41] and utilised as micro-scale waveguides, interferometers and ring resonators [42] by Bozhevolnyi and co-workers. In addition, the modal properties of CPPs have been extensively studied in literature [227, 216, 324, 301].

It has been shown in theory and experiment [305] that nanoscale WGM res-

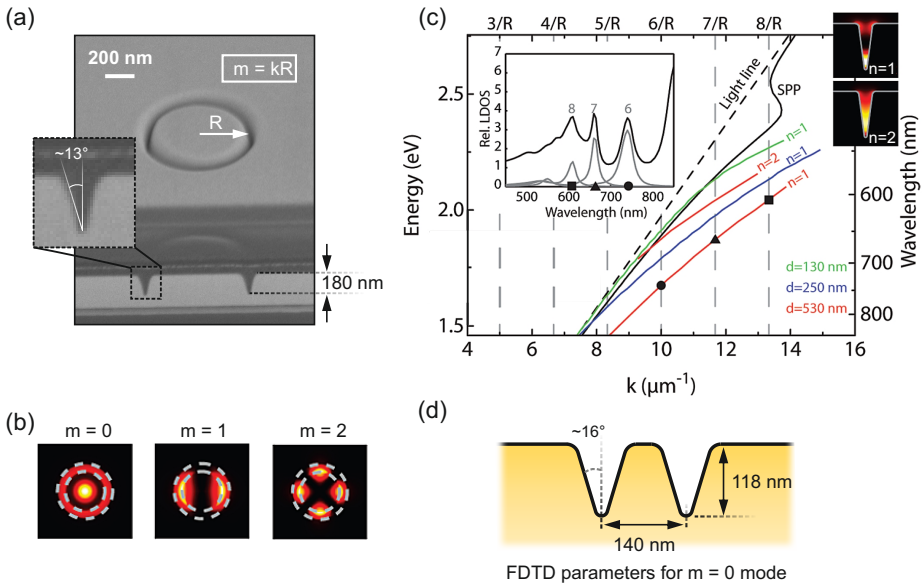

Fig. 1.4: Annular grooves used as nano-antennas: The whispering gallery mode (WGM) resonator. (a) Scanning electron microscopy image of two WGM antennas with $R = 350$ nm and and a depth of 180 nm in a single crystalline gold plate. The upper WGM antenna demonstrates smooth structures after fabrication with focused ion beam (FIB) milling, which is also seen in the cross-section and groove structure of the lower antenna. The image is taken at an angle of 52° to surface normal. Images and structures were produced with the support of Thomas Löber (NSC, TU Kaiserslautern). (b) Lateral cross-sections of electric field intensities $|E|^2$ associated with different azimuthal antenna mode numbers m. Dashed lines sketch the annular groove. The image is reproduced from [305]. (c) Comparison of the dispersion relation of straight groove plasmons (coloured lines) for different groove depth d and radial mode numbers n with expected WGM antenna resonances $k = mR$ for $m = 6,7,8$ (black cricle, triangle and square). Top-left inset: Calculated spectrum of the local density of states for $d = 530$ nm and $R = 600$ nm. The black symbols (square, triangle and circle) indicate the WGM resonances and correspond to the symbols in the dispersion relation for straight grooves. Top-right inset: $|E|^2$ distribution in straight grooves with different radial number n.The image is reproduced from [305]. (d) Cross-section of the WGM antenna structure that is used in FDTD simulations in the present thesis. Corners are rounded and the geometric parameters correspond to a $m = 0$ resonance.

onators like in Fig. 1.4(a), as well as microscale WGM resonators for SPPs [214], feature resonant modes if the circumference ($2\pi R$) of the circular groove matches the wavelength of the propagating CPP. This is expressed by the condition

$$m = kR, \tag{1.1}$$

where m is the so-called *azimuthal* mode number which takes on integer values $m \geq 0$. In this case a standing wave pattern is localised inside the groove. The corresponding lateral distributions of the electric field intensity $|E|^2$ for $m = 0, 1, 2$ are shown in Fig. 1.4(b) (reproduced from [305]). For $m = 1$ the circumference is matched to the CPP wavelength resulting in two nodes and two anti-nodes in the lateral mode pattern. Due to its dipolar character this mode can be efficiently excited from the far-field when the electric field vector oscillates parallel to the substrate [306]. The mode corresponding to $m = 2$ exhibits a quadrupolar character and couples less to far-field radiation.

According to condition (1.1) WGM antenna resonances can be envisioned as circulating CPPs which originate from plasmons in straight grooves that have just been bend to a ring of radius R. This analogy is shown in Fig. 1.4(c) (reproduced from [305]) which shows the dispersion relation of CPPs confined to straight and infinitely long V-grooves of depth d. A straight groove of constant depth can also feature different modes that are classified by the *radial* mode number n which relates to the number of anti-nodes in the cross-section of the electric field intensity, as shown in the upper right inset. The upper left inset shows the calculated resonances $(m,n) = (6,1), (7,1), (8,1)$ of a WGM antenna with radius $R = 600$ nm and depth $d = 530$ in terms of the local density of states (see equation (2.11) in Section (2.2.1)). The resonant vacuum wavelengths are marked by a black circle, triangle and square, respectively. In the dispersion relation of the straight groove with identical depth $d = 530$ nm (red solid line, $n = 1$) these wavelengths indeed correspond to CPP wave vectors that satisfy $k = m/R$ with $m = 6, 7, 8$ (vertical grey-dashed lines) as marked by the aforementioned black symbols.

In contrast to this resonance mechanism the $m = 0$ mode is not related to a propagating CPP and it exhibits the demanded radial symmetric lateral mode pattern Fig. 1.4(b). It has been shown that this special mode can be excited with an electron beam at normal incidence focused on the central part of the antenna [306]. Taking into account the radial symmetry and that the induced image charges move perpendicular to the substrate the electric field distribution is related to an electric dipole moment that points out of the substrate [306]. A dipole oscillating perpendicular to the substrate is expected to predominantly inject its energy into lateral directions and therefore into SPP excitations. Hence, the annular groove

WGM antenna operated in the $m = 0$ mode seems to be suited for a strong coupling of single LSPs with extended surface plasmons and it will be used throughout the entire chapter.

Before presenting the results of WGM antennas incorporated in all-plasmonic cavities the $m = 0$ mode is characterised by FDTD simulation with respect to particular geometrical properties. The geometrical antenna profile, as used in the FDTD software, is shown in Fig. 1.4(d). The groove is modelled with circular rounded edges which are connected by tangential straight lines. The opening angle of the groove amounts to $\approx 16^\circ$ and is hence comparable to the angle estimated from FIB treatment (see inset Fig. 1.4(a)). To use the presented antenna design in the FDTD software a script has been written that allows to implement WGM antennas with variable parameters via polygon meshes. By looking at the groove milled with FIB it might also be appropriate to model the cross-section profile with a Lorentzian or Gaussian peak function like in the early works about CPPs [227]. However, since other studies use the same approach as depicted in Fig. 1.4(d) (e.g. [216]) and since most of the FDTD simulations presented here have been done before the experiments, the modelling of alternative groove profiles should be addressed in future work.

1.2.2 Resonant near-field distributions

This section is concerned with the electric near-field distribution of the $m = 0$ - WGM antenna mode (labelled 'm_0-mode' during the rest of this chapter) in order to qualitatively asses the interaction of the LSP with a spatially extended SPP mode.

Electric near-fields are retrieved from FDTD simulations and the corresponding setup is depicted in Fig 1.5(a). The WGM antenna is modelled according to the parameters given in Fig.1.4(d). A refined mesh with a resolution of 2 nm in all directions encases the structure. Note that a further refined mesh is avoided since the antennas, as well as the refined meshes, will be incorporated in larger cavity structures which then utilise nearly the maximum amount of computer RAM (32 GB). The overall simulation volume in the present case assures that there is

no direct interaction of the antenna near-fields with the perfectly matched layer (PML) boundaries. Using symmetric boundary conditions in x- and y- direction reduces the effective simulation volume by a factor of 4. An electric dipole serves as the source of electromagnetic fields and it is buried inside the Au substrate and positioned in the lateral centre of the antenna mesa. This configuration assures that the WGM antenna is predominantly excited when it is incorporated in the cavities. The dipole inside the antenna therefore depicts the initial deflection of only one pendulum as sketched in Fig. 1.1(a). Note that it is avoided to position the dipole close to enhanced fields near interfaces to prohibit self-interaction.

The electric near-field of the axial antenna cross-section is shown in Fig. 1.5(c) (x-z-plane) while the near-field of the lateral cross-section (x-y-plane), 10 nm below the gold surface, is shown in Fig. 1.5(d). Arrows represent 2D-projections of the electric field vector $\mathbf{E} = (E_x, E_y, E_z)^{\mathrm{T}}$ onto the axial and lateral plane, i.e. $\mathbf{E}_{x,z} = (E_x, E_z)^{\mathrm{T}}$ and $\mathbf{E}_{x,y} = (E_x, E_y)^{\mathrm{T}}$, respectively. The underlying contour plot represents the electric field amplitude within the respective plane and is hence directly related to the arrow length. Note that the arrows as well as the contour plots are scaled by the decimal logarithm. This accounts for the large spread in field strength that arises by a simultaneous comparison of electric fields at sharp metallic structures in vacuum to the field inside metals.

The bright spot featuring maximum field values inside the antenna mesa is an imprint of the electric dipole source (Fig. 1.5(c)). Its dipole moment points perpendicular to the substrate which can be directly seen by the nearby field vectors that resemble dipolar flux lines. The dipole moment of the source mimics the consequence of the aforementioned excitation geometry of an impinging electron beam and it is hence expected to predominantly excite the m_0-mode. This is verified by observing the frequency-resolved and squared response amplitude 10 nm above the mesa centre (Fig. 1.5(b), black circles): The shape of the spectral intensity reveals a pronounced peak while the phase response (black-dashed line) is typical for a harmonic oscillator. The presented near-field distributions in Fig. 1.5(c) and (d) correspond to the resonance frequency of 375 THz (800 nm).

Since the WGM antenna is resonantly driven by the centrally-positioned dipole source its characteristic field distribution is imprinted onto the entire antenna structure: The near-field vectors inside the mesa point downwards according to the source field and then they are oriented around the groove bottom in the fashion

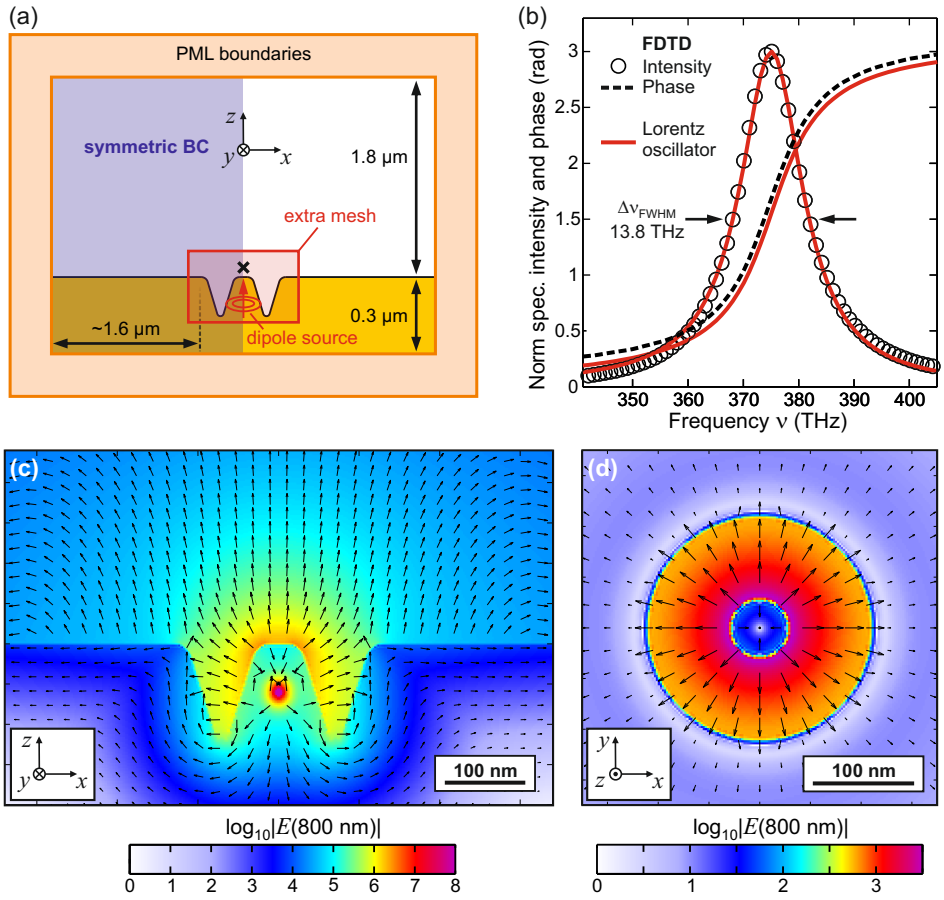

Fig. 1.5: Spectral response and near-field distribution of the $m = 0$ mode of WGM nano-antennas. (a) Sketched FDTD setup: The WGM antenna is modelled by a polygon mesh and the geometric parameters are identical to those shown in Fig. 1.4. An extra mesh (300 nm $\times$ 300 nm $\times$ 138 nm, 2 nm resolution) encases the antenna structure while the overall accuracy of the graded mesh is set to 22 sampling points for the centre wavelength in the respective material. Symmetric boundary conditions are used in x- and y-direction so that the simulation volume is reduced by a factor of 4. The electric dipole source is located 58 nm below the Au-vacuum interface and gold's dielectric function is modelled according to [155] (see Section A.1). The black cross marks the position of the retrieved spectral information (10 nm above the interface). (b) Near-field spectrum (black circles) and phase (black-dashed line, shifted by $+\pi$) as retrieved from FDTD simulations. A Lorentzian oscillator model (red lines, respectively) was fitted to the simulation data (see main text). (c) and (d) Near-field distribution at 375 THz (800 nm): The arrows represent only in-plane field components, i.e. (E_x,E_z) and (E_x,E_y), respectively. The underlying contour plot represents the arrow length. Data for (d) is related to a monitor located 10 nm below the interface, inside the Au substrate.

of a lobe. In contrast to a pure point-like dipole the machining direction of the field vectors changes across the antenna groove due to the induced surface charges of the extended structure. However, the rotational symmetry of the dipolar pattern is maintained when observing the electric field vectors in the plane that has its surface normal parallel to the dipole moment (x-y-plane, see Fig. 1.5(d)). The radial symmetry in this plane guarantees that electromagnetic fields injected into the proposed circular cavity, i.e. SPPs, are refocused in phase at the WGM antenna due to reflection at the cavity walls.

The SPP injection is clearly visible outside the WGM antenna at the Au-vacuum interface: Electric field vectors point out of the surface into the vacuum half-space at the outer groove edges and are successively rotated to point towards the interface after some hundred nanometres. The corresponding field vectors inside the metal substrate feature a similar behaviour by pointing in the opposite z-direction. This field distribution resembles the hybrid electromagnetic and conduction electron excitations that are bound to the flat metallic surface. Hence SPP injection appears to be an appreciable loss channel of the antenna which is more quantitatively assessed below.

Besides the electric field orientation of the m_0-mode also the corresponding field strength distribution is of importance: The electromagnetic energy is mainly concentrated at the flat mesa top of the WGM antenna. This is in general an unusual behaviour since the WGM antenna resonances are linked to CPPs which are confined close to the antenna groove and are described by the radial mode number $n \geq 1$ (see Fig. 1.4(c), upper right inset). The field intensity at the upper edges is usually linked to the evanescent part of the fundamental CPP mode [122]. Esteban Moreno and co-workers could show that the electric field is more and more expelled from the groove with decreasing groove depth [216]. In this case the wave vector k gets smaller and the CPP is less confined and its dispersion line crosses that of a so-called wedge plasmon polariton (WPP). These WPPs propagate along the upper edge of both groove sides in the same way as the CPP propagates inside the channel [324, 217]. In a more shallow groove the CPP dispersion line would finally cross the common SPP dispersion for a flat surface and the delocalised plasmon is radiated away as an SPP [216]. Although the m_0-mode does not exhibit features of propagation the argumentation also holds in this case since the (0,1)-mode usually has concentrated fields near the groove bottom

(see [305], centre of Fig. 3(d)) whereas the present geometry leads to concentrated fields at the upper mesa edges.

Having the electromagnetic energy confined close to the substrate surface is beneficial for two reasons: First, it has been shown that WPPs exhibit longer propagation lengths than CPPs [217]. Extended decay times might also hold for the m_0-mode in Fig. 1.5 since Ohmic losses are reduced by less concentrated fields. Second, the main part of the electromagnetic energy of the resonant mode is not buried inside the groove where an overlap with propagating SPPs can hardly be achieved. In contrast to that the present geometry favours the interaction with SPPs by sharing the same electron gas as well as a common mode volume.

1.2.3 Q-factor of the m_0-mode and buried dipole sources

In this section the quality factor (Q-factor) of the m_0-mode is retrieved from the same FDTD simulations that have already been used in the previous section. This is done for several reasons: On the one hand assigning Q-factors allows to quantitatively compare the m_0-mode of the WGM antenna to other nano-antennas and on the other hand it will be shown that placing a dipole source inside the WGM antenna does not alter the temporal dynamics of the resonant system. Additionally, an oscillator model is applied to describe plasmonic resonances.

The Q-factor is a dimensionless parameter, used in resonator physics, that compares the stored energy of a resonator to the energy loss per cycle ([260], Chapter 10.1):

$$Q = 2\pi \frac{\text{stored energy}}{\text{energy loss per cycle}}. \tag{1.2}$$

In the case of surface plasmon resonances the parameter Q comprises radiative decay as well as non-radiative processes like the electron-hole pair generation by plasmon induced intra- and interband excitations [278]. The Q-factor of optical resonators is also often written as the ratio of the resonance frequency ν_0 to the homogeneous linewidth $\Delta\nu$ ([260, 108]):

$$Q = \frac{\nu_0}{\Delta\nu}. \tag{1.3}$$

The formulation in (1.3) becomes equivalent to (1.2) for $Q > 1$ since in this case the squared response amplitude of a harmonic oscillator can be described by a simple Lorentzian peak function with a full-width at half the peak value: $\Delta\nu = \Delta\nu_{\mathrm{FWHM}}$. The energy of the system then decays to e^{-1} of its initial value after a time $\tau = (2\pi \cdot \Delta\nu_{\mathrm{FWHM}})^{-1}$. In the case of a harmonic oscillator this decay time is expressed as $\tau = (2\gamma)^{-1}$, where γ^{-1} is the time, i.e. the inverse decay constant, in which the electric field amplitude decays to e^{-1} of its initial value. The factor 2 accounts for the fact that the electromagnetic energy is proportional to the field intensity, i.e. the absolute square of the electric field.

The Q-factor of the WGM antenna is now retrieved from the spectrally resolved near-field intensity shown in Fig. 1.5(b). The related data stems from a position 10 nm above the mesa centre (black cross in Fig. 1.5(a)). Due to this choice it is sufficient to evaluate the complex E_z-component since the electric near-field, which contains the relevant spectral information about the resonance, can be almost completely projected onto the z-axis. The spectral intensity ($|E_z|^2$, black circles in Fig. 1.5(c), normalised to 3) clearly shows a resonant peak structure without any additional background. Accordingly, the spectral phase (black dashed line in Fig. 1.5(c)) exhibits the typical sigmoidal shape running from 0 to π across the resonance. Please note that the original phase data from the FDTD simulation file runs from 0 to $-\pi$ and has been multiplied with a factor -1 to agree with the conventional definition that a harmonic oscillator lags behind the driving force by a phase of $\pi/2$ on resonance. The conjugated phase evolution in the simulation is related to the phase jump of the electric field at the Au-vacuum interface. This phase jump occurs because positive surface charges accumulate at the mesa top so that the E_z-component points into opposite directions in the respective material.

The spectral information in Fig. 1.5(b) suggests to formally treat the problem as a harmonic oscillator. In the electrodynamics of dielectrica an applied source field deflects the electrons bound to an atom and the driven oscillator is described in the so-called *Lorentz-oscillator* model ([260], Chapter 5.5C). This concept also applies to plasmonic resonances in which deflected electrons in nano-antennas experience a restoring force due to excess charges at nearby interfaces [34]. Instead of formulating the problem in terms of deflected electric charges [193] the ordinary differential equation is written in terms of near-fields generated by these surface charges [5]:

$$\frac{d^2}{dt^2}E_{loc}(t) + 2\gamma\frac{d}{dt}E_{loc}(t) + \omega_0^2 E_{loc}(t) = g \cdot E_L(t). \tag{1.4}$$

In this equation $E_{loc}(t)$ is the local electric field which is the convolution of the response function $R(t)$ with the driving laser field $E_L(t)$, i.e. $E_{loc}(t) = R(t) \circ E_L(t)$, according to Merschdorf and co-workers [210]. The other parameters are the decay constant γ (e^{-1} decay of the field amplitude) in units of s^{-1}, the resonance frequency ω_0 in units of $rad \cdot s^{-1}$ and the constant g in units of $rad^2 \cdot s^{-2}$ which determines the coupling strength of the external laser source to the plasmonic system. To model the FDTD simulation data in Fig. 1.5(b) equation (1.4) is converted to the frequency domain by assuming that only linear processes occur so that $E_{loc}(t) = E_{loc}e^{-i\omega t}$ and $E_L(t) = E_L e^{-i\omega t}$. Inserting these test solutions in (1.4) is formally equivalent to apply the Fourier transformation in equation (A.7) to the left and right side of equation (1.4).

At this point it has to be noted that the fast Fourier transformation (FFT) in MATLAB uses the opposite sign convention in contrast to the definition in (A.7). The only consequence of this difference is that the electric field with a phase term ($-i\omega t$) evolves towards negative (earlier) times instead of positive (later) times in MATLAB. To be consistent with common notation subsequent analytical approaches and figures use the phase term and phase depiction according to the aforementioned Fourier transformation. Equation (1.4) reads in frequency-domain:

$$-\omega^2 E_{loc}(\omega) - 2\gamma i\omega E_{loc}(\omega) + \omega_0^2 E_{loc}(\omega) = g \cdot E_L(\omega). \tag{1.5}$$

Solving for the local electric field yields:

$$E_{loc}(\omega) = \frac{1}{-2\gamma i\omega + \omega_0^2 - \omega^2} g \cdot E_L(\omega). \tag{1.6}$$

Since the FDTD software provides the spectral information in terms of an impulsive response (δ-pulse excitation) the laser spectrum reduces to $E_L(\omega) = 1$. Likewise g is set to unity (w.l.o.g.) since only normalised data is considered. With these conditions the local electric field directly transforms into the complex local response function $R_{loc}(\omega)$:

$$E_{loc}(\omega) \underset{\left(\substack{E_L=1 \\ g=1}\right)}{=} R_{loc}(\omega) = \frac{1}{2\gamma i\omega + \omega_0^2 - \omega^2}. \tag{1.7}$$

Equation (1.7) is utilised to fit the FDTD data shown in Fig. 1.5(b) with the function $|R_{loc}(\omega)|^2$. Fitting is performed with a self-written MATLAB script that uses the non-linear data-fitting algorithm `lsqcurvefit` in which ω_0 and γ are the free parameters. The fitted spectral intensity and spectral phase are shown as red lines in Fig. 1.5(b), respectively: Indeed the near-field data is in excellent agreement with the Lorentz oscillator model. Only small deviations occur in the spectral intensity at the side wings which might be explained by a missing dielectric permittivity in the oscillator model.

The excellent agreement allows to specify the centre frequency $\omega_{0,wgm}$ as well as the decay constant γ_{wgm} of the WGM antenna:

$$\begin{aligned} \omega_{0,wgm} &= 2\pi \cdot 375.2 \text{ THz} \\ \gamma_{wgm} &= 43.4 \text{ THz} \end{aligned} \tag{1.8}$$

With these results the Q-factor Q_{wgm} of the m_0-mode is determined to be:

$$Q_{wgm} = \frac{\nu_{0,wgm}}{\Delta\nu_{FWHM}} = \frac{\pi\nu_{0,wgm}}{\gamma_{wgm}} = 27.2. \tag{1.9}$$

This is a rather high Q-factor compared to Au-nanoparticle antennas that only exhibit $Q \approx 2$ at resonance frequencies near 375 THz (800 nm) [278]. Interestingly, Vesseur and co-workers also found Q-factors of ≈ 27 for the dipolar $(1,1)$-mode of WGM antennas with large groove depths of 500 nm [304]. Comparable Q-factors of ≈ 20 have been found for Au-nano-rods in theory [34] and experiment [278]. Similar to the utilised WGM antennas the resonant behaviour of nano-rods can be explained in the model of a Fabry-Pérot resonator [53, 34]. Sönnichsen and co-workers have shown that the Q-factor of nano-rods increases with decreasing resonance frequency and they attributed this behaviour to a reduced plasmon-induced interband transition, i.e. the plasmon energy is too low to create a hole in the Au d-band and a corresponding electron in a free conduction band state [278]. The low Q-factors for Au-nanoparticles near resonance wavelengths of $\lambda = 800$ nm is explained by increased radiation damping [278]: Scattering-resonances at longer wavelengths require larger particles which in turn

feature a higher polarisability (see e.g. Chapter 4.1.1 in [34]). It was then shown by Sönnichsen that the decay time of nano-rods is close to that of a quasistatic-approximation in which only Ohmic losses (inter- and intraband transitions) are considered.

However, the results retrieved from nano-rods cannot be completely translated to WGM antennas since in both systems the constructive wave interference of the resonances is linked to retardation effects and hence these antennas should generally not be treated in the quasistatic-limit. Interestingly, Feigenbaum and Orenstein could show that Q-factors beyond the material-dependent quasistatic limit [309] can be reached by utilising the usually non-existing $m = 0$ -mode in deep sub-wavelength Fabry-Pérot resonators together with negative phase accumulation at the resonator 'mirrors' [103]. Similar effects could therefore be responsible for the rather high Q-factor of the non-propagating m_0-mode in WGM nano-antennas, but investigation of the exact mechanisms is beyond the scope of this work. Here, the assessment of the ratio of different plasmon decay channels will be further supported by far-field projections in the upcoming section.

Two important deductions can be made by concerning the retrieved Q_{wgm} together with the application of WGM antennas inside plasmonic cavities: First, high Q-factors lead to stronger local field-enhancement [309], especially in combination with sharp metallic structures. This is interesting with view to an enhanced interaction of plasmons with quantum systems inside the cavities. Second, due to the corresponding rather small bandwidth of the nano-antenna more electromagnetic energy is stored in spectral regions which are shared with the even sharper cavity mode. This should lead to an enhanced interaction of both constituents.

In the remainder of this section it is shown that the temporal electric field dynamics of the m_0-mode does not crucially depend on the location of the dipole source, even when the source is located inside a lossy and dispersive material. To do this, the Q-factor of the m_0-mode is retrieved in time-domain for two source positions: inside the WGM antenna, like in the previously shown FDTD simulations, and 10 nm above the mesa centre at the position of the black cross in Fig. 1.5(a). The latter configuration is close to the experimental excitation geometry of cathodoluminescence [261] in which a focused electron beam at normal incidence excites an oscillating surface-dipole in the mesa centre by means of induced image charges. However, one should be aware of the fact that a dipole source in FDTD

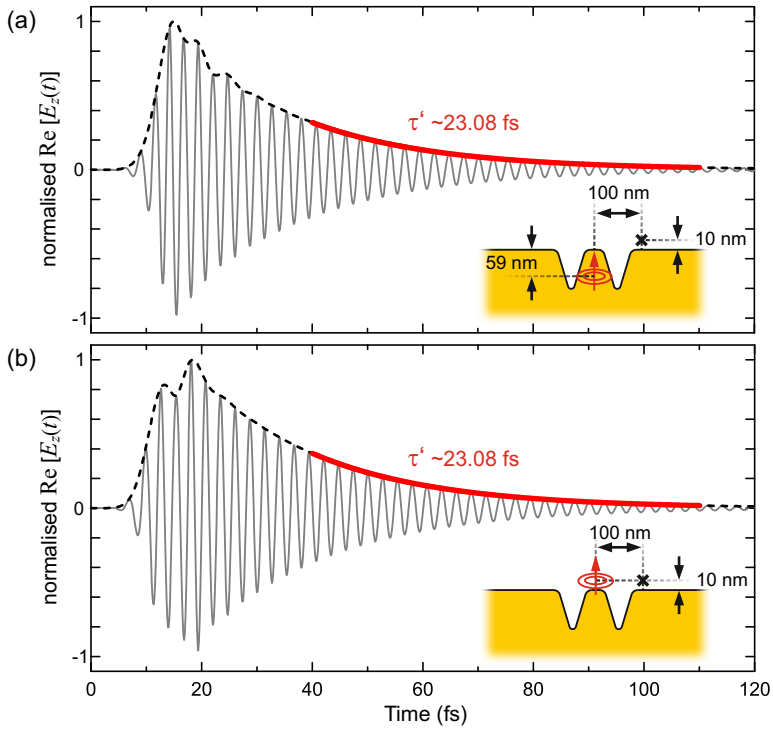

Fig. 1.6: Q-factors of the m_0-mode of WGM antennas retrieved in time-domain. (a) Temporal evolution of $E_z(t)$ (grey solid line) at the position marked by the black cross in the lower right inset. The dipole source is buried 59 nm inside the Au substrate and laterally positioned in the centre of the antenna mesa. The field envelope (black-dashed line) is fitted with an exponential decay function $\exp(-t/\tau')$ (red thick line) in which τ' is the time constant for the e^{-1}- decay of the electric field. (b) The same as in part (a) but with the dipole source 10 nm above the Au-vacuum interface.

simulations can be understood as a quantum emitter like a molecule or quantum dot (see Section 2.2.1). Their emitted power crucially depends on the inhomogeneous environment, e.g. the WGM antenna, due to self-interaction [245, 229] as will be extensively investigated in Chapter 2. Nevertheless, this excitation geometry is used since only relative electric field strength is of interest for the present question.

The recorded temporal electric fields induced by a dipole source inside and above the antenna mesa are presented in Fig. 1.6(a) and (b), respectively. The data is collected at a position 100 nm away from the antenna centre in lateral

direction and 10 nm above the Au-vacuum interface (black cross in the insets of Fig. 1.6). At this position the electric field dominantly points into z-direction (see Fig. 1.5(c)) and it is hence sufficient to evaluate $E_z(t)$. First of all it is pointed out that the temporal evolution of $E_z(t)$ is quite similar for both excitation conditions: The field envelope, retrieved by the `hilbert` command in MATLAB, rapidly increases in the first few femtoseconds as the ~ 4 fs pulse enters the simulation and then the envelope decays slowly to zero after reaching maximum field amplitude. Deviations occur only during the transient phenomenon around $t = 20$ fs but the associated modulation depths of the envelope are rather small. To retrieve the Q-factor in time-domain the slowly decaying envelope was fit using an exponential decay $\exp(-t/\tau')$ (red thick line) in which τ' is the time constant for the e^{-1}-decay of the electric field amplitude. The fit was applied in the range of $t = 40$ fs to $t = 110$ fs in order to exclude features of transient phenomena. For both excitation geometries the decay constant amounts to $\tau' = 23.08$ fs, revealing that the relevant system dynamics is matched with a precision of about 10 as. The corresponding homogeneous line width is calculated to be $\Delta\nu_{\mathrm{FWHM}} = (2\pi\cdot\tau)^{-1} = 13.79$ THz by considering that the time constant of the e^{-1}-decay of the intensity amounts to $\tau = \tau'/2 = 11.54$ fs. According to equation (1.3) and $\nu_{0,wgm} = 375$ THz the Q-factor retrieved in time-domain amounts to $Q_{wgm,t} = 27.2$ which is in perfect agreement with (1.9). This result leads to the conclusion that the dipole source can be incorporated into the lossy and dispersive material of the WGM antenna while still maintaining the important plasmonic dynamics. However, great care must be taken whenever absolute power values or exact field enhancement values are retrieved.

1.2.4 Far-field properties of the m_0-mode and SPP injection efficiency

In this section the efficiency of plasmon excitation as a decay channel of the m_0-mode will be further investigated by far-field projections. The amount of energy radiated by a dipole source to the far-field allows to assess the energy that is injected into localised and propagating surface plasmons in a complementary fashion. Furthermore, the geometrical characteristics of the emitted radiation

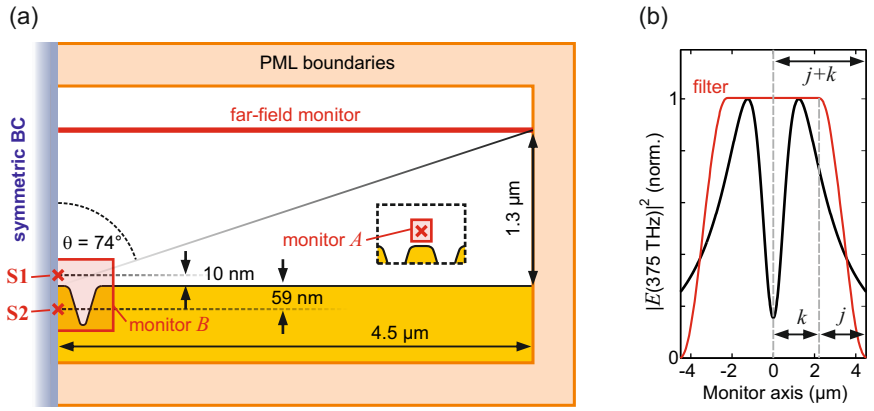

Fig. 1.7: Sketched FDTD setup for far-field projections. (a) Far-field projections are obtained with a built-in function of the frequency-domain field monitor located 1.3 μm above the Au-vacuum interface. In combination with a lateral width of the simulation volume of 9 μm this enables projections featuring inclination angles of $\theta = 70°$ up to $\theta = 74°$. Two different dipole source positions are considered: above ($S1$) and below ($S2$) the interface, in the lateral centre of the WGM antenna. The monitor boxes A and B (8 nm $\times$ 8 nm $\times$ 8 nm and 300 nm $\times$ 300 nm $\times$ 300 nm, respectively) measure the transmitted radiation. Together with the measured transmission of the far-field monitor the efficiency of SPP injection is assessed. (b) A built-in function allows to smoothly truncate the data (black line) for far-field projections at the far-field monitor edges. The parameter j can vary between 0 and 1 whereupon $j+k \stackrel{!}{=} 1$. The presented 1D electric field intensity is linked to a lateral cut through the simulation centre.

allows to find the optimum excitation geometry for an external light source like a laser. It will be shown that the experimental setup in the working group of Martin Aeschlimann (TU Kaiserslautern) nicely fits to the theoretical considerations. At the end of the section concrete scattering and absorption cross sections for far-field plane wave excitation will be given.

The FDTD setup for far-field projections is depicted in Fig. 1.7(a). It is very similar to the setup already presented in Fig. 1.5(a), only the lateral simulation size is extended to 9 μm in x- and y-direction. This extension guarantees, from a geometrical point of view, that radiation emitted under an inclination angle of $\theta = 74°$ can be detected by the far-field monitor which laterally spans across the entire FDTD simulation. The distance of this monitor to the material interface was set to 1.3 μm to ensure that the near-field of plasmonic excitations has sufficiently decayed at the monitor position. A built-in function of the LUMERICAL software is then used to perform far-field projections based on radiated electric fields. Before

the projection procedure is applied the recorded data can be smoothed with a flat-top filter as shown in Fig. 1.7(b) (red line). By setting the parameter $j = 0$ the unfiltered data is used for the projection which leads to diffraction effects when the electric field is appreciably strong at the monitor edge. In this case it acts like an aperture. Here, the recorded electric field intensity $|\mathbf{E}(x, y = 0)|^2$ at 375 THz (800 nm) along the centreline of the monitor is partially truncated, but it has already decayed to less than e^{-1} of the peak value and the main features are captured (black line in Fig. 1.7(a)). Since the problem exhibits radial symmetry and since the monitor is of quadratic shape a truncation along the diagonal bisecting line has a minor effect.

Like in the investigation of Q-factors two excitation geometries are considered: an electric dipole source above (S1) and below (S2) the mesa centre (see Fig. 1.7(a)). Retrieved angular far-field distributions of electric field intensity at the resonance frequency of 375 THz (800 nm) are shown in Fig. 1.8(a) and (b). The far-field radiation is projected onto a hemisphere in the vacuum half-space so that the azimuthal angle ϕ runs from 0° to 360° and the inclination angle θ from 0° (the surface normal) to 90° (parallel to interface). The unfiltered angular distribution of the m_0-mode, excited by an electric dipole 10 nm above the antenna ($S1$, $j = 0.0$), shows zero intensity at normal incidence ($\theta = 0°$) and is hence hardly addressable by standard far-field illumination. Most of the radiated energy is found in a ring-like structure around inclination angles of $\theta = 60°$ with a spread of 15°. The radiation pattern exhibits a 4-fold rotational symmetry instead of the expected radial symmetry of the problem. This 4-fold character emerges from the enhanced intensity along the diagonal directions of the x-y-plane ($\phi = 45°, 135°, 225°$ and 315°) and can be ascribed to the cuboid shape of the simulation volume: As described above more energy can be collected along the diagonals of the monitor since the electric field data is not truncated as early as along the x- or y-direction. This also allows for detecting the emitted radiation at larger θ-angles more properly. The overall angular distribution pattern is hence a combination of radiation emitted with circular symmetry in a distinct direction ($\theta \approx 60°$) and the sinc-like interference pattern of a rectangular mask. Utilizing the built-in filter function with $j = 0.1$ (Fig. 1.8(a)) removes for the most part the imprint of a diffraction pattern and hence the radial symmetry is clearly visible. However, it should also be noted that the filter also limits the detection, i.e. the

amplitude, at large θ-angles. Compared to $j = 0$ the emission direction is now located at lower inclination angles ($\theta \approx 55°$). However, this deviation is rather small. By considering the likewise small deviations in amplitude and θ for different azimuthal angles ϕ in the case $j = 0$ and the geometrical limitation $\theta = 74°$, it can be deduced that most of the radiated energy is properly detected by the far-field monitor.

The angular distributions of far-field radiation of the m_0-mode excited by an electric dipole source located inside the WGM antenna (S2 configuration) is shown in Fig. 1.8(b). No deviations are observable in the patterns retrieved with ($j = 0.0$) and without ($j = 0.1$) filtering compared to the excitation geometry S1. It can hence be concluded that also the spatial emission properties are not crucially altered by comparing mode excitation inside or above the antenna.

The radial symmetric emission of radiation by the m_0-mode of WGM antennas was experimentally observed by Vesseur and co-workers with cathodoluminescence [306]. They also pointed out that the angular pattern is related to the far-field radiation of a dipole located above a flat metal surface and to that of transition radiation, which occurs when an electron is impinging on a metal surface and subsequently cancels with the induced image charge (see Fig. 22 in [111]). Vesseur and co-workers used WGM antennas with a resonance wavelength of $\lambda = 750$ nm, a groove depth of 100 nm and a radius $R = 120$ nm . This configuration lead to radial symmetric emission at an inclination angle $\theta = 45°$. In contrast to that the chosen antenna geometry in this thesis ($\lambda = 800$ nm, $R = 70$ nm and $d = 118$ nm) suggests a maximum emission intensity at larger inclination angles $\theta \approx 60° - 70°$ (see Fig. 1.8 for $j = 0.0$). Such emission angles perfectly fit to the experimental setup that will be introduced in Section 1.5.4: A Ti:sapphire laser hits the sample in the photoelectron emission microscope at grazing incidence, more precisely at $\theta \approx 65°$. Using p-polarised light provides oscillating electric fields with a major field component perpendicular to the substrate which matches the m_0-mode character.

Before commenting on expected absorption and scattering cross-sections related to the experimental excitation geometry the far-field monitor is utilised to asses the different decay channels in the system by using the S1 configuration. In order to do this three quantities are introduced: The transmission T_{ff} of radiation through the far-field monitor, the transmission T_B through the monitor box B surrounding

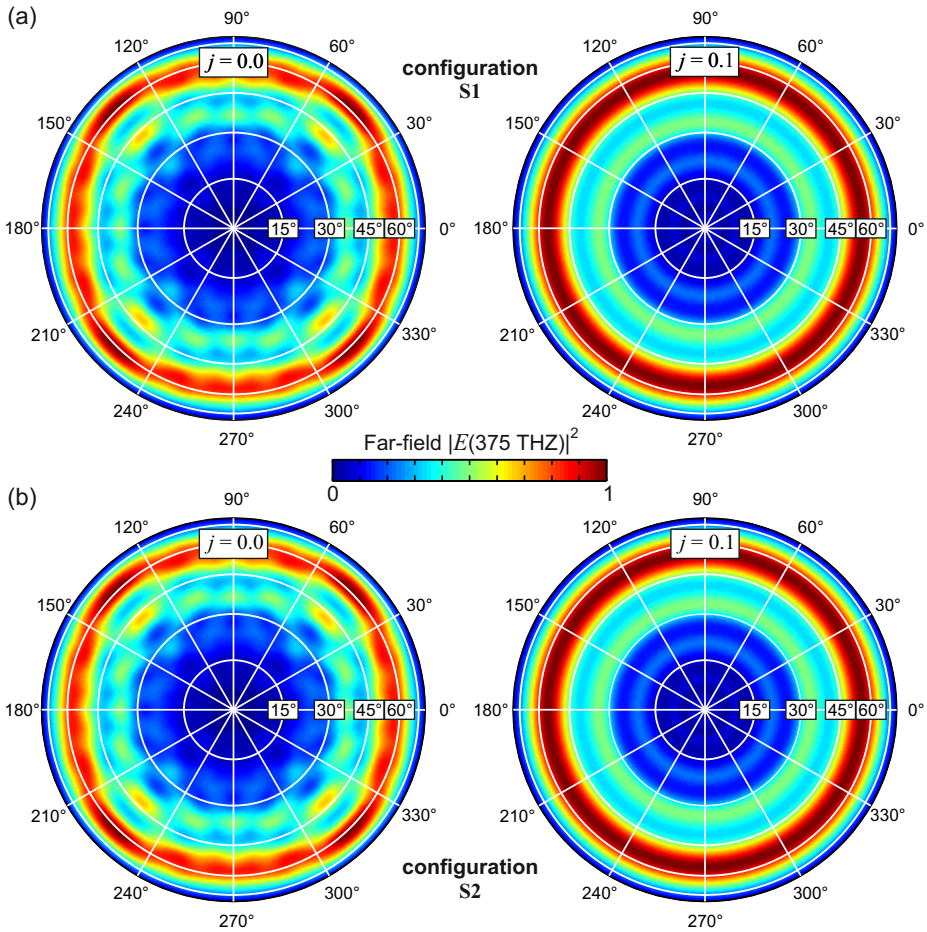

Fig. 1.8: Far-field projection of the electric field intensity at 375 THz of the m_0 antenna mode for an electric dipole source above (a) and below (b) the Au-vacuum interface (see the configurations $S1$ and $S2$ in Fig. 1.7(a), respectively) and for different filter values j. The azimuthal angle ϕ, running from 0° to 360°, is defined in a plane parallel to the substrate, while the inclination angle θ, running from 0° to 90°, is plotted on the radial axis of the polar plot. All data is normalised to respective maxima.

the WGM antenna structure and the transmission T_A through the monitor box surrounding the dipole source (see Fig. 1.7(a)). The dimensionless transmission is calculated by a built-in function that relates the power transmitted through the respective monitor structure to the power that is emitted by an electric dipole in vacuum. The results are presented in Fig. 1.9: The power injected by the dipole

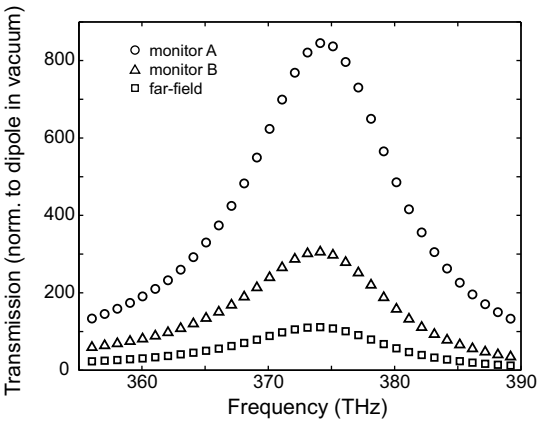

Fig. 1.9: Assessing SPP injection efficiency by power transmission: The figure displays the transmission T_A of radiation through monitor box A surrounding the dipole source, T_B through monitor box B encasing the entire WGM structure and T_{ff} through the 2D far-field monitor (see Fig. 1.7(a) for details). The transmission is the ratio of electromagnetic power passing the monitors normalised to the power emitted by an electric dipole source in vacuum.

source into the simulation serves as the reference and the related transmission is $T_A = 845$ at $\nu = 375$ THz. This value is the *Purcell enhancement* of a quantum emitter which will be extensively discussed in Chapter 2.2. Here, it serves just as a reference. The transmission related to the WGM antenna amounts to $T_B = 305$ and it can hence be deduced that approximately 64% $(1 - T_B/T_A)$ of emitted power remains in the vicinity of the antenna as a localised surface plasmon polariton which decays mainly by intraband electron-hole generation. The transmission trough the far field monitor amounts to $T_{ff} = 111$. Hence, about 87% $(1 - T_{ff}/T_A)$ of emitted power are injected to propagating or localised surface plasmons that will be absorbed by the Au substrate instead of being radiated to the far-field. More precisely, besides the 63% of power transferred to the LSP the amount of energy launched into SPPs amounts to 23% $(T_B - T_{ff})/T_A$ of the total radiated dipole power. Especially the latter ratio shows quantitatively that the m_0-mode exhibits a non-negligible interaction with propagating surface plasmons, as already inferred from the near-field distribution in Fig. 1.5(c). It is also interesting to note that the ratio of energy radiated by the WGM antenna (T_B) to the energy lost to the far-field (T_{ff}) is the same for different excitation geometries S1 and S2: In both cases $1/3$ (T_{ff}/T_B) of radiated energy is lost to the far-field and 2/3 of radiated energy are hence injected to SPPs. This confirms once more that the dipole source inside the WGM antenna is a proper excitation geometry to initiate the evolution of the combined system in later sections. Finally, it should be noted that the reported values have to be treated with caution since the recorded data of the far-field

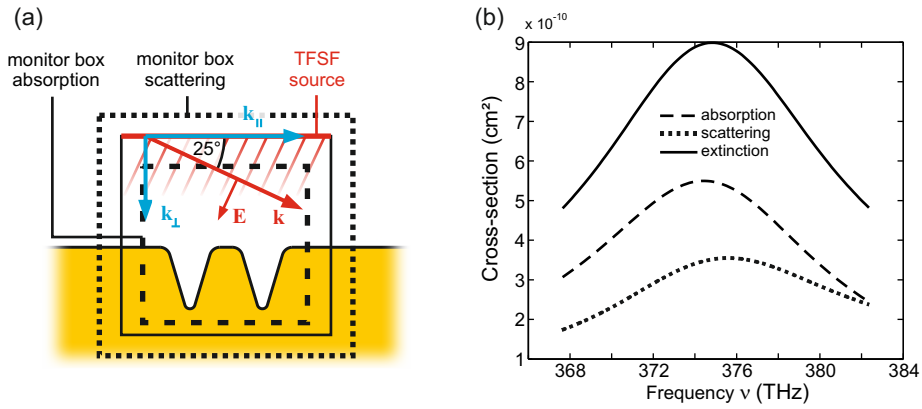

Fig. 1.10: Scattering- and absorption cross-sections of the m_0-mode. (a) FDTD setup: The WGM antenna is excited by a total-field scattered-field (TFSF) source that injects a plane wave at an inclination angle of $\theta = 65°$ only inside the defined volume of the TFSF box. The corresponding wave vector **k** can be decomposed into a component parallel to the red injection plane ($\mathbf{k}_\parallel$) and perpendicular to the injection plane ($\mathbf{k}_\perp$). To match the field phase at the source boundaries, $\mathbf{k}_\parallel$ is calculated for the central pulse frequency and is then fixed for all other frequencies ν. Hence the actual injection angle will change as a function of frequency. The transmission box monitor inside the TFSF source (black-dashed lines, 290 nm $\times$ 290 nm $\times$ 225 nm) is used for calculating the absorption cross-section while the monitor outside the TFSF source (black-dotted lines, 400 nm $\times$ 400 nm $\times$ 500 nm) is used for retrieving the scattering cross-section. (b) Cross-sections are retrieved by the operation $\texttt{transmission}(\nu)\cdot\texttt{sourcepower}(\nu)\cdot\texttt{sourceintensity}^{-1}(\nu)\cdot\cos(65°)$. Since `sourceintensity` is normalised to $\theta = 0°$ the trigonometric function is required as a correction term for the angular injection.

monitor in Fig. 1.7(b) implies an underestimation of power radiated to the far-field due to an insufficient monitor size. More computer resources are needed to model this problem properly. However, even if the power radiated to the far-field doubles ($2T_{ff}$) $1/3$ of the overall radiated power is ascribed to propagating SPPs.

The last far-field property that is presented is the accessibility of the m_0 - mode by an external light source, e.g. a laser. It was already shown in the far-field patterns in Fig. 1.8(a) and (c) that the angular distribution of emitted antenna radiation peaks at an inclination angle θ around 60°. Here, the scattering and absorption cross-sections are determined for an incoming plane wave at an inclination angle of $\theta = 65°$. This particular angle is chosen because it matches the inclination angle of the laser setup that is available for PEEM experiments in Kaiserslautern (see Section 1.5.4).

The reduced sketch of the FDTD simulation setup is shown in Fig. 1.10. It is similar to the setup presented in Fig. 1.5(a) but here the symmetric boundary condition in x-direction is omitted and the dipole source is replaced by a total-field scattered-field source which injects a plane wave only inside the defined volume (black solid rectangle) and subtracts it outside the source box. This allows to record the net transmission through the inner and outer transmission box monitor (black-dashed rectangle and black-dotted rectangle, respectively). Since the injected plane wave cannot penetrate the outer box only scattered fields are recorded, while the inner box gives a measure for the ratio of incoming and outgoing radiation, i.e. the absorption. Both cross-sections are calculated with the built-in commands $\texttt{transmission}(\nu)\cdot\texttt{sourcepower}(\nu)\cdot\texttt{sourceintensity}^{-1}(\nu)\cdot\cos(65^\circ)$. A multiplication with $\texttt{sourcepower}(\nu)$ withdraws the usual power normalisation and the integrated power is instead normalised to the source intensity, giving the cross-section in m^2. The factor $\cos(65^\circ)$ accounts for the angular injection since in LUMERICAL FDTD the command `sourceintensity` refers to normal incidence ($\theta = 0^\circ$) and hence to the complete injection area (sketched as a red line in Fig. 1.10(a)). The incoming plane wave is p-polarised to match the electric field of the m_0-mode that points out of the antenna mesa.

Results are shown in Fig. 1.10(b). The absorption as well as the scattering cross-section (black-dashed and black-dotted line, respectively) clearly peak at $\nu \approx 375$ THz, therefore confirming the excitation of the resonant mode with a plane wave light source injecting radiation from a well defined direction ($\theta = 65^\circ$, $\phi = 180^\circ$). The absorption cross-section σ_a turns out to be larger than the scattering cross-section σ_s. This behaviour is explained by the previous observation that most of the emitted power of a dipole source is injected into a LSP (see Fig. 1.9) that will mainly decay by intraband absorption. On resonance ($\nu = 375$ THz) the absorption cross-section amounts to $\sigma_a = 5.5 \times 10^{-10}$ cm^2. Taking into account the circular structure size of the WGM antenna of 6.2×10^{-10} cm^2 (diameter $d \approx 280$ nm) leads to the statement that nearly every photon that hits the WGM structure under the specific angle will be absorbed. With view to the even higher extinction cross-section $\sigma_e = \sigma_s + \sigma_a$ of about 9.0×10^{-10} cm^2 the WGM antenna geometry presented here seems to be perfectly suited for addressing the overall system in the experiments (see Section 1.5).

It has to be noted that only the cross-section value at the centre frequency

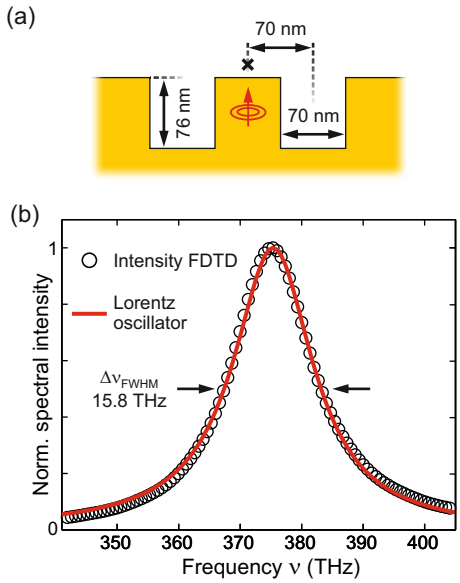

Fig. 1.11: Cylindrical WGM antenna for excitation of the m_0-mode at $\nu = 375$ THz. (a) Alternative and simplified geometry for a WGM antenna: The groove is modelled by a cylinder barrel (vacuum) while the antenna mesa is just a cylindrical protrusion. The black cross marks the position, 10 nm above the interface, at which spectral information is recorded. The dipole source is located 38 nm below the interface. (b) Near-field spectrum (black circles) retrieved from FDTD simulations at the position of the black cross in (a). A Lorentzian oscillator fit (red solid line) was applied in the same way as in Fig. 1.5(b).

$\nu_0 = 375$ THz is exact with respect to its absolute value and the defined inclination angle θ. All other frequencies are injected at larger ($\nu < \nu_0$, $|\mathbf{k}| < |\mathbf{k}_0|$) and smaller angles ($\nu > \nu_0$, $|\mathbf{k}| > |\mathbf{k}_0|$) because the FDTD code keeps the parallel component $\mathbf{k}_{\|}$ (see Fig. 1.10(a)) of the wave vector $\mathbf{k}$ constant for all frequencies. This procedure is necessary since the field is injected similar to periodic boundary conditions and the phases at opposing TFSF boundaries need to be matched. However, the deviations of $\pm 5°$ are rather small since a small-band laser pulse with a temporal duration of 30 fs was used in the simulation. It has also been verified that no severe numerical errors occur by disabling the WGM structure in a subsequent simulation and by checking that electric fields do not leak out of the TFSF volume.

Alternative WGM antenna geometry for the m_0-mode

At the end of this section about the m_0-mode of WGM antennas a simplified geometrical groove structure is introduced in short. As depicted in Fig. 1.11(a) the antenna groove can be modelled by a standard cylinder barrel object in LUMERICAL FDTD instead of the more complicated V-shaped grooves with rounded

edges. The functionality is demonstrated by the near-field spectrum that is shown by black circles in Fig. 1.11(b): A resonant mode is clearly visible around $\nu = 375$ THz. Like in the case of V-groove antennas the FDTD data is fitted with a Lorentzian oscillator model (red-line). The corresponding decay constant amounts to $\gamma = 49.5$ THz which leads to the associated e^{-1} life-time of the field intensity of $\tau = 10.1$ fs. Translating these values into the FWHM of a Lorentzian peak function, i.e. $\Delta\nu_{FWHM} = 15.8$ THz, gives a quality factor of $Q = 23.8$. This value is only 12% smaller than that of WGM antennas with a V-shaped groove (see equation (1.9)) and these simple structures hence provide a good functionality. The WGM antennas with barrel-shaped grooves will be used in Chapter 2 for a more conservative estimation of energy transport between incorporated quantum emitters: The structure-induced electric field enhancement is smaller because of the broader antenna mesa.

1.3 Hybridisation of SPPs with single LSPs in circular all-plasmonic cavities

In this section the hybridisation of a m_0-mode of a single WGM antenna with a single extended surface plasmon mode inside a circular all-metallic cavity is demonstrated by FDTD simulations. First, the cavity scheme and the associated mode characteristics will be presented in Section 1.3.1. Then, the temporal evolution in the combined antenna-cavity system will be examined in Section 1.3.2. In Section 1.3.3 it will be shown that the corresponding spectral signature of the combined system can be described by a simple model of two coupled harmonic oscillators, therefore confirming the hybridisation of the single systems. Finally, near-field distributions of the new eigenmodes are presented in Section 1.3.4 and it is shown that the observed temporal dynamics can be explained by a superposition of these modes.

1.3.1 Circular plasmonic arena cavities

The cavity scheme that is utilised for the prearranged hybridisation of LSPs and SPPs is a cylindrical pit inside a metal substrate (Au), as already shown in Fig. 1.3(a).: SPP modes, injected by the incorporated WGM antenna, will be bound to the cavity floor, i.e. at the Au-vacuum interface of the pit. The circular shaped upright walls serve as cavity mirrors for the propagating SPPs and the concentric wave fronts will be refocused at the source point in the cavity centre. Using upright metallic walls for SPP reflection is a straight forward approach which is historically inspired by the random coupling of LSPs and SPPs in the work of Aeschlimann and co-workers [6]. Additionally, Sorger and co-workers demonstrated that two straight and upright standing Ag-walls of a simple Fabry-Pérot nano-cavity exhibit a reflectivity of approximately 98% [279]. An alternative approach would be to use distributed Bragg reflector mirrors to build an annular nano-resonator, also known as a bull's eye structure [139]. However, it was theoretically shown that two-dimensional straight Bragg reflector mirrors are limited to a maximum reflection of approximately 90% [232]. This value is below the above reported coefficients that can be reached by using metallic walls. Furthermore, Bragg mirrors of high reflectivity only work at a particular surface plasmon wavelength. An appreciable mode splitting in strongly coupled systems is hence not attainable. In contrast, the metallic walls used in the research presented here are expected to exhibit broadband operation in the Vis-NIR spectral region with respect to SPP reflectivity. In the following the cylindrical pits in the metal substrate, serving as plasmon cavities, will be abbreviated by the acronym CPAC (circular plasmonic arena cavity).

The first experiments of standing mode patterns confined in metallic rings on dielectric and metallic substrates were demonstrated by Babayan and co-workers in 2009 [25]. However, the height of their optical corrals stayed well below 100 nm, therefore providing a large loss channel due to scattering of SPPs and waveguide modes at the upper corner of wall structures. A similar cavity scheme as used in this research has been investigated in theory and experiment by Zhu and co-workers [335]. They also used all-metallic cylindrical open cavities with heights of up to 550 nm. It has to be noted that the thesis author was not aware of this research until all theoretical and experimental results had been obtained.

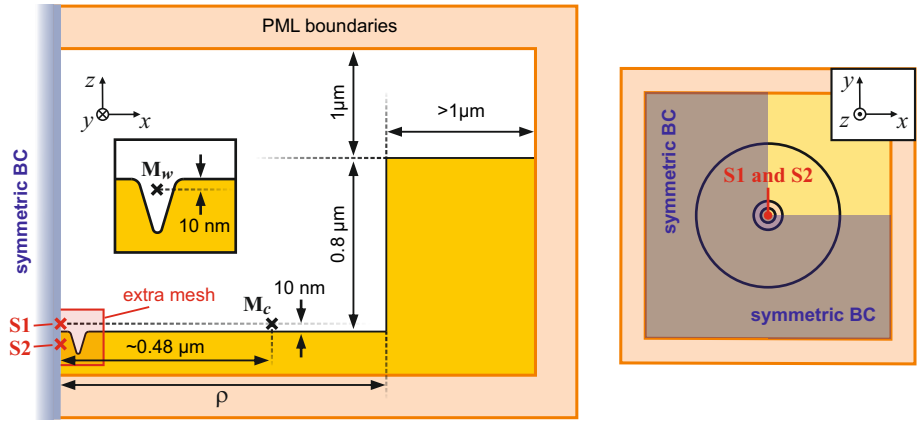

Fig. 1.12: FDTD simulation setup for WGM antennas incorporated in circular plasmonic cavities (CPACs). The cavity radius ρ is a variable that allows to distinctively select spatial modes that require the same surface plasmon energy while the CPAC has a constant height of 800 nm in all simulations. Likewise the extra mesh (300 nm $\times$ 300 nm $\times$ 138 nm, 2 nm resolution) stays constant and it is also present in simulations in which only the pure cavity is considered. In the case of pure cavity simulations the dipole source is placed 10 nm above the central antenna mesa ($S1$) while in simulations which include the nano-antenna the dipole source is located inside the mesa ($S2$) like in Fig. 1.5(a). To compare the electric field dynamics to the model of coupled oscillators in Section 1.3.3 the frequency-domain monitors M_w and M_c are used to record amplitude and phase of the response function in the vicinity of the antenna and the cavity mode, respectively. Due to the radial symmetry of the structure and dipole source, symmetric boundary conditions are used in x- and y-directions.

However, some important differences still exist: Here, gold is used in theory and experiments instead of silver and hence the surface structure and quality will not be affected by the environment on long time scales. Furthermore different fabrication processes are utilised: Here, single-crystalline and atomically flat gold microplates are used in combination with focused ion beam milling [143] (see Section 1.5.1) instead of template stripping that involves sputtering of metal layers [336]. Using single-crystalline gold microplates is closer to FDTD conditions since no enhanced scattering at grain boundaries has to be considered. Furthermore the cavity design of Zhu and co-workers is comparable to a thick cylinder barrel and hence offers more corners for unwanted scattering of incident laser light.

The fundamental plasmonic properties of circular nano-cavities, which depend on parameters like structure height and diameter, have already been studied by Zhu and co-workers [335]. Therefore only selected and specific cavity features

that are important for the hybridisation scheme, as well as corresponding FDTD simulations, are introduced and presented in the remainder of this section. The FDTD setup for subsequent investigations is sketched in Fig. 1.12. All cavities exhibit a height of 800 nm to assure proper reflection at the cavity walls since the e^{-1} penetration depth δ_{vac} of SPP intensity into the vacuum half-space at frequencies of 375 THz (800 nm) is about 610 nm according to equation (A.3) and the FDTD dispersion model of Au (see Section A.1). The cavity radius ρ is a variable that serves to select cavity modes of different order. In all cases the minimum horizontal distance of the upper wall corner to the PML boundary is kept larger than 1 μm and the vertical distance of the upper Au surface to the PML boundary is set to 1 μm according to $\delta_{vac} = 610$ nm. The WGM antenna in the centre of the cavity can be disabled to perform FDTD simulations concerning the pure CPAC and the extra mesh is of the same size as in Section 1.2. The mesh is also enabled in pure cavity simulations and hence the resonant modes of the WGM antenna and the pure CPAC are not shifted due to different meshing procedures. All FDTD simulations are allowed to use symmetric boundary conditions in x- and y-direction since the electric dipole source, oscillating in z-direction, is placed in the cavity centre (position S1 or S2).

Near-field distributions of a resonant cavity mode at approximately 375 THz (800 nm) are shown in Fig. 1.13 and the corresponding cavity radius $\rho = 662$ nm is the same as will be later used for hybridisation. The mode is labelled $(0,2)$-mode in which '0' is the azimuthal mode number and '2' is the radial mode number. The particular meaning of these mode numbers will be itemised below. Fig. 1.13(a) shows a lateral cross-section through the cavity centre ($y = 0$ plane) of the near-field excited in S1-configuration. Black arrows represent the full electric field information since E_y vanishes due to symmetry reasons. The contour plot in the background represents the absolute field strength $|\mathbf{E}|$. Both, the contour plot as well as the arrows are scaled according to the decimal logarithm in order enhance visibility due to different field strengths in vacuum and the metal substrate. The contour plot reveals three sub-wavelength regions of enhanced electric fields which are bound to the cavity floor and decay exponentially into both half-spaces. Nearly all electromagnetic energy in these regions is attributed to the E_z-component of the electric field. Here, the arrows are retrieved by taking the imaginary part of the response function $\mathbf{R}(\nu)$ as directly retrieved from FDTD simulations. This

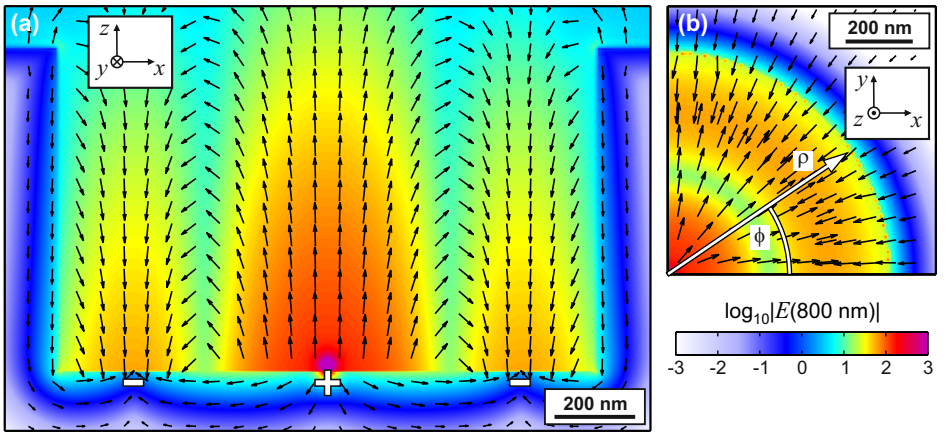

Fig. 1.13: Near-field distribution of the (0,2)-CPAC-mode at $\nu_0 = 375$ THz. (a) The black arrows represent a cross-section of the near-field (E_x,E_z) in the xz-plane ($y = 0$). Due to symmetry reasons there is no E_y-component in this plane. The contour plot in the background represents the overall field amplitude $|\mathbf{E}|$ and the plus and minus sign depict accumulated charges due to non-vanishing Gaussian pill box integrals $\int_V \nabla \mathbf{E}\, dV$ at the Au-vacuum interface. (b) Lateral cross-section through the near-field (E_x,E_y) 10 nm above the cavity floor. All arrows and the contour plots are scaled according to the decadic logarithm.

operation seems to give the appropriate phase relation of the oscillating field with respect to the maximum field amplitude. The electric field structure resembles that of a propagating surface plasmon. Associated surface charges can be revealed by integrating Gauss's law (A.12) in a small pill box at the Au-vacuum interface. The net flux through the box surface then indicates the presence of electric charges which are sketched by $+$ and $-$ signs in Fig. 1.13(a) according to the common convention that electric flux lines start at positive charges. The phase of the electric field mode in this snapshot is related to the turning point of an oscillating pendulum: All energy is stored in the separation of charges. The evanescent fields will then be reflected at the cavity walls and the charges are redistributed to cancel out and subsequently change their sign. These charge distributions will be affected in the hybridisation process as shown later in Section 1.3.4.

An excerpt of the lateral electric near-field $(E_x,E_y)^{\mathrm{T}}$ 10 nm above the cavity floor is shown in Fig. 1.13(b). The amplitude as well as the direction of the near-field distribution exhibit radial symmetry with respect to the rotation-axis that points perpendicular through the lateral centre of the cavity floor. This distribution

perfectly fits to the m_0-mode of the WGM antenna (see Fig. 1.5(c,d)) and the mode overlap is expected to appreciably support the hybridisation process.

The lateral mode structure can be decomposed by treating the electromagnetic problem in a similar fashion like radio- or microwaves confined in cylindrical metal cavities ([151], Chapter 3.7 and 3.8) as pointed out by Zhu and co-workers [335]. To retrieve the eigenmodes of the CPACs, i.e. the surface charge induced electrostatic potential Φ inside the cavity, one has to solve Laplace's equation in cylindrical coordinates. Utilising separation of variables the general solution $\Phi = R(\rho)Q(\phi)Z(z)$ can be written as a product state of the radial part $R(\rho)$, the angular part $Q(\phi)$ and the axial part $Z(z)$. The axial part is of minor interest here and it is hence ignored. The angular part $Q(\phi)$ exhibits the general form [151]:

$$Q(\phi) = A\sin(m\phi) + B\cos(m\phi), \tag{1.10}$$

in which A and B are amplitudes, m is an integer value and the angle ϕ is sketched in Fig. 1.13(b). Due to the radial symmetry of the resonant mode in Fig. 1.13(b) there is no angular contribution so that $Q(\phi) = const.$ and hence $m = 0$. The radial part $R(\rho)$ is solved according to

$$R(\phi) = CJ_m(k\rho) + DN_m(k\rho), \tag{1.11}$$

in which $J_m(k\rho)$ and $N_m(k\rho)$ are Bessel functions of the first kind and Neumann functions (Bessel functions of the second kind), respectively [151]. C and D are amplitudes that need to be determined and k can be associated with the real part of the SPP wave vector. Since the mode exhibits an anti-node in its centre at $\rho = 0$ and a finite electric field strength the diverging Neumann functions ($\rightarrow -\infty$ for $k\rho = 0$) have no contribution to the problem and hence $D = 0$. Another restriction is that Φ vanishes at the cavity wall position $\rho = a$ where a is the cavity radius. This gets clear by looking at the near-field cross-section in Fig. 1.13(a): The energy of the mode is mainly contained in the field component perpendicular to the cavity floor. This component is highly concentrated at the sketched surface charges since they serve as the source for electric fields. Moving the surface charges that are related to Φ close to the cavity wall would lead to strong electric field components parallel to metal walls. Such a field orientation is not favoured since the electric field lines tend to point perpendicular to an equipotential surface. Therefore $\Phi = 0$ at $\rho = a$ requires:

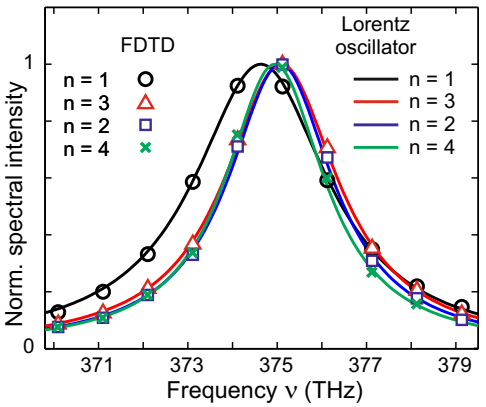

Fig. 1.14: Circular cavity modes retrieved from FDTD simulations (symbols, $|E_z(\omega)|^2$) fitted by a Lorentzian oscillator model in frequency-domain (solid lines). The modes refer to a constant azimuthal number $m = 0$ and different radial mode numbers $n =$ 1,2,3,4 which are linked to different radii ρ of 274 nm, 662 nm, 1052 nm and 1443 nm, respectively. Data for $n = 2,3,4$ is recorded with the monitor M_c (see Fig. 1.12) at the position of the first mode ring (see Fig. 1.13) while data for $n = 1$ (no mode ring) is recorded at $x = 150$ nm.

$$ka = x_{mn}. \tag{1.12}$$

Here, x_{mn} is the nth root of the Bessel function J_m and hence $\Phi \propto J_m(ka) = J_m(x_{mn}) = 0$. n is the above mentioned radial mode number which gives the number of anti-nodes in radial direction and m is the azimuthal mode number. Modes of CPACs are therefore labelled by (m,n) and the particular field distribution presented in Fig. 1.13 is referred to as $(0,2)$.

Equation (1.12) can now be utilised to find the cavity radius a for different orders n of the radial symmetric mode. Using the plasmon wavelength $\lambda_{SPP,inf} =$ 782.4 nm at a plasmon frequency of 375 THz, according to the real part of equation (A.1), as well as the first four roots of the Bessel function $x_{01} = 2.405$, $x_{02} = 5.520$ $x_{03} = 8.654$ and $x_{04} = 11.781$ (see [151], Section 3.7), gives the following CPAC radii:

$$\begin{aligned} a_{01} &= 299 \text{ nm} \\ a_{02} &= 687 \text{ nm} \\ a_{03} &= 1078 \text{ nm} \\ a_{04} &= 1467 \text{ nm} \end{aligned} \tag{1.13}$$

The retrieved radii can serve as a starting point to find the radius a_{0n}^{FDTD} that fits to a CPAC resonance frequency of 375 THz in FDTD simulations. For $n = 2,3,4$ the spectral intensity of the SPP mode is recorded with the frequency-domain

monitor M_c shown in Fig. 1.12 at $\rho = 480$ nm. This is approximately the position of the first ring anti-node for all $(0, n > 1)$-modes (see Fig. 1.13) and it is hence sufficient to evaluate the $E_z(\nu)$-component. In the case of $n = 1$ the response function is determined at $\rho = 150$ nm. A resonance at $\nu_0 \approx 375$ THz is then obtained at CPAC radii of $a_{01}^{FDTD} = 274$ nm, $a_{02}^{FDTD} = 662$ nm, $a_{03}^{FDTD} = 1052$ nm and $a_{04}^{FDTD} = 1443$ nm (see Fig. 1.14 for spectral positions). Although these values are close to the predicted radii in (1.13) there exists a systematic deviation: The radii obtained with FDTD simulations are smaller than those from analytic calculations. More precisely, the deviation is about 8% for the smallest mode volume $n = 1$ and decreases monotonously to $< 2\%$ for the largest mode volume $n = 4$. This is attributed to the fact that strongly confined modes require a smaller surface plasmon wavelengths λ_{SPP} and hence larger wave vectors k_{SPP}. As a consequence, the condition (1.12) is fulfilled for a smaller cavity radius a. In the case of the $(0,1)$-mode the calculated diameter $2 \cdot a_{0,1}$ is even smaller than the wavelength $\lambda_{SPP,inf} = 782.4$ nm ($\nu_0 = 375$ THz) of an SPP on an infinitely large surface. With increasing n the cavity floor area grows larger and λ_{SPP} gets closer to the large area limit $\lambda_{SPP,inf}$, which has been used in the analytic calculations.

The spectrally-resolved intensity of all four modes is shown in Fig. 1.14 (coloured symbols). To better analyse the closely packed data in the rather small frequency range all four modes are fitted according to the Lorentzian oscillator model introduced in equation (1.7). The analytic model (coloured lines) accurately describes the FDTD simulation data and the respective decay constants γ_{mn} are determined to be $\gamma_{01} = 11.4$ THz, $\gamma_{02} = 9.7$ THz, $\gamma_{03} = 9.0$ THz and $\gamma_{04} = 8.5$ THz. Obviously the decay rate of the CPAC mode decreases with increasing mode area. This trend can be explained by the relative part of the CPAC mode that interacts with the annular cavity wall. In the case of the smallest $(0,1)$-mode a large part of the mode volume is located in the vicinity of the cavity walls, while only a small part of the $(0,4)$-mode interacts with the metallic boundaries. The explanation is corroborated by checking that the skin depth of the modes in the cavity floor is not influenced by the presence of the metallic walls.

The e^{-1} life-time τ_{04} of the $(0,4)$-mode is calculated to be $\tau_{04} = (2 \cdot \gamma_{04})^{-1} = 59$ fs. Determining the propagation length (see equation (A.2)) and the phase velocity of an infinitely extended surface plasmon at $\nu_0 = 375$ THz by using the dispersion relation in Fig. A.1(b) gives an SPP life-time of $\tau_{SPP,inf} = 165$ fs. The interaction

of the CPAC mode with the cavity walls hence reduces the SPP life-time by a factor of three. In order to compare the retrieved decay rates to literature the Q-factors of all modes have been determined: $Q_{01} = 103$, $Q_{02} = 121$, $Q_{03} = 131$ and $Q = 139$. Obviously, these values cannot compete with dielectric toroid microcavities ($Q = 10^7$) [21] or optical microsphere resonators ($Q = 10^{10}$) [119]. Therefore the retrieved Q-factors should be compared to other all-metallic systems: Hofmann and co-workers measured a maximum Q-factor of about 36 in annular Ag-nanocavities consisting of Bragg reflector mirrors (Bull's eye structures) [139]. The rather low values, compared to the quality factors predicted here, might be explained by the aforementioned reflectivity limit of 2D Bragg reflector mirrors [232]. Zhu and co-workers found Q-factors < 25 in square-shaped Ag-pits [337], but it should be noted that these cavities exhibited a wall height of only 300 nm. Later, Zhu and co-workers measured maximum Q-factors of about 73 in 500 nm high cylindrical-shaped Ag nano-cavities [335] which are closely related to the systems presented here. However, the Ag material was sputtered in the fabrication process and hence grain boundaries exist.

1.3.2 Time-domain characteristics of the composite system

Before investigating the composite system of CPAC and WGM antenna with respect to its spectral features a numerical 'experiment' is conducted according to the introductory sketch in Fig. 1.1(a): One of the pendulums, i.e. the WGM antenna, is initially deflected and the temporal evolution of the overall system in the FDTD simulations is monitored. It can be inferred from the observed dynamics that the design of the combined cavity and nano-antenna indeed gives rise to a spring that connects the two individual pendulums. This conjecture will be corroborated in the next sections by describing the system as two coupled oscillators in frequency-domain and by decomposing the system into new and old eigenmodes which are related to specific, spatially-resolved electric near-field distributions.

The rudimentary setup of the FDTD simulation has already been depicted in Fig. 1.12. Here, the radius of the CPAC is set to $\rho = a_{02}^{FDTD} = 662$ nm and therefore

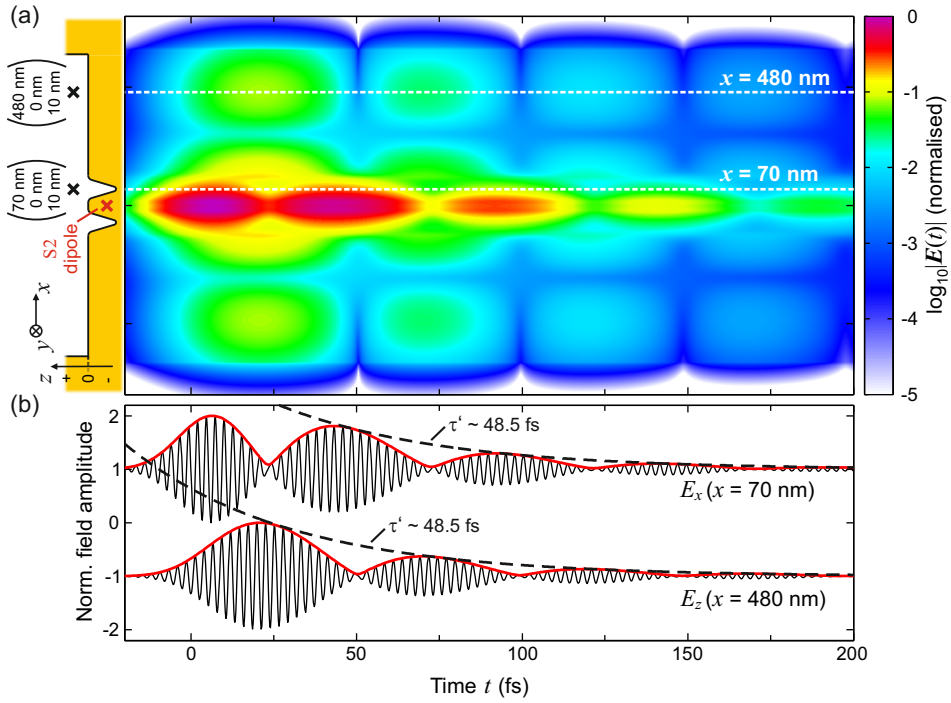

Fig. 1.15: Simulated temporal evolution of the electric field in a CPAC with an incorporated WGM antenna. The presented data is obtained by multiplying the recorded multi-dimensional response function $\mathbf{R}(\nu,x,y=0\text{ nm},z=10\text{ nm})$ with a Gaussian function $p_{gauss}(\nu)$ that represents the spectral amplitude of a coherent light pulse of 15 fs duration, centred at $\nu_0 = 375$ THz (800 nm). Applying a fast Fourier transformation to $\mathbf{R}(\nu)\cdot p_{gauss}(\nu)$ gives the local electric field $\mathbf{E}(t,x,0\text{ nm},10\text{ nm})$. An electric dipole inside the WGM antenna serves as the source of the electric field (*S2* configuration, see Fig. 1.12). The WGM antenna geometry supports the m_0-mode ($\nu_0 = 375$ THz, see Fig. 1.5) and the CPAC parameters relate to the (0,2)-mode at $\nu_0 = 375$ THz, as presented in Section 1.3.1. (a) Slowly varying envelope $|\mathbf{E}(t,x,0\text{ nm},10\text{ nm})|$ of the oscillating electric field. (b) Oscillating electric field components $E_x(t)$ and $E_z(t)$ (black solid lines) at the positions $x = 70$ nm and $x = 480$ nm, respectively, as marked by the white-dashed lines and black crosses in part (a). Red lines are the corresponding field envelopes. Black dashed lines sketch the exponential decay of the electric field evolution with manually adjusted life-times of $\tau' = 48.5$ fs. All curves for $x = 70$ nm are artificially offset by $+1$ and for $x = 480$ nm by -1.

the cavity features the $(0,2)$-mode at a resonance frequency $\nu_0 = 375$ THz. The geometrical parameters of the WGM antenna are those shown in Fig. 1.5 so that the m_0-mode can also be resonantly excited at $\nu_0 = 375$ THz. To ensure that only the pendulum of the WGM antenna is initially deflected, an electric dipole

source is placed inside the antenna mesa (S2-configuration in Fig. 1.12 and Fig. 1.15(a)). It was shown in Section 1.2.3 that this excitation condition is capable to qualitatively and quantitatively describe the relevant system dynamics. The simulation time was set to 500 fs in order to ensure that all electric fields have sufficiently decayed after system excitation.

The depiction in figures is restricted to two spatial dimensions and the temporal electric field dynamics in Fig. 1.15(a) is therefore shown on a line in x-direction along the central cross-section of the system ($y = 0$ nm), 10 nm above the cavity floor. This is sufficient to capture the relevant dynamics since the antenna mode as well as the cavity mode exhibit radial symmetry. Instead of using a simple time-domain monitor in the LUMERICAL software to record the electric field data the information is obtained by using a frequency-domain monitor and post-processing of the obtained data. This is done for two reasons: First, the recorded response function in frequency-domain can be filtered with a custom spectral profile to account for different excitation scenarios and to exclude modes that are not relevant to the problem. This will get important in the investigation of hybridisation of elliptic cavities with nano-antennas in Chapter 1.4. Second, the data can be interpolated to account for non-uniform meshing.

The post-processing procedure is executed as follows: The impulsive response function of the system $\mathbf{R}(\nu, x, y = 0\,\text{nm}, z = 10\,\text{nm})$ is obtained in the range of $\nu = 300$ THz (1000 nm) to $\nu = 500$ THz (600 nm) with 200 sampling points by using the dipole source S2 which injects a short pulse of about 4.3 fs. Then $\mathbf{R}(\nu, x)$ is zero-padded in MATLAB with respect to ν whereby the sampling point distance is left unaltered. Afterwards a linear interpolation of $\mathbf{R}(\nu, x)$ with respect to the x-axis is performed so that all data points are spaced by the minimum grid point distance of the extra mesh (2 nm). The response function $\mathbf{R}(\nu, x)$ is then multiplied with a spectral envelope of Gaussian shape $p_{gauss}(\nu)$ that represents a coherent pulse of 15 fs duration centred at $\nu_0 = 375$ THz. This gives the local electric field $\mathbf{E}(\nu, x) = \mathbf{R}(\nu, x) \cdot p_{gauss}(\nu)$ in frequency domain. A fast Fourier transformation is applied to retrieve the complex and spatially-resolved electric field data $\mathbf{E}(t, x)$ in time-domain.

The temporal evolution of the electric field envelope $|\mathbf{E}(t, x)|$ along the x-axis is shown as a contour plot in Fig. 1.15(a), in which values are scaled according to the decimal logarithm. The envelope, emphasising the relevant dynamics, was

retrieved by a Hilbert transformation. Due to the specific excitation geometry the electromagnetic energy ($\propto |\mathbf{E}(t,x)|^2$) is localised at the WGM antenna in the first few femtoseconds of the simulation. After reaching maximum electric field strength at $t \approx 6$ fs the energy near the nano-antenna diminishes. At the same time $|\mathbf{E}|$ increases appreciably inside the cavity. The amount of energy stored inside the cavity reaches a maximum around $t \approx 20$ fs while simultaneously the energy stored at the WGM antenna is significantly decreased with respect to $t \approx 6$ fs. However, after reaching this minimum, the energy stored inside the cavity seems to flow back into the WGM antenna until a local maximum of field strength is reached near $t \approx 42$ fs. This process is continuously repeated while the overall field envelope and hence the entire energy stored inside the system steadily decreases to zero. The oscillation period T_E of back and forth transfer of electromagnetic energy can be assessed by the interval of field nodes and it amounts to $T_E = 49$ fs.

The fast oscillating electric field $\mathbf{E}$(t) at the position of the WGM antenna ($x = 70$ nm) and inside the cavity ($x = 480$ nm) is shown in Fig. 1.15(b) (black solid lines, artificially offset by $+1$ and -1 for visibility). By interpreting the electric field oscillations at the specific position as the deflection of the specific pendulum the temporal beating behaviour of both time traces closely resembles the time evolution of mechanically coupled pendulums in the introductory figure Fig. 1.1(b). It is emphasised that in the mechanical scenario, as well as in the electromagnetic scenario, only one pendulum was initially deflected. It is hence inferred that incorporating a WGM nano-antenna into a circular plasmonic arena cavity indeed leads to a prearranged coupling of a single localised surface plasmon and a propagating surface plasmon.

The coupling strength can be qualitatively assessed by comparing the characteristic decay time of field amplitudes to the beating period T_E. Therefore an exponential decay function $\exp(t/\tau')$ (black-dashed lines in Fig. 1.15(b)) has been manually adjusted to the respective envelopes (red lines in Fig. 1.15(b)). In the case of the WGM antenna ($x = 70$ nm) the first anti-node has been ignored since the transient phenomenon disturbs the comparison of field amplitudes. The decay constant τ' of the electric field $\mathbf{E}(t)$ amounts to $\tau' = 48.5$ fs at both positions: inside the cavity and at the WGM antenna. Strikingly, the system appears to be strongly coupled since the electric field amplitude can be restored to a local maximum while loosing only 63% (e^{-1}-criterion) of field strength with respect to the

former maximum. This is especially interesting in the case of the nano-antenna since the decay time τ' of the isolated system was determined to be around 23 fs (see Section 1.2.3). It is hence inferred that according to hybridisation the longevity of the cavity plasmon mode has been imprinted onto the nano-antenna resonance.

1.3.3 Frequency-domain characteristics of the composite system

The beating behaviour of the electric field evolution suggests the existence of two clearly distinguished spectral components although both subsystems are tuned to the same resonance frequency. Therefore the spectral intensity and phase of the composite system is observed at characteristic positions: In the groove of the WGM antenna, labelled M_w, and in an anti-node of the pure cavity mode, labelled M_c (see Fig. 1.16 and Fig. 1.12). This approach is similar to analyse the deflections $x_1(t)$ and $x_2(t)$ of both pendulums in Fig. 1.1(a) in frequency-domain. It can be deduced from the near-field distribution of the m_0-antenna-mode and the $(0,2)$-cavity-mode (see Fig. 1.5(c) and Fig. 1.13, respectively) that the electric field dynamics inside the groove (M_w) is dominated by the x-component of the electric field while the z-component is dominating inside the cavity (M_c). Hence, it is sufficient to analyse the corresponding complex spectral amplitudes $E_x^{WGM}(\nu)$ and $E_z^{cavity}(\nu)$. Observing the electric field inside the groove is of particular interest since in the case of hybridisation a redistribution of charges can be expected which should lead to pronounced effects between adjacent metallic surfaces. For the rest of this chapter the subscripts x and z are omitted and the scalar field quantities $E_w(\nu)$ and $E_c(\nu)$ of the WGM antenna and the cavity are always linked to the x- and z-component of the electric field, respectively.

The spectral intensity (black circles) and phase (black-dashed lines) at the positions M_w and M_c are shown in Fig. 1.16. The data is retrieved from the same FDTD simulation that was utilised in the previous Section 1.3.2. Unlike the previous analysis it is emphasized that the FDTD data is not filtered by a finite source spectrum and hence the curves represent the complex spectral response functions $R_w(\nu)$ and $R_c(\nu)$. As expected both spectral intensities, $|R_c(\nu)|^2$ and

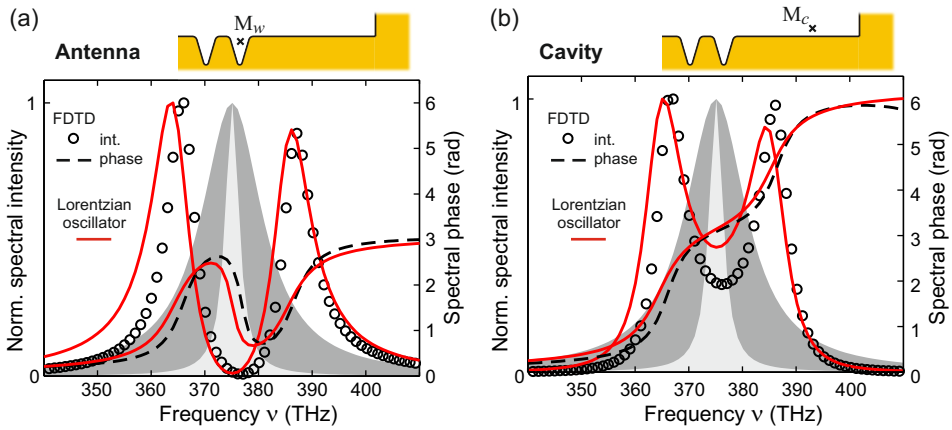

Fig. 1.16: Spectral response function of the composite antenna-CPAC system compared to a model of two coupled point-like oscillators at two characteristic positions: (a) Inside the antenna groove at $M_w = (x = 70$ nm $, y = 0$ nm $, z =$ -10 nm $)$. The spectral intensity and phase as retrieved from FDTD simulations (black circles and black-dashed line, respectively) relate to the x-component of the response function, i.e. $R_x^{FDTD}(\nu, M_w)$, which is labelled $R_w(\nu)$. (b) Inside the cavity at $M_c = (x =$ 480 nm $, y = 0$ nm $, z = 10$ nm $)$. The spectral intensity and phase (black circles and black-dashed line, respectively) relate to the z-component of the response function, i.e. $R_z^{FDTD}(\nu, textM_c)$, which is labelled $R_c(\nu)$. Red lines: The respective spectral intensity and phase as retrieved from the model of two coupled oscillators in equation (1.19). Characteristic oscillator parameters are set to the values for the m_0-mode and the (0,2)-mode in previous sections, i.e. $\omega_{w,0} = 2\pi \cdot$ 375.2 THz, $\gamma_w = 43.4$ THz, $\omega_{c,0} = 2\pi \cdot$ 375.1 THz and $\gamma_w = 9.7$ THz. The coupling constant is set to $\kappa = 0.32$ rad^2 fs^{-2} to match the frequency splitting. Dark shaded area: Spectral intensity of the m_0-antenna-mode (see Fig. 1.5(b)). Light shaded area: Spectral intensity of the (0,2)-cavity-mode (see Fig. 1.14). The FDTD setup is shown in Fig. 1.12 and the cavity radius was set to $a_{02}^{FDTD} = 662$ nm.

$|R_w(\nu)|^2$, feature two clearly separated modes which are shifted to lower and higher frequencies with respect to the overlapping spectral intensities of the isolated WGM antenna and the pure cavity (light and dark shaded areas, respectively, in Fig. 1.16). The width of these shifted modes (~ 6 THz FWHM) is narrower than the m_0-antenna-mode but broader than the (0,2)-cavity-mode and it perfectly fits to the observed decay time of the temporal electric field evolution (see Fig. 1.15(b)). The respective mode distance at M_w and M_c amounts to approximately $\Delta^{(0,2)} = 22$ THz which leads to a beating period of $\tau_{beat}^{(0,2)} = 45.5$ fs in accordance to temporal field dynamics. Interestingly, the spectral intensity $|R_w(\nu)|^2$ at M_w is completely suppressed near the resonance frequency $\nu_0 = 375$ THz of both subsystems whereas an appreciable amount of spectral intensity $|R_c(\nu = 375\text{ THz})|^2$

persists inside the cavity at M_c. As a consequence no electromagnetic energy is located near the WGM antenna although it is directly driven by the source dipole. This behaviour resembles the plasmonic analogue of *electromagnetically induced transparency* (EIT) [39]: If a high-Q oscillator is coupled to a low-Q oscillator the motion of the bright mode can be quenched by the dark mode at excitation frequencies located in the so-called *transparency window* [331, 193]. The quenching can be directly related to a destructive interference of both oscillators: $R_c(\nu)$ and $R_w(\nu)$ run out of phase by π while ν goes through the transparency window.

To further corroborate the hybridisation of antenna and cavity the response functions $R_c(\nu)$ and $R_w(\nu)$ are compared to a scalar model of coupled oscillators in which the only free parameter is the coupling constant κ measured in units of $\mathrm{rad}^2\ \mathrm{fs}^{-2}$. With view to the Lorentzian oscillator equation in (1.4) the coupling of local electric field amplitudes $E_w(t)$ and $E_c(t)$ is expressed by coupled ordinary differential equations (ODEs):

$$\begin{aligned} \frac{d^2}{dt^2}E_w(t) + 2\gamma_w\frac{d}{dt}E_w(t) + \omega_{w,0}^2 E_w(t) &= p_{gauss}(t) + \kappa E_c(t) \\ \frac{d^2}{dt^2}E_c(t) + 2\gamma_c\frac{d}{dt}E_c(t) + \omega_{c,0}^2 E_c(t) &= \kappa E_w(t) \end{aligned} \tag{1.14}$$

Here, $E_w(t)$ and $E_c(t)$ represent the time-resolved deflection of the antenna pendulum and the cavity pendulum, respectively, while γ_w and γ_c are the decay constants and $\omega_{w,0}$ and $\omega_{c,0}$ the resonance frequencies of the corresponding isolated subsystems. Only the WGM antenna is driven by the electric dipole source and hence the term $p_{gauss}(t)$ exclusively appears in the first equation in (1.14) on the right hand side. Coupling is mediated by treating the cavity field amplitude $E_c(t)$ as an additional driving term in which the coupling strength is tuned by the coupling constant κ. Likewise the dynamics inside the cavity is driven by the WGM antenna and hence $\kappa E_w(t)$ is the driving term of $E_c(t)$. The model presented in equation (1.14) and especially the mathematical incorporation of the coupling mechanism is inspired by the works of Zhang [331] and Ghoshal [115]. It has to be noted that in classical mechanics coupling between two identical oscillators is proportional to the difference in the respective instantaneous deflection e.g. $\propto \kappa[E_w(t) - E_c(t)]$ [228]. However, adopting this approach is not suited for plasmonic systems: In plasmonics the new symmetric and anti-symmetric

eigenmodes shift to lower and higher frequencies with respect to the uncoupled oscillators, whereas in classical mechanics the energy of the anti-symmetric mode experiences a blueshift and the energy of the symmetric mode does not shift and exactly coincides with the energy of the uncoupled oscillators [34].

Since the spectrally-resolved FDTD data is obtained in the impulsive response mode the source term $p_{gauss}(t)$ can be expressed by a Dirac delta function $\delta(t)$. By applying a Fourier transformation to (1.14) the coupled equations can be formulated in frequency-domain:

$$\begin{aligned} -\omega^2 R_w(\omega) - 2\gamma_w \omega \mathrm{i} R_w(\omega) + \omega_{w,0}^2 R_w(\omega) - \kappa R_c(\omega) &= 1 \\ -\omega^2 R_c(\omega) - 2\gamma_c \omega \mathrm{i} R_c(\omega) + \omega_{c,0}^2 R_c(\omega) - \kappa R_w(\omega) &= 0. \end{aligned} \tag{1.15}$$

Due to the δ-pulse excitation the spectral amplitudes E_w and E_c are identical to the response functions R_w and R_c. By using vector notation the problem can be expressed as:

$$\underbrace{\begin{pmatrix} \omega^2 - 2\gamma_w \omega \mathrm{i} + \omega_{w,0}^2 & -\kappa \\ -\kappa & \omega^2 - 2\gamma_c \omega \mathrm{i} + \omega_{c,0}^2 \end{pmatrix}}_{\overleftrightarrow{\mathbf{H}}} \begin{pmatrix} R_w(\omega) \\ R_c(\omega) \end{pmatrix} = \begin{pmatrix} 1 \\ 0 \end{pmatrix}. \tag{1.16}$$

The FDTD data in Fig. 1.16 describes the deflection of the respective pendulums in frequency-domain and hence equation (1.16) has to be solved for $R_w(\omega)$ and $R_c(\omega)$. Therefore the left hand side is multiplied with $\overleftrightarrow{\mathbf{H}}^{-1} = \overleftrightarrow{\mathbf{K}}$:

$$\begin{pmatrix} R_w(\omega) \\ R_c(\omega) \end{pmatrix} = \underbrace{\begin{pmatrix} \omega^2 - 2\gamma_w \omega \mathrm{i} + \omega_{w,0}^2 & -\kappa \\ -\kappa & \omega^2 - 2\gamma_c \omega \mathrm{i} + \omega_{c,0}^2 \end{pmatrix}^{-1}}_{\overleftrightarrow{\mathbf{K}}} \begin{pmatrix} 1 \\ 0 \end{pmatrix}, \tag{1.17}$$

in which the elements of $\overleftrightarrow{\mathbf{K}}$ are labelled

$$\overleftrightarrow{\mathbf{K}} = \begin{pmatrix} K_{11} & K_{12} \\ K_{21} & K_{22} \end{pmatrix}. \tag{1.18}$$

For the particular excitation geometry, described by the vector $(1,0)^{\mathrm{T}}$, the response functions $R_w(\omega)$ and $R_c(\omega)$ are determined to be

$$\begin{aligned} R_w(\omega) = K_{11} &= \frac{\omega_{c,0}^2 - \omega^2 - 2\gamma_c\omega\mathrm{i}}{-\kappa^2 + \left(\omega^2 - \omega_{w,0}^2 + 2\gamma_w\omega\mathrm{i}\right)\left(\omega^2 - \omega_{c,0}^2 + 2\gamma_c\omega\mathrm{i}\right)} \\ R_c(\omega) = K_{21} &= \frac{-\kappa}{\kappa^2 + \left(-\omega^2 + \omega_{w,0}^2 - 2\gamma_w\omega\mathrm{i}\right)\left(\omega^2 - \omega_{c,0}^2 + 2\gamma_c\omega\mathrm{i}\right)}, \end{aligned} \tag{1.19}$$

in which the terms for K_{11} and K_{21} have been obtained with the MATHEMATICA software package by using matrix inversion. To compare the spectral intensities and phases of (1.19) to the FDTD simulation data in Fig. 1.16 the characteristic oscillator parameters are set to the values retrieved for the m_0-mode and the $(0,2)$-mode in previous sections, i.e. $\omega_{w,0} = 2\pi \cdot 375.2$ THz, $\gamma_w = 43.4$ THz, $\omega_{c,0} = 2\pi \cdot 375.1$ THz and $\gamma_w = 9.7$ THz.

The resulting spectral intensities and phases of the coupled oscillator model are shown as red lines in Fig. 1.16. Given the fact that the coupling constant κ is the only free parameter in the analytic terms (1.19) the agreement of the coupled oscillator model and the numerical FDTD simulations is nearly perfect. The coupling strength κ was adjusted by hand to match the mode splitting of $\Delta^{(0,2)} = 22$ THz and it amounts to $\kappa = 0.32$ rad^2 fs^{-2}. This sound set of parameters serves to reproduce all characteristic features of the complex system response. Only two systematic deviations can be observed: First, the spectral intensity and phase, as retrieved from the ODE model, appear to be slightly shifted to lower frequencies for both subsystems. And second, the peak width of the modes retrieved from FDTD simulations is appreciably smaller compared to the peaks retrieved from the coupled oscillator model. The frequency shift is attributed to the ODE model since the presence of a spring shifts the natural frequencies of the pendulums [135]. Hemmer and co-workers pointed out that this 'self-energy'-effect is forbidden in quantum mechanics due to electric-dipole selection rules [135].

Deviations in relative peak height and width are attributed to the fact that the electromagnetic properties of a three-dimensional structure are modelled with point-like oscillators. The local spectral signature of the different electric field components inside the antenna-decorated CPAC varies significantly (not shown

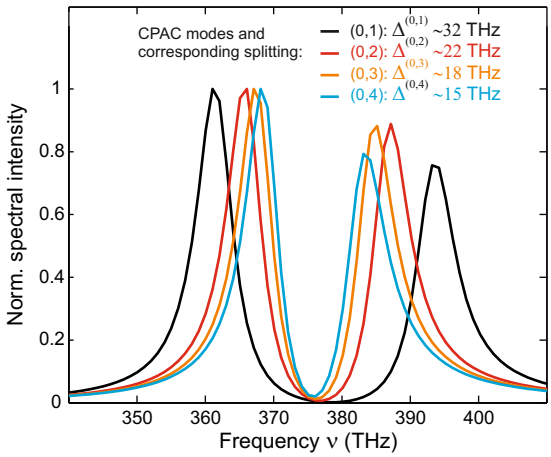

Fig. 1.17: Cavity-mode dependent frequency splitting of the response function near the WGM antenna at the position M_c (see Fig. 1.16). The solid lines represent the FDTD data of $|R_w(\nu)|^2$ for different cavity radii $a_{01}^{FDTD} = 299$ nm (black), $a_{02}^{FDTD} = 687$ nm (red), $a_{03}^{FDTD} = 1078$ nm (orange) and $a_{04}^{FDTD} = 1467$ nm (cyan).

here) because the overlap and hence the interaction of the LSP and SPP mode is location-dependent, i.e. retardation effects are present. However, the good agreement of the ODE model and the FDTD simulation at the specific positions M_c and M_w, as well as the temporal evolution of the entire system, suggest that indeed an appreciable coupling of WGM antenna and cavity mode has been established and that the essential physics of the extended three-dimensional problem can be reduced to point-like oscillators.

Coupling strength of the WGM antenna with different CPAC modes

The coupling strength in a plasmonic systems depends on the spatial and spectral mode overlap of the different constituents and it is hence expected that the observed splitting of resonance frequencies decreases with increasing CPAC mode size. To verify this behaviour FDTD simulations of the composite system have been performed with different cavity radii. Fig. 1.17 shows the FDTD response function $|R_w(\nu)|^2$ at the position M_w inside the WGM antenna groove for cavity radii $a = 299$ nm, $a = 687$ nm, $a = 1078$ nm and $a = 1467$ nm. While the radius $a = 687$ nm corresponds to the already presented (0,2)-mode of the cavity subsystem the other radii are linked to cavities with different radial mode numbers, i.e. $(0,1)$, $(0,3)$ and $(0,4)$, and the same resonance frequency $\nu_0 \approx 375$ THz (see Fig. 1.14 for pure cavity resonances). It can be observed that with increasing radial

mode number n the splitting of modes, and hence the effective coupling strength, indeed reduces. For the smallest mode with $n = 1$ the peak splitting amounts to $\Delta^{(0,1)} = 32$ THz (black solid curve in Fig. 1.17) which is nearly 10% of the resonance frequency ν_0 of both participating subsystems. For the next higher $(0,2)$-mode the splitting is significantly reduced to $\Delta^{(0,2)} = 22$ THz (red solid curve). The coupling strength further decreases for the $(0,3)$- and $(0,4)$-mode ($\Delta^{(0,3)} = 18$ THz and $\Delta^{(0,4)} = 15$ THz) but the relative modification in coupling strength with increasing radial mode number n is also reduced. The trend of a reduced relative modification can be explained in the following way: The $(0,1)$-mode exhibits only a single anti-node in the cavity centre and a major part of the CPAC mode energy is hence concentrated at the WGM antenna structure. In the case of the $(0,2)$-mode a significant part of the overall CPAC mode energy can be found in the annular anti-node which surrounds the cavity centre and exhibits no geometrical overlap with m_0-mode of the WGM antenna. For ever higher radial mode numbers n the relative amount of energy located in the outermost ring decreases compared to the overall mode energy. Therefore a smaller change in mode splitting can be expected for increasing n. Additionally, it was shown in Section 1.3.1 that the dissipation in the cavity is smallest for the $(0,4)$-mode so that a reduction in mode-splitting is compensated by smaller mode widths.

Since the peaks of the response functions $R_w(\nu)$ and $R_c(\nu)$ are well-resolved it is appropriate to classify the combination of a CPAC and a WGM nano-antenna as a strongly coupled system. To the best of the author's knowledge this is the first demonstration of strong coupling between a single SPP and a single LSP. As a consequence the amount of mode splitting, as a measure of coupling strength, can only be compared to systems in which many LSPs couple to SPPs or to systems which consist of a bright nano-antenna coupled to a dark nano-antenna. For example the mode-splitting in dolmen structures amounts to $\Delta = 40$ THz in theory [331] and experiment [193]. Considering that these coupled nano-antennas can exchange energy just two times faster than in the extended system presented here gives a first hint that the coupling of WGM antenna resonances and cavity modes is an interesting approach for long range coherent energy transfer. The rather strong coupling can furthermore be assessed by comparing it to the mode-splitting found in systems in which a propagating SPP couples to a nano-antenna array. For example Ghoshal and co-workers theoretically demonstrated that placing an array

of elliptic nanoparticles 80 nm above a metal surface leads to a mode-splitting of just $\Delta = 12$ THz although 23 nano-antennas per μm^2 contribute to the process [115]. A stronger splitting of $\Delta = 30$ THz was experimentally obtained by Chu and co-workers by using Au nano-discs located 20 nm above an Au-film [66]. The density of nano-antennas in this case was about 1.6 per μm^2. Taking into account that CPACs and WGM antennas achieve a mode-splitting of $\Delta^{(0,2)} = 22$ THz while there is only a single antenna associated with the cavity floor area of 1.5 μm^2 demonstrates that the cavity approach makes the large amount of nano-antennas redundant in LSP-SPP coupling.

1.3.4 Eigenmodes of the hybridised system

In the previous section it was shown that the local spectral properties can be perfectly described by a simple model of two coupled oscillators. Against this backdrop, the newly emerging peaks in the response function of the WGM antenna and cavity have been interpreted as the new eigenmodes of the composite system. Before moving to the more sophisticated elliptical cavities in the next sections the proof-of-principle investigation will be completed by looking at the specific eigenmode structure, i.e. the corresponding near-field distribution. According to the common hybridisation scheme in plasmonics (see [244]) it will be shown that the new near-field distributions correspond to charge distributions that require different excitation energies. Furthermore the near-field data serves to demonstrate that the same problem can be described by different sets of basis vectors, therefore underlining the hypothesis about hybridisation in the context of WGM antennas incorporated in CPACs. This section uses the FDTD simulation data that is related to previous section in which the $(0,2)$-cavity-mode was used for LSP-SPP coupling.

In the context of coupled systems the deflection of one subsystem can be expressed as a superposition of the new eigenmodes [228]. The superposition of eigenmodes corresponds to the shifted peaks occurring in both response functions $R_w(\nu)$ and $R_c(\nu)$ in Fig. 1.16(a) and (b). For convenience the blue-shifted peak at $\nu = \nu_A = 386.6$ THz (776 nm) is referred to as the anti-symmetric eigenmode

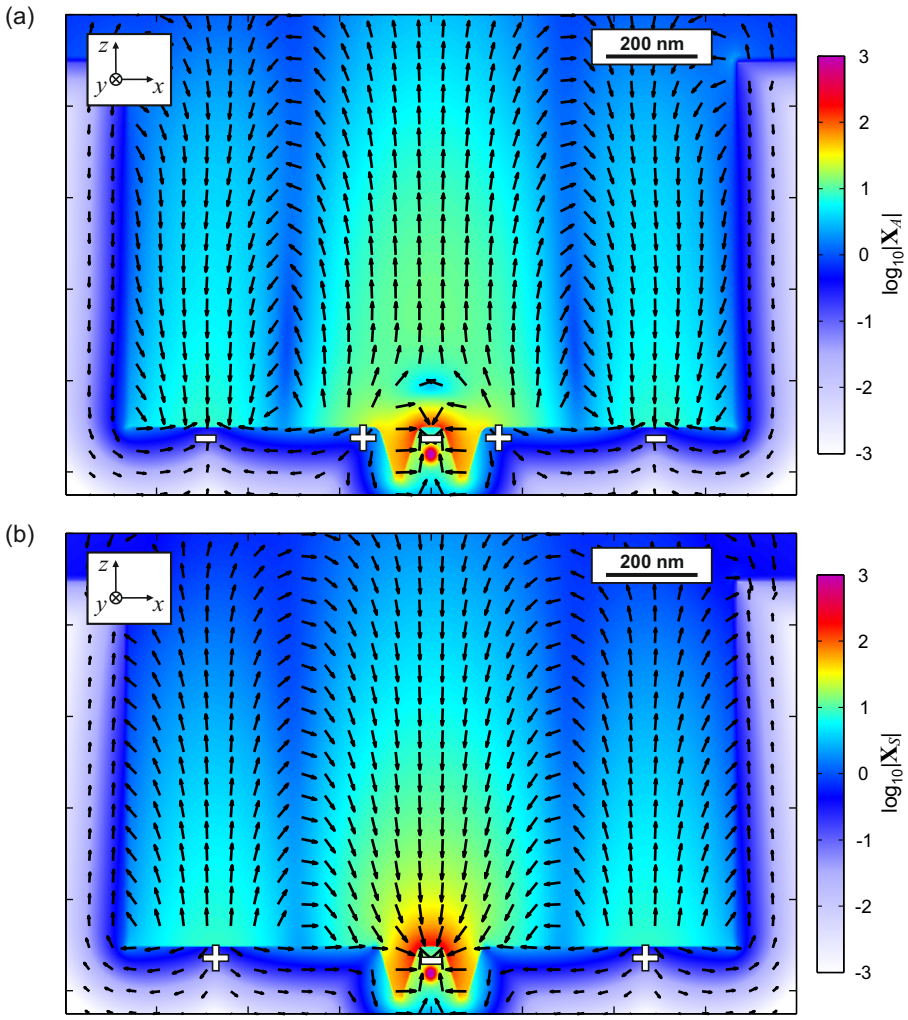

Fig. 1.18: Near-field distribution of the new eigenmodes in the composite system of WGM antenna (m_0-mode) and CPAC ((0,2)-mode). (a) Anti-symmetric eigenmode $\mathbf{X}_A$ as retrieved from the FDTD response function $\mathbf{R}(x,z,\nu = 386.6\ \text{THz})$. (b) Symmetric eigenmode $\mathbf{X}_S$ as retrieved from the FDTD response function $\mathbf{R}(x,z,\nu = 366.7\ \text{THz})$. The contour plot in the background represents the overall field amplitudes $|\mathbf{X}_A|$ and $|\mathbf{X}_S|$, and the plus and minus signs depict accumulated charges due to non-vanishing Gaussian pill box integral $\int_V \nabla\mathbf{E}\ dV$ at the Au-vacuum interface. All arrows and the contour plots are scaled according to the decadic logarithm.

and the associated near-field distribution is labelled $\mathbf{X}_A$. The red-shifted peak at

$\nu = \nu_A = 366.7$ THz (818 nm) is referred to as the symmetric eigenmode and the associated near-field distribution is labelled $\mathbf{X}_S$. The near-fields of $\mathbf{X}_A$ and $\mathbf{X}_S$ are shown in Fig. 1.18(a) and (b), respectively. Due to the radial symmetry of the problem it is sufficient to consider only the axial cross-section (plane at $y = 0$ nm) in which all the field information is represented by the x- and z-components while the y-component vanishes.

Although both near-field distributions look quite similar at first sight a significant difference in excitation energy exists ($\Delta^{(0,2)} \approx 22$ THz ≈ 90 meV). Since surface plasmons are bound to electrons it is once again helpful to integrate the electric field flux over the surface of a Gaussian pillbox that encases the Au-vacuum interface at different positions of the cavity floor. A net flux indicates an accumulation of surface charges and the corresponding polarity is roughly sketched by $+$ and $-$signs. While the symmetric $\mathbf{X}_S$-mode exhibits only a single annular anti-node inside the cavity (linked to the positive charges) the anti-symmetric $\mathbf{X}_A$-mode features two annular anti-nodes of different polarity. This additional separation of charges demands energy and hence leads to a blueshift of the mode. In the picture of the surface plasmon dispersion an additional anti-node requires a larger plasmon wave vector which is usually found at higher energies. The higher surface plasmon energy of the $\mathbf{X}_A$-mode also becomes obvious by the additional surface charges at the outer antenna grooves: a repulsion of likely charges occurs which is represented by the electric field vectors that avoid each other above the WGM antenna. At the same time, the outer anti-node exhibits a higher charge concentration, resulting in energetically unfavourable field components parallel to the cavity walls. For the symmetric $\mathbf{X}_S$-mode precisely the opposite is the case: The negative surface charges of the antenna mesa are confined to a smaller volume compared to the pure cavity mode in Fig. 1.13(a). The positive charges of the annular anti-node are hence less concentrated which leads to a reduced field strength at the cavity wall and the corresponding field components favour a perpendicular orientation to the metallic boundary as expected from electric fields near an equipotential surface.

The resonance peaks representing the new eigenmodes $\mathbf{X}_A$ and $\mathbf{X}_S$ are present in both eigenfunctions $R_w(\nu)$ and $R_c(\nu)$ in Fig. 1.16. If their presence is viewed as a superposition then the π-difference in phase evolution of $R_w(\nu)$ and $R_c(\nu)$ reflects the different symmetries: the symmetric case $\mathbf{X}_S + \mathbf{X}_A$ and the anti-symmetric

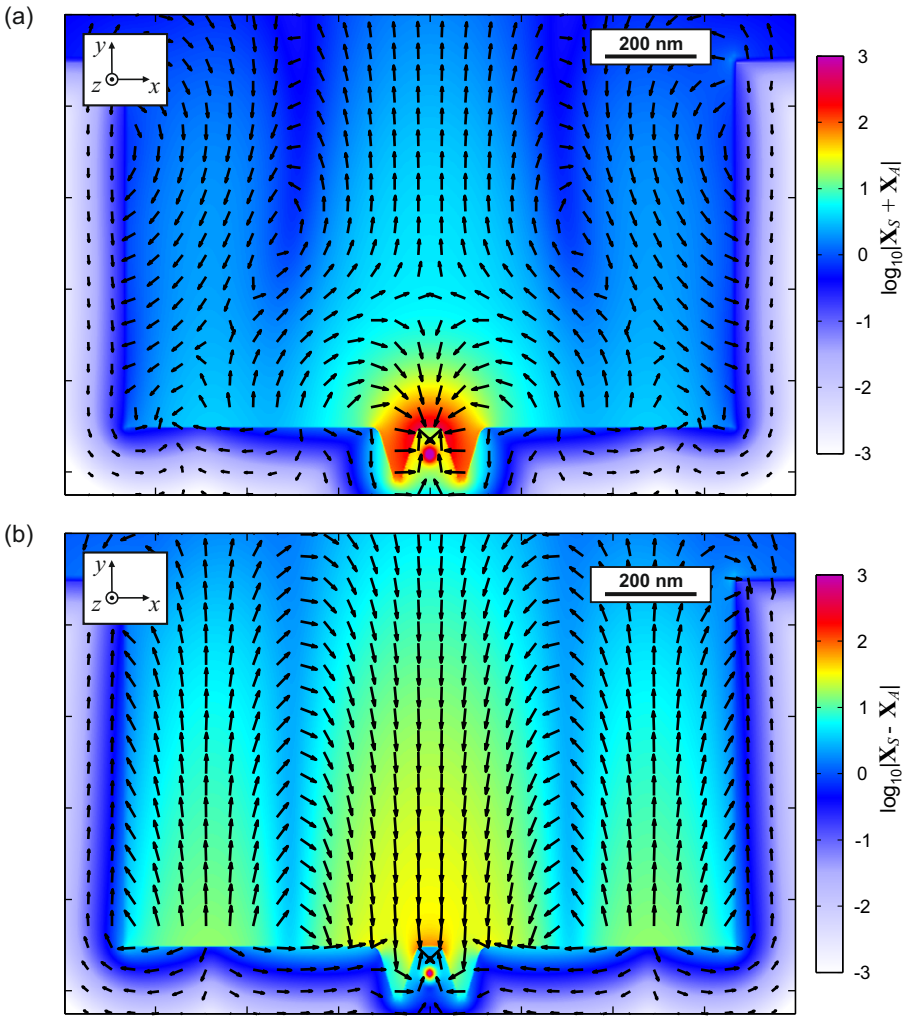

Fig. 1.19: Near-field distribution of the superposition of new eigenmodes $\mathbf{X}_S$ and $\mathbf{X}_A$ in the composite system of WGM antenna (m_0-mode) and CPAC ((0,2)-mode). (a) Symmetric superposition $\mathbf{X}_S + \mathbf{X}_A$. (b) Anti-symmetric superposition $\mathbf{X}_S - \mathbf{X}_A$. All arrows and the contour plots are scaled according to the decadic logarithm.

case $\mathbf{X}_S - \mathbf{X}_A$. Since R_w at the position M_w and R_c at the position M_c represent the deflection of the antenna pendulum and the cavity pendulum the superposition of eigenmodes $\mathbf{X}_S + \mathbf{X}_A$ and $\mathbf{X}_S - \mathbf{X}_A$ should lead to spatial near-field distributions

which resemble the near-field mode of the WGM antenna and the pure cavity, respectively.

Here, some cautionary words are necessary: Using the simple coefficients '$+1$' and '-1 in the above given superpositions is related to a hand waving explanation. Generally, these coefficients are non-trivial and they can become a complex-valued and frequency-dependent quantity when treating the model of two-coupled pendulums with non-matching resonance frequencies or different decay constants of single constituents. Using coefficients '$+1$' and '-1' is valid in the case of e.g. non-decaying identical pendulums. However, despite this limitation the simple approach is qualitatively applicable in the systems presented here, as can be seen in Fig. 1.19(a) for the symmetric superposition $\mathbf{X}_S + \mathbf{X}_A$ and in Fig. 1.19(b) for the anti-symmetric superposition $\mathbf{X}_S - \mathbf{X}_A$: In the case of the symmetric superposition in part (a) the electric field is mainly located at the WGM antenna and the field intensity in the cavity is orders of magnitude lower (note the logarithmic scale). Additionally, the field vectors point strongly towards the antenna mesa. The opposite is true for the anti-symmetric superposition of the near-fields $\mathbf{X}_S$ and $\mathbf{X}_A$: The electric field strength is significantly reduced at the WGM antenna compared to Fig. 1.18. Also the direction of electric field vectors seems to be unaffected by the WGM antenna groove and they simply resemble the mode structure inside a pure CPAC.

The superposition of the new eigenmodes also explains the temporal behaviour investigated earlier in Fig. 1.15: There, the plasmonic excitation was periodically exchanged between the WGM antenna and the cavity. This means that the spatial mode distribution periodically changes from the $(\mathbf{X}_S + \mathbf{X}_A)$ in Fig. 1.19(a) to the cavity mode $(\mathbf{X}_S - \mathbf{X}_A)$ Fig. 1.19(b). The specific time evolution occurs due to beating since the new eigenmodes $\mathbf{X}_S$ and $\mathbf{X}_A$ exhibit different eigenfrequencies and the π phase shift between $(\mathbf{X}_S + \mathbf{X}_A)$ and $(\mathbf{X}_S - \mathbf{X}_A)$ ensures that nearly all energy can be found near the antenna while there is no energy in the cavity and vice versa.

The specific charge distributions leading to energetically split modes, as well as the possibility to describe the same physics by a different set of modes, correspond to the main features of coupled systems and hence the strong coupling of an LSP and an SPP is successfully demonstrated.

1.4 A plasmonic analogue of the Tavis-Cummings model

Having demonstrated the strong coupling between a localised surface plasmon of a nano-antenna and a standing SPP mode inside a circular all-metallic cavity, the question arises: Is it possible to establish a rather strong coupling between several, separately addressable nano-antennas, which is mediated by a plasmonic cavity mode? Such a structure would allow to coherently control the energy transfer between well-separated nanostructures and might find applications in on-chip routing of surface plasmon wave packets [254]. Furthermore, the properties of electric field enhancement and long-lived excitations could help to enhance the energy transfer between different quantum systems coupled to the incorporated nano-antennas, as will be shown in Chapter 2.

To couple at least two nano-antennas it suggests itself to deform the CPACs of the previous section to an elliptical shape. An ellipse exhibits two focal spots and therefore an enhanced interaction can be expected by incorporating the WGM antennas in those spots: A surface plasmon injected by a nano-antenna in one spot of the cavity will be imaged to the nano-antenna placed in the opposite focal spot (see Fig. 1.3(c)). Projecting the information of one spot to a remote location was impressively demonstrated in another branch of physics: Manoharan and co-workers demonstrated in 2000 that the electronic structure near a cobalt atom placed in the focal spot of an elliptical-shaped copper quantum corral can be projected to the opposite focal spot [201]. More precisely, the cobalt atom served as a magnetic impurity that was screened by a collective resonance of the conduction electrons (see *Kondo effect* [165]). Due to the resonant mode pattern of the electron concentration a spectroscopic replica of the cobalt atom was found in the empty focus with scanning tunnelling microscopy. The first elliptical corral for surface plasmon propagation was fabricated and demonstrated by Drezet and co-workers in 2005 [91]. They showed that a plasmon launched at a non-resonant gold protrusion in one focal spot can be focused at a protrusion in the opposite focal spot by using an elliptical Bragg reflector, also consisting of protrusions. However, considering the above mentioned goal the focal spot distance of 30 μm appears too large for a coherent back transfer of excitation energy. Moreover, spectrally sharp Bragg reflectors do not support an appreciable mode splitting of the system and a strong coupling cannot be established. Optical corrals of much

smaller size (few μm) and of elliptical shape have been investigated by Babayan and co-workers regarding the mode pattern of confined standing surface plasmon and wave guide modes [25]. They used shallow, and hence lossy, metallic dykes for SPP reflection, nevertheless the observed mode patterns were similar to those emerging in quantum corrals [201]. Finally, a gold CPAC of elliptical shape and a few hundred nanometre height, as sketched in the introduction (Fig. 1.3(c)), was fabricated by Schoen and co-workers [268]. The major and minor axis size stayed well below 2 μm, therefore offering pronounced focal spots in the standing SPP pattern which were made visible by cathodoluminescence. They could show that a quasi-2D elliptical plasmonic arena cavity (EPAC) can be used as a 3D broadband unidirectional parabolic antenna if the focal spot of the imaginary parabola coincides with the focal spot of a corresponding elliptical parabola cross-section.

In this section it is demonstrated in theory that the focal spots of an EPAC facilitate indirect coupling between two WGM antennas separated by twice the vacuum wavelength of corresponding resonances. It will be shown in Section 1.4.2 that the interaction is strong enough to perceivably alter the response function of the single constituents and that the new hybridised system can be qualitatively described by a simple model of three coupled harmonic oscillators. Thereby it is emphasized that one pendulum is the cavity mode itself and hence the description depicts an all-plasmonic analogue of the quantum mechanical Tavis-Cummings model [290], which describes the interaction of N atoms with a common light field. In Section 1.4.3 it will be shown that excitation energy can be coherently exchanged between the widely separated nano-antennas whereupon the amount of energy and the fashion of temporal evolution crucially depends on dissipation and excitation conditions. Cavity dissipation is controlled via the cavity height and hence two distinct specimen with different Q-factors for FDTD simulations will be introduced in the upcoming Section 1.4.1.

1.4.1 Elliptic plasmonic arena cavities

The FDTD setup is shown in Fig. 1.20. In subsequent sections two types of elliptic cavities will be used, labelled LQ and HQ, which differ in wall height h. Due to the interaction of the evanescent tail of standing SPP modes with the upper wall edge the parameter h determines the cavity dissipation rate. The wall height is set to $h_{LQ} = 500$ nm and $h_{HQ} = 800$ nm. Considering the penetration depth of a SPP mode at $\nu = 375$ THz into the vacuum half-space of $\delta_{vac} = 610$ nm renders the LQ-cavity as rather lossy while the HQ-cavity is expected to feature long-living surface plasmon modes.

It important to note that the two cavities will not inherit the same type of WGM antenna: The WGM antennas with V-shaped grooves are incorporated in the LQ-cavity while the barrel-shaped WGM antennas can be found in the floor of the HQ-cavity (see central insets in Fig. 1.20). This is done for two reasons: First, the combination boosts the contrast in Q-factors of the different constituents in the composite systems. It will be shown in Section 1.4.3 that WGM antennas exhibit a periodic energy exchange inside the cavity when their dissipation rate is matched to the EPAC. Second, the HQ-cavity will be used in Chapter 2 to model the energy transfer of quantum emitters located on top of the respective antenna mesa. By avoiding sharp structures and the associated larger field-enhancement light-matter interaction is assessed conservatively.

It has to be noted that in the case of the LQ-cavity the extra meshes surrounding the WGM antennas do not extend above the Au-vacuum interface due to historical reasons. However, it has been checked that the slightly coarser mesh size does not lead to a shift in the m_0-mode resonance compared to the previously shown simulations. The extra meshes and the WGM antennas are positioned at maximum field intensity of the resonant cavity mode, i.e. the electromagnetic focal spots. This leads to an antenna distance of $d_{wgm} = 1646$ nm in the LQ case and $d_{wgm} = 1630$ nm in the HQ case. Since a single source dipole is located at one of the antennas (deflection of a single pendulum) a symmetric boundary condition can only be applied along the y-direction.

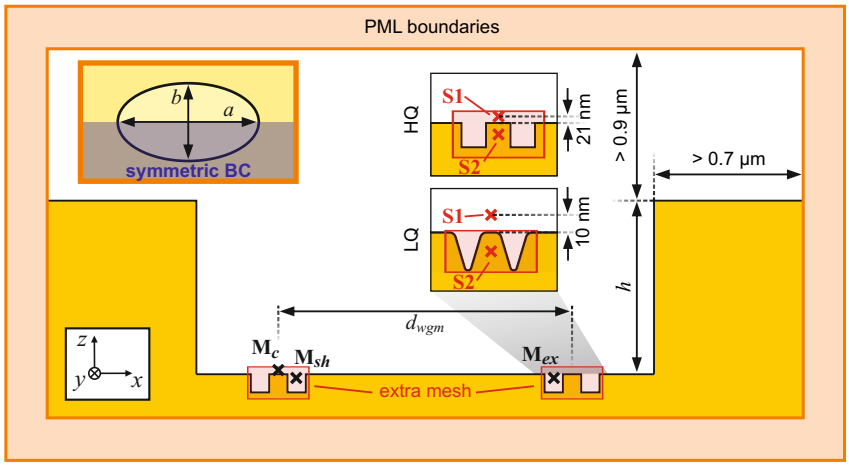

Fig. 1.20: FDTD simulation setup for WGM antennas incorporated in elliptic plasmonic arena cavities (EPACs). The cavity height h determines the amount of dissipation. Two cases are considered: a high-Q cavity with $h_{HQ} = 800$ nm and a low-Q cavity with $h_{LQ} = 500$ nm. The V-shaped groove antenna is used in the LQ-cavity and the barrel-shaped antenna in the HQ-cavity. Corresponding extra meshes (300 nm $\times$ 300 nm $\times$ 118 nm, 2 nm resolution) and (300 nm $\times$ 300 nm $\times$ 138 nm, 2 nm resolution), respectively, are also present in simulations in which only the pure cavity is considered. Antennas and meshes are separated by $d_{wgm} = 1646$ nm (LQ-cavity) and $d_{wgm} = 1630$ nm (HQ-cavity) and therefore centred at the location of maximum field intensity of the pure cavity modes. In the case of pure cavity simulations the dipole source is located 21 nm (10 nm, respectively) above the central antenna mesa ($S1$) while in simulations which include the nano-antenna the dipole source is located inside the mesa ($S2$). Frequency-domain monitors M_{ex}, M_{sh} and M_c are used to record amplitude and phase of the response function in the vicinity of the *excited* antenna, the *shaded* antenna and the cavity mode, respectively. The excitation of a single antenna breaks symmetry and therefore symmetric boundary conditions can only be applied in y-direction. The major and minor axes are set to $a_{HQ} = 2072$ nm and $b_{HQ} = 1450$ nm, and $a_{LQ} = 2092$ nm and $b_{LQ} = 1450$ nm. The eccentricity in both cases is around $e \approx 0.71$.

Mode pattern

The mode pattern of a HQ-cavity resonance at 375 THz is represented by the response function $|R_{c,z}(x,y)|$ in Fig. 1.21(a). A restriction to the z-component is valid according to the associated near-field distribution of the axial cross-section in Fig. 1.21(b) and the considerations about how eigenmodes form in the presence of metallic walls in Section 1.3.1. The out-of-plane component reveals pronounced anti-nodes near the respective apex of the major axis a. It should be noted that these outer anti-nodes do not exactly coincide with the distance of geometrical

focal spots of $\approx 1.480\ \mu$m when considering a major and minor axis size of 2.072 μm and 1.451 μm, respectively. Despite this discrepancy the bright anti-nodes are still referred to as focal spots for simplicity. Together with the other three elongated anti-nodes this mode can be described by the solution $\mathrm{Je}_4 \cdot \mathrm{ce}_4$ in which Je_m and ce_m are even angular and even radial Mathieu functions [128]. Such modes are classified by the roots of the respective functions in the form of (m,n). The parameter m describes the number of angular nodal lines and n the number of radial nodal lines in the pattern. Here, the pattern is denoted as the $(4,1)$-mode since the vanishing field at the metallic boundary counts as a node [128].

The $n = 1$-class of even Mathieu functions, featuring the pronounced anti-nodes near the geometrical focal spots, reflects the common conception of imaging properties of an ellipse. Here, the widely separated hot spots are beneficial to demonstrate a strong long-range coupling and therefore a coherent energy transfer between incorporated WGM antennas. Beyond that the rich variety of Mathieu functions allows for more sophisticated distributions of more than two intense hot-spots which might get interesting for designing complex networks of coupled antennas.

Spectral features

In what follows the spectral parameters of the LQ- and HQ-cavity resonance at 375 THz are retrieved for subsequent analyses. The spectral intensity and phase, as retrieved from FDTD simulations, are shown in Fig. 1.22 for both cavities. Four resonant peaks can be identified in the range of 300 THz to 500 THz with a slightly non-uniform frequency spacing of about 55 THz: the $(3,1)$-mode near 317 THz (946 nm), the $(4,1)$-mode near 375 THz (800 nm), the $(5,1)$-mode near 431 THz (696 nm) and the $(6,1)$-mode near 481 THz (624 nm). It has to be noted that modes with odd m exhibit an anti-symmetric behaviour: The out-of-plane field component at one focal spot exhibits a phase shift of π with respect to the opposite focal spot. For even m the z-components point in the same direction, as can be seen in Fig. 1.21(b).

The (4,1)-mode near 375 THz is significantly broadened in the LQ-cavity compared to the the same mode in the HQ-cavity. Broadening occurs because the evanescent tail of the standing SPP pattern interacts with the upper wall edge and

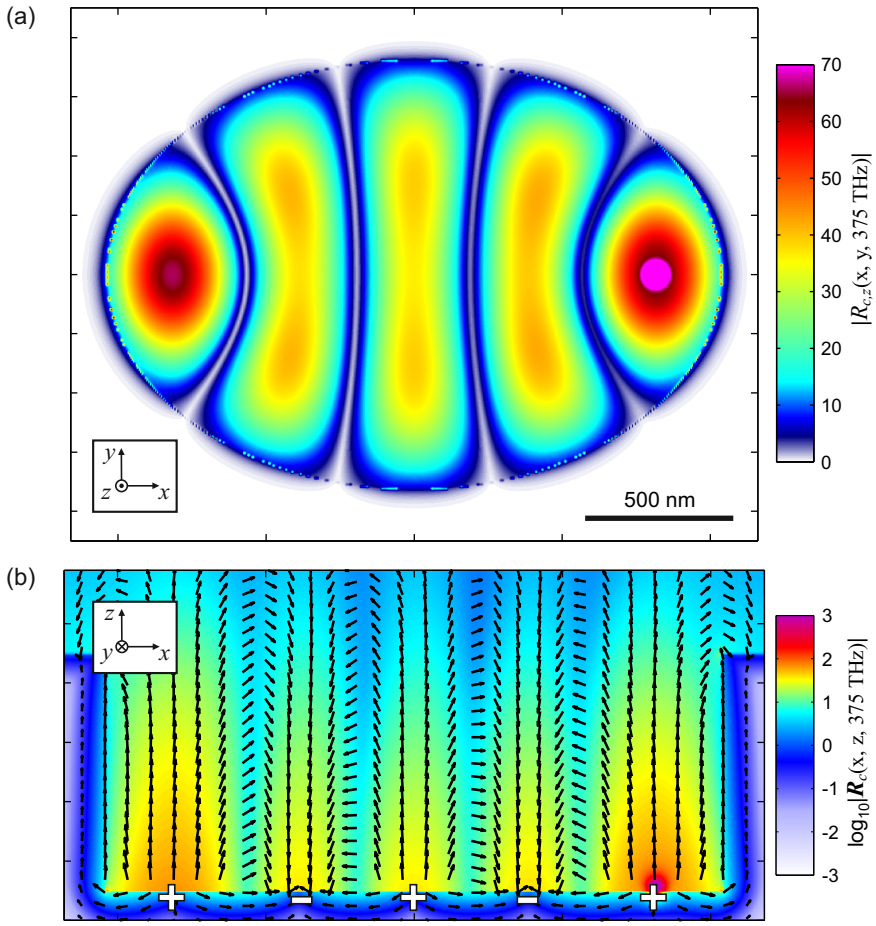

Fig. 1.21: Mode pattern and near-field distribution of the (4,1) EPAC mode at $\nu_0 = 375$ THz. (a) Lateral mode pattern 10 nm above the cavity floor. The mode pattern is dominated by the z-component of the response function $|\mathbf{R}_c(x,y)|$ and it is hence sufficient to show $|R_{c,z}(x,y)|$. The focal spot on the right side is overexposed with respect to the linear colour scale due to the bright dipole source ($S1$-configuration). (b) Black arrows represent a cross-section through the near-field ($R_{c,x}$,$R_{c,z}$) in the plane at $y = 0$. Due to symmetry reasons there is no $R_{c,y}$-component in this plane. The contour plot in the background represents the response amplitude $|\mathbf{R}_c(x,z)|$ and the $+$ and $-$ signs depict accumulated charges due to non-vanishing Gaussian pill box integrals $\int_V \nabla\mathbf{E}\ dV$ at the Au-vacuum interface.

hence energy is coupled out of the cavity into propagating SPPs bound to the top surface. Modes at higher resonance frequencies feature a smaller decay length δ_{vac} and are hence less affected (see Fig. A.1(d)).

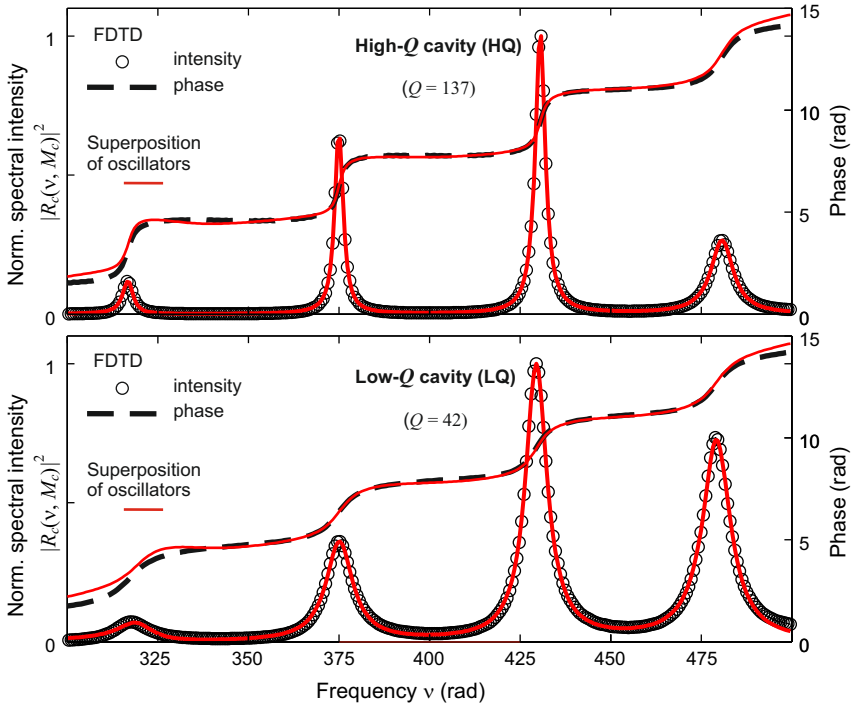

Fig. 1.22: Fitting the spectral intensities (black circles) of low-Q and high-Q EPAC resonances with the `lsqcurvefit` kit in MATLAB according to equation (1.20) (red solid lines). The squared response functions are recorded at the focal spot opposite to the one of the dipole source (position M_c in Fig. 1.20). Since the z-component of the near field is dominating only $|R_{c,z}|^2$ is considered. The offset of FDTD phases (black-dashed lines) and oscillator phases is arbitrarily adjusted by hand. Furthermore, the oscillator phases gain an additional linear phase corresponding to a time delay of 6.6 fs in order to account for the delay of electric fields emitted at the source and arriving at M_c. Fit parameters for the (4,1)-mode: $\nu_{0,(4,1)} = 375.0$ THz and $\gamma_{(4,1)} = 8.6$ THz (HQ-cavity), $\nu_{0,(4,1)} = 375.2$ THz and $\gamma_{(4,1)} = 28.0$ THz (LQ-cavity).

To retrieve the exact resonance frequency ν_0 and decay constant γ for the later utilised $(4,1)$-mode the absolute square of the FDTD response function of the LQ- and HQ-cavity is fitted with four coherently added Lorentzian oscillators:

$$|R_c(\nu, M_c)|^2 = \left| a_0 + \sum_{j=1}^{4} \frac{a_j}{\omega_{0,j}^2 - \omega^2 - 2\gamma_j \mathrm{i}\omega} \mathrm{e}^{\mathrm{i}\phi_i} \right|^2 . \tag{1.20}$$

The running index $j = 1, \ldots, 4$ identifies the modes from $(3,1)$ to $(6,1)$, respectively. The free parameters are the corresponding resonance frequencies $\omega_{0,j}$, the

decay constants γ_j, the amplitudes a_j and a general offset a_0. One of the amplitudes is fixed to 1 so that a_j gives relative amplitudes. Here, the amplitudes are considered to be complex and the associated phase factors ϕ_j are also treated as free parameters. This is necessary because the FDTD data is related to the z-component at the fixed position M_c (see Fig. 1.20). Since the various mode patterns provide focal spots of different size and since every focal spot itself exhibits a non-uniform spectral phase it is not appropriate to fix the relative phase between the oscillators to the same value. Additionally, symmetry introduces phase shifts of π between modes with even and odd m. Moreover, the reflection of SPPs at the cavity walls introduces an additional phase shift which depends on the penetration depth to vacuum δ_{vac}.

The data in Fig. 1.22 was fitted according to equation (1.20) with a self-written MATLAB script, in which the `lsqcurvefit` function was utilised, and the results are represented by red solid lines in Fig. 1.22: The spectral intensity of the HQ- and LQ-cavity can be perfectly reproduced by the proposed model of four coherently added oscillators. The quality of the fit can also be assessed by the matched spectral phase which did not enter the fit routine as a quality criterion (see figure caption for details). The retrieved parameters for the $(4,1)$-mode in the HQ-cavity are:

$$\nu_{0,(4,1)}^{HQ} = 375.0 \text{ THz}, \qquad \gamma_{(4,1)}^{HQ} = 8.6 \text{ THz} \tag{1.21}$$

These values give a Q-factor of $Q^{HQ} = 137$ which is similar to the Q-factor of the $(0,3)$-CPAC-mode that is bound to a cavity floor of comparable size. The parameters for the $(4,1)$-mode in the LQ-cavity amount to:

$$\nu_{0,(4,1)}^{LQ} = 375.2 \text{ THz}, \qquad \gamma_{(4,1)}^{LQ} = 28.0 \text{ THz} \tag{1.22}$$

Accordingly, the Q-factor of $Q^{LQ} = 42$ is more than three times smaller than that of the HQ-cavity. Furthermore, the Q-factor of the WGM antenna with V-shaped grooves (see equation (1.9)) is only a factor of 1.5 smaller compared to the LQ-cavity. This rather small difference between the different constituents will lead to interesting dynamics in energy transport as will be shown in the next sections.

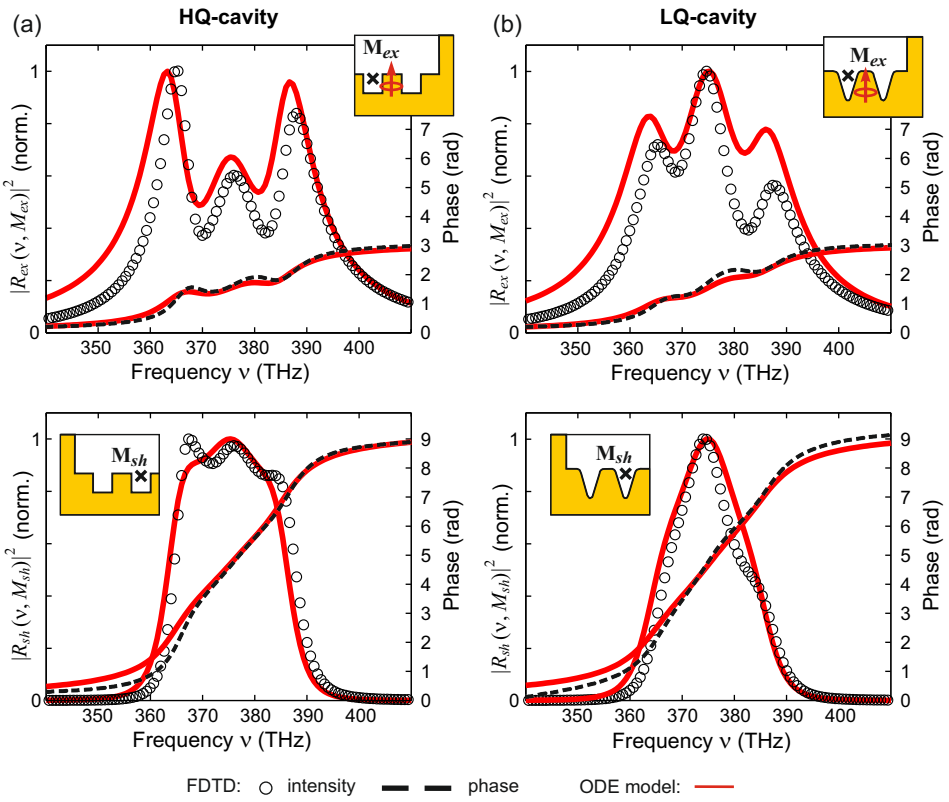

Fig. 1.23: Comparing the x-component of FDTD response functions of the composite EPAC-antenna system (black circles for spectral intensity and black-dashed lines for phase) to a model of three coupled oscillators (ODE, red solid lines) presented in equation (1.26). FDTD data is recorded at the position indicated in the respective insets according to the setup in Fig. 1.20. All phase offsets and signs are adjusted to common notation. The only free parameter is the coupling constant κ which is adjusted by hand to match the mode splitting of the FDTD data. All other parameters are retrieved from fits of the single constituents. (a) ODE parameters LQ-cavity: $\nu_{0,ex} = \nu_{0,sh} = \nu_{0,c} = 375.2$ THz, $\gamma_{ex} = \gamma_{sh} = 43.4$ THz, $\gamma_c = 28.0$ THz and $\kappa = 0.22$ rad^2 fs^{-2}. (b) ODE parameters HQ-cavity: $\nu_{0,ex} = \nu_{0,sh} = 375.5$ THz, $\nu_{0,c} = 375.0$ THz, $\gamma_{ex} = \gamma_{sh} = 49.5$ THz, $\gamma_c = 8.6$ THz and $\kappa = 0.23$ rad^2 fs^{-2}.

1.4.2 Frequency-domain characteristics of the composite system

The response function of the composite system consisting of two WGM antennas located in the respective focal spots of an EPAC is expected to be more complicated than that of two coupled oscillators in Section 1.3.3. Additionally,

the temporal dynamics of a system is sensitive to the specific excitation conditions and hence the spectral properties are studied first.

FDTD simulations for the HQ- and LQ-cavity have been performed according to the setup shown in Fig. 1.20. The S2-configuration is used for excitation and the response function is recorded in the groove of both antennas, i.e. at the positions M_{ex} and M_{sh}. In the rest of the chapter the subscripts *ex* and *sh* are used for the directly excited antenna and its counterpart, respectively. Since the observation points are located between opposing groove walls the problem is reduced to the x-component of the electric field and the respective response functions are labelled $R_{ex}(\nu,\mathrm{M}_{ex})$ and $R_{sh}(\nu,\mathrm{M}_{sh})$.

The retrieved spectral intensities and phases for both cavity designs are presented in Fig. 1.23 (black circles and black-dashed lines, repsectively): In the case of the HQ-cavity (Fig. 1.23(a)) three clearly separated peaks can be observed in $|R_{ex}(\nu, \mathrm{M}_{ex})|^2$ at the excited antenna although the isolated cavity itself as well as the WGM antennas exhibit a resonant response solely at 375 THz. Therefore it is inferred that the additional peaks emerge due to hybridisation of the WGM antennas and the EPAC and that their spectral position determines the normal mode energies of the composite system. The additional peaks are located at $\nu_{nm_1}^{HQ} \approx 365$ THz (822 nm) and $\nu_{nm_3}^{HQ} \approx 388$ THz (773 nm) which results in an overall mode splitting of $\Delta_{HQ} \approx 23$ THz. This splitting is comparable to the hybridisation strength of one WGM antenna located inside a CPAC featuring the $(0,2)$-mode (see Fig. 1.17), although the EPAC exhibits a factor $\sqrt{2}$ larger cavity floor area. It has also to be noted that especially the outer peak widths are smaller than 10 THz and thus they are smaller than the line width of the pure antenna resonance (see Fig. 1.11). This implies an imprinted SPP feature and underlines the hybridisation conjecture. The phase evolves from 0 to π across the resonances. Small phase dips can be observed between the peaks which might be related to transparency windows of lower quality. The spectral intensity $|R_{sh}(\nu, \mathrm{M}_{sh})|^2$ at the opposite WGM antenna also features three peaks which, however, can be hardly resolved. The corresponding phase runs from 0 to 3π and hence exhibits an extra step of π compared to the circular system. This behaviour is ascribed to the presence of a third resonance peak.

The characteristic features of response functions at the WGM antennas inside the LQ-cavity are similar to those of the HQ-cavity. However, due to the enhanced

dissipation of the LQ-cavity the peaks are broadened. As a consequence, tails of the outer peaks add up at the position of the central peak so that the latter one is pronounced in contrast to the peak structure of the HQ-cavity system. This effect is visible at both antennas. Nevertheless the peak positions and hence the mode splitting remains unaltered, i.e. $\Delta_{LQ} \approx 23$ THz. The phase evolution at both antennas resembles that of the HQ-cavity system, but characteristic features are less pronounced.

In the following a model of three coupled oscillators is introduced in order to quantitatively describe the response functions and to proof hybridisation. In doing so the question arises how coupling is implement in the case of WGM antennas incorporated in EPACs. It seems unlikely that a direct coupling exists between the antennas since they are separated by a distance of more than 1 μm. Hence it is assumed that the antennas are coupled indirectly via the cavity mode, i.e. both antennas couple directly to the cavity, as in the case of CPACs, but not among themselves. The scenario resembles the quantum mechanical Tavis-Cummings model in which multiple quantum emitters interact with each other via a common mode of the light field [290]. This model is discussed in Chapter 2.4.1 in detail. Here, it is sufficient to know that the coupling of two quantum emitters and a cavity mode leads to three non-degenerate new eigenstates of the system. By identifying the quantum emitters with the WGM antennas and using the new set of eigenstates (2.60) the new eigenmodes of the plasmonic system (HQ-cavity) can be sketched in Dirac notation as

$$
\begin{aligned}
|nm_1\rangle &= \frac{1}{2}\left(|WGM_{ex}\rangle + |WGM_{sh}\rangle + \sqrt{2}\,|cavity\rangle\right) \quad \text{at } \nu_{nm_1}^{HQ} \approx 365 \text{ THz} \\
|nm_2\rangle &= \frac{1}{\sqrt{2}}\left(|WGM_{ex}\rangle - |WGM_{sh}\rangle\right) \quad \text{at } \nu_{nm_2}^{HQ} \approx 375 \text{ THz} \\
|nm_3\rangle &= \frac{1}{2}\left(|WGM_{ex}\rangle + |WGM_{sh}\rangle - \sqrt{2}\,|cavity\rangle\right) \quad \text{at } \nu_{nm_3}^{HQ} \approx 388 \text{ THz}
\end{aligned}
\tag{1.23}
$$

in which the normal modes $|nm_1\rangle$, $|nm_2\rangle$ and $|nm_3\rangle$ correspond to the three resonance peaks in Fig. 1.23. All three modes at the respective frequencies are related to a specific electric near-field distribution labelled $\mathbf{X}_{nm_1}(\nu_{nm_1}^{HQ})$, $\mathbf{X}_{nm_2}(\nu_{nm_2}^{HQ})$ and $\mathbf{X}_{nm_3}(\nu_{nm_3}^{HQ})$. These considerations are similar to those about hybridisation in circular cavities in Section 1.3.4. According to equation (1.23) a symmetric

superposition $\mathbf{X}_{nm_1} + \mathbf{X}_{nm_3}$ should lead to a state in which the electromagnetic energy is mainly located at both WGM antennas. On the contrary to the symmetric case, an anti-symmetric superposition $\mathbf{X}_{nm_1} - \mathbf{X}_{nm_3}$ is expected to expel the energy from the antennas and to concentrate it inside the cavity. For the sake of brevity the near-field distributions $\mathbf{X}_{nm_1}$, $\mathbf{X}_{nm_3}$, $\mathbf{X}_{nm_1} + \mathbf{X}_{nm_3}$ and $\mathbf{X}_{nm_1} - \mathbf{X}_{nm_3}$ are shown in Appendix A.4. Indeed, the symmetric and anti-symmetric superposition of near-fields conform the conjectures derived from the Tavis-Cummings model in (1.23). It is once again noted that the notation in (1.23) with its superposition coefficients is a stark simplification by considering that the involved oscillators exhibit e.g. different decay constants and non-zero line-width. Therefore caution should be taken by applying the above given Tavis-Cummings model in plasmonics.

As a consequence of the above considerations the system of two coupled ordinary differential equations (ODEs) in (1.14) is extended by the equation for the second WGM antenna and the linear system of equations reads in frequency-domain:

$$\underbrace{\begin{pmatrix} \omega^2 - 2\gamma_{ex}\omega\mathrm{i} + \omega_{ex,0}^2 & -\kappa & 0 \\ -\kappa & \omega^2 - 2\gamma_c\omega\mathrm{i} + \omega_{c,0}^2 & -\kappa \\ 0 & -\kappa & \omega^2 - 2\gamma_{sh}\omega\mathrm{i} + \omega_{sh,0}^2 \end{pmatrix}}_{\overleftrightarrow{\mathbf{H}}} \begin{pmatrix} R_{ex}(\omega) \\ R_c(\omega) \\ R_{sh}(\omega) \end{pmatrix} = \begin{pmatrix} 1 \\ 0 \\ 0 \end{pmatrix}, \tag{1.24}$$

in which the subscripts *ex*, *sh* and *c* denote the excited WGM antenna mode, the shaded WGM antenna mode and the cavity mode, respectively. The direct coupling of antennas is prohibited by setting $H_{13} = H_{31} = 0$. The response functions can be retrieved by inverting $\overleftrightarrow{\mathbf{H}}$:

$$\begin{pmatrix} R_{ex}(\omega) \\ R_c(\omega) \\ R_{sh}(\omega) \end{pmatrix} = \overleftrightarrow{\mathbf{H}}^{-1} \begin{pmatrix} 1 \\ 0 \\ 0 \end{pmatrix} = \underbrace{\begin{pmatrix} K_{11} & K_{12} & K_{13} \\ K_{21} & K_{22} & K_{23} \\ K_{31} & K_{32} & K_{33} \end{pmatrix}}_{\overleftrightarrow{\mathbf{K}}} \begin{pmatrix} 1 \\ 0 \\ 0 \end{pmatrix}. \tag{1.25}$$

Due to the specific excitation conditions only the first column of $\overleftrightarrow{\mathbf{K}}$ has to be considered and the response functions are expressed by $R_{ex}(\omega) = K_{11}$, $R_c(\omega) = K_{21}$ and $R_{sh}(\omega) = K_{31}$:

$$
\begin{aligned}
R_{ex}(\omega) &= \frac{-\kappa^2 + (2\mathrm{i}\gamma_c\omega + \omega^2 - \omega_{0,c}^2)(2\mathrm{i}\gamma_{sh}\omega + \omega^2 - \omega_{0,sh}^2)}{\zeta} \\
R_c(\omega) &= \frac{\kappa(-2\mathrm{i}\gamma_{sh}\omega - \omega^2 + \omega_{sh}^2)}{\zeta} \\
R_{sh}(\omega) &= \frac{\kappa^2}{\zeta},
\end{aligned}
\tag{1.26}
$$

in which common denominator is

$$
\begin{aligned}
\zeta =& \kappa^2(2\mathrm{i}\gamma_{ex}\omega + \omega^2 - \omega_{0,ex}^2) + ... \\
&... + (-\kappa^2 + (2\mathrm{i}\gamma_{ex}\omega + \omega^2 - \omega_{0,ex}^2)(2\mathrm{i}\gamma_c\omega + \omega^2 - \omega_{0,c}^2)) \cdot ... \\
&... \cdot (-2\mathrm{i}\gamma_{sh}\omega - \omega^2 + \omega_{0,sh}^2).
\end{aligned}
\tag{1.27}
$$

This analytic model is now applied to reproduce the FDTD simulation data in Fig. 1.23. The specific parameters of the single constituents are determined by the previously shown FDTD simulations (see figure caption for details). The results are shown as red solid lines in Fig. 1.23 for the HQ- and the LQ-cavity: In both cases the analytic model perfectly reproduces all specific features of the spectral intensity. It has to be noted that relative peak heights in the spectral intensity are highly sensitive to the spatial observation point in the extended 3D-simulation and hence a rough agreement is sufficient. Additionally, the matched phase evolution in all cases corroborates the coupled oscillator model. The systematic deviations like the narrower peaks in FDTD simulations and the shift in frequency are the same as observed in the CPAC simulations in Fig. 1.16. The frequency shift is again ascribed to the selfenergy of the pendulums that exists due to the presence of the spring in the classical model [135].

It is once again stressed that the only free parameter in the complex equations (1.26) and (1.27) is the coupling constant κ which has been adjusted by hand to match the amount of mode splitting of ≈ 23 THz. The corresponding value is $\kappa \approx 0.225$ rad^2 fs^{-2} in both cavities and hence the amount of dissipation does not generally influence the coupling strength between the m_0-antenna-mode and the $(4,1)$-EPAC-mode. Interestingly, the amount of mode splitting in elliptical cavities is the same as in the case of circular cavities (see Fig 1.16) although the

coupling constant in EPACS ($\kappa_{EPAC} \approx 0.225$ rad^2 fs^{-2}) is a factor $\sqrt{2}$ smaller as in CPACS ($(2,1)$-mode, $\kappa_{CPAC} = 0.32$ rad^2 fs^{-2}). The reduced coupling constant in the case of elliptical cavities can be explained by the non-annular mode shape of the focal spots (see Fig. 1.21) which negatively affects the mode overlap with the radial-symmetric m_0-antenna-mode. The reduced coupling strength seems to be compensated by the presence of a second nano-antenna in the opposite focal spot. This is at least a well-known behaviour in quantum mechanics: The amount of Rabi-splitting increases with $\sqrt{n}$ where n describes the number of coupled quantum emitters [295, 108]. Here, the analogue effect is observed in classical physics. With view to the Tavis-Cummings model it can be deduced that the system presented here facilitates for the first time an appreciable long-range coupling of single plasmonic nano-antennas.

1.4.3 Time-domain characteristics of the composite system

The presence of three normal modes and the different spectral phase evolutions at the deflected pendulums imply a complex temporal dynamics of plasmonic excitation that will crucially depend on the source spectrum. When sophisticated devices like a pulse shaper are neglected the common shape of a source spectrum is similar to a Gaussian curve. Therefore two specific excitation conditions suggest itself: A spectrum that spans across the entire response function of, for instance, the excited antenna (upper part of Fig. 1.23) and a spectrum that selects two adjacent peaks. These two scenarios are simulated for the LQ- and the HQ-cavity leading to four different data sets that need to be examined.

Data processing

Data processing routines follow the one that was used in the investigation of the temporal behaviour in circular cavities in Section 1.3.2: The impulsive response function of the system $\mathbf{R}(\nu, x, y = 0 \text{ nm}, z = -10 \text{ nm})$ is obtained 10 nm below the cavity floor in the spectral range of $\nu = 300$ THz (1000 nm) to $\nu = 500$ THz (600 nm) with 300 sampling points. The associated electric dipole source injects a short

pulse of about 4.3 fs and it is operated in the source configuration S2. Then $\mathbf{R}(\nu,x)$ is zero-padded in MATLAB with respect to ν whereby the sampling point distance is left unaltered. Afterwards a linear interpolation of $\mathbf{R}(\nu,x)$ with respect to the x-axis is performed so that all data points are spaced by the minimum distance of the extra mesh (2 nm). The response function $\mathbf{R}(\nu,x)$ is then multiplied with a spectral envelope of Gaussian shape $p_{gauss}(\nu)$ that represents either a pulse of 15 fs duration centred at $\nu_0 = 376.4$ THz (797 nm) or a pulse of 30 fs duration centred at $\nu_0 = 383.6$ THz (782 nm). This gives the local electric field $\mathbf{E}(\nu,x) = \mathbf{R}(\nu,x) \cdot p_{gauss}(\nu)$ in frequency-domain. A fast Fourier transformation is applied to retrieve the complex and spatially-resolved electric field data $\mathbf{E}(t,x)$ in time-domain.

LQ-cavity

First of all the temporal dynamics inside the LQ-cavity is discussed (see Fig. 1.24). The evolution of the electric field envelope $|\mathbf{E}(t,x)|$ initiated by the small-band source pulse of 30 fs duration is presented as a contour plot in Fig. 1.24(a) (note the logarithmic colour scale): In the first few femtoseconds around $t = 0$ fs the field builds up at the initially excited antenna. After a short delay time the electric field strength also increases at the opposite (shaded) antenna. The electromagnetic field energy ($\propto |\mathbf{E}|^2$) at the shaded antenna reaches its climax at $t \approx 50$ fs. Interestingly, at this instant of time there is hardly any field energy located at the initially excited antenna. Then, a re-focusing of energy occurs at the initially excited antenna while energy is absent at the opposite one, as clearly indicated by the field node near $t \approx 100$ fs. The electric field dynamics continuous until the end of the simulation at which the overall field amplitude has decayed by four orders of magnitude compared to its maximum value.

For a more detailed analysis $|\mathbf{E}(t)|$ is shown at the well-known positions M_{ex} and M_{sh}, inside the groove of the excited and shaded antenna (Fig. 1.24(c)). The alternating occurrence of field nodes and anti-nodes at the different positions is clearly visible and both curves decay with a time constant of $\tau' \approx 31$ fs. Compared to a field life-time of the pure WGM antenna of 23 fs (see equation (1.9)) the presence of the cavity yields a life-time enhancement of a factor 1.5. This is quiet efficient when considering that the LQ-cavity mode itself exhibits a life-time of

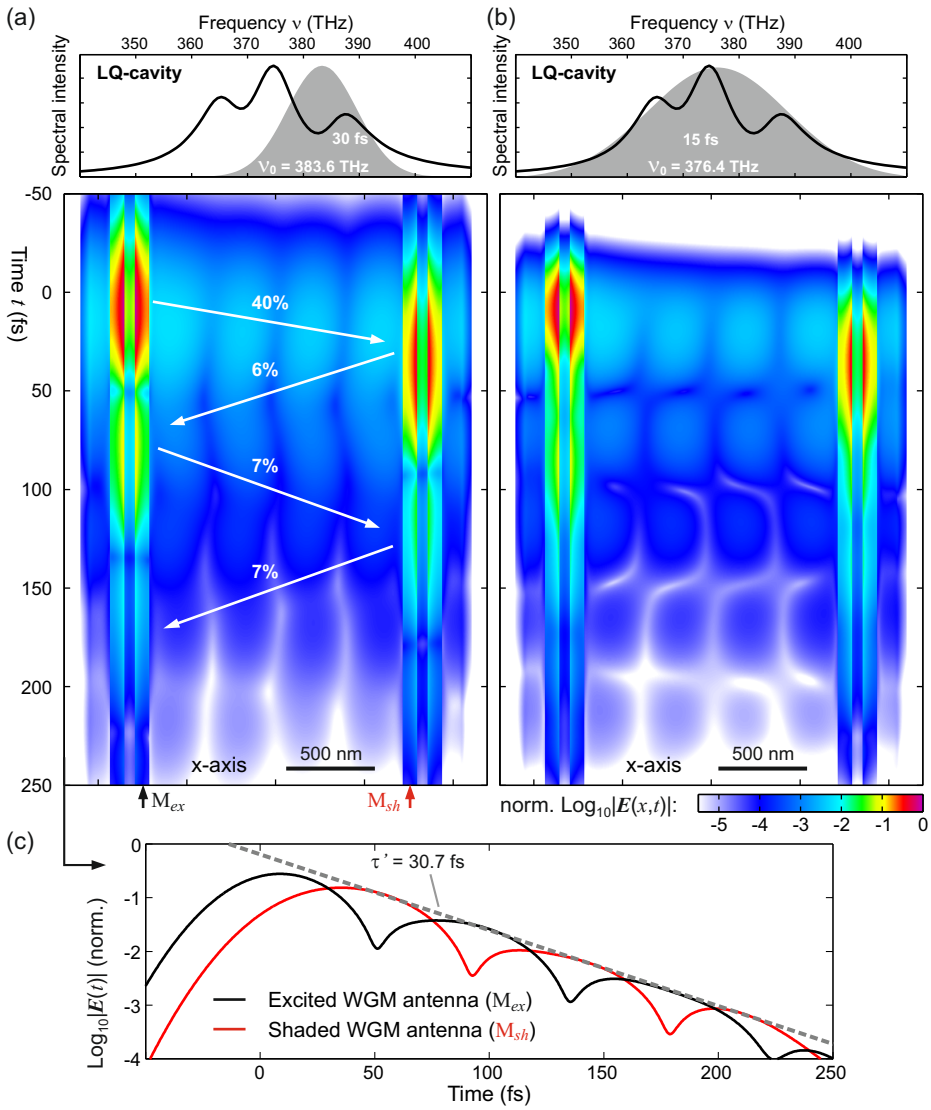

Fig. 1.24: Temporal evolution of the electric field envelope in the hybridised LQ-cavity system 10 nm below the Au-vacuum interface along the major axis ($S2$-configuration). $|\mathbf{E}(x,t)|$ is obtained by filtering the response function $\mathbf{R}(\nu,x)$ with a Gaussian spectral amplitude $p_{gauss}(\nu)$. (a) Narrow-band excitation: Grey-shaded area represents $\left|p_{gauss}(\nu)\right|^2$ with $\nu_0 = 383.6$ THz (782 nm) and $\Delta t = 30$ fs. (b) Broad-band excitation: $\nu_0 = 376.4$ THz (797 nm) and $\Delta t = 15$ fs. Black solid line: $|R_{x,ex}(\nu, \mathrm{M}_{ex})|^2$ from FDTD simulations. (c) Details of field evolution upon small-band excitation at the indicated positions.

only 36 fs (see equation (1.22)). The life-time of the electric field and the beating period then determine the amount of energy that can be transferred from one antenna to the other. Due to the uniform field evolution at the respective antennas it is appropriate to assume that the electric field information at M_{ex} and M_{sh} is sufficient to determine the amount of transferred energy. To do this, the absolute square of both curves is integrated from field node to field node which gives a measure for the energy comprised in a single field anti-node. The ratio of these values, i.e. the relative amount of transferred energy, is indicated in the contour plot in Fig. 1.24(a) for subsequent processes: Despite dissipation nearly 40% of electromagnetic energy located at the initially excited antenna is transferred in the first 90 fs to the opposite one. After the transient effect 7% of energy are transferred in a subsequent emission-absorption processes. As a consequence, nearly 3% of energy emitted at M_{ex} are transferred back to the initially deflected pendulum. The extraordinarily high transfer efficiency of 40% in the first process is ascribed to the transient phenomenon: A constructive superposition occurs between the surface plasmons directly injected by the excited antenna (delayed by 10 fs to 20 fs at M_{sh}) and the temporal beating pattern of the steady state dynamics ($\tau_{beat} \approx 86$ fs). This is deduced from the temporal duration of the first anti-node at the shaded antenna which is increased compared to the duration of all subsequent anti-nodes.

After the discussion of energy transfer efficiencies the question may arise: Why is there a periodic energy transfer between the WGM antennas at all? As a matter of course the peak structure and spectral phases of the response functions in Fig. 1.23(b) can answer this question since they are connected with the temporal field evolution via the Fourier transformation. Furthermore, split peaks and spectral phases which exhibit the character of a third order dispersion imply a beating behaviour and a train of delayed sub-pulses. However, this gives no intuitive explanation for the specific timing. A more fundamental insight can be obtained by considering the Tavis-Cummings model in equation (1.23): The shifted peaks in the response functions can be related to the normal modes $|nm_1\rangle$, $|nm_2\rangle$ and $|nm_3\rangle$ whereupon each of them includes information about the deflection of all pendulums. It was already shown in Appendix A.4 that a superposition of near-fields at frequencies close to the resonance frequencies of $|nm_1\rangle$ and $|nm_3\rangle$ allowed to selectively locate electromagnetic energy at the WGM antennas or inside the

HQ-cavity. Here, the specific filtering of the response function with the source spectrum (see Fig. 1.24(a)) implies the superposition $|nm_2\rangle + |nm_3\rangle$ and $|nm_2\rangle - |nm_3\rangle$. The different symmetries for the superpositions are deduced from the spectral phase evolution at the antenna pendulums in Fig. 1.23(b). With respect to the equations in (1.23) the symmetric superposition $|nm_2\rangle + |nm_3\rangle$ leads to an enhancement of the state $|WGM_{ex}\rangle$ and a suppression of the other antenna state $|WGM_{sh}\rangle$. The anti-symmetric case leads to the opposite behaviour and the energy difference between these two stationary states then leads to the observed periodic energy transfer as it is naively expected from coupled oscillators. The cavity state $|cavity\rangle$ remains unaffected, as can be seen in the contour plot, since it is only included in $|nm_3\rangle$.

The electric field evolution upon simultaneous excitation of a all three normal modes with a 15 fs pulse is shown in Fig 1.24(b). Obviously, there is no periodic energy transfer between the WGM antennas. Field nodes of the temporal envelope at both antennas are hardly visible. Using a 1D-representation similar to Fig. 1.24(c) actually reveals a weak beating behaviour with small modulation depths (not shown here). But in contrast to the dynamics upon small-band excitation the anti-nodes here appear synchronised in time at both antennas. Instead the broad-band excitation leads to visible electric field nodes and anti-nodes inside the cavity which can be expected by considering that the symmetric and anti-symmetric superpositions of $|nm_1\rangle$ and $|nm_3\rangle$ eliminates or enhances the cavity state $|cavity\rangle$. According to the superpositions $|nm_1\rangle \pm |nm_3\rangle$ the electromagnetic energy should be located at the antennas when it leaves the cavity and vice versa. Although indications of such a field evolution are visible, e.g. the antenna synchronisation, the overall dynamics seems to be smeared out due to dissipation or unmatched peak heights, i.e. mode contributions.

HQ-cavity

In the case of the HQ-cavity, which features reduced loss, the just predicted electric field evolution is indeed visible upon broad-band excitation (Fig. 1.25(a)): After the transient phenomenon ($t > 70$ fs) the clearly visible field anti-nodes of both WGM antennas are synchronised. It can also be observed that the antenna system periodically exchanges energy with the cavity as deduced from the static

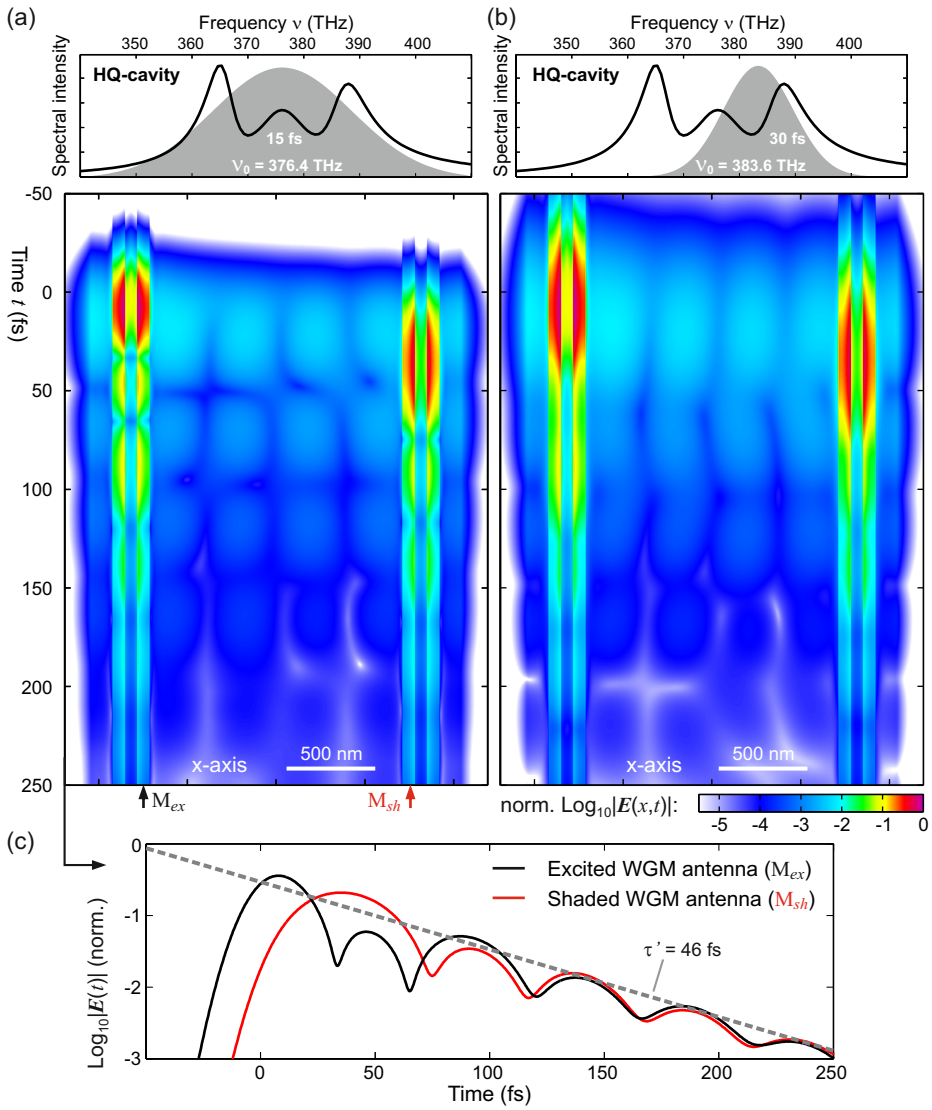

Fig. 1.25: Temporal evolution of the electric field envelope in the hybridised HQ-cavity system 10 nm below the Au-vacuum interface along the major axis ($S2$-configuration). $|\mathbf{E}(x,t)|$ is obtained by filtering the response function $\mathbf{R}(\nu,x)$ with a Gaussian spectral amplitude $p_{gauss}(\nu)$. (a) Broad-band excitation: $\nu_0 = 376.4$ THz (797 nm) and $\Delta t = 15$ fs. (b) Narrow-band excitation: Grey-shaded area represents $\left|p_{gauss}(\nu)\right|^2$ with $\nu_0 = 383.6$ THz (782 nm) and $\Delta t = 30$ fs. Black solid line: $|R_{x,ex}(\nu, \mathrm{M}_{ex})|^2$ from FDTD simulations. (c) Details of field evolution upon broad-band excitation at the indicated positions.

superposition of near-fields in Appendix A.4 and the Tavis-Cummings model in equation (1.23).

A well-arranged temporal evolution of the electric field amplitude at the specific positions M_{ex} and M_{sh} is shown in Fig. 1.25(c). The synchronisation of the antennas after a time $t > 70$ fs is clearly visible and field amplitudes at both antennas decay with a time constant $\tau' \approx 46$ fs. Considering the field life-time of the barrel-shaped WGM antenna ($\tau' = 20.2$ fs) the hybridisation process in the HQ-cavity enhances the antenna life-time by more than a factor of 2. Since the electric field life-time of the system is now comparable to the faster beating period $\tau_{beat} \approx 50$ fs upon broad-band excitation, the energy transfer at a specific antenna is greatly enhanced: Well-above 10% of energy are transferred from anti-node to anti-node at both antennas in the steady state regime. In the case of the LQ-cavity the successive emission and absorption processes lead to a rather small energy re-occurrence of $\approx 0.5\%$ (conditional transfer rates: $7\% \cdot 7\%$, see contour plot in Fig. 1.24(a)).

An interesting analogy to energy transport in quantum systems can be drawn by considering the WGM antennas as quantum emitters: If the energy transfer rate between the quantum emitters is larger than the dissipation rate of the overall system the transfer process can no longer be described in terms of a *donor* and an *acceptor* like in the weak coupling regime. Instead the well split peaks in the response function of the HQ-cavity system imply a strong coupling regime in which a coherent interaction between the sub-systems gets dominant (see Chapter 2.4.1). Considering these normal modes as new quantum sates of the hybridised system the isochronal location of energy at both antennas can be interpreted analogously to the interaction of quantum emitters: The energy transfer in the plasmonic system is so fast that a distinction between an emitting WGM antenna and a receiving WGM antenna is not possible. This interpretation might get important when dealing with single surface plasmons in the composite system. Therefore the device might serve as a toy model in the research field of quantum plasmonics [289]. However, analogies should not be overstressed and here it is important to note that the excitation of all eigenmodes by a simple Gaussian pulse leads to a coherent electric field evolution with characteristic features that appear on faster time-scales than the decay of the field amplitude to 10% of its initial value. Hence the device is a promising candidate for ultra-fast coherent control of plasmonic

energy transfer by using e.g. shaped laser pulses, just like the evolution of coupled quantum systems can be affected by an external stimulus.

The temporal evolution of the electric field upon small-band excitation is shown in Fig. 1.25(b). Interestingly, the filtering of two peaks with a Gaussian spectrum does not lead to a periodic energy transfer as in the case of the LQ-cavity. Instead, there are indications that again the anti-nodes at both antennas are synchronised. However, the modulations depth is small and the entire temporal dynamics of the electric field envelope appears washed-out like in the broad-band excitation of the LQ-cavity system. The reason for the observed behaviour is of course comprised in the spatially dependent complex response function, but a deeper insight into the problem can be obtained by considering a universal phenomenon: *critical coupling*, also known as *impedance matching*.

Impedance matching

Impedance matching is best known in electrical engineering where the input impedance of a sub-system needs to be matched to the output impedance of another sub-system in order to maximise the transfer of power between them. Otherwise a signal reflection can occur which leads to standing waves in the connecting cable and hence no power is effectively transferred. This phenomenon is universal and applies to different branches of physics: Light incident on an open 1D Fabry-Pérot resonator, which exhibits an opaque back-reflector, will be perfectly absorbed inside the device if the dissipation in the resonator is equal to the leakage of the front mirror [37]. These resonator schemes are technologically relevant in building graphene electro-optic modulators [239] or to enhance the absorption in thin-film solar cells by Anderson-localised photonic modes [4]. With view to the quantum mechanical Tavis-Cummings model it is interesting to note that impedance matching also applies to quantum systems like quantum dots: The resonant absorption of light is maximised when the absorption cross-section equals the scattering cross-section [181] (see equation (2.45) and the related discussion). Impedance matching is also a known phenomenon in plasmonic systems since the work of Alù and Engheta in 2008 [11]. Only one year later Huang and co-workers could show that the concept of impedance matching can be applied to optimise the energy transfer between interconnected nano-optical elements [144].

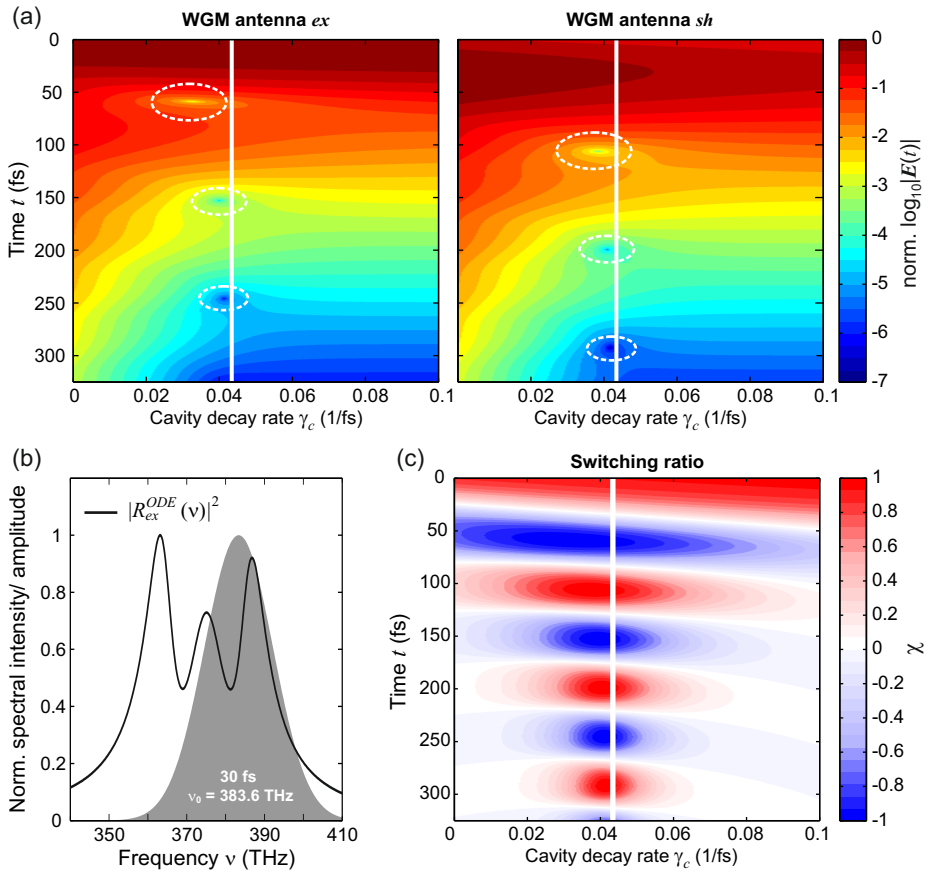

Fig. 1.26: Impedance matching in hybridised EPAC-antenna systems. (a) Temporal evolution of $|E(t)|$ as a function of the cavity decay rate γ_c at the excited and shaded WGM as retrieved from the ODE model in equation (1.26). The applied parameters are related to barrel-shaped WGM antennas ininside the HQ-cavity: $\nu_{0,ex} = \nu_{0,sh} = 375.5$ THz, $\nu_{0,c} = 375.0$ THz, $\gamma_{ex} = \gamma_{sh} = 49.5$ THz and $\kappa = 0.23$ rad^2 fs^{-2}. (b) Visualisation of mode filtering: The temporal dynamics in part (a) is initiated by a small-band Gaussian spectral amplitude (grey-shaded area, $\nu_0 = 383.6$ THz (782 nm) and $\Delta t = 30$ fs). The black solid curve represents $|R_{x,ex}(\nu, \mathrm{M}_e x)|^2$ as retrieved from the ODE model with $\gamma_c = \gamma_{ex}$. (c) Switching ratio $\chi(t, \gamma_c)$ as a function of γ_c according to equation (1.28). The vertical white line marks the scenario $\gamma_c = \gamma_{ex}$.

The idea that impedance matching is important in the hybridised system presented here stems from the aforementioned work of Huang and co-workers, since the cavity is used as an interconnecting waveguide. Moreover, it has been shown that the coupling strength of WGM antennas and plasmonic cavity modes is nearly

identical for low-Q and high-Q cavities. Hence the major difference between the systems is indeed the amount of dissipation.

The impact of impedance matching is verified by exploiting the approved ODE model of three coupled oscillators: The response functions at the excited antenna, $R_{ex}^{ODE}(\nu)$, and at the shaded antenna, $R_{sh}^{ODE}(\nu)$, are obtained via equation (1.26) for a fixed dissipation of the WGM antenna γ_{WGM} and a variable cavity decay rate γ_c. The temporal electric field envelope is then calculated via the fast Fourier transformation and a subsequent Hilbert transformation in MATLAB. The decimal logarithm of the field envelope $|E(t)|$ at both antennas is shown as a function of the cavity decay rate γ_c in the contour plot in Fig. 1.26(a). It has to be noted that $E(t)$ was obtained by multiplying the response functions $R_{ex}^{ODE}(\nu)$ and $R_{sh}^{ODE}(\nu)$ with a Gaussian source spectrum $p_{gauss}(\nu)$ centred at $\nu_0 = 383.6$ THz and the spectral width is related to a pulse of 30 fs (see Fig. 1.26(b)). The excitation conditions coincide with the FDTD simulations presented in see Fig. 1.24(a) for the LQ-cavity and Fig. 1.25(b)) for the HQ-cavity.

The contour plots in Fig. 1.26(a) perfectly fit to the hypothesis of impedance matching: At both antennas the temporal dynamics of the electric field is smeared out for cavities of high quality ($\gamma_c < 0.02$ THz) and a slow modulation of the envelope is hardly visible. This behaviour resemble the FDTD simulations for the HQ-cavity in Fig. 1.25(b). However, when the cavity decay rate matches the antenna decay rate, i.e. $\gamma_c \approx \gamma_{WGM} = 43.2$ THz, characteristic features appear in the electric field evolution. More precisely, the features are identified as nodes of the field envelope which exhibits an appreciable modulation depth (marked by white-dashed ellipses). Furthermore the field nodes of the respective antennas are shifted relative to each other in time so that an anti-node of one antenna coincides with a node of the other antenna and vice versa. This behaviour is in accordance with FDTD simulations of the LQ-cavity presented Fig. 1.24(a). For ever higher cavity decay rates ($\gamma_c > 0.5$) the peaks of the response functions get very broad and the temporal dynamics of the electric field envelope is smeared out again. As a consequence, the periodic energy transfer occurs only in the region $\gamma_c \approx \gamma_{WGM}$. This behaviour corroborates the conjecture that impedance matching facilitates an efficient energy transfer between the nano-antennas.

For technological applications it is interesting to examine the quality of switching during the periodic energy transfer. The quality can be assessed by comparing

the amount of energy located at each nano-antenna to the overall amount of energy at both antennas. The switching ratio $\chi(t,\gamma_c)$ is hence determined as a function of time and cavity dissipation by

$$\chi(t,\gamma_c) = \frac{|E(t,\gamma_c)_{ex}|^2 - |E(t,\gamma_c)_{sh}|^2}{|E(t,\gamma_c)_{ex}|^2 + |E(t,\gamma_c)_{sh}|^2}, \tag{1.28}$$

in which $|E(t,\gamma_c)_{ex}|^2$ and $|E(t,\gamma_c)_{sh}|^2$ are proportional to time-averaged intensities at the respective antenna. A switching ratio $\chi = +1$ means that all energy is located at the initially excited antenna while for $\chi = -1$ all energy is located at the shaded antenna. The result is shown in Fig. 1.26(c): After a transient phenomenon a switching ratio of $\chi \approx \pm 1$ is maintained for time-scales > 300 fs, if the decay rate of the cavity is matched to the decay rate of the nano-antennas. Otherwise the switching ratio rapidly decreases to zero. Although this result underlines the general benefit of impedance matching the number of transfer events is very small since the beating period is large compared to typical decay times: The field envelope has decayed by two orders of magnitude after 150 fs due to the rather low quality factor of the combined cavity-antenna system. Therefore, it is worthwhile to bring the quality factor of the antenna system closer to that of the high-Q cavities. For instance, Feigenbaum and Orenstein could show that Q-factors > 100 are actually available in structures featuring ultra-small plasmon volumes and retardation effects at the same time [103].

1.5 Experimental realisation of cavity-mediated LSP coupling

After the demonstration of cavity-mediated coupling of two widely separated nano-antennas via FDTD simulations, this section is dedicated to the experimental realisation of the above developed concept. Before showing and discussing the successfully implemented back and forth transfer of electromagnetic energy between the WGM antennas in the final Section 1.5.4, the sample preparation will be presented in Section 1.5.1. Then, the experimental setup will be introduced in Section 1.5.2. By measuring the non-linear photoelectron emission of WGM antenna arrays, it will be verified in Section 1.5.3 that structural parameters of

plasmonic resonances found with FDTD simulations approximately coincide with experimental results.

1.5.1 Sample preparation

The device presented here is a complex combination of three different plasmonic structures, i.e. two WGM antennas and one EPAC, and the margin of fabrication tolerance is hence very small. Especially the m_0-mode of WGM antennas is very sensitive to structural modifications: FDTD simulations revealed that changing the groove depth by just 10 nm results in a resonance shift of 20 THz (not shown here). Using standard preparation methods for Au thin-films like thermal evaporation is not suited for the fabrication of such sophisticated structures due to the multi-crystalline structure of evaporated thin-films: The particular crystal grains exhibit a size of 40 nm [143] and show different resistance to FIB milling [59] which makes it impossible to obtain well-defined and reproducible nanostructures.

To avoid structural inaccuracy, the samples in this work have been realised by using chemically-grown single-crystalline gold microplates: These plates take the shape of hexagons or triangles with edge lengths of some micrometres and a thickness of some hundred nanometres [127] while their surface remains atomically flat (surface roughness < 1 nm over an area of 1 μm^2 [143]). It was recently shown that the single-crystalline character of gold microplates allows for a fabrication of smooth and well-defined nanostructures with improved plasmonic performance [143]. The latter statement refers to the observation that roughness and small grain boundaries support scattering and dephasing of surface plasmon resonances [64]. With a view to this it was experimentally demonstrated by Kuttge and co-workers that the propagation length of SPPs on single-crystalline metal films is in perfect agreement with predictions from the dielectric function according to equation (A.2) [177]. Hence atomically flat single-crystalline gold microplates are perfectly suited to be used as the cavity floor which is at the same time the substrate for

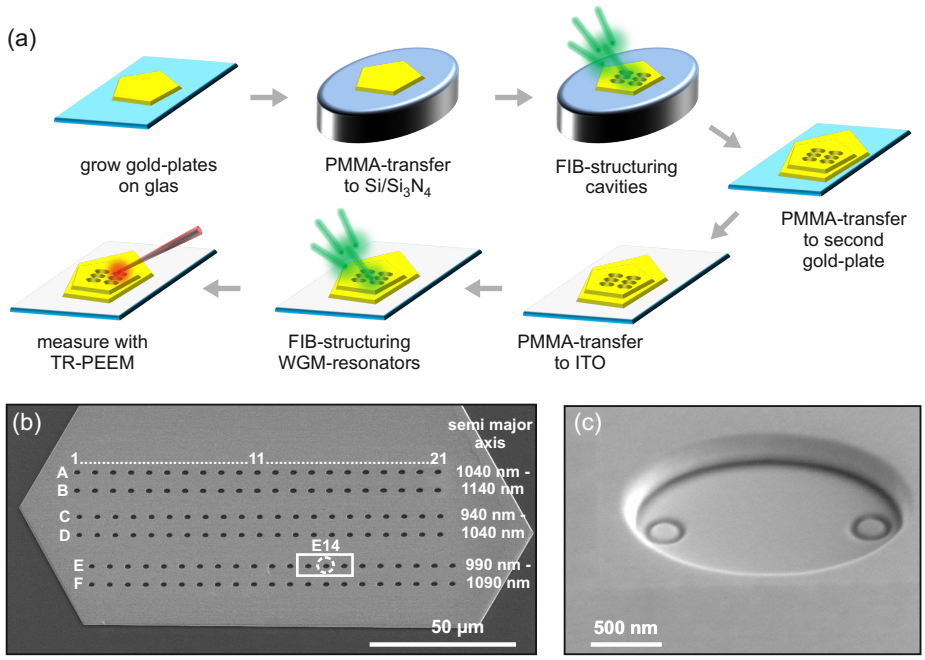

Fig. 1.27: Sample preparation with single-crystalline Au microplates. (a) The main idea is to use two microplates for the fabrications of cavities: One microplate is perforated with elliptical holes and it is then mechanically drawn over a second microplate. The atomically flat surface of the lower plate serves as the cavity floor and FIB substrate for writing WGM antennas into the focal spots. Single-crystalline Au microplates are grown on a substrate by Enno Krauss (University of Würzburg) who also performs all subsequent steps until WGM antennas are incorporated. This step is accomplished with the support of Thomas Löber (NSC, TU Kaiserslautern). (b) SEM image upper microplate. For a variety of cavities and resonant modes the upper plate is perforated with elliptical holes which increase in major axis size. Rows A and B are identical, likewise C and D as well as E and F. The major axis size increases in 10 nm steps from column 1 to column 21 and the range of the semi major axis is indicated. (c) SEM image (SEM column tilted by 52°) of a representative EPAC ready for experiments.

the FIB structuring of WGM antennas. Furthermore, the single-crystalline character and the associated consequences are expected to yield a performance close to the predictions of FDTD simulations and should in principal allow for higher Q-factors than the well-defined multi-crystalline metallic wall cavities of Zhu and co-workers [335].

The overall device is composed of two different gold microplates: By utilising FIB milling one plate is perforated with elliptic holes and it is then stacked onto another microplate. The lower microplate serves as the cavity floor and WGM

antenna substrate, thereby maintaining an untreated atomically flat surface. In contrast to this approach, Schoen and co-workers recently fabricated monolithic EPACs out of a single-crystalline polished gold pellet by just milling the elliptical pits with FIB technique [268]. Although a monolithic device is often desirable the FIB treatment excludes the existence of an atomically flat surface.

General fabrication process

The single-crystalline Au microplates are fabricated and pre-processed by Enno Krauss from the Nano-Optics and Biophotonics group of Bert Hecht (Würzburg University). The fabrication process is sketched in Fig 1.27(a): Here, a new approach is utilised in which Au microplates are directly grown on a glass substrate instead of drop-casting or spin-coating solution-grown microplates onto a substrate. It has been observed that direct growth on glass prevents small-particle contamination, microplate aggregation and rejects the tendency of plates to roll up and bend due to large aspect ratios and accumulated strain during the growth process [319]. In a next step the microplates are transferred to a hard silicon substrate with a silicon nitride layer (Si_3N_4) for the first FIB process in which the microplate is perforated with elliptical holes of different size. Using silicon nitride prevents a FIB-induced welding of structures and substrate [318] so that the perforated microplate can be mechanically transferred and stacked onto another microplate that has also been grown on a glass substrate. Then the stacked microplates are transferred to a transparent conducting oxide (ITO) and are shipped to the Nano Structuring Center in Kaiserslautern (NSC, TU Kaiserslautern). At the NSC the second FIB treatment is performed with the support of Thomas Löber: A particular choice of WGM antennas is milled into the cavity floor (see Section 1.5.3 for details of this process). Then the samples are ready for time-resolved photoelectron emission microscopy (TR-PEEM) experiments (see Section 1.5.4). Using ITO as a sample substrate is necessary since it avoids charging effects.

Specific EPAC pattern

A scanning electron microscopy (SEM) image of the perforated microplate that is used in the experiments is shown in Fig. 1.27(b). It exhibits the shape of a

truncated triangle with edge lengths of some ten micrometres up to some hundred micrometres so that it is visible to the naked eye. Enno Krauss determined the thickness of the microplate to 440 nm which is comparable to the LQ-cavity in Section 1.4.2. Six different rows of elliptical holes have been written labelled by the capital letters A to F. The 21 holes in each row increase in major axis size a in 10 nm steps while the minor axis is kept constant at $b = 1450$ nm. The reason for this specific pattern is to provide a selection of cavities and to assure that at least one of them features a resonance frequency that coincides with the WGM antenna resonance. Changing the major axis size leads to a factor of 3.5 stronger shift of the resonance frequency than changing the minor axis size. A step of 10 nm in major axis length results in a frequency shift of ≈ 1.7 THz (not shown here). It has to be noted that row B is a copy of row A, likewise is D a copy of C and F a copy of E. A and B increase (left to right) from 2080 nm to 2280 nm, C and D increase from 1880 nm to 2080 nm and E and F increase from 1980 nm to 2180 nm. The rows E and F are of particular interest since FDTD simulations predict a resonance at 375 THz for cavities with $a = 2092$ nm which would relate to cavities in the vicinity of $E(F)12$. Indeed this will turn out to be true and cavity $E14$ (marked by a white-dashed circle) will be thoroughly investigated in Section 1.5.4.

Visual quality and incorporation of WGM antennas

A SEM image (column tilted by 52°) of a representative cavity equipped with two WGM antennas near the focal spots is shown in Fig. 1.27(c). The surface, as well as the written WGM antennas, appears very smooth and well-defined due to the single-crystalline character of the Au microplates. The crescent-shaped shadow at the interface of the upper and lower microplate implies a small elevation of the former one, leading to a horizontal notch. However, such a crescent-shaped shadow also appears in the tilted-view SEM image of monolithic EPACs in the work of Schoen [268] and hence the shadow appears to be an artefact that is related to the SEM geometry.

The distance d_{WGM} between the WGM antennas was defined by the equation $d_{WGM} = a \cdot (3/4.5)$. The factor 4.5 relates to the uncertainty in PEEM experiments with empty EPACs: It could not be clearly identified whether four or five anti-

nodes exist between the walls. In the case of cavity $E12$ this distance amounts to $d_{WGM} = 1393$ nm while FDTD simulations predict a distance $d_{WGM} = 1646$ nm. This procedure seems to be inappropriate with view to the experimental results in Sections 1.5.3 and 1.5.4 which render the results of FDTD simulation as reliable. However, it will be shown that these discrepancies do not eliminate hybridisation but the coupling strength is found to be reduced compared to simulations. It can also be shown with FDTD simulations that hybridisation features are hardly altered when reducing the ideal d_{WGM} value by e.g. 100 nm.

1.5.2 Experimental setup

Measurement scheme

Similar to the first observation of LSP-SPP-coupling on corrugated Ag films by Aeschlimann and co-workers [6] the temporal dynamics of plasmons in antenna-decorated EPACs is investigated by time-resolved photoelectron emission microscopy (TR-PEEM) [265, 173]. In short, a PEEM consists of a system of electrostatic lenses, sketched in Fig. 1.28(a), which facilitate to image the electrons ejected by a sample upon light irradiation onto a combined system of fluorescence screen and CCD-camera (see [29] for a brief summary of PEEM). The contrast of this image is determined by the spatially-resolved number of emitted electrons and is among other influences (e.g. surface topography [252] and magnetic domains [12]) a measure for the strength of the local electric field according to the photo effect [96]. Since the detection scheme is based on electrons the theoretical resolution of a PEEM image is determined by the de Broglie wavelength of electrons [48, 49] which is about 1 nm for kinetic energies of 1 eV and thereby well below the optical diffraction limit. Using a PEEM with a Vis-NIR light source is especially suited to refine contrast and to investigate upon optical near-fields at small nanostructures due to the non-linear emission character of photoelectrons [102, 67]: The work function of gold is about 5.1 eV and the photon energy at frequencies of $\nu = 375$ THz amounts to 1.55 eV. Hence, four photons need to be absorbed by the electronic system to eject a single electron. In the absence of resonant intermediate states the yield Y in this *multi-photon regime* scales with the

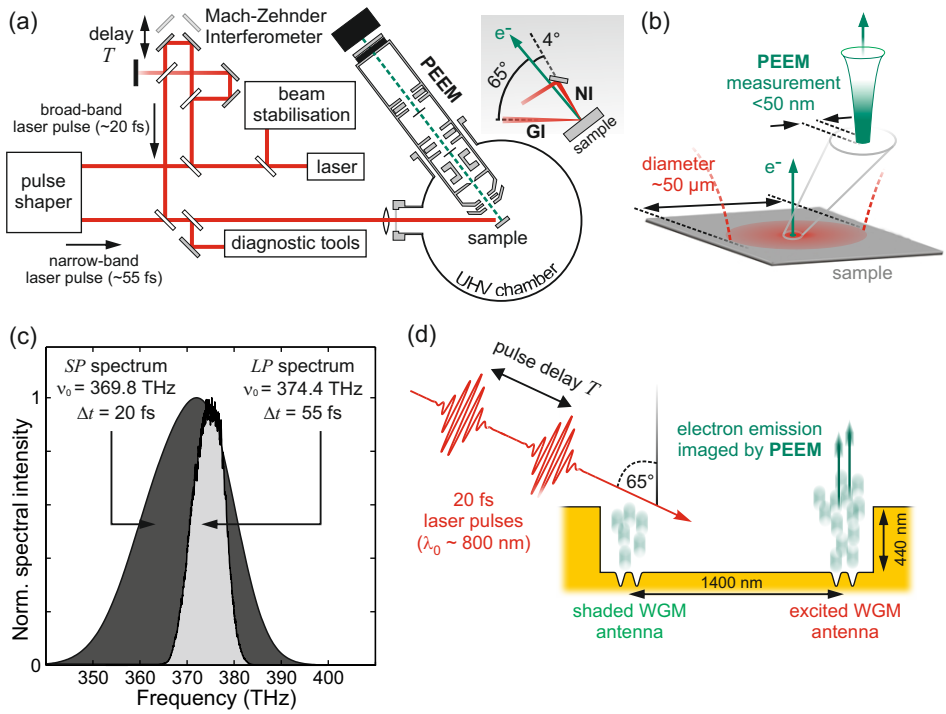

Fig. 1.28: Setup and schemes for time-resolved photoelectron emission microscopy (TR-PEEM) experiments. (a) Laser and PEEM setup. The PEEM can be operated under normal incidence (NI) of laser light or under grazing incidence (GI) so that e.g. different WGM antenna modes can be selectively excited. (b) Sketch of enhanced resolution: While a large area is illuminated by the laser with a focus spot size of about 50 μm (e^{-2}-diameter) the PEEM image offers a resolution of about 50 nm which is limited by the de Broglie wavelength of the matter wave and the electrostatic lens system. (c) Broad-band (*SP*, direct laser output) and narrow-band (*LP*, pulse shaper output) spectrum for PEEM experiments measured in the *diagnostic tools* section with an OCEAN OPTICS spectrometer. (d) For TR-PEEM the GI-geometry is used because it provides electric field components perpendicular to the substrate which allow to excite the m_0-mode of WGM antennas. The cavity wall shadows one of the antennas so that only one pendulum is initially excited.

intensity dependent power function according to

$$Y(I) = I^N \tag{1.29}$$

in which I is the light intensity and N the number of absorbed photons [118]. Therefore the photoelectron emission is greatly enhanced at nanostructures due to the field enhancement effect of sharp edges (lightning rod effect) or surface

plasmon resonances, and the enhanced spatial resolution allows to map the confinement of associated near-fields.

The above considerations are now embedded in a more formal context in order to shortly discuss which information can be retrieved in the experiments presented in Section 1.5.4. First, it is recalled from Section 1.3.2 that under homogeneous light irradiation the local electric field $\mathbf{E}_{loc}(\mathbf{r},t)$ at a specific position $\mathbf{r}$ on the sample surface is given by

$$\mathbf{E}_{loc}(\mathbf{r},t) = \mathscr{F}^{-1}\left\{\mathbf{R}(\mathbf{r},\nu)E_L(\nu)\right\}, \tag{1.30}$$

in which $E_L(\nu)$ is the complex spectral amplitude of the laser pulse, $\mathbf{R}(\mathbf{r},\nu)$ the complex spectral response function at $\mathbf{r}$ related to the specific excitation geometry and $\mathscr{F}^{-1}$ the inverse Fourier transformation. According to the plasmon-assisted multi-photon photoelectron emission model of Merschdorf and co-workers [210] the local probability for photoelectron emission can be approximated as a transition rate that depends on the local electric field intensity:

$$\mathscr{P}_{loc}(\mathbf{r},t) \propto \left(\mathbf{E}_{loc}(\mathbf{r},t)\right)^{2N} = I_{loc}(\mathbf{r},t)^N, \tag{1.31}$$

in which N is the number absorbed photons. The coherent character of the electronic system can be neglected since dephasing of intermediate electronic states takes place instantaneously due to the continuous electronic band structure above the Fermi energy of metals [314]. This can be envisioned as the elution of the overall interference pattern in a double-slit experiment in which a broad-band light source is utilised. Since the detection device in a PEEM experiment is much slower than optical frequencies of some hundred THz the local yield $Y_{loc}(\mathbf{r})$ is calculated by integrating (1.31) over time:

$$Y_{loc}(\mathbf{r}) \propto \int_{-\infty}^{\infty} \left(I_{loc}(\mathbf{r},t)\right)^N dt = \int_{-\infty}^{\infty} \left(\mathscr{F}^{-1}\left\{\mathbf{R}(\mathbf{r},\nu)E_L(\nu)\right\}\right)^{2N} dt, \tag{1.32}$$

Equation (1.32) might imply at first sight that a pump-probe geometry facilitates to directly image the temporal evolution of plasmonic excitations in the system. However, the outcome of such an experiment is quiet more complex which gets clear by substituting the spectral amplitude of a single laser pulse $E_L(\nu)$ with the spectral amplitude $E_{PP}(\nu,T)$ of a pump-probe geometry, i.e.:

$$E_{PP}(\nu,T) = \left[E_L^+(\nu)+E_L^-(\nu)\right] + \left[E_L^+(\nu)\mathrm{e}^{\mathrm{i}2\pi\nu T} + E_L^-(\nu)\mathrm{e}^{-\mathrm{i}2\pi\nu T}\right], \qquad (1.33)$$

in which T is the temporal pulse delay. By inserting the laser field (1.33) into (1.32) the local photoelectron yield can be written as:

$$Y_{loc}(\mathbf{r},T) \propto \int_{-\infty}^{\infty} \left(E_{loc}(\mathbf{r},t) + E_{loc}(\mathbf{r},t-T)\right)^{2N} dt, \qquad (1.34)$$

Hence, the photoelectron yield is determined by the interference of the local electric fields excited by the pump and the probe pulse. In specific cases $Y_{loc}(\mathbf{r},T)$ might give a first clue of plasmon dynamics but should in general not be confused with $(E_{loc}(\mathbf{r},t))^{2N}$. A more reliable interpretation of $Y_{loc}(\mathbf{r},T)$ in TR-PEEM experiments is feasible if a concrete physical model is applied to the response function $\mathbf{R}(\mathbf{r},\nu)$ which is further supported by excluding other models through argumentation [6, 4, 5]. This approach is also applied to the TR-PEEM experiments in this thesis since it has been shown in Section 1.4.2 via FDTD simulations that the LSPs of WGM antennas couple to the SPP cavity mode and the collective dynamics of the plasmonic excitation was sufficiently described by an analytic model of three coupled oscillators. Here, it should be mentioned that the single particle dynamics, e.g. the energy dependent life-time of excited electrons, is not considered in contrast to [210], since a quantitative fitting of the temporal evolution is not be pursued.

Detailed setup

The most important devices of the experimental setup are shown in Fig. 1.28(a): The photoelectron emission microscope is the FOCUS IS-PEEM ([174, 68, 69], see the thesis of Christian Schneider for an elaborate description [267]). The sample, mounted in an ultra-high vacuum chamber, can be excited by a laser in two different geometries: under grazing incidence (GI, 65° to surface normal of the sample) and under normal incidence (NI, 4° to surface normal of the sample), as sketched in the inset of Fig. 1.28(a). The NI-geometry is made possible by the reflection of the laser beam from a rhodium mirror (2 mm × 2 mm) which is positioned close to the electron beam. It features broad-band high reflectivity

for s- and p-polarised light. Although the NI-geometry is slightly offset from the electron optical axis by 4° the polarisation of the incoming beam lies almost completely parallel to the sample surface and hence facilitates to excite the m_1-mode of WGM antennas. The GI-geometry with p-polarised light provides a dominant polarisation component perpendicular to the sample surface and hence this configuration facilitates to excite the m_0-mode of WGM antennas. In NI-geometry the focus spot size is about 50 μm (e^{-2}-diameter, see Fig. 1.28(b)) and the resolution of the PEEM image can be optimised to ≈ 50 nm (the supplementary information [6]).

The light source in the experiments is a Ti:sapphire laser oscillator (SHORT PULSE TSUNAMI, SPECTRA PHYSICS, 80 MHz repetition rate, < 30 fs laser pulses at $\lambda_0 = 800$ nm). When the laser beam arrives at the optical table of the experiments it is actively stabilised with the TEM MESSTECHNIK BEAMLOK 4D system so that no beam pointing fluctuations occur during the measurements. Then, two options exist for time-resolved measurements which can be selected with a beam splitter: In previous experiments of the collaboration the temporal and spatial control of optical near-fields was investigated with a pulse shaper [3] which also allows to shape pulse sequences for time-resolved experiments and multi-dimensional spectroscopy [6]. Due to the geometry of the pulse shaper and the size of the liquid crystal display the band-width limited pulse duration is about 55 fs. A second scheme with much shorter pulses (≈ 20 fs) can be implemented by using the direct output of the Ti:sapphire oscillator and by directing the beam through a phase-stabilised Mach-Zehnder interferometer to create a pulse sequence of variable delay T. The temporal duration of the laser pulses was determined with the FROG method (frequency-resolved optical gating [296]) in front of the PEEM where both beams can be picked out with a beam splitter. Additionally, the spectrum of both laser beams were recorded with a spectrometer. It has to be noted that the spectrum of the broad-band laser pulse (dark-shaded area in Fig. 1.28(c)), now labelled by the abbreviation *SP*, has been fitted by two Gaussian functions because the spectrometer detection range was too small to record the entire spectral intensity. However, the result is in agreement with the spectrum that can be measured with a different spectrometer in the vicinity of the Ti:sapphire oscillator in the laser laboratory. The small-band spectrum of the pulse shaper (light-shaded area in Fig. 1.28(c)), now labelled by the abbreviation *LP*, was used

to identify the parameters of WGM antennas which are resonant near 375 THz (see Section 1.5.3). The *SP* pulses are then used to observe the collective dynamics in the composite antenna-cavity systems since the broad-band spectrum gives a better chance to excite the entire response function (see Section 1.5.4).

Laser pulses are then focused with a lens onto the sample. The glass window of the UHV chamber introduces a chirp which is pre-compensated with a prism-compressor (not shown here). For time-resolved experiments the GI-geometry with p-polarised laser pulses is selected because of the pronounced electric field component that oscillates perpendicular to the sample surface (Fig. 1.28). In Section 1.2 it was shown that the m_0-mode of the specific WGM antenna can be predominantly excited from far-field at an incident angle of $\approx 65^\circ$ (see Fig. 1.8). This perfectly fits to the PEEM setup of the experiments. Another benefit of the GI-geometry is that the laser pulses mainly excite one of the antennas while the other one is screened from the incoming radiation by the cavity wall. Hence, this antenna is labelled *shaded* and the directly excited antenna *excited*. This excitation geometry approximately reflects the configurations of FDTD simulations in which one of the antennas was initially excited to mimic the situation of coupled pendulums in the introduction (Fig. 1.1).

1.5.3 Compliance of antenna resonances and FDTD simulations

An array of WGM antennas with different radii and groove depths was written into a gold microplate with FIB at the NSC in Kaiserslautern in order to demonstrate the addressability of different WGM antenna modes in NI- and GI-geometry and to retrieve the geometrical parameters for the particular m_0-mode. The subsequent PEEM experiments were performed by Philip Thielen, Martin Piecuch and the thesis author.

A PEEM image of the antenna array recorded in NI-geometry and with the *LP* laser spectrum ($\nu_0 = 374.4$ THz) is shown in Fig. 1.29(a). The ring radii in the array range from 75 nm to 350 nm in 25 nm steps (vertical axis) and the groove depth is increased from 50 nm to 200 nm in 10 nm steps (horizontal axis). To facilitate photoelectron emission upon laser irradiation the work function of gold

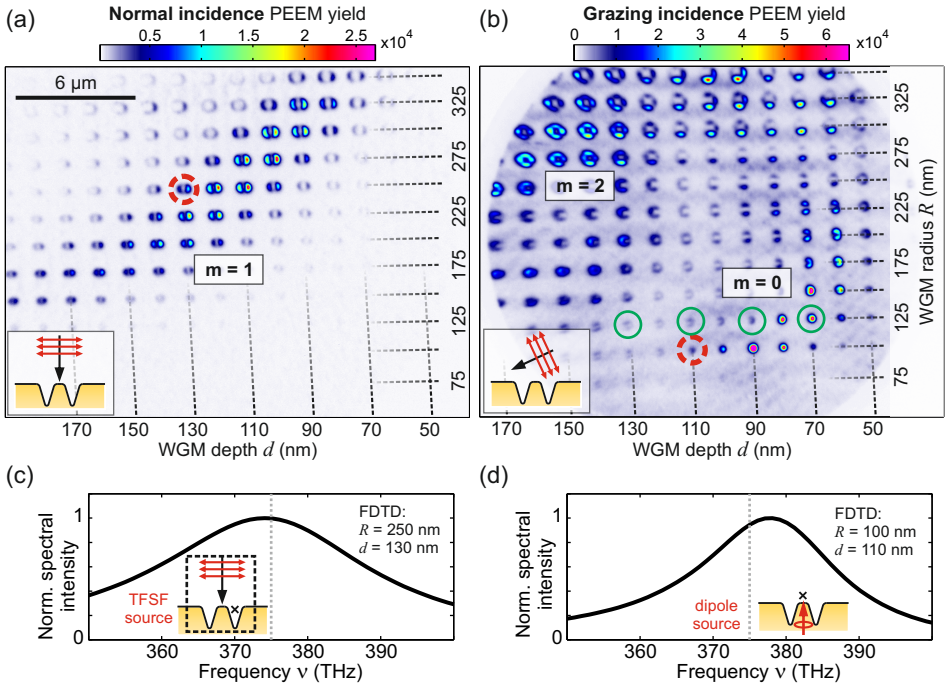

Fig. 1.29: Experimental demonstration of selecting various WGM antenna modes in an antenna array by using grazing and normal incidence with PEEM. The array provides WGM antennas of different radii (vertical direction) and groove depth (horizontal direction), and the work function of the single-crystalline Au microplate was lowered by cesiation. (a) NI-geometry: The polarisation of the incoming laser is mainly parallel to the substrate. An electron emission band indicates a $m = 1$ resonance showing the characteristic lobes. (b) GI-geometry: The laser hits the sample under 65° therefore providing electric field components perpendicular to the substrate. The region of resonant $m = 2$ and $m = 0$ excitation are indicated. Additionally, the periodic structure of the antenna array serves as a grating coupler for SPPs (see horizontal electron emission lines). Green circles indicate antennas that are used in hybridisation experiments. (c) and (d) FDTD simulations for comparison: The presented spectral intensity $|\mathbf{R}(\nu)|^2$ refers to respective positions marked by the black cross. Antennas of the same parameters are indicated by red-dashed circles in the WGM antenna array.

was lowered by vapour deposition of caesium. The work function is reduced in this case since alkali metals adsorbed on metal surfaces induce an electric dipole at the interface [159]. The photoelectron emission yield shows a systematic behaviour: There is hardly any photoelectron emission from WGM antennas with large radius and large groove depth. The same holds for antennas with small radius and small groove depth. However, between those two extremes there is an ideal relationship

between radius and groove depth leading to an enhanced electron yield along a band spanning from the lower left corner of the array to the upper right corner. The highest electron yield is found for WGM antennas in the middle of this band with a radius around $R = 250$ nm and a depth of $d = 110$ nm. The emission pattern of each antenna shows lobes at opposite groove sides and the lobes are in line with the incident p-polarised electric field oscillations projected onto the substrate. Due to this specific emission characteristics and the fact that resonances lead to enhanced near-fields, and hence to an increased electron yield according to (1.29), it can be inferred that the associated antenna parameters support the $m = 1$ mode (compare Fig. 1.4(c)).

This conjecture is verified by the FDTD simulation shown in Fig. 1.29(c): A plane wave (TFSF source) excites a WGM antenna with $R = 250$ nm and a depth of $d = 130$ nm under normal incidence and the frequency dependent near-field intensity $|\mathbf{R}(\nu)|^2$ is recorded inside the groove (black cross). The spectral intensity shows a clear resonant behaviour and peaks near $\nu = 375$ THz (grey-dashed line). The antenna with the corresponding parameters in the experiment is marked by the red-dashed circle in Fig. 1.29(a). Obviously, the prediction of FDTD simulations is quite accurate. Small deviations are attributed to the particular shape of the upper groove edges: FDTD simulations suggest that for a groove depth of 130 nm no pronounced near-fields exist at the groove bottom and hence the radial mode number n is not well-defined, i.e. the CPP is pushed out of the groove and is bound to the upper groove edges in the form of a WPP [216].

The photoelectron emission of the same WGM antenna array, but now illuminated in GI-geometry, is presented in Fig. 1.29(b). Interestingly, the trend of the emission pattern has changed: There is hardly any photoelectron yield from WGM antennas featuring the $m = 1$ resonance at normal incidence. In contrast to that the photoelectron emission is enhanced for antennas with large radii and large depth, or for antennas with small radii and more shallow grooves. In the case of large radii the specific antenna emission pattern of four lobes around the groove clearly indicates a quadrupole, i.e. a $m = 2$ resonance, which is most efficiently excited at $d = 150$ nm and $R = 300$ nm. The quadrupole resonance can be excited from far-field because the incident angle of 65° breaks the NI-symmetry and the p-polarised light exhibits an appreciable field component perpendicular to the substrate.

It is exactly this field component that also facilitates a far-field excitation of the m_0-mode of WGM antennas (see Fig. 1.10). The systematic enhancement of electron yield at small radii and shallow grooves is therefore attributed to a resonant excitation of the radial symmetric mode. A resonant behaviour at a specific laser frequency is presumed because the photoelectron emission signal of antennas with constant radii increases with groove depth until a certain depth is reached, and then the signal fades away by further increasing the groove depth. If the near-field enhancement was attributed to a simple lightning-rod effect, like in the case of sharp nano-tips, the electron yield would further increase with increasing groove depth. Or, at least, it would not decline that fast. The existence of the m_0-mode resonance is corroborated by FDTD simulations in Fig. 1.29(d): A dipole source excites a WGM antenna with radius $R = 100$ nm and groove depth $d = 110$ nm and the near-field intensity $|\mathbf{R}(\nu)|^2$ is recorded 10 nm above the antenna mesa centre (black cross). A clear resonant behaviour can be observed and the utilised parameters lead to a maximum field enhancement near 378 THz. The corresponding antenna parameters suitably lead to a slightly enhanced electron emission in the experiment (red-dashed circle in Fig. 1.29(b)). However, maximum electron emission is reached with a reduced groove depth of 20 nm. Despite this deviation the compliance of antenna resonances and FDTD predictions is rated very good since the m_0-mode resonance is extremely sensitive to the groove depth, especially when no proper radial mode n exists and near-fields interact across the small antenna-mesa: It was found with FDTD simulations that changing the depth from $d = 100$ nm to $d = 130$ nm, at a constant radius $R = 100$ nm, drastically shifts the resonance frequency from $\nu = 340$ THz to $\nu = 400$ THz (not shown here).

The remaining measuring field in Fig. 1.29(b) is commented in short: There seems to be a $m = 1$-mode at $R = 225$ nm and $d = 70$ nm which has its lobes oriented in vertical direction and hence perpendicular to the incident light polarisation. It has to be noted that the enhanced electron yield is not attributed to the direct excitation of a resonant mode. In contrast, the periodicity of the WGM antenna array seems to facilitate the excitation of a standing SPP pattern due to grating coupling: The photoelectron yield shows a structure of horizontal, equally spaced lines with small signal amplitude. At the aforementioned position the WGM antennas are located in a node of this pattern and only the opposite groove sides interact with the plasmonic excitation. This effect is even more pronounced

for WGM antennas with a radius of $R = 325$ nm and a depth ranging from 60 nm to 100 nm. Hence, care must be taken when interpreting photoelectron emission data of WGM antenna arrays in the grazing incidence geometry.

Selecting antennas for the cavities

The PEEM experiments on WGM antenna arrays serve to find the geometrical parameters for the m_0-mode resonance in the vicinity of $\nu = 375$ THz. However, it is not possible to examine the arrays and to remove them from the PEEM in order to write antennas into the cavities during an additional FIB session. When the sample is removed from the UHV chamber the caesium on the surface tends to form clots that irreversibly contaminate the Au surface for further treatment. Caesium may be desorbed by sample heating but this treatment also tends to melt and smear out fine nanostructures. Therefore the FIB performance is gauged.

The procedure is as follows: Six WGM antennas with a constant radius and varying groove depth are written with FIB on a free area of the lower single-crystalline microplate. The gallium ion beam is operated at rather low intensities ($41.66\ \mu\mathrm{C\ cm^{-2}}$) and single annular grooves are milled in repetitive steps called *loops* so that the depth can be precisely controlled. The number of loops varies from 100 to 1100 in steps of 200 for the six antennas. Then they are covered with a protecting platinum layer by using ion beam-induced deposition. Subsequently, the gallium ion beam of the FIB cuts through the antenna structures as well as through the entire microplate so that the axial cross-section of the grooves is disclosed and can be imaged with the SEM column tilted by 52° (see Fig. 1.4(a) for instance). This procedure allows to retrieve a linear relationship between the number of FIB loops to the groove depth, which amounts to 100 loops for every 16 nm. It can be ensured that antenna resonances are not severely shifted by checking this ratio before the WGM antennas are incorporated into the cavities. See the diploma thesis of Benjamin Frisch for more details [109].

Despite this gauge procedure the m_0-mode of a WGM antenna is still quite sensitive to deviations of geometric features and it has been observed that the emission band of the radial symmetric mode can vary by two or three columns in Fig. 1.29(b) on different microplates: Therefore, four different nominal groove depths have been selected at a constant radius of $R = 125$ nm; the corresponding

antennas are marked by green circles. Pairs of WGM antennas are then written with FIB milling in an alternating order into the elliptic cavities shown in Fig. 1.27(b). Since the cavities only vary by 10 nm in major axis size and the related shift of the resonance frequency is expected to be small there is an appreciable chance to find at least one composite system in which antenna and cavity resonances are matched.

1.5.4 Demonstration of LSP-SPP hybridisation with time-resolved PEEM

In this section the coherent and periodic long-range energy transfer between two WGM antennas, incorporated in elliptical plasmonic arena cavities, is demonstrated with TR-PEEM. First experiments were performed during a two weeks long measurement campaign with the sample shown in Fig. 1.27(a) at the TU Kaiserslautern. The campaign was a collective effort from the working group of Martin Aeschlimann at the TU Kaiserslautern (Philip Thielen, Martin Piecuch and Benjamin Frisch), the working group of Tobias Brixner at the University of Würzburg (Christian Kramer and Bernhard Huber) and the working group of Walter Pfeiffer at the University of Bielefeld (thesis author). These first experiments utilised the pulse shaper and the *LP*-spectrum. Although indications of hybridisation have been identified a detailed analysis was hardly possible since the small-band spectrum only probes a minor part of the response function. The results that will be presented in this section were obtained by Benjamin Frisch at the same sample position by using the broad-band *SP*-spectrum and the phase stabilised Mach-Zehnder interferometer after the measurement campaign was over. Evaluation and model fitting of the TR-PEEM data was performed by the thesis author.

Time-integrated PEEM

A PEEM image of the cavity-antenna system investigated in GI-geometry is shown in Fig. 1.30(a). The field of view is linked to the area marked by the white rectangle in Fig. 1.27(b) and the cavity in the centre (shape marked by black-

dashed line) is the $E14$ cavity with a major axis size of $a = 2110$ nm and a minor axis size of $b = 1450$ nm. The sample region in the vicinity of the $E14$-cavity appeared to be most interesting because some cavities showed a nano-localised electron emission at both of their focal spots although one antenna is mainly shaded by the cavity wall. Furthermore, FDTD simulations of the elliptic cavity reveal a resonant $(4,1)$-mode at $\nu = 375$ THz for a major axis size of 2092 nm (see Fig. 1.22) which is close to the $E14$ geometry.

Here, it is recalled that different types of antennas have been written into different cavities: $E13$ and $E15$ are both equipped with WGM antennas of radius $R = 125$ nm and depth $d = 70$ nm (labelled A_{70}^{125}) and the cavity $E14$ is equipped with WGM antennas of radius $R = 125$ nm and depth $d = 90$ nm (labelled A_{90}^{125}). While there is an appreciable nano-localised photoelectron emission at the focal spots of $E14$, hardly any electron yield is obtained from the adjacent cavities. This behaviour turns out to be systematic: The $F14$ system which exhibits the same major and minor axis size as $E14$ also shows hardly any photoelectron emission like $E13$ and $E15$ (not shown here). The only difference between the bright $E14$ system and the dark $F14$ system is that the latter one incorporates the WGM antennas A_{110}^{125} which exhibit 20 nm deeper grooves than the antennas in $E14$. Interestingly, $E12$ and $E16$ are equipped with the same antennas as $E14$ and both cavities provide an appreciable photoelectron emission near the focal spots, similar to the $E14$ system (not shown here).

The stark contrast in photoelectron emission of the different systems in GI-geometry cannot be explained by a lightning-rod effect which occurs near sharp nanostructures because there is no reason why the A_{90}^{125}-antenna should be distinguished from the other antennas. This was checked by changing the excitation geometry to normal incidence. In the NI-geometry the electric field polarisation is parallel to the substrate and the m_0-mode cannot be addressed. Without exception, all cavities show a pronounced photoelectron emission near their focal spots and the different systems cannot be distinguished, as expected in the case of non-resonant near-field enhancement. It is also implausible that the stark contrast in photoelectron emission under GI illumination is linked to the excitation of the pure m_0-mode of A_{90}^{125}: With view to Fig. 1.29(b) (linear colour scale) it is expected that at least the adjacent antennas A_{70}^{125} (more shallow) or A_{120}^{125} (deeper grooves) would show a noticeable electron yield on the logarithmic colour scale

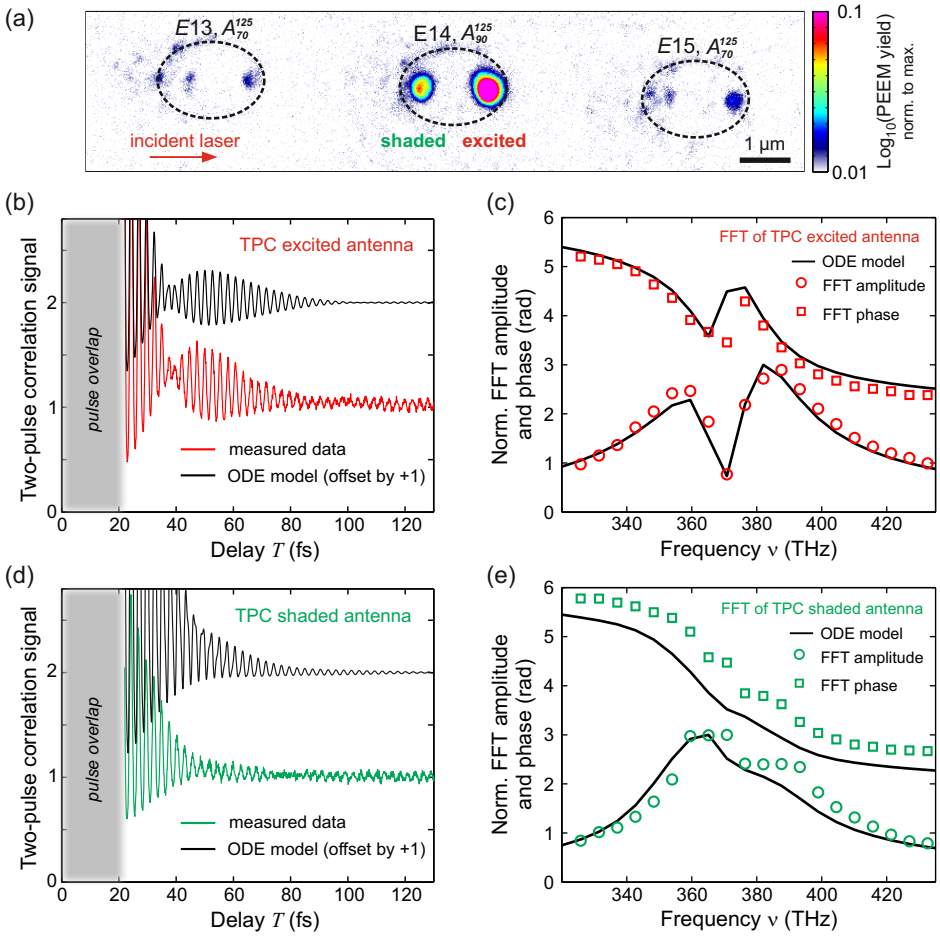

Fig. 1.30: TR-PEEM experiments. (a) Static PEEM image (GI-geometry) of the region of interest marked by the white dashed-rectangle in Fig. 1.27(b) showing the EPACs $E13$, $E14$ and $E15$. The radius and the groove depth of incorporated antennas A are indicated by upper and lower subscripts. (b) and (d) Measurements conducted by Benjamin Frisch: Integrated (30×30 pixels) time-resolved electron yield averaged over five subsequent measurements at the excited and shaded antenna of $E14$. The time step of the phase-stabilised Mach-Zehnder interferometer was set to 0.2 fs and data is normalised to the base-line value. The non-linearity of the photoelectron emission process was determined to be $N = 2.2$. (c) and (d): FFT of the TR-PEEM data at the fundamental frequency component. All black lines correspond to the ODE model of three coupled oscillators with a partial excitation of the shaded antenna (see main text), and the photoelectron yield is calculated according to equation (1.34). Manually set parameters: $\nu_{0,ex} = \nu_{0,c} = \nu_{0,sh} = 370.8$ THz, $\gamma_{ex} = \gamma_{sh} = 78.4$ THz, $\gamma_c = 22.3$ THz, $\kappa = 0.16$ rad^2 fs^{-2}, $\alpha = 0.89$, $\phi = \pi/10$.

of Fig. 1.30(a). Hence, it is inferred that the combination of the cavity $E14$ and the WGM antenna A_{90}^{125} leads to an appreciable hybridisation so that the larger Q-factor of the cavity resonance is imprinted onto the antenna resonance leading to enhanced near-fields and photoelectron emission. This statement is now closer examined with TR-PEEM experiments.

TR-PEEM experiments

The TR-PEEM data of the $E14$ system from the region shown in Fig. 1.30(a) was provided by Benjamin Frisch. He used the Mach-Zehnder Interferometer and the SP-spectrum and recorded PEEM images for pulse delays of $T = 20$ fs to $T = 300$ fs with a step size 0.2 fs. Omitting the first 20 fs, i.e. the period of pump and probe overlap, serves to exploit the dynamical range of the CCD camera in order to observe plasmonic dynamics. The delay dependent photoelectron yield at the directly excited and shaded antenna was retrieved for data evaluation by integrating the signal at the respective positions in a region of interest of 30×30 pixels. The experiment was repeated without interruption for five times to improve data quality. The five different 1D-signal traces at both antennas were added up by the thesis author and it was checked that no artefacts occur due to shifted traces.

The two-pulse correlation (TPC) signal at the excited antenna is represented by the red curve in Fig. 1.30(b) while the TPC for the shaded antenna is shown by the green curve in Fig. 1.30(d). Both curves are normalised to the respective TPC signal at large delay times T so that the baseline takes the value 1. The amplitudes of the TPCs are asymmetric with respect to the baseline and the peak-to-baseline ratio is slightly larger than $8:1$ at $T = 0$ for the excited antennas. This fits to the order of the multi-photon photoelectron emission process which was determined to be $N = 2.2$ by measuring the power dependent electron yield at WGM antenna arrays.

The TPC of the excited antenna shows a striking feature: After the signal has declined to a minimum value at a delay of $T = 40$ fs a revival occurs and the TPC signal increases once again to culminate at $T = 50$ fs, although pump and probe pulse are considerably separated in time. This behaviour reflects the experimental results of Aeschlimann and co-workers on a corrugated silver surface, as shown in Fig. 1.2(b). Here, the beating of the TPC envelope is interpreted in a similar

fashion: Due to the presence of the cavity, plasmonic energy is refocused at the initially excited antenna. This leads to an enhanced photoelectron emission. In contrast to that the TPC of the shaded antenna is rather featureless. There are faint indications of nodes in the envelope of the signal at $T = 45$ fs and $T = 80$ fs but the overall amplitude is quite small for delay times larger than 40 fs.

As explained earlier the interpretation of the temporal evolution of the non-linear TPC signal is usually not straight forward according to equation (1.34). Thus the model of three coupled oscillators, developed in Section 1.4.2, is applied to reproduce the measured data. The spectral response functions of the excited antenna and the shaded antenna, i.e. $R_{ex}(\nu)$ and $R_{sh}(\nu)$, are retrieved via equation (1.26). In order to simulate the TPC signal, $R_{ex}(\nu)$ and $R_{sh}(\nu)$ are multiplied with the double pulse sequence E_{pp} in equation (1.33) in which the spectral amplitude $E_L(\nu)$ is represented by the measured *SP*-spectrum (dark-shaded area in Fig. 1.28(c)). By applying a fast Fourier transformation the delay dependent electron yield can be calculated via (1.34) in which the non-linear order is set to $N = 2.2$, according to power law measurements.

It is important to know that the excitation vector $(1,0,0)^{\mathrm{T}}$ is replaced by the more refined excitation $(\alpha,0,(1-\alpha)\mathrm{e}^{\mathrm{i}\phi})^{\mathrm{T}}$. Here, $\alpha \in [0,1]$ is an amplitude ratio and ϕ introduces a relative phase between the entries. The non-zero third entry lifts the dark-mode character of the shaded antenna and allows for a direct excitation by the incoming laser pulse sequence. A direct excitation might occur due to diffraction of light at the upper cavity edge. To keep the model as simple as possible the relative strength of the excitation α as well as the relative phase ϕ are assumed to be independent of frequency. Using this excitation condition the new response functions of the TPC simulation read:

$$\begin{aligned} R_{ex}(\nu) &= \alpha K_{11} + (1-\alpha)K_{13}\mathrm{e}^{\mathrm{i}\phi} \\ R_{sh}(\nu) &= \alpha K_{31} + (1-\alpha)K_{33}\mathrm{e}^{\mathrm{i}\phi}, \end{aligned} \tag{1.35}$$

It is noted that ϕ has different signs for positive and negative frequencies and that the frequency-dependent K-coefficients are not given in detail for reasons of brevity.

Since the TPC signals contain a lot of sampling points the problem is reduced to a small number of data points by applying a FFT to the measured and simulated

TPC signals. The simulated time signals as well as the corresponding FFT data near the fundamental frequency are shown as black curves in Fig. 1.30(b,d) and Fig. 1.30(c,e), respectively, and they are labelled *ODE model*. The curves have been simulated with the following parameters:

$$\begin{aligned} \nu_{0,ex} = \nu_{0,c} = \nu_{0,sh} &= 370.8 \text{ THz} \\ \gamma_{ex} = \gamma_{sh} &= 78.4 \text{ THz} \\ \gamma_c &= 22.3 \text{ THz} \\ \kappa &= 0.16 \text{ rad}^2 \text{ fs}^{-2} \\ \alpha &= 0.89 \\ \phi &= \pi/10, \end{aligned} \tag{1.36}$$

in which the subscripts *ex*, *sh* and *c* denote the excited and shaded antenna mode and the cavity mode, respectively. The above parameters were manually determined by the thesis author and it was found by Christian Kramer that it is difficult to apply fitting algorithms with view to convergence and fit results. Despite the manual adjustment the above parameters nicely resemble the measured data. Especially the anti-node of the TPC signal at the excited antenna (Fig. 1.30(b)) is accurately modelled with respect to oscillation amplitudes and phasing. This is reflected by the corresponding FFT data in Fig. 1.30(c): The dip in the spectral amplitude of the ODE model and the associated modulation depth in the phase coincide with the measured data. In the case of the shaded antenna (Fig. 1.30(d)) also the shoulder in the spectral amplitude is reproduced in the range of 375 THz to 400 THz. This shoulder is of particular interest since its existence is based on the partial excitation of the shaded antenna. The chosen values of α and ϕ force the TPC signal in time-domain (Fig. 1.30(d)) to decline faster so that a kink occurs near $T = 45$ fs. Otherwise the TPC amplitude would be much higher and would decline slower. This approach appears to be justified when taking into account the rather weak excitation of the shaded antenna.

The decay constants of the cavity mode and the antenna mode are equal or higher than those retrieved from FDTD simulations (compare to (1.22) and (1.8)). This seems to be realistic with respect to the findings of Section 1.3.3 and Section 1.4.2 that the peaks of the hybridised modes appear more narrow-band in FDTD simulations compared to those of spectral response functions retrieved from the

ODE model and the parameters of the single constituents. Using smaller values for γ and hence longer life-times results in more pronounced features in the spectral phase of the FFT signals. The resonance frequencies of the single systems have been fixed to the same value of $\nu_0 = 370.8$ THz. This congruence is reliable since the measured spectrum used for the calculation of the local electric fields is also fixed and shifting the resonance frequencies of the antennas or the cavity would crucially shift the features of the amplitude and phase of FFT signals in Fig. 1.30(c,e). Moreover, the $E14$ cavity exhibits a slightly larger major axis than the cavities used in FDTD simulations which showed a resonant behaviour at 375 THz. A red-shift by 5 THz in the experiments is hence conceivable.

By gathering all evidence of the experimental data and by considering that the ODE model facilitates to mimic measured TPC signals with realistic parameters it can be claimed that for the first time a prearranged coherent and periodic energy transfer between widely separated nano-antennas has been successfully demonstrated.

Retrieved response functions and electric field reconstruction

Having a set of reliable parameters for the model of three coupled oscillators at hand, the temporal dynamics of plasmonic excitation can be visualised by filtering the retrieved response functions at the excited antenna $R_{ex}(\nu)$ and at the shaded antenna $R_{sh}(\nu)$ with the measured *SP*-spectrum. The absolute square of the response functions related to (1.36) are depicted in Fig. 1.31(a). The splitting of the outer normal modes is symmetric with respect to the centre frequency $\nu_0 \approx 370$ THz of the single constituents and amounts to 16.6 THz (68.7 meV) at the directly excited antenna (red solid curve). In contrast to that the absolute square of the response function of the shaded antenna exhibits an asymmetric spectral shape and its spectral weight is located at lower frequencies. It was verified that the asymmetric shape is a consequence of the partial excitation: Interestingly, a similar effect can be observed when looking at the response function retrieved from FDTD simulations in which the LQ-cavity system of Section 1.4.2 is illuminated by a plane wave source at an incidence angle of 40°.

The response function $|R_{ex}(\nu)|^2$ was experimentally investigated by Benjamin Frisch. He used a short pulse laser system with variable centre frequency (MAITAI

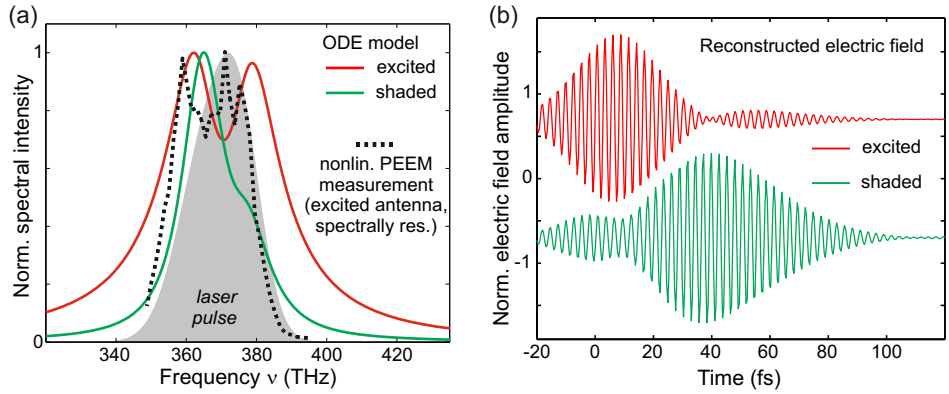

Fig. 1.31: Corroboration of experimentally retrieved response functions and electric field reconstruction. (a) Response functions $|R_{ex}(\nu)|^2$ (red curve) and $|R_{sh}(\nu)|^2$ (green curve) calculated according to equation (1.35) with the parameters of (1.36). The resonant behaviour in the vicinity of $|R_{ex}(\nu)|^2$ is corroborated by spectrally-resolved PEEM at the excited antenna (black-dashed curve) with a tunable laser oscillator (MAITAI HP from SPECTRA PHYSICS, experiments performed by Benjamin Frisch). The Data is non-linear according to N =2.2. The grey shaded area is the SP-spectrum used for reconstruction of the electric field oscillations that lead to the TR-PEEM data in Fig. 1.30. (b) Reconstructed field at the excited antenna (red) and shaded antenna (green) according to the SP-spectrum and the retrieved response functions in part (a).

HP, SPECTRA PHYSICS, 80 MHz repetition rate, 140 fs laser pulses, tuneable from 690 nm to 1040 nm) and recorded the photoelectron yield at the excited antenna in the $E14$ system while tuning the laser through the spectral resonance. The laser power was kept constant in front of the PEEM at all centre frequencies. The result is shown in Fig. 1.31(a) as a black-dashed line: Strikingly, the photoelectron emission is greatly enhanced in the spectral window in which $|R_{ex}(\nu)|^2$ was retrieved by the combination of TR-PEEM experiments and the ODE model. The enhanced photoelectron emission implies the existence of a resonance and the non-uniform shape suggests a contribution of several constituents, therefore corroborating the hybridisation hypothesis of TR-PEEM experiments. An interpretation of the detailed structure and peak heights is difficult due to the non-linear character of the experiment and the included convolution with the excitation spectrum. Here, the data is represented as-measured with $N \approx 2.24$. By taking the square of the peak structure the shape will broaden and hence an even better qualitative agreement with the ODE model is achieved.

The temporal electric field has been reconstructed by multiplying $R_{ex}(\nu)$ and

$R_{sh}(\nu)$ with the spectral amplitude of the measured *SP*-spectrum and applying a FFT to the data. The results are presented in Fig. 1.31(b): First, field oscillations increase at the excited (red) and shaded (green) antenna since also the shaded antenna is partially excited at the beginning. While the field energy at the excited antenna further increases the field oscillations at the shaded antenna are suppressed and reach a local minimum at $t \approx 10$ fs. Then, the electromagnetic energy leaves the excited antenna and the field oscillations at the shaded antenna are no longer restrained and reach a maximum at a time instant at which the excited antenna shows a node in the electric field envelope. Finally, the electromagnetic energy returns to the directly excited antenna. Bearing in mind that the temporal behaviour is retrieved from an experiment, in combination with an approved analytical model, it is stated that for the first time a coherent back-and-forth transfer of energy between a localised surface plasmon resonance and an extended surface plasmon has been demonstrated. The coherent character of this process is emphasised by the temporarily suppression of field oscillations at the shaded antenna at the expense of increasing field oscillations at the excited antenna. Such an effect has also been observed in FDTD simulations in the LQ-cavity system when using plane wave excitation and the narrow-band excitation parameters.

1.6 Summary and outlook

For the first time ever a prearranged strong coupling of single localised surface plasmons (LSPs) and a plasmonic cavity mode was demonstrated in theory, i.e. finite-difference time-domain (FDTD) simulations and an analytical model of coupled oscillators (ODE), and experiment, i.e. time-resolved photoelectron emission microscopy (TR-PEEM). Plasmonic whispering gallery mode (WGM) resonators [305, 304, 306] were utilised as nano-antennas for LSPs while pits of circular and elliptical shape [335, 268] served as cavities for propagating surface plasmon polaritons (SPPs). Confinement of plasmon modes inside the cavities is facilitated by using the upright metallic pit walls of some hundred nanometre height as cavity mirrors. In the case of elliptic cavities, light concentration at the focal spots lead to an enhanced interaction between WGM antennas placed

there and the common cavity mode, hence facilitating a coherent energy transfer between the widely separated nano-antennas

The cavity character of WGM nano-antennas and the $m = 0$ operation mode provide a suitable trade-off between nano-localised electric fields and comparatively low dissipation. Rather high Q-factors of ~ 27 occur due to impeded far-field coupling; this allows for elongated interaction times with surface plasmons inside the cavity. The selective excitation of this mode under inclination angles of 60° perfectly fits to the utilised PEEM setup. Furthermore, their small mode size and radial mode symmetry are perfectly suited for surface plasmon injection in the hot-spots of extended, but confined, surface plasmon modes.

Using FDTD simulations, the incorporation of a single antenna in the centre of non-detuned circular plasmonic cavities of high quality ($Q > 100$), and of different size, lead to a mode splitting of Δ of 15 THz - 32 THz at centre frequencies of $\nu = 375$ THz. The newly emerging modes were attributed to hybridisation according to mode-dependent near-field distributions and according to the applied ODE model which provides the coupling strength as the only free parameter. This mode splitting is comparable to that of an SPP interacting with many LSPs of a nano-disc array ($\Delta = 30$ THz) [66]. Therefore, the cavity approach makes the large number of nano-antennas redundant. The splitting found here is also comparable to nanoscale systems like dolmen structures ($\Delta = 40$ THz) [331, 193].

It was then found with FDTD simulations that cavities of elliptical shape and an eccentricity of about $e \approx 0.71$ feature SPP mode patterns that provide two lobes of enhanced field strength near the geometrical focal spots. Inserting WGM antennas in the respective spots, lead to a strong mode splitting of $\Delta = 23$ THz that is independent of cavity wall height and hence the amount of dissipation. The spectral features of the overall three normal modes were qualitatively described with a modified ODE model in which the two LSP modes couple indirectly via the cavity mode. Therefore, the composite system and its description resemble the quantum mechanical Tavis-Cummings (TM) model. However, the dissipationless TM model failed in providing a hand-waving explanation for the temporal dynamics of plasmonic excitations inside the cavity upon spectrally filtering specific modes: A periodic energy transfer from one antenna to the opposite one is only observed when the dissipation of the antennas and the cavity are matched. Otherwise both antennas are excited simultaneously and exchange energy with the

cavity in a synchronised fashion. This behaviour was reproduced with the ODE model. As a consequence the composite system obeys the universal phenomenon of impedance matching.

The elliptical cavities have been fabricated for experiments by using single-crystalline and atomically flat gold microplates. A microplate perforated with elliptical holes was mechanically drawn over another microplate. The lower microplate therefore provided at the same time the atomically-flat cavity floor as well as the substrate for writing very smooth WGM antenna structures with focused ion beam milling. Using a rather low-Q cavity according to FDTD simulations (440 nm wall height), the coherent back-and-forth transfer of energy between a directly excited antenna and the opposite one, separated by > 1 μm , was demonstrated via time-resolved experiments: Response functions for electric field reconstruction were retrieved by modelling the spatially-resolved PEEM data of non-linear two-pulse correlation measurements at the position of both antennas with the coupled oscillator model. According to this model, the outer modes of the response function of the directly excited antenna are split by 16 THz and the presence of such non-trivial spectral features was corroborated by spectrally-resolved PEEM.

The successfully observed back-and-forth transfer of energy is a huge step forward in LSP-SPP coupling: In contrast to the preliminary works of Aeschlimann and co-workers [6], energy has not only been exchanged between an SPP and an LSP but also between two different LSPs that are separated by more than 1 μm. Moreover, the system presented here was designed in advance and it is hence promising for on-chip technology. However, to fully exploit the benefits provided by a plasmonic system of three coupled oscillators, some work will be required: A detailed characterisation of response functions and spatially resolved mode patterns of single constituents and composite systems will be necessary for a reliable fabrication of structures with desired properties. This could be successfully accomplished by using spatially-resolved cathodoluminescence since the impinging electron beam is the most natural way to excite an electric dipole that oscillates perpendicular to the substrate [111, 261]. A refined technology is currently developed at the AMOLF institute (Amsterdam, Netherlands) that will even allow to combine spatially-resolved cathodoluminescence with time resolution.

In order to improve performance and to increase mode splitting (to speed up energy exchange), the operating frequency should be lowered. First of all, lower

frequencies are less affected by absorption in metallic systems and hence higher Q-factors can be expected. Furthermore, the SPP dispersion relation is steeper for smaller wavevectors k and the surface charge patterns of the normal modes in the hybridised system might be linked to widely separated eigenfrequencies.

The technological relevance of the antenna-cavity systems with respect to the energy transfer between incorporated quantum emitters is discussed in the next chapter.

2 Cavity-enhanced energy transfer of quantum emitters

This chapter is concerned with a theoretical study on incoherent and coherent energy transfer between single quantum emitters (e.g. quantum dots and molecules) positioned on widely separated whispering gallery mode (WGM) antennas inside the elliptical plasmonic arena cavities, which were presented in Chapter 1 of this thesis. After providing a more detailed overview of the questions that will be addressed in this chapter, the investigation starts in Section 2.2 with a determination of the general interaction strength of quantum emitters to the plasmonic structure. The following Section 2.3 is then dedicated to the determination of relative and absolute energy transfer rates by assuming a weak interaction between two quantum emitters, located on opposed nano-antennas in the elliptical cavity. In Section 2.4 it will be estimated whether a strong, i.e. coherent, interaction can be established by considering the mediating cavity plasmon as a part of the corresponding stationary system state. For the sake of completeness, the strong-coupling regime is also investigated in circular arena cavities. At the end of this chapter, in Section 2.5, the weak coupling regime is considered again in order to asses the feasibility of cooperative emitter effects (*Dicke effect*), which have not been experimentally demonstrated in literature so far.

The idea to investigate on this research topic and the implementation of required FDTD simulations, including their evaluation, are ascribed to the author of this thesis alone.

2.1 Introduction

In the previous chapter it was shown that hybridisation of a propagating SPP cavity mode with localised surface plasmon resonances of well-separated nano-

antennas facilitates the exchange of excitation energy between the antennas. Accordingly, all investigations about the hybridised system were up to now concerned with the plasmonic properties of the structure itself. In both, theory and experiment, broadband coherent laser pulses were utilised as an excitation source since the illustrative transfer of plasmonic energy between the WGM antennas can only be realised if a sufficiently broad part of the response function is excited: The observation of an oscillating excitation of separated nano-antennas is only visible when the beating period, i.e. the splitting of hybridised modes, is faster than the decay time of the plasmonic excitation. An obvious question is to what extent the hybridised system also facilitates energy transfer between distinct quantum emitters like molecules or quantum dots. This problem is highly relevant with respect to various research areas like incoherent and coherent energy exchange in biological processes like photosynthesis [72, 47] and the related fabrication of artificial light harvesting complexes [27, 166], as well as in quantum information science [198] and thresholdless lasing [256]. Especially the two latter ones require that interaction between quantum emitters occurs in the strong-coupling regime, i.e. the splitting of new system modes can be resolved so that a coherent transfer is established before the transient evolution of the system decays. Since WGM antennas in circular or elliptical arena cavities can be deterministically equipped with one or two quantum emitters respectively, it is of great interest whether a strong coupling between this minimum number of emitters and a single cavity photon (plasmon) can be achieved. This splitting of modes is then called *vacuum Rabi splitting* and it is usually small compared to the splitting of the hybridised plasmonic modes in Chapter 1 (e.g. 20 GHz for two quantum dots in a photonic crystal cavity [160]). It is strongly emphasised that at this juncture the strong-coupling regime of single emitters and a single excitation of the radiation field has so far not been demonstrated in any plasmonic experiment [295].

On the way to strong single emitter-plasmon coupling: A short overview

The pioneering first observation of strong coupling between a single atom and a single electric field mode was accomplished by Gerhard Rempe and co-workers in 1987 with a superconducting cavity operating at microwave frequencies [251]. In 1992 vacuum Rabi splitting was demonstrated by Thompson and co-workers in the

optical regime with a high-finesse cavity and a frequency-stabilised Ti:sapphire laser [292]. First solid-state strong-coupling experiments were simultaneously realised in 2004 by Reithmaier [250] and co-workers and Yoshie [328] and co-workers, by using In(Ga)As quantum dots in semiconductor micro-pillar cavities and photonic crystal cavities respectively. These first experiments were conducted at temperatures < 20 K and a vacuum Rabi splitting of about 40 GHz was demonstrated. In the same year, first strong-coupling experiments with surface plasmon polaritons (SSPs) and cyanide dye J-aggregates were demonstrated by Bellessa and co-workers [31]. An enormous Rabi splitting of 144 THz was observed at room temperature by exciting a propagating SPP at the interface of coupled molecules and a silver film. Although the amount of mode splitting is impressive, one has to bare in mind that this is only achieved by the large number of participating molecules. However, the benefit of strong plasmonic near-field excitations in light-matter interaction is obvious: In 2009 Bellessa and co-workers utilised the localised plasmon resonance of an Ag nano-disc array covered with cyanide dye J-aggregates to experimentally demonstrate a giant Rabi splitting of 108 THz [32]. When going to the single emitter strong-coupling regime only theoretical approaches exist. They frequently utilise standard plasmonic nano-antennas offering large field-enhancement: nanoparticle dimers (15 THz vacuum Rabi splitting in interparticle gap) [263] or a chain of nano-spheroids [272], cigar-shaped nano-rods (12 THz vacuum Rabi splitting) [297] and sharp nano-tips [77]. The drawback of these structures is simply the cumbersome preparation since a single emitter has to be positioned and fixed in the nanometer-sized hot-spot of small structures.

A more promising approach, with view to preparation, is the coupling of single emitters to 1D plasmonic waveguides [148]. In these structures field enhancement of the plasmonic modes is utilised, as well as cavity features due to Bragg reflector mirrors at both waveguide ends. A moderate vacuum Rabi splitting of up to 1 THz is predicted by simulations. These microscopic structures seem to be worthwhile for an experimental realisation of single emitter - single plasmon coupling since they were already used for the demonstration of single plasmon injection by exciton decay of a coupled quantum dot [9]. Moreover, the elongated geometry allows for the insertion of a second quantum emitter and hence the mutual interaction can be studied.

Enhanced light-matter interaction in hybridised cavity-antenna systems

Here, the WGM antenna decorated elliptic arena cavities serve as an alternative system to investigate on the just mentioned two subjects: A potentially strong coupling of single quantum emitters to single plasmons and the incoherent, and maybe coherent, mutual interaction of two well-separated quantum emitters. Once the strong-coupling regime is established the coherent or incoherent character of the quantum emitter interaction can be selected by adjusting the dissipation inside the system via the cavity wall height.

For the purpose of enhanced emission and absorption of light, the mere presence of the elliptical cavity presented here is beneficial. According to Section 1.4.1, and Fig. 1.21(a) therein, the highest electric field intensity of the resonant cavity mode is found in the vicinity of the focal spots, which are associated with the specific geometrical elliptic shape. The high field intensities suggest a concentration of light leading to an enhanced light-matter interaction for quantum emitters, which are placed nearby these spots. Additionally, the insertion of spectrally matching WGM antennas at the focal spots and the associated hybridisation of plasmonic sub-system is promising to amplify light-matter interaction even further: First of all, metallic nano-antennas intrinsically provide a substantial enhancement of electric fields near their respective interface. Secondly, as a consequence of the hybridisation, the long-living character of the pure cavity mode is imprinted onto the new emerging modes of the coupled system although these modes might be mainly localised at the antenna structure. Consequently, energy is stored for longer times and the associated larger electric fields additionally increase the field enhancement provided by the antenna alone. It needs to be emphasised that the term 'enhanced light-matter interaction' is intended to cover two distinct effects: The enhanced coupling of an emitter to the radiation field provided by an inhomogeneous environment, i.e. the Purcell effect (see Section 2.2), and the enhanced chance for interaction with photons due to light concentration at the position of another quantum emitter, similar to surface enhanced Raman scattering (see Chapter 4).

In addition to the plasmonic properties, the rather macroscopic and well-defined structure of the cavity system should facilitate a deterministic positioning of quantum emitters. Once positioned on the mesa of the WGM antennas, they can be addressed and probed from above with the appropriate tools.

Chapter aim and outline

The central question of this chapter is: "To which extent can plasmonic modes inside the WGM antenna decorated elliptic arena cavities influence energy transfer between widely separated quantum systems operated at Ti:sapphire wavelengths ($\lambda_0 = 800$ nm)". This question requires a quantitative assessment of the amount of transferred energy between the emitters. If it turns out that the rate of energy transfer is sufficiently high, the separated quantum emitters might interact in a coherent manner. Besides the benefits that arise alone from the efficient energy transfer between well-separated quantum systems, the system presented here would be marked as a promising candidate for the first experimental demonstration of strong coupling between a single plasmons and a quantum emitter. To tackle the agenda this chapter is structured as follows:

First of all, the coupling strength of quantum emitters to the plasmonic structures of Chapter 1 is quantified in terms of the *Purcell enhancement* in Section 2.2. A mathematical introduction to this standard criterion will be presented in Section 2.2.1. The introduction will also help to understand why FDTD simulations and classical dipole sources can be utilised to model the interaction of quantum emitters with their electromagnetic environment. Results of Purcell enhancement retrieved from FDTD simulations will then be discussed in Section 2.2.2. For this investigation the focus lies on the hybridised system of elliptical-shaped HQ-cavities and barrel-shaped WGM antennas (see Chapter 1 for plasmonic properties). In the Sections 2.3.1 and 2.3.2 FDTD simulations will be utilised to determine the normalised energy transfer rate (nETR) and the absolute energy transfer rate (ETR) in the formalism of weak coupling, respectively. While the former one is independent of particular emitter properties and takes only the contribution of the plasmonic structure into account, the latter one gives absolute transfer rates which are determined by specific properties of quantum emitters attached to the plasmonic structures. Section 2.4 is concerned with the question if both quantum emitters couple strongly, i.e. coherently, to the cavity mode. For this purpose FDTD simulations are utilised together with electric field quantisation in the dyadic Green's function formalism in order to assess the vacuum Rabi splitting (VRS) of the combined emitter-plasmon system. Since both systems, the elliptical and the circular cavity, are close to the onset of a visible VRS for the specific set of structural parameters, improvements will be discussed to achieve

a clear coherent interaction. Section 2.5 will then be dedicated to the effect of collective spontaneous emission, also called *superradiance*. Although assigned to weak light-matter interaction, this dissipative channel can be utilised to generate a stationary entangled state, according to ideas taken from literature [205]. With the help of FDTD simulations, it is shown that this state might also be prepared in the elliptical cavities presented here. This investigation presents an alternative route if the strong-coupling regime cannot be reached despite all efforts. Besides that, superradiance, like strong coupling, has so far not been demonstrated in a plasmonic experiment and it is hence an appealing issue.

Please note that this chapter contains and mentions a lot of references to literature and that important concepts are explicitly discussed and adapted to the present problem. The purpose behind this elaborate approach is a largely self-consistent text. Hopefully, a reader who is not familiar with the topic of energy transfer between quantum emitters can follow the text without additional literature.

2.2 Purcell enhancement in hybridised cavity-antenna systems

2.2.1 Modelling light-matter interaction with classical dipole sources

Actually, it is well known, since the early works of Edward Mills Purcell [245] and Karl-Heinz Drexhage [90], that the spontaneous decay rate of a quantum emitter is modified by the environment in which it is being placed; a prominent continuation of this research lead to the field of cavity quantum electrodynamics (QED) in which atoms are exposed to cavities that favour the existence of only well defined electromagnetic modes [120, 132]. In order to describe the above considerations about enhanced electric fields and associated increased light-matter-interaction in a mathematical framework, the so called Purcell factor F_{Purcell} is introduced as ([229], Chapter 8):

$$\frac{P}{P_0} = F_{\mathrm{Purcell}} = \frac{\gamma}{\gamma_0}. \tag{2.1}$$

Both sides of the equation represent the normalised rate of energy dissipation of an emitter. The left hand side treats the emitter as a classical oscillating dipole

source which looses power P in an inhomogeneous environment, while P_0 represent the power loss in a homogeneous environment which exhibits a background medium matching the one that also encases the dipole in the inhomogeneous environment. The right hand side treats the radiation source as a quantum emitter in the dipolar approximation: γ is the modified spontaneous decay rate in the inhomogeneous environment and γ_0 represents the appropriate free-space decay rate. Hence, the Purcell factor determines the enhancement ($F_{\text{Purcell}} > 1$) or suppression ($F_{\text{Purcell}} < 1$) of radiation and it crucially depends on the emitter position in the inhomogeneous environment.

At first, the behaviour of an enhanced or suppressed emission is described in the classical picture. In classical electrodynamics Poynting's theorem connects the rate of energy dissipation P with power dissipated by the Lorentz force acting on charged particles [229]:

$$P(\omega) = -\frac{1}{2}\int_V \mathrm{Re}\left\{\mathbf{j}^*(\mathbf{r},\omega)\cdot\mathbf{E}(\mathbf{r},\omega)\right\} dV. \tag{2.2}$$

Here, $\mathbf{j}$ is the free current density corresponding to motion of charge. Keeping in mind that the time harmonic oscillating charge of a dipole $\mathbf{p}(\omega)$ located at $\mathbf{r}_0$ is related to a current density by

$$\mathbf{j}(\mathbf{r},\omega) = -\mathrm{i}\omega\mathbf{p}(\omega)\delta(\mathbf{r}-\mathbf{r}_0) \tag{2.3}$$

(see [229]), the rate of energy dissipation of a dipole in the small source volume V can be rewritten as

$$P(\omega) = \frac{\omega}{2}\mathrm{Im}\left\{\mathbf{p}^*(\omega)\cdot\mathbf{E}(\mathbf{r}_0,\omega)\right\}. \tag{2.4}$$

In the last step the relation $\mathrm{Re}\{x+\mathrm{i}y\} = \mathrm{Im}\{\mathrm{i}(x+\mathrm{i}y)\}$ was used. According to equation (2.4) the rate of energy dissipation depends on the electric field strength at the position of the dipole. If the dipole is the only source of electric fields equation (2.4) states that the dipole acts on itself. The electric field at position $\mathbf{r}$ of a dipole source located at $\mathbf{r}_0$ in an arbitrary environment is determined by

$$\mathbf{E}(\mathbf{r},\omega) = \omega^2\mu_0\mu_r\overleftrightarrow{\mathbf{G}}(\mathbf{r},\mathbf{r}_0,\omega)\mathbf{p}(\mathbf{r}_0,\omega), \tag{2.5}$$

in which the information about the ambient structure is encoded in the Dyadic Green's function $\overleftrightarrow{\mathbf{G}}(\mathbf{r},\mathbf{r}_0,\omega)$ [229]. Hence, setting $\mathbf{r}=\mathbf{r}_0$ and inserting (2.5) into (2.4) leads to

$$P(\omega)=\frac{\omega^3\left|\mathbf{p}(\omega)\right|^2}{2c^2\varepsilon_0\varepsilon_r}\left[\mathbf{n}_\mathrm{p}\cdot\mathrm{Im}\left\{\overleftrightarrow{\mathbf{G}}(\mathbf{r}_0,\mathbf{r}_0,\omega)\right\}\cdot\mathbf{n}_\mathrm{p}\right], \tag{2.6}$$

in which $\mathbf{n}_\mathrm{p}$ denotes the unit vector of the dipole moment. The radiated power P_0 in homogeneous space is finally obtained by using Green's function of free space $\overleftrightarrow{\mathbf{G}}_0(\mathbf{r}_0,\mathbf{r}_0,\omega)$ [229]:

$$P_0(\omega)=\frac{\left|\mathbf{p}(\omega)\right|^2}{12\pi}\frac{\omega^4}{\varepsilon_0\varepsilon_r c^3}. \tag{2.7}$$

In the classical picture a dipole radiates more ($P>P_0$) or less ($P<P_0$) power because of its own retarded field which is determined by the surrounding environment. In the context of quantum mechanics this means that in unit time more or less quanta of a specific energy are emitted by the molecule or quantum dot compared to its spontaneous decay rate in a homogeneous environment. The spontaneous decay rate γ can be derived by Fermi's golden rule [229]:

$$\gamma=-\frac{2\pi}{\hbar^2}\sum_f\left|\left\langle f\left|\hat{\mathbf{p}}\cdot\hat{\mathbf{E}}\right|i\right\rangle\right|^2\delta(\omega_i-\omega_f). \tag{2.8}$$

Here, $-\hat{\mathbf{p}}\cdot\hat{\mathbf{E}}$ is the interaction Hamiltonian in the dipolar approximation and $|i\rangle=|e\rangle\,|0_\mathbf{k}\rangle$ denotes the initial state of the combined emitter-photon system, while $|f\rangle=|g\rangle\,|1_\mathbf{k}\rangle$ denotes its final state. Furthermore, $|g\rangle$ and $|e\rangle$ denote the ground and excited sate of the emitter while $|0_\mathbf{k}\rangle$ and $|1_\mathbf{k}\rangle$ denote the zero-photon and one-photon state of the quantised radiation field. The subscript $\mathbf{k}$ represents different modes of the radiation field which exhibit the same energy $\hbar\omega_\mathbf{k}$ and thus might be populated by the emitted photon with energy $E_g-E_e=\hbar\omega$. These modes originate from quantisation of the radiation field by writing it as a denumerable Fourier series. This can be considered as solving the problem in momentum space. Thereby one should keep in mind that $\mathbf{k}$ indicates the appropriate spatial modes and not a wave vector. According to this procedure the vacuum electric field operator $\hat{\mathbf{E}}$ can be written as [229]:

$$\hat{\mathbf{E}} = \sum_{\mathbf{k}} \sqrt{\frac{\hbar\omega_{\mathbf{k}}}{2\varepsilon_0}} \left[\mathbf{u}_{\mathbf{k}}(\mathbf{r},\omega_{\mathbf{k}}) \hat{\mathrm{a}}_{\mathbf{k}}(t=0) \mathrm{e}^{-i\omega_{\mathbf{k}}t} + \mathbf{u}^{*}_{\mathbf{k}}(\mathbf{r},\omega_{\mathbf{k}}) \hat{\mathrm{a}}^{\dagger}_{\mathbf{k}}(t=0) \mathrm{e}^{i\omega_{\mathbf{k}}t} \right]. \tag{2.9}$$

In this equation $\hat{\mathrm{a}}_{\mathbf{k}}(0)$ and $\hat{\mathrm{a}}^{\dagger}_{\mathbf{k}}(0)$ denote the annihilation and creation operators for photons, respectively, and $\mathbf{u}_{\mathbf{k}}(\mathbf{r},\omega_{\mathbf{k}})$ represents the decomposition of the field into normal modes. The last quantity that needs to be specified is the dipole moment operator $\hat{\mathbf{p}}$ which connects the ground and excited state of the quantum emitter. Due to its odd symmetry it only connects different states and it can be written as $\hat{\mathbf{p}} = \mathbf{p}\left(|e\rangle\langle g| + |g\rangle\langle e|\right)$ [229], in which $\mathbf{p}$ is the transition dipole moment. Inserting equation (2.9) into (2.8) and considering self-interaction ($\mathbf{r} = \mathbf{r}_0$) gives [229]:

$$\gamma = \frac{2\omega}{\hbar\varepsilon_0} |\mathbf{p}|^2 \sum_{\mathbf{k}} \left[\mathbf{n}_{\mathbf{p}} \cdot \left(\mathbf{u}_{\mathbf{k}}(\mathbf{r}_0,\omega_{\mathbf{k}}) \otimes \mathbf{u}_{\mathbf{k}}(\mathbf{r}_0,\omega_{\mathbf{k}}) \right) \cdot \mathbf{n}_{\mathbf{p}} \right] \delta(\omega_{\mathbf{k}} - \omega), \tag{2.10}$$

in which $\otimes$ denotes the outer product. In the final step, the normal modes $\mathbf{u}_{\mathbf{k}}(\mathbf{r},\omega_{\mathbf{k}})$ can be utilised as basis vectors for the expansion of the dyadic Green's function $\overleftrightarrow{\mathbf{G}}(\mathbf{r},\mathbf{r}',\omega)$. By determining the expansion coefficients and using complex contour integration the spontaneous decay rate reads [229]:

$$\gamma = \frac{\pi\omega}{3\hbar\varepsilon_0} |\mathbf{p}|^2 \underbrace{\frac{6\omega}{\pi c^2} \left[\mathbf{n}_{\mathbf{p}} \cdot \mathrm{Im}\left\{ \overleftrightarrow{\mathbf{G}}(\mathbf{r}_0,\mathbf{r}_0,\omega) \right\} \cdot \mathbf{n}_{\mathbf{p}} \right]}_{=\rho_{\mathrm{P}}\text{ , the partial local density of states}}. \tag{2.11}$$

For a given quantum emitter with a defined transition dipole moment $\mathbf{p}$ and dipole orientation $\mathbf{n}_{\mathbf{p}}$ the spontaneous decay rate γ depends on the partial local density of states (LDOS) ρ_{p}. The LDOS determines the number of modes per unit volume and frequency which are available for a potentially emitted photon during the spontaneous decay process. If the number of modes is increased in a particular spot than the probability for a decay to occur is enhanced. Hence, the presence of a cavity or arbitrarily shaped object can facilitate or hinder the stimulated emission of photons due to vacuum field fluctuations.

In the light of the LDOS, the conjecture about enhanced light-matter interaction in nano-antenna decorated cavities at the beginning of this section can be fortified

by a quantum mechanical point of view: According to (2.10) the LDOS is represented by the normal modes $\mathbf{u}_\mathbf{k}(\mathbf{r},\omega_\mathbf{k})$ of the environment. It seems plausible that especially objects with sharp edges, e.g. nano-antennas, need a dense and broad distribution of spatial frequencies in order to be properly rendered. This concept is transferred in a hand-waving manner to the normal modes $\mathbf{u}_\mathbf{k}(\mathbf{r},\omega_\mathbf{k})$. Due to the numerous available states at the nano-antenna the probability of finding a photon nearby this structure is higher than finding a photon in a smooth environment with a low LDOS. Therefore, by placing the WGM antennas, and their respective quantum systems, in the focal spots of the elliptic cavity an increased probability is expected for both processes: the emission of a photon by one emitter, due to the increased LDOS, and the subsequent absorption by its counterpart, due to resonant light concentration. Despite these qualitative considerations the above equations refer to the enhanced emission of a single emitter. The energy transfer to a second system will be discussed in more detail in Section 2.3.

It remains to specify the normalisation factor γ_0 which is the spontaneous decay rate in a homogeneous medium [229]:

$$\gamma_0 = \frac{2\omega|\mathbf{p}|^2}{3\hbar\varepsilon_0}\cdot\frac{\omega^2}{\pi^2c^3} = \frac{\omega^3|\mathbf{p}|^2}{3\hbar\varepsilon_0\pi c^3}. \tag{2.12}$$

This equation is obtained from (2.11) by inserting the density of modes as encountered in black-body-radiation, i.e. $\omega^2\pi^{-2}c^{-3}$, into ρ_p.

With the retrieved expressions for $P(\omega)$, $P_0(\omega)$, γ and γ_0 it is verified that the Purcell enhancement F_Purcell can be equivalently described by a full quantum mechanical treatment as well as with classical oscillating dipole sources. This is an important statement since it allows to use FDTD simulations in the upcoming sections to model the mutual interaction of quantum systems with the included classical dipole sources. Specific emitter properties, like the dipole moment $\mathbf{p}$, cancel out via normalisation with $P_0(\omega)$ or γ_0.

2.2.2 Purcell enhancement retrieved with FDTD simulations

This subsection is dedicated to quantify the interaction of a quantum emitter with its environment ere the energy transport from one quantum system to another

is investigated. As a measure of the interaction the Purcell factor of different geometries is determined by utilising FDTD simulations. These geometries include, in addition to the combined nano-antenna decorated cavity system, the single constituent parts, i.e. the pure elliptic cavity and a single WGM antenna. It is emphasised that potentially high Purcell factors are not a surety for enhanced interaction between separated quantum systems since this additionally relies on the coupling rate of emitted photons into plasmonic cavity modes.

FDTD setup

The simulation setup is identical to the HQ-cavity system with a cavity wall height of 800 nm and barrel-shaped WGM antennas, as already investigated in Section 1.4. But in contrast to former simulations the dipole source is now located 10 nm above the gold substrate (see Fig. 2.1(a)) in order to mimic a real quantum emitter. This corresponds to the S1-configuration in Fig. 1.20. The elevation of the source is favourable in different ways: First, due to a mesh resolution of 2 nm at the WGM antenna there is a spacing of only four Yee cells to the substrate. A further lowering of the source might increase Purcell enhancement and coupling to plasmonic cavity modes but also increases the influence of numerical artefacts at the interface. Second, if the quantum emitter is very close to the surface its transition dipole moment $\langle g|\,\hat{\mathbf{p}}\,|e\rangle$ might be perturbed leading to quenching of emission properties [229]. Furthermore it is reported in literature that fluorescence of molecules is suppressed if the distance to a metallic nanoparticle surface is reduced below 5 nm [18]. The reduction in fluorescence is due to the non-radiative coupling of excitation energy to the metal leading to increased ohmic losses [229]. This quenching also reduces the plasmonic coupling between multiple quantum emitters and hence negatively affects the prospect of superradiance [206]. To circumvent quenching, the quantum emitter is lifted by 10 nm. This might be implemented by a sputtered Al_2O_3 layer, as demonstrated in literature [321].

The charge oscillation of the dipole source is oriented perpendicular to the substrate. This choice guarantees overlap with the plasmonic $m = 0$ mode of the WGM antenna. Hence, the presented Purcell factors do not account for orientation averaging and the successful implementation is spared for the designated experimenter. For instance, InAs quantum dots could be used since they exhibit a

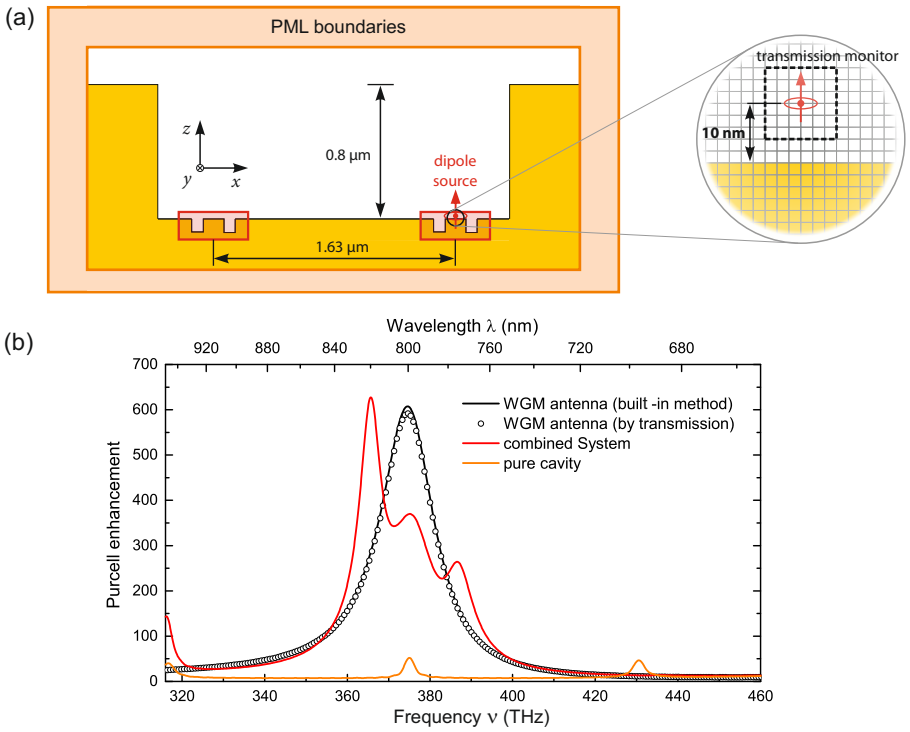

Fig. 2.1: Purcell enhancement in elliptic cavities. (a) The simulation setup is identical to setup of the HQ-cavity presented in Fig. 1.20. The dipole source is located 10 nm above the substrate and is surrounded by transmission box monitor in order to compare the thereby measured Purcell enhancement to the factor retrieved from a built-in function of the LUMERICAL software. (b) Comparison of frequency resolved Purcell enhancement in different environments by either, the built-in function (lines) and the transmission box monitor (empty circles).

trapezoidal shape and therefore feature anisotropic properties (see [13] and Section 2.3.2 for details).

The Purcell factor F_{Purcell} is directly retrieved with a built-in function provided by the Lumerical software. In this case the software uses equations (2.6) and (2.7) to calculate the normalised rate of energy dissipation. The only unknown quantity of the evaluation is the dyadic's Green function $\overleftrightarrow{\mathbf{G}}(\mathbf{r}_0, \mathbf{r}_0, \omega)$ which is determined by the relation of the applied dipole moment $\mathbf{p}(\mathbf{r}_0, \omega)$ of the injection source and the retrieved spectral amplitude $\mathbf{E}(\mathbf{r}_0, \omega)$ at the emitter position according to (2.5). The reliability of the retrieved Purcell factor is verified with a tight-fitting

transmission box monitor surrounding the dipole (Fig. 2.1(a)). The power $P(\omega)$ flowing out of this box is obtained by a surface integral of the spatially-resolved Poynting vector. The obtained power of the radiating dipole is then divided by the built-in `sourcepower` function which simply gives the power radiated by a dipole in vacuum $P_0(\omega)$ as determined by the analytical equation (2.7). Hence the transmission box monitor directly gives the Purcell factor F_{purcell}. This second method is required if the mesh resolution approaches a cell size of $\lambda/1000$ or if the dipole is placed in a dispersive medium. In the latter case depolarisation of the dipole's microscopic environment influences the local field at the dipole position, which is used in the first method of the built-in Purcell function, and corrections similar to the Clausius-Mossotti relation have to be applied to equation (2.7) [229].

Results and discussion

The Purcell factors F_{purcell} for the combined cavity-antenna system, as well as for the single constituents, are shown in Fig. 2.1(b) as a function of frequency and values of F_{purcell} range from 7 (base line of the pure cavity mode) to a maximum value of 627 (combined system). Interestingly, the maximum Purcell enhancement of the WGM antenna at the resonance wavelength of 375 THz (800 nm) is nearly identical to that of the combined system. The latter one is distinguished from the pure antenna system by offering Purcell factors well above 200 over a wider range of frequencies. The black empty circles represent F_{purcell} of the pure WGM antenna retrieved by the transmission box method. The values match the ones retrieved by the Lumerical built-in function very well. Hence the discussion about Purcell factors is now restricted to the latter method.

Bare cavity: The detailed discussion starts with the Purcell factors of the pure cavity modes: The desired cavity mode at 375 THz (800 nm) exhibits a maximum Purcell enhancement of 52. This means that an excited quantum dot or molecule which is located in the focal spot of an elliptic arena-like cavity would radiate one and a half orders of magnitude more photons in unit time than its counterpart in free space. The same holds for the adjacent modes at 317 THz (947 nm) and 430 THz (697 nm) which exhibit a F_{purcell} of 40 and 45, respectively. A dipole emitter that radiates under non-resonant conditions, i.e. the range of frequencies between resonant modes, experiences a uniform Purcell enhancement of 7.5. This value

is comparable to analytical results of a perpendicular oriented dipole sandwiched between a glass substrate and an aluminium layer at 10 nm distance, showing a Purcell factor of 10 (see Fig. 10.5 in [229]). Experimental Purcell factors reported in literature amount to $F_{\text{purcell}} = 32$ for InAs quantum dots emitting at 327 THz (918 nm) in a semiconductor micropillar cavity consisting of distributed Bragg reflectors (DBR) [114] and $F_{\text{purcell}} = 75$ in a photonic crystal cavity doped with InGaAs quantum wells emitting at 317 THz (945 nm) [10]. Taking into account that these non-metallic systems were operated at cryogenic temperatures renders the metallic system presented here at ambient conditions with a maximum Purcell factor of 52 at 375 THz emission frequency as a promising candidate for enhanced plasmonic light-matter interaction.

Actually, other plasmonic systems promise higher Purcell factors: Plasmonic nano-disc resonators (MIM cavities), in which a 50 nm thick circular SiO_2 layer is sandwiched between 100 nm thick Ag layers, is expected to give a Purcell enhancement of 900 [176]. This was deduced from the very small near-field mode volume $V_0 = 0.00033\lambda^3 n^{-3}$ of and the measured quality factor ($Q = 16$) of the system according to the relation [108]:

$$F_{\text{Purcell}} = \frac{3}{4\pi^2}\frac{Q}{V}\left(\frac{\lambda}{n}\right)^3, \tag{2.13}$$

in which n is the refractive index of the cavity medium. However, this result is not confirmed by direct observation of an enhanced spontaneous decay rate of emitters, which appears to be a cumbersome task since the hardly accessible emitters are buried between two metal layers. Here, the open cavity geometry allows to directly address and observe the quantum emitters. This comes, according to equation (2.13), at the expense of a larger mode volume so that the Purcell enhancement in the resonators presented here is one order of magnitude below that of nano-disc resonators. Inserting $F_{\text{Purcell}} = 52$, $Q = 137$ (see Section 1.4.1) and $\lambda = 800$ nm into (2.13) gives an effective mode volume of $V_0 = 0.1\ \mu\text{m}^3$, which resembles a cube of 464 nm side length. This volume is larger than the geometrical extents of the nano-disc resonators. The condition for using equation (2.13) is that the emission frequency of the emitter is only resonant to a single resonance of the cavity. Typical emission peaks of CdSe quantum dots emitting near 545 THz (550 nm) exhibit a spectral full-width tenth-maximum of 80 THz

[229], and InAs/GaAs quantum dots emitting at 231 THz (1.3 μm) exhibit an emission peak FWHM of 35 THz [294]. Hence the criterion is fulfilled by the elliptic cavity since the adjacent modes of the 375 THz resonance are separated by approximately 100 THz.

Purcell factors of several thousands seem to be achievable with plasmonic wedge waveguide cavities [148] which require DBR mirrors, offering at least 95% reflection. Recently, a reflectivity of this quality has been achieved with 1D waveguides [78].

WGM nano-antenna: Next, the Purcell enhancement of the barrel-shaped WGM antenna with parameters matching the $m = 0$ mode at 375 THz excitation is discussed (black curve in Fig. 2.1(b)). An easily accessible dipole emitter which is located 10 nm above the surface exhibits a factor F_{Purcell} of about 600. This emitter is expected to radiate two and a half orders of magnitude more photons in unit time than its counterpart in free-space. Purcell factors of 100 are available in a spectral range of approximately 30 THz, which is nearly 10% of the emission frequency, and hence a broadband coupling of the emitter to the antenna is feasible. According to equation (2.13) the higher Purcell factor of the WGM antenna is assigned to a smaller effective mode volume V which amounts to 0.0015 μm^3 by inserting $F_{\text{Purcell}} = 600$ and $Q = 24$ (see Section 1.2.3). Thus, the volume V is 60 times smaller than the effective mode volume of the pure cavity mode. By using the WGM antenna with V-grooves optimised for the $m = 0$ mode operation at 800 nm, as presented in Fig. 1.4(d), the Purcell factor is further increased to 900 while the Q-factor is also slightly increased to $Q = 27$ (see equation (1.9)). The increasing F_{Purcell} is attributed to a sharper, tip-like form of the WGM antenna which favours a larger field enhancement and thus a higher LDOS at the emitter position.

Actually, it is already known for 5 years that WGM resonators theoretically feature high Purcell factors of up to 2000 according to the publication of Vesseur and co-workers [304]. However, these factors have been retrieved for emitter positions inside the 10 nm wide groove of barrel-shaped WGM antennas where highest field strengths prevail. Although a fabrication of such fine structures might be feasible [79], the positioning of a single emitter in the groove will be a cumbersome task. Despite a surface-emitter distance of only 5 nm the authors expect no quenching effects due to resonant plasmon coupling [304]. A first study of WGM antenna

grooves filled with ATTO680 molecules revealed a fluorescence enhancement of about 5 [303]. Another characteristic difference is that the investigation in [304] only covers the $m = 1$ resonance of WGM antennas. In this scenario Purcell factors do not exceed values of 500 if V-shaped grooves are used instead of the above mentioned grooves with a constant width of only 10 nm. The smaller values of F_{Purcell}, with respect to the $m = 0$ excitation, are attributed to the larger structural extents required for the $m = 1$ resonance which leads to larger mode volumes. Additionally, the antennas presented here exhibit a shallow depth of 76 nm and do not resemble a proper $n = 1$ mode, as already discussed in Chapter 1: The electric field is for the most part localised at the metal-vacuum interface and not at the groove bottom, which is beneficial for self-interaction of emitters placed on top of the antenna.

Hybridised system: At last, the hybridised system of two WGM antennas in the focal spots of the elliptic cavity is discussed. Interestingly, the dipole emitter experiences a maximum enhancement of its spontaneous emission rate (red curve in Fig. 2.1(b)) which is comparable to the single antenna (black curve in Fig. 2.1(b)). This may seem disappointing at first sight, but the benefit of the combined system lies in the even further broadened spectral distribution of Purcell factors. The splitting of modes due to hybridisation leads to a Purcell enhancement of 200 in the range of 30 THz. It is worth striving for a broader distribution of large Purcell factors since quantum emitters, like the above mentioned InAs/GaAs quantum dots, exhibit a similar width of emission spectra (35 THz FWHM) at room temperature. Otherwise the effective enhancement of the spontaneous decay rate is reduced through spectral selectivity, as investigated in the enhanced luminescence of non-thermalised excitons in whispering core-shell nanowire-cavities [65]. Here, in the scenario of energy transport it is desirable to have a broad distribution of Purcell factors to cover the overlapping emission and absorption spectra of the separated quantum systems. Concerning transport it is worth mentioning that the constant maximum Purcell factor might be attributed to the fact that emission from one antenna is imaged to the other one: A certain part of energy emitted by the quantum system will be localised and absorbed at the second antenna due to enhanced near-fields. In Section 2.4.3 it will be shown that if the cavity is circular, and both WGM antennas are merged to a single one at the cavity centre, the dipole emitter self-interaction is increased and the maximum Purcell factor

will be doubled compared to the scenario without cavity.

In summary, the pure cavity mode at 800 nm offers a moderate Purcell factor of 52. In contrast to numerous other plasmonic geometries F_{Purcell} should be easily accessible due to the exposed focal spots, rendering the elliptic arena-like cavity alone a robust system for enhanced light-matter interaction. Likewise, an emitter on top of a WGM antenna appears to be easily addressable in contrast to systems embedded in the antenna groove. By utilising the $m = 0$ resonance the exposed emitter exhibits appreciable Purcell factors of 600 to 900 and the associated mode geometry is promising for an efficient excitation of surface plasmons (see Fig. 1.9 and the related discussion). The hybridised system of cavity and antennas further broadens the spectral range of large Purcell factors provided by the antenna alone. The Purcell factor, as a benchmark, renders the presented system of WGM antenna decorated elliptic cavities a promising candidate for an enhanced energy transport on comparatively large spatial scales.

2.3 Enhanced energy transfer rates of widely separated quantum emitters

In Section 2.2 it was shown that the presence of elliptic plasmonic cavities and incorporated WGM antennas significantly enhance the emission rate of single quantum emitters. Consequently, this section addresses the question of how the electromagnetic environment supports the interaction of two quantum systems placed on top of the opposing WGM antennas (Fig. 2.2). Since interaction implies both processes, emission and absorption, the previously used term *quantum emitter* is in the following specified to *quantum dot*. This is done without loss of generality and simply accounts for the fact that all upcoming examples refer to absorption and emission properties of particular quantum dots.

As sketched in Fig. 2.2 the interaction between two quantum dots can be described in the picture of a dipole-dipole interaction. This can be inferred from a classical point of view by hand-waving argumentation: The interaction of two particles is generally expressed as a multi-pole expansion of the Coulomb interaction. Since the quantum dots are uncharged, interactions like charge-charge, charge-

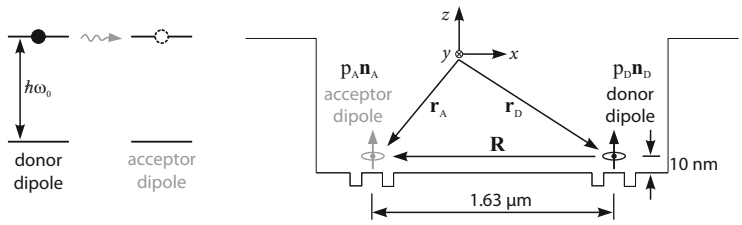

Fig. 2.2: Resonant energy transfer between quantum systems in elliptic cavities. The donor system is in an excited state and transfers the stored energy radiatively to the acceptor system. The shown greyed acceptor dipole illustrates that no re-emission of the absorbed photon is considered (weak-coupling limit). The dipole moments $\mathbf{p}_\mathrm{D}$ and $\mathbf{p}_\mathrm{A}$ are expressed in terms of their magnitudes p_D and p_A and unit vectors $\mathbf{n}_\mathrm{D}$ and $\mathbf{n}_\mathrm{A}$ which are bot fixed in z-direction.

dipole and related higher order terms vanish. All terms including a quadrupole interaction decay faster than a R^{-3}-law which is ascribed to the dipole-dipole interactions, leaving the latter one as the dominant mechanism ([229], Chapter 8.1).

A more precise classification of the distance-depended interaction is given in the following: Within the range of 1 nm transfer of excitation energy is described by the exponentially decaying Dexter process [83] which is caused by overlapping wave functions of the donor and acceptor system. The Förster resonant energy transfer (FRET) [107] then dominates on scales of up to 10 nm and it describes the radiationless resonant dipole-dipole interaction in the near-field of the donor system. Finally, on larger scales, the transfer of excitation energy is described by the radiative long-range transfer theory [24]. Similar to the concept of near- and far-fields a clear distinction between radiative and non-radiative regimes is not possible. As a rule of thumb, the radiative energy transfer rate is valid for $R/\lambda \gg 1$ and obeys R^{-2}, while the non-radiative energy transfer rate dominates if $R/\lambda \ll 1$ and it decays like R^{-6}, as known from Förster's theory. Actually, it has been shown that these two regimes can be understood as the limiting cases of a more general theory using the formalism of QED [74].

The quantum dots investigated here are separated by two times the excitation wavelength. In this case the transfer process can be described by the pathway of successive emission and absorption of a photon rather than the superposition of non-intuitive quantum pathways [204]. In contrast, the separation of donors and

acceptors was on the order of some 10 nm in the first pioneering experiments of enhanced resonant dipole-dipole interaction in Fabry-Pérot microcavities [142, 15] and on thin metallic films which support surface plasmon polaritons [16]. More recent experiments will be discussed together with the results at the end of this section.

A second classification can be made according to the coherent or incoherent nature of the transfer process. If the oscillating dipoles couple strongly to the vibrational modes of the host structure their phase information is lost during the transfer. A coherent resonant energy transfer (CRET) requires that the energy transfer rate (ETR) is faster than dephasing and damping rates of the environment. If the donor emits a photon and damping rates are smaller than the ETR, there is an appreciable chance of re-emission of the photon by the acceptor. In this case it is not possible to distinguish between the donor and acceptor and the excitation becomes delocalised over the quantum dots [229]. The CRET is hence attended by the so-called strong-coupling regime.

To classify the system presented here with respect to its transfer properties the next section will be concerned with the evaluation of the normalised energy transfer rate (nETR). The nETR describes the transfer rate of photons from the donor quantum dot to the acceptor quantum dot in the presence of the plasmonic structure compared to the energy transfer rate of the same quantum dots in free-space. Since specific properties like dipole moments and absorption cross-sections cancel out in this ratio the nETR is an appropriate factor to rank the transfer properties of the hybridised system in a more general way. Then, real quantum dot properties will be introduced in order to estimate the plasmon-enhanced Förster transfer rate which can be directly compared to the damping rate of the cavity-antenna system. To fathom the possibility of a strong-coupling scenario the temperature dependent absorption cross-section serves as a tuning parameter.

2.3.1 The normalised energy transfer rate (nETR)

The following derivation of the nETR is closely related to the approach in *Principles of Nano-Optics* ([229]) written by Bert Hecht and Lukas Novotny, and

it is adapted to the present system geometry. The power transferred from the donor to the acceptor quantum dot is calculated by describing both constituents as classical dipoles and by using Poynting's theorem as in (2.2):

$$P_{\mathrm{DA}}(\omega) = -\frac{1}{2}\int_{V_{\mathrm{A}}} \mathrm{Re}\left\{\mathbf{j}_{\mathrm{A}}^{*}(\mathbf{r},\omega)\cdot\mathbf{E}_{\mathrm{D}}(\mathbf{r},\omega)\right\} dV. \tag{2.14}$$

Here, the electric field of the donor dipole $\mathbf{E}_{\mathrm{D}}(\mathbf{r},\omega)$ drives the acceptor charge, leading to the associated current density $\mathbf{j}_{\mathrm{A}}(\mathbf{r},\omega)$. This is further specified by using the connection between the current density and the dipole moment at $\mathbf{r}_{\mathrm{A}}$ according to (2.3):

$$P_{\mathrm{DA}}(\omega) = \frac{\omega}{2}\mathrm{Im}\left\{\mathbf{p}_{\mathrm{A}}^{*}(\mathbf{r}_{\mathrm{A}},\omega)\cdot\mathbf{E}_{\mathrm{D}}(\mathbf{r}_{\mathrm{A}},\omega)\right\}. \tag{2.15}$$

The clear distinction between donor and acceptor implies the weak-coupling regime in which the transferred photon does not return to the donor dipole. Hence, the acceptor dipole remains passive and it is therefore shown greyed in Fig. 2.2. Accordingly, the transfer rate can be retrieved from FDTD simulations by using just a single dipole source. This is explicitly verified in [97], where it is shown that knowing just the response function, i.e. the electric field of the donor dipole at the position of the acceptor dipole, yields the same results for resonant dipole-dipole interaction as solving the problem in quantum mechanics with second order Rayleigh-Schrödinger perturbation theory. The method of second order perturbation theory only holds in the weak-coupling regime [97] and therefore the knowledge of the response function of a single dipole is no longer sufficient to accurately model strong interaction between the quantum dots.

Since the acceptor dipole moment $\mathbf{p}_{\mathrm{A}}$ is induced by the electric field of the donor $\mathbf{E}_{\mathrm{D}}(\mathbf{r}_{\mathrm{A}})$ both quantities are linked by the polarisability tensor of the acceptor quantum dot $\overleftrightarrow{\alpha}_{\mathrm{A}}$. Like in the evaluation of Purcell factors the induced charge oscillation is assumed to be perpendicular to the substrate according to the $m = 0$ mode of the WGM antennas. The unit vector of the acceptor dipole moment $\mathbf{n}_{\mathrm{A}}$ is therefore parallel to $\mathbf{n}_{\mathrm{z}}$ and $\mathbf{p}_{\mathrm{A}}$ can be written as:

$$\mathbf{p}_{\mathrm{A}}(\mathbf{r}_{\mathrm{A}},\omega) = \alpha_{\mathrm{A}}(\omega)\mathbf{n}_{\mathrm{z}}\mathbf{n}_{\mathrm{z}}\mathbf{E}_{\mathrm{D}}(\mathbf{r}_{\mathrm{A}},\omega). \tag{2.16}$$

Inserting (2.16) into (2.15) and taking account of the complex conjugation leads to:

$$P_{\mathrm{DA}}(\omega) = \frac{\omega}{2}\mathrm{Im}\left\{\alpha_{\mathrm{A}}(\omega)\right\}\left|\mathbf{n}_{\mathrm{z}}\cdot\mathbf{E}_{\mathrm{D}}(\mathbf{r}_{\mathrm{A}},\omega)\right|^2. \tag{2.17}$$

To be consistent with literature the polarisability $\mathrm{Im}\{\alpha_{\mathrm{A}}\}$ will be expressed in terms of the absorption cross section $\sigma_{\mathrm{A}}(\omega)$ of the acceptor quantum dot. The absorption cross-section can be defined as the ratio of transferred power $P_{\mathrm{DA}}(\omega)$ to the incident intensity $I(\omega)$:

$$\sigma_{\mathrm{A}}(\omega) = \frac{P_{\mathrm{DA}}(\omega)}{I(\omega)}. \tag{2.18}$$

According to literature the definition of the intensity in equation (A.37) is inserted into the upper equation and the absorption cross section then reads,

$$\sigma_{\mathrm{A}}(\omega) = \frac{(\omega/2)\mathrm{Im}\left\{\alpha_{\mathrm{A}}(\omega)\right\}\left|\mathbf{n}_{\mathrm{z}}\cdot\mathbf{E}_{\mathrm{D}}(\mathbf{r}_{\mathrm{A}},\omega)\right|^2}{(1/2)\sqrt{(\varepsilon_0/\mu_0)}n(\omega)\left|\mathbf{E}_{\mathrm{D}}(\mathbf{r}_{\mathrm{A}},\omega)\right|^2} = \omega\sqrt{\frac{\mu_0}{\varepsilon_0}}\frac{\mathrm{Im}\left\{\alpha_{\mathrm{A}}(\omega)\right\}}{n(\omega)}, \tag{2.19}$$

in which $n(\omega)$ is the refractive index of the embedding medium. In the last step it has been assumed that the electric field mainly points into the z-direction, according to the $m = 0$ WGM antenna mode, and hence the squared field amplitude in the denominator cancels with the projection of the field along z in the numerator. Inserting the retrieved absorption cross-section into equation (2.17) gives the power transferred from the donor to the acceptor quantum dot as:

$$P_{\mathrm{DA}}(\omega) = \frac{1}{2}\sqrt{\frac{\varepsilon_0}{\mu_0}}n(\omega)\sigma_{\mathrm{A}}(\omega)\left|\mathbf{n}_{\mathrm{z}}\cdot\mathbf{E}_{\mathrm{D}}(\mathbf{r}_{\mathrm{A}},\omega)\right|^2. \tag{2.20}$$

The above equation is similar to the expression for the time averaged electric field intensity multiplied by an absorption cross-section. By expressing the electric field $\mathbf{E}_{\mathrm{D}}(\mathbf{r}_{\mathrm{A}},\omega)$ of the donor quantum dot in terms of the dyadic Green's function according to (2.5) the transferred power can also be written as [229]:

$$P_{\mathrm{DA}}(\omega) = \frac{n(\omega)\sigma_{\mathrm{A}}(\omega)\omega^4\left|\mathbf{p}_{\mathrm{D}}\right|^2}{2\varepsilon_0 c^3}\left|\mathbf{n}_{\mathrm{z}}\cdot\overleftrightarrow{\mathbf{G}}(\mathbf{r}_{\mathrm{A}},\mathbf{r}_{\mathrm{D}},\omega)\cdot\mathbf{n}_{\mathrm{z}}\right|^2. \tag{2.21}$$

Interestingly, the transferred power increases with the refractive index of the embedding medium. Although n is set to 1 (vacuum) in the remainder of this chapter, the cavity design presented here might be improved by using highly

refractive dielectrics to concentrate the electric field and to further reduce its mode volume, leading to even more enhanced light-matter interaction. Since the skin depth into the dielectric half-space would be reduced according to equation (A.3) the Q-factor of the plasmon modes might be increased due to avoided loss at the upper cavity edges. However, according to equation (A.1) the propagation length will be reduced with increasing n and therefore it is required to determine optimum conditions for the given task.

A shortcoming of the classical derivation of (2.21) is the missing influence of an emitter spectrum with finite width. This is accounted for in quantum mechanics by representing the ground and excited state of the two quantum systems as a set of vibrational sub-levels ([92, 204]). Summing over these manifolds with respect to associated overlap integrals of ground and excited state directly leads to the above mentioned absorption cross-section $\sigma_{\mathrm{A}}(\omega)$ and the so called *equilibrium single-photon emission spectrum* $f_{\mathrm{D}}(\omega)$ which can be represented by a normalised distribution function [229]:

$$\int_0^\infty f_{\mathrm{D}}(\omega)d\omega = 1. \tag{2.22}$$

With this distribution function (2.21) can be written as [229]:

$$P_{\mathrm{DA}}(\omega) = \int_0^\infty \frac{\sigma_{\mathrm{A}}(\omega) f_{\mathrm{D}}(\omega)\omega^4 |\mathbf{p}_{\mathrm{D}}|^2}{2\varepsilon_0 c^3} \left| \mathbf{n}_{\mathrm{z}} \cdot \overleftrightarrow{\mathbf{G}}(\mathbf{r}_{\mathrm{A}}, \mathbf{r}_{\mathrm{D}}, \omega) \cdot \mathbf{n}_{\mathrm{z}} \right|^2 d\omega. \tag{2.23}$$

Note that both, $f_{\mathrm{D}}(\omega)$ and $\sigma_{\mathrm{A}}(\omega)$, refer to emission and absorption spectra in free-space [93]. Hence, the transferred power $P_{\mathrm{DA}}(\omega)$ is in general a composition of contributions weighted by the overlap of the absorption and emission spectrum of the respective quantum dots. In order to simplify (2.23) it can be assumed that $f_{\mathrm{D}}(\omega) = \delta(\omega - \omega_0)$. This simplification implies a discussion in the cryogenic limit of few K sample temperature in which the quantum dot emission line is dominated by the zero-phonon line [249], i.e. it is not broadened by energy dissipation into phonons of the environment (Debye-Waller factor) or the quantum dot itself (Franck-Condon factor). Another simplification can be introduced by considering the spontaneous emission rates of quantum dots which can be as high as 1 GHz [148]. Since characteristic changes of the cavity's dyadic Green's function are on the scale of a few THz (see Fig. 2.1) the absolute square, including

the term $\overleftrightarrow{\mathbf{G}}(\mathbf{r}_\mathrm{A}, \mathbf{r}_\mathrm{D}, \omega)$, is a constant function with respect to ω and it is hence not involved in the integration.

The enhanced energy transfer properties of the designed plasmonic system are now ranked in a very general sense by calculating the normalised energy transfer rate (nETR), which is defined as:

$$\mathrm{nETR} = \frac{\gamma_\mathrm{DA,struc}(\omega)}{\gamma_\mathrm{DA,vac}(\omega)} = \frac{P_\mathrm{DA,struc}(\omega)}{P_\mathrm{DA,vac}(\omega)}. \tag{2.24}$$

Here, $\gamma_\mathrm{DA,struc}(\omega)$ and $\gamma_\mathrm{DA,vac}(\omega)$ are the quantum mechanical energy transfer rates (see [92]) of the donor and acceptor quantum dot placed in the designed plasmonic environment and in vacuum, respectively. The quantities $P_\mathrm{DA,struc}(\omega)$ and $P_\mathrm{DA,vac}(\omega)$ describe the transferred power in the different geometries by classic dipoles according to (2.20). Equation (2.24) establishes a safe link between classical electrodynamics and the quantum mechanical picture like in the case of Purcell factors (see (2.1)) and the nETR is hence not limited to a particular formalism. By inserting (2.20) into (2.24) the nETR finally reads

$$\mathrm{nETR} = \frac{\left|\mathbf{n}_\mathrm{z} \cdot \mathbf{E}_\mathrm{D,struc}(\mathbf{r}_\mathrm{A}, \omega)\right|^2}{\left|\mathbf{n}_\mathrm{z} \cdot \mathbf{E}_\mathrm{D,vac}(\mathbf{r}_\mathrm{A}, \omega)\right|^2} = \frac{\left|E^{(z)}_\mathrm{D,struc}(\mathbf{r}_\mathrm{A}, \omega)\right|^2}{\left|E^{(z)}_\mathrm{D,vac}(\mathbf{r}_\mathrm{A}, \omega)\right|^2}. \tag{2.25}$$

It is emphasised that the specific form of equation (2.25) is based on the approximation that the dyadic Green's function is constant with respect to $f_\mathrm{D}(\omega)$. This approximation is also explicitly validated with respect to $\sigma_\mathrm{A}(\omega)$ in Section (2.3.2). Hence, the nETR in equation (2.25) is independent of specific quantum dot properties and it is therefore suited to describe the influence of the electromagnetic environment on the transfer process. In the present geometry with its fixed dipole axes the only information required for calculating the nETR factor is the squared modulus of the z-component of the donor's electric field at the position of the acceptor quantum dot. This information is easily accessible with FDTD simulations and the results are presented in the upcoming section.

nETR retrieved from FDTD simulations

The parameters of the FDTD simulations for retrieving the nETR are identical to those utilised for determination of Purcell factors in Section 2.2.2. Again, the single dipole source is located 10 nm above the lateral centre of one WGM antenna in order to avoid quenching and enhanced ohmic loss (Fig. 2.3(a)).

Likewise both WGM antennas inside the elliptic cavity are resolved with additional meshes of 2 nm resolution in every direction. According to the determination of Purcell factors for different geometries the nETR is also separately evaluated for the two constituents of the hybridised cavity-antenna system, i.e. the cavity and both antennas alone, as sketched in Fig. 2.3(a). Hence four simulations are necessary to retrieve the three distinct nETR factors: Three for the numerator in (2.25), i.e. the configurations sketched in Fig. 2.3(a), and one reference simulation for the denominator in (2.25), i.e. a dipole radiating in vacuum.

The elliptic cavity is expected to show a plasmonic-enhanced energy transfer by electric field concentration at both focal spots. They offer a dominating z-component of the electric field fitting to the fixed orientation of the quantum dot dipole moments. The third configuration, i.e. the WGM antennas in the absence of elliptic cavity walls, might increase the transfer rate compared to the rate in vacuum by near-field enhancement of the antenna structure alone. This latter simulation configuration and the reference simulation of an oscillating dipole in vacuum are most prominently affected in their mesh properties: Since the automatic meshing algorithm takes into account the refractive index of the present environment the absence of cavity walls and substrates will make the overall mesh more coarse compared to the hybridised and cavity-alone system. However, all four simulations exhibit the same fine meshes in the important regions, i.e. around the actively radiating emitter dipole and the intended position of the acceptor quantum dot.

The results are presented in Fig. 2.3(b). The nETR is shown as a function of the lateral position of the virtual acceptor quantum dot 10 nm above the Au substrate. The lateral displacement ranges from one side of the inner mesa-like structure of the WGM antenna to the other. Two different emission frequencies are considered here: The data for 366 THz (819 nm) relates to the spectral position of highest Purcell enhancement in the case of the hybridised system (see Fig. 2.1(b)), while data for 375 THz (800 nm) relates to spectral resonance of the

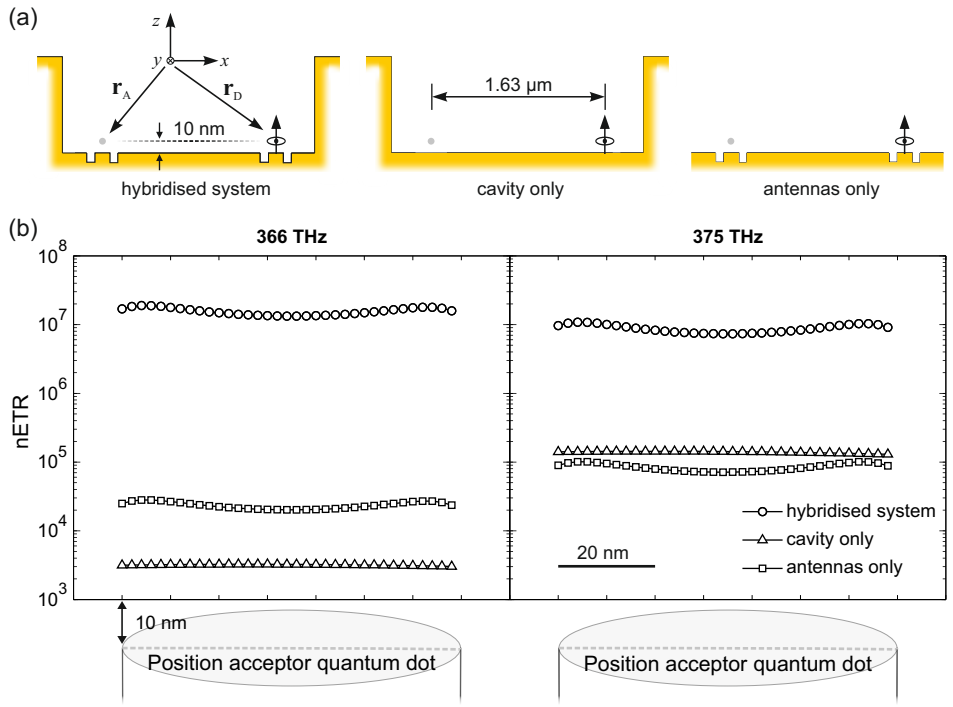

Fig. 2.3: Normalised energy transfer rate (nETR) of quantum dots coupled to WGM antennas in elliptic arena cavities as retrieved from FDTD simulations (a) The nETR is calculated for the hybridised antenna-cavity system and its distinct constituents. FDTD simulation parameters are identical to those utilised in Section 2.2.2. The grey dot marks the position of data evaluation. (b) Evaluated nETR for different excitation frequencies 366 THz (819 nm) and 375 THz (800 nm). The retrieved values relate to an acceptor quantum dot positioned 10 nm above the left WGM antenna. Its lateral position ranges, as sketched, from one groove edge to the other.

single constituents. Obviously, the nETR is highest for the hybridised system at both emission wavelengths and amounts to values well above 10^7. This means that 10^7 times more photons are transferred in the plasmonic environment from the donor to the acceptor than in free-space. Minimum values for the transfer rate amount to 3×10^3. Hence, the energy transfer rate alters by four orders of magnitude depending on the environment.

The detailed discussion starts with 366 THz (819 nm) emission: Both, the hybridised system and the two WGM antennas show an increased nETR of factor

1.5 near the groove edges compared to the mesa centre which is assigned to the enhanced electric fields near the abrupt structural inhomogeneity (see Fig. 1.5(c)). The exact nETR for an acceptor quantum dot laterally located in the centre of the WGM antenna amounts to 1.3×10^7 which is reduced by a factor of 500 to 2.0×10^4 if the cavity walls are removed ('antennas only'). Interestingly, by removing the WGM antennas and inserting the cavity walls again ('cavity only') the nETR is further reduced to a value of 3.2×10^3, although the cavity should prevent the photons from escaping the quantum dot environment. This can be explained by the LDOS of the system: The cavity mode is located at 375 THz and exhibits a sharp spectral width of below 3 THz (FWHM). The emission of the donor quantum dot at 366 THz is therefore far off-resonant and photons of this energy are not allowed to exist inside the cavity. To this effect the spontaneous emission of the emitting quantum dot is reduced compared to the other configurations which negatively affects the energy transfer rate. However, the spontaneous emission in this off-resonant case is still enhanced compared to free-space by the presence of the Au interface which gives a constant Purcell factor of 7.5 (see Fig. 2.1(b)). Here, it should be emphasised that although the WGM antennas are also not resonantly excited their broader spectral feature renders the excitation at 366 THz as 'near-resonant'. The associated enhanced electric field strength is sufficient to provide a nETR that exceeds that of the off-resonant cavity despite the fact that most of the radial symmetric emission of the source dipole will never reach the acceptor quantum dot. The orders of magnitude higher nETR in the presence of different plasmonic geometries is a result of the large donor-acceptor distance R in the present study, since the electric field amplitude of an oscillating dipole emitting in vacuum falls off with R^{-3} in the near-field and with R^{-1} in the far-field (see Fig. 8.3 in [229]). Hence the nETR is expected to drastically increase with R if photon emission into a 4π solid angle is prevented by an inhomogeneous environment. At very large separations R the exponentially decaying propagation length of SPPs starts to dominate and the nETR decreases to zero after reaching its maximum value [206].

At 375 THz (800 nm) donor quantum dot emission the hybridised system offers a nETR of 7.3×10^6 at the WGM centre which is a factor of two smaller compared to 366 THz emission. This reduction is explained by the two times smaller Purcell factor of the 375 THz mode of the hybridised system (see Fig. 2.1(b)). If the

quantum dots are placed inside the cavity without antennas the photon transfer rate is enhanced by 1.4×10^5. In the case of WGM antennas without the cavity walls the enhancement is about 7.1×10^4 and hence a factor of two smaller compared to the pure cavity. At resonant excitation the one order of magnitude higher Purcell factor of the WGM antennas and the associated larger LDOS is insufficient to compensate the loss of photons emitted into other directions than the WGM antenna decorated with the acceptor quantum dot. Like in the discussion of Purcell factors the plasmonic cavity alone is a very interesting device to enhance the energy exchange between widely separated quantum systems by utilising light concentration at the focal spot.

Comparing the retrieved nETR to literature

The quality of the enhanced dipole-dipole interaction in the plasmonic cavity system presented here is further assessed by comparing it to other devices enabling plasmon-mediated energy transfer. This is a cumbersome endeavour because, as discussed above, the nETR is highly sensitive to the donor-acceptor separation. However, a plasmonic system that has been theoretically investigated with view to nETR values on spatial scales of up to $R = 17$ μm is a metallic wedge waveguide (Martín-Cano and co-workers [206]). Due to light confinement in two dimensions and the possibility to use simple 1D Bragg reflector mirrors at the waveguide ends this structure is predicted to reach the strong-coupling regime and to be a suitable candidate for plasmonic cavity-QED (Hümmer and co-workers [148]). In the work of Martín-Cano and co-workers donor and acceptor quantum systems are positioned 10 nm above the wedge to avoid quenching effects just like in the present study. Likewise, the donor and acceptor dipole axis is fixed and no orientation averaging is applied. In contrast to the present study the donor quantum system, i.e. the emitting dipole source, radiates at 600 nm and the wedge is modelled according to the dielectric constant of Ag. The largest nETR values of up to 10^5 are obtained for a quantum system separation of $R = 3$ μm. Beyond this separation the exponential decay of the propagating wedge plasmon-polariton mode starts to dominate. At a comparable distance of $R = 2$ μm, like in the elliptic cavities, the nETR is approximately 5×10^4. Remarkably, the hybridised plasmonic system of elliptic cavity and WGM antennas, which has been developed

in this thesis, exceeds the nETR retrieved for metallic wedge waveguides in this case by more than two orders of magnitude. Even the pure elliptic cavity system without the antennas provides a superior performance with respect to nETR values at $R = 2\ \mu$m.

The observed superior performance of elliptic cavities is expected when considering propagations lengths of SPPs at a flat surface compared to those of wedge and channel plasmon-polaritons. Esteban-Moreno and co-workers theoretically studied the modal shape, dispersion relation and losses of channel plasmon-polaritons (CPP) in V-grooves and wedge plasmon-polaritons (WPP) [216] as utilised in the work of Martín-Cano. They found that the propagation length of a pure SPP is longer than that of fundamental CPPs and even longer than that of WPPs, which are not disturbed by the presence of a substrate featuring the wedge. The shorter propagation lengths of WPPs and CPPs are directly related to the field enhancement at corners and related field confinement [216].

The above discussion is restricted to fixed donor and acceptor dipole moment orientations. A study on the non-parallel configuration of these quantum systems and the associated impact on the nETR in the presence of metallic nano-rods, i.e. waveguides, was performed by Yu and co-workers in [329]. They could show that two nearby waveguides forming an angle compensate the non-parallel orientation of dipole moments of quantum emitters placed at opposing ends of the 250 nm long waveguides. nETR values amount to 8×10^4 and are hence similar to the results of Martín-Cano and co-workers. The non-parallel orientation of dipole moments is assumed to be the most severe drawback of the hybridised cavity system: If the acceptor quantum dot has its dipole moment aligned parallel to the Au substrate (x- and y-direction) and hence perpendicular to one of the donor quantum dot the m = 0 mode of the WGM antenna with its prominent electric field in z-direction will greatly suppress the energy transfer.

A comparison of plasmonic-enhanced energy transfer rates in two-dimensional systems is not possible since, to the best of the author's knowledge, the study presented here is the first one in this research field.

2.3.2 Absolute transfer rates and feasibility of strong-coupling regime

This section is concerned with the discussion of absolute transfer rates between the donor and acceptor quantum dots. As mentioned in the previous section, retrieved nETR values are sometimes not easy to interpret since they tend to rapidly grow with distance. Fortunately, they could be compared to a system that is predicted to facilitate plasmonic cavity QED and it turned out that the designed cavity-antenna system is more than a promising competitor. However, knowledge about the absolute transfer rate will give deeper insight into the efficiency of the transfer process and allows an estimation whether the system is suited to reach the strong-coupling regime with single, separated quantum systems. First, the idea of how to calculate the absolute transfer rate is introduced. In this context the retrieved nETR values will turn out to be very useful. Then, a specific type of quantum dot will be presented since the equation for energy transfer (2.20) requires knowledge about properties like the absorption cross-section $\sigma_{\mathrm{A}}(\omega)$ of the acceptor quantum dot.

The determination of the energy transfer rate $\gamma_{\mathrm{DA,struc}}(\omega)$ actually calls for a full quantum mechanical treatment of the problem. This can be simplified by making use of an expression exhibiting a comparing character like in (2.24) or (2.1), which links the quantum mechanical formulation to classical dipole sources. In this spirit the energy transfer rate in the plasmonic environment $\gamma_{\mathrm{DA,struc}}(\omega)$ is related to the rate of spontaneous decay $\gamma_0(\omega)$ by

$$\frac{\gamma_{\mathrm{DA,struc}}(\omega)}{\gamma_0(\omega)} = \frac{P_{\mathrm{DA,struc}}(\omega)}{P_0(\omega)} = \xi(\omega), \tag{2.26}$$

in which $P_{\mathrm{DA,struc}}(\omega)$ is the power absorbed by the acceptor and $P_0(\omega)$ the radiated power of the donor dipole in free space. Equation (2.26) relates the energy transfer rate to the spontaneous decay rate by the dimensionless factor $\xi(\omega)$. Since the spontaneous decay rate is known for a specific quantum dot the energy transfer rate can be evaluated in units of s^{-1}. The fraction in (2.26) is expanded by $P_{\mathrm{DA,vac}}(\omega)$, which is the absorbed power of the acceptor in free space:

$$\xi(\omega) = \frac{P_{\mathrm{DA,struc}}(\omega)}{P_{\mathrm{DA,vac}}(\omega)} \cdot \frac{P_{\mathrm{DA,vac}}(\omega)}{P_0(\omega)}. \tag{2.27}$$

Comparison with equation (2.24) leads to:

$$\xi(\omega) = \mathrm{nETR}(\omega) \cdot \underbrace{\frac{P_{\mathrm{DA,vac}}(\omega)}{P_0(\omega)}}_{\eta(\omega)} = \mathrm{nETR}(\omega) \cdot \eta(\omega). \tag{2.28}$$

The nETR has already been evaluated in the previous section. The factor $\eta(\omega)$ describes the the ratio of power $P_{\mathrm{DA,vac}}(\omega)$ absorbed by an acceptor quantum dot positioned in vacuum to the power $P_0(\omega)$ radiated by the donor quantum dot, which is also placed in vacuum, in the absence of the acceptor. If $\eta(\omega)$ and hence $\xi(\omega)$ is known the energy transfer rate is simply obtained by multiplying the latter factor with the spontaneous decay rate of the quantum dot according to (2.26). The ratio $\eta(\omega)$ can be calculated fully analytical by dividing (2.21) with (2.7) and setting the refractive index of the environment to $n = 1$:

$$\eta(\omega) = 6\sigma_{\mathrm{A}}(\omega)\pi \left| \mathbf{n}_{\mathrm{z}} \cdot \overleftrightarrow{\mathbf{G}}(\mathbf{r}_{\mathrm{A}}, \mathbf{r}_{\mathrm{D}}, \omega) \cdot \mathbf{n}_{\mathrm{z}} \right|^2. \tag{2.29}$$

Note, that (2.29) ignores the influence of a donor emission spectrum $f_{\mathrm{D}}(\omega)$. To be consistent with literature the following definition is applied [229]:

$$T(\omega) = 16\pi^2 k^4 R^6 \left| \mathbf{n}_{\mathrm{z}} \cdot \overleftrightarrow{\mathbf{G}}(\mathbf{r}_{\mathrm{A}}, \mathbf{r}_{\mathrm{D}}, \omega) \cdot \mathbf{n}_{\mathrm{z}} \right|^2. \tag{2.30}$$

Hence, $\eta(\omega)$ can be rewritten as:

$$\eta(\omega) = \frac{3c^4 \sigma_{\mathrm{A}}(\omega)}{8\pi R^6 \omega^4} T(\omega). \tag{2.31}$$

The function $T(\omega)$ generally accounts for an arbitrary orientation and separation of the donor and acceptor dipole moments. Due to the fixed orientation along the z-axis in the present discussion $T(\omega)$ is evaluated by inserting the dyadic Green's function of free-space to give the simple term [229]:

$$T(\omega) = 1 - k^2 R^2 + k^4 R^4. \tag{2.32}$$

Now, $\eta(\omega)$ can be written as:

$$\eta(\omega) = \frac{3c^4 \sigma_{\mathrm{A}}(\omega)}{8\pi \omega^4 R^6} - \frac{3c^2 \sigma_{\mathrm{A}}(\omega)}{8\pi \omega^2 R^4} + \frac{3\sigma_{\mathrm{A}}(\omega)}{8\pi R^2}. \tag{2.33}$$

The first term on the right hand side, rapidly decaying with R^{-6}, describes the non-radiative energy transfer in the donor's near-field, also known as Förster resonant energy transfer (FRET). At large donor-acceptor separation, like in the present elliptic cavities, the last term on the right hand side dominates. It describes energy transfer in the radiative limit in which the acceptor quantum dot absorbs a photon which was beforehand emitted by the donor quantum dot. The term with the R^{-4} dependence is related to an intermediate regime in which all terms contribute significantly ($kR \approx 1$).

For the sake of generality the normalised emission spectrum $f_{\mathrm{D}}(\omega)$ is considered according to (2.23) and hence equation (2.33) can be written as:

$$\begin{aligned}\eta(\omega) = &\frac{3c^4}{8\pi R^6}\int_0^\infty \frac{\sigma_{\mathrm{A}}(\omega) f_{\mathrm{D}}(\omega)}{\omega^4} d\omega - \frac{3c^2}{8\pi R^4}\int_0^\infty \frac{\sigma_{\mathrm{A}}(\omega) f_{\mathrm{D}}(\omega)}{\omega^2} d\omega + \ldots \\ &\ldots + \frac{3}{8\pi R^2}\int_0^\infty \sigma_{\mathrm{A}}(\omega) f_{\mathrm{D}}(\omega) d\omega.\end{aligned} \tag{2.34}$$

In its present form equation (2.34) is similar to literature except a missing orientation averaging (see equation (14.23) in [224]). With the knowledge of $\eta(\omega)$ the absolute energy transfer rate $\gamma_{\mathrm{DA,struc}}(\omega)$ can now be calculated according to (2.26) and (2.28):

$$\gamma_{\mathrm{DA,struc}}(\omega) = \mathrm{nETR}(\omega, R) \cdot \eta(\omega, R) \cdot \gamma_0. \tag{2.35}$$

in which the R-dependence is explicitly mentioned. Evaluating (2.35) requires the information about the specific absorption cross-section $\sigma_{\mathrm{A}}(\omega)$, emission spectrum $f_{\mathrm{D}}(\omega)$ and the spontaneous decay rate γ_0 of a real quantum dot.

Specific and general properties of quantum dots

All-solid-state emitters like quantum dots are perfectly suited for light-matter interaction in the presented plasmonic cavities since they feature deterministic positioning and remain stationary [266] compared to single molecules. For an experimental realisation of the above described long-range light-matter interaction InAs/GaAs quantum dots are of special interest: These quantum systems

exhibit a strong interaction with the radiation field due to high oscillator strength of about 11, belonging to the fundamental $0-0$ transition, which was theoretically estimated and measured by integrated absorption at temperatures below 10 K by Warburton and co-workers [310]. The oscillator strength corresponds to a spontaneous decay rate of $\gamma_0 \approx 1$ GHz which was confirmed by time-resolved photoluminescence only one year later by Gérard and co-workers [114]. These decay rates are faster than those of alternative quantum emitters at room-temperature like nitrogen vacancies in nanodiamonds [7] and CdSe quantum dots [9]: Both systems feature $\gamma_0 \approx 0.05$ GHz. Fitting to the utilised cavity and WGM antenna parameters InAs/GaAs quantum dots can be operated in the spectral range around 1.3 eV (950 nm), which lies within the spectrum of well-established Ti:sapphire oscillators. On the way to a solid-state analogue of cavity QED within the range of the optical spectrum InAs/GaAs quantum dots had been incorporated into micropillar cavities almost twenty years ago [113], showing a Purcell enhancement of 32 [114]. Already in that time they had been a promising candidate for reaching the strong-coupling regime [14]. By choosing an appropriate cavity scheme, i.e. the above mentioned 1D plasmonic waveguides with DBR mirrors, a theoretical study has recently shown that a plasmonic "one atom + one mode" system is actually feasible [148]. The upcoming evaluation of equation (2.35) is therefore performed with:

$$\gamma_0 = 1 \text{ GHz}. \tag{2.36}$$

InAs/GaAs quantum dots are fabricated by self-assembly according to the idea of Stranski and Krastanow [285]. This method exploits the mismatch in the lattice constant during epitaxial growth of semiconductor heterostructures. In this specific case InAs is deposited onto GaAs, which explains the denomination as InAs/GasAs quantum dots. After the first few layers of InAs, the so-called *wetting layer*, strain introduced by the lattice mismatch forces subsequently deposited InAs to build three-dimensional islands exhibiting a trapezoidal or pyramidal structure. A capping layer made of GaAs is further required to complete the structure [229]. For the useage of single InAs quantum dots a lateral periodic growth is required and specific quantum dots may be cut out by focused ion beam milling, while positioning is achieved by atomic force microscopy.

The base edge size of the pyramidal structure and its height determine the

electronic transition energies. Marzin and co-workers calculated the fundamental transition energies by an effective mass treatment and by approximating the structure as a cone [207]: Diameters of about 12 nm and heights in the nanometre regime should give fundamental transition energies of the 'electron - light hole' excitations around 1.55 eV (800 nm). Transition energies below 1.2 eV (1000 nm) have been realised with a base size of 20 nm $\times$ 20 nm and a height of 6 nm by Andersen and co-workers [13]. The geometrical extents of the active volume is much larger than that of spherical CdSe quantum dots with effective radii of about 2 nm [229]. Interestingly, Andersen and co-workers could experimentally show that with rather mesoscopic InAs quantum dots the dipole approximation of light-matter interaction is no longer valid because the extent of electron and hole wave functions becomes comparable to that of field gradients of plasmonic excitations. Depending on the exact configuration, the rate of decay to surface plasmons can vary by nearly an order of magnitude [13]. However, for the sake of simplicity and until an experimental realisation of the suggested scheme takes form the dipole approximation is assumed to be valid throughout the rest of the thesis.

At ambient temperatures the size of quantum dots also influences another parameter that has to be known for a quantitative analysis of absolute energy transfer rates: the absorption cross-section σ_{A}. Osborne and co-workers investigated on the absorption cross-section of InAs quantum dots with a base area of 100 nm^2 and a height of 7 nm for the fundamental transition around 1.0 eV (1.24 μm) [231]. From their data they deduce a peak absorption cross-section of 0.7×10^{-12} cm^2 (70 nm^2) in the absence of inhomogeneous broadening. The retrieved value is close to the geometric size of the base area which is a common trend for quantum dots operated at room temperature ([229], Chapter 9.2). For the upcoming determination of absolute energy transfer rates the absorption cross-section σ_{A} is set to:

$$\sigma_{\mathrm{A}}(\omega) = \sigma_{A,peak} \frac{\frac{\Gamma_{A,hom}^2}{4}}{(\omega - \omega_e)^2 + \frac{\Gamma_{A,hom}^2}{4}}, \tag{2.37}$$

in which $\sigma_{A,peak} = 0.7 \times 10^{-12}$ cm^2 , ω_e is the resonance frequency of the quantum dot, and $\Gamma_{A,hom}$ is the homogeneous line-width of the Lorentzian absorption peak. According to Osborne and co-workers [231] the line-width amounts to

$$\Gamma_{A,hom} = 2\pi \times 0.05 \text{ THz}. \tag{2.38}$$

The normalised emission spectrum $f_{\mathrm{D}}(\omega)$ of the quantum dot is modelled according to:

$$f_D(\omega) = \frac{1}{\pi} \frac{\frac{\Gamma_{em}}{2}}{(\omega - \omega_e)^2 + \frac{\Gamma_{em}^2}{4}}. \tag{2.39}$$

Since the above derived formalism requires the free-space emission spectrum [92], the emission line-width Γ_{em} is set equal to the spontaneous decay rate γ_0, i.e. $\Gamma_{em} = 2\pi \times \gamma_0 = 2\pi \times 1$ GHz. It may seem odd to use the emission spectrum at cryogenic temperatures and the absorption spectrum at room temperature. However, this is a conservative estimate since the peak absorption at cryogenic temperatures is increased (Chapter 9.2 in [229]), as will be discussed below. The upcoming discussion is assigned to the cryogenic temperature regime.

Determination and discussion of absolute energy transfer rates

This section is dedicated to the evaluation of absolute energy transfer rates (ETR) of widely separated quantum dots positioned on nanoantennas inside a plasmonic cavity. Finally, all results and information obtained in this chapter serve to derive the ETR according to the developed concept comprised in equation (2.34) and (2.35).

Here, the ETR between two widely separated quantum dots of different systems is derived: On the one hand the hybridised system of elliptical cavity and WGM antennas, and on the other hand the pure cavity for reasons of comparison. The associated nETR factors in (2.35) are those retrieved from FDTD simulations in Section 2.3.1. More precisely, the nETR of the hybridised system refers to the mode at 366 THz (819 nm), while the nETR of the cavity without antennas refers to the pure cavity mode at 375 THz (800 nm). Both values are taken at the centre of the circular mesa-like WGM antenna structure (nETR $\approx 1.3 \times 10^7$) and the focal spot of the cavity mode (nETR $\approx 1.4 \times 10^5$), respectively (see Fig. 2.3).

By utilising the information about the specific InAs quantum dot properties in the previous section the energy transfer rates for both systems are calculated according to (2.34) and (2.35):

$$\begin{aligned} \gamma_{\mathrm{DA,struc}}(\omega_e = 2\pi \times 366\ \mathrm{THz}) &\approx 40\ \mathrm{GHz} \quad \text{(hybridised system)} \\ \gamma_{\mathrm{DA,struc}}(\omega_e = 2\pi \times 375\ \mathrm{THz}) &\approx 0.4\ \mathrm{GHz} \quad \text{(pure cavity)} \end{aligned} \tag{2.40}$$

In the case of combined antenna-cavity system the rate of energy transfer is about 40 GHz which means that 40×10^9 photons are absorbed by the acceptor quantum dot every second. By considering that the nETR contributes with a factor of 1.3×10^7 the energy transfer rate in vacuum amounts to $\gamma_{\mathrm{DA,vacuum}} \approx 3$ kHz, i.e. 3000 photons per second. When comparing the transfer rate of 40 GHz to the Purcell-enhanced decay rate of the quantum dot of approximately 627 GHz it can be deduced that 6% of all emitted photons are safely delivered to the acceptor.

In the case of the pure elliptic cavity the rate of energy transfer is about 0.4 GHz which means that 4×10^8 photons are absorbed by the acceptor quantum dot in unit time. When comparing this energy transfer rate to the Purcell-enhanced decay rate of the quantum dot of approximately 54 GHz it can be deduced that 0.7% of all emitted photons are safely delivered to the acceptor. The only one order of magnitude lower efficiency compared to the hybridised system is attributed to the reduced dissipation of the pure cavity setup.

It can be summarised that both plasmonic structures, the hybridised system and the pure cavity, appreciably enhance the absolute energy transfer between widely separated quantum systems. This is also underscored by considering the rather low transfer rates of the quantum emitters in vacuum. The transfer efficiency in the latter case is about 3×10^{-6}, which corresponds to 3000 absorbed photons per second compared to 1×10^9 emitted photons per second. To achieve transfer efficiencies in vacuum that are comparabel to those of the hybridised system the distance between the specific quantum dots should be reduced from 1630 nm to 55 nm.

Enhanced cross-sections and cryogenic temperatures

A transfer efficiency of 6% in the case of the hybridised system is a decent performance, however, the absolute transfer rate stays below the transfer limit that is given by the Purcell-enhanced emission rate. It should be noted that the geometry-limited value of $\sigma_{A,peak}$ in equation (2.37) is only a lower boundary

since cross-sections in light-matter interaction can increase significantly at very low temperatures if the energy of irradiated photons $\hbar\omega$ matches the energy difference $\hbar\omega_e$ of particular quantum states, i.e. excitons in the case of semiconductor quantum dots. Basic quantum-mechanical light-scattering theory treats the scattering of a photon by an arbitrary multi-level system in second-order perturbation theory [195]. The associated two interactions represent the excitation of the quantum system from its initial state $|i\rangle$ to an excited state $|e\rangle$ due to the absorption of a photon, and the subsequent emission of a photon while the system decays from $|e\rangle$ to the final state $|f\rangle$. If the final state is identical to the initial state ($|f\rangle = |i\rangle$) and if the photon energy $\hbar\omega$ matches the transition energy $\hbar\omega_e$ of this two-level system the scattering process is also known as *resonant light scattering* and the scattering cross-section σ_S takes the simple form [195]

$$\sigma_S = \frac{3\lambda^2}{2\pi}, \tag{2.41}$$

which is completely independent from the transition dipole moment $\langle f|\,\hat{\mathbf{p}}\,|i\rangle$. Using $\lambda = 800$ nm gives $\sigma_S = 3 \times 10^{-9}$ cm^2 μm which is nearly four orders of magnitudes larger than the room temperature absorption cross-section in equation (2.37).

The approach of a pure elastic process and the approximation of a two-level system are restricted to ambient temperatures of ~ 0 K and to the decoupling of the quantum dot from a dissipative environment. The related transition is the $0-0$ transition represented by a zero-phonon line [249]. With increasing temperature dephasing events become more significant. The probability for phonon excitation and absorption grows so that the single final state transforms to a manifold of substates. This process is called *inelastic Raman scattering* and it can be shown that the scattering cross-section retrieved from perturbation theory in (2.41) decreases [195, 229]:

$$\sigma_S = \frac{3\lambda^2}{2\pi} \cdot \frac{\gamma_0}{\gamma_{\text{inh}}}, \tag{2.42}$$

Here, γ_0 and γ_{inh} are the homogeneous and inhomogeneous line-width, respectively. This ratio can be expressed in terms of Franck-Condon- and Debye-Waller-factors describing energy dissipation into phonons of the environment or the quantum dot itself [57] and it is of the order 0.1 for many molecules at low temperatures

[242]. The anti-correlation between resonance amplitudes and the line-width of single molecule resonances, as implied by equation (2.42), has been experimentally verified by Butter and co-workers [58].

The present discussion has been limited to the scattering cross-section under resonant conditions. From a quantum mechanical point of view the scattering process always includes the absorption of a photon. Using the large cross-section (2.41) as the absorption cross-section in previous calculations will lead to transfer rates of 100%. However, in the present formulation the derivation, starting at Poynting's theorem in (2.14), suggests to treat 'absorption' as a process in which the energy after donor excitation is irreversibly transferred into heat or chemical reactions like in photosynthesis. Therefore, the present discussion is continued in this picture:

Resonant light absorption, which is explicitly linked to a non-radiative decay rate γ_{nr} [180], has been theoretically investigated for semiconductor quantum dots by Lang and Pavlov [181]. In contrast to quantum mechanical perturbation theory they use a semi-classical approach with retarded potentials that takes into account all orders of light-electron interaction. The total light scattering and absorption cross-sections σ_S and σ_A, respectively, for an excitonic excitation are given by:

$$\sigma_S(\omega) = \frac{3\lambda^2}{2\pi} \cdot \frac{\gamma_r^2/4}{(\omega-\omega_e)^2 + \Gamma^2/4}, \tag{2.43}$$

$$\sigma_A(\omega) = \frac{3\lambda^2}{2\pi} \cdot \frac{\gamma_r\gamma_{nr}/4}{(\omega-\omega_e)^2 + \Gamma^2/4}, \tag{2.44}$$

in which λ and ω are the wavelength and angular frequency of the incident light, ω_e the resonance frequency of the exciton, and $\Gamma = \gamma_r + \gamma_{nr}$ the total decay rate with its radiative and non-radiative contributions, respectively. The results resemble the scattering and absorption cross-section of a bound electric charge in classical electrodynamics (Lorentz oscillator) [151]. It is noted that in the absence of non-radiative damping of excitons ($\gamma_{nr} = 0 \Rightarrow \sigma_A(\omega) = 0$) and on resonance ($\omega = \omega_e$) the scattering cross-section in (2.43) is identical to the resonant scattering cross-section as retrieved form second order quantum mechanical perturbation theory in (2.41).

A maximum peak absorption occurs for the special case of $\gamma_{nr} = \gamma_r$:

$$\sigma_{\mathrm{A}}^{Res} = \sigma_{\mathrm{S}}^{Res} = \frac{3\lambda^2}{8\pi}, \tag{2.45}$$

which is only four times smaller than the peak scattering cross-section. Interestingly, the requirement of equal non-radiative and radiative loss rates is similar to *impedance matching* and the condition for the phenomenon of *critical coupling*, in which an open resonator absorbs all incident energy [37].

To summarise the investigation of energy transfer rates in the weak-coupling regime, an appropriate choice and preparation of sample temperature and specific system properties, e.g. $\gamma_r = \gamma_{nr}$, will facilitate to push the evaluated decent transfer rates in (2.40) close to 100% efficiency. This result suggests to tackle the interaction of emitters in hybrid cavity-antenna systems in the formalism of quantum electrodynamics. Calculating the vacuum Rabi splitting of emitters attached to the system in the upcoming section will unambiguously reveal that the interaction of emitters is close to the strong-coupling regime and that a quantum mechanical description is indeed required.

2.4 Strong light-matter interaction in plasmonic arena cavities

This section is concerned with the coupling strength of quantum systems inside the elliptic arena cavity. With a view to literature a theoretical model will be proposed in form of the Tavis-Cummings Hamiltonian [290] while a sophisticated investigation of the master equation of an open quantum system is beyond the scope of this work. During the discussion it will turn out that under certain conditions both, the elliptic cavity as well as the circular cavity, are promising candidates for strong and ultra-fast light-matter interaction involving single quantum emitters.

2.4.1 Introduction to the Tavis-Cummings model

The coupling between oscillators has already been discussed in terms of localised and propagating SPPs in Chapter 1. According to those results and the simple oscillator model (see Section 1.4.2) the strong-coupling regime features the splitting of energy levels if two or more systems with identical resonance frequencies are combined to a new system. In the case of a WGM antenna embedded in a circular arena cavity the splitting of modes leads to an oscillatory exchange of electromagnetic energy between the individual constituents, whereupon the rate of energy exchange increases with the splitting magnitude. It was also shown that the new corresponding eigenmodes are a linear combination of the modes of the isolated systems (Section 1.3.4).

This concept also applies in a similar fashion to quantum dots: The eigenstates of two quantum dots can be written as $|g_1\rangle$, $|g_2\rangle$, $|e_1\rangle$ and $|e_2\rangle$, in which the subscripts denote the particular quantum dot, and g and e denote the ground and excited state, respectively. If the quantum dots are isolated, the corresponding systems are separable and the eigenstates can be written in form of product states, e.g. $|g_1\rangle \cdot |e_2\rangle = |g_1, e_2\rangle$. By switching on the interparticle interaction Hamiltonian $\hat{V}_{12}$ the entire system has to be described by a new set of eigenstates which can be represented as a linear combination of the former unperturbed eigenstates ([229], Chapter 8.7.3). Besides the ground state $|g_1, g_2\rangle$ and the double excited state $|e_1, e_2\rangle$ the single excited states are of particular interest:

$$\begin{aligned} \left|\psi^+\right\rangle &= \frac{1}{\sqrt{2}}\left(|e_1, g_2\rangle + |g_1, e_2\rangle\right) \\ \left|\psi^-\right\rangle &= \frac{1}{\sqrt{2}}\left(|e_1, g_2\rangle - |g_1, e_2\rangle\right) \end{aligned} \tag{2.46}$$

If the coupled system resides in one of the stationary states $|\psi^+\rangle$ or $|\psi^-\rangle$, it is impossible to distinguish which of both quantum dots is excited and which one is in its ground state. The eigenenergies associated with those two stationary states shift to lower and higher energies with respect to the eigenenergy of the isolated system state $|e_{1,2}\rangle$ and they are separated by $M \propto \langle e_1, g_2 | \hat{V}_{12} | g_1, e_2 \rangle$ ([229], Chapter 8.7.3). The increasing splitting of energy levels with higher coupling strength M was shown by Bayer and co-workers [30]. They varied the coupling strength by

increasing the distance between InAs quantum dot layers. A complex manifold of such optical signatures, so-called *anti-crossings*, are realised by applying electric fields to neighbouring InAs quantum dots embedded in Schottky diodes by Stinaff and co-workers [284].

The interaction Hamiltonian $\hat{V}_{12}$ connects states in which opposite quantum dots are excited and hence $M/\hbar$ can be taken as a measure for the rate of excitation exchange [74]. If this process is faster than competing processes responsible for dephasing, e.g. phonon interaction, it is not possible to distinguish which quantum dot is excited and the single excited states of the system have to be described by the stationary states (2.46). The inverse of this rate can also be interpreted as the time $\tau_c = h/M$ that is required to establish coherence between the states $|e_1, g_2\rangle$ and $|g_1, e_2\rangle$ ([229], Chapter 8.7.3). Temperature-dependent dephasing times of InAs quantum dots were measured by Borri and co-workers by four-wave mixing spectroscopy [40]: At temperatures of 25 K to 7 K they determined dephasing times of 170 ps to 630 ps, respectively. The dephasing time near liquid helium temperature is close to the lifetime $(1/\gamma_0)$ of InAs quantum dots in vacuum and hence the 40 times larger ETR in elliptic arena cavities, retrieved in equation (2.40), seems to facilitate stationary states like in (2.46) at first sight.

However, another process that destroys the coherence of the superposition of states is spontaneous emission [108], since in this case the photon is generally lost to the radiation field and the system ultimately resides in the ground state $|g_1, g_2\rangle$. The interaction of quantum systems separated by distances on the order of the Förster radius occurs in a non-radiative manner. For emitter separations larger than the vacuum wavelength of involved photons the transport is dominated by the intuitive quantum pathway in which a photon (plasmon) is emitted by one quantum system and successively absorbed by the other quantum system ([224], Chapter 14). From this considerations it can be deduced that a strong coupling in the exact form of the eigenstates in (2.46) is not possible. This is because the transfer process requires ultimately the emission of a photon into the cavity.

Fortunately, this latter point can be utilised to formulate a different coupling scheme: Unlike in common spontaneous emission, the photon is not irreversible lost in free-space but it is stored as a surface plasmon excitation inside the cavity. In this case it is not sufficient to only consider the Hilbert spaces of both quantum emitters. Additionally, a sub-space of photons has to be considered in which the

eigenstate $|n\rangle$ describes the number n of photons (plasmons) stored inside the cavity. The new product state then reads, for instance, $|g_1, g_2, 1\rangle$, meaning that both quantum dots are in the ground state and one photon is stored in the cavity. The same approach was recently utilised by Kim and co-workers to describe the experimental results of two separated quantum dots strongly coupled to a photonic crystal cavity [160]. They were able to control the detuning between individual exciton spin states and the cavity resonance by applying external magnetic fields and temperature tuning. The uniform density of InAs quantum dots was about 20 μm^{-2} and hence the single emitters were separated by at least 200 nm. They successfully modelled the measured photoluminescence, as well as the retrieved vacuum Rabi splitting, by the following Hamiltonian:

$$\begin{aligned}\hat{H}_{TC} = & \underbrace{\hbar\omega_c \hat{a}^\dagger \hat{a}}_{\text{energy in radiation field}} + \underbrace{\frac{\hbar}{2}\left(\omega_1 \hat{\sigma}_{1z} + \omega_2 \hat{\sigma}_{2z}\right)}_{\text{energy in QDs}} \\ & + \underbrace{\hbar g_1 \left(\hat{\sigma}_{1+}\hat{a} + \hat{a}^\dagger \hat{\sigma}_{1-}\right)}_{\text{coupling of photons to QD1}} + \underbrace{\hbar g_2 \left(\hat{\sigma}_{2+}\hat{a} + \hat{a}^\dagger \hat{\sigma}_{2-}\right)}_{\text{coupling of photons to QD2}} .\end{aligned} \tag{2.47}$$

This is the so-called *Tavis-Cummings Hamiltonian* which describes the interaction of N identical multi-level atoms with a single cavity mode [290]. Since only a particular transition of the quantum dot is considered the formulation of (2.47) is restricted to two-level systems and the corresponding formalism becomes mathematically equivalent to that of spin-1/2 particles in a magnetic field [199]. In the following the particular constituents and properties of $\hat{H}_{TC}$ are presented in short.

The first term on the right-hand side describes the energy contained in the radiation field. The operators $\hat{a}^\dagger$ and $\hat{a}$ are the creation and annihilation operators for photons with frequency ω_c. Their subsequent application $\hat{a}^\dagger\hat{a}$ on the eigenstate $|n\rangle$ gives the number of photons inside the cavity and hence the overall energy $\hbar\omega_c n$:

$$\hat{a}^\dagger \hat{a}\,|n\rangle = n\,|n\rangle\,. \tag{2.48}$$

This can be easily shown with the relations

$$\hat{a}^\dagger |n\rangle = \sqrt{n+1}\,|n+1\rangle\,, \tag{2.49}$$

and

$$\hat{a}\,|n\rangle = \sqrt{n}\,|n-1\rangle\,, \tag{2.50}$$

and the special case $\hat{a}\,|0\rangle = 0$, in which $|0\rangle$ denotes the vacuum state of the quantised radiation field ([108], Chapter 8).

The second term on the right-hand side represent the amount of energy stored in the quantum dots. This quantity is measured with the Pauli matrix $\hat{\sigma}_{i,z}$ [247], where the subscript i denotes the particular quantum dot:

$$\hat{\sigma}_x = \begin{pmatrix} 0 & 1 \\ 1 & 0 \end{pmatrix}, \hat{\sigma}_y = \begin{pmatrix} 0 & -\mathrm{i} \\ \mathrm{i} & 0 \end{pmatrix} \text{ and } \hat{\sigma}_z = \begin{pmatrix} 1 & 0 \\ 0 & -1 \end{pmatrix}. \tag{2.51}$$

The ground state $|g_i\rangle$ and the excited state $|e_i\rangle$ of the quantum dots may be represented by

$$|g\rangle = \begin{pmatrix} 0 \\ 1 \end{pmatrix} \text{ and } |e\rangle = \begin{pmatrix} 1 \\ 0 \end{pmatrix}. \tag{2.52}$$

The application of $\hat{\sigma}_{i,z}$ on $|g_i\rangle$ or $|e_i\rangle$ thus gives the ground state energy $-\frac{\hbar}{2}\omega_i$ or the excited state energy $\frac{\hbar}{2}\omega_i$ and leaves the state itself unaltered.

The last two terms on the right-hand side finally describe the coupling of the individual quantum dots to the cavity. If the operator $\hat{a}^\dagger\hat{\sigma}_{2-}$ acts on the state $|g_1, e_2, 0\rangle$, the excited second quantum dot returns to its ground state by emitting a photon into a cavity and hence the former state is altered to $|g_1, g_2, 1\rangle$. The operators $\hat{\sigma}_{i-}$ and $\hat{\sigma}_{i+}$ are the so-called lowering and raising operator for the specific quantum dot and they are built by a linear combination of Pauli matrices [247]:

$$\hat{\sigma}_- = \frac{1}{2}(\hat{\sigma}_x - \mathrm{i}\hat{\sigma}_y) = \begin{pmatrix} 0 & 0 \\ 1 & 0 \end{pmatrix} \quad \text{and} \quad \hat{\sigma}_+ = \frac{1}{2}(\hat{\sigma}_x + \mathrm{i}\hat{\sigma}_y) = \begin{pmatrix} 0 & 1 \\ 0 & 0 \end{pmatrix}. \tag{2.53}$$

The raising and lowering of quantum dot states can then be easily verified with (2.52):

$$\hat{\sigma}_+ |g\rangle = \begin{pmatrix} 0 & 1 \\ 0 & 0 \end{pmatrix} \begin{pmatrix} 0 \\ 1 \end{pmatrix} = \begin{pmatrix} 1 \\ 0 \end{pmatrix} = |e\rangle \,. \tag{2.54}$$

On this note it is important to realise that operations like $\hat{\sigma}_- |g\rangle$ or $\hat{\sigma}_+ |e\rangle$ are pointless in a two-level system and they will give the null vector $\mathbf{0}$ according to (2.53) and (2.52).

Since the concept of the elliptical arena cavity setup is quite similar to the one presented by Kim and co-workers, and since both devices only differ in the specific design, the Tavis-Cummings Hamiltonian is applied to the system presented here. Interestingly, the coupling scheme for the quantised system in (2.47) resembles that of the pure plasmonic properties investigated in Chapter 1.4.2. There it was shown that the coupling of localised plasmonic modes of widely separated WGM antennas (the emitters) is mediated by the resonant cavity mode. The response function of the system was correctly modelled by ordinary differential equations which exhibit a direct coupling only between both antenna modes to the cavity mode, respectively, and no direct coupling between the antennas is required.

The question may arise which properties distinguish the system presented here from the coupling scheme in the above mentioned photonic crystal cavities in [160]. An important difference can occur in the strength of coupling which is measured in terms of the coupling constant g in (2.47). The coupling constant g is related to the so-called *vacuum Rabi frequency* $\Omega_{\mathrm{VRS}} \propto g$ which determines the time-scale of coherent and time-harmonic switching between probabilities of finding the quantum dot in the ground or excited state. These coherent operations are the building blocks for e.g. quantum information processing. Hence, a stronger interaction between the radiation field and the quantum system allows faster and more stable operations. Additionally, a strong interaction is needed to explore specific phenomena like thresholdless lasing, or quantum plasmonics [289] and quantum nonlinear optics [63] in general. Plasmonic nanostructures with small mode volumes, like the utilised WGM antennas inside the arena cavities, are promising for increasing this coupling strength since they offer a high LDOS and hence many options are available for the emitter to interact with the radiation field. It is further interesting to note that up to now no experiment exists that reports on the successful realisation of strong-coupling between a single quantum system and an SPP mode [295].

Therefore, the next section will present the criterion for the observation of strong coupling in the case of the Hamiltonian in (2.47). The coupling strength g will then be derived from FDTD simulations and it will be estimated whether the criterion is fulfilled.

2.4.2 Determination of coupling strength g in elliptic arena cavities

The criterion for strong light-matter interaction is to resolve the splitting of energy levels of the coupled quantum dots-cavity-system in the limit of a single cavity photon. This is similar to the case of coupled plasmonic modes in Chapter 1: If the splitting of mode peaks is too small compared their spectral width, no periodic exchange of excitation (beating) is observed in the time-signal before it is has decayed due to cavity loss. First, the participating states and the associated magnitude of energy level splitting is derived from the Tavis-Cummings model.

By considering a weak excitation of the system and n cavity photons the derivation of eigenenergies is restricted to the following three states [160]: $|e_1, g_2, n-1\rangle$, $|g_1, e_2, n-1\rangle$ and $|g_1, g_2, n\rangle$. Accordingly, the double excited state is not considered in the weak excitation limit. Applying the Hamiltonian in (2.47) to these three states gives the following results:

$$\hat{H}_{TC}\,|e_1, g_2, n-1\rangle = \left[\hbar\omega_c(n-1) + \frac{\hbar}{2}(\omega_1 - \omega_2)\right]|e_1, g_2, n-1\rangle + \hbar g_1\sqrt{n}\,|g_1, g_2, n\rangle \tag{2.55}$$

$$\hat{H}_{TC}\,|g_1, e_2, n-1\rangle = \left[\hbar\omega_c(n-1) + \frac{\hbar}{2}(\omega_2 - \omega_1)\right]|g_1, e_2, n-1\rangle + \hbar g_2\sqrt{n}\,|g_1, g_2, n\rangle \tag{2.56}$$

$$\hat{H}_{TC}\,|g_1, g_2, n\rangle = \left[\hbar\omega_c n - \frac{\hbar}{2}(\omega_2 + \omega_1)\right]|g_1, g_2, n\rangle + \hbar g_1\sqrt{n}\,|e_1, g_2, n-1\rangle + \hbar g_2\sqrt{n}\,|g_1, e_2, n-1\rangle \tag{2.57}$$

As can be seen from the equations (2.55 - 2.57) the three states $|e_1,g_2,n-1\rangle$, $|g_1,e_2,n-1\rangle$ and $|g_1,g_2,n\rangle$ are no longer eigenstates of the coupled system. For simplicity it is assumed that the cavity resonance frequency is equal to both quantum dot transition frequencies ($\omega=\omega_c=\omega_1=\omega_2$) and that the coupling constants are identical ($g=g_1=g_2$). The Hamilton operator $\hat{H}_{TC}$ in matrix form then reads:

$$\hat{H}_{TC,n}=\begin{pmatrix}\hbar\omega(n-1) & 0 & \hbar g\sqrt{n}\\ 0 & \hbar\omega(n-1) & \hbar g\sqrt{n}\\ \hbar g\sqrt{n} & \hbar g\sqrt{n} & \hbar\omega(n-1)\end{pmatrix}. \tag{2.58}$$

Using the methods of linear algebra the Hamiltonian in (2.58) can be diagonalised by finding the roots of the characteristic polynomial:

$$\hat{H}_{TC,n}=\begin{pmatrix}\hbar\omega(n-1)-\hbar g\sqrt{2n} & 0 & 0\\ 0 & \hbar\omega(n-1) & 0\\ 0 & 0 & \hbar\omega(n-1)+\hbar g\sqrt{2n}\end{pmatrix}. \tag{2.59}$$

According to (2.59) the maximum energy splitting between the lowest and the highest level is $\Delta E_{max}=\hbar 2g\sqrt{2n}$. This is a factor of $\sqrt{2}$ larger than in the case of a single emitter and a cavity described by the Jaynes-Cummings model ([108], Chapter 10.4). Since the strong-coupling regime is concerned with a single cavity photon ($n=1$) the eigenenergies and the corresponding new eigenstates can finally be written as [160]:

$$\begin{aligned}
|\psi_+\rangle &= \frac{1}{2}\left(|e_1,g_2,0\rangle+|g_1,e_2,0\rangle+\sqrt{2}\,|g_1,g_2,1\rangle\right), \quad E_+=\hbar g\sqrt{2}\\
|\psi_0\rangle &= \frac{1}{\sqrt{2}}\left(|e_1,g_2,0\rangle-|g_1,e_2,0\rangle\right), \quad E_0=0\\
|\psi_-\rangle &= \frac{1}{2}\left(|e_1,g_2,0\rangle+|g_1,e_2,0\rangle-\sqrt{2}\,|g_1,g_2,1\rangle\right), \quad E_-=-\hbar g\sqrt{2}
\end{aligned} \tag{2.60}$$

The eigenstate $|\psi_0\rangle$ is a so-called *dark dressed state* [106] which is not seen in photoluminescence because it cannot decay to the system ground state by dipole radiation or the decay of a photon into the cavity [106, 160]. In order estimate the feasibility of strong-coupling in elliptic arena cavities only the two states $|\psi_+\rangle$ and $|\psi_-\rangle$ and the corresponding level splitting $\Delta E_{max}=\hbar 2g\sqrt{2}$ will be considered.

It is interesting to note that in the investigation of *superradiance* with FDTD simulations it will later turn out (see Section 2.5) that the central, non-shifted mode of the hybridised system also vanishes due to destructive interference if dipoles on separated WGM antennas are oscillating in phase.

Since the involved modes and the corresponding energy splitting have been identified it remains to determine the coupling strength g for an estimation of the strong-coupling regime. In the case of quantised plasmonic interaction the coupling strength can be expressed in general by the *spectral density* $|g(\omega)|^2$ like in the plasmonic QED publication of Hümmer and co-workers [148]:

$$|g(\omega)|^2 = \frac{1}{\hbar\pi\varepsilon_0}\frac{\omega^2}{c^2}\mathbf{p}^T \cdot \mathrm{Im}\left\{\overleftrightarrow{\mathbf{G}}_{\mathrm{SPP}}(\mathbf{r}_0,\mathbf{r}_0,\omega)\right\}\cdot\mathbf{p}. \tag{2.61}$$

Here, $\mathbf{p}$ is the (transposed) transition dipole moment and $\overleftrightarrow{\mathbf{G}}_{\mathrm{SPP}}(\mathbf{r}_0,\mathbf{r}_0,\omega)$ is the plasmonic contribution to the electromagnetic Green's tensor of the nanostructure at the position $\mathbf{r}_0$ of the emitting quantum dot. By comparing equation (2.61) with (2.11) it follows that the spectral density $|g(\omega)|^2$ differs from the enhanced spontaneous decay rate of an emitter by only a factor of 2π. Note, that although the spectral density is represented by a squared value it is measured in units of s^{-1}. Analogue to Hümmer and co-workers it is assumed that the dyadic Green's function retrieved from FDTD simulations is dominated by the plasmonic contribution, which is underscored by the fact that most of the power emitted by a dipole source is injected into localised and propagating surface plasmons (see Chapter 1.2.3). In this formulation the Hamiltonian for a single quantum dot (QD) with a transition frequency ω_0 coupled to a resonant cavity reads [148]:

$$\begin{aligned}\hat{H} =& \hbar\frac{\omega_0}{2}\hat{\sigma}_{z,\mathrm{QD}} + \int_0^\infty \hbar\omega\hat{a}^\dagger(\omega)\hat{a}(\omega)d\omega \\ &+ \int_0^\infty \hbar\left(g(\omega)\hat{a}^\dagger(\omega)\hat{\sigma}^-_{\mathrm{QD}} + g(\omega)\hat{\sigma}^+_{\mathrm{QD}}\hat{a}(\omega)\right)d\omega,\end{aligned} \tag{2.62}$$

in which $\hat{a}^\dagger(\omega)$ and $\hat{a}(\omega)$ are the creation and annihilation operators for collective modes, i.e. plasmon-polaritons [148]. An elaborate quantisation scheme for the electromagnetic field in dispersive and lossy linear dielectrics can be found in [149] and [240]. If $|g(\omega)|^2$ exhibits a resonant-like shape it can be expressed in terms of a Lorentzian line shape function [148]:

$$|g(\omega)|^2 = g^2 \frac{1}{\pi} \frac{\frac{1}{2}(2\pi\Delta\nu_{\mathrm{cav}})}{(\omega-\omega_0)^2 + \left(\frac{1}{2}(2\pi\Delta\nu_{\mathrm{cav}})\right)^2}. \tag{2.63}$$

Here, g is identified as the coupling constant between a quantum dot inside the elliptic arena cavity and the plasmonic cavity mode and it can thus directly be inserted into the Tavis-Cummings Hamiltonian (2.47). It is important to note that the full value of g describes the coupling strength at a sharp frequency ω_0 which is assumed to coincide with the transition frequency of the quantum dots and the plasmonic cavity mode. The peak width $\Delta\nu_{\mathrm{cav}}$ represents the amount of loss due to SPP propagation or cavity wall reflection. It is this peak-broadening mechanism that can obscure the Rabi vacuum splitting of $\Omega_{\mathrm{VRS}} = 2g\sqrt{2}$ since in the presence of loss also the emission lines in e.g. photoluminescence will broaden. For modelling the full system, i.e. the temporal evolution of the density matrix ρ, including loss, the representation of $|g(\omega)|^2$ in the form of (2.63) is advantageous: The quantum dots and the elliptic cavity are described in the form of a sharp two-level system (TLS) with the coupling constant g according to (2.47), while all terms describing loss mechanisms (emitter loss, cavity loss, pure dephasing,...) are encoded in a bosonic bath that is additionally coupled to the pure TLS. This is the approach of the so-called *Markovian Lindblad Master equation* [73, 46], which lies beyond the scope of this work.

Here, the splitting $\Omega_{\mathrm{VRS}} = 2g\sqrt{2}$ will be determined and the corresponding sharp modes will be convoluted with a Lorentzian peak function of width $\Delta\nu_{\mathrm{cav}}$. The sum of both peaks then renders a photoluminescence signal. The sole consideration of cavity loss is motivated by the fact that peak broadening due to enhanced emission rates lies well below 1 THz and operation at temperatures of 4 K eliminates pure dephasing as mentioned above. Since $|g(\omega)|^2$ is identical to the enhanced emission rate of the quantum dot except for a constant factor the peak shape in (2.63), defined by $\Delta\nu_{\mathrm{cav}}$, is assumed to render the spectral resolved photoluminescence signal. This procedure is a visual verification of the rule of thumb which states that the coupling constant should be preferably larger than half the width of the emission peak [295, 108]:

$$g > \frac{\Delta\nu_{\mathrm{cav}}}{2} \tag{2.64}$$

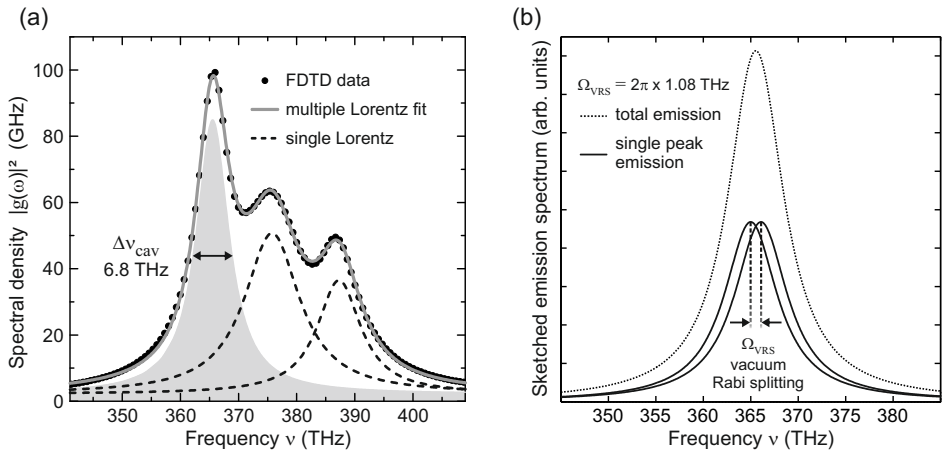

Fig. 2.4: Coupling strength of a quantum dot to an elliptic plasmonic cavity. (a) Spectral density (black filled circles) calculated from the imaginary part of the dyadic Green's function according to equation (2.11) and a dipole moment of 1.4×10^{-28} Cm ($\gamma_0 = 1$ GHz). The spectral features are fitted with three Lorentz peaks whereupon the grey curve is the cumulative result. One of the peaks (grey shaded area) is further investigated since it exhibits the strongest coupling to cavity photons. Its fitted spectral width of $\Delta\nu_{\text{cav}} = 6.8$ THz is mainly attributed to cavity loss. (b) Sketched photoluminescence yield: The black solid lines represent the grey shaded peak at 365 THz shifted by $\pm\Omega_{\text{VRS}}/2$, respectively, according to the vacuum Rabi splitting retrieved from the Tavis-Cummings model. The black-dotted line is the sum of both shifted peaks.

The coupling constant g is retrieved from FDTD simulation via the spectral density $|g(\omega)|^2$ in (2.61). The FDTD simulations and corresponding parameters are the same as utilised for the determination of Purcell enhancement (see Section 2.2) and energy transfer rates (see Section 2.3.1 and 2.3.2). The decisive component of dyadic Green's function at the emitter position is $G_{zz}(\mathbf{r}_0, \mathbf{r}_0, \omega)$ since the dipole moment of the emitter points in z-direction. A script provided by Lumerical was adapted to the present problem to calculate $\text{Im}\{G_{zz}\}$ according to equation (2.5). By utilising equation (2.12) and the previously used spontaneous decay rate γ_0 of 1 GHz at 366 THz (819 nm) the strength of the transition dipole moment $\mathbf{p}$ amounts to 1.4×10^{-28} Cm. This value was taken as a constant and the calculated spectral density $|g(\omega)|^2$ is represented in Fig. 2.4(a) by black filled circles.

The shape of the curve is dominated by three features which are the well-known modes already encountered in the investigation of plasmonic modes and the frequency-resolved Purcell factor. At 366 THz (819 nm) the spectral density

exhibits a peak value of about 100 GHz. Taking into account that $|g(\omega)|^2$ can also be retrieved by dividing the enhanced spontaneous emission rate $\gamma \approx 600$ GHz by 2π approves the aforementioned procedure for calculating the spectral density. To carve out the modal parameters of the peak at 366 THz, which is most promising for strongest emitter-plasmon coupling, a sum of three single Lorentzian line shape functions is fitted to the entire curve. The single Lorentzian peak functions are given by equation (2.63) and the cavity loss rate of the mode at 366 THz amounts to $\Delta\nu_{\mathrm{cav}} = 6.8$ THz, while the spectral density peaks at $|g(366\ \mathrm{THz})|^2 = 85$ GHz. Taking this peak position as the sharp resonance frequency $\omega_0 = 2\pi \times 366$ THz of both, the TLS and the cavity mode, the coupling strength is evaluated according to (2.63):

$$g = \sqrt{|g(\omega_0)|^2 \pi^2 \Delta\nu_{\mathrm{cav}}}. \tag{2.65}$$

Finally, the coupling strength and the vacuum Rabi splitting in the elliptic arena cavity amount to

$$g = 2\pi \times 0.38\ \mathrm{THz} \qquad \Omega_{\mathrm{VRS}} = 2g\sqrt{2} = 2\pi \times 1.08\ \mathrm{THz}. \tag{2.66}$$

The chance to observe vacuum Rabi splitting, i.e. the strong-coupling of a single cavity photon to the quantum emitters, appears to be unlikely when comparing the splitting of $\Omega_{\mathrm{VRS}}/(2\pi) = 1.08$ THz to the peak width of $\Delta\nu_{\mathrm{cav}} = 6.8$ THz. This is depicted in Fig. 2.4(b): Two Lorentzian peaks are shown which are separated by $\Omega_{\mathrm{VRS}}/(2\pi)$ and exhibit a width of $\Delta\nu_{\mathrm{cav}} = 6.8$THz. The single peaks are well separated for the naked a eye and can be clearly distinguished on the THz-scale. However, if these sketched emission spectra are added up, the separation smears out and the result has to be described as a single peak. Hence, for a real experiment the vacuum Rabi splitting is assumed to be too small for detection.

To better assess the strength of splitting the results are compared to the coupling of two InAs quantum dots to the mode of a photonic crystal cavity which has already been mentioned earlier [160]. Kim and co-workers retrieved a maximum coupling strength of $g_{\mathrm{Kim}} = 20$ GHz from their experiments, whereat g_{Kim} includes the additional factor of $\sqrt{2}$ due to the presence of two quantum emitters. By direct comparison the coupling strength of the elliptic arena cavities presented here exhibits values of about $\sqrt{2} \cdot 0.38$ THZ, which is 26 times higher than that in

the photonic crystal cavity. Unfortunately, the higher coupling constant in the plasmonic system is dearly bought since metallic systems also provide higher loss rates. Here, a cavity loss rate of $\Delta\nu_{\mathrm{cav}} = 6.8$ THz was retrieved, whereas the photonic crystal cavity of Kim and co-workers offers a 186 times smaller damping of $\Delta\nu_{\mathrm{Kim}} = 36.4$ GHz. In order to enhance interaction and to see a Rabi splitting despite the plasmonic losses, more photons have to be stored inside the cavity according to the n-photon Hamiltonian in (2.59). Approximately 10 photons have to be kept inside the cavity to satisfy at least the rule of thumb in (2.64) because the splitting increases with $\sqrt{n}$.

Although this chapter is dedicated to the interaction of multiple quantum systems the next section will be concerned with the circular arena cavity and a single emitter. The results of this section raise the hope that a smaller mode area and the perfect radial symmetry of plasmonic modes and metallic structures lead to higher coupling strength.

2.4.3 Determination of coupling strength g in circular arena cavities

The coupling of a single quantum system with a single cavity mode is a limiting case of the more general Tavis-Cummings Hamiltonian. This problem is known in literature as the *Jaynes-Cummings* model. The Jaynes-Cummings Hamiltonian $\hat{H}_{JC}$ can be obtained directly from (2.67):

$$\hat{H}_{JC} = \underbrace{\hbar\omega_c\hat{a}^\dagger\hat{a}}_{\text{energy in radiation field}} + \underbrace{\frac{\hbar}{2}\omega_{\mathrm{QD}}\hat{\sigma}_{QD,z}}_{\text{energy in QD}} + \underbrace{\hbar g\left(\hat{\sigma}_{QD,+}\hat{a} + \hat{a}^\dagger\hat{\sigma}_{QD,-}\right)}_{\text{coupling of photons to QD}}. \tag{2.67}$$

Again, the weak excitation of the system is considered with a general number of n cavity photons. The corresponding product states, which represent the old eigenstates of the uncoupled system, are $|e,n-1\rangle$ and $|g,n\rangle$. Letting these two states act on the Jaynes-Cummings Hamiltonian in (2.67) and obeying the rules defined in (2.48) to (2.54) the matrix representation of $\hat{H}_{JC}$ is given by:

$$\hat{H}_{JC,n} = \begin{pmatrix} \hbar\omega_c(n-1) + \frac{\hbar\omega_{\mathrm{QD}}}{2} & \hbar g\sqrt{n} \\ \hbar g\sqrt{n} & \hbar\omega_c n - \frac{\hbar\omega_{\mathrm{QD}}}{2} \end{pmatrix}. \tag{2.68}$$

Assuming that the frequency of the resonant cavity mode coincides with the transition frequency of the TLS ($\omega_0 = \omega_c = \omega_{\mathrm{QD}}$) the diagonalised Hamiltonian reads:

$$\hat{H}_{JC,n} = \begin{pmatrix} \hbar\omega_0(n-\frac{1}{2}) + \hbar g\sqrt{n} & 0 \\ 0 & \hbar\omega_0(n-\frac{1}{2}) - \hbar g\sqrt{n} \end{pmatrix}. \tag{2.69}$$

The new eigenstates and eigenenergies can be summarised:

$$\begin{aligned} |\psi_+\rangle &= \frac{1}{\sqrt{2}}\left(|g,n\rangle + |e,n-1\rangle\right), \quad E_+ = \hbar\omega_0(n-\frac{1}{2}) + \hbar g\sqrt{n} \\ |\psi_-\rangle &= \frac{1}{\sqrt{2}}\left(|g,n\rangle - |e,n-1\rangle\right), \quad E_- = \hbar\omega_0(n-\frac{1}{2}) - \hbar g\sqrt{n} \end{aligned} \tag{2.70}$$

The formal appearance of the new eigenstates is now similar two those of two quantum dots in (2.46) and it cannot be distinguished whether the quantum dot or the cavity is in the excited state. The eigenenergies of this system build the famous *Jaynes-Cummings ladder* [108] and degeneracy is lifted if at least a single photon is inside the cavity. The energy splitting amounts to $\Delta E = \hbar 2g\sqrt{n}$, which is a factor of $\sqrt{2}$ less than in elliptical cavities since the second quantum system is missing which raises the chance of interaction. The vacuum Rabi splitting is then defined by $\Omega_{\mathrm{VRS}} = 2g$.

In the following the circular arena cavity with one circular anti-node in the resonant mode pattern will be investigated ($(0,2)$-mode, see Chapter 1.3.1) with view to the spectral density $|g(\omega)|^2$. The FDTD setup is the same as in the case of the pure plasmonic investigation (see Section 1.3.2) and the proportions are once again depicted in Fig. 2.5(a). The only difference is that the emitting source dipole is now positioned 10 nm above the lateral centre of the WGM antenna just like in the case of elliptic arena cavities. It should also be noticed that the shape of the WGM antenna is not the same as in the investigation of elliptic cavities. According to the pure plasmonic investigation the shape is chosen to match real FIB processing results and its sharper mesa might further enhance light-matter interaction.

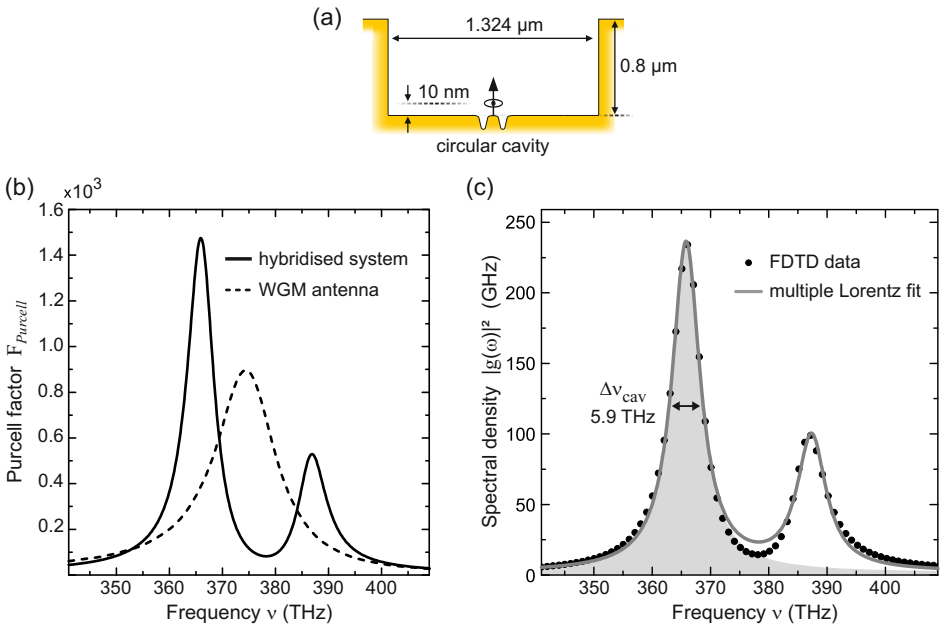

Fig. 2.5: Coupling strength of a quantum dot to a circular plasmonic cavity. (a) The FDTD parameters are identical to those in Section 1.3.1 and are related to a cavity mode showing a circular anti-node, i.e. the (0,2)-mode. As with elliptic cavities the dipole emitter is positioned 10 nm above the lateral centre of the WGM antenna. (b) The Purcell factor F_{Purcell} is calculated with the built-in function for both, the hybridised system (solid black line) as well as for the WGM antenna alone (black-dashed line). (c) Spectral density (black filled circles) calculated from the imaginary part of the dyadic Green's function according to equation (2.11) and a dipole moment of 1.4×10^{-28} Cm ($\gamma_0 = 1$ GHz). The spectral features are fitted with two Lorentz peaks whereupon the grey curve is the cumulative result. One of the peaks (grey shaded area) is further investigated since it exhibits the strongest coupling to cavity photons.

For the sake of completeness and to shed light on the different antenna shapes the spectrally resolved Purcell factor is discussed prior to the spectral density. The solid black line represents the Purcell enhancement of the hybridised system in Fig. 2.5(b), while the black-dashed line is assigned to the pure WGM antenna. The latter one exhibits a Purcell factor of $F_{\text{Purcell}} = 900$, which exceeds the Purcell factor of the barrel-shaped WGM antenna by a factor of $3/2$. Hence, the sharper shape of the mesa facilitates higher field enhancement and thus an enhanced spontaneous emission rate due to the higher LDOS. The hybridised system shows two separated peaks which are assigned to the new eigenmodes of the coupled

oscillators. A Purcell factor of about 1470 is provided by the red-shifted mode at 366 THz (819 nm) and this factor exceeds those of the hybridised elliptic arena cavities by more than a factor of two.

To retrieve the actual coupling strength g the same procedure as in the case of elliptical cavities is applied: The imaginary part of Green's tensor $\mathrm{Im}\{G_{zz}\}$ is retrieved from the FDTD simulation at the emitter position with an adapted LUMERICAL script that makes use of equation (2.5). Again, the transition dipole moment is set to 1.4×10^{-28} Cm which corresponds to a spontaneous decay rate of $\gamma_0 = 1$ GHz at a photon frequency of 366 THz (819 nm). The resulting spectral density is shown in Fig. 2.5(c) and its shape resembles that of Purcell enhancement. The data is fitted with a sum of two Lorentzian peaks, whereupon the fit of the single modes is only visualized for the mode at 366 THz by the grey shaded area. This mode is further investigated since it facilitates a stronger light-matter interaction than the blue-shifted mode at 387 THz (775 nm). The width of the mode amounts to $\Delta\nu_{\mathrm{cav}} = 5.9$ THz while the peak spectral density is about $|g(366\ \mathrm{THz})|^2 = 235$ GHz. By considering the TLS and the cavity mode to be on resonance at $\omega_0 = 2\pi \times 366$ THz the coupling strength and the vacuum Rabi splitting in the particular circular arena cavity yield:

$$g = 2\pi \times 0.59\ \mathrm{THz} \qquad \Omega_{\mathrm{VRS}} = 2g = 2\pi \times 1.18\ \mathrm{THz}. \tag{2.71}$$

The coupling strength of the quantum system and the radial symmetric cavity mode is a factor of $3/2$ stronger than that of a quantum dot inside the elliptic cavity (see equation (2.66)). This can be deduced from the fact that the Purcell enhancement of WGM antennas embedded in circular cavities is two times larger than that of antennas in elliptic cavities. This factor contributes in the derivation of g through the square root of the spectral density $|g(\omega_0)|^2$ (see equation (2.65)) and the latter is directly proportional to the two times higher enhanced decay rate. The vacuum Rabi splitting Ω_{VRS} in elliptic and circular cavities is nearly identical and hence not effectively improved. In the case of elliptic cavities the missing factor of $\sqrt{2}$ in the coupling strength of a single emitter is balanced by the additional factor $\sqrt{2}$ due to the second quantum emitter on top of the opposite WGM antenna. Therefore, the effective coupling strength is the same in both cavity schemes despite the fact that the coupling of individual quantum dots to plasmons is improved in circular arena cavities.

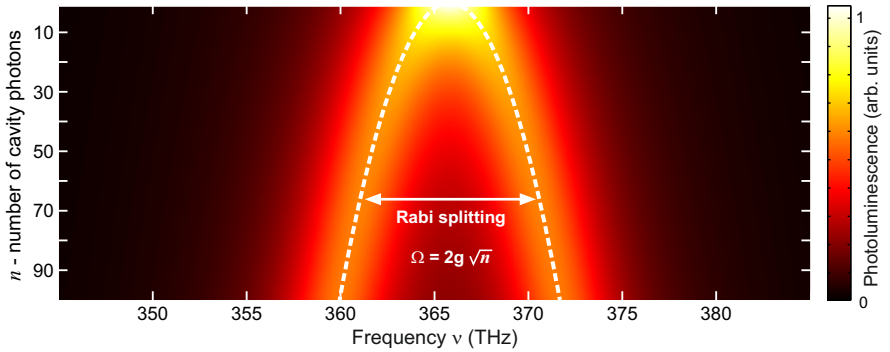

Fig. 2.6: Rabi splitting Ω in circular plasmonic cavities as a function of the number of photons n inside the cavity according to the Jaynes-Cummings model. The sketched photoluminescence signal is taken to be proportional to the spectral density of the grey shaded mode in Fig. 2.5(c). The associated Lorentz peak retrieved from fitting is shifted to $\nu_0 + \Omega/(4\pi)$ and $\nu_0 - \Omega/(4\pi)$, respectively. The sum of both peaks gives the resulting photoluminescence signal as a function of photons n inside the cavity. White-dashed lines mark the respective peak positions.

At last, the Rabi splitting $\Omega = 2g\sqrt{n}$ of the single excited states (2.70) is presented as a function of cavity photons n in Fig. 2.6: Two Lorentzian line shape functions broadened by $\Delta\nu_{\mathrm{cav}} = 5.9$ THz are shifted to $\nu_0 \pm \Omega(n)/(4\pi)$ and then added up to sketch photoluminescence spectra. First evidence for two separable resonances occurs at $n = 10$ and is then clearly visible for $n = 20$ in the contour plot. Due to the similar amount of Rabi splitting for two emitters on WGM antennas in elliptic cavities and the single emitter placed on a WGM antenna in a circular cavity it can be deduced that the same photon numbers are required in both types of cavities.

Although the vacuum Rabi splitting cannot be resolved, the strong-coupling regime of single quantum emitter(s) with few cavity photons is clearly demonstrated. 'Few' means that e.g. resonance shifts upon addition or removal of a single photon have to be described by QED and cannot be explained in the limit for large n in which $\sqrt{n}$ grows linear and the correspondence principle of quantum mechanics leads to a Rabi splitting proportional to the electric field strength.

2.4.4 Perspectives for single emitter-plasmon interaction

In the above considerations it has been shown that the proposed system of plasmonic arena cavities with implemented WGM antennas is close to the limit of coherent single plasmon-exciton operation. Some improvements will now be discussed that might help to overcome remaining obstacles. In doing so the results of Hümmer and co-workers serve as a benchmark since they also used cavities (1D plasmonic waveguides with DBR mirrors) to reach the strong-coupling regime in the single plasmon limit [148]. Many other works simply rely on the huge field enhancement near sharp nanostructures like metallic tips and spheroids or on the enhanced coupling of emitters to the radiation field in nanometre-sized gaps of chains of spheroids [263, 297, 272, 62, 77].

The coupling strength g of various 1D plasmonic waveguide modes to InAs quantum emitters, operating at 1550 nm, exhibits values of 1 GHz up to 1 THz, which are comparable to the values retrieved here (see Hümmer and co-workers [148]). However, in contrast to the elliptic and circular arena cavities, the damping rates $\Delta\nu_{\mathrm{cav}}$ of plasmonic waveguides stay well below 1 THz and can be as low as 10 GHz. This is achieved by assuming a strongly reduced population of phonons in the metal substrate at operating temperatures of 4 K [116]. The consequently reduced scattering of electrons then leads to surface plasmon propagation lengths which are increased by nearly two orders of magnitude [148].

The extended life-time of SPPs inside the resonator has two beneficial contributions: First, the reduced damping rates result in a smaller line-width of spectral features in the appropriate measurement channel and hence a more clear vacuum Rabi splitting. Second, the amount of mode splitting is increased since the interaction time of the emitter with its own field is extended. Accordingly, the LDOS is enhanced and the resonator configuration increases the Purcell factor by up to one order of magnitude in the work of Hümmer and co-workers. A requirement for an increased SPP propagation length at cryogenic temperatures is that scattering events of electrons are dominated by phonon interaction instead of scattering at rough surfaces, grain boundaries or impurities [148]. These criteria are to a certain extent met by single-crystalline and atomically flat gold microplates utilised for the arena cavity sample preparation in Chapter 1. The limiting factor of these systems is, however, the incorporated WGM antenna which transfers a

small but non-negligible amount of plasmonic excitation into the far-field. This radiative decay sets an absolute limit to the minimum mode line-width which can be approximated by replacing the cavity resonance with a Dirac delta function $\delta(\omega - \omega_0)$ in the set of differential equations in Chapter 1.3.3 and Chapter 1.4.2. Hence, a mode decay rate below that of pure cavities at room temperature, i.e. 2 THz to 3 THz, is not expected when sticking to WGM antennas.

With view to this latter point it would be very interesting to use the elliptic and circular areana cavities without the WGM antennas at 4 K and to just place the quantum dots in the focal spots of the eigenmodes. By reducing the propagation length by one order of magnitude due to a suppressed electron-phonon interaction the enhanced emission rate could be as high or even exceed cavity damping rates. This is especially expected when changing the operating wavelength of the quantum dots to telecom wavelengths around 1400 nm (214 THz), promising nearly two-orders of magnitudes enhanced SPP life-time and emitter-plasmon interaction [148]. First FDTD simulation for pure silver WGM antennas in the $m = 0$ configuration and operated at 1450 nm offer enhanced decay rates > 5000 for dipole emitters placed 10 nm above the antenna mesa (not shown here). With view to this result it seems worthy to again consider the combined antenna-cavity system and to push the strength of single emitter and single photon interaction g near to 10% of the operating angular frequency ω. In this regime it is, for instance, questionable to omit counter-rotating terms in the system Hamiltonian.

The specific parameters of the presented hybridised plasmonic systems are, according to the above discussion, not exhausted yet. If the strong-coupling regime is reached, a manifold of experiments come into mind: Having single emitters and mediating photons at hand the most prominent application would be quantum computation [202] on plasmonic time scales. Here, the cavity allows a non-local coupling of well separated and hence easily accessible qubits, i.e. the quantum dots. It serves as a so-called *quantum bus* that allows the coherent transfer of quantum states between the single quantum systems [198, 333]. Particular quantum dots might be selectively accessible and addressable by tightly focused laser beams.

From a more fundamental point of view it would also be interesting to exploit the non-linear character of the Jaynes-Cummings model in (2.67) or the Tavis-Cummings model in (2.47) with respect to the non-linear spacing of energy

eigenvalues (see (2.70) and (2.60), respectively). According to the considerations of Hümmer and co-workers an external stimulus will lead to a non-linear response of the system [148] and the Jaynes-Cummings Hamiltonian in (2.67) is proposed to be written in the form of an effective Kerr Hamiltonian $\propto \hbar\omega\hat{a}^\dagger\hat{a} + \hbar\kappa(\hat{a}^\dagger\hat{a})^2$ [152] when the detuning $\omega_c - \omega_{\mathrm{QD}}$ is larger than the coupling constant g (the so-called *dispersive regime* [339]). Analogue to the demonstration in circuit QED [326] such a system might be used to generate squeezed quantum plasmonic states. Another phenomenon that relies on the non-linear spacing of energy levels would be the plasmonic version of a *photon-blockade* [35, 138]: By injecting a plasmon into the plasmonic arena cavities the energy levels of the stationary states are determined by (2.70) and (2.60). Due to plasmon-plasmon interaction the energy level spacing is modified, depending on the number n of excited plasmons. Hence, the required excitation energy of an additional plasmon is also altered.

The so far mentioned applications all require that the coupling strength g of plasmonic modes to the quantum emitters exceeds the rate of cavity damping $\Delta\nu_{\mathrm{cav}}$ and emitter line-width broadening. Interestingly, the dominating dissipative channels in plasmonics might be utilised for a new way of doing quantum computation without the need for coherent dynamics: Recent works have shown that many-body open quantum systems can be driven into various kinds of quantum states by interaction with the dissipative environment, which is usually represented by a bath of harmonic oscillators [85, 302]. Diehl and co-workers theoretically demonstrated that engineering with quantum jump operators facilitates a dissipatively driven Bose-Einstein condensate [85]. Concurrently, Verstraete and co-workers introduced their approach for universal quantum computation which is labelled *dissipative qunatum computation (DQC)* [302]. The developed formalism does not require the preparation of states or unitary dynamics and it implemets quantum random walks [158]. If it turns out that sample cooling is a valid parameter for controlling plasmon dissipation the hybridised antenna-cavity systems presented here might serve as an experimental toy model for testing the aforementioned schemes in solid-state systems.

In the upcoming last section of this chapter FDTD simulations will be utilised to investigate another dissipative channel that is predicted to lead to entangled states between distant quantum emitters: The so-called *superradiant* and *subradiant* decay of multiple quantum emitters which share the same radiation field [94, 205].

2.5 Super- and subradiance in plasmonic arena cavities

In 1954 Robert Henry Dicke predicted that in a gas of N two-level atoms, in which an isolated atom would decay with a rate Γ, every single atom decays N times faster than usual ($N\Gamma$), if the wavelength of the common light field is larger than the spatial emitter separation [84]. This collective emission behaviour is assigned to the interaction between atoms through the vacuum field.

In last section it has been stated that two quantum dots placed on separated WGM antennas cannot reside in an entangled state (2.46) since emission of a photon leads to decoherence. Accordingly, the enhanced radiative decay due to superradiance, a dissipative channel, is expected to even worsen the chance for qubit entanglement at first glance. However, the presence of a superradiant state, e.g. $\sqrt{0.5}\left(|e_1,g_2\rangle + |g_1,e_2\rangle\right)$, is always accompanied by a subradiant state $\sqrt{0.5}\left(|e_1,g_2\rangle - |g_1,e_2\rangle\right)$ which exhibits a reduced spontaneous emission rate [199]. Due to a reduction in the decay rate a prepared entangled state might be maintained for elongated times, especially when dephasing due to interaction with the environment is attenuated at low temperatures [40]. An experimental demonstration of enhanced and suppressed life-times was accomplished with two barium ions in a Paul trap by DeVoe and Brewer [82]. In plasmonics, a theoretical study of Martín-Cano and co-workers showed that spatially separated quantum emitters placed on 1D plasmonic channel waveguide can be entangled if the system evolves through a subradiant state [205]. The forced depopulation in this transient phenomenon can be compensated by coherent pumping in contrast to usual cavity QED in which incoherent pumping is utilised. Besides interesting applications it is desirable to experimentally demonstrate for the first time super- and subradiance of quantum emitters in plasmonics systems since the first prediction by Pustovit and Shahbazyan [246]. Here, it will be shown via FDTD simulations that the WGM antenna decorated plasmonic arena cavities are a promising candidate for cooperative quantum emitter interaction. Before results are presented and further applications are assessed a short mathematical outline is given for a description of cooperative decay rates by means of dyadic Green's function.

2.5.1 The cooperative decay rate

Super- and subradiance do not require a strong-coupling regime. More precisely, they occur in the so-called *bad-cavity limit* [70, 291] in which cavity loss dominates over light-matter coupling strength ($\Delta\nu_{\mathrm{cav}} \gg g$) and the radiation field is treated as a reservoir showing no back reaction effects [105]. If the proposals for reaching the strong-coupling regime listed in Section 2.4.4 are not successfully implemented, the bad-cavity limit is the conventional operating regime of plasmonic arena cavities without any additional effort. Nevertheless, the mathematical treatment of cooperative effects between N quantum emitters starts with the Tavis-Cummings Hamiltonian already mentioned in equation (2.47) and it is here explicitly decomposed into spatial modes $\mathbf{k}$, with polarisation index s, of the quantised electric field $\hat{\mathbf{E}}(\mathbf{r}_i, \omega_{\mathbf{k}})$ [105] (see equation (2.9)):

$$\begin{aligned}\hat{H} = &\underbrace{\sum_{\mathbf{k},s} \hbar\omega_{\mathbf{k}} \hat{a}^{\dagger}_{\mathbf{k},s}\hat{a}_{\mathbf{k},s} + \sum_{i=1}^{N} \hbar\omega_i \sigma_i^z}_{\hat{H}_0} \\ &\underbrace{-\mathrm{i}\hbar \sum_{i=1}^{N}\sum_{\mathbf{k},s} \left[\mathbf{p}_i \cdot \mathbf{g}_{\mathbf{k},s}(\mathbf{r}_i)\left(\hat{\sigma}_i^{+} + \hat{\sigma}_i^{-}\right)\hat{a}_{\mathbf{k},s} \;+\; h.c.\right]}_{\hat{H}_I}.\end{aligned} \tag{2.72}$$

While $\hat{H}_0$ denotes the unperturbed Hamiltonian of the field and the N atoms, the operator $\hat{H}_I = \sum_{i=1}^{N} -\mathbf{p}_i(\hat{\sigma}_i^{+} + \hat{\sigma}_i^{-})\hat{\mathbf{E}}(\mathbf{r}_i, \omega_{\mathbf{k}})$ comprises their interaction. The coupling constant $\mathbf{g}_{\mathbf{k},s} = \mathbf{e}_{\mathbf{k},\mathrm{s}}\sqrt{\omega_{\mathbf{k}}/(2\varepsilon_0\hbar V)}$ at location $\mathbf{r}_i$ is that of normal modes where V is the normalisation volume and $\mathbf{e}_{\mathbf{k},\mathrm{s}}$ is a unit polarisation vector.

Since the analysis below will rely on FDTD simulations a representation of the quantised radiation field in terms of dyadic Green's function $\overleftrightarrow{\mathbf{G}}$ is beneficial since $\overleftrightarrow{\mathbf{G}}$ itself can be represented in terms of the quantised field modes $\mathbf{k}$ according to equations (2.10) and (2.11). A mathematical treatment of quantised fields near inhomogeneous and dispersive media can be found in the textbook of Vogel and Welsch ([307], Chapter 2), in the book edited by Peřina ([236], Chapter 1), and in the paper about quantised dipole-dipole interaction in the presence of dispersing

and absorbing surroundings by Dung and co-workers [93]. The Hamiltonian in (2.72) is then written as

$$\begin{aligned}\hat{H} = &\underbrace{\int d\mathbf{r} \int_0^\infty d\omega\, \hbar\omega\, \hat{a}^\dagger(\mathbf{r},\omega)\hat{a}(\mathbf{r},\omega) + \sum_{i=1}^{N} \hbar\omega_i \sigma_i^z}_{\hat{H}_0} \\ &\underbrace{-\sum_{i=1}^{N} \int_0^\infty d\omega\, \left[\mathbf{p}_i \left(\hat{\sigma}_i^+ + \hat{\sigma}_i^-\right) \hat{\mathbf{E}}(\mathbf{r}_i,\omega) \;+\; h.c.\right]}_{\hat{H}_I},\end{aligned} \tag{2.73}$$

in which the quantised electric field is expressed in terms of the dyadic Green's function [205]:

$$\hat{\mathbf{E}}(\mathbf{r},\omega) = \mathrm{i}\sqrt{\frac{\hbar}{\pi\varepsilon_0}} \frac{\omega^2}{c^2} \int d\mathbf{r}' \sqrt{\varepsilon_i(\mathbf{r}',\omega)} \overleftrightarrow{\mathbf{G}}(\mathbf{r},\mathbf{r}',\omega) \hat{a}(\mathbf{r}',\omega). \tag{2.74}$$

Here, $\hat{a}$ are bosonic field operators, i.e. the plasmons, and $\varepsilon_i(\mathbf{r}',\omega)$ the permittivity of a surrounding dielectric medium. The detailed temporal dynamics of the combined atom(A)-field(F) system can be obtained by investigation of the joint density operator $\hat{\rho}_{AF}$[105]:

$$\frac{\partial}{\partial t}\hat{\rho}_{AF} = \frac{1}{\mathrm{i}\hbar}\left[\hat{H}, \hat{\rho}_{AF}\right]. \tag{2.75}$$

To concentrate on the consequences of atom-field coupling, equation (2.75) is transferred to the interaction picture by unitary transformation of quantum mechanical operators, i.e. multiplication with $\exp(\mathrm{i}\hat{H}_0 t/\hbar)$ from the left side and $\exp(-\mathrm{i}\hat{H}_0 t/\hbar)$ from the right side. Equation (2.75) then reads

$$\frac{\partial}{\partial t}\hat{\rho}_{AF}^{IP}(t) = \frac{1}{\mathrm{i}\hbar}\left[\hat{V}^{IP}(t), \hat{\rho}_{AF}^{IP}(t)\right], \tag{2.76}$$

in which the superscript IP identifies the operators in the interaction picture [105]. Note that here $\hat{V}^{IP}(t)$ is the unitary transformation of the interaction part $\hat{H}_I$ of the Hamiltonian. This first order differential equation can be solved in an iterative way according to standard procedures in quantum mechanics. Approximating (2.75) up to second order in $\hat{V}^{IP}(t)$ gives the following integro-differential equation [105]:

$$\begin{aligned}\frac{\partial}{\partial t}\hat{\rho}_A^{IP}(t) &= \frac{1}{\mathrm{i}\hbar}\mathrm{Tr}_F\left[\hat{V}^{IP}(t),\hat{\rho}_A^{IP}(0)\hat{\rho}_F^{IP}(0)\right] \\ &\quad -\frac{1}{\hbar^2}\int_0^t dt'\mathrm{Tr}_F\left(\left[\hat{V}^{IP}(t),\left[\hat{V}^{IP}(t'),\hat{\rho}_A^{IP}(t')\hat{\rho}_F^{IP}(0)\right]\right]\right).\end{aligned} \tag{2.77}$$

Here, the operation Tr_F denotes the trace over the vacuum field so that (2.77) only describes the temporal evolution of the atomic system, i.e. $\hat{\rho}_A^{IP}(t)$ is a reduced density operator. This is connected to the so-called *Born approximation*, in which the atom only interacts weakly with the vacuum field so that the latter one does not change over time and hence the former density operator in (2.77) is split into two parts, i.e. $\hat{\rho}_{AF}^{IP}(t') = \hat{\rho}_A^{IP}(t')\hat{\rho}_F^{IP}(0)$ is a product state. Another important approximation that is usually applied for solving the above differential equation is the *Markov approximation*, which states that the system will lose its past memory on very short time scales [307]. To fulfil this requirement the bandwidth of the reservoir spectrum has to broader than the radiative line-width of the embedded quantum emitter [307]. In the case of the elliptic plasmonic arena cavities discussed here the cavity bandwidth is about 6 THz, while the Purcell enhanced emission rate of InAs quantum dots was assumed to be around 0.6 THz. The difference of an order of magnitude suggests that the Markov approximation can be applied without any concerns. Finally, by applying the rotating wave approximation and by using (2.74) in $\hat{V}^{IP}(t)$, one finally arrives at the *master equation* after some cumbersome calculations [105, 205]:

$$\frac{\partial}{\partial t}\hat{\rho} = -\frac{\mathrm{i}}{\hbar}\left[\hat{H}_{coh},\hat{\rho}\right] - \frac{1}{2}\sum_{i,j}\gamma_{ij}\left(\hat{\rho}\hat{\sigma}_i^\dagger\hat{\sigma}_j + \hat{\sigma}_i^\dagger\hat{\sigma}_j\hat{\rho} - 2\hat{\sigma}_i^\dagger\hat{\rho}\hat{\sigma}_j\right). \tag{2.78}$$

For simplicity the sub- and superscripts IP and A are omitted from now on and it should be clear that equation (2.78) describes the temporal evolution of the atomic system represented by $\hat{\rho}$. The operator $\hat{H}_{coh}$ describes the the coherent interaction of the various quantum emitters according to [205]:

$$\hat{H}_{coh} = \sum_i \hbar(\omega_0+\delta_i)\hat{\sigma}_i^\dagger\hat{\sigma}_i + \sum_{i\neq j}\hbar g_{ij}\hat{\sigma}_i^\dagger\hat{\sigma}_j \tag{2.79}$$

In (2.79) δ_i represents the Lamb-shift of the quantum emitter in the presence of the plasmonic arena cavities and it is usually very small ([229], Appendix B) and

it can be neglected for emitter-metal distances larger than 10 nm [205]. A very important parameter is the dipole-dipole coupling energy given by $\hbar g_{ij}$ [205]:

$$g_{ij} = \frac{\omega_0^2}{\hbar\varepsilon_0 c^2}\mathbf{p}_i^* \mathrm{Re}\left\{\overleftrightarrow{\mathbf{G}}(\mathbf{r}_i, \mathbf{r}_j, \omega_0)\right\}\mathbf{p}_j. \tag{2.80}$$

More precisely, $\hbar g_{ij}$ represents the dipole-dipole interaction potential $\hat{V}_{ij}$ that has been mentioned in Section 2.4.1. As stated there, it gives a measure for the time scale needed to establish a coherence directly between the distinct quantum emitters. The dyadic Green's function $\overleftrightarrow{\mathbf{G}}(\mathbf{r}_i, \mathbf{r}_j, \omega_0)$ enters the dipole-dipole coupling constant g_{ij} through the quantised representation of the electric field in (2.74) and the insertion of $\hat{\mathbf{E}}$ into the interaction operator $\hat{V}^{IP}$. The commutator in the second line of euqation (2.77) then leads to the mixing terms of quantum emitters i and j.

To underline the statement in Section 2.4.2 that a direct dipole-dipole coupling is unlikely to occur for quantum emitters positioned on 1.63 μm separated WGM antennas in an elliptic plasmonic arena cavity, equation (2.80) has been evaluated by utilising the FDTD simulations already presented in the strong-coupling and nETR investigation (see Fig. 2.3(a), left cavity). By assuming a transition dipole moment of 1.4×10^{-28} Cm (spontaneous decay rate $\gamma_0 = 1$ GHz), according to the discussion in Section 2.4, the maximum dipole-dipole coupling rate amounts to:

$$\max(g_{12}) = 2\pi \cdot 0.04 \text{ THz}. \tag{2.81}$$

Hence, the corresponding energy shift is only small compared to the broad cavity mode with a width of e.g. 6 THz at a centre frequency of 366 THz (819 nm).

The last term in (2.78) describes the dissipative part of the evolution of the atomic system. In this equation γ_{ij} denotes the the decay rate arising from self ($i = j$) and mutual ($i \neq j$) quantum emitter interaction. It can also be expressed in terms of dyadic Green's function by [205]:

$$\gamma_{ij} = \frac{2\omega_0^2}{\hbar\varepsilon_0 c^2}\mathbf{p}_i^* \mathrm{Im}\left\{\overleftrightarrow{\mathbf{G}}(\mathbf{r}_i, \mathbf{r}_j, \omega_0)\right\}\mathbf{p}_j. \tag{2.82}$$

The reader should be aware of the fact that the case of enhanced decay by self-interaction has already been presented and derived at the beginning of this chapter in Section 2.2.1 and equation (2.11). This effect is better known as *Purcell enhancement*. In this spirit the effect of superradiance can be viewed as a "field amplification and stimulated emission by some atoms of the field emitted by others", as formulated by Serge Haroche and Michel Gross [125]. The interested reader is referred to their essay, which also tackles the semantical confusion about the interpretation of the effect with view to the formulation of the problem in the Schrödinger picture and the Heisenberg picture of quantum mechanics.

Before evaluating equation (2.82) in the light of the WGM antenna decorated plasmonic arena cavities, a last view is taken on literature to visualise that γ_{ij} leads to enhanced or suppressed decay rates. To describe the atom-field system properly it is convenient to diagonalise the Hamiltonian $\hat{H}_{coh}$ which leads to the following set of states when two quantum emitters are considered [205]:

$$\begin{aligned} \rho_{gg}: &\quad |g_1,g_2\rangle \\ \rho_{+}: &\quad |+\rangle = \sqrt{1/2}\,(|g_1,e_2\rangle + |e_1,g_2\rangle) \\ \rho_{-}: &\quad |-\rangle = \sqrt{1/2}\,(|g_1,e_2\rangle - |e_1,g_2\rangle) \\ \rho_{ee}: &\quad |e_1,e_2\rangle \end{aligned} \tag{2.83}$$

While $|g_1,g_2\rangle$ and $|e_1,e_2\rangle$ describe the ground and double excited state, respectively, $|+\rangle$ and $|-\rangle$ represent symmetric and anti-symmetric entangled states in which the excitation cannot be clearly assigned to one of the emitters. These states are the diagonal elements ρ_{gg}, ρ_{+}, ρ_{-} and ρ_{ee} of the density operator $\hat{\rho}$ in (2.78) and their temporal evolution can be summarised by the following four simple equations [205]:

$$\begin{aligned} \partial_t \rho_{gg}(t) &= (\gamma+\gamma_{12})\rho_{+}(t) + (\gamma-\gamma_{12})\rho_{-}(t) \\ \partial_t \rho_{+}(t) &= (\gamma+\gamma_{12})\rho_{ee}(t) - (\gamma+\gamma_{12})\rho_{+}(t) \\ \partial_t \rho_{-}(t) &= (\gamma-\gamma_{12})\rho_{ee}(t) - (\gamma-\gamma_{12})\rho_{-}(t) \\ \partial_t \rho_{ee}(t) &= -2\gamma\rho_{ee}(t) \end{aligned} \tag{2.84}$$

The above equations relate to the case that $|\gamma_{12}| = |\gamma_{21}|$ and $|\gamma_{11}| = |\gamma_{22}| = |\gamma|$. While the latter condition holds for identical quantum emitters, the former is only

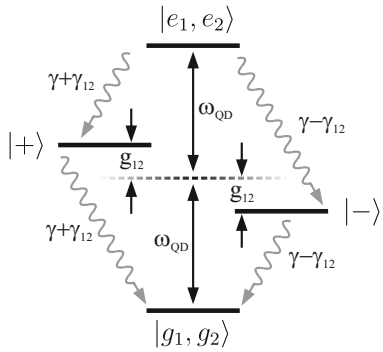

Fig. 2.7: Level diagram for super- and subradiant decay of two quantum emitters according to equation (2.84). The super- and subradiant states, i.e. $|+\rangle$ and $|-\rangle$, are detuned from the quantum emitter transition frequency ω_{QD} by $\pm g_{12}$ due to dipole-dipole interaction. Here, it is assumed that mutual enhanced decay is symmetric ($\gamma_{12} = \gamma_{21}$) and that self-interaction is of equal strength ($\gamma_{11} = \gamma_{22} = \gamma$). Wiggled arrows indicate decay rates.

valid in WGM antenna decorated plasmonic arena cavities when both emitters have a relative phase of 0 and π, i.e. the state ρ_+ and ρ_-, respectively. Figure 2.7 visualises the consequences of equations (2.84) and (2.80).

The ground state $|g_1, g_2\rangle$ and the double-excited state $|e_1, e_2\rangle$ are separated by two times the transition frequency ω_{QD} of an isolated quantum emitter. Due to dipole-dipole interaction the single excited state is shifted by $\pm g_{12}$ with respect to the former transition frequency ω_{QD}, depending on whether it is superradiant $(+)$ or subradiant $(-)$. Equation (2.84) directly gives the rate by which the population of the diagonal elements change, i.e. $\gamma + \gamma_{12}$ and $\gamma - \gamma_{12}$. If γ_{12} is positive and if $\gamma_{12} \approx \gamma$ the decay route over the superradiant state $|+\rangle$ is much faster than the decay route involving the subradiant state $|-\rangle$.

2.5.2 FDTD results

Here, the strength of super- and subradiance in WGM antenna decorated arena cavities is determined via FDTD simulations. According to equation (2.82) only knowledge about dyadic Green's function of one dipole emitter *i* at the position of the second emitter *j* is required for evaluation of the mutual decay rate γ_{ij}. For descriptive reasons, the total decay rate of one emitter, influenced by the presence of a second emitter, is first evaluated with the built-in *Purcell-function* of the LUMERICAL software before the general approach via equation (2.82) is

utilised. The built-in approach has already been used in Section 2.2.2 and it directly measures the enhanced decay rate of an emitter without the need for user-scripting. The drawback of this simple function is the following: While the general approach requires only a single dipole source and a single simulation to calculate the mutual enhanced decay of a second emitter anywhere inside the simulation volume, the former built-in approach requires a single simulation for every spatial configuration of the two dipole sources and their relative phases.

The setup for the built-in approach is shown in Fig. 2.8(a): Two simultaneously oscillating dipole sources with a relative phase of $\Delta\phi$ are positioned in the mesa centre of opposed WGM antennas inside an elliptic arena cavity. Geometrical cavity extents are the same as in the investigation about strong coupling (Section 2.4) and Purcell enhancement (Section 2.2). The metal-emitter distance of 10 nm is also adopted.

The results of the built-in Purcell function are presented in Figure 2.8(b). A relative emitter phase $\Delta\phi = 0$ is represented by the solid black curve while the case of anti-phased emitters ($\Delta\phi = \pi$) is represented by the black-dashed curve. The grey shaded area in the background is the Purcell enhancement for a single emitter as already shown in Fig. 2.1 (solid red curve) and it serves as a reference. Interestingly, only the outer peaks are maintained if the dipoles oscillate in phase ($\Delta\phi = 0$) and the Purcell enhancement in the spectral centre near 375 THz (800 nm) drops from nearly 400 to 60. In contrast to this, the low frequency peak at 366 THz (820 nm) suggests an enhanced Purcell factor which is increased from 600 in the case of a single emitter to 1000 in the case of two in-phase emitters. The same is true for the high frequency peak at 387 THz (775 nm) which is increased from 260 to 370. Since the Purcell function of one dipole source measures the enhanced or suppressed radiated power, deviations from single emitter simulations suggest that the second emitter has a non-negligible influence on the observed emitter. More precisely, the radiated fields interfere at the emitter positions leading to the injection of more or less power into the simulation for a particular frequency. Hence the distinct peaks in Fig. 2.8(b) can be attributed to phase differences at the emitter positions imprinted by the plasmonic resonances, i.e. the response function of the hybridised system. It is anticipated that the enhanced radiated power at 366 THz and at 387 THz for in-phase emitters relies on a response function phase difference of integer multiples of 2π, while the anti-phased emitters

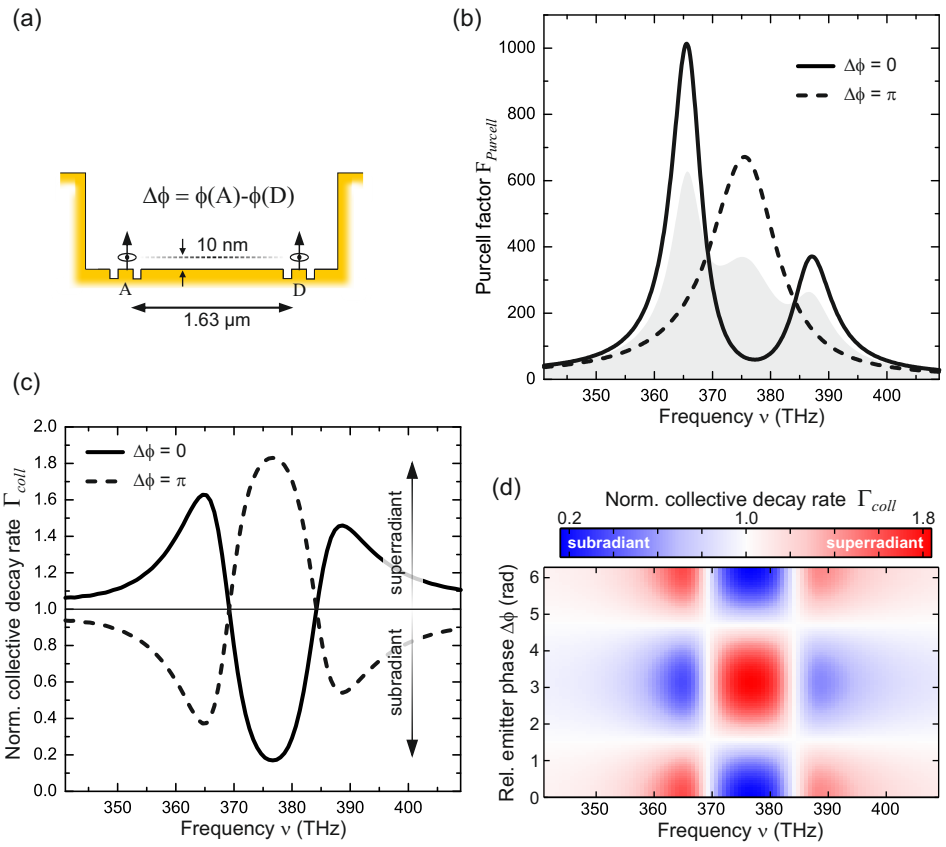

Fig. 2.8: Collective emission in elliptic arena cavities. (a) Sketch of FDTD setup which is identical to that of the investigation of strong coupling and Purcell enhancement (see Fig. 2.1). Two dipole sources (A and D) with phase difference $\Delta\phi$ are used to determine the enhanced decay rate of every dipole with the built-in function of the LUMERICAL software. Dipole A is omitted in a general approach which utilises scripting language. (b) Purcell enhancement of dipole D retrieved from LUMERICAL'S built-in function. (c) Determination of frequency-resolved super- and subradiant states according to equation (2.90) using scripting language and dipole source D only. (d) Determination of frequency-resolved super- and subradiant states as a function of the dipole source phase difference $\Delta\phi$ from 0 to 2π using equation (2.90).

need a structure-induced phase shift of π to get in phase again for the 375 THz mode. This is verified by utilising a FDTD simulation in which the dipole source A is omitted and dipole source D is positioned in the substrate to retrieve the pure plasmonic response of the system. Since the on-top dipole sources are usually

located at the mesa centre where mainly field components perpendicular to the substrate exist it is sufficient to compare the phase of the respective E_z-components 10 nm above each WGM antenna. The relative phases $\Delta\phi_{plasm}$ for the three modes are:

$$\begin{aligned}\Delta\phi_{plasm}(366\text{ THz}) &= 13.29\text{ rad} = 2\pi\cdot 2.1\\ \Delta\phi_{plasm}(375\text{ THz}) &= 15.35\text{ rad} = \pi\cdot 4.9\\ \Delta\phi_{plasm}(387\text{ THz}) &= 17.61\text{ rad} = 2\pi\cdot 2.8\end{aligned} \tag{2.85}$$

The results in (2.85) confirm the assumption that the enhanced and suppressed power injection for particular modes can be assigned to the plasmonic properties of the system. Deviations from a full integer value arise since the selected frequencies are chosen according to peak maxima of the grey shaded area in Fig. 2.8(b) which do not necessarily coincide with central mode frequencies.

For a quite clearly representation the results of Fig. 2.8(b) can be expressed by a normalised decay factor Γ_{coll} which compares the decay caused by mutual- and self-interaction to the decay rate of single emitters [206]:

$$\Gamma_{coll} = \frac{\gamma_{AA}+\gamma_{AD}+\gamma_{DD}+\gamma_{DA}}{\gamma_{AA}+\gamma_{DD}}. \tag{2.86}$$

In order to evaluate equation (2.86) the general approach is chosen in which mutual- and self-induced decay rates can be calculated with a single simulation containing only a single dipole source. Hence, dipole source A is deactivated in Fig. 2.8(a) and only source D is radiating. The following derivation shows how the evaluation of (2.86) is organised. In a first step the decay rates of (2.82) are inserted into (2.86) and prefactors cancel out:

$$\begin{aligned}\Gamma_{coll} = &\frac{\mathbf{p}_A^*\mathrm{Im}\left\{\overleftrightarrow{\mathbf{G}}(\mathbf{r}_A,\mathbf{r}_A,\omega_0)\right\}\mathbf{p}_A + \mathbf{p}_A^*\mathrm{Im}\left\{\overleftrightarrow{\mathbf{G}}(\mathbf{r}_A,\mathbf{r}_D,\omega_0)\right\}\mathbf{p}_D}{\mathbf{p}_A^*\mathrm{Im}\left\{\overleftrightarrow{\mathbf{G}}(\mathbf{r}_A,\mathbf{r}_A,\omega_0)\right\}\mathbf{p}_A + \mathbf{p}_D^*\mathrm{Im}\left\{\overleftrightarrow{\mathbf{G}}(\mathbf{r}_D,\mathbf{r}_D,\omega_0)\right\}\mathbf{p}_D}\\ &+\frac{\mathbf{p}_D^*\mathrm{Im}\left\{\overleftrightarrow{\mathbf{G}}(\mathbf{r}_D,\mathbf{r}_D,\omega_0)\right\}\mathbf{p}_D + \mathbf{p}_D^*\mathrm{Im}\overleftrightarrow{\mathbf{G}}(\mathbf{r}_D,\mathbf{r}_A,\omega_0)\mathbf{p}_A}{\mathbf{p}_A^*\mathrm{Im}\left\{\overleftrightarrow{\mathbf{G}}(\mathbf{r}_A,\mathbf{r}_A,\omega_0)\right\}\mathbf{p}_A + \mathbf{p}_D^*\mathrm{Im}\left\{\overleftrightarrow{\mathbf{G}}(\mathbf{r}_D,\mathbf{r}_D,\omega_0)\right\}\mathbf{p}_D}.\end{aligned} \tag{2.87}$$

In a next step it is included that the electric field at the emitter positions A and D solely points in z-direction. Hence, only one out of nine components of dyadic Green's function needs to be known, i.e. G_{zz}. Likewise the dipole moments, pointing also in z-direction, are reduced to scalar values p:

$$\begin{aligned}\Gamma_{coll} = &\frac{p_A^* \mathrm{Im}\{G_{zz}(\mathbf{r}_A,\mathbf{r}_A,\omega_0)\}\, p_A + p_A^* \mathrm{Im}\{G_{zz}(\mathbf{r}_A,\mathbf{r}_D,\omega_0)\}\, p_D}{p_A^* \mathrm{Im}\{G_{zz}(\mathbf{r}_A,\mathbf{r}_A,\omega_0)\}\, p_A + p_D^* \mathrm{Im}\{G_{zz}(\mathbf{r}_D,\mathbf{r}_D,\omega_0)\}\, p_D} \\ &+ \frac{p_D^* \mathrm{Im}\{G_{zz}(\mathbf{r}_D,\mathbf{r}_D,\omega_0)\}\, p_D + p_D^* \mathrm{Im}\{G_{zz}(\mathbf{r}_D,\mathbf{r}_A,\omega_0)\}\, p_A}{p_A^* \mathrm{Im}\{G_{zz}(\mathbf{r}_A,\mathbf{r}_A,\omega_0)\}\, p_A + p_D^* \mathrm{Im}\{G_{zz}(\mathbf{r}_D,\mathbf{r}_D,\omega_0)\}\, p_D}.\end{aligned} \tag{2.88}$$

To consider an arbitrary phase between the two dipole emitters it is assumed that dipole D and A only differ by an additional phase so that $p_A = p_D \cdot \exp(\mathrm{i}\Delta\phi)$. In this case the dipole transition moments cancel out and Γ_{coll} can be written as:

$$\begin{aligned}\Gamma_{coll} = &\frac{\mathrm{Im}\{G_{zz}(\mathbf{r}_A,\mathbf{r}_A,\omega_0)\} + \mathrm{Im}\{G_{zz}(\mathbf{r}_A,\mathbf{r}_D,\omega_0)\}\, \mathrm{e}^{\mathrm{i}\Delta\phi}}{\mathrm{Im}\{G_{zz}(\mathbf{r}_A,\mathbf{r}_A,\omega_0)\} + \mathrm{Im}\{G_{zz}(\mathbf{r}_D,\mathbf{r}_D,\omega_0)\}} \\ &+ \frac{\mathrm{Im}\{G_{zz}(\mathbf{r}_D,\mathbf{r}_D,\omega_0)\} + \mathrm{Im}\{G_{zz}(\mathbf{r}_D,\mathbf{r}_A,\omega_0)\}\, \mathrm{e}^{-\mathrm{i}\Delta\phi}}{\mathrm{Im}\{G_{zz}(\mathbf{r}_A,\mathbf{r}_A,\omega_0)\} + \mathrm{Im}\{G_{zz}(\mathbf{r}_D,\mathbf{r}_D,\omega_0)\}}.\end{aligned} \tag{2.89}$$

Since the emitters are positioned on the antennas in the exact same manner it is allowed to make the simplification $\mathrm{Im}\{G_{zz}(\mathbf{r}_A,\mathbf{r}_A,\omega_0)\} = \mathrm{Im}\{G_{zz}(\mathbf{r}_D,\mathbf{r}_D,\omega_0)\}$. Additionally, due to symmetry the electric field emitted by dipole D and experienced by dipole A is identical to field emitted by dipole A and experienced by dipole D, and hence $\mathrm{Im}\{G_{zz}(\mathbf{r}_D,\mathbf{r}_A,\omega_0)\} = \mathrm{Im}\{G_{zz}(\mathbf{r}_A,\mathbf{r}_D,\omega_0)\}$. With these simplifications (2.89) is re-written as:

$$\Gamma_{coll} = 1 + \frac{\mathrm{Im}\{G_{zz}(\mathbf{r}_A,\mathbf{r}_D,\omega_0)\}}{\mathrm{Im}\{G_{zz}(\mathbf{r}_D,\mathbf{r}_D,\omega_0)\}} \cos(\Delta\phi). \tag{2.90}$$

The normalised decay factor Γ_{coll} is shown for the special case of $\Delta\phi = 0$ and $\Delta\phi = \pi$ in Fig. 2.8(c) as solid and dashed black lines, respectively. The superradiant ($\Gamma_{coll} > 1$) and subradiant ($\Gamma_{coll} < 1$) behaviour is clearly visible and verifies the suggestions inferred from the Purcell enhancement in Fig. 2.8(b): Dipoles which oscillate in-phase with a frequency near the outer two modes (366 THz and 387 THz) show a faster radiative decay as expected from a single dipole. Near the central mode (375 THz) the in-phase emitters show a more slow radiative

decay as expected from a single dipole. The normalised decay factor Γ_{coll} for all relative phases $\Delta\phi$ is depicted in Fig. 2.8(d). It is interesting to note that super- and subradiant behaviour vanishes for a relative phase of $\Delta\phi = \pm\pi/2$. This follows directly from equation (2.90) and may be interpreted as the mutual cancellation of enhanced and suppressed decay at opposite emitters.

The most prominent effect is expected when working with quantum emitters which are operated at 375 THz (800 nm). In this case Γ_{coll} is well above 1.8 ($\Delta\phi = \pi$) suggesting that the mutual decay rate γ_{AD} is nearly identical to γ_{DD}, although the emitters are separated by two times the vacuum emission wavelength. Vice versa, if the emitters are in phase ($\Delta\phi = 0$) the emission can be effectively suppressed ($\Gamma_{coll} < 0.2$) in spite of the enhanced LDOS of the inhomogeneous environment. Note that the size of the elliptic arena cavity exhibits three antinodes in the mode pattern between the WGM antennas. Shrinking the size of the structure might lead to an even more enhanced effect.

2.5.3 Perspectives for collective effects in plasmonic arena cavities

The observed high contrast of the collective decay factor Γ_{coll} raises hope that a collective enhanced or suppressed emitter decay can be experimentally observed in WGM antenna decorated elliptic arena cavities. An experimental proof of this effect has not been demonstrated in literature so far since the first prediction by Pustovit and Shahbazyan in 2009 that a plasmonic mode is able to serve as a hub for mediating cross-talk of nearby emitters [246]. The device presented here provides the benefit that it can be prepared deterministically, i.e. a known number of quantum emitters can be deposited on the mesa of WGM antennas. The quantum dots in the steady state configuration are then exposed to irradiated light and the cross-talk would occur over large distances d ($d > \lambda_0$) which makes the system presented here even more appealing and challenging.

A coequal candidate for realising a long-range plasmonic Dicke effect are 1D plasmonic wedge and channel waveguides, mainly investigated by Diego Martín-Cano, Alejandro González-Tudela and co-workers [206, 205, 117]. The Ag channel waveguides are operated at 600 nm (1.7 μm propagation length) and two quan-

tum emitters separated by $d = 2\lambda_0$ exhibit a minimum collective decay factor of $\Gamma_{coll} \approx 0.35$ [206]. Here, it has been shown that emission at 375 THz is suppressed to values well below $\Gamma_{coll} \approx 0.2$ (see Fig. 2.8(c)). Additionally, Martín-Cano theoretically demonstrated that this subradiant behaviour is sufficient to generate entanglement between two separated quantum emitters [205, 117]. Subradiance is beneficial because it hinders the entangled state $|-\rangle$ (see equation (2.83) and Fig. 2.7) from decaying and hence coherence of the prepared state is maintained. The pronounced subradiant behaviour of the elliptic arena cavities at 375 THz is attributed to quantum emitters that are in phase ($\Delta\phi = 0$). This state is usually described by the symmetric state $|+\rangle = \sqrt{1/2}(|g_1, e_2\rangle + |e_1, g_2\rangle)$. However, the presence of a plasmonic resonance can change the sign of the mutual decay rate γ_{ij} and, consequently, the decay route over $|+\rangle$ in Fig. 2.7 can lead to subradiance, while the decay route over the anti-symmetric state $|-\rangle$ is the new superradiant channel.

It was suggested and shown by Diego Martín-Cano, Alejandro González-Tudela and co-workers that a steady state entanglement can be facilitated by continuously pumping the quantum emitters with an external laser source, which calls for an additional term in the coherent Hamiltonian in (2.79). To populate the symmetric state $|+\rangle$, which leads to subradiant behaviour at 375 THz in elliptic arena cavities, both quantum emitters i and j should have an equal relative phase to the driving laser, i.e. the emitters are pumped with identical Rabi frequencies $\Omega_i = \Omega_j$ [205, 117]. For steady state entanglement Rabi frequencies of $0.1 \cdot \gamma_{ii}$ up to $1 \cdot \gamma_{ii}$ are suggested [205], in which γ_{ii} denotes the self-induced decay rate of a single emitter. These values correspond to 0.2 mW - 20 mW continuous wave irradiation and a focus size of 10 μm when the well-known InAs quantum dots with a dipole moment of 1.4×10^{-28} Cm are utilised in elliptic cavities.

The plasmonic structures for these experiments have already been fabricated and successfully tested as shown in Chapter 1. While the quantum emitter experiments can be directly prepared it should also be investigated if the cavity walls near the WGM antennas have a negative influence on the plane wave front of the incident laser beam and hence on the symmetric pumping of opposite quantum dots with identical Rabi frequencies. Likewise it should be checked how laser-excited plasmonic modes influence the experiment. For the very first experiments it may also be sufficient to place the quantum dots in the anti-nodes of the pure

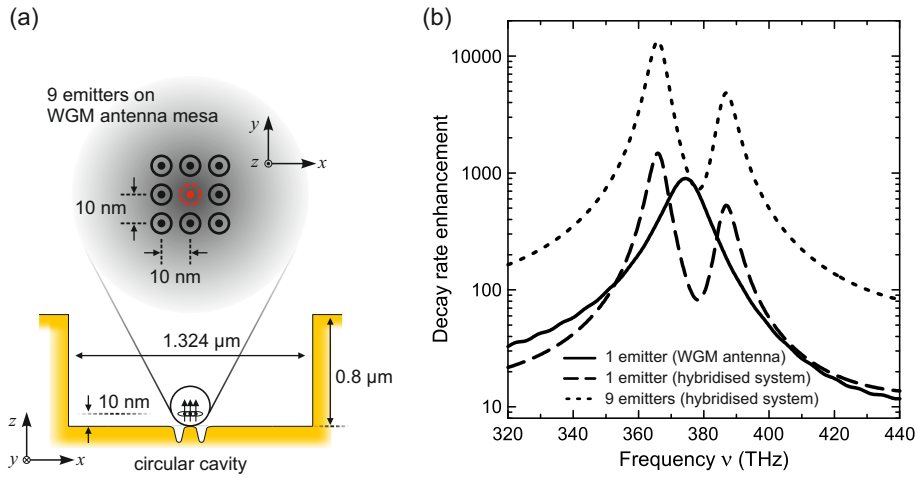

Fig. 2.9: Decay rate enhancement of many emitters in circular cavities. (a) Sketch of FDTD setup including a circular cavity with $n = 2$ and 9 dipole sources on top of the WGM antenna mesa. (b) The decay rate enhancement experienced by the central dipole source (red-marked dipole in part (a)) was obtained by simply using the built-in Purcell function of the LUMERICAL software. While the dotted black line represents the simulation with 9 emitters, the dashed and solid lines represent reference simulations with a single dipole source in the hybridised system and without cavity walls, respectively.

cavity modes without any WGM antenna. This would render a plasmonic hub with clearly separated quantum emitters.

Besides the proposed experiments about entanglement it will also be interesting to go beyond configurations involving only two emitters and to investigate the cooperative behaviour of many emitters in plasmonic systems. In Fig. 2.9(a) the FDTD setup of a circular Au arena cavity is shown which contains nine dipole sources oscillating in phase. All emitters are positioned 10 nm above the WGM antenna mesa and the lateral spacing resembles a grid with emitter distances of 10 nm. The fabrication of such an emitter structure is feasible since semiconductor quantum dots grow by self-assembly in array structures. One of the dipole sources (red dashed line in Fig. 2.9(a)) serves as the probe and its frequency resolved enhancement of the decay rate is shown as the black dotted line in Fig. 2.9(b). The decay rate enhancement of a single dipole inside an identical cavity is shown as a reference (black-dashed line). Likewise, the Purcell enhancement of a dipole source on top of a pure WGM antenna, without cavity walls, is presented. In these latter two cases the single emitter decay rate enhancement of 900 (non-hybridised

mode) is increased to 1473 for the hybridised mode at 366 THz. In the case of nine emitters the central dipole exhibits a decay rate enhancement of 13400. This equates a nine times higher decay rate compared to the single emitter in the hybridised system. Hence, if the quantum emitters are arranged in an array structure like in Fig. 2.9(a) the mutual decay rate will be equal to the decay rate through self-interaction, i.e. $\gamma_{ij} = \gamma_{ii}$.

By assuming that the quantum emitters are InAs quantum dots with a vacuum decay rate $\gamma_0 = 1$ GHz the enhanced decay rate will amount to ≈ 13.4 THz for all nine emitters. Recalling that the damping rate of the hybridised cavity mode is about $\Delta\nu_{cav} \approx 6$ THz leads to the conclusion that every time a photon is lost in a dissipative channel two new photons are inserted into the cavity by every emitter. This effect might be even enhanced if multiple layers of quantum dot arrays are grown. It would be interesting to model the exact behaviour of the radiative system and the atomic system and to pursue the question whether it is possible to establish a traditional lasing regime in which coherence is carried by plasmons.

One could also go into the other direction and investigate on the recently demonstrated plasmonic analogue of a so-called *superradiant laser* which operates in the bad-cavity limit [38]. This laser facilitates stimulated emission by storing the coherence in the collective atomic dipole of the lasing medium (in this case ^{87}Ru atoms) while there is less than one photon on average inside the cavity. It would also be interesting to tune the quantum dot spacing in the presented system to investigate about a systematic effect on collective coherent interaction.

Hence, the plasmonic arena cavities turn out to be an interesting system beyond the usual strong-coupling goal in light-matter interaction. It has been shown that they constitute a serious alternative to widely studied plasmonic waveguides for first-time demonstration of cooperative effects mediated by plasmon modes. The presence of a cavity, in addition to structure-induced resonant electric field enhancement, serves as an intriguing tuning parameter to experimentally study the behaviour of a prepared quantum dot ensemble across the validity of the Markov approximation.

2.6 Summary and outlook

This chapter was motivated by the question to which extent plasmonic modes inside the WGM antenna decorated elliptic arena cavities, i.e. light-concentration far below the optical diffraction limit, can influence energy transfer between widely separated quantum systems operated at Ti:sapphire wavelengths ($\lambda_0 = 800$ nm). It was shown that under cryogenic conditions the system configuration presented here is close to the regime in which energy is reversibly exchanged between widely separated quantum emitters and the radiation field, allowing for coherent interaction of single quantum systems. Furthermore, they are suited for the first experimental realisation of the plasmonic version of the Dicke-effect which is a cooperative interaction of quantum emitters in the weak-coupling regime of light-matter interaction.

By utilising FDTD simulations with single dipole sources, it was shown that the coupling of emitters to the radiation field is quiet efficient, i.e. the emitters decay 600 to 1400 times faster than in vacuum if they are positioned on WGM antennas in elliptic or circular arena cavities, respectively. It turned out that due to this enhanced injection of photons into the hybridised cavity modes and due to resonant field enhancement at opposite WGM antennas, the transfer rates of incoherent energy transfer between widely separated quantum emitters ($d = 2\lambda_0$) are boosted by a factor (nETR) of 10^7 compared to emitters in vacuum. These values even exceed the ones of emitters coupled to 1D plasmonic waveguides which are considered as a promising candidate for strong single emitter-plasmon coupling [206, 148]. Sticking to formalism of incoherent energy transfer, absolute energy transfer rates have been assessed by utilising particular properties of InAs quantum dot emitters, e.g. their comparably high decay rates in vacuum ($\gamma_0 = 1$ GHz) and their temperature dependent absorption cross-section. In a conservative estimate, i.e. using a rather low absorption cross-section in the geometric limit, the efficiency of transferred photons to emitted photons amounts to $\approx 6\%$ in hybridised cavity-antenna systems.

This result suggests that under suitable conditions the transfer of energy is no longer an incoherent process and a quantum-mechanical model, i.e. the Tavis-Cummings-Hamiltonian, was applied to the combined system of photons and two

quantum emitters positioned on opposed WGM antennas insides elliptical arena cavities. By utilising FDTD simulations and quantised electrodynamics, including dyadic Green's function, it was shown that the vacuum Rabi splitting (VRS) of the new eigenmodes is around 1 THz. This splitting is nearly 30 times larger than the VRS of two quantum systems in a photonic crystal cavity [160]. However, cavity damping rates of a few THz are expected to hinder strong coupling of single emitters and a single plasmon. The same is true for VRS of an emitter and a plasmon inside circular arena cavities. Note that this conclusion is restricted to the configuration investigated here: Varying several parameters might help to reach this strong-coupling regime. These include enhanced surface plasmon life-times by reducing scattering events due to sample cooling, operating the system at telecom wavelengths and incorporation of dielectrics for electric field concentration. At least it turned out that a description in the context of QED is mandatory for the configuration presented here .

In the last part of this chapter, it was shown that the dissipative character of the present configuration is promising for realising the first experimental demonstration of a plasmonic version of the Dicke effect, i.e. superradiance and subradiance [246]. By utilising FDTD simulations and Green's function formalism, it was demonstrated that a cooperative interaction of quantum emitters will lead to an appreciably enhanced (superradiant, 1.8 times the single emitter decay rate) or suppressed (subradiant, 0.2 times the single emitter decay rate) decay rate of the collective system. Besides such a fundamental proof, the existence of a subradiant state would, according to ideas from literature [205], also facilitate the entanglement of quantum emitters since the suppressed decay of the system helps to maintain coherence. The quality of the system presented here competes with coequal system, e.g. 1D plasmonic waveguides, which theoretically provide entanglement of emitters via this dissipative channel.

To summarise, the combined system of plasmonic arena cavities and incorporated WGM antennas presented here is an intriguing structure for plasmon-mediated interaction between quantum emitters. Applications and research questions range from incoherent energy transfer to coherent interaction with related topics like cooperative emitter effects or quantum information technology respectively. Furthermore, the combination of both regimes in different structure

constituents, e.g. plasmon-emitter or emitter-emitter, might facilitate the study or realisation of artificial and plasmon-supported light harvesting complexes. The plasmonic structures have already been prepared, as shown in Chapter 1 and are ready for experiments. Besides some fundamental questions that need to be answered like a quantitative investigation of coupling efficiency of emitters to plasmonic modes or a concrete measurement setup with data acquisition channels, the present results render the system as interesting and desirable.

3 Nano-antenna supported current injection in MIM-junctions

3.1 Introduction

A short introduction to hot-electron devices

One of the topics in this thesis is concerned with surface-enhanced Raman scattering (SERS): Light concentration in a small gap between adjacent metallic nanoparticles is utilised to greatly enhance the scattering efficiency of gap-bridging molecules and to transfer spectroscopic information to the far-field. Related to SERS, it was speculated in the early 1980s whether light concentration could also be exploited to drive photochemical reactions of molecules adsorbed on the surface of nanoparticles [223]. During following years it turned out that excited electrons near the surface are equal candidates for doing this job [55, 110]. These excited electrons emerge from the non-radiative decay channel of plasmonic resonances, the so-called *Landau damping*, in which electron-hole pairs are created by the plasmon-induced electric field [140, 98, 190, 200] (see Fig. 3.2(a)). As a consequence, the electron is energetically excited to states above the Fermi level which are according to the Fermi-Dirac distribution less likely occupied at ambient temperature. If the anti-bonding orbital of a molecule at the particle surface exhibits the same energy, the hot electron can be transferred into this state and induce a dissociation process. Usually this transfer is affected by relaxation of the carrier through scattering processes, hence so-called *ballistic* electrons, which did not suffer from scattering, are favoured.

In the context of light harvesting, the separation of hot electrons and holes is an important scheme for energy conversion. Recently, it was shown that combining this scheme with plasmonics culminates in a photosynthetic device which splits water in a completely autonomous fashion [219]. A reproduced sketch of the operation principle is shown in Fig. 3.1: Localised surface plasmons of gold

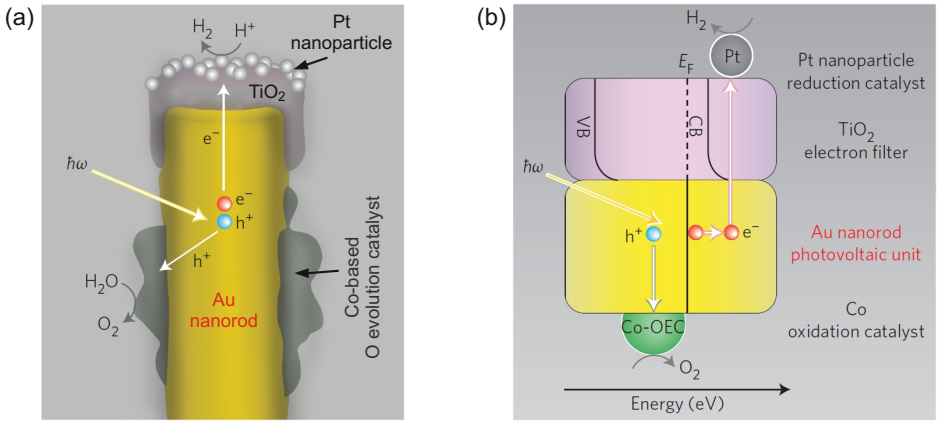

Fig. 3.1: A plasmon-enhanced autonomous water splitting unit. (a) The structure: Solar light resonantly excites localised surface plasmons of gold nano-rods. These plasmons can non-radiatively decay via electron-hole pair creation (Landau damping). The electrons are used by the platinum nanoparticles for hydrogen ion reduction while the created holes are filled with with electrons from the cobalt-based oxygen evolution catalyst (OCE). The associated water oxidation reaction resupplies the OCE with electrons. (b) Sketched energy level diagram: CB, conduction band; VB, valence band; E_f Fermi energy; Pt nano-particles and the Au nano-rod are separated by a TiO_2 layer. A Schottky-barrier builds up and filters the hot electrons created by plasmon decay. The figure is reproduced from [219].

nano-rods, embedded in water, are excited by incident sunlight. After decaying through creation of electron-hole pairs, the holes are refilled with electrons from a cobalt-based hydrogen evolution catalyst which splits the surrounding water by an oxidation reaction. Additionally, hot electrons are directed to platinum nanoparticles which carry out hydrogen ion reduction. The separation is implemented by using TiO_2 as a spacer between the nano-rod and the nanoparticles: A Schottky barrier comes into existence which only allows the hot-electrons to pass the oxide via its conduction band (see Fig. 3.1(b). Using nano-rods of different size broadens the overall absorption spectrum of the device and hence a large part of the solar spectrum can be exploited.

In General, separating charges by a potential barrier is a fundamental concept in light harvesting applications. In this chapter another class of barrier devices is investigated, although in a different context than photosynthesis: *metal-insulator-metal* (MIM) junctions. In these devices an electron is excited by incident light in one of the electrodes. Depending on the barrier height of the oxide the electron

can cross the barrier either by tunnelling or by *internal photoemission* (IPE) above the barrier (see Fig. 3.2). The latter process is identified as most efficient and usually involves ballistic electrons excited near the metal-oxide interface [168].

The application of MIM devices as photodetectors in the optical and mid-IR regime was already studied in the 1970s [134, 101] but it turned out that the efficiency of electron injection into the opposite electrode is far too low for any practical application [56]. In the spectral range of radio-frequencies the efficiency of rectifying devices was enormously enhanced by using antennas for injection of electromagnetic energy [52, 327] and power conversion efficiencies of 90% had been achieved [51]. Based on the progress in nano-technology and the ability to design antennas for visible light [34], separation of charges in rectifying devices has gained large interest in recent years. Plasmon-enhanced conversion of electromagnetic radiation into hot electrons was extensively studied in the fields of solar energy conversion [71], surface-chemistry and photo-detection [50], leading to artificial photosynthetic devices as described above. In the case of MIM junctions different approaches have been realised to utilise plasmonics: depositing nanoparticles as light concentrators on the top-electrode [22], reshaping the top-electrode into a stripe antenna [61] or exciting surface-plasmons in Kretschmann coupling geometry [308]. Although great enhancement has been achieved compared to light irradiation of the bare devices, the power conversion efficiencies or quantum yields stayed well below 1% in all cases. The same holds for nano-plasmonic Schottky-devices [162, 163].

Optical switching by plasmon-enhanced non-linear current injection

So far, recent research about plasmon-induced currents in MIM junctions focused on application of the devices and less attention was paid to more fundamental phenomena like e.g. photo-assisted tunnelling [293]. Focussing on applications for energy conversion tends to restrict the operating regime of the junctions to single-photon processes since they are more likely to occur than multi-photon processes, which require the simultaneous or successive absorption of many photons (see Fig. 3.2). As a consequence of conditional probabilities, such higher-order processes depend on the irradiated intensity in a non-linear fashion and they require usually intense light sources ([136], Chapter 5).

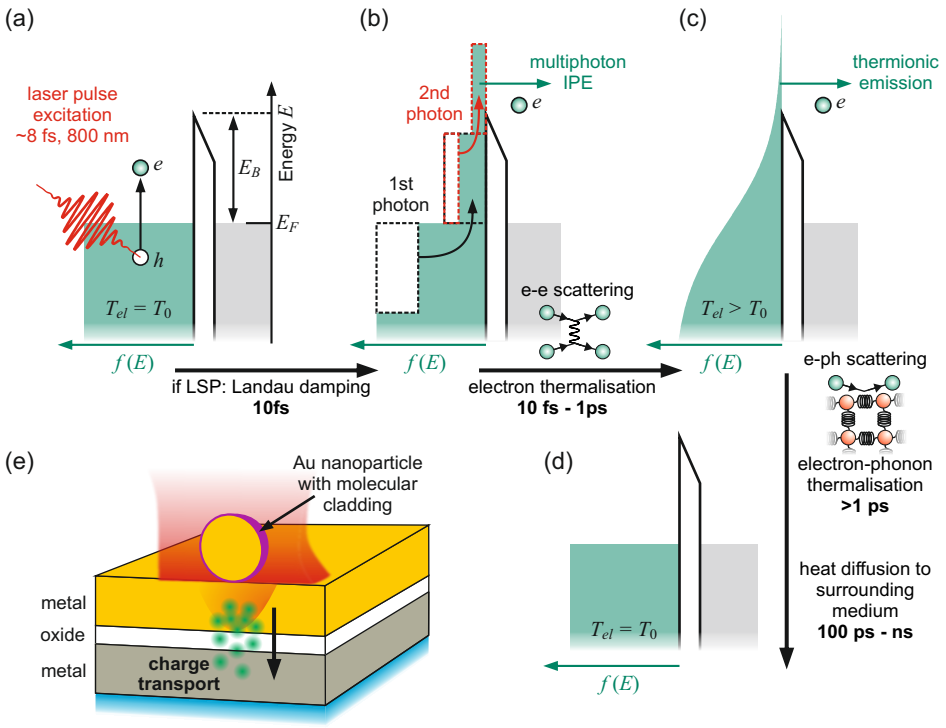

Fig. 3.2: Typical time scales of the electron gas dynamics of a femtosecond laser pulse excited metal-insulator-metal junction. The electron distribution function $f(E)$ of the excited top-electrode is sketched by green-shaded area while the back-electrode (grey-shaded area) is ignored. E_F, Fermi energy; E_B, potential barrier height; T_{el}, temperature of the electronic system; T_0 ambient temperature. (a,b) An electron-hole pair is generated by ultra-short laser pulse irradiation or by plasmon decay. On very short time-scales $f(E)$ forms an athermal staircase-like distribution due to Pauli blocking. The absorption of several photons may be required to inject a current of mainly ballistic electrons by multi-photon internal photoemission (IPE). (c) Thermalisation of electrons: Inelastic electron-electron and electron-surface scattering redistribute $f(E)$ to the form of a Fermi-Dirac distribution (thermal equilibrium) at elevated electron gas temperatures. (d) Electron-phonon thermalisation: The electronic system cools down by collision with phonons so that the lattice and the electrons are in thermal equilibrium after picoseconds. Both sub-systems arrive at room temperature by heat diffusion to the environment after nanoseconds. (e) Proposed scheme for the experiments: A nanoparticle acts as a light concentrator to generate electrons near the metal-oxide interface. The non-linear character of the process and a thick top-electrode render an optical current switch.

A first demonstration of an up to three-photon-induced photocurrent in bare Ag-Al_2O_3-Al junctions (film thickness: 15 nm - 2nm - 40 nm, barrier height: 3.9 eV) was accomplished by Diesing and co-workers [88], as well as by Thon and

co-workers in a different context [293], by using a Ti:sapphire oscillator providing laser pulses of 20 fs duration centred at 1.55 eV photon energy. A connection between plasmonic and non-linear excitations was demonstrated eight years later by Dominik Differt, Detlef Diesing and Walter Pfeiffer at the University of Bielefeld [89]: The spatially-resolved photocurrent injection in a Ag-TaO_x-Ta junction (film thickness: 30 nm - 4.5nm - 30 nm, barrier height: 1.8 eV) was measured by using similar illumination conditions as described above. Interestingly, two-photon IPE into the back-electrode was only observed at particular hot-spots while for all other positions the injected current stayed below the detection limit. The current injection at these pronounced positions was ascribed to field enhancement at structural defects. In addition to that, interferometric two-pulse correlations at those hot-spots implied that a localised plasmonic resonance could be responsible for enhanced electric fields and the corresponding IPE signal.

Based on the latter results, one motivation for this chapter is to demonstrate the plasmon-enhanced injection of non-linear IPE currents by using pre-arranged antennas instead of exploiting random structural defects. Here, antenna-supported current injection is accomplished by drop-casting citrate-stabilised nanoparticles onto the top-electrode of the MIM junction. Due to results of FDTD simulations, it is expected that the nanoparticles act as lenses which transfer the irradiated electromagnetic energy to the metal-oxide interface of a closed top-electrode of appreciable thickness (see Fig. 3.2(e)). According to the experiments of Diesing and Thon, a detectable non-linear current injection could also be facilitated by rather thin electrodes. However, by exploiting the non-linear character of the dominating above-barrier IPE the geometry presented here ensures that a measurable current is only injected when the tightly-focussed laser spot excites the selected nanoparticle. Hence, a presumably nano-localised current is injected and the device can be considered as a nano-scale light-controlled current switch.

The approach of using nanoparticles as light concentrators on top of MIM junctions is similar to the work of Atar and co-workers [22]. However, they used a xenon lamp to illuminate the entire active area of the junction in order to asses the device in the context of solar energy conversion. Neither did the experimenters use intense light pulses nor did they examine current injection at selected antennas. Additionally, in their work the nanoparticle and top-electrode are separated by a spacer layer of 10 nm thickness while in the study presented

here the thin citrate cladding of the nanoparticles serves as a spacer. Hence, a stronger field enhancement is achieved in the present study.

Plasmon-enhanced non-linear and non-equilibrium dynamics

In addition to the aspect of local current injection, further experimental and theoretical results imply that strong light concentration below the nanoparticle gives access to an unusual regime in non-equilibrium dynamics of the electronic system: In contrast to previous work, the dominating current injection mechanism is identified to be *thermionic emission* rather than multi-photon-induced above-barrier injection of charge carriers, although dynamics in the system is excited with an ultra-short laser pulse of ≈ 10 fs duration. Thermionic emission usually occurs when the temperature of the electronic system is high enough so that a significant part of the corresponding Fermi-Dirac distribution lies above the work function. Since the Fermi-Dirac (FD) distribution determines, in the case of thermal equilibrium, the probability to find an electron at a specific energy, there is an appreciable chance for many electrons to be ejected from the metal into the environment [167] or, in the present case, to surmount the potential barrier of the oxide and to reach the back-electrode. The improbable case of dominating thermionic emission can be envisioned by tracking the system evolution upon light excitation as sketched in Fig. 3.2(a-d):

Absorption of electromagnetic energy. The electron distribution (ED) function $f(E)$ of the top-electrode is represented by the green-shaded area and it is assumed that the ED function of the back-electrode (grey-shaded area) is not affected at any time. At the beginning the electronic system is in thermodynamic equilibrium and it obeys the FD distribution which resembles a Heaviside step function around the Fermi energy E_F at ambient temperature T_0. A laser pulse impinging on the electrode excites electrons into states of higher energy by photon absorption. Alternatively, in the case of a bright localised plasmon resonance, electron-hole pair generation occurs due to Landau damping on time scales of the pulse duration. Because of Pauli blocking only electrons between E_f and $E_f - \hbar\omega$ are initially excited, in which $\hbar\omega$ is the photon energy, and $f(E)$ resembles a step-like shape (experimentally demonstrated in [100]). Due to absorption of successive photons this shape is copied to higher energies and a staircase evolves. Electrons with

energies above E_B can reach the back-electrode via the conduction band of the oxide and this multi-photon process was identified as the dominating channel for non-linear current injection in MIM junctions [88, 89].

Thermalisation of electronic system. In its present state, the electronic system is driven out of thermal equilibrium: It cannot be described by the smooth FD distribution and hence the concept of an electron gas temperature T_{el} fails. The electronic system tends towards equilibrium mainly by electron-electron scattering processes and a redistribution of $f(E)$ occurs [253]. The time it takes the electronic system to reach its thermal equilibrium, and therefore to regain the shape of a FD distribution with an associated temperature T_{el}, is the thermalisation time τ_{therm}. It depends on specific excitation conditions and definitions [220], reported values range from 100 fs for nanoparticles [150] to some hundred femtoseconds for metallic single-crystals [191]. Electrons residing in the high energetic tail of the FD distribution can also contribute to current injection via thermionic emission, but their contribution to the overall current is usually insignificant with respect to the above reported results.

Electron-phonon thermalisation and external heat diffusion. The absorption of photons is mainly attributed to the electronic system. As a result, the electronic temperature T_{el} is highly elevated while the temperature of the lattice T_{la} is usually much lower. A thermal equilibrium between both systems, i.e. $T_{el} = T_{la} > T_0$, is established via electron-phonon collisions. The cooling time of the electronic system occurs on time scales > 1 ps (see [147] for e.g. nanoparticles) because the maximum phonon energy is small compared to the kinetic electron energy and hence many electron-phonon collisions are necessary to decrease the energy stored in the electron gas [253]. Finally, heat diffusion requires 100 ps up to a few nanoseconds in order to establish thermal equilibrium with the environment [26], i.e. $T_{el} = T_{la} = T_0$.

The above processes have been described in the fashion of discrete steps but actually they overlap in time. For instance, a dominating thermionic emission of electrons from a nano-object is realised by irradiation of nanosecond laser pulses [322]. In this case the laser pulse duration is longer than the typical time scales for electron-phonon thermalisation and the object is continuously heated. In contrast to that, the previous MIM experiments of Differt and Diesing have been performed with laser pulse durations which are expected to be shorter than the thermalisation

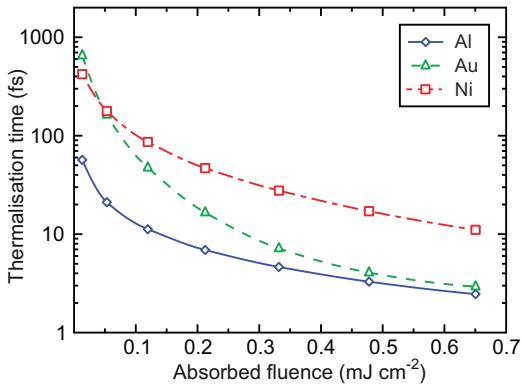

Fig. 3.3: Thermalisation time of the electronic system as a function of absorbed fluence for aluminium (Al), gold (Au) and nickel (Ni). The homogeneous excitation ignores heat transport and involves a 10 fs laser pulse with a singular photon energy of $\hbar\omega = 1.55$ eV (800 nm). The thermalisation time is derived from the e^{-1} time constant of the transient entropy which tends to be constant at thermal equilibrium. Figure is reproduced from [220].

time τ_{therm} of the electronics system. In this case most of the current injection occurs due to multi-photon-induced above-barrier processes of the athermal ED function and relaxation, i.e. electron-electron scattering, reduces the available number of electrons above the required injection energy.

With respect to the above consideration, a dominating thermionic emission initiated by an ultra-short laser pulse will only occur if the electronic system is instantaneously thermalised after the excitation. Recently, Mueller and Rethfeld investigated theoretically on relaxation dynamics in laser-excited metals under non-equilibrium conditions and found that the thermalisation time of the electronic system depends on the absorbed fluence of the laser pulse [220] (Fig. 3.3). They used the microscopic framework of the Boltzmann equation and Boltzmann collision integrals, and defined τ_{therm} by the transient entropy of the system: According to the second law of thermodynamics, the entropy of an isolated system increases or, in the case of thermal equilibrium, remains constant ([123], Chapter 2.3). The transient entropy revealed an exponential-like behaviour and the characteristic e^{-1} time constant was identified as τ_{therm} which can be as short as a few femtoseconds for strong and ultra-fast energy deposition (Fig.3.3). These fast thermalisation times are ascribed to the increased phase space of the electrons [220].

The experimental results presented in this chapter suggest that antenna-enhanced light concentration at the metal-oxide interface of MIM junctions facilitates to reach this high-intensity regime of non-equilibrium dynamics. Furthermore, it will be deduced from a theoretical model that the present nano-scale geometry

might allow for injection of ultra-short current pulses, which is in stark contradiction to the common regime of thermionic emission.

Field-driven and popuplation-driven light-matter interaction

At the end of the introduction, an attempt will be made to place the presented topic into a larger context. This will be done by separating light-matter interaction into field-driven processes, which are characterised by coherence, and non-equilibrium processes, which are significantly influenced by population. Both classes are sketched in the low and high intensity limit in Fig. 3.4:

Field-driven - low intensity. The irradiated laser field induces a collective motion of the conduction electrons in the nanoparticle. For sufficiently high field strength the potential for the collective motion is no longer harmonic due to the presence of the metal-vacuum interface, a non-uniform particle shape or the presence of a substrate. Hence, the potential of the electronic motion becomes anharmonic which leads to a polarisation at low order harmonics of the external field (blue pulse). It was shown that the non-linear polarisation can be mathematically treated in perturbation theory like in standard non-linear optics [213] and second and third-harmonic generation have been demonstrated for various plasmonic systems [221, 131, 130].

Field-driven - high intensity. The research field of strong laser fields interacting with nano-scale systems has emerged in the last ten years. In this scenario, the external light field cannot be treated as a perturbation because it competes with the potential that keeps the electrons inside the e.g. nanoparticle. As a consequence, electrons escape from the system by field or tunnel ionisation [157] and are accelerated in the external laser field. Analogous to atomic attosecond physics [169] the electrons are driven back to the nano-object by the laser field and scatter elastically off the surface, therefore gaining even more energy in a subsequent field cycle. In this process, harmonics of high order are generated in the electron spectrum and special features explicitly depended on the exact waveform of the laser pulse. This regime has been achieved with metallic nano-tips [172, 241] and SiO_2 particles [334]. Here, two important points are noted: First, interaction of the ejected electrons with optical near-fields can form a train of attosecond electron pulses [104], i.e. electronic pulses shorter than expected from multi-photon

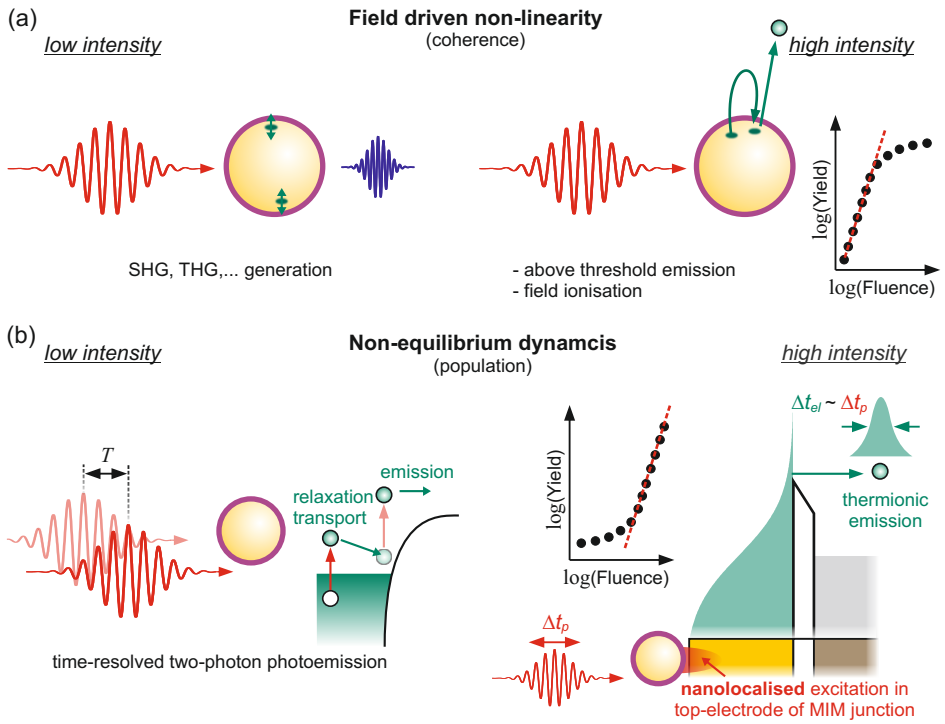

Fig. 3.4: Sketch of field-driven and non-equilibrium processes in nano-scale systems for low and high intensity of irradiated laser pulses. (a) Field-driven: At relatively low intensity an anharmonic collective motion of electrons is induced due to the presence of metal-vacuum interfaces, a non-uniform particle shape or a supporting substrate, leading to second- or third harmonic generation of the incident light. At high intensities electrons are extracted from the nano-system and are accelerated in the time-varying electric field. High-harmonic generation and strong field effects similar to the gas phase occur. The non-linear yield-to-fluence dependence decreases due to saturation and electronic pulses shorter than the laser pulse are created. (b) Non-equilibrium dynamics: Athermal electron distributions are generated to facilitate charge transfer or to study the interactions of system constituents. 'Low-order harmonics' of electronic energies can be created (see Fig. 3.2(b)) in analogy to field-driven processes. At high intensities an unexplored regime occurs: The electronic system is instantaneously thermalised leading to thermionic emission as the dominating current injection mechanism. Similar to field-driven processes the yield-to-fluence dependence is altered and electron pulses are created that are shorter than expected from thermionic emission.

ionisation. And second, the non-linear dependence of the overall electron yield with irradiated fluence decreases until saturation occurs ([136], Chapter 8).

Population-driven - low intensity. Driving a nanoparticle with an external field does not result solely in generation of low order harmonic radiation. As in the

case of MIM junctions in Fig. 3.2(a-d) the electronic system of the nano-particle can also be driven out of equilibrium upon laser pulse excitation and it will hence pass trough the different steps of relaxation (time-domain study in [211]). Usually the initiated dynamics, i.e. the time-dependent state of $f(E)$, is probed with a second laser pulse in so-called *time-resolved two-photon photoemission*. The non-linearity is introduced through the second absorbed photon which is required to eject excited electrons. Creating non-equilibrium states of the electronic system facilitates to observe interesting phenomena like charge transport between the nanoparticle and the supporting substrate [238] or to determine the important electron-phonon interaction in single-wall carbon nanotubes [137].

Population-driven - high intensity. The non-linear character in population-driven processes may also be attributed to the staircase shape of the athermal electron distribution. At low intensities only the second step would be significantly populated compared to energetically higher steps, in a similar way only low-order harmonics are generated in field-driven processes. At high intensity higher steps are significantly populated which might be compared to the high-harmonic generation in field-driven processes. For an increasing energy absorption, it is shown that the non-equilibrium electron distribution behaves similar to an equilibrium electron distribution of the same inner energy [220]. This behaviour supports fast thermalisation times and equilibrium is achieved almost instantaneously [220]. Compared to field-driven processes, two important similarities have to be noted: First, the non-linearity of yield-to-fluence dependence is also altered in population-driven processes but in an opposite sense. The low gradient of the multi-photon IPE gets steeper in thermionic emission due to the highly non-linear character of the associated Richardson-Dushman equation (see equation (3.11)). And second, the temporal duration Δt_{el} of the injected electron pulse is assumed to be similar to the duration Δt_p of the ultra-short laser pulse. This is much faster compared to the expected thermal related time scales.

At this point the question arises whether coherent processes or non-equilibrium processes dominate a measurable quantity in an experiment. This question becomes especially important when metallic nano-structures are considered in the high intensity regime. For instance, a lowered non-linearity of the yield-to-fluence dependence might indicate the onset of strong field effects. However, depending on the multi-photon order for ejecting electrons at a given laser frequency, the non-

linear character of the process might also be reduced because of the decreased non-linearity in thermionic emission at very high temperatures. The results of the present chapter reveal that dissipative effects should not be ignored and that great care must be taken when discussing strong-field effects in nano-plasmonic systems.

Chapter outline

The chapter is structured as follows: Section 3.2 is dedicated to the experimental results. After a short introduction of the setup and the preparation methods, the nano-localised current injection is demonstrated with two MIM junctions featuring different barrier heights. It will be shown that the antenna-supported current injection depends in a highly non-linear fashion on the incident laser pulse energy and the injection mechanism can no longer be explained by multi-photon-induced above-barrier injection of charge carriers. Finite-difference time-domain simulations are utilised in Section 3.3 to asses the absorbed energy density in the top-electrode underneath the nanoparticle. It will turn out, with respect to the results of Mueller and Rethfeld, that the experimental conditions meet the criterion to assume an instantaneous thermalisation of the electronic system. Therefore, it is allowed to model the temporal dynamics of the electronic system, i.e. the heat diffusion, according to the two-temperature-model. These spatially-resolved simulations are utilised in Section 3.4 to calculate the thermionic current injection at the metal-oxide interface. It will turn out that thermionic emission model adequately describes the experimental results. A summary and an outlook can be found in Section 3.5

The results in this chapter have been obtained in cooperative work: Detlef Diesing (University of Duisburg-Essen) fabricated and provided the MIM junctions. Experiments on current injection with ultra-short laser pulses were performed by Dominik Differt (University of Bielefeld) and the thesis author. The thesis author was also responsible for FDTD simulations. Simulations about heat-diffusion and thermionic emission were performed by Felix Becker (University of Bielefeld). The overall data evaluation was accomplished by Felix Becker and the thesis author, with support of Dominik Differt. Walter Pfeiffer (University of Bielefeld) supervised the work.

3.2 Experimental demonstration of nano-localised current injection

3.2.1 Experimental setup

Laser setup

A sketch of the device setup on the optical table is shown in Fig. 3.5(a). The laser system used in the experiments is the Ti:sapphire oscillator FEMTOSOURCE RAINBOW from FEMTOLASERS. Its Ti:sapphire crystal is pumped with a power of 4.9 W from a low noise ($< 0.03\%$ rms) diode-pumped solid-state laser (VERDI V5, COHERENT) at a light frequency of 563.5 THz (532 nm). The radiation of 563.5 THz is closely located to the maximum of the absorption spectrum of the Ti^{3+} ion inside the Ti:sapphire crystal [259]. Pulsed emission occurs at a centre frequency of 375 THz (800 nm, 1.55 eV) with a repetition rate of 80 MHz due to the Kerr lens mode locking mechanism. Advanced optics inside the laser cavity, like chirped mirrors [43], facilitate to maintain a broad-band emission spectrum (see Fig.3.5(b)) and the oscillator is specified to deliver ultra-short sub-7 fs laser pulses. Two beams are provided by an internal beam splitter: One beam is provided for attosecond streaking experiments in which the author has also been involved [212], and the other one is used in the experiments presented here (output power: ≈ 210 mW).

Due to the broad-band spectrum the laser pulse is severely affected by any dispersive element on the way to the MIM experiment at the three-axis stage. To maintain the ultra-short character of the pulse three different elements for dispersion management are utilised: First, the chirped mirror compressors CMC1 and CMC2 are used to compensate the group velocity dispersion (GVD) which is usually the dominant contribution in pulse stretching due to a frequency-dependent speed of light in materials with normal dispersion. Second, a third-order dispersion (TOD), as well as additional GVD, can be compensated with the prism compressor. The prisms (Brewster prisms for 800 nm with $< \lambda/10$ wave front distortion, BERNHARD HALLE NACHFL. GMBH) are mounted on linear and rotation stages and have been aligned by identifying the minimum deflection angle with a beam profiler camera. The Ag mirror at the second prism is slightly tilted in vertical direction so that the reflected laser beam can be picked out at a shallow beam height of 75.5 mm. And third, thin glass wedges (OA924, FEMTOLASERS)

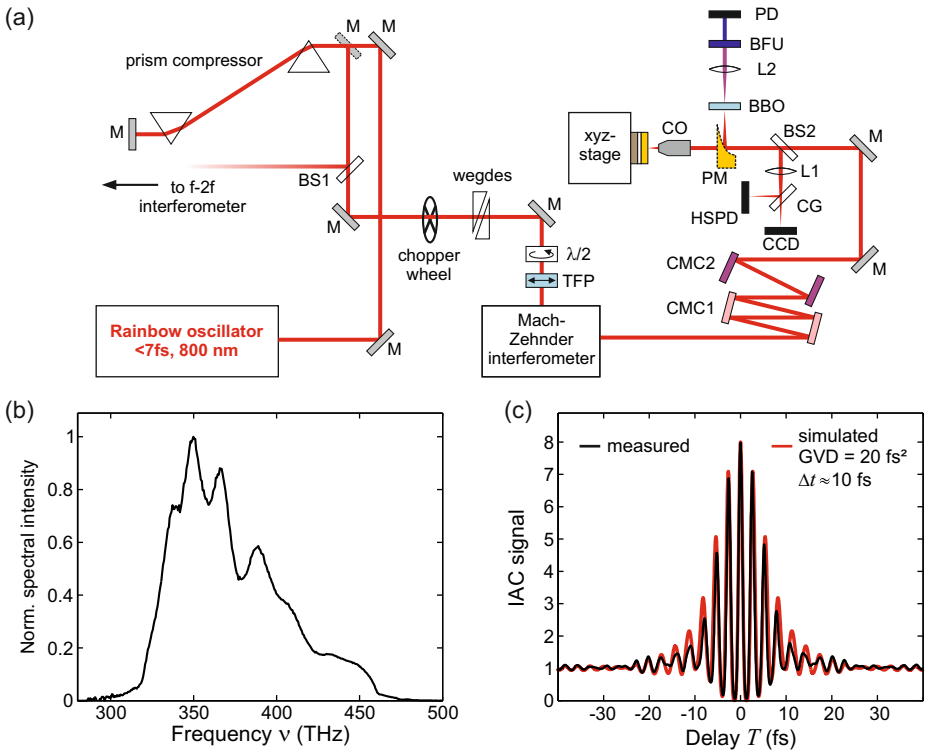

Fig. 3.5: Experimental setup. (a) Explained abbreviations. M: mainly enhanced Ag mirrors (OA022, FEMTOLASERS). BS1: 50% beam splitter (108222, LAYERTECH). $\lambda/2$: achromatic $\lambda/2$ waveplate (OA232, FEMTOLASERS). TFP: ultra-broad-band achromatic thin film polariser (OA512, FEMTOLASERS). CMC1: chirped mirror compressor (FEMTOLASERS). CMC2: chirped mirror compressor (DCM7, VENTEON). BS2: ≈5% beam splitter. L1: plano-convex lens (THORLABS). CG: cover glass (MARIENFELD). HSPD: high-speed photo-detector (DET100A/M, THORLABS). CCD: small-board charge-coupled device (CONRAD). PM: off-axis gold-coated parabolic mirror (OA175, FEMTOLASERS). BBO: mounted beta-barium-borate crystal (FO030, FEMTOLASERS). L2: plano-convex lens (THORLABS). BFU: blue light transmission filters (see [129]). PD: blue sensitive photo-diode (1961, HAMAMATSU PHOTONICS). CO: Cassegrain objective (5006-120, DAVIN OPTRONICS). (b) Spectral intensity of the laser measured with an USB spectrometer (USB4000, OCEAN OPTICS). (c) Measured (black solid line) IAC in front of the CO and simulated IAC (red solid line). The IAC is simulated by using the spectrum in (b) and imprinting a GVD of 20 fs^2.

mounted on individual linear stages are used for fine-tuning of the dispersion.

The temporal duration of the laser pulses is monitored with non-linear interferometric autocorrelations (IAC, see Chapter 9 in [86]) by using a Mach-Zehnder interferometer which was built during the bachelor thesis of Henning Hachmeister

[129]. The detection unit is closely located to the MIM experiment: An off-axis gold-coated parabolic mirror (PM, 50 mm focal length, OA175, FEMTOLASERS) is used to focus the pulses into a thin beta-barium-borate crystal (BBO, 20 μm, FEMTOLASERS) for second-harmonic generation. The blue light is filtered with several optical components (BFU, see [129]) and focused onto a blue-sensitive photo-diode (G 1961, HAMAMATSU PHOTONICS) which is connected with a pico-ammeter. Alternatively, the IAC can be measured by focussing the laser on the chip of the photo-diode in order to generate a two-photon absorption process.

A typical IAC is shown by the black solid line in Fig. 3.5(c): The peak-to-baseline signal is close to the optimum second-harmonic IAC ratio of 8 : 1. Additionally, there is no significant indication for satellite pulses which typically originate from e.g. TOD. To asses the pulse duration an IAC has been simulated by using the measured laser spectrum shown in Fig. 3.5(b). The IAC is simulated with a GVD of 20 fs^2 (red solid line in Fig. 3.5(c)) so that the corresponding temporal intensity profile is broadened to approximately 10 fs at full-width half-maximum. Although no fitting procedure is applied there is a good agreement in general shape between simulation and experiment. Actually, the fringe amplitude of the measured IAC is lower compared to the simulated IAC which is associated with a 10 fs laser pulse. Hence the actual laser pulse duration is shorter than 10 fs in the experiments (here, $\approx$ 8 fs). Note that applying a fitting routine is cumbersome since the spectral phase emerges from self-phase modulation inside the Ti:sapphire crystal so that it cannot be describes by a smooth low-order power function. This has been verified by SPIDER ([86], Chapter 9) measurements.

MIM setup

The parabolic mirror for IAC measurements is mounted with a magnetically coupled kinematic base so that the PM can be reproducibly inserted. Once removed the beam enters a Cassegrain objective (CO, 5006 – 120, DAVIN OPTRONICS) and is focused onto the MIM junction which is fixed to a three-axis stage. The CO is an all-reflective objective which mainly consists of two spherical mirrors, as sketched in Fig. 3.6(a) and its transmission was determined to be $\approx$ 37% for the incident laser beam (e^{-2}-diameter: 5.4 mm). Due to the reflective character no material dispersion will broaden the laser pulses in time. The magnification

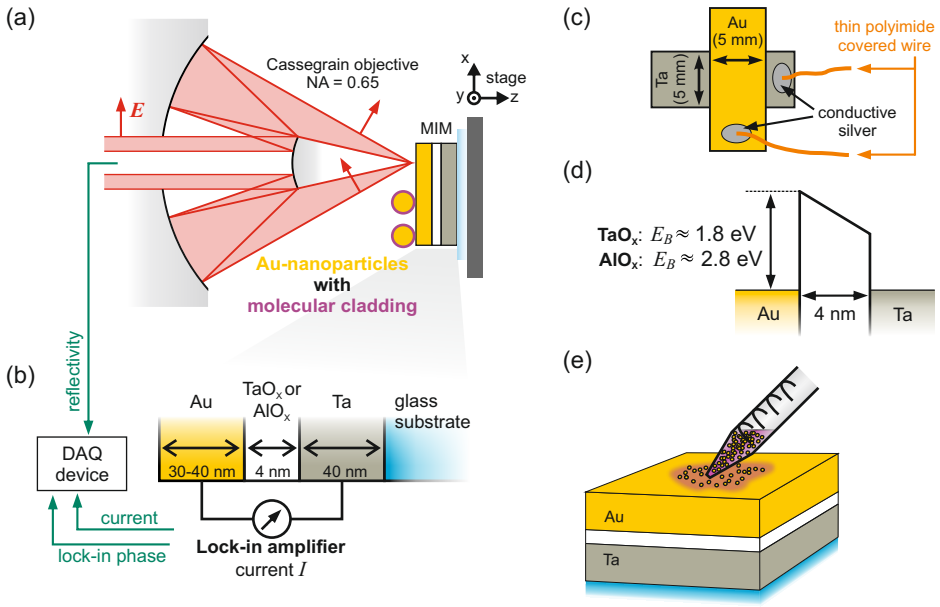

Fig. 3.6: Details of the MIM setup and preparation of experiments. (a) Path of optical rays in the all-reflective Cassegrain objective and the impact on electric field polarisation E. (b) The re-collimated light reflected by the sample surface is recorded with an USB DAQ device (NI USB-6211, NATIONAL INSTRUMENTS) in referenced single-ended configuration. It also serves to measure the current and phase signal (differential terminal configuration) of a lock-in amplifier (7265, EG&G INSTRUMENTS) that is connected to the electrode of the MIM junction. Two different junctions are used for experiments with nano-particles: The junction with TaO_x exhibits a top-electrode thickness of 40 nm and the AlO_x-junction features a 30 nm top-electrode. (c) The evaporated electrodes are connected with conductive silver and thin polyimide covered wires to the lock-in amplifier via an BNC cable. (d) Barrier heights. For TaO_x see [282] while the value for AlO_x is estimated by Detlef Diesing. Similar values can be found in [146, 112]. (e) Au nano-particles are deposited by the drop casting method using an Eppendorf pipette. Only a few μL of solution are used. The TaO_x-junction is decorated with citrate stabilised nano-particles fabricated by Ingo Heesemann (100 nm - 200 nm diameter) while the AlO_x-junction is prepared with commercial nano-particles from SIGMA ALDRICH (250 nm diameter).

factor is about $\times 52$ and the mirrors are coated with inert gold to ensure long-time operation under normal ambient conditions.

While the CO remains fixed after coarse positioning with a linear stage the MIM surface can be laterally scanned in the laser focus with a three-axis stage. During the experiments two different stages have been used: A piezo stage from MADCITYLABS (NANO-LP300, 300 μm travel distance, closed loop) and a piezo electric inertial drive stage from MECHONICS (8 mm travel distance, closed loop).

While the piezo stage features a repositioning accuracy of about 1 nm, the latter stage offers a more coarse repositioning accuracy of about 50 nm. Lateral scans can be controlled with a LABVIEW VI which was mainly written and updated by Dominik Differt.

During a scan three signals are recorded and saved: Light-induced currents in the MIM junctions are measured with a lock-in amplifier (7265, EG&G INSTRUMENTS). To ensure that the injected current is related to laser irradiation the lock-in phase signal is simultaneously recorded. An optical chopper system (model 3501, NEW FOCUS) provides the corresponding trigger-signal for the lock-in amplifier (note the chopper wheel in Fig. 3.5(a)). The lock-in amplifier current, as well as the phase, are recorded in differential terminal configuration with an USB data acquisition device from NATIONAL INSTRUMENTS (NI USB-6211, see Fig. 3.6(b)). The third signal that is recorded with spatial resolution is the light which is reflected by the sample and re-collimated by the CO. The reflected light is picked up with a beam splitter of $\approx 5\%$ reflection, as shown in Fig. 3.6(a), and then focused with a lens onto the high-speed photo-detector HSPD (DET100A/M, THORLABS). The signal is amplified by a current-voltage converter (FEMTO) and then recorded with the DAQ device in referenced single-ended configuration. This reflection signal depends e.g. on junction topography and it supports orientation as well as the interpretation of obtained results. Here, it will be used together with scanning electron microscopy (SEM) to identify single nanoparticles which have been excited by the laser. All three measurement signals, current, phase and reflectivity, can be monitored with a digital oscilloscope (WAVESURFER, LECROY) while scans are running.

A cover glass (CG) allows to split the reflected light so that the beam can be additionally recorded with a CCD image sensor of a small board camera. If the axial laser (or flashlight) focus is located on the surface of the MIM junction the CCD sensor delivers live images in terms of a microscope. It can be used for orientation as well as to adjust the axial focus on the MIM junction.

MIM junction preparation

The MIM junctions are fabricated and provided by Detlef Diesing: Two metal electrodes are evaporated orthogonal to each other onto a cover glass (see Fig.

3.6(c)). Before the top-electrode is prepared the oxide is grown on the back-electrode by a wet-chemical procedure. The geometrical dimensions of the electrode are affected by the evaporation mask so that the active area of the junctions measures approximately 5 mm $\times$ 5 mm. Away from this area thin Kapton covered wires are connected to the respective electrode by using conductive silver. These wires are then connected to the core and the metallic shield of a sliced BNC cable, respectively, that is wired to the lock-in amplifier.

Here, MIM junctions with two different barrier heights are investigated while the top-electrode and the back-electrode are made out of gold and tantalum in both cases. One junction is prepared with tantalum oxide which exhibits a barrier height at the top-electrode-oxide interface of 1.8 eV [282], which is slightly higher than the central photon energy of the laser setup (Fig. 3.6(d)). The second MIM junction is prepared with aluminium oxide which leads to a significantly increased potential barrier of approximately 2.8 eV, as estimated by Detlef Diesing (see [87], Fig. 6, upper part, wet preparation). This estimate for the Au-Al_2O_3 interface is corroborated by reported literature values of 2.6 eV for metal-insulator-semiconductor junctions [146, 112] and it is expected that two-photon and three-photon absorption processes are required for the above barrier injection of charge carriers. It should be noted that the top-electrode thickness of the devices is different: The AlO_x-junction exhibits a top-electrode thickness of approximately 30 nm while the TaO_x-junction features a thickness of about 40 nm.

Due to historical reasons the junctions are equipped with different types of Au nanoparticles: The TaO_x-junction is operated with nanoparticles fabricated by Ingo Heesemann in a similar manner like in the SERS experiments presented Chapter 4. In this case the size of the nanoparticles varies from 100 nm to 200 nm. In contrast to that the AlO_x-junction is equipped with as-received Au nanoparticles from SIGMA ALDRICH which exhibit a highly mono-disperse size of 250 nm. Both types of nanoparticles come with a molecular citrate cladding of unknown thickness [298]. The cladding ensures that the nanoparticles are not electrically connected with the top-electrode otherwise it is expected that any antenna effects are greatly reduced. For both junctions the particles are deposited on the top-electrode by the drop casting method using a few μL of the colloidal solutions (Fig. 3.6(e)). In the case of the TaO_x-junction the solution is vaporised at air

while in the case of the AlO_x-junction the drop was vaporised much faster by using a desiccator. In both cases it was successfully checked that drop-casting and vaporisation did not damage the junctions via measuring the non-linear laser-related current injection.

3.2.2 Laser-induced current injection at the top-electrode edge

Laser-related current injection is now presented at the edge of a bare MIM junction to demonstrate the measurement scheme in a more visual way and to show the typical behaviour of a MIM junction irradiated with ultra-short laser pulses of 1.55 eV photon energy. The system is a Au-TaO_x-Ta junction with a top-electrode thickness of 100 nm. At the edge of the active area the top-electrode thickness smoothly decreases because of the evaporation mask. This allows to position the excitation volume of the focused laser close to the metal-oxide interface where it is expected that the excited ballistic electrons may easily travel to the back-electrode via the conduction band of the oxide (see [89] and Fig. 3.7(a)).

Once the axial focus is adjusted to the top-electrode surface by maximising the signal on the HSPD or by improving the image on the CCD the laser spot is scanned laterally across a predefined area for a point-by-point data acquisition. In the context of MIM junctions this spatially-resolved method has been labelled as *scanning internal photoemission microscopy* [89]. The acquisition period at each position should be adjusted to the time constant of the lock-in amplifier so that the current and phase detection gives reliable values. If the scanning speed is too fast a significant spatial displacement occurs between simultaneously recorded features related to current injection and reflectivity.

The spatially-resolved reflectivity is shown in Fig. 3.7(b). From left to right the voltage signal of the HSPD is steadily decreasing. The signal reduction indicates a decreasing film thickness at the edge of the active array since this leads to a reduction of reflectivity. The simultaneously recorded current is shown in Fig. 3.7(c). A significant current of a few nanoampere is detected at medium reflectivity and an impinging laser pulse energy of 10.2 pJ. Note that specific features appear sharper than expected from a laser focus size of 1-2 μm (e^{-2}-diameter, see Section

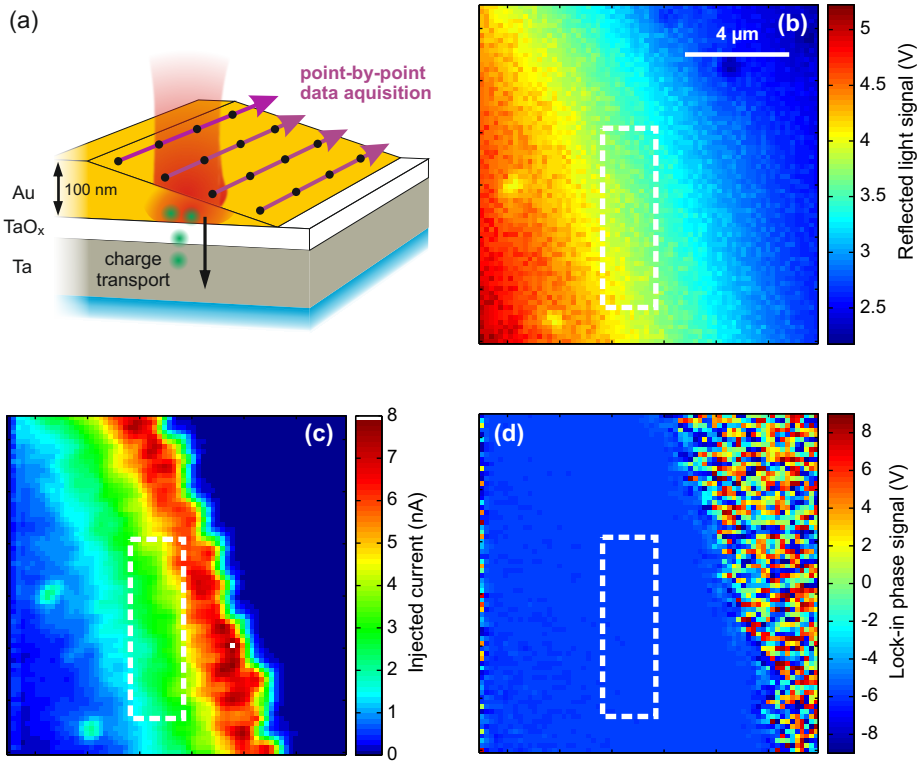

Fig. 3.7: Laser-induced current injection at thin top-electrodes. (a) Sketch of scanning internal photoemission microscopy [89]. At every position induced current, lock-in phase and reflectivity are simultaneously recorded by the USB DAQ device. Light-induced currents can be easily detected at the edge of the active MIM area: In this region the top-electrode thickness is continuously reduced because of the shadow mask in the evaporation process and hence the excitation volume of the laser moves closer to the metal-oxide interface. (b-d) Reflectivity, induced current and lock-in phase at the active area edge of a TaO_x-junction. The lock-in phase is given in volts: Voltages of +9V and -9V correspond to angles of +180° and -180° respectively. The white-dashed rectangle marks the region for the power law measurement in Fig. 3.9(a). Lock-in sensitivity: 10 nA. Lock-in time-constant: 50 ms. Chopper frequency: 73 Hz. Laser pulse energy: 19 pJ

3.3.2). However, this can be attributed to the non-linear character of the current injection process which is discussed in Section 3.2.4.

The corresponding lock-in phase in this region takes constant values (see Fig. 3.7(d)) which strongly corroborates that the injected current is attributed to laser pulse excitation. Moving the laser further to the right part of the scan area leads

to a random distribution of lock-in phase values since no current can be detected. The signal has dropped to the noise level of ≈ 0.02 nA, which is given by the lock-in amplifier parameters. Moving the laser to the left part of the scan area also leads to a reduction of the injected current. This reduction is not as abrupt as on the right side and the lock-in phase only shows small deviations from values found in the region of maximum current injection. However, moving the laser further to the left will finally decrease the detected current to noise level (not shown here).

The results from above suggest that an optimum thickness exists for laser-induced current injection: In the left part of the scan area the Au film thickness exceeds the typical penetration depth of ≈ 13 nm for 375 THz light at the Au-vacuum interface, as well as the inelastic mean free path of about 10 nm for electrons with an energy of 2 eV [270]. In the right part of the scan area current injection is simply limited by the vanishing top-electrode thickness: The injected current will take higher values close to the cut-off because the excitation volume of the laser moves closer to the metal-oxide interface, but then the electrode thickness falls below the percolation limit which precludes current detection.

3.2.3 Demonstration of nano-localised current injection

After presenting the measurement scheme this section is now dedicated to the demonstration of nano-antenna-assisted laser-induced current injection. The preparation of the junctions and the deposition of nanoparticles has already been described in Section 3.2.1 and hence the results are immediately discussed.

At the beginning of the experiments a large area of 300 μm $\times$ 300 μm is scanned with a rather high resolution of 1 μm to get an overview. This area is much smaller than that of the circular shaped dried out drop of the colloidal solution which exhibits a diameter of about 2 mm. For a better orientation it is therefore preferable to perform the experiments at the rim of this structure. It looks like a coffee stain because the nanoparticles tend to accumulate near the rim and the specific area can be easily identified in later SEM investigation. Then a specific region is chosen which shows a significant current amplitude. Due to the ratio of scan resolution to nanoparticle size this amplitude should be restricted to one or

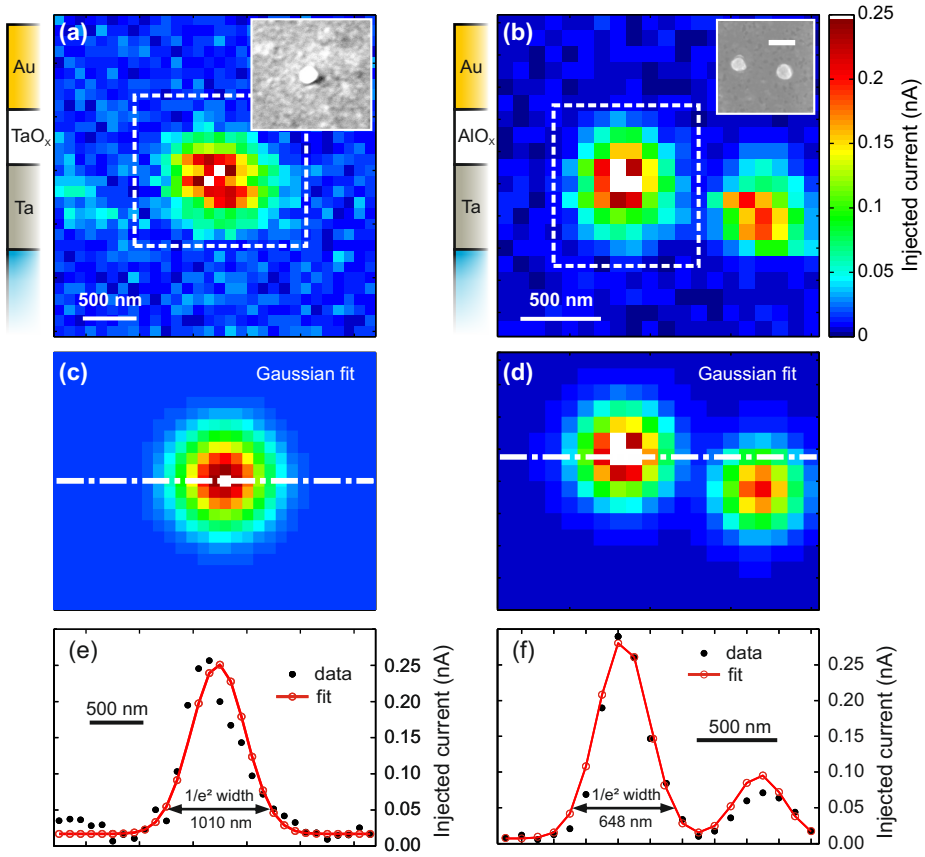

Fig. 3.8: Nano-antenna-assisted laser-induced current injection using the TaO_x-junction (a,c,e) and the AlO_x-junction (b,d,f). (a) The spatially-resolved current is measured with the following parameters: 10 nA lock-in sensitivity, 50 ms lock-in time-constant, 143 Hz chopper frequency and 7.4 pJ laser pulse energy. Inset: SEM image of the same scale. (b) The spatially-resolved current is measured with the following parameters: 1 nA lock-in sensitivity, 50 ms lock-in time-constant, 143 Hz chopper frequency and 27.8 pJ laser pulse energy. Inset: SEM image with a 500 nm scale bar. White-dashed rectangle in (a) and (b): Evaluation area for power laws. (c) and (d): Two-dimensional Gaussian fits of the injected current according to equation 3.1. The white-dashed-dotted line marks the position of the one-dimensional cut that is shown together with the experimental values in (e) and (f).

only a few pixels. By performing successive scans with ever smaller area size and higher resolution it is attempted to localise single spots with a diameter below 1 μm in the field-of-view of the spatially-resolved current signal. The successive scans also facilitate to verify if a signal in the current map stays constant so that it

can be related to laser irradiation.

The localised current injection is successfully demonstrated in Fig. 3.8(a) and 3.8(b) for the TaO_x-junction and the AlO_x-junction, respectively, by performing the above given procedure. The field-of-view has been reduced to a few micrometer and the scan resolution is 100 nm. Both junctions reveal a significant current injection of about 250 pA which is restricted to a hot-spot region of ≤ 1 μm. In the case of the AlO_x-junction two hot-spots can be clearly resolved while they are separated by a distance less than 1 μm, close to the diffraction limit of the utilised light source. Outside this region the current signal has dropped below the noise floor which is about 6 pA in the case of AlO_x. The noise floor is comparable to earlier works (2 pA, [168]) in which a slightly higher barrier of 3.9 eV was used. It was verified that the injected current is related to laser irradiation through the observation of a constant lock-in phase signal.

So far, current injection was discussed based on a nanoparticle-assisted process. Still a proof is required for this scenario since field enhancement can also occur at random defects [89]. This is done by taking SEM images of the two specimens after the experiments. Indeed it turned out that efficient local current injection was supported by individual deposited nanoparticles. The corresponding SEM images are shown as insets in Fig. 3.8(a) and (b). Identifying one nanoparticle out of 10^6 other particles seems to be a cumbersome endeavour. However, the task can be fulfilled by taking an overview map of the injection current and reflectivity, as well as several other images at different zoom stages, and by comparing this information with SEM images. Details of the procedure are presented in Appendix A.2 for both junctions. In these figures it can also be seen that many nanoparticles facilitate current injection so that the antennas of the present section do not exhibit a unique character with respect to functionality.

At the end of this subsection the injected current shown in Fig. 3.8(a) and (b) is fitted by using Gaussian peaks. The results are required for the evaluation in the next sections. More precisely, the fits will be used for estimating the laser spot size and for finding a scaling factor between the injected peak current and the spatially averaged current of the entire hot-spot. Fitting is accomplisched with a self-written MATLAB script that uses the nonlinear data-fitting algorithm `lsqcurvefit`. The fit function $GP_m(i,j)$ for m peaks is defined by

$$GP_m(i,j) = \text{offset} + \sum_m A_m \mathrm{e}^{-2\left(\frac{i-x_{i,m}}{\sigma_m}\right)^2} \mathrm{e}^{-2\left(\frac{j-x_{j,m}}{\sigma_m}\right)^2}, \tag{3.1}$$

in which i and j are pixel indices in both directions, A_m the peak current amplitude, $x_{i,m}$ and $x_{j,m}$ the peak coordinates in pixels, and $2\sigma_m$ the peak width at e^{-2}-level. The fits are presented in a two-dimensional representation in Fig. 3.8(c) and (d), and a one-dimensional cut (white dashed-dotted line in (c) and (d)) is shown in Fig. 3.8(e) and (f), respectively. Especially the injected current of the AlO_x-junction is reproduced very well and the peak width of the bright peak amounts to $2\sigma = 650$ nm.

3.2.4 Fluence-dependent current injection

The barrier heights, as well as the small hot-spot size of 650 nm, which is close to the optical diffraction limit, suggest that a non-linear process is involved in the charge separation. To identify the non-linear order of the process power law measurements are performed: The non-linear dependence of the injected current on incident pulse intensity determines the order of the associated multi-photon process when assuming that ballistic electrons dominate the charge transfer (see Fig. 3.2(a,b) and [89]).

Power law measurements have been performed at the sample positions that have already been presented in the previous subsection. In the case of the AlO_x-junction only the bright left spot has been evaluated because it also provides a significant current at low laser pulse intensity. For comparison the intensity dependent current strength is also detected without the nano-antennas at the edge of the active area where the top-electrode thickness gets thinner. In the latter scenario the injected current was averaged (current per pixel) over an area of 14 μm $\times$ 29 μm for the AlO_x-junction. The bare TaO_x-junction is represented by the device in Fig. 3.7 and the current is averaged over an area of 2 μm $\times$ 7 μm marked by the white dashed rectangle. The data that is associated with antenna-supported power laws is also marked by white-dashed rectangles in Fig. 3.8(a,b).

It has to be mentioned that in the case of nanoparticles the average current

(current per pixel) was initially determined. However, this is not an appropriate procedure for hot-spots since the resulting average current strongly depends on the size of the evaluated area. Therefore the averaged data is scaled so that the values represent peak currents. This procedure is valid since the spatially-resolved current in Fig. 3.8(a,b) belongs to the power law data sets and represents the results for highest pulse energies. Also note that in the following the injected current is given as a function of incident pulse energy U instead of power or intensity. This is valid as long as pulse duration and focus spot size remain constant.

The results are presented in Fig. 3.9 as double logarithmic plots so that the linear slope of data points gives an idea of the non-linear order N of the pulse energy dependence. However, the data itself is fitted with a power law. For the bare TaO_x-junction (black empty squares) the injected average current as a function of U gives a straight line which can be described by $N = 2.48 \pm 0.05$. This result indicates a mixture of two- and three-photon-induced processes. By considering the barrier height of 1.8 eV and a photon energy of 1.55 eV, whereupon lowest photon energies in laser spectrum amount to ≈ 1.24 eV, current injection is attributed to multi-photon-induced above-barrier injection of charge carriers. The results and interpretation are in good agreement with earlier studies which have been concerned with barrier heights of 1.8 eV and pulsed excitation spectrally centred at 1.55 eV [89]. It has to be noted that the retrieved value of N is for the most part independent of the evaluated area. Only at some positions at which highest currents are injected the non-linearity increases to $N = 2.8$.

In the case of the bare AlO_x-junction the power law measurement also shows a straight line in double logarithmic presentation. Compared to the AlO_x-junction the average current is slightly lower which may be attributed to the higher potential barrier. As a consequence the data points at low pulse energies deviate from the straight line since they are close to the detection limit of a few pA. The power law fit of the data gives a non-linearity of $N = 2.70 \pm 0.09$. This result indicates a mixture of two- and three-photon-induced processes with a dominating three-photon contribution. By considering a barrier height of approximately 2.6 eV up to 3 eV the current injection process is once again attributed to multi-photon-induced above-barrier injection of charge carriers. Diesing and co-workers determined a non-linearity of ≈ 3 for a slightly higher 3.9 eV barrier by using 1.55 eV photons and hence the conclusions presented here are reliable [88].

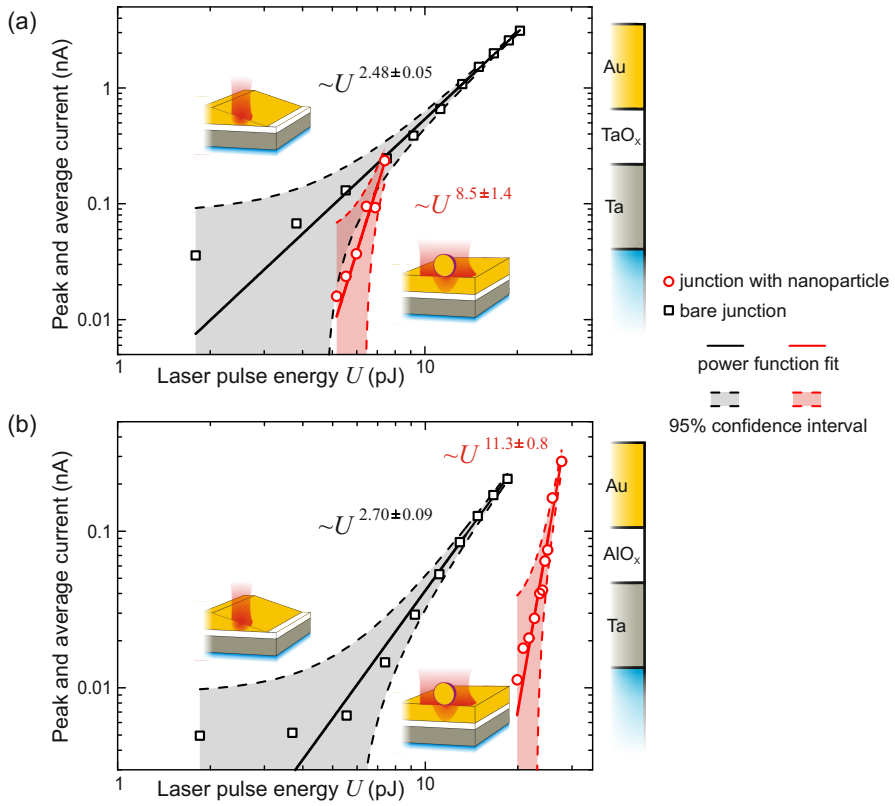

Fig. 3.9: Local dependence of the injected current on incident laser pulse energy for MIM junctions with and without antennas. (a) Using TaO_x: Black empty symbols represent the injected average current (SEN: 10 nA, TC: 50 ms, trigger: 73 Hz) of the bare MIM junction evaluated in the white-dashed rectangle shown in Fig. 3.7. The injected peak current (SEN: 10 nA, TC: 50 ms, trigger: 143 Hz) at the nanoparticle encased by the white-dashed rectangle in Fig. 3.8(a) is represented by red empty circles. (b) Using AlO_x: Black empty symbols represent the injected average current (SEN: 10 nA, TC: 100 ms, trigger: 143 Hz) of the bare junction, while red empty circles represent the injected peak current (SEN: 1 nA, TC: 100 ms, trigger: 143 Hz) at the nanoparticle encased by the white-dashed rectangle in Fig. 3.8(b) on the same junction. Average current: The current is added up in the evaluation region and divided by the number of pixels. Peak current: The average current is evaluated in the specific region and translated to a peak current by multiplying with a constant factor retrieved from the fit in equation 3.1. Data and fits (red and black lines) are shown without offset.

In contrast to the bare junctions the antenna-assisted current injection shows a strikingly different behaviour: While both power law measurements (red empty circles) follow a straight line in the double logarithmic presentation of the pulse

energy dependence, the steepness of the slopes greatly exceed that of the bare junctions. More precisely, the power law measurement of the TaO_x-junction can be fitted with $N = 8.5 \pm 1.4$ and the data of the AlO_x-junction is described by an even higher value of $N = 11.3 \pm 0.8$. Note that the incident laser pulse energy is restricted to a small interval due to this highly non-linear behaviour of the system.

Such an extreme non-linear pulse energy dependence has recently been reported in the context of light concentration in thin-film solar cells and it was explained by the model of thermionic emission [4]: The enhanced absorption of radiation in Anderson localised modes heated the electron gas in the absorber layer so that electrons with an energy higher than the material work function can be ejected and detected. Thermionic emission is the dominating process in this special case because the highly localised modes ($\approx 1\ \mu$m) correspond to an increased energy absorption density and they exhibit life-times of 100 fs. Hence, they temporally overlap with thermalisation processes of the electron gas. However, here, the laser pulses are ultra-short and the electron distribution function exhibits a highly athermic character after excitation. As already mentioned in the introduction, Mueller and Rethefld demonstrated theoretically that thermalisation times of the electron gas can be as short as a few femtoseconds given that the absorbed laser fluence is sufficiently large [220]. By assessing the antenna-assisted absorption in the top-electrode via FDTD simulations, it is shown in the next section that the regime of instantaneous thermalisation can be reached and that thermionic emission is responsible for the observed experimental results.

Alternative explanations appear to be unlikely: Multi-photon-induced current injection would imply that the successive or simultaneous absorption of 8 up to 11 photons is the dominating excitation channel. In this case the electrons would be excited by more than 14 eV in energy which is enough to overcome the work function of the involved materials. Furthermore, even in above threshold ionisation [95] the lowest orders of multi-photon absorption always dominate the overall signal. Even if the fields are very strong so that the first or second above-threshold channel can be closed due to a laser-induced AC stark shifts ([45], Chapter 15), the closing of three and more channels is unlikely to occur. Additionally, in the case of strong laser fields tunnel ionisation becomes an important process [157] and usually the non-linearity of the signal decreases due to saturation effects ([241], Chapter 8 in [136]).

At the end of this subsection it needs to be mentioned that particle-MIM systems are susceptible to laser-induced damage. Although the system is obviously stable on short time-scales during the spatially-resolved mapping of injection currents, as can be seen in Fig. 3.8(b), something gets damaged on the long run. This issue needs further investigation. However, the high non-linearities have been observed at different hot-spot locations and the retrieved values therefore seem to be reliable.

3.3 FDTD simulations

3.3.1 General simulation setup

In order to find evidence for the mechanism which is responsible for the highly non-linear nanoparticle-supported current injection in MIM junctions finite-difference time-domain (FDTD) simulations have been performed by utilising the commercial software package from LUMERICAL SOLUTIONS.

A sketch of the simulation setup and corresponding details are depicted in Fig. 3.10. Three axes with lengths of 4 μm in the lateral direction and 2 μm in the axial direction, perpendicular to the plane of the MIM junction, define the overall simulation volume. Perfectly matched layers (PMLs) truncate the computational region and prevent reflection of scattered waves at the volume boundaries. The nanoparticle is centred in lateral directions and has a spacing of $> 2\lambda_0$ to the corresponding PML boundaries and $> \lambda_0$ to the top PML boundary in order to reduce interaction with evanescent near-fields.

To keep things simple a particular and exemplary layer system was considered in the simulations. The MIM device is modelled by four flat layers, i.e. a 30 nm thick gold top-electrode (built-in data from Johnson and Christy), a 4 nm thick tantalum oxide layer (built-in data, Palik), a 40 nm tick tantalum back-electrode (built-in data, CRC handbook) and a 520 nm thick glass substrate (built-in data, Palik). The nanoparticle rests 1 nm above the top-electrode to inhibit electric interaction by direct contact. As mentioned earlier this is experimentally implemented by a citrate shell around the nanoparticle [298]. Actually, citrate shells might

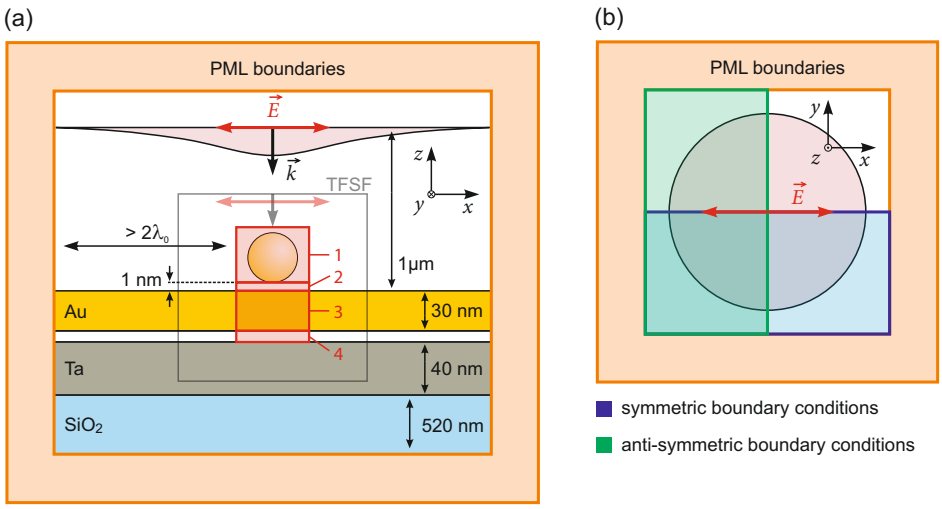

Fig. 3.10: Sketch of the general FDTD simulation setup and symmetry conditions for MIM junctions. (a) The size of the simulation volume is 5 μm $\times$ 5 μm $\times$ 1.7 μm ($x \times y \times z$). These proportions assure that near-fields originating from excitation of the nanoparticle do not interact with the perfect matched layer (PLM) boundaries. The red shaded areas depict a refinement of the simulation mesh. The following list gives the spatial extents of the meshes according to their numbering; Yee cell size follows in brackets: 1. 300 nm $\times$ 300 nm $\times$ 260 nm (0.8 nm in all directions), 2. 300 nm $\times$ 300 nm $\times$ 1.2 nm (0.8 nm $\times$ 0.8 nm $\times$ 0.2 nm), 3. 300 nm $\times$ 300 nm $\times$ 40 nm (0.8 nm $\times$ 0.8 nm $\times$ 1.5 nm), and 4. 300 nm $\times$ 300 nm $\times$ 4 nm (0.8 nm $\times$ 0.8 nm $\times$ 0.5 nm). A full vectorial Gaussian source with linear polarization **E** and injection direction **k** is positioned 1 μm above the top-electrode. Alternatively a total-field scattered-field (TFSF) source can be used (2.2 μm $\times$ 2.2 μm $\times$ 0.7 μm). (b) Non-scaled top-view: Since particle and sources are laterally centred symmetric boundary conditions are applied in the x-z-plane and anti-symmetric boundary conditions in the y-z-plane. According to this only two out of eight octants have to be evaluated during the simulation. The simulation time was set to 70 fs and the general accuracy of the graded mesh is about 22 sampling points for the centre wavelength in the respective material. The reddish circle is a sketch of the Gaussian beam source.

even exhibit a smaller thickness due to their molecular character. To properly render such gaps between top-electrode and nanoparticle would require a very small simulation mesh size. However, the FDTD method cannot accurately describe electromagnetic field dynamics on length scales smaller than 1 nm because quantum effects have to be considered [203]. Therefore the minimum gap size is here restricted to 1 nm.

The mesh of the FDTD simulation is non-uniform and adapts itself to Yee cell edge lengths of approximately $\lambda/22$, where λ is the effective wavelength in the corresponding material with respect to the refractive index. To achieve a higher

accuracy and more data points in other regions of the simulated domain meshes are inserted with smaller cell sizes. There are overall four refined meshes which enclose the nanoparticle, the gap between particle and top-electrode, the part of the top-electrode directly located below the particle and the 4 nm thick oxide, respectively. Specific mesh details and a sketch of their setup can be found in Fig. 3.10.

The illumination source is a full vectorial Gaussian beam launched 1 μm above the gold-vacuum interface, which also serves as the focus plane. The retrieved complex response function $\mathbf{R}(x,y,z,\nu)$ for all three components of the electric field is normalised to the input spectrum $E_0(\nu)$ in the injection plane (impulsive response mode). Multiplying $\mathbf{R}(x,y,z,\nu)$ with an arbitrary input spectrum and performing an inverse Fourier transformation then gives the temporal evolution of the injected electric field at any position of the simulation. Note once again that the input spectrum is defined in the injection plane and hence the corresponding temporal peak electric field increases until the beam has reached the focal plane. For subsequent FDTD simulations a laser pulse of 4 fs duration is injected at a centre frequency ν_0 of 400 THz (750 nm) to retrieve the response function $\mathbf{R}(x,y,z,\nu)$ in the range from 250 THz (1200 nm) to 500 THz (600 nm). This range is sufficient to cover the entire spectrum of the laser oscillator used in the previously described experiments.

The full vectorial character of the source implicates the existence of three different transverse modes which are attributed to different polarisation directions: parallel to the main polarisation axis (x-axis), perpendicular to the main polarisation axis parallel to the injection plane (y-axis) and along the axial direction and hence perpendicular to the injection plane (z-axis) (see Fig. 3.10 in [229]). The FDTD software uses a principle established by Richards and Wolf to generate the beam [257]: The field distribution in the injection plane emerges from a superposition of plane waves. The distinct wave vectors $\mathbf{k}$ are distributed according to rays that have been refracted by a thin lens (see Fig. 3.11). This concept is discussed in more detail in the next subsection in which the focus size is set.

In all subsequent FDTD simulations the computational region can be mirrored with respect to the included objects and hence symmetric boundary conditions are applied (Fig 3.10(b)). The polarisation direction of the source requires symmetric boundary conditions for the x-z-plane and anti-symmetric boundary conditions

for the y-z-plane. Applying the conditions reduces the computational region from eight to two octants which results in a four times shorter evaluation duration.

3.3.2 Considerations about the beam size

In the best case scenario the spot size in the focus is directly characterised during the experiments. The nano-localised current injection is promising to retrieve an estimate of the focus size since the laser is scanned over an object that is smaller than the optical diffraction limit and the measured signal reveals a spot like shape (see Fig. 3.8). Here, the Gaussian fit of the spatial current profile of the AlO_x-junction is utilised (see Fig. 3.8(c,f)) to calculate the beam waist because the current profile is more symmetric than that of the TaO_x-junction. The fit of the profile revealed a e^{-2}-diameter of about 650 nm. It is important to note that the profile is connected to a non-linear injection process with $N \approx 11$ and hence the Gaussian profile should not be confused with the focal spot of the laser. The actual beam waist w_0 is larger which can be seen by expressing the measured signal in terms of the electric field intensity in cylindrical coordinates: $\left[\exp(-2 \cdot r^2/w_0^2)\right]^{11}$, in which r is the radius. The term can be rewritten to regain its common shape: $\exp(-2 \cdot r^2/(w_0/\sqrt{11})^2)$. Hence the current profile is a factor of $\sqrt{11}$ smaller than the beam waist so that the e^{-2}-diameter of the laser amounts to $\sqrt{11} \cdot 0.65\ \mu$m $\approx 2.16\ \mu$m.

Since the CO exhibits a high numerical aperture (NA = 0.65) it is expected to perform better and the previously retrieved value for the beam waist w_0 is taken as an upper limit. The lower limit is estimated by applying the Richards-Wolf (RW) method to the actual geometry of CO, i.e. the focus size of the CO is calculated by a superposition of plane waves (Fig. 3.11). The required geometrical and optical parameters were kindly provided by the manufacturer DAVIN OPTRONICS in the form of a CAD drawing and a ZEEMAX file. Important parameters are the the obscuration radius o, the aperture radius R and the effective focal length f. The implementation of the CO geometry is sketched in Fig. 3.11(b) and the field $\mathbf{E}_{focal}(\mathbf{r})$ in the the focus is obtained by a superposition of plane waves with wave vectors $\mathbf{k}(\theta, \phi)$ pointing towards the origin of the coordinate system in the centre

of the focus [280]:

$$\mathbf{E}_{focal}(\mathbf{r}) = \int_{\theta_{min}}^{\theta_{max}} \int_{0}^{2\pi} u(\theta)\sqrt{\cos\theta}\sin\theta\ \mathbf{p}(\theta,\phi)\mathrm{e}^{\mathbf{ikr}}\mathrm{d}\phi\mathrm{d}\theta, \tag{3.2}$$

in which the unit vector $\mathbf{p}(\theta,\phi)$ translates the x-polarised plane wave components into the focal region according to

$$\mathbf{p}(\theta,\phi) = \begin{pmatrix} (\cos\theta - 1)\sin^2\theta - \cos\theta \\ (\cos\theta - 1)\cos\phi\sin\phi \\ \sin\theta\cos\phi \end{pmatrix}. \tag{3.3}$$

The above equation is evaluated for a single frequency, i.e. the centre frequency $\omega = 2\pi \cdot 375$ THz, similar to the method in FDTD. The scalar product $\mathbf{kr}$ is the projection of the respective wave vector $\mathbf{k}(\theta,\phi)$ onto the position vector $\mathbf{r}$ and consequently $\mathrm{e}^{\mathbf{ikr}}$ determines the phase of electric field corresponding to the plane wave $\mathbf{k}(\theta,\phi)$. To model the CO geometry the integral over the polar angle is evaluated in region between θ_{min} and θ_{max}. The angle $\theta_{min} = \arctan(o/f)$ is determined by the obscuration radius o and the angle $\theta_{max} = \arctan(R/f)$ is determined by the aperture radius R. The input mode profile is modelled according to a collimated beam with a transverse Gaussian profile $u(\theta) = \exp(-f^2\sin^2\theta/\sigma^2)$ in which σ is the e^{-1} beam radius.

The beam radius σ is the only free parameter in this calculation and it has been estimated by the transmission (37%) of the CO: In the RW model a mask was built so that $u(\theta)$ was integrated in the region $[\theta_{min}, \theta_{max}]$ and then compared to the value retrieved from full integration of $u(\theta)$ for different values of σ. A transmission around 37% was achieved for an input beam radius of $\sigma = 3.6$ mm. This is slightly larger than the estimated beam size in the experiments of about ≈ 2.8 mm (measured with a beam profiler camera). However, a comparison is cumbersome since the laser spot is asymmetric and hence $\sigma = 3.6$ mm is utilised in the calculation. The intensity profile of the focal spot for an input beam radius of $\sigma = 3.6$ mm is shown in Fig. 3.11(d). As expected the obscuration acts as a Fourier filter leading to a circular lobe. A cut trough the main peak was fitted with a Gaussian curve which revealed an effective e^{-2}-diameter of ≈ 1.21 μm. This value serves as a lower boundary for the focus size.

The minimum and maximum focal spot has been reproduced in the FDTD software package by using the thin lens mode and the resulting focal intensity

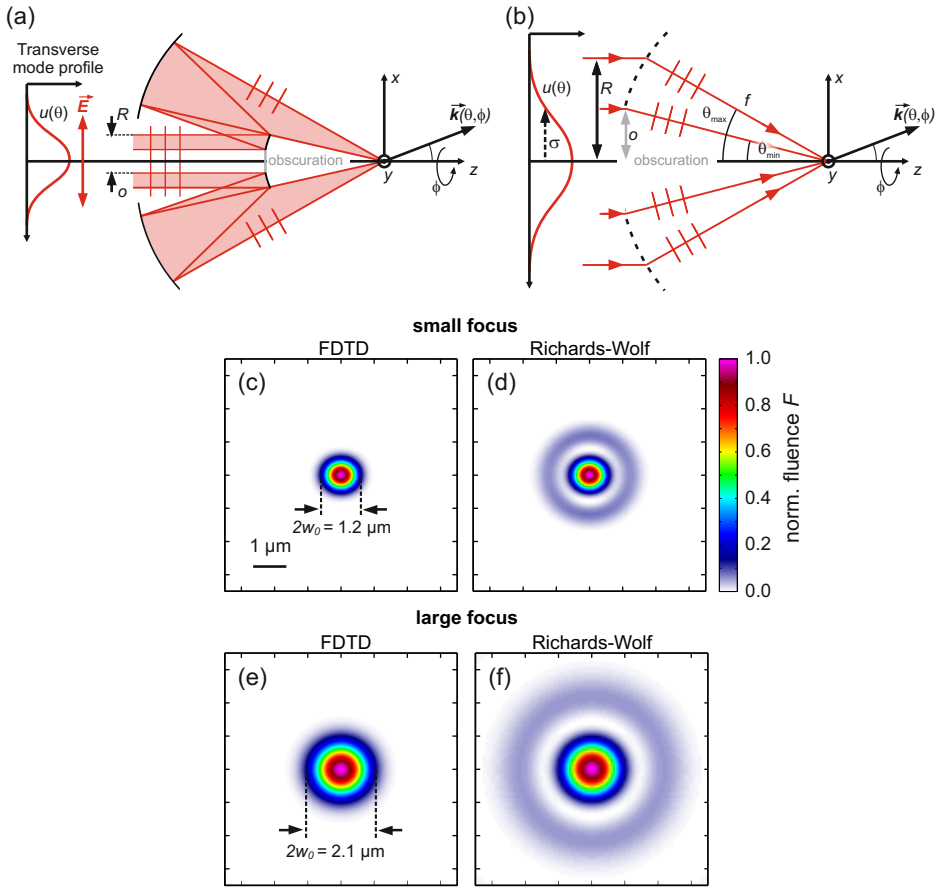

Fig. 3.11: Defining lower and upper bounds of laser spot size to compare simulations to experimental results. For realistic focal field distributions the CO is modelled according to the Richards-Wolf (RW) method. (a) Sketch of beam path in CO. R: aperture radius (2.259 mm). o: obscuration radius (0.8 mm). Effective focal length: $f = 3.55$ mm (not shown). Parameters are provided by DAVIN OPTRONICS. (b) Implementation of the RW-method: Calculating the electric field distribution in the focal plane by a superposition of plane waves with wave vector $\mathbf{k}(\theta, \phi)$. $u(\theta)$: Transverse beam profile with e^{-1}-radius σ. (c,d): Smallest focus size implemented in FDTD and with RW, respectively. The spot generated with the RW-method and $\sigma = 3.6$ mm takes into account the measured 37% CO transmission. The obscuration of the CO leads to diffraction rings, but central peaks of FDTD and RW are similar. (e,f): Largest spot size retrieved from the measured spatial profile of injected current (Fig. 3.8(f)), taking into account the non-linear character of the signal ($2w_0 = 2.1$ μm). Deviating parameters to artificially enlarge RW-generated spot: $\sigma = 1.2$ mm, $f = 5.6$ mm, $R = 2.259$ mm. (c-f): The peak fluence can be adjusted so that spatial integration of the spot gives the laser pulse energy.

profiles are depicted in Fig. 3.11(c) and (e), respectively. To keep the evaluation as short as possible only the small focus was used in FDTD simulation of the MIM structure. Although this approach is one-sided with respect to laser peak fluence it is justified by considering that the actual absorption cannot be reliably retrieved since many factors contribute to this quantity, e.g. surface roughness, specific particle size and shape, local top-electrode thickness and the gap size between nanoparticle and top-electrode. Here, the overall absorption in the top-electrode is the important information rather than the specific contribution of distinct factors

The large focal spot with $2w_0 \approx 2.1\ \mu$m, as retrieved from the experiments, was also modelled with the RW method and it is depicted in Fig. 3.11(f). The utilised calculation parameters (see figure caption for details) lead to a central peak which exhibits a e^{-2}-diameter of $\approx 2.1\ \mu$m. This diameter value matches the Gaussian fit of the current injection profile in Fig 3.8(d,f) when the non-linear character of the injection process is considered. The large and the small focus in Fig. 3.11(f) and (d) then serve as the lower and upper limits of the incident peak fluence in the experiments, respectively. This will allow to compare the measured power laws in Fig. 3.9 to simulated curves of a thermionic emission model in Section 3.4.2.

3.3.3 Resonances in the particle-MIM system

Before investigating on the current injection mechanism the composed system of nanoparticle and MIM junction is characterised with respect to its optical properties. The absorption and scattering cross-sections of different regions of the combined system are shown in Fig. 3.12(a). Results have been obtained by using the total-field scattered-field (TFSF) source which injects a plane wave in a defined region. Using plane waves for this endeavour is the only valid option with respect to the definition of a cross-section.

The scattering cross-section of the isolated 200 nm Au nanoparticle is represented by the black solid line. It exhibits a scattering resonance at 485 THz (625 nm) with a peak cross-section of about 1.33×10^{-9} cm^{-2}, which is four times larger than the geometrical cross-section (3.14×10^{-10} cm^{-2}). This is in good agreement with Mie theory, hence indicating converged results. Bringing

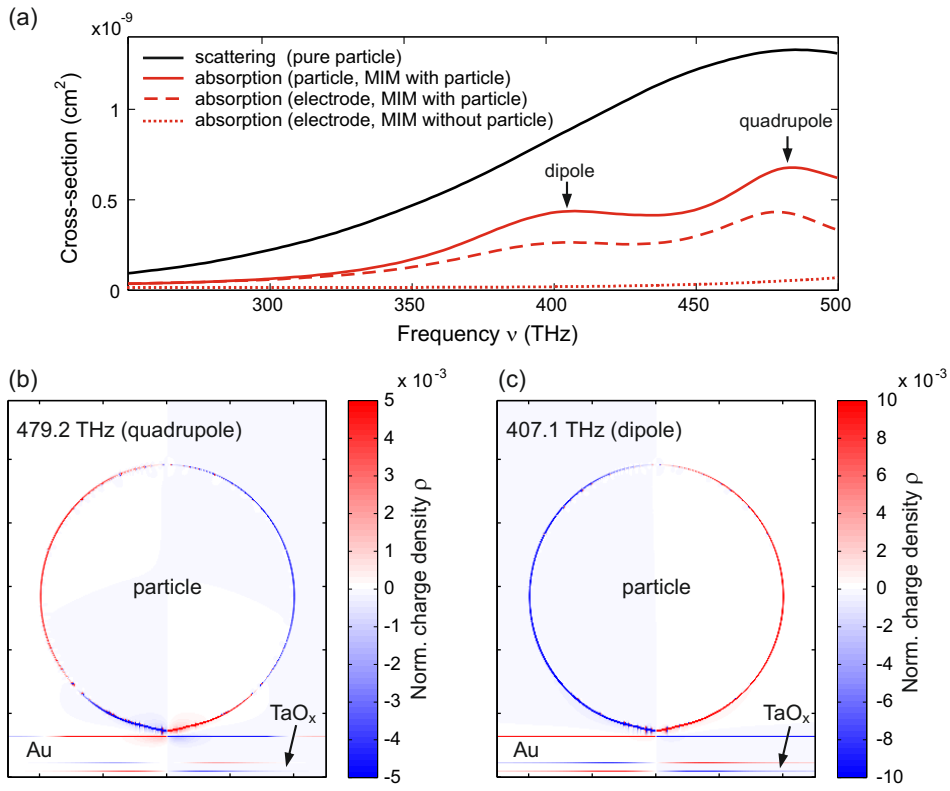

Fig. 3.12: Identification of plasmonic resonances in the combined particle-MIM system by using plane wave excitation under normal incidence. Only TFSF sources are used. (a) Comparison of different cross-sections σ. Pure particle (black solid line): σ_{scatt} is calculated by integrating the Poynting flow through a transmission box encasing a TFSF source and the nano-particle, without the MIM structure. The transmitted power is normalised to incoming intensity to retrieve σ_{scatt}. Particle on MIM junction (red solid line): A 3D-field and index monitor surrounds the particle and σ_{abs} is calculated with a built-in script according to the method related to equation (4.5). Absorption cross-section σ_{abs} of a volume identical to the refined mesh 3 in Fig. 3.10(a), underneath the nano-particle: with (red-dashed line) and without (red-dotted line) nano-particle. Data is retrieved with 3D-field and index monitors according to equation (4.5). (b,c): Electric charge densities retrieved with a built-in script and 3D-field and index monitors according to the law of Gauss in (3.4). The relative phase of the time-harmonic problem is chosen to maximise the amount of accumulated surface charge and to emphasize the character of the resonant modes. Blue: negative charge. Red: positive charge.

the nanoparticle close to the surface is expected to alter its resonant properties. Even in the case of dielectric substrates symmetry breaking lifts the degeneracy of dipoles oscillating parallel and perpendicular to the substrate. This permittivity-

dependent energy splitting was experimentally observed by Knight and co-workers [164]. In the case of metallic substrates Nordlander and co-workers pointed out that the localised plasmon resonance (LSP) of the particles is additionally affected by induced image charges and, even more important, by coupling of the LSP to the surface plasmon of the substrate [225]. An experimental study of the gap size dependent properties can be found in the publication of Mock and co-workers [215]. It was also theoretically shown by Nordlander and co-workers that the spectral signature of these structures strongly depends on the thickness of the metallic film [185]. Furthermore, Sobhani and co-workers found experimentally that the substrate facilitates a coupling between adjacent dipolar and quadrupolar modes, leading to a line-narrowing of the dipolar mode [274]. This effect is prominent when radiative decay dominates the resonance line-width.

The absorption cross-section of the nanoparticle, which rests 1 nm above the MIM junction, is shown in Fig. 3.12(a) by the red solid line. Data has been retrieved as follows: The absorbed power density $p_{abs}(x,y,z,\nu)$ is evaluated at every mesh point of the particle by a built-in script according to equation (4.5). Integration over all space gives the overall absorbed power $P_{abs}(\nu)$. Then, $P_{abs}(\nu)$ is divided by the command `sourceintensity(`ν`)` in order to determine the frequency-dependent cross-section. The absorption cross-section reveals two distinct features at 407 THz (736 nm) and 481 THz (623 nm) with reduced amplitudes compared to the scattering efficiency of the isolated particle and close to the geometrical cross-section. These features are also observed in the absorption cross-section of the the top-electrode (red-dashed line). It has to be noted that the data stems from a monitor that coincides in size with the proportions of the refined mesh 3 in Fig. 3.10(a), hence it only covers the volume below the particle. The amplitude is smaller than that of the particle absorption cross-section but significantly higher than that of a bare MIM junction (red-dotted line). This indicates that the presence of the nanoparticle is expected to enhance light matter interaction irrespective of the specific mechanism.

To identify the nature of the two resonances requires a closer look at the respective distribution of surface charges in the particle-MIM system. The spatially-resolved charge density for the resonance at 479.2 THz is shown in Fig. 3.12(b) while the charge density for the resonance at 407.1 THz is shown in Fig. 3.12(c). A built-in script has been used to generate the data according to Gauss's law and

with respect to time-harmonic fields (impulsive response mode):

$$\nabla \mathbf{E}(x,y,z,\nu) = \frac{\rho(\nu)}{\varepsilon_0}. \tag{3.4}$$

Here, $\rho(\nu)$ is the complex-valued volume charge density. In the case of time-harmonic fields the induced distribution of surface charges also varies harmonically in time. For Fig. 3.12(b) and (c) the relative phase was set to maximise charge accumulation and to underline the mode character. The resonance at 407.1 THz clearly exhibits a dipolar character as can be seen by the positive (red) and negative (blue) charges accumulated on opposing sides of the particle surface. As a consequence charges are additionally induced at all interfaces of the system. The resonance at 479.2 THz shows four regions of opposite charges on the nanoparticle surface. Hence, the presence of the metallic substrate breaks symmetry and facilitates to excite a quadrupolar resonance of the particle which can be hardly excited in free space by impinging plane waves. A detailed investigation about coupling of the different modes in the spirit of [274] is omitted here. Just two important points are mentioned: The quadrupolar resonance is very sensitive to the separation of particle and top-electrode due to a tighter confinement of charges near the top-electrode. By lifting the nano-particle 10 nm above the top-electrode the resonance position of this mode crucially shifts (see Fig. 3.13(b)). In contrast to that the dipolar mode appears to be unaffected in resonance energy when lifting the particle by 10 nm. This is explained by the rather large size of the nanoparticle in comapirson to gap size and, additionally, by less concentrated charges on the particle surface.

This information might be useful for future design of the system. Here, it is highlighted that the following investigation is performed at a centre frequency of 375 THz which is located at the slope of the dipolar resonance.

3.3.4 Calculation of the absorbed energy density

In this section the absorption is quantified by calculating the absorbed energy density ε_{abs} below the nanoparticle in the top-electrode. Similar to the results in the previous Section 3.3.3 the evaluation region is restricted to volume of the

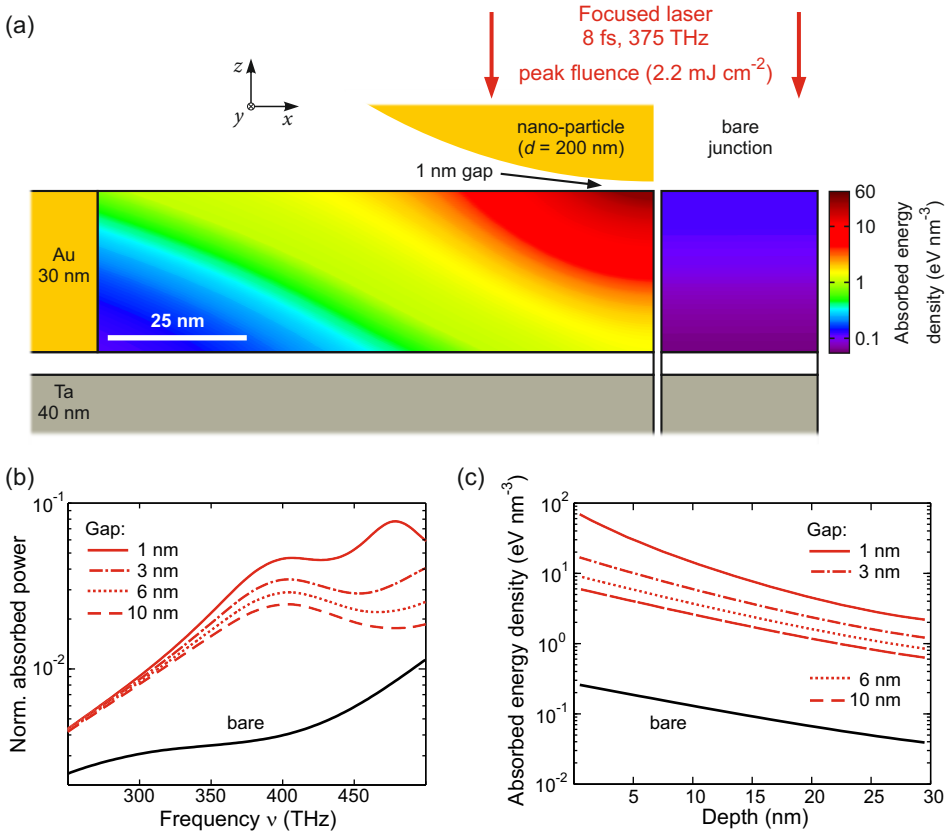

Fig. 3.13: Calculation of the spatially-resolved absorbed energy density $\varepsilon_{abs}(x,y,z)$ in the top-electrode of MIM junctions by using FDTD simulations. The excitation source is a Gaussian beam which corresponds to the focus spot shown in Fig. 3.11(c) and the oxide is modelled according to Al_2O_3. (a) Central cross-section through $\varepsilon_{abs}(x,y,z)$ with and without the nanoparticle on top of the MIM junction. Clearly, the nanoparticle acts as a lens and concentrates the electromagnetic energy in a nano-scale volume. $\varepsilon_{abs}(x,y,z)$ is calculated according to the derived equation in (3.5) and by using the data of a 3D-field monitor. Laser parameters are given in the figure and the imaginary part of the dielectric function was set to $\mathrm{Im}[\varepsilon_r(x,y,z,\nu_0)] = 1.44$, which corresponds to Au at 375 THz. (b) Gap-dependent absorbed power in the same monitor as used in (a), normalised to the incoming power of the Gaussian beam. The calculation is performed with a built-in script and the data refers to cw-excitation. (c) $\varepsilon_{abs}(z)$ directly underneath the lateral centre of the nanoparticle ($x = y = 0$ nm). $z = 0$ nm (0 nm depth): Au-vacuum interface. $z =$ -30 nm (30 nm depth): Au-oxide interface.

refined mesh 3 in Fig. 3.10(a). The excitation source in the FDTD simulation is a full vectorial Gaussian beam which exhibits the focus profile shown in Fig.

3.11(c). The absorbed energy density $\varepsilon_{abs}(x,y,z)$ is calculated according to the derivation in Appendix A.3:

$$\varepsilon_{abs}(x,y,z) = \int_0^\infty \frac{2\pi\nu_0\varepsilon_0 \,\mathrm{Im}(\varepsilon_r(x,y,z,\nu_0))}{\pi} \left|\mathbf{R}(x,y,z,\nu)\cdot E^{(+)}(\nu)\right|^2 \mathrm{d}\nu \qquad (3.5)$$

The equation is similar to (4.5) but it additionally accounts for calculating the absorbed energy density upon pulsed excitation. Here, $E^{(+)}(\nu)$ is the spectral amplitude of an 8 fs laser pulse at positive frequencies, centred around $\nu_0 = 375$ THz (800 nm). Considering the transverse beam profile in the injection plane and setting the incident pulse energy to typical experimental values of 12.5 pJ (1 mW average power at 80 MHz repetition rate) leads to a peak electric field of 1.2×10^9 V m^{-1} in the injection plane and to a peak fluence in the focal plane of 2.2 mJ cm^{-2}. The exact form of equation (3.5) corresponds to the the form of the Fourier transformation defined in Appendix A.3 and it also accounts for the associated specific formulation of Parseval's theorem, i.e. energy conservation in time- and frequency-domain. One should bear in mind that equation (3.5) is an approximation and it is only valid when the temporal envelope of the laser pulse is a slowly varying function of time. More precisely, it varies slowly relative to both, the inverse of the centre frequency ν_0 and the inverse of the frequency range over which the dielectric function $\varepsilon(\nu)$ changes appreciably. The important step in the derivation is the Taylor expansion of $\nu\varepsilon(\nu)$ with respect to ν in which all terms of second and higher order are neglected. Fortunately, $\varepsilon(\nu)$ varies in a linear fashion around $\nu = 375$ THz, far away from interband transitions, so that the approximation is valid in the present case (see Fig. A.1).

By using the imaginary part of the relative permittivity of gold at 375 THz, i.e. $\varepsilon_r(375\ \mathrm{THz}) = 1.44$ (see Fig. A.1), the absorbed energy density ε_{abs} is calculated by using the above given parameters via a self-written MATLAB script and the results are shown in Fig. 3.13. A cross-section through the centre of the combined system and the bare junction is presented in Fig. 3.13(a). In the case of the nanoparticle assisted current injection the absorbed energy density is highly concentrated underneath the particle. Peak values amount to 65 eV nm^{-3} and fall of by one and a half orders of magnitude in lateral direction (note the logarithmic colour scale). In the case of the bare MIM junction the absorbed energy density is much smaller and shows no spatial features due to the relatively large laser spot.

Peak values amount to 0.26 eV nm^{-3}. At the metal-oxide interface ε_{abs} is one and a half orders of magnitude smaller than in the case of the nanoparticle on top of the electrode (see Fig. 3.5(c)). This underlines the statement that the nanoparticle acts as a lens which facilitates concentrating the energy in the top-electrode.

Integrating ε_{abs} over all spatial dimension gives the overall absorbed energy E_{abs} inside the monitor box. In the above example the absorbed energy amounts to $E_{abs} = 0.39$ pJ. Considering that the incoming pulse energy is set to 12.5 pJ leads to the conclusion that 3.1% of the incident energy are absorbed underneath the particle. Applying the same evaluation to the bare junction gives an energy absorption of 0.3% in the same volume. This behaviour is also seen in continuous wave simulations in which the same monitor was used to calculate the absorbed power density according to equation (4.5) with a built-in script: The frequency-resolved absorption normalised to incoming laser power is shown in Fig. 3.13(b) for different gap sizes. In the case of a 1 nm gap 3% up to 4% of power are absorbed around $\nu = 375$ THz. This corroborates the results of pulsed laser excitation and renders equation (3.5) as a good approximation.

With the information about the absorbed energy density it is possible to estimate whether an instantaneous thermalisation of the electron gas occurs according to the work of Mueller and Rethfeld [220]. In their theoretical investigation they assumed that the laser spot is much larger than the film thickness. Using this excitation condition they found that the thermalisation time τ_{therm} of gold is faster than 10 fs when the absorbed fluence is larger than 0.3 mJ cm^{-2}. The corresponding absorbed energy density can be looked up in Fig. 6(a) of their publication and it amounts to 25 eV nm^{-3}. By considering that the enhanced absorption is due to the excitation of surface plasmons, so that the electronic system behaves like a free electron gas, the required absorbed energy density for $\tau_{therm} < 10$ fs is further reduced to values around 10 eV nm^{-3} (see results for aluminium in [220]). Comparing these limits to the absorbed energy density retrieved from the FDTD simulation in Fig. 3.13(a) for moderate incident pulse energies of 12.5 pJ leads to the conclusion that the particle-MIM system indeed facilitates to prepare conditions in which the significant part of the excited electronic system is instantaneously thermalised.

3.4 Temporal dynamics of the electronic system modelled by heat diffusion

This section is dedicated to the presentation of a theoretical model based on thermionic emission and to compare its predictions, based on FDTD simulations, to the experimental results. Heat-diffusion simulations and calculations of injected currents via thermionic emission were performed by Felix Becker. Hence technical details about the utilised method will be kept short in this thesis.

3.4.1 Heat diffusion in the top-electrode

According to the results of Mueller and Rethfeld it is expected that the excited electron distribution is instantaneously thermalised in the present case and it can hence be described in the formalism of an electron gas in thermodynamic equilibrium. To convert deposited energy into a temperature the heat capacity of the electron gas is required and it is given by [124]:

$$C_{el} = \frac{\pi^2 k_B^2 n T_{el}}{2E_F}, \tag{3.6}$$

in which E_F is the Fermi-energy

$$E_F = \frac{\hbar^2}{2m_e}(3\pi^2 n)^{\frac{2}{3}}. \tag{3.7}$$

In the above equations k_B is the Boltzmann constant, m_e the electron mass, $\hbar$ the reduced Planck constant, n the electron density and T_{el} the temperature of the electronic system. By assuming that one electron per gold atom contributes to electric conduction and using the mass density of crystalline gold (19.32 g cm^{-3}) as well as the mass of a gold atom (3.271×10^{-22} g) the electronic heat capacity amounts to:

$$C_{el} = 62 T_{el} \ \frac{\mathrm{J}}{\mathrm{m^3 K}}, \tag{3.8}$$

which is close to the value used for thin Au films by Groeneveld and co-workers [124]. In the case of a thermalised system the deposited energy density is retrieved

by comparing the increase in energy at an elevated temperature T_{el} to room temperature:

$$\varepsilon_{abs} = \int_{300\,\mathrm{K}}^{T_{el}} 62T\,\mathrm{d}T = \frac{1}{2}62T_{el}^2 \ \frac{\mathrm{J}}{\mathrm{m^3K^2}} - 2.79\times10^6 \ \frac{\mathrm{J}}{\mathrm{m^3}}. \tag{3.9}$$

According to equation (3.9) deposited energies of 65 eV nm^{-3} in Fig. 3.13(a) correspond to electron gas temperatures of $T_{el} \approx 11500$ K, while lowest temperatures in this cross-section amount to $T_{el} \approx 450$ K. As a consequence steep heat gradients exist in the electronic system and the corresponding dynamics will be modelled in the so-called *two-temperature model* [19].

The thermionic emission model

The spatially-resolved temporal dynamics of the electronic temperature T_{el} and the lattice temperature T_{la} are modelled according to the following two coupled differential equations [19, 316]:

$$\begin{aligned} C_{el}\frac{\partial T_{el}}{\partial t} &= \nabla(K_e\nabla T_{el}) - g(T_{el}-T_{la}) \\ C_{la}\frac{\partial T_{la}}{\partial t} &= g(T_{el}-T_{la}), \end{aligned} \tag{3.10}$$

in which K_e is the thermal conductivity of the electron gas and g the coupling constant for energy exchange between the electrons and the lattice. The lattice is described by its temperature T_{la} and heat capacity C_{la}. A thermal conductivity of the lattice is ignored since the time-scales of heat-diffusion are large compared to electrons and the lattice only serves as an energy reservoir for the electronic system. An external source term, i.e. the laser pulse, is also ignored because the pulse-duration is below 10 fs and hence faster than typical time-scales of thermal processes (see Fig. 3.2).

To simplify the problem, the cylindrical symmetry of the structure is exploited and the equations in (3.10) are solved in cylindrical coordinates, therefore reducing the problem to two spatial dimensions (see inset of Fig. 3.14(b)). A finite-difference method is used with derivatives calculated in second order approximation and by implementing reflective boundary conditions. The cylinder

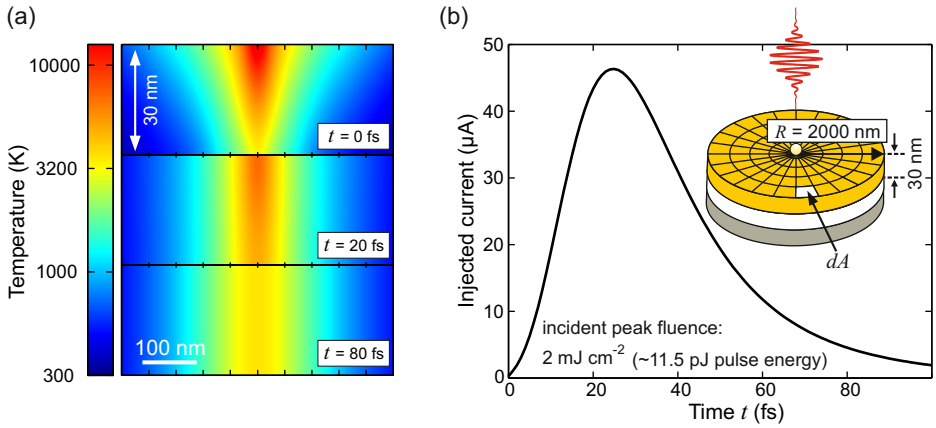

Fig. 3.14: Thermionic emission modelled with heat-diffusion of the electron gas according to the two-temperature model presented in equation (3.10) and by assuming instantaneous thermalisation. The initial values for the spatially-resolved electron gas temperature T_{el} are retrieved by converting the absorbed energy density $\varepsilon_{abs}(x,y,z)$ in Fig. 3.13(a) into a temperature via equation (3.9). Due to the linear character of the absorption process, $\varepsilon_{abs}(x,y,z)$ can be scaled with a simple factor to account for different incident peak fluences. Here: 2 mJ cm^{-2}, 11.5 pJ pulse energy. The coupling constant g was set to 2×10^{16} [316, 80, 81] and K_e is modelled according to standard Fermi gas theory [156]. (a) Snap-shots of T_{el} inside the top-electrode at different time instants. The problem is solved in cylindrical coordinates so that the lateral direction represents the radius and the vertical direction the depth inside the electrode. (c) Transient current calculated according to the Richardson-Dushman equation in (3.11). The required electron gas temperature refers to the respective unit cell at the metal-oxide interface and the current is retrieved by integrating $j \cdot dA$ over all surface elements dA.

radius was set to 2 μm so that the influence of the boundaries on the rest of the simulation volume is precluded. The initial distribution of T_{el} is that of Fig. 3.13(a) whereupon the energy-to-temperature conversion is performed using equation (3.9). Note that the FDTD monitor data is restricted to a radius of 150 nm, therefore the slope of the cross-section data in Fig. 3.13(a) is fitted with an exponential decay and extrapolated to the full radius of 2 μm.

The current injected into the back-electrode is calculated according to the thermionic emission model by using the Richardson-Dushman equation [167]:

$$j = A \cdot T_{el}^2 \mathrm{e}^{-\frac{E_B}{k_B T_{el}}}, \tag{3.11}$$

where j is the thermionic current density (A m^{-2}) and T_{el} the temperature of the electron gas inside the volume element directly in front of the metal-oxide

interface. The barrier height at the interface is represented by E_B and A is the Richardson constant in units of A m^{-2} K^{-2}. Usually, the Richardson constant A depends on the effective charge carrier mass in the oxide. However, Knight and co-workers experimentally found an effective Richardson constant $A_{eff} = 1.1 \times 10^6$ A m^{-2} K^{-2} at a nano-structured Au-Si Schottky-interface, which is close to the value of the universal constant $A_0 = 1.2 \times 10^6$ A m^{-2} K^{-2} [163]. Since A is just a multiplicative factor and since the most sensitive term in equation (3.11) is the exponential function it is assumed that $A = A_0$.

Transient currents

The overall injected transient current is finally calculated by adding up all partial contributions $j \cdot \mathrm{d}A$ of the distinct volume elements. An example of the above formalism is shown in Fig. 3.14. Here, the parameters are similar to the FDTD simulations shown in Fig. 3.13, i.e. AlO_x is used as the oxide ($E_B = 3.0$ eV) and the incoming laser pulse contains an energy of 11.5 pJ ($\approx$ 1mW at 80 MHz repetition rate). The radial- and depth-dependent distribution of T_{el} underneath the nanoparticle is presented in Fig. 3.14(a) for different time instants. The initial distribution simply reflects ε_{abs} as retrieved from FDTD simulations, converted to an electron gas temperature via equation (3.9). The diffusion is quiet fast due to the large gradients of the initial distribution so that after 80 fs the temperature is appreciably lowered and appears to be constant in axial direction. It has to be noted that in lateral direction the size of volume elements increases with radius so that an alteration in this direction is less pronounced for larger radii. At an intermediate time of 20 fs significantly high temperatures have reached the metal-oxide interface and it is expected that current injection is most efficient at this point of temporal evolution.

The transient injected current is shown in Fig. 3.14(b). As predicted by the distribution of T_{el} current injection is most efficient about 20 fs after the excitation. After reaching its maximum the signal declines with a time constant of approximately 40 fs (e^{-2}-decay of signal). The ultra-short time-scale is the result of a strongly localised deposition of energy which leads to fast and laterally non-restricted heat diffusion. Fast diffusion lowers the temperature at the metal oxide interface on very short time-scales so that the number of electrons energet-

ically lifted above the potential barrier is significantly lowered. The time-scales reported here are much faster than those usually encountered in thermal processes, e.g. thermalisation itself. Furthermore, the current injection seems to be nano-localised: The signal has declined after 80 fs and the spatial distribution of T_{el} is below 1000 K for radii larger than 200 nm so that an efficient current injection is only expected in the vicinity of the nanoparticle.

3.4.2 Comparison of the FDTD-supported thermionic emission model to experimental results

The current in Fig. 3.14(b) is given in SI units and it is hence possible to compare the injected current of the experiments to the thermionic emission model. In the experiments the lock-in amplifier measures a current that is averaged over 10^6 impinging laser pulses. In the simulations a comparable value can be retrieved by integrating the current pulse profile over time which gives the number of electrons injected into the back-electrode for a single excitation pulse. Multiplying this quantity with the repetition rate of the laser then represents a measurable current.

In order to allow a good comparison, injected currents should be simulated for a broad range of laser pulse energies and it is appropriate to compare the results to the experimental power law measurements in Fig 3.9. Due to the linear character of the absorption process, no additional FDTD simulations are required: The absorbed energy density distribution for 12.5 pJ laser pulse energy in Fig. 3.13(a) can be scaled with a linear factor to account for other pulse energies. The subsequent heat diffusion simulations are then performed for both potential barriers, AlO_x and TaO_x. Thereby it is assumed that the difference in the respective dielectric function of both oxides has no significant influence on the spatial profile of the absorbed energy density in the top-electrode. Additionally, it is ignored that both junctions exhibit a slightly different top-electrode thickness.

Experimental and theoretical curves of pulse energy dependent current injection are presented in Fig. 3.15. In contrast to the experimental section the injected currents are given as a function of incident peak fluence. The peak fluence is the relevant quantity because the nano-antenna is much smaller than the laser

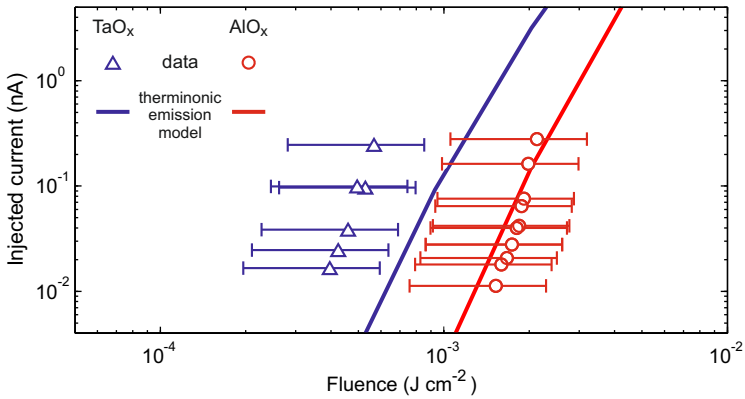

Fig. 3.15: Comparison of the FDTD-supported thermionic emission model to experimental results. The experimental data corresponds to the data shown in Fig. 3.9. Here, the measured laser pulse energy in converted into peak fluence by using the focus spot profiles which have been calculated with the RW method and are presented in Fig. 3.11(d) and (f). The peak fluence is a scaling factor of the normalised profiles and spatial integration gives the corresponding pulse energy. The error bars reflect the uncertainty of the excitation focus diameter. The upper and lower fluence values correspond to the lower and upper limit of the illumination focus diamter. Data points for the TaO_x-junction (blue empty triangles) and the AlO_x-junction (red empty circles) are placed in the centre of these extrema. Note that the error bars represent a systematic error. The respective theoretical curves (blue and red solid lines) are retrieved from the thermionic emission model. The initial distribution of the absorbed energy density (electron gas temperature) shown in Fig. 3.13(a) is multiplied with a scaling factor which is related to different pulse energies (peak fluences). The peak fluence at a given pulse energy is retrieved by integrating the scaled laser spot profile in Fig. 3.11(c). The theoretical curves are therefore related to the smaller excitation focus, i.e. the upper fluence bound. The simulated injected current current is calculated by integrating the transient current profile from the thermionic emission model and by multiplying the retrieved charge with the laser repetition rate. This procedure mimics the rather slow detection of a lock-in amplifier.

focus and the absorbed energy underneath the particle crucially depends on the electric field intensity in the vicinity of the particle. According to the discussion in Section 3.3.2 the size of the laser focus is not exactly known and hence the focus profiles calculated with the Richards-Wolf method presented in Fig. 3.11(d) and (f) are utilised as upper and lower boundaries for the peak fluence. These bounds indicate a systematic deviation. The peak fluence for the simulation data is calculated according to the FDTD injection profile in Fig. 3.11(c) (smaller focus size, upper fluence bound).

The experimental data of power law measurements are represented by blue empty triangles and red empty circles for the TaO_x-junction and the AlO_x-junction,

respectively. Upper and lower boundaries for the incident peak fluence are marked with error bars and the data points have been centred between these extrema. It is emphasised that the fluence uncertainty is a systematic error. The theoretical curves, as retrieved from FDTD simulations and the thermionic emission model, are represented by solid lines of associated colour. Strikingly, both curves can be found in the vicinity of the experimental data without further adjustments and both curves exhibit slopes that imply a non-linear behaviour similar to experiments. It is remarkable that despite the involved non-linearities the simulated injected current is on the same order of magnitude as indicated by the error margins.

However, a small quantitative deviation still remains which is especially apparent in the case of the TaO_x-junction. As mentioned before, the exact amount of absorbed energy, and hence the subsequent heat diffusion, crucially depends on many local factors like surface roughness, top-electrode thickness, the resonant behaviour of nanoparticles or the gap size, just to name a few. Furthermore, the equation for retrieving the absorbed energy density from FDTD simulations is only an approximation and hence errors are expected. It is also interesting to note that the simulation results of the TaO_x-junction reproduce the experimental data when artificially increasing the absorption in the top-electrode from 3% to 5%, i.e. multiplying $\varepsilon_{abs}(x,y,z)$ with a higher factor for the same incident peak fluence, which seems to be a realistic deviation. Taking into account all of the above factors, it is concluded that the thermionic emission is the dominating mechanism for current injection in the present excitation scheme.

3.4.3 Ultra-fast current injection in the thermionic regime

At the end of this chapter a brief comment is given on the temporal duration of thermionic current injection. The simulated transient current of four different peak fluences is shown in Fig. 3.16. The fluence values cover the range of AlO_x results in Fig. 3.15 and the barrier height corresponds to an AlO_x-junction. All four transient profiles have at least decayed within 200 fs and the temporal duration of the current pulses is further deceased with decreasing peak fluence. In order to give more quantitative information about the corresponding time-constants, all four

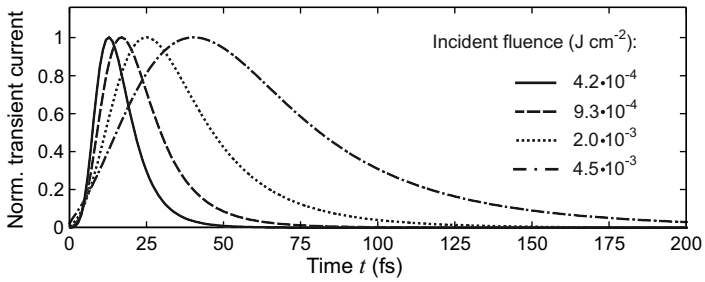

Fig. 3.16: Simulation of transient currents injected at different peak fluences. The temporal profiles are the basis for calculating the temporal averaged current in Fig. 3.15. The potential barrier corresponds to the AlO_x-junction, i.e. $E_B = 2.8$ eV.

profiles have been fitted with an exponential decay after reaching maximum signal strength. The e^{-2}-decay constants from lowest to highest incident fluence read 7 fs, 12 fs, 22 fs and 41 fs. Although an experimental demonstration of such ultrafast features is missing in the present study, the unambiguous identification of the injection mechanism and the consistency of the effect with respect to peak fluence suggests that ultra-short electron pulses have been generated in the experiments presented here.

It might be argued that a non-resonant multi-photon process, involving ultrashort laser pulses, also leads to a short temporal duration of injected currents. However, a dominating multi-photon process is only found for low pulse energies since otherwise the electron gas will be efficiently heated. In the experiments a transition from the multi-photon regime to the thermionic emission regime was not observed and it is hence expected that injected multi-photon currents are below the detection limit. In contrast, the nano-localised excitation and the subsequent heat diffusion help to maintain the ultra-short character of the external stimulus and provide the opportunity for strong peak currents. The important question that needs to be answered is how the dynamics of such an electron pulse evolves. Will it spread or is it tightly directed until it reaches the back-electrode surface for further application in the subject of hot-electron injection?

3.5 Summary and outlook

In this chapter laser-induced current injection in metal-insulator-metal junctions was demonstrated by utilising the plasmonic near-field enhancement of prearranged gold nanoparticles deposited on the top-electrode. The investigated nano-systems have been clearly identified among 10^6 other antennas by using the techniques of scanning internal photoemission microscopy [89] and scanning electron microscopy. Spatially resolved current injection was restricted to a region of 650 nm in diameter which is smaller than the focal laser spot size. Outside this region currents, declined below the detection limit.

It was found that the enhanced spatial resolution is related to a highly-nonlinear current injection mechanism. In the commonly accepted picture of multi-photon induced above barrier injection of charge carriers, the measured signal-to-pulse-intensity relation would suggest that an electron absorbs more than eight incident photons. This was found to be in stark contrast to both, measurements without nano-antennas and to previous experiments in which electrons overcome comparable potential barriers by the absorption of two or three photons [88, 89]. Strong-field effects have been ruled out since they tend to decrease the non-linearity of the signal-to-pulse-intensity relation [241].

In recent research, it was found that in the context to light localisation such unexpected high non-linearities can be explained by thermionic emission [4]. Hence, it was suggested that the nanoparticle on top of the MIM junction concentrates a large amount of energy in a nano-scale volume of the top-electrode. As a consequence the associated electron gas is efficiently heated so that electrons are injected into the back-electrode by internal thermionic emission. This model was verified by FDTD simulations which revealed that absorbed energy densities of > 50 eV nm^{-3} are achieved in the top-electrode by using moderate 12.5 pJ laser pulses (1 mW at 80 MHz repetition rate). Such energy densities correspond to electron gas temperatures of about 10^4 K.

Furthermore, it was found that the energy, deposited in a few femtoseconds, is high enough to reach a regime in which the electron gas thermalises on ultrafast time scales (< 10 fs). In this regime the non-equilibrium character of the excited electron distribution is elided and it directly transforms into an electron gas which is in thermal equilibrium [220]. The assumption of a nearly instantaneous

thermalisation allowed to use the spatially resolved absorbed energy density from FDTD to investigate on the dynamics of the excited electron gas by means of heat-diffusion simulations. The injected current in MIM junctions was calculated with internal thermionic emission at the metal-oxide interface and the measured data was reproduced without further adjustments.

These simulations also show that the injected transient current pulses are on the order of some ten femtoseconds which is much shorter than expected from thermal processes. Those ultra-fast time-scales were ascribed to the highly localised excitation volume provided by the nanoparticle. In contrast to many previous studies, lateral diffusion of excited charge carriers cannot be neglected in the present geometry due to the steep temperature gradients. The fast heat diffusion, in combination with the potential barrier, seems to facilitate ultra-fast and nano-localised current injection. Hence, the preparation of an instantaneously thermalised and highly localised hot electron distribution helps to maintain the ultra-short character of the external stimulus, even in the regime of intense energy deposition.

The research presented here about the plasmonic-enhanced generation of hot charge carriers in MIM junctions goes beyond the general trend of recent years to exploit linear phenomena in such systems for energy conversion. The rather low reported efficiency factors of these devices suggests to move further to more specialised applications in which high energetic electron pulses might be utilised for surface chemistry or in which the ultra-fast, and intense, character of the generated electron pulses is exploited. However, this will require further research about the spatial and temporal dynamics of the excited electron system in the the back-electrode or while crossing the oxide.

It might also be interesting for future research to bring the MIM junctions from the regime of population driven systems to the regime of field driven systems (see Fig. 3.4). FDTD simulations revealed that the nanoparticle facilitates to transfer the peak electric field strength of the incoming laser pulse to the oxide. Interestingly, this field is dominated by the component perpendicular to the interfaces. Typical field strengths of a focused sub-10 fs laser pulse of 1 V nm^{-1} will considerably alter the potential barrier of the system and hence offer the opportunity for all-optical coherent control of current injection on the nano-scale. Recently, it was shown by Schiffrin and co-workers that an intense few-cycle laser pulse can

switch an oxide from insulating behaviour to conducting behaviour on time-scales of 1 fs by inducing a level-crossing of valence and conduction bands [264]. Using nano-antennas and MIM junctions, like in the present study, might facilitate to bring these strong field phenomena for all-optical control to the nano-scale. First experiments on controlling the injected current by influencing the tunnel barrier with coherent light have already been reported [293]. However, the results presented here suggest that the common metal-insulator-metal junctions might not be the best choice for this endeavour due to thermal effects at high field intensities. This obstacle might be overcome by using transparent and conductive materials so that absorption is reduced and coherent effects are favoured.

Finally, it has to be said that all the new emerging questions and ideas render the results of this chapter as a fertile ground for future research in the field of optically controlled electronics on the nano-scale.

4 Surface-enhanced Raman scattering with dithiol-linked gold nanoparticles

This chapter is dedicated to nanoparticle dimers systems which act as a light harvesting complex for spectroscopic applications. Extreme light concentration, i.e. plasmon-induced field-enhancement inside the nanometre wide gap of two adjacent nanoparticles, is utilised to overcome the generally small cross-section of Raman scattering so that the unique spectroscopic information is transferred to the far-field with significant signal strength. In contrast to many other studies using similar approaches, here, as-prepared colloidal dispersions are utilised for Raman scattering experiments. In this scenario, the ensemble of nanoparticle aggregates is in exchange equilibrium with the Raman-active molecules in the solution and a desorption of molecules bound to the nano-particles is prevented. Thus, it is possible to reliably quantify the density of Raman-active molecules on the nanoparticle surface. The knowledge of this quantity is crucial when assessing the quality and signal enhancement factor of the device. Furthermore, a new Raman-active molecule is used in the experiments which provides a unique vibrational spectroscopic signature and it allows to form well-defined inter-particle gaps due to its rigid structure.

The exploitation of intense near-fields generated in plasmonic systems for boosting the signal strength of Raman scattering experiments is called *surface-enhanced Raman scattering*. At the beginning of this chapter a short introduction will be given into this research field. A detailed investigation of the device will follow afterwards.

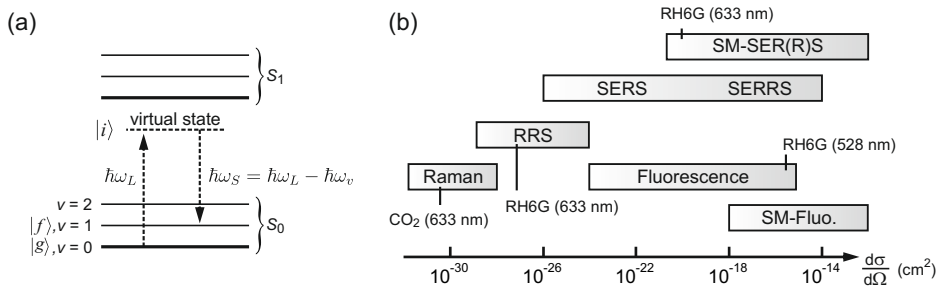

Fig. 4.1: Comparison of cross-sections of various spectroscopy techniques. (a) Simplified Jablonski diagram illustrating a non-resonant Raman scattering process. An incident laser photon of energy $\hbar\omega_L$ excites the molecule from its ground state $|g\rangle$ into a virtual intermediate state $|i\rangle$. The intermediate state instantaneously decays to the final state $|f\rangle$ which is an excited vibrational level (quantum number v) of the electron singlet state S_0. As a consequence the energy of the scattered photon $\hbar\omega_S$ is reduced by the energy required for the vibrational excitation $\hbar\omega_v$. (b) Required cross-sections for for different spectroscopic techniques, reproduced from [187]. Abbreviations: resonant Raman scattering (RSS), surface enhanced (resonant) Raman scattering(SER(R)S), and single molecule (SM).

4.1 Surface-enhanced Raman scattering - a short introduction

The inelastic scattering of light by molecular bonds, which is the basis of Raman scattering, provides highly specific information about organic and inorganic substances [182]. Since molecular vibrations depend on the molecular structure, a spectral fingerprint can be obtained that is unique to each molecule.

Raman scattering is in general a non-resonant process. In contrast to fluorescence spectroscopy, an electronic transition of the molecule is not required and hence the selection of excitation sources is not restricted to a narrow spectral region. Instead, infrared excitation can be used for investigating living tissues [189]. Furthermore, Raman scattering is attractive for applications in imaging and the characterisation of living cells and biomedical samples because it avoids the need for fluorescent labelling [313]. The excitation scheme is sketched in the Jablonski diagram shown in Fig. 4.1(a): An incident photon of energy $\hbar\omega_L$ excites the molecule from its initial ground state $|g\rangle$ (singlet state S_0, vibrational quantum number $v = 0$), to an intermediate virtual level $|i\rangle$. Due to the non-resonant character of the process, the intermediate state instantaneously decays via emission of a photon to the electronic ground state S_0. A vibrational mode of the molecule is excited when the final state $|f\rangle$ of the radiative process is e.g. the $v = 1$ state.

The emitted photon is then reduced in energy by the amount $\hbar\omega_v$ which is the energy required to excite the molecular vibration. The red-shift in this inelastic scattering process is called *Stokes-shift* and its particular strength, measured in units of cm^{-1}, depends on the dynamic of the excited molecular bond.

In contrast to the above discussion, it has to be mentioned that a non-resonant excitation process is not purely beneficial. A severe drawback is its low efficiency which can be inferred from quantum mechanical perturbation theory: The probability of the scattering process decreases with increasing detuning from a real transition ([195], Chapter 8.9). Consequently, inelastic Raman scattering exhibits a very low scattering cross-section of about 10^{-30} cm^{-1} (see Fig. 4.1(b)) and a high concentration of molecules is usually required for data acquisition. Sensing applications seem to be out of reach due to this restriction.

Surface enhanced Raman scattering with nano-particle dimers

This restriction was overcome since the first works of Jeanmaire and co-workers in 1977 [153]: They deposited molecules on a roughened metal surface and utilised the associated near-field enhancement of surface plasmons, i.e. the concentration of photons to a small volume, to compensate for the small scattering cross-section. Since then many substrates have been designed for tailoring electric field enhancement and surface-enhanced Raman scattering (SERS) evolved to a wide research field combining physics, chemistry and biology (see [283, 218, 188] for detailed reviews). Nowadays even the vibration of a single molecule has been observed with time-resolved methods and by exploiting the strong near-field enhancement in the nanometre-wide gap of two adjacent nanoparticles [323]. This particular SERS substrate is also subject of the research presented here. But before discussing the specific problems that will be addressed throughout the chapter, a short introduction will be given into the SERS mechanism by means of this particular substrate.

The excitation geometry is sketched in Fig. 4.2. An electric field of angular frequency ω_L and field strength E_0 excites charge oscillations in both nanoparticles. Due to the small distance of surface charges, these oscillations influence each other and both sub-systems get coupled. The adjacent nano-particles built a new, hybridised system which features its own resonant modes [244, 225]. The

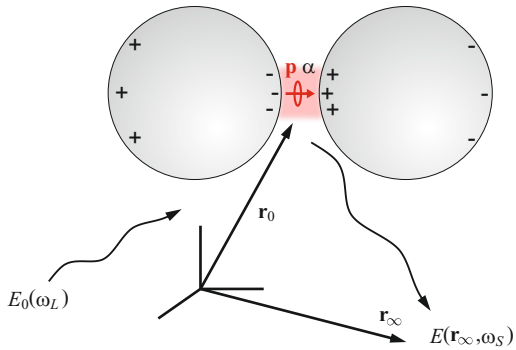

Fig. 4.2: Sketch of surface-enhanced Raman scattering with molecules inside the gap of a nanoparticle dimer structure: Incident light of photon energy $\hbar\omega_L$ and field strength E_0 excites the localised surface plasmon resonance of a hybridised nanoparticle system which leads to an enhanced electric field inside the gap (red-shaded area). Plus and minus signs represent positive and negative surface charges that are associated with the bright hybridised mode of the nanoparticle dimer. The molecular dipole **p** with its Raman polarisability α inelastically scatters the electric field back into far-field ($\mathbf{r}_\infty$). The scattered field strength of the molecular dipole E is also enhanced compared to free-space due to the presence of a metallic nanostructure.

charge distribution that allows coupling to the far-field is explicitly shown in Fig. 4.2: An elongated dipole is excited by the incoming electric field so that charges of different sign are accumulated at the respective outward surface of the particles. As a consequence of charge separation, surface charges of different sign are also accumulated in the gap region giving rise to strong field enhancement (red shaded area): A capacitor with nanometre spaced electrodes is formed. The resonance frequency of the combined system is shifted to lower frequencies with respect to the single particle resonance [225]. Due to its dipolar character, this mode is efficiently driven when the electric field polarization is parallel to the inter-particle axis and this mode is called a *plasmonic dimer resonance* for the rest of this chapter.

The enhancement of the electric field in the gap region is the first step in the SERS process. The intense local field interacts with a molecule inside the gap and induces a dipole moment **p** that is associated with Raman scattering. In the following the vector character of the dipole moment is ignored without loss of generality. The corresponding polarizability $\alpha(\omega_S, \omega_L)$ can be phenomenologically described in classical perturbation theory: The oscillator-like motion of the atoms introduces

a small perturbation to the electronic states of the molecule so that the molecular dipole also exhibits Stokes-shifted frequency components at $\omega_S = \omega_L - \omega_v$, in which ω_v is the frequency of the oscillating atoms ([187], Chapter 2.5). Due to the plasmonic dimer mode the Raman dipole p is driven by the field $f_1 E_0$ in which f_1 is the field enhancement factor with respect to the incoming field [229].

The second step in the SERS process is then the re-emission of radiation by this dipole. Radiation emitted by a dipole source into the far-field can be mathematically treated in Green's function formalism according to equation (2.5). It can be shown that the intensity in the far-field $I(\mathbf{r}_\infty, \omega_S)$ is then given by [229]:

$$I(\mathbf{r}_\infty, \omega_S) = \frac{\omega_S^4}{\varepsilon_0^2 c^4} \left| [1 + f_2(\omega_S)] G_0(\mathbf{r}_\infty, \mathbf{r}_0) \alpha(\omega_S, \omega_L) [1 + f_1(\omega_L)] \right|^2 I_0(\mathbf{r}_0, \omega_L). \tag{4.1}$$

Equation (4.1) is a purely scalar approximation and the Green's function for the scattered radiation G_S was expressed by $f_2(\omega_S) G_0$, in which f_2 is an enhancement factor and G_0 the free-space Green's function. A similar result is obtained by a full-tensorial treatment [229]. In the case of large enhancement ($f_1, f_2 \gg 1$) the Raman signal $I(\mathbf{r}_\infty, \omega_S)$ is enhanced by the factor

$$F = |f_1(\omega_L)|^2 |f_2(\omega_S)|^2 . \tag{4.2}$$

By using the optical reciprocity theorem ([179], §69) in a hand-waving fashion the Green's function related enhancement factor f_2 can be envisioned as the plasmonic dimer enhancement induced by E_0 at the Stokes-shifted frequency ω_S ([187], Chapter 4.3.5). Therefore, (4.2) can be rewritten as:

$$F = \frac{|E_{loc}(\omega_L)|^2 |E_{loc}(\omega_S)|^2}{|E_0(\omega_L)|^2 |E_0(\omega_S)|^2}, \tag{4.3}$$

in which the subscript *loc* denotes the local electric field at the position of the molecule. For a negligible Stokes-shift the famous E^4-law of SERS is obtained:

$$F = \frac{|E_{loc}(\omega_L)|^4}{|E_0(\omega_L)|^4}, \tag{4.4}$$

One should be deeply aware of the fact that the excitation and emission process are actually not separable due to the instantaneous character of non-resonant

Raman scattering.

At the end of this section it should be noted that excitation of intense near-fields is not the only mechanism that facilitates enhancement of signal strength in Raman scattering experiments. Any effect that directly modifies the Raman polarisability $\alpha(\omega_S, \omega_L)$ to give an enhanced signal strength is classified as *chemical enhancement*. Such modifications can occur when the molecule is linked to a surface and various schemes, e.g. charge transfer, are commonly discussed in literature ([187], Chapter 4.8). However, these effects are still a subject of debate [218]. Furthermore, typical enhancement factors are expected to lie in the range of 10^0-10^2. Interestingly, such factors have been recently reported in a combined theoretical and experimental approach of Valley and co-workers [300]. Nevertheless, these factors are several orders of magnitude smaller than those expected from the E^4-law [188] and hence they will be ignored throughout this chapter.

Aim of this chapter

To use the intense electric field enhancement in the gap of a nanoparticle dimer for Raman signal enhancement of nearby molecules was already suggested in 1981 by Aravind and co-workers [20]. Such structures can be easily produced by chemical synthesis and hence these SERS devices and colloidal solutions have gained a lot of interest [320, 288, 189, 76, 317, 234, 161]. The research presented here stands out from previous studies by the following features:

To the best of the authors knowledge this study determines for the first time the nanoparticle dimer induced plasmon-resonant Raman enhancement factor for an as-prepared dispersion of nano-particle aggregates, i.e. for an ensemble of aggregates that is in exchange equilibrium with the Raman reporter molecules in solution. Hence, the actual concentrations are known for both bound and unbound Raman reporter molecules. Knowledge of these quantities is essential to determine reliable enhancement factors from the comparison of measured Raman signals strengths [188]. Previous works which focused on nanoparticle dimers often used centrifugation with speed gradients and additional substances to sort out the desired aggregates for experiments in solution [317]. Or the aggregates are dried on a substrate so that they can be specifically addressed by an excitation source [288, 161]. Sometimes a combination of these methods is used [76, 234]. In all

of these approaches the number of bound Raman reporter molecules can hardly be estimated. In this context it will also be quantified for the first time how many molecules are bound to the nanoparticles when the final and non-fractionated dispersion is optimised for the production of nanoparticle dimers.

Another novelty of the presented research is the synthesised Raman molecule itself: Here, alkyne-rich acetyl protected dithiol molecules are used as both, thiol-supported active linkers between the gold nanoparticles and efficient Raman reporter molecules due to the four alkyne groups (C≡C bonds) (see Fig. 4.3(a)). Using alkyne bonds is interesting from several points of view: For instance, the Stokes-shifted signal of the C≡C bond is located in the so-called *Raman-silent region* (1800 cm^{-1} 2800 cm^{-1}) of acquired spectra [141]. The signature of e.g. solvents is found for shifts < 1800 cm^{-1} and hence the alkyne mode is unaffected by other features which makes the system interesting for live-cell imaging [141]. Moreover, the triple bonds form a rigid backbone and it will be interesting to see how this structure affects the linking process. In this context a second molecule was synthesised for reasons of comparison which also features the alkyne bonds but exhibits only one of the thiol groups (see Fig. 4.3(b)). Therefore, the choice of either an acetyl protected dithiol or an acetyl protected monothiol is expected to strongly influence the aggregation process and thus also the yield of nano-particle dimers.

A last key point is that Raman experiments are performed with a setup that allows to take spectra at various excitation frequencies. Using frequency-resolved UV-Vis extinction measurements for detecting plasmonic resonances then enables to relate these resonances to the signal strength of plasmon-enhanced Raman spectra. This is particularly interesting because it was recently reported that no correlation was observed between localised plasmon resonances of nanoparticle aggregates and the frequency-resolved SERS enhancement [161].

Finally, comparing the information of all sub-sections to the predictions of finite-difference time-domain simulations about resonance frequencies and expected SERS signal enhancement will allow to fully asses the functionality of the dithiol Raman reporter molecule. More precisely, the obtained results will imply that the fully-conjugated dithiol molecules act as a nano-scale tunnel junction. According to literature, a tunnel junction between the nanoparticles might be responsible for a red-shift of resonances and for decreasing electric field enhance-

ment [203].

Chapter outline

The presented research is the collaborative work of three different working groups at the University of Bielefeld. All contributions will be explicitly mentioned in the following chapter outline.

The synthesis and characterisation of colloidal solutions with either, acetyl-protected dithiol and monothiol, is presented in Section 4.2. Ingo Heesemann (Adelheid Godt's group, *Organic Chemistry and Polymer Chemistry*) performed the synthesis procedure. He was also responsible for both characterisation of the number of bound and unbound molecules with UV-Vis extinction measurements and the associated interpretation of the results about nanoparticle aggregation with alkyne-rich dithiol and monothiol linker molecules (see his dissertation [133]). Electron energy loss spectroscopy and energy-dispersive X-ray spectroscopy for visualising the large amount of bound Raman reporter molecules were conducted at the companies of JEOL and FEI, respectively, on behalf of Andreas Hütten (University of Bielefeld). Overview images of nano-particle aggregates recorded with transmission electron microscopy have been evaluated by the thesis author.

Section 4.3 is dedicated to the determination of absorption cross-sections of nanoparticle aggregates with finite-difference time-domain simulations. These simulations are required to estimate the number of nanoparticle dimers which contribute to UV-Vis extinction measurements. The quantity will be later used to estimate the number of bound molecules taking part in SERS so that reliable enhancement factors can be retrieved. Theoretically expected SERS enhancement factors will be estimated from the retrieved three-dimensional electric field response function. All simulations, as well as corresponding evaluations, have been performed by the thesis author.

Experiments about wavelength-resolved Raman scattering utilising six different excitation wavelengths across the visible spectrum will be presented in Section 4.4. The setup was built by Elina Oberländer (Thomas Huser's group, *Biomolecular Photonics*) who also performed the Raman scattering experiments. Furthermore she carried out the evaluation about SERS signal enhancement by using MATLAB code that was written by the thesis author.

UV-Vis extinction measurements of the colloidal dispersions are presented in Section 4.5 to support the interpretation of wavelength-resolved Raman scattering experiments. The extinction experiments were performed by Ingo Heesemann and Elina Oberländer.

Finally, in Section 4.6 SERS enhancement factors will be calculated by means of FDTD simulations and compared to experimentally retrieved values. For this endeavour, additional Raman scattering experiments were performed by the thesis author with a commercial setup, which provides a higher spectral resolution than the self-built one. The results are used to relate the Raman signal of a reference solution containing only the Raman reporter molecules to the Raman signal of the colloidal dispersions. The corresponding evaluation, which uses information of previous sections, is also performed by the thesis author.

A short summary and outlook can be found in Section 4.7.

4.2 Nanoparticle aggregation with acetyl protected thiol molecules

This section describes the preparation of colloidal dispersions as they were investigated with Raman spectroscopy and their characterisation with techniques like TEM or UV-Vis extinction. The entire preparation process, including the synthesis of the dithiol and monothiol Raman reporter molecules and the growth of gold nanoparticles, was solely conducted by Ingo Heesemann. For an elaborate description and discussion of all single steps the reader is referred to his dissertation [133]. Here, only the major steps, i.e. the growth of the gold nanoparticles and the subsequent reaction with acetyl protected thiols (Fig. 4.3) are sketched. Despite the sketchy character of the description specific information about concentration and the amount of substance is provided since some important estimations in this chapter are based on those values and assumptions. Furthermore, results will be presented in this section that originate from samples which have been synthesised in an analogous manner prior to the experiments reported here in order to support associated findings. Those previous results can also be found in [133].

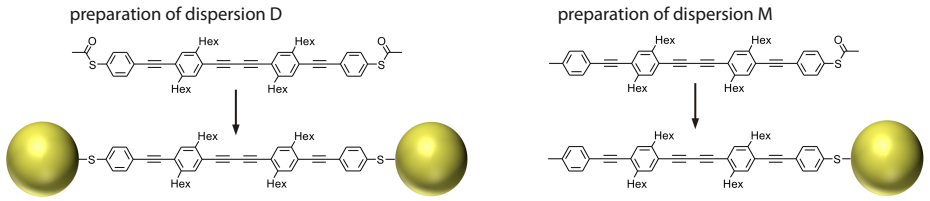

Fig. 4.3: Chemical concept of nanoparticle aggregation using either acetyl protected dithiol or acetyl protected monothiol. (a) In a simple picture the acetyl protected dithiol of dispersion D is intended for favoring the formation of nanoparticle dimers by linking the sulphur atoms at the respective molecular ends covalently to the gold surface (left panel). A missing sulphur atom in the monothiol counterpart is expected to negatively affect the formation of nanoparticle dimers in dispersion M (right panel).

4.2.1 Synthesis of the colloidal dispersions

The synthesis of colloidal dispersions in which aggregation is driven by dithiol linker molecules or its monothiol analogue is accomplished in three steps: preparation of the seed particle dispersion, growth of the particles to a requested size and inducing the reaction of these particles with acetyl protected thiols.

The preparation of a gold seed dispersion was run in air at room temperature according to the method provided by Grabar and co-workers [121]. The gold source is a solution of tetrachloroauric acid $HAuCl_4$ (10 mg, 25 μmol), which corresponds to 5 mg of gold. The seed particle concentration was estimated by considering a reported seed particle diameter of 2.6 nm [121] and assuming that the density of gold incorporated in these particles is equal to that of the bulk (19.32 g cm^{-3}). With an overall reaction volume of 103 mL a seed particle concentration of 2.7×10^{14} mL^{-1} is obtained. From this dispersion 50 μL, including 1.4×10^{13} seed particles, were removed for the growth of citrate stabilized Au nanoparticles according to the procedure published by Perrault and co-workers [237]. It is assumed that the distinct seed particles do not form aggregates during this growth process. The product was centrifuged to give a highly concentrated dispersion of 10 μL containing 5.7×10^{12} citrate stabilized Au nanoparticles. Note that the number of particles is an upper bound implying that no loss occurs due to pipetting or centrifugation itself.

In a last step the reaction of the highly concentrated Au nanoparticles with either acetyl protected dithiol (0.105 mg, 0.12 μmol) or acetyl protected monothiol

(0.105 mg, 0.13 μmol) is induced in 1 mL of acetone. During this process the acetyl moiety is cleaved off *in situ* and a covalent gold-sulphur bond is formed. [299]. For subsequent Raman experiments both colloidal dispersions of 1 mL were filled into 1.4 mL cuvettes. In order to avoid air bubbles during experiments the cuvettes were filled up with acetone to maximum volume. The cuvettes are closed so that the volatility of the solvent acetone is suppressed. Throughout the entire chapter the as-prepared colloidal dispersion obtained with dithiol molecules is labelled *dispersion D*, and the colloidal dispersion obtained with monothiol molecules is labelled *dispersion M*.

4.2.2 Characterisation of the colloidal dispersions

A particular aim of using rod-like dithiol molecules for linking nanoparticles in dispersion D is to foster the formation of nanoparticle dimers. Earlier experiments revealed that using an amount of 0.105 mg of dithiol molecules, as in the synthesis described above, gives a good yield of the desired structures [133]. It was also shown that increasing the amount of linker molecules does not increase the number of nanoparticle dimers compared to other types of aggregates, but results in large clusters of particles. Using a lower amount of dithiol molecules, i.e. 0.04 mg, leads to an increased ratio of nanoparticle monomers to dimers. Considering the excess supply of dithiols in all cases the conjecture arises that a multiplicity of dithiol molecules benefits the linking of Au nanoparticles. This contrasts with the idea that only a single molecule bridges the nanoparticles and thereby contributes solely to an enhanced Raman scattering signal. The assumption about a minimum number of dithiol molecules required for nanoparticle dimer formation is furthermore supported by the consideration that the colloidal dispersion should be susceptible to further aggregation if a single molecule alone is sufficient for stable linking.

Element specific EELS and EDX investigation of previous dispersions

To gain qualitative information about the actual surface coverage of nanoparticle aggregates with dithiol molecules element specific and spatial resolved techniques like electron energy loss spectroscopy (EELS) and energy-dispersive X-ray spectroscopy (EDX) incorporated in high resolution TEM devices were utilised. EDX measurements were conducted at the company of JEOL and EELS measurements were conducted at the company FEI on behalf of Andreas Hütten. Note that the examined sample is not the above mentioned dispersion D but it is synthesised in an analogue manner.

The spatially resolved EELS measurements of nanoparticle aggregates synthesised with acetyl protected dithiols are presented in Fig. 4.4(a-b). The TEM image shows an overview of the region which had been examined with regard to the presence of sulphur and oxygen (see Fig. 4.4(c)). The grey level shading in Fig. 4.4(a) and (b) reflects the local sulphur concentration in this region measured by the sulphur L-edge related EELS signal and the local oxygen concentration measured by the oxygen K-edge, respectively. Both element specific maps suggest a homogeneous distribution of the respective elements across the entire nanoparticle surface. The only source of sulphur in the synthesis described above is the acetyl protected dithiol molecule. An inferred homogeneous distribution of dithiol molecules on the nanoparticle surface corroborates the assumption that a multiplicity of these molecules is required to link adjacent particles. The presence of oxygen is attributed to the stabilising citrate cladding which is only partially removed while acetyl is cleaved off the dithiol and sulphur covalently binds to gold [133].

The detection of a significant amount of sulphur in the nanoparticle gap would suggest linking by acetyl protected dithiol molecules. Therefore EDX line scans on particular aggregates were performed. The evaluation of a nanoparticle dimer is shown in Fig. 4.4(d). A high resolution TEM (HR-TEM) image is presented in the upper right inset while the upper left inset depicts the region for the EDX line scan. The signal yield of the respective elements is accumulated in the direction perpendicular to the yellow bold dashed line whereupon the latter indicates the scan direction. The green line in the EDX scan is assigned to gold and shows two maxima with a width that matches the geometrical size of the nanoparticles. Inside the dimer gap the gold signal does not completely vanish. This is explained

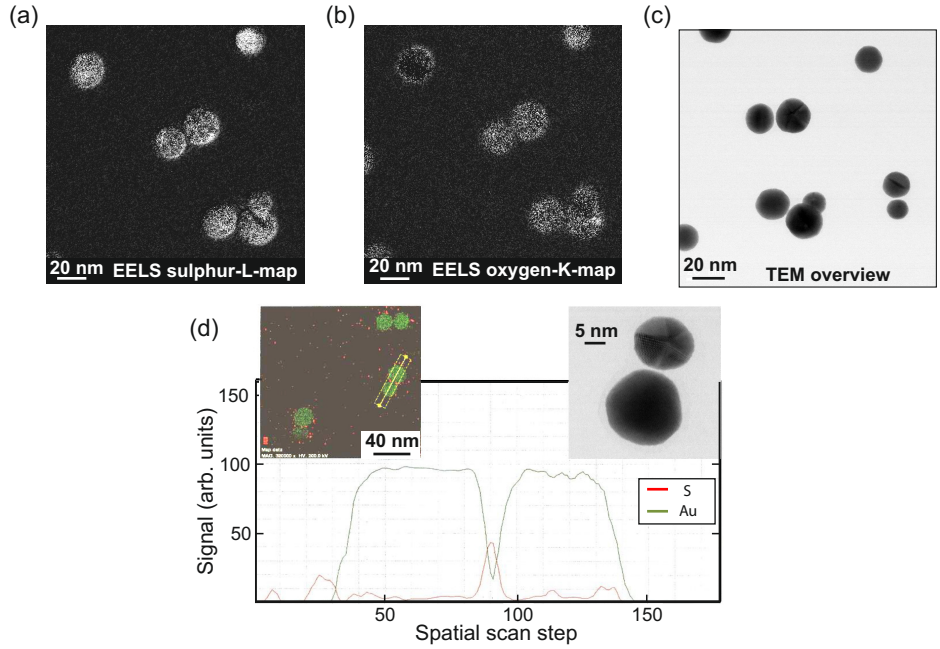

Fig. 4.4: Element specific characterization of nanoparticle aggregates. (a) Spatially resolved detection of sulphur atoms on the surface of a nanoparticle dimer by electron energy loss spectroscopy (EELS) incorporated in a high-resolution transmission electron microscope (at JEOL, Germany): The grey scale reflects the amount of detected sulphur, which is clearly distributed across the entire particle surface. (b) Detection of oxygen in the same region. (c) TEM overview of the examined region. (d) A line scan with element specific energy-dispersive X-ray spectroscopy (EDX) (at FEI, Czech Republic): The electron signal stems approximately from the area marked by the yellow rectangle in the upper left inset. The yield, red curve for sulphur and green curve for gold, is accumulated in the direction perpendicular to the yellow bold dashed line.

by scattering of primary electrons: The spatially resolved signal is broadened and hence a complete decay to zero is prevented. The sulphur signal, represented by the red line, significantly increases in the dimer gap region. Since, again, the only source for sulphur is acetyl-protected dithiol its importance for the nanoparticle linking process is a reasonable suspicion. The sulphur signal increases again at the rim of the dimer since the primary electrons are less disturbed by gold and pass many dithiol molecules in the organic shell. A non-zero sulphur signal along the entire line confirms that other regions on the nanoparticle surface are covered with dithiol molecules, as already shown by EELS maps of the sulphur L-edge in

Fig. 4.4(a).

UV-Vis extinction measurements of supernatant solutions

HR-TEM experiments revealed the qualitative result that many acetyl protected dithiol molecules bind to the surface of citrate stabilized Au nanoparticles. In SERS experiments it is of great importance to know the exact number of molecules of the respective substrate that contribute to the measured Raman signals. Otherwise it is not possible to assign a reliable enhancement factor, which is the most important aspect in SERS [188]. By avoiding any fractionation, purification, or single aggregate selection and by using as-prepared dispersions for Raman experiments the equilibrium between bound and unbound thiol molecules is maintained. In order to quantify the average surface coverage UV-Vis extinction measurements are performed on the supernatant solutions of dispersion D and dispersion M, respectively.

The supernatant solution of dispersion D is obtained by a centrifugation process in which the nanoparticle aggregates are concentrated at the bottom of the vessel. The segregated clear solution which contains all the unbound thiol molecules is removed. This process constitutes the last step of the experiments and is conducted by Ingo Heesemann who also takes care of the subsequent evaluation. From measured molar extinction coefficients he determined an amount of unbound dithiol molecules of 0.062 mg (7×10^{-5} mmol) according to Beer's law (see equation (4.14)). Recalling that the dispersion is synthesized with 0.105 mg of dithiol leads to the conclusion that 41% of the molecules bind to Au nanoparticles. Taking into account the molar mass of acetyl protected dithiol of 887.34 g mol^{-1} gives an absolute number of 2.9×10^{16} bound molecules. Since the dispersion contains 5.7×10^{12} nanoparticles, as estimated in Section 4.2.1, approximately 5100 dithiol molecules are attached to the surface of a single particle. The nanoparticle diameter was determined with TEM to be 38 ± 7 nm (average of 157). Hence, the overall surface coverage amounts to $c_D \approx 1$ nm^{-2}.

To assess the retrieved surface coverage it is compared to similar systems in literature. Yang et al. report on a surface coverage of approximately 4 nm^{-1} for an ordered self-assembled monolayer (SAM) of upright standing benzenethiol molecules on an Au(111) surface [325]. The lower surface coverage of the

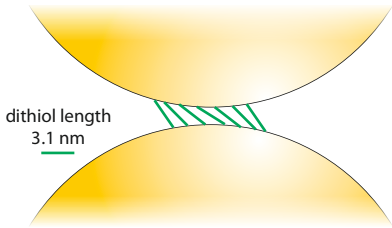

Fig. 4.5: Sketch of tilted dithiol molecules in the interparticle gap. An average gap width of 1.64 nm was determined by TEM.

nanoparticle structure presented here is explained as follows: First, the prepared dithiol and monothiol molecules possess hexyl side chains which require more space. Second, according to the oxygen concentration detected by EELS measurements the citrate shell is not entirely removed by the tethered dithiol molecules which leads to a less dense coverage of Raman reporter molecules. As a consequence of the lower surface coverage it is expected that the reporter molecules do not stand upright on the nanoparticle surface. Interestingly the average gap size of 60 nanoparticle dimers was determined to be 1.64 ± 0.35 nm [133]. Taking into account the length of the rod-like dithiol and monothiol molecules of approximately 3.1 nm [133] corroborates the assumption of tilted molecules and the absence of a densely packed SAM. A sketch of tilted molecules in the interparticle gap is shown in Fig. 4.5.

An analogue investigation of dispersion M reveals an identical surface coverage of nanoparticles with monothiol molecules of 1 nm^{-2}. This is attributed to the fact that acetyl protected monothiol molecules exhibit a nearly identical structure as synthesised dithiol molecules. Furthermore monothiol molecules are also able to replace citrate on the nanoparticle surface in the same manner as dithiol molecules.

TEM aggregate statistics

For assessment of the yield in nanoparticle dimers of a chemically driven aggregation process with acetyl protected thiols TEM images of resulting aggregates were taken of both, dispersion D and dispersion M, respectively. TEM images were recorded by Ingo Heesemann and subsequent evaluation was performed by the thesis author.

A CM 100 ST transmission electron microscope from PHILIPS with a tungsten cathode was operated at an acceleration voltage of 80 kV. Approximately 3 μL

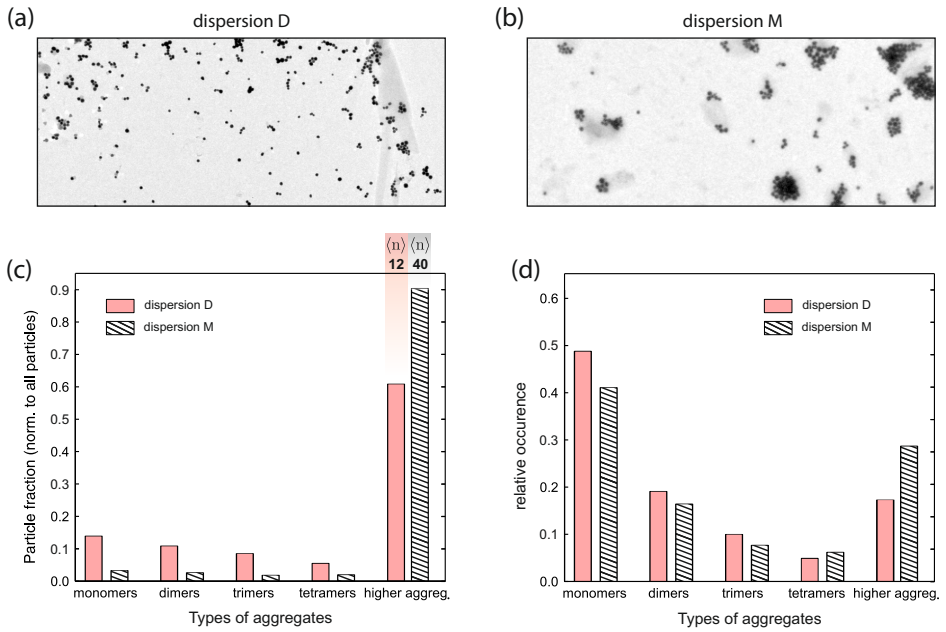

Fig. 4.6: Nanoparticle aggregate statistics obtained from evaluation of transmission electron microscopy (TEM) images. (a) and (b) show representative images of dispersion D (left panel) and dispersion M (right panel), in which nanoparticle aggregation was induced by adding acetyl protected dithiol or acetyl protected monothiol, respectively, to a prepared dispersion of Au nanoparticles. (c) shows the fraction of nanoparticles which are incorporated in distinct nanoparticle aggregates like monomers, dimers, trimers or tetramers. Nanoparticle aggregates with a coordination number $n > 4$ are merged with respect to the expectation value $\langle n \rangle$. Approximately 1700 aggregates were analysed for dispersion D (pink bars) and 700 aggregates for dispersion M (black hatched bars). (d) In order to present the relative occurrence of distinct aggregates the height of the bars is divided by the respective coordination number.

of the colloidal dispersion were dropped on a TEM grid (400-mesh copper grids coated with carbon, PLANO) and most of the dispersion was immediately sucked off using filter paper. Since the retrieved histograms only show a relative difference of less than 15% between aggregates of different coordination numbers in two days it is of no importance if TEM images are recorded and evaluated before Raman measurements or afterwards. The coordination number describes the number of particles in a particular aggregate, e.g. dimers have the coordination number 2.

A typical section of a TEM image of dispersion D is shown in Fig. 4.6(a) while a typical section of dispersion M is presented in Fig. 4.6(b). Both dispersions

feature a mix of distinct particle aggregates which was also previously observed with structurally related dithiol molecules by Novak and co-workers [226]. The presented sections indicate that aggregation with monothiol molecules in dispersion M leads to the incorporation of more particles in lager aggregates compared to dispersion D. For a quantitative assessment 1726 aggregates of dispersion D and 715 aggregates of dispersion M were evaluated. The statistics of relative occurrence of nanoparticle aggregates with different coordination numbers is presented in Fig. 4.6(d). Both dispersions show a similar distribution while the impression that dispersion M incorporates more aggregates with coordination numbers $n > 4$ is confirmed. The precise distribution of dispersion D reads 48.8% nanoparticle monomers, 19.1% dimers, 10.0% trimers, 4.9% tetramers, and 17.3% higher order aggregates. This is in very good agreement with dispersions previously synthesised by Ingo Heesemann [133] and the preparation process hence appears to be repeatable.

The nanoparticle dimers, which are of particular interest in the SERS investigation presented here, make one-fifth of all aggregates in dispersion D without any purification. Moreover, aggregates with low coordination numbers from $n = 2$ to $n = 4$ account for almost 70% of all aggregates with more than one particle. These findings suggest that acetyl protected dithiol obviously fosters the formation of small aggregates. However, the statistics of relative occurrence does not reveal the ratio of particular aggregates with small coordination numbers between dispersion D and dispersion M. To this end it is essential to know the fraction of all particles which are incorporated in different types of aggregates. Therefore the average number of particles in higher order aggregates $\langle n \rangle$ is determined: On average 12 particles are incorporated in higher order aggregates in dispersion D and 40 particles in dispersion M, respectively. Knowing the number of particles representing each aggregate type allows to multiply the bars in Fig. 4.6(d) with the appropriate number and to normalise them to all particles of the preparation process. This procedure gives the fraction of particles incorporated in different aggregates, which is presented in Fig. 4.6(c). Since three times more particles can be found in larger aggregates with $n > 4$ of dispersion M compared to dispersion D and since the statistics of relative occurrence is quite similar for both dispersions, less particles are available for the smaller aggregates in dispersion M. It is retrieved from Fig. 4.6(c) that approximately five times more nanoparti-

cle dimers are obtained by driving the aggregation process with acetyl protected dithiol compared to its monothiol analogue.

Finally, the question is addressed why larger aggregates form by using a mono-functional Raman reporter molecule like the acetyl-protected monothiol. Interestingly, it was already reported in literature that the usage of mono-functional 4-mercaptobenzoic lead to the formation of larger particle clusters [183, 288]. It is likewise reported that the usage of bi-functional linker molecules such as 4-aminobenzenethiol proved to facilitate dimer formation [183]. Here, it is presumed that acetone is too polar for the hydrophobic methyl group which is exposed to the solvent. To avoid exposure the nanoparticles tend to agglomerate ([133], page 127).

4.3 FDTD simulations

This section is dedicated to a numerical study of the properties of nanoparticle dimers and other aggregates with the finite-difference time-domain (FDTD) method. The general setup for subsequent simulations and analysis methods is introduced in Section 4.3.1. Section 4.3.2 is concerned with the calculation of absorption spectra of distinct nanoparticle aggregates. These spectra will support the interpretation of Raman scattering and UV-Vis extinction measurements in Section 4.4 and 4.5, respectively. Furthermore the simulations are utilised for a more quantitative evaluation of the SERS systems presented here: Inspired by the work of Pazos-Perez and co-workers [234] the as-prepared dispersion will be described in the model of so-called *effective dimers*. In this model the non-fractionated dispersion, containing also nanoparticle trimers and tetramers, is treated in the picture of dimer-like resonators. In Section 4.6 their quantity is retrieved with the help of the previously presented extinction measurements in order to specify a particular enhancement factors for the investigated SERS system.

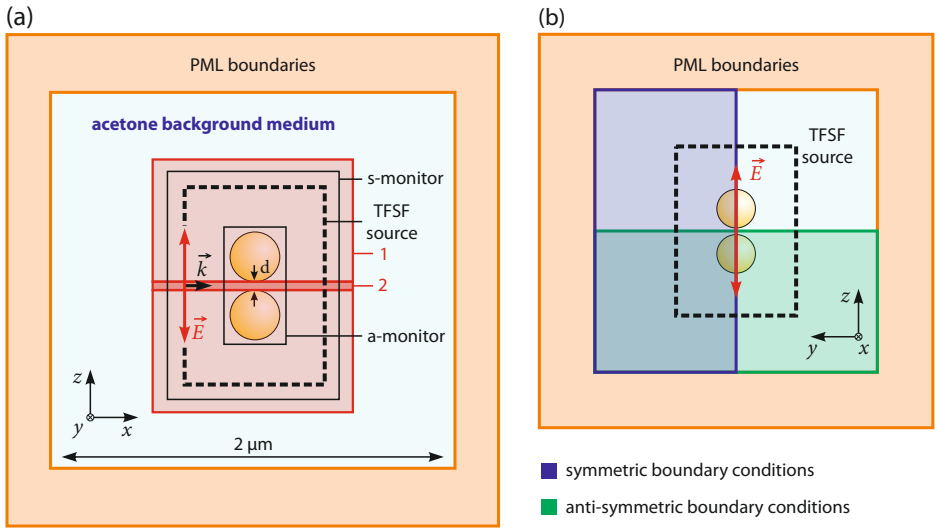

Fig. 4.7: Sketch of the general FDTD simulation setup and symmetry conditions. (a) The size of the simulation volume is 2 μm $\times$ 2 μm $\times$ 2 μm ($x \times y \times z$). These proportions assure that near-fields originating from excitation of the nanoparticle do not interact with the perfect matched layer (PLM) boundaries. The red shaded areas depict a refinement of the simulation mesh. Mesh 1 encases the entire particle structure and mesh 2 additionally refines the inter-particle gap. The a-monitor usually records 3D-data of the electric field and the spatially resolved refractive index. For simulations with more than 2 nanoparticles the a-monitor and the s-monitor only record the transmission through their respective surface. The total-field scattered-field source is located between these two monitors. (b) Symmetric boundary conditions are applied in the x-z-plane and anti-symmetric boundary conditions in the x-y-plane. According to this only two out of eight octants have to be evaluated during the simulation.

4.3.1 General FDTD setup

The general setup for FDTD simulations with nanoparticle aggregates is sketched in Fig. 4.7. Depending on the number of nanoparticles involved in the simulation, the object properties like monitor types and additional meshes are adjusted. Therefore specific definitions will be emphasised in the respective case.

The simulation volume in all cases is a cube with side lengths of 2 μm. Since the wavelength sampling points for evaluation range from 450 nm to 800 nm the perfectly matched layer (PML) boundaries exhibit at least a distance of one wavelength to the scattering structure in order to prevent interaction with evanescent

tails of the resonant surface plasmon modes. The mesh size is set to 3 or 4 which gives Yee cell sizes of approximately $1/14$ to $1/18$ of the wavelength prevailing in the respective material. However, in all cases the scattering structure is encased by an additional mesh, entitled *mesh* 1 in Fig. 4.7, with a minimum resolution of 0.5 nm to better resolve the curved nanoparticle surface and to minimise the occurrence of numerical artefacts due to staircasing effects. When simulating light-scattering with nanoparticle dimers an additional mesh is introduced which refines the resolution in the gap between both particles to 0.2 nm in z-direction.

According to results of the TEM analysis the diameter of the nanoparticle monomers was set to 40 nm. The dielectric function $\varepsilon(\nu)$ of gold was fitted to the experimental data of Johnson and Christy [155] in order to account for interband transitions in the short wavelength range. The dielectric function of the embedding medium acetone was implemented by using the Cauchy dispersion formula with parameters evaluated by Rheims and co-workers [255].

Whenever possible symmetry conditions are utilised as sketched in Fig. 4.7(b). In most cases it is possible to restrict the simulation volume to two octants which reduces the required time by a factor of four. This applies to single nanoparticle monomers, dimers or chains of more than two particles. If three particles are arranged as an equilateral triangle the structure is assigned to the D_3 symmetry group. In the latter case only a single symmetry plane is present and four octants have to be evaluated. Symmetric boundary conditions were used in the plane spanned by the wave vector and the electric field vector of incoming light, and anti-symmetric boundary conditions in the plane that is rotated by $\pi/2$ around the wave vector axis with respect to the former plane.

Calculation of absorption cross-sections

The frequency specific absorption cross-section is calculated via the absorbed power density (see equation (A.36) in Appendix A.2) by using a built-in script:

$$p_{abs}(x,y,z,\nu) = -\frac{1}{2} 2\pi\nu \, |\mathbf{R}(x,y,z,\nu)|^2 \, \mathrm{Im}\{\varepsilon_0 \varepsilon_r(x,y,z,\nu)\}, \qquad (4.5)$$

in which $|\mathbf{R}(x,y,z,\nu)|$ is the local absolute value of the impulsive response function in the frequency domain and $\mathrm{Im}\{\varepsilon_0\varepsilon_r(x,y,z,\nu)\}$ is the imaginary part of the

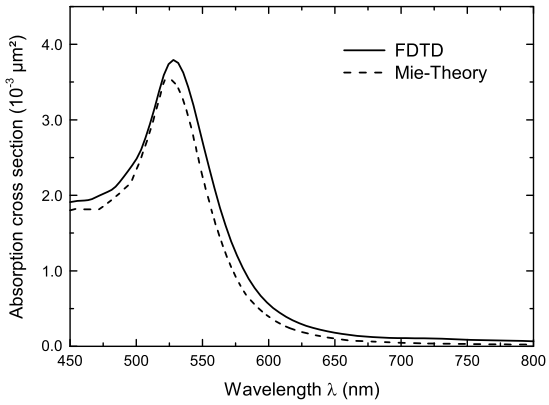

Fig. 4.8: Comparison of the nanoparticle absorption cross-section of a 40 nm gold nanoparticle calculated with FDTD and Mie theory (MIEPLOT by Philip Laven). In both cases gold's dielectric function is modelled according to data of Johnson and Christy [155]. The background medium of the Mie calculations is water and acetone [255] in the FDTD simulation.

local dielectric function. Both quantities represent four dimensional data stored in the a-monitor sketched in Fig. 4.7(a). Since the spectral field amplitude $|\mathbf{R}(\nu)|$ is usually given in V s m^{-1} and $\varepsilon = \varepsilon_0\varepsilon_r$ is given in A^2 s^4 kg^{-1} m^{-3} the according units of the absorbed power density $p_{abs}(x,y,z,\nu)$ are W m^{-3}. Integrating this quantity over all space and dividing it by the source intensity $I(\nu)$ gives the spectrally-resolved absorption cross-section. The source intensity $I(\nu)$ is available through the script command `sourceintensity(`ν`)`.

The functionality of this procedure was tested by calculating the absorption cross-section of a single Au nanoparticle with a diameter of 40 nm. The result is compared to the absorption cross-section retrieved from Mie theory in Fig. 4.8. In the latter case the free available software MIEPLOT, written by Philip Laven [184], was utilised. Although both curves match quite well small deviations remain. These deviations are attributed to the dielectric functions: First, in FDTD simulations the data of Johnson and Christy is fitted with a polynomial function while MIEPLOT uses the exact values. And second, the embedding medium in Mie theory calculations is water which exhibits a slightly smaller refractive index than acetone leading to a smaller absorption cross-section. Hence, the above described procedures and parameters are sufficient for reliable FDTD simulations.

An important theme that remains to be discussed is the calculation of the absorption cross-section of a nanoparticle dimer freely floating in a dispersion, as it is the case in the presented experiments. As a consequence the interparticle axis of the dimer exhibits an arbitrary orientation to the linear polarised light. The overall cross-section $\sigma_A(\omega)$ is therefore the equally weighted sum of the absorption

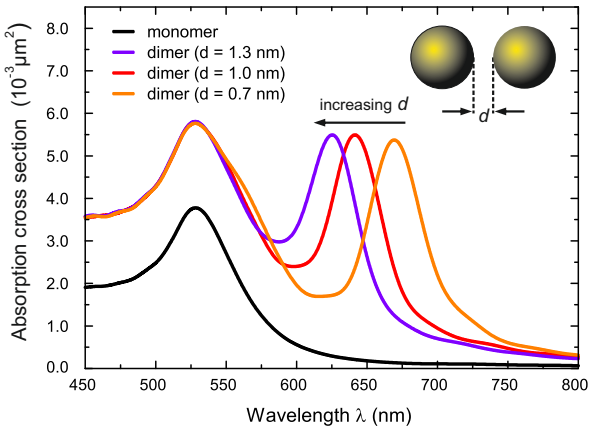

Fig. 4.9: Orientation averaged absorption cross-sections of Au nanoparticle dimers with various gap widths d. The structure is illuminated by a linearly polarized plane wave (TFSF source) and acetone serves as the surrounding medium. All simulations were run with a duration of 50 fs. In this time electric field amplitudes decay by more than an order of magnitude with respect to maximum field amplitude. The mesh encasing the dimers has an extent of 60 nm $\times$ 60 nm $\times$ 100 nm with a resolution of 0.5 nm. An additional interparticle mesh exhibits a size of 60 nm $\times$ 60 nm $\times$ 5 nm with 0.2 nm resolution along the latter axis.

cross-section $\sigma_{A,1}(\omega)$ with the polarisation vector along the inter-particle axis, and $\sigma_{A,2}(\omega)$ and $\sigma_{A,3}(\omega)$ with the polarisation vector along the other two axes of the right-handed coordination system:

$$\sigma_A(\omega) = \frac{\sigma_{A,1}(\omega) + \sigma_{A,2}(\omega) + \sigma_{A,3}(\omega)}{3}. \tag{4.6}$$

This procedure is well known from the rotational averaging of transition dipole moments and a detailed mathematical treatment can be found in [17].

4.3.2 Absorption spectra of nanoparticle dimers

Nanoparticle dimers

Orientation averaged absorption cross-sections for Au nanoparticle dimers with different interparticle distance d are shown in Fig. 4.9. The data of $|\mathbf{R}(x,y,z,\nu)|^2$ and $\varepsilon_r(x,y,z,\nu)$ is collected in the a-monitor (42 nm $\times$ 42 nm $\times$ 85) and subsequently evaluated according to equations (4.5) and (4.6).

For comparison the absorption cross-section of an Au nanoparticle is also shown

(black solid curve) and it peaks at the plasmonic Mie resonance near 525 nm [170]. This resonance is also clearly imprinted into the cross-section of the nanoparticle dimers. The pronounced character is attributed to the fact that two out of three independent excitation geometries feature an incoming electric field polarisation perpendicular to the interparticle axis. For these modes the interaction between the charge oscillations in the two nanoparticles is weak and consequently the resonance deviates only slightly from the isotropic monomer resonance. The resonance peak is approximately a factor 1.5 higher than in the case of a monomer, although two particles are involved. Here, it has to be taken into account that one of these two excitation geometries effectively excites a single nanoparticle while the other one is shadowed.

Besides this single particle resonance a second peak is present in the absorption cross-section at longer excitation wavelengths. This resonance is attributed to the dipolar mode excited along the interparticle axis, i.e. the dimer plasmon resonance. It can be conceived as a hybridised plasmon resonance of two adjacent nano-particles [244] leading to a red-shift of the symmetric mode compared to the single particle resonance. With increasing gap distance d the hybridised mode significantly shifts to smaller excitation wavelengths, as was previously described by Zhao and co-workers [332].

4.3.3 Absorption spectra of higher order nanoparticle aggregates

The TEM analysis in Section 4.2.2 revealed that the prepared dispersions also contain aggregates with more than two nanoparticles. To asses their influence on subsequent measurements the absorption cross-section of selected aggregate types is shown in Fig. 4.10. For simplicity only the non-averaged cross-sections have been calculated and the specific excitation geometry of different aggregates with respect to electric field and wave vectors is sketched in the inset. In the case of the triangular-shaped trimer it is not possible to insert cuboid-shaped refined meshes into the Cartesian grid inside the gaps due to the structural D_3 symmetry. Therefore only a single refined mesh is used for all aggregates. It encases the aggregates and the accuracy in all spatial directions is set to 0.2 nm.

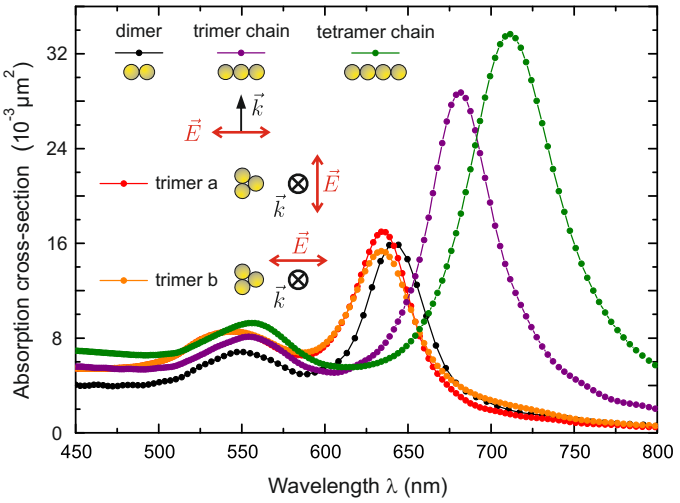

Fig. 4.10: Absorption cross-sections of larger Au nano-particle aggregates. Electric field vectors (red) and wave vectors (black) sketch the specific excitation geometry. No spatial averaging was performed for the presented absorption cross-sections.

Due to the larger structure size compared to dimers the a-monitor (see Fig. 4.7(a)) was exchanged by a transmission box monitor which spatially integrates the net Poynting vector on the monitor surface. The cross-section, given in m^2, is then obtained by dividing the resulting power in units of W by the source intensity via the command `sourceintensity(ν)`.

All of the aggregates exhibit a small resonance peak near 550 nm which is ascribed to the monomer resonance. The residual peaks are therefore attributed to hybridisation of plasmonic resonances. The hybridised resonance of the triangular-shaped trimer (red and orange curve) is located close to the dimer resonance (black curve) and exhibits similar oscillator strength. This is explained by the fact that for the triangular trimer the dimer-like mode between the two particles, which have their interparticle axes aligned parallel to the incident electric field vector, is predominantly excited. For a trimer consisting of linearly arranged nanoparticles, where both interparticle axes are parallel to the electric field vector, the absorption cross-section of the long-wavelength resonance is almost doubled in strength. Following the hybridisation model the additional red-shift for this aggregate can be attributed to an additional hybridisation of the two dimer modes in the collinear

aligned gaps. Accordingly, the resonance of a chain of four nanoparticles (green curve) is shifted even further. As a consequence the dimer resonance is no longer the dominating plasmon mode in very large aggregates, especially when these aggregates exhibit a chain-like structure. Complex hybridisation phenomena will lead to spatially more extended plasmon modes with spectrally broad and red-shifted resonances.

4.4 Wavelength-resolved Raman scattering

As discussed in the introduction and the previous subsections, nanoparticle dimers are interesting SERS systems due to their strong field enhancement in the interparticle gap and the possibility to tune the according hybridised plasmonic resonance by parameters like the particle size or gap distance. It was shown in Section 4.2.2 that especially the synthesised dispersion D gives a good yield in nanoparticle dimers without any purification mechanisms. Additionally, the gap distance turned out to be well-defined. Hence it is expected that Raman spectra recorded at different excitation wavelengths should give a clear fingerprint of the plasmonic properties of the presented SERS system.

In this section Raman spectra of the as-prepared dispersion D will be presented for six different excitation wavelengths, ranging from 473 nm to 785 nm, and the spectra will be evaluated with view to enhanced Raman bands. The utilised Raman scattering setup, which is presented in Section 4.4.1 was built and operated by Elina Oberländer. The subsequent data evaluation of enhanced Raman signals relies on a MATLAB-code written by the thesis author. Since the as-prepared dispersion M also exhibits nanoparticle dimers the whole procedure is also conducted with this dispersion for reasons of comparison.

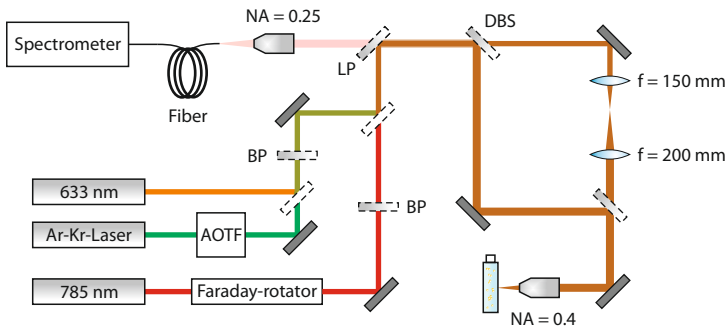

Fig. 4.11: Setup for wavelength-resolved Raman scattering. Only essential optical elements are shown. Excitation at a wavelength of 633 nm is provided by a helium-neon laser while excitation at 758 nm is performed with a laser diode. The abbreviated optical elements are an acousto-optical tunable filter (AOTF), a long-pass razor edge filter (LP), optical band-pass filters (BP), and a dichroic beam splitter (DBS).

4.4.1 Raman scattering setup

The optical setup for wavelength-resolved Raman scattering is shown in Fig. 4.11. A total of six different excitation wavelengths are available: A water-cooled argon-krypton laser (INNOVA 70C SPECTRUM, COHERENT) is utilised for excitation at 473 nm, 514 nm, 560 nm and 647 nm. A particular excitation wavelength was selected by using an acousto-optical tunable filter (AOTFnC-VIS-TN, AA OPTOELECTRONICS) and optical band-pass filters for spectral cleaning (SEMROCK). Excitation at 633 nm was provided by a helium-neon laser (COHERENT) while excitation in the NIR region at 785 nm was realised with a diode laser (INNOVATIVE PHOTONIC SOLUTIONS). Similar to the argon-krypton laser the other two light sources are also spectrally cleaned with optical band-pass filters. The beam width of the respective light source was then widened with a lens telescope so that the subsequent microscope objective (OLYMPUS, $\times 20$, 0.4 NA) was well illuminated. The dispersion specimen is placed in the laser focus and the backscattered photons are collected by the same objective. After passing a dichroic beam splitter and a long-pass razor edge filter (SEMROCK) for blocking Rayleigh-scattered photons, light is coupled with a second microscope objective (OLYMPUS, $\times 10$, 0.25 NA) into a multi-mode step-index fibre (THORLABS, AFS 105/125Y, 105μm, 0.22 NA, $400 - 2400$ nm). The fibre directs the light to a

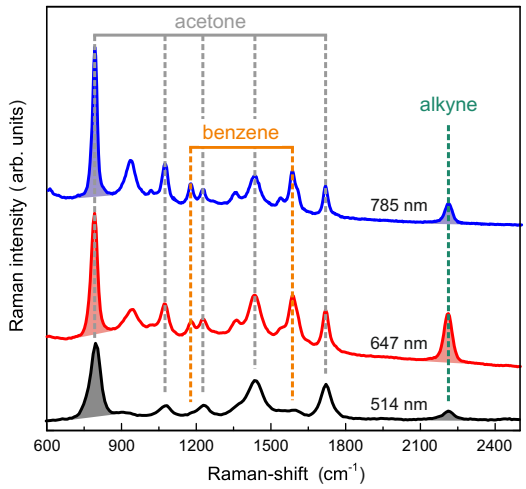

Fig. 4.12: Raman spectra of dispersion D recorded at different excitation wavelengths. An artificial offset is added to the spectra to allow a clear comparison. The height of each spectrum is adjusted so that the shaded area of the foremost Raman peak at 787 cm^{-1} is the same at all excitation wavelengths.

monochromator (ACTON 2300I, PRINCETON INSTRUMENTS) which includes an air-cooled CCD-camera (NEWTON, DU 920P BR-DD, ANDOR) and a 300 mm^{-1} grating. The SERS spectra, which will be presented in the following subsection, were recorded with an integration time of 1 s and a laser power of 10 mW.

4.4.2 Discussion of Raman spectra

Raman spectra recorded of dispersion D at three different excitation wavelengths are shown in Fig. 4.12. For clear comparison an artificial offset is added. All spectra reveal intense vibrational modes of the solvent acetone: At 787 cm^{-1} and 1223 cm^{-1} the a_1 and b_1 C−C stretching mode, respectively, at 1066 cm^{-1} and 1431 cm^{-1} the CH_3 rocking and deformation mode, respectively, and at 1709 cm^{-1} the C=O stretching mode. The Raman spectrum at 514 nm mainly features this solvent signature. By increasing the excitation wavelength to 647 nm and 785 nm additional peaks emerge which are attributed to the benzene ring of the dithiol and acetyl protected dithiol molecules: The peak at 1179 cm^{-1} relates to the C−H bending mode of the benzene ring and the peak at 1596 cm^{-1} is assigned to the benzene ring stretching mode. All peaks were identified according to [44] and [273].

A distinct feature that is clearly visible in all spectra is the peak located at 2200 cm^{-1}. This feature is attributed to the stretching mode of the four alkyne moieties (C≡C bonds). Interestingly the alkyne signal appears to be enhanced at 647 nm excitation while it is smaller at longer and shorter excitation wavelengths. Here, the signal is defined as the peak area as it is indicated by the shaded area in Fig. 4.12. Note that the presented spectra are adjusted in peak height so that the shaded area of the foremost Raman peak of acetone at 787 cm^{-1} is the same at all excitation wavelengths.

An enhanced signal of the alkyne moieties at 647 nm excitation is remarkable since the scattering efficiency usually follows the λ^{-4}-law ([195], Chapter 8) and should therefore increase towards shorter excitation wavelengths. In Section 4.2.2 spatially-resolved EELS and EDX measurements revealed that numerous dithiol molecules are attached to the surface of gold nanoparticles. Moreover, it is assumed that plenty of these molecules are required to link distinct nanoparticles [133]. Hence the corresponding alkyne moieties are also located in the interparticle gap and are exposed to strongly enhanced fields when the nanoparticle dimer is excited at its plasmonic resonance. The Mie-scattering resonance of isolated Au nanoparticles with a diameter of 40 nm is located near 525 nm (see Fig. 4.9). The bright hybridised mode of the nanoparticle dimer is the red-shifted one, which results from an effectively elongated dipole with respect to the charge distribution of the combined system. Accordingly, the enhanced alkyne signal at 2200 cm^{-1} for an excitation wavelength which is longer than the single nanoparticle resonance might be attributed to the plasmonic resonance of nanoparticle dimers in dispersion D.

To quantify the enhancement of the alkyne signal its peak area is compared to that of the solvent acetone at 787 cm^{-1}, whose signal strength is expected to be independent from the particle systems, for all six excitation wavelengths. The distinct peak areas are retrieved as follows: Lower and upper bounds of the Raman-shift axis were set in the vicinity of the respective signal peak. Averaging the signal height at the border with those of adjacent data points lead to the definition of two fixed points for a linear background subtraction. The linear signal was subtracted from the measured spectrum and the background-free peak was numerically integrated according to a trapezoidal method. The resulting peak areas are sketched as shaded areas in Fig. 4.12. This procedure is done for both dispersions,

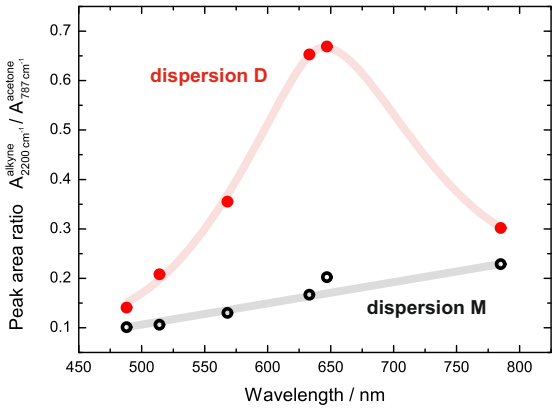

Fig. 4.13: Wavelength resolved signal enhancement for dispersion D and M. The alkyne-related Raman signal at 2200 cm^{-1} normalized to the acetone signal at 787 cm^{-1} is shown as a function of the excitation wavelength for dispersion D (red, filled circles) and M (black, open circles). Peak areas were normalized after background subtraction. The continuous curves are intended to guide the eyes and do not relate to a particular model.

D and M. Fig. 4.13 displays the peak area ratio of the alkyne signal at 2200 cm^{-1} to that of acetone at 787 cm^{-1} versus the excitation wavelength.

As already expected from the presented Raman spectra the peak area ratio for dispersion D exhibits a clear maximum at 647 nm with falling values to both, increasing and decreasing excitation wavelengths. Unfortunately, more data points are needed between 647 nm and 785 nm excitation to determine a particular wavelength for most efficient alkyne signal enhancement. However, the flat slope between the data points of 633 nm and 647 nm excitation suggests a maximum of the curve near 650 nm. In contrast to that, dispersion M shows only a slight monotonous rise of the peak area ratio with increasing excitation wavelength. The signal enhancement at the pronounced maximum of dispersion D is approximately five to six times higher than for dispersion M. Interestingly, this factor fits quite well to the statement of the statistics in Fig. 4.6(c) that dispersion D contains five times more nanoparticle dimers than dispersion M. Although dispersion M contains less nanoparticle dimers the few existing systems should contribute to an enhanced signal near the supposed plasmonic dimer resonance. Furthermore, the statistics in Fig. 4.6(c) and (d) reveals that more higher order aggregates incorporating many particles are found in dispersion M. According to a simple oscillator model the plasmonic resonance in bigger systems is further shifted towards longer wavelengths since the respective charges are separated on large spatial scales and hence the effective restoring force is smaller [34]. This behaviour has also been shown with FDTD simulations in Section 4.3.3. Therefore the slight increase of the ratio for dispersion M is attributed to residual field enhancement effects in

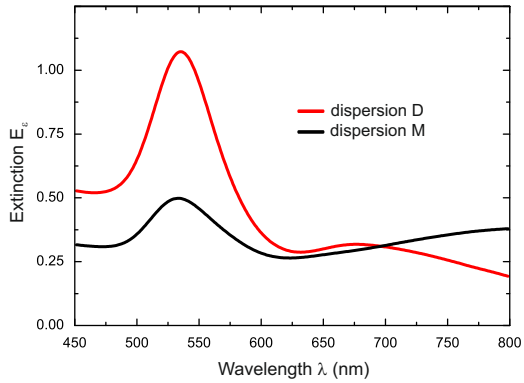

Fig. 4.14: UV-Vis extinction spectra of dispersion D and M, respectively. The spectra show no variation before and after the conducted Raman experiments.

larger nanoparticle aggregates in which resonances occur above 1000 nm.

4.5 UV-Vis extinction measurements

To further investigate the plasmonic properties of the colloidal dispersions UV-Vis extinction measurements were performed with a commercial spectrometer (LAMBDA 25, PERKIN ELMER). The measurements were conducted by Ingo Heesemann before and after the Raman scattering experiments. The dispersions are stable during this time and no changes in the extinction spectra occurred [133].

In UV-Vis extinction measurements the amount of transmitted light through the colloidal dispersions is measured. The extinction E_ε is defined as the negative decadic logarithm of the ratio of transmitted light to the incident light ([312], Chapter 3.4.1). The transmittance is altered by two processes: absorption and scattering. Since plasmonic resonances lead to features in the absorption and scattering cross-sections they also exhibit a fingerprint in extinction spectra. The spectra for dispersion D and M are presented in Fig. 4.14 as the red and black solid curve, respectively. Both extinction spectra have a pronounced feature at an excitation wavelength of 530 nm which is attributed to the plasmonic resonance of a single Au nanoparticle with a diameter of approximately 40 nm (see Section 4.3 for details). Additionally, the spectrum of dispersion D exhibits a second, weaker peak centred at 675 nm. The spectral position of this feature fits quite well to the

highest Raman signal enhancement of the alkyne moieties near 650 nm which has been discussed in the previous section. Hence the extinction peak at 675 nm is attributed to the presence of a plasmonic nanoparticle dimer resonance.

For dispersion M the feature of a nanoparticle dimer resonance near 675 nm excitation is not clearly visible. The extinction spectrum shows a broad feature which reaches its maximum at wavelengths well beyond 800 nm. Since TEM analysis revealed that nanoparticles are predominantly part of higher order aggregates (see Section 4.2.2) the increasing extinction at the NIR part of the spectrum is attributed to more complex hybridisation phenomena which lead to more extended plasmon modes with spectrally broad and red-shifted resonances. This conjecture is corroborated by the wavelength resolved Raman spectra presented in Section 4.4.2 and the related monotonously increasing enhancement of the alkyne signal towards excitation wavelengths beyond 800 nm.

Comparing UV-Vis extinction to Raman experiments

Further information can be retrieved by comparing the UV-Vis extinction measurements (Fig. 4.14) and the wavelength-dependent Raman signal enhancement (Fig. 4.13) since both signals exhibit specific features. In the case of Raman enhancement it was inferred that the maximum of the curve is located near 650 nm, i.e. blue-shifted by about 25 nm with respect to the extinction maximum of the dimer-related plasmon resonance in dispersion D. A blue-shift of the excitation wavelength for maximum signal enhancement is known from multi-colour SERS experiments performed using ensembles of individual nano-antennas that are characterized by distinct localised plasmon resonances [209]. It is attributed to the fact that SERS is most efficient if the product of the field enhancement at the excitation wavelength and at the Stokes-shifted wavelength reaches a maximum (see equation 4.3 and [209]). This occurs for a symmetric displacement of both lines to the left and to the right of the resonance wavelength.

Interestingly, nanoparticle aggregates or more generally speaking, hot-spot dominated SERS substrates were shown to behave differently. Kleinman et al. reported highest SERS enhancement for SiO_2 coated nano-particle aggregates at excitation wavelengths far red-shifted with respect to the dominant plasmon peak in the scattering cross-section [161]. The behaviour is explained in this work by

dark modes which are excited by the re-emitting dipoles near the nanoparticle surface inside the aggregate. However, the data presented here shows the opposite behaviour, although it lacks data points beyond 800 nm where Kleinman and co-workers observed maximum SERS enhancement for dimers and trimers: The Raman enhancement coincides almost perfectly with the dimer-related extinction.

The different behaviour might be explained by the dithiol linker molecule used in the experiments presented here, since the aggregates in the work of Kleinman lack such a molecule. As will be shown below, the dithiol-linked aggregates experience a reduced field enhancement in the gap region. It is suggested that this leads to a SERS enhancement mechanism that is less hot-spot-like [161] and more like the enhancement of individual single nanoparticle antenna structures [209] .

4.6 Determination of SERS substrate enhancement factors

As discussed in the introduction, surface-enhanced Raman scattering is intended to overcome the low scattering cross-section of the Raman process and to amplify the strength of the desired spectroscopic signal. Therefore it is obvious that the so-called *SERS enhancement factor* (SERS EF) is one of the important parameters that need to be characterised in order to allow a comparison of SERS devices. However, assigning SERS EFs is a tedious endeavour because they crucially rely on the specific definitions and experimental conditions [186, 188]. Here, the widely spread and straightforward SERS substrate enhancement factor (SSEF) is utilised:

$$SSEF = \frac{I_{SERS}/N_{SERS}}{I_{RS}/N_{RS}}, \tag{4.7}$$

in which I_{SERS} is the SERS signal intensity of the device, and I_{RS} the spontaneous Raman signal intensity of a reference sample containing only the Raman reporter molecules. The number of molecules in the reference sample N_{RS} and the number of molecules bound to the SERS device N_{SERS} serve to normalise the respective signal strength.

The synthesised nanoparticle dispersions have been used as-prepared without further purification and therefore an identical solution of acetyl protected dithiol

in acetone, in which no nanoparticles were added, was used as a reference. Both solutions ($\approx$ 1 mL) exhibit initially the same concentration of dithiol and acetone molecules which is not affected by adding the small volume fraction of nanoparticles ($\approx$ 10 μL, see Section 4.2.1). First, the SERS experiments are presented in Section 4.6.1. Then the average *SSEF* is determined in Section 4.6.2 by considering all nanoparticles in the dispersion. Finally, an attempt is made to assign a SSEF value to dimer-related aggregates in Section 4.6.3. The subsequent experiments, evaluation and FDTD-supported analysis was performed by the thesis author.

4.6.1 SERS experiments for SSEF determination

The utilised Raman setup is a commercial Raman system (LABRAM ARAMIS, HORIBA) and it is hence shortly introduced: The confocal setup allows for measurements with an excitation wavelength of 473 nm (COBOLT BLUES DPSS laser, 25 mW) and 633 nm (COHERENT, 17 mW). Laser light is filtered with a neutral density optical filter (OD 0.3) and focused with an $\times$10 microscope objective (OLYMPUS, NA 0.25). A 600 mm^{-1} grating is used for 633 nm excitation and a 1200 mm^{-1} grating for 473 nm excitation.

The obtained data is presented in Fig. 4.15 for off-resonant excitation at 473 nm laser wavelength (a) and at near-resonant excitation at a laser wavelength of 633 nm (b). In the case of 473 nm excitation the alkyne mode, appearing at about 2200 cm^{-1}, is clearly visible and it features similar intensity in dispersion D and the reference solution. According to the procedure introduced in Section 4.4.2 the signal enhancement is quantified by using the acetone related Raman signal at 787 cm^{-1} as a reference in order to account for both, slightly different wavelength-dependent Raman detection efficiencies and the difference in scattering efficiency at different wavelengths: The peak area of the acetone mode is normalised separately for dispersion D (red solid line) and the reference dispersion (black solid line). The strength of the alkyne peak signal is represented by the respective scaled peak area. Comparing dispersion D and the reference solution yields a nanoparticle related signal enhancement of 1.8. Here, it should be noted that the signal of

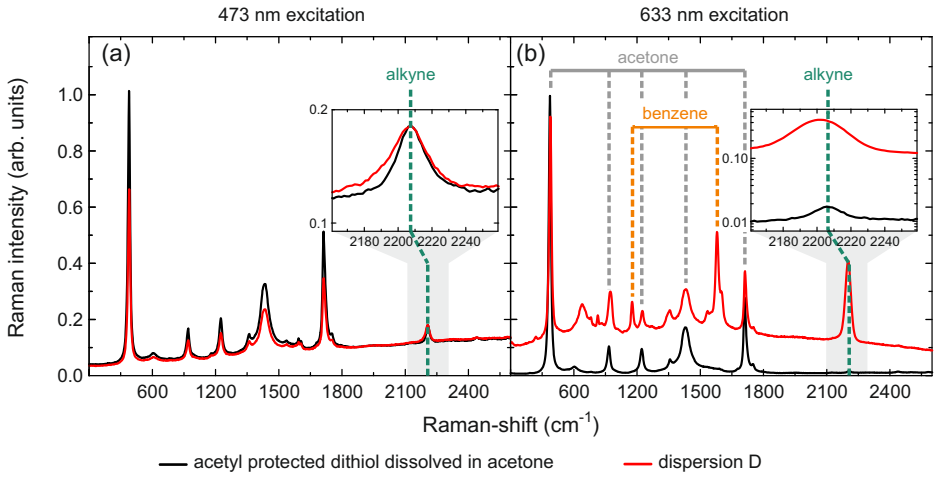

Fig. 4.15: SERS experiments for the determination of SSEF values. Raman spectra of acetyl protected dithiol dissolved in acetone (black solid line) and of dispersion D (red solid line) are obtained at an excitation wavelength of 473 nm excitation (a) and at 633 nm excitation (b). The insets in both spectra highlight the signal strength of the alkyne peak at $\approx$ 2200 cm^{-1} on a logarithmic scale. The nature of distinct Raman peaks was already discussed in Section 4.4.2.

dispersion D contains the contribution of nanoparticle aggregates as well as that of free floating dithiol molecules and it is labelled I_{sum}. The ratio I_{SERS}/I_{RS} is then calculated according to:

$$473\text{ nm: } \frac{I_{SERS}}{I_{RS}} = \frac{I_{sum} - \alpha I_{RS}}{I_{RS}} = \frac{I_{sum}}{I_{RS}} - \alpha = 1.80 - 0.59 = 1.21 \tag{4.8}$$

It is assumed that Raman scattering of free floating dithiol molecules occurs with the same efficiency in dispersion D as in the reference solution so that I_{SERS} is retrieved by subtracting the contribution αI_{RS} from the overall signal I_{sum}. The factor α accounts for the fact that 59% of dithiol molecules are not bound to nanoparticles (see Section 4.2.2).

It is expected from the Raman spectrum in Fig. 4.15(b) that the signal enhancement is increased in the case of near-resonant excitation at 633 nm. Indeed, it is found that $I_{sum}/I_{RS} = 73$ and hence:

$$633\text{ nm: } \frac{I_{SERS}}{I_{RS}} = \frac{I_{sum} - \alpha I_{RS}}{I_{RS}} = \frac{I_{sum}}{I_{RS}} - \alpha = 73 - 0.59 = 72.41 \tag{4.9}$$

4.6.2 Determination of the average SSEF

The quantities I_{SERS} and I_{RS} have been retrieved for 633 nm and 473 nm excitation in Section 4.6.1. To calculate the average $SSEF$ value N_{SERS} and N_{RS} need to be determined. Since the same Raman scattering geometry is used for dispersion D and the reference sample it is sufficient to retrieve the respective concentration c_{SERS} and c_{RS}.

For homogeneously distributed aggregates and homogeneous surface coverage the concentration of adsorbed Raman reporter molecules in dispersion D is obtained as $c_{SERS} = 2.0 \times 10^{16}$ mL^{-1} (2.9×10^{16} dithiol molecules are bound Au nanoparticles inside 1.4 mL cuvettes). The concentration of Raman reporter molecules in the reference sample is known by the initial preparation conditions and it amounts to $c_{RS} = 5.1 \times 10^{16}$ mL^{-1} (7.1×10^{16} dithiol molecules freely floating in 1.4 mL cuvettes). Using the retrieved values for I_{SERS}, I_{RS}, c_{SERS} and c_{RS} together with equation (4.7) the average $SSEF$ for 633 nm and 473 nm excitation amounts to:

$$SSEF_{avg}(633\text{ nm}) \approx 185 \qquad \text{and} \qquad SSEF_{avg}(473\text{ nm}) \approx 3 \tag{4.10}$$

Although a significant signal enhancement occurs at 633 nm excitation the overall $SSEF$ value is several orders of magnitude smaller than enhancement factors reported by e.g. Kleinman and co-workers who estimated that their Au nanoparticles are covered with 14000 SERS probe molecules. However, they investigated on single aggregates while here the quantitative assessment is related to a sample average.

4.6.3 Estimating a dimer-related SSEF

The spectroscopic signature of UV-Vis extinction measurements and the wavelength-dependent Raman scattering enhancement give a clear hint that a dimer-related field enhancement is responsible for the signal enhancement in (4.10) and it is thus interesting to compare the observed enhancement with that expected from nanoparticle dimers.

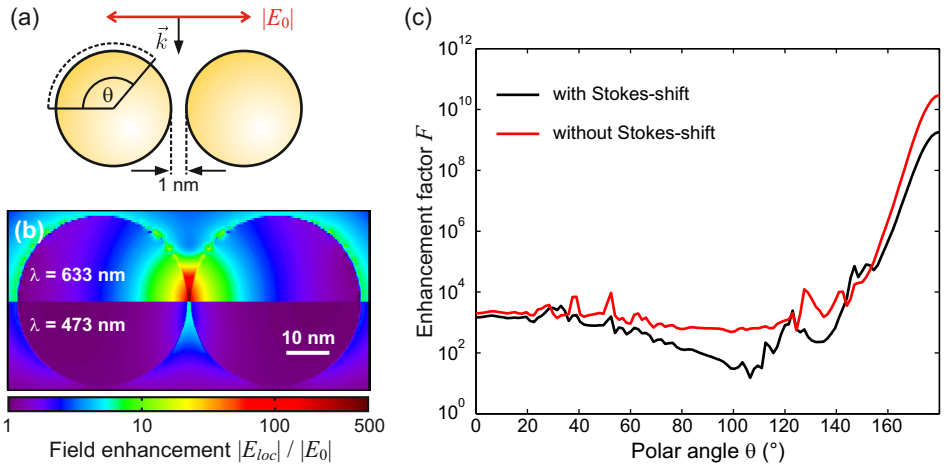

Fig. 4.16: Field and signal enhancement of nanoparticle dimers modelled with FDTD simulations. (a) Sketch of the excitation geometry. The incoming field strength is $|E_0|$. (b) The corresponding spatially-resolved field enhancement $|E_{loc}|/|E_0|$ for 633 nm and 473 nm excitation, i.e. near-resonant and off-resonant, respectively. $|E_{loc}|$ is the local electric field upon excitation. (c) The signal enhancement $F = (|E_{loc}(\theta)|/|E_0|)^4$ as a function of the polar angle θ (see (a)) with (black solid line) and without (red solid line) considered Stokes-shift. The radius was chosen to be 20.5 nm. It has to be noted that a specific θ sampling point does not necessarily coincide with a grid point due to the Cartesian mesh. Therefore the field enhancement is obtained by weighting the contribution of adjacent grid points with a three-dimensional Gaussian distribution (standard normal deviate: 0.8 grid points).

Predicted enhancement factors

In a theoretical approach Le Ru and co-workers numerically calculated the average signal enhancement factor $\langle F \rangle$ for a homogeneous coverage of the surface with analyte molecules and showed that the strong hot-spot enhancement in the dimer gap leads in general to single-molecule sensitivity in SERS measurements [258]. For varying nanoparticle diameters (25 nm - 50 nm), gap widths (1 nm - 3 nm), and materials (gold and silver) they show that 0.3% to 1.1% of the adsorbed molecules are responsible for 80% of the total Raman yield [258]. Here, 102000 dithiol molecules are bound to a nanoparticle dimer. In this simple assessment ≈ 30 molecules are responsible for the major part of the acquired signal yield.

According to Le Ru and co-workers the average signal enhancement $\langle F \rangle$ can be obtained by:

$$\langle F \rangle = \int_0^{\pi} F(\theta) \frac{\sin\theta}{2} \, \mathrm{d}\theta. \tag{4.11}$$

Here, $F(\theta)$ is the angle-dependent SERS signal enhancement $(|E_{loc}(\theta)| / |E_0|)^4$ upon plane wave excitation as sketched in Fig. 4.16(a). The field enhancement $(|E_{loc}(\theta)| / |E_0|)$ is directly retrieved from FDTD simulations via the three-dimensional a-monitor (see Fig. 4.7(a)) and the factor $\sin(\theta)/2$ accounts for spherical surface elements. A cross-section through the field enhancement data is shown in Fig. 4.16(b) for both excitation conditions, near- and off-resonance, to emphasise the difference in electric field strength. The angle-dependent signal enhancement $F(\theta)$ (equation (4.16)) of the monitor data in the near-resonant case upon 633 nm excitation is shown in Fig. 4.16(c) (red solid line). Matching to the above statement that only a few tens of molecules are responsible for the SERS yield the signal enhancement is largest in the gap near $\theta = 180°$ and it rapidly falls off by many orders of magnitude outside the gap. Applying equation (4.11) to this curve yields an average signal enhancement of $\langle F \rangle = 6 \times 10^7$ which is similar to the results found in [258].

The obtained result is valid for the specific excitation geometry in 4.16(a) and for a negligible Stokes-shift, i.e. the wavelength of incident light is identical to that of scattered light. In contrast to these assumptions the nanoparticle aggregates exhibit a random orientation to the incident electric field vector in the experiments and scattering of light by alkyne bonds introduces a non-negligible Stokes-shift of 2200 cm^{-1} (66 THz, from 633 nm to 735 nm). The evaluation of $\langle F \rangle$ is hence refined by considering the Stokes-shift according to $F(\theta) = (|E_{loc}(\theta, 633\ \mathrm{nm})|^2 \, |E_{loc}(\theta, 735\ \mathrm{nm})|^2) / |E_0|^4$ and by applying rotational averaging of the term $\cos^4\theta$ according to equation (8.157) in [229] (reduction of $\langle F \rangle$ by a factor of 0.2). The procedure yields an average signal enhancement of

$$\langle F \rangle_{theory} = 8.4 \times 10^5. \tag{4.12}$$

Calculating the concentration of effective nano-particle dimers

The evaluated quantity $\langle F \rangle_{theory}$ takes into account experimental conditions and it can hence be compared to an experimentally-retrieved SSEF that only considers

nanoparticle dimers. But applying equation (4.7) is not straightforward since the signal of dispersion D at the dimer-related resonance of 675 nm (see UV-Vis measurements in Fig. 4.14) is also influenced by the dimer-like contributions of smaller aggregates like triangular-shaped trimers (see the absorption cross-section in Fig. 4.10). Therefore this subsection is dedicated to identify the number of *effectively contributing dimers*, which is expected to be higher than the number of pure dimer aggregates as retrieved by TEM analysis.

As will be shown now, the concentration of effective dimers can be obtained from the UV-Vis extinction measurements. According to the Beer-Lambert law the extinction of radiation in a material of thickness d can be written as ([312], Chapter 3.4.1):

$$I(d) = I_0 \mathrm{e}^{-c\sigma_{ext}d}, \tag{4.13}$$

in which I_0 is the impinging intensity, $I(d)$ the intensity reduced by extinction, c the concentration of the specific material and σ_{ext} the extinction cross-section. The extinction itself is define by:

$$E_\varepsilon = \log_{10}\frac{I_0}{I(d)} = \varepsilon_{ext} c d, \tag{4.14}$$

in which ε_{ext} is the extinction coefficient. Inserting (4.13) into (4.14) gives the relation between extinction coefficient and cross-section:

$$\varepsilon_{ext} \approx 0.434\sigma_{ext}. \tag{4.15}$$

If the extinction E_ε is known from experiments the concentration of the material is retrieved by:

$$c = \frac{E_\varepsilon}{0.434\sigma_{abs}d}. \tag{4.16}$$

In the last step it is exploited that for small nanoparticles and small aggregates the extinction spectrum is dominated by the plasmon absorption cross-section and that scattering from larger aggregates is negligible because of the low concentration. The peak absorption cross-section of nano-particle dimers is given by Fig. 4.9 and it amounts to $\sigma_{abs} = 5.5 \times 10^{-15}$ m^2. To account for the absorption of

dimer-like structures that are shifted in wavelength with respect to 675 nm the absorption cross-section is reduced by a factor α of

$$\alpha = \frac{\int_0^\infty a(FWHM \approx 34 \text{ THz}) g(FWHM \approx 66 \text{ THz})}{g(FWHM \approx 66 \text{ THz})} \approx 0.5. \tag{4.17}$$

The specific form of (4.17) is related to the fact that only the reduction of extinction at the specific wavelength of 675 nm is required. Here, $a(\nu)$ is a Cauchy distribution with a full-width half-max of 34 THz describing the Lorentzian-like dimer resonance and $g(\nu)$ is a Gaussian distribution accounting for an inhomogeneous broadening of approximately 66 THz. With this information (4.16) can be re-written to:

$$c = \frac{E_\varepsilon}{0.217 \sigma_{abs} d}. \tag{4.18}$$

For an extinction value of $E_\varepsilon = 0.32$ at 657 nm and a cuvette thicknes of 0.01 m one obtains the effective dimer concentration c_{dim}:

$$c_{dim} = 2.6 \times 10^{10} \text{ mL}^{-1}. \tag{4.19}$$

This implies that roughly 1% of the nanoparticles in dispersion D are incorporated in a dimer or dimer-like resonator. According to the TEM-based particle distribution shown in Fig. 4.6(c) at least 10% of the nanoparticles should be part of a dimer and if dimer-like excitations in higher order aggregates are considered an even higher percentage of the nanoparticles should experience a dimer or dimer-like environment. Hence the above estimated $c_{dim} = 2.6 \times 10^{10}$ mL^{-1} represents a lower limit which is based on the theoretically determined absorption cross-section. The discrepancy between the estimated c_{dim} and the TEM analysis can be attributed to an overestimation of the absorption cross-section.

Dimer-related SSEF and discussion

The dimer-related concentration of SERS substrate molecules, participating in the evaluation of (4.7), are obtained by recalling that approximately 10^4 molecuels are bound to a nanoparticle dimer. Together with the concentration of dimer-like structures of $c_{dim} = 2.6 \times 10^{10}$ mL^{-1} the concentration of SERS substrate

molecules amounts to $c_{SERS}^{dim} = 2.6 \times 10^{14}$ mL^{-1}. The evaluation of equation (4.7) leads to an experientially determined dimer-related $SSEF_{dim}$ of

$$SSEF_{dim} = 1.4 \times 10^4. \tag{4.20}$$

The value is obtained by using the signal enhancement in equation (4.9) and the concentration of reference molecules $c_{RS} = 5.1 \times 10^{16}$ mL^{-1}.

The experimentally retrieved value is 60 times smaller than the predicted average Raman signal enhancement $\langle F \rangle_{theory}$ in (4.12). Taking into account that $SSEF_{dim}$ is only an upper limit, since c_{dim} is a lower limit for the concentration of dimer-like structures, the discrepancy between both values might be even larger. As a consequence the actual electric field in the experiments is expected to be at least three times smaller than the theoretically predicted value since the enhanced Raman signal scales with the fourth power of electric field enhancement. When comparing $SSEF_{dim}$ to the maximum signal enhancement factors $F > 10^9$ in the interparticle gap (see Fig. 4.16(c)) the effective field enhancement is only slightly larger than ten.

A lower field enhancement in the gap indicates a stronger dampening of the dimer resonance. This could be, again, related to the presence of the linker molecules. As indicated by its structure shown in Fig. 4.3(a), the dithiol molecule is a fully conjugated system. The dithiol molecule binds to both nanoparticles forming an electrical connection as it is also known from transport measurements in single molecule junctions [275]. Such an electrical link acts like a tunnel junction between the nanoparticles and for a shrinking tunnel barrier width quantum mechanical modelling of the plasmon resonances shows a red-shift and increasing damping [203]. It was also experimentally observed that SERS signals decrease when the resistance of a molecular junction decreases [311]. This effect might be even more pronounced by the fact that many linker molecules connect the two nanoparticles and thus the resistance of a single molecule junction is even further reduced.

A tunnel-junction induced red-shift of the plasmon resonance would also explain the discrepancy between FDTD simulations and UV-Vis extinction measurements. FDTD simulations predicted a hybridised plasmon resonance at 625 nm for the experimentally observed gap width of about 1.3 nm (Fig. 4.9). In contrast to this prediction, UV-Vis measurements revealed a dominating plasmon mode at

675 nm (Fig. 4.14). The large red-shift of 50 nm (35 THz) cannot be explained by numerical inaccuracies and it is hence ascribed to quantum mechanical effects [203].

With respect to the above discussion the strikingly small SERS enhancement is attributed to the quenching of the dimer resonance by electrical shortcuts between the nanoparticles. In other words, the electric field strength in the gap between the particles is greatly reduced due to the fact that electrons can flow between the particles.

4.7 Summary and outlook

In this chapter surface-enhanced Raman spectroscopy was performed with as-prepared dispersions of nanoparticle aggregates. A novel alkyne-rich and acetyl-protected molecule with thiol end-groups was synthesised to actively link two Au nanoparticles and to serve as a Raman reporter in the interparticle gap. The four incorporated alkyne triple bonds build the rigid backbone of the molecule and feature a Raman signal in the Raman-silent region (2200 cm^{-1}) that is undistorted by the solvent signature. Several key results will be shortly summarised:

- The optimum amount of nanoparticle dimers (20% of all aggregates) was found for an initial dithiol concentration that leads to a total number of 5100 molecules bound to a single nanoparticle, as retrieved from UV-Vis extinction measurements of the supernatant solution. This corresponds to a rather dense surface coverage of one molecule per nm^{-2}, which was corroborated by spatially-resolved sulphur detection using HR-TEM electron energy loss spectroscopy (EELS) and energy dispersive X-ray spectroscopy (EDX). These findings are in stark contradiction with a previous report about attaching nanoparticle dimers with a single bi-functional linker molecule [317] and ultra-low synthesis conditions were not mentioned explicitly in this report.

- The gap size of nanoparticle dimers was found to exhibit a narrow distribution of (1.64 ± 0.35) nm. This was perfectly explained by the molecule

length of 3.1 nm and the measured surface coverage that allows a tilting of molecules by approximately 45°. Hence, the devices synthesised here are well-defined with respect to the gap geometry.

- The multi-colour Raman study revealed a clear signal enhancement for the alkyne bond at excitation wavelengths that are slightly blue-shifted to a dimer-related resonant feature at 675 nm in the UV-Vis extinction measurements of the colloidal dispersion. This is in agreement with the general perception that SERS is most efficient if the product of the field enhancement at the excitation wavelength and at the Stokes-shifted wavelength reaches a maximum [209]. Therefore, the preparation of aggregates presented here, with a well-defined molecule-gap geometry, leads to a SERS enhancement mechanism of designed antenna structures rather than to an erratic hot-spot-like behaviour which was observed by Kleinman and co-workers with silica-coated dimer and trimer aggregates [161].

- The dimer-related peak in the extinction measurements was used to retrieve the number of *effective nano-particle dimers* since it was found with FDTD simulations that under certain geometric excitation conditions small aggregates like trimers or tetramers can exhibit resonances of similar strength and resonance frequency. The retrieved value of $c_{dim} = 2.6 \times 10^{10}$ mL^{-1} is ten times smaller than what is expected from TEM analysis for pure nanoparticle dimers. Hence, the number of effective dimers should be even higher and it is inferred that the absorption cross-section of the aggregates is much smaller than predicted by FDTD simulations.

- By using as-prepared dispersions the number of bound and unbound dithiol molecules is known in Raman experiments. Based on these values the SERS enhancement factor of effective dimers was determined to $SSEF_{dim} = 1.4 \times 10^4$, which is 60 times smaller than the average enhancement $\langle F \rangle_{theory} = 8.4 \times 10^5$ expected from FDTD simulations under near-resonant excitations and by considering the Stokes shift. Recalling that the absorption cross-section might be overestimated the value of $SSEF_{dim}$ might be even smaller.

- The plasmonic resonance measured with UV-Vis extinction exhibits a rather large red-shift of 50 nm with respect to FDTD simulations when using

nanoparticle dimers with a gap of 1.3 nm like in the experiments. This additional red-shift of the hybridised resonance, the smaller absorption cross-section and the associated lower field enhancement suggest that the linker molecules build an electrical connection between the nano-particles and act as a tunnel junction. It was found by Marinica an co-workers through quantum mechanical modelling that a reduction of the interparticle tunnel barrier, here an increasing number of linker molecules, induces a red-shift of the plasmonic dimer resonance and increases damping in the system [203].

- Nanoparticle aggregates formed by monothiol molecules do not show a significant dimer-related plasmonic resonance or Raman signal enhancement. TEM analysis revealed that using monothiol for synthesis leads to large nanoparticle aggregates which obscure the contribution of dimer structures.

To summarise, nanoparticle dimers synthesised with alkyne-rich dithiol molecules are an interesting SERS substrate since they show a systematic enhancement mechanism that is in agreement with general perceptions. This systematic behaviour and the associated well-defined gap rely on a rather dense surface coverage of the nanoparticles and the rigid character of the linker molecule. However, it is presumed that these properties will be at the expense of a decreased signal enhancement because the large number of fully-conjugated linker molecules might reduce the electrical resistance of the particle junctions.

In future experiments the concentration of rigid dithiol molecules should be systematically varied in the aggregation process and the different parameters, like gap width and Raman signal enhancement, should be monitored. With this approach it might be possible to find a trade-off between reliability and strong SERS enhancement in an as-prepared nano-scale system. Since the alkyne mode is located in the Raman-silent region of natural cellular molecules [141], these devices might be used for enhanced imaging applications. Furthermore, alkyne based dithiol Raman reporter molecules form an interesting model system to experimentally investigate the impact of chemical linkers and the related electrical coupling [75] on plasmonic resonances and local field enhancement in general.

Summary and Outlook

Several contributions to the field of nano-plasmonics, light harvesting and light-matter interaction have been presented in this thesis, ranging from molecular spectroscopy to the rather strong coupling of single quantum systems over microscopic distances. All of these contributions have benefited from the sub-wavelength concentration of light which was supported by resonant or coupled nano-structures. In this section the key results, suggestions for improvement of the devices, as well as their future perspective, will be separately discussed with respect to the distinct topics.

Chapter 1 - Cavity-mediated coupling of widely separated nano-antennas

A device was presented that allows for the first time ever a strong coupling between single localised surface plasmon (LSP) resonances with propagating surface plasmon polaritons (SPPs), which are confined to circular and elliptical shaped metallic pits. Therefore, the device enables to exploit the benefit of two worlds: strong electromagnetic field enhancement of metallic nano-antennas and the longevity of resonant cavity modes. Finite-difference time-domain (FDTD) simulations revealed that the $m = 0$ mode of whispering gallery mode (WGM) antennas [306] is perfectly suited for LSP-SPP coupling since approximately 24% of mode energy is injected into propagating surface plasmons. Positioning these structures into the central mode hot-spot of circular plasmonic cavities, where light is highly concentrated, leads to a mode splitting of 15 THz - 32 THz at operating frequencies of 375 THz, depending on the size of the respective cavity mode.

Cavity-mediated coupling of nano-antennas separated by 1.6 μm was then theoretically demonstrated by placing the WGM antennas in the electric field anti-nodes near the geometrical focal spots of an elliptical shaped cavity. The frequency

data of FDTD simulations revealed three distinct mode peaks with an overall splitting of 23 THz. The results are in qualitative agreement with a model of three coupled harmonic oscillators, a classical analogue of the Tavis-Cummings model [290], in which the coupling strength is the only free parameter. Furthermore, it was found that the temporal dynamics of energy transfer inside the coupled system obeys the universal phenomenon of impedance matching [11, 144]: An alternating coherent energy transfer between the nano-antennas, featuring a maximum switching ratio for several 100 fs, only occurs when the dissipation of the cavity and the nano-antennas is matched. Otherwise both antennas are simultaneously excited and periodically exchange energy with the cavity mode.

For an experimental realisation of the coherent energy transfer, atomically-flat single-crystalline gold microplates were utilised in the fabrication process of cavity-antenna structures in order to ensure superior plasmonic performance [143]. The coherent back-and-forth transfer of energy between the antennas was demonstrated via time-resolved experiments: Response functions for electric field reconstruction were retrieved by modelling the spatially-resolved photoelectron emission microscopy data of non-linear two-pulse correlation measurements at the position of both antennas with the coupled oscillator model, which revealed a maximum mode splitting of 16 THz.

The successfully demonstrated coherent back-and-forth transfer of energy between widely separated plasmonic systems is a huge step forward in coherent control and routing of surface plasmons for on-chip applications. In this work the cavity design was limited to Mathieu functions offering modes with two hot-spots. More than two hot-spots can be exploited by using more complex Mathieu functions which correspond to different ellipse parameters and hence the system presented here is suited to be used as a plasmonic hub. For a reliable fabrication of structures with desired properties response functions and spatially resolved mode patterns of single constituents and composite systems should be characterised with spatially-resolved cathodoluminescence [261]. Furthermore, the operating frequency should be lowered to decrease absorption and to enhance Q-factors of the single constituents.

Chapter 2 - Cavity-enhanced energy transfer of quantum emitters

This chapter was concerned with the question to which extent light concentration inside the antenna-decorated elliptic cavities can influence the energy transfer between single quantum emitters which are attached to the widely separated WGM nano-antennas. FDTD simulations revealed that dipolar emitters decay 600 times faster when positioned on-top of the WGM antennas due to the increased local density of states for photons near metallic nano-structures. By assuming an incoherent dipole-dipole interaction and applying the classical dyadic Green's function formalism it was found that the energy transfer rate between the emitters is 10^7 times faster compared to emitters in vacuum separated by the same distance of 1.6 μm. An estimation of absolute energy transfer rates for InAs quantum dots at cryogenic temperatures revealed that approximately 6% of photons emitted by one quantum dot are absorbed by the other quantum dot. This estimation is based on the conservative assumption that the absorption cross-section is similar to the quantum dot size.

By using the dyadic Green's function formalism in the context of quantum electrodynamics, a vacuum Rabi splitting of 1 THz was retrieved. Although such a mode splitting is 26 times larger than in photonic crystal cavities [160], a strong coupling between the quantum emitters cannot be established due to the slightly higher cavity loss rate of about 7 THz. However, a proper assessment of the impact of cavity loss requires the Markovian Lindblad formalism which has not been applied in the present thesis. Furthermore, only a single configuration of the cavity-antenna system was considered and varying several parameters might help to reach the strong coupling regime. These variations include e.g. a reduction of the cavity size, the consideration of reduced plasmon scattering due to decreased sample temperatures, the incorporation of a dielectric embedding medium and switching to operating wavelengths in the telecom regime.

An alternative route to entangled emitters is to exploit their collective interaction according to the *Dicke-effect*, i.e. super- and subradiance [84], in the weak coupling regime: Mutual interaction can lead to either enhanced (superradiant) or suppressed (subradiant) decay of excited emitters. According to literature, entanglement is facilitated by preparing subradiant states since the suppressed decay helps to maintain coherence [205]. Using FDTD simulations, it was found that the enhanced decay rate of one emitter can be quenched by a factor of five due to the

presence of a second emitter attached to the opposite WGM antenna. This value is comparable to that of 1D plasmonic waveguides which theoretically provide entanglement via subradiance [205].

To summarise, light concentration in the plasmonic device presented here is interesting for the investigation of the plasmon-mediated interaction of pre-arranged quantum emitters in both, the weak and strong coupling regime. Placing many emitters in circular or elliptical shaped cavities, and tuning the coupling via emitter distance or cavity loss, might even allow to study incoherent and coherent energy transport, like in light harvesting complexes, with nanometre-resolution by using the technique of 2D Nanoscopy [6].

Chapter 3 - Nano-antenna supported current injection in MIM-junctions

Nanoparticles deposited on Au-insulator-Ta junctions were used as light harvesting units to concentrate electromagnetic energy in the subjacent $30-40$ nm thick Au top-electrode and to facilitate a current flow via above-barrier injection of charge carriers. Tantalum oxide (TaO_x) and aluminium oxide (AlO_x) were used as the insulator, featuring potential barriers of 1.8 eV and 2.8 eV, respectively. Scanning the samples laterally with sub-10 fs laser pulses ($\lambda_0 = 800$ nm) revealed that current injection is restricted to a region of some 100 nm in diameter, smaller than the focal laser spot size (>1 μm). The improved spatial resolution was attributed to the highly non-linear injection process: The injected current as a function of incident laser fluence could be described by a power law with an exponent N of 8.5 (TaO_x) and 11.3 (AlO_x), which highly exceeds the $N \approx 2.5$ dependence measured on thin top-electrodes. With regard to photon energies and barrier heights, the highly non-linear character of the injection process could neither be explained by multi-photon above-barrier injection of charge carriers, which is the dominating excitation channel according to previous research [88, 89], nor by strong field effects at nano-structures, which usually tend to lower the non-linearity [241]. Hence an unexpected current injection mechanism is responsible for the observed behaviour which was identified with numerical methods:

The concentration of light to a small volume in the top-electrode underneath the nano-particle was confirmed by modelling the system with FDTD simulations. They also revealed that the absorbed energy density in this region amounts to

values > 50 eV nm^{-3} for typical pulse energies of 12.5 pJ. In this regime the electron gas is thermalised in less than 10 fs according to the work of Mueller and Rethfeld [220]. This allowed to model the transient current injection with heat-diffusion simulations. The related current injection mechanism is thermionic emission of thermal electrons over the barrier which was modelled according to the Richardson-Dushman equation. Within the scope of the uncertainties, the experimental current-to-fluence dependence was quantitatively reproduced by assuming 3% of absorbed laser pulse energy according to FDTD simulations . This statement is furthermore justified when taking into account that the actual amount of absorption depends on many particular aspects like the unknown gap size between nano-particle and top-electrode, i.e. the thickness of the molecular particle cladding. Hence, extreme light concentration with few-cycle laser pulses facilitated to prepare a system state that is usually encountered in the limit of laser pulses with a temporal duration longer than typical thermalisation times in the low-intensity regime (> 100 fs).

To the best of the author's knowledge the device presented here enables the exploitation of the yet unexplored regime of instantaneous thermalisation for technological applications for the first time, e.g. ultra-fast current injection. According to heat-diffusion simulations the injected transient currents exhibit pulse durations of only some 10 fs despite their thermal character. This is explained by the high energy gradients of the spatial excitation profile (fast diffusion) in combination with the potential barrier that exceeds the single photon energy. The intense and presumably nano-localised current pulses might find application in ultra-fast and spatially selective surface chemistry. However, a reliable operation will require the identification of the yet unknown reason for long term degradation of performance. Another perspective for the device is to exchange the metallic electrodes with less-absorbing material like conductive oxides. This might allow to maintain a coherent character during the excitation so that the intense laser fields can switch the current on and off in the sub-cycle regime on smallest spatial scales. Such phenomena were recently shown on microscopic scales in the strong field regime of light-matter interaction [264].

Chapter 4 - Surface-Enhanced Raman Scattering with dithiol-linked gold nanoparticles

In this chapter the strong light concentration in the gap of adjacent nanoparticles, which were actively linked by rigid alkyne-rich dithiol molecules, was exploited to overcome the low cross-section in Raman scattering experiments. The focus here was on nanoparticle dimer aggregates, featuring a single well-defined interparticle gap. The preparation process yielded an optimum amount of nanoparticle dimers (20% of all aggregates) for an initial dithiol concentration that leads to a total number of 5100 molecules bound to a single nanoparticle and a rather dense surface coverage of one molecule per nm^{-2}. The rigid character of the four alkyne bonds and the dense surface coverage indeed resulted in a well-defined gap size of (1.64 ± 0.35) nm.

The results of spectroscopic measurements are in agreement with the general perception that SERS is most efficient when the product of the field enhancement at the excitation wavelength and at the Stokes-shifted wavelength reaches a maximum [209]: A multi-colour Raman study revealed a maximum alkyne-related signal enhancement at an excitation wavelength of 647 nm, while UV-Vis extinction spectra, probing the plasmonic properties, show a resonant feature near 675 nm. Although the as-prepared dispersions contain a mixture of different nanoparticle aggregates, it was found that these spectroscopic features are dominated by the dimer-related plasmon resonance: The alkyne-related signal enhancement is five times larger than that of a comparative sample in which aggregation was driven by monothiol molecules, leading to five times less nanoparticle dimers. Interestingly, the spectral position of the plasmonic dimer resonance, as retrieved from UV-Vis extinction measurements, could not be reproduced at all with FDTD simulations which predict a resonant feature at 625 nm. The rather large red-shift of 50 nm cannot be assigned to numerical errors.

Further deviations occurred when estimating the number of *effective dimers*, i.e. structural nanoparticle dimers as well as dimer-like resonances in larger aggregates: Using the measured dimer-related extinction and the corresponding absorption cross-section retrieved from FDTD simulations lead to an estimated concentration which was ten times smaller than than the concentration of structural dimers as expected from evaluated TEM images.

Since as-prepared dispersion are utilised the number of molecules attached to

particles stays constant throughout all experiments. By knowing the concentration of effective dimers as retrieved from extinction measurements and by comparing the signal enhancement to a pure dithiol solution, a SERS enhancement factor was calculated that is 50 times smaller than expected from theory. Taking into account that the actual number of structural dimers is expected to be ten times larger, the SERS enhancement is further reduced.

All the above mentioned deviations give reasons for the assumption that the large number of gap-bridging, fully conjugated dithiol molecules built an electrical link that reduces the tunnel barrier of the vacuum gap between the nanoparticles. As reported in literature, the reduced tunnel barrier gives rise to a red-shift of the plasmonic dimer resonance and decreases electric field enhancement, as well as the related absorption cross-section [203].

To summarise, the nanoparticle dimers linked by rigid alkyne-rich dithiol molecules are an interesting device to find a trade-off between structural reliability and strong SERS enhancement: In future experiments the different parameters like gap width and Raman signal enhancement should be monitored while systematically varying the concentration of linker molecules in the aggregation process. Additionally, it would be interesting to study the impact of chemical linkers and the related electrical coupling on plasmonic resonances and local field enhancement in general. An optimisation of the device is especially desirable since the alkyne mode is located in the Raman-silent region of e.g. living cells natural cellular molecules [141] and the device might be used for enhanced imaging applications.

A Appendix

A.1 Specific properties of SPPs at Au-vacuum interfaces in FDTD-simulations

In all projects presented in this thesis gold plays a central role for concentrating light by plasmonic resonances: Due to its chemically inert character it offers a broad range of applications. Therefore, this section introduces in short some important properties of the material itself and the corresponding consequences for surface plasmons at gold-vacuum interfaces. Here, the focus lies on propagating surface plasmon polaritons (SPPs) since the associated length scales of light confinement and propagation lengths provide a basis for the considerations about strong light-matter interaction presented in Chapter 1 and 2.

All subsequent calculations rely on the material data used in the FDTD simulations of plasmonic cavities in Chapter 1 and 2, as well as in light-induced current injection in MIM junctions shown in Chapter 3. The utilised real and imaginary part of the frequency-dependent dielectric function $\varepsilon(\nu)$ are shown in Fig. A.1(a) by the black and red solid line, respectively. These curves emerge from a multi-coefficient fitting model which was matched to the experimental data measured by Johnson and Christy [155] (black and red empty cricles). The utilised fit parameters allow to accurately describe the material in the range of 200 THz (1500 nm) up to 800 THz (375 nm).

For low excitation frequencies up to 430 THz (700 nm) the response of the electronic system to an external stimulus is dominated by the contribution of free electrons. The dynamics in the system can therefore be described by the Drude-Sommerfeld theory ([229], Section 12.1.1). At higher frequencies beyond ≈ 545 THz (550 nm) the photon energy is sufficient to excite electrons from d-bands to s-bands (interband transitions, [229], Section 12.1.2). As a consequence the imaginary part of $\varepsilon(\nu)$ is considerably increased and light is predominantly absorbed. Here it is emphasised that $\varepsilon(\nu)$ around $\nu = 375$ THz is dominated by

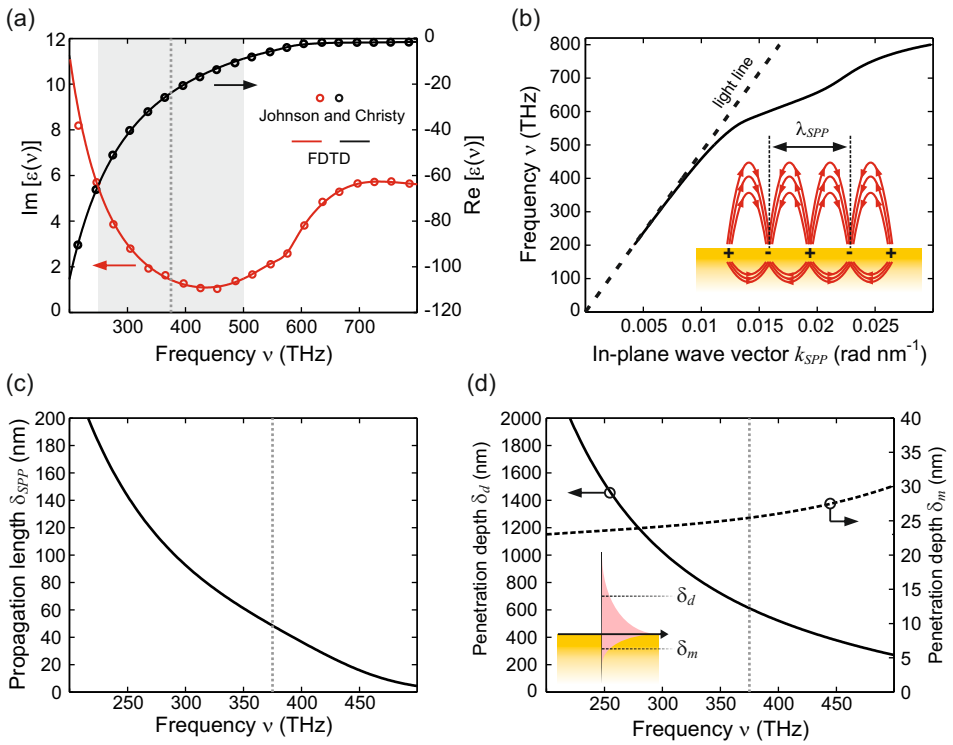

Fig. A.1: Properties of SPPs at a gold-vacuum interface as retrieved from the material data used in FDTD simulations. (a) Real (black solid line) and imaginary (red solid line) part of the dielectric function used in FDTD simulations. The curves emerge from a fit of the experimental data of Johnson and Christy (corresponding empty circels). (b) SPP dispersion relation: The black solid line represents the real part of the in-plane wave vector in euqation (A.1). The dispersion relation of freely propagating light is represented by the black-dashed line. (c) SPP propagation length for $\varepsilon_d = 1$ according to equation (A.2). (d) SPP penetration depth into the dielectric and metal half-space for $\varepsilon_d = 1$ according to (A.3) and (A.4), respectively. Grey vertical dashed lines indicate a frequency of 375 THz (800 nm).

its real part which shows no characteristic feature in the region of 250 THz (600 nm) up to 500 THz (1200 nm) (grey shaded area). This range was evaluated in the FDTD simulations in Chapter 3 on condition that $\varepsilon(\nu)$ can be approximated by a linear function (see Section A.2, equation (A.28)). Since most of the pulse energy in the simulations is spectrally centred around $\nu = 375$ THz the approximation is valid, although deviations can be expected, especially at lower frequencies.

SPPs are collective oscillations of surface charges which are coupled to the electromagnetic waves which, in turn, emerge due to surface charge accumulation.

The properties of these surface waves can be obtained by retrieving the associated wave vector k_{SPP} from the eigenmode of the wave equation at the gold-vacuum interface ([229], Section 12.2). By considering boundary conditions the complex dispersion relation reads [28]:

$$k_{SPP}(\nu) = \frac{2\pi\nu}{c}\sqrt{\frac{\varepsilon_m(\nu)\varepsilon_d(\nu)}{\varepsilon_m(\nu)+\varepsilon_d(\nu)}}, \tag{A.1}$$

in which $\varepsilon_d(\nu)$ is the dielectric function of vacuum ($\varepsilon_d(\nu)$=1) while $\varepsilon_m(\nu)$ describes that of gold (see A.1(a)). For reasons of generality $\varepsilon_d(\nu)$ is not set to unity in the upcoming equations. The real part of the wave vector is shown in Fig. A.1(b) as a function of frequency (solid line), together with the dispersion relation of light in vacuum (dashed line). The wavelength $\lambda_{SPP} = 2\pi k_{SPP}^{-1}$ is shorter than that of freely propagating light and the wave is hence bound to the interface [28]. Deviations from the light-like character are most prominent at high frequencies where absorption dominates the electron dynamics and therefore SPP propagation is hampered. The propagation length δ_{SPP} of an SPP, i.e. the distance over which the electromagnetic intensity decays to e^{-1} of its initial value, is given by the imaginary part of the complex wave vector [28]:

$$\delta_{SPP} = \frac{1}{2\cdot \mathrm{Im}\left[k_{SPP}(\nu)\right]} = \frac{\mathrm{Re}[\varepsilon_m(\nu)]^2}{k_0\cdot \mathrm{Im}[\varepsilon_m(\nu)]}\left(\frac{\mathrm{Re}[\varepsilon_m(\nu)]+\varepsilon_d(\nu)}{\mathrm{Re}[\varepsilon_m(\nu)]\varepsilon_d(\nu)}\right)^{\frac{3}{2}}, \tag{A.2}$$

in which k_0 is the wave vector in vacuum. The propagation length for an SPP at a gold-vacuum interface is shown in Fig. A.1(c): SPP propagation is hampered by absorption at high frequencies and the propagation length approaches zero near the interband transitions. For lower frequencies the propagation length is enhanced and δ_{SPP} exhibits values greater than 200 μm in the spectral range of telecom frequencies near 200 THz (1500 nm). At lower frequencies the electric field is pushed out of the metal substrate (see Fig. A.1(d)) so that the SPP is less affected by absorption. For operating frequencies of a Ti:sapphire laser (375 THz) the propagation length amounts to ≈ 50 μm.

To achieve a stronger coupling of plasmonic resonances and to enhance light-matter interaction in the Chapters 1 and 2 it is tempting to operate the systems at frequencies $\nu < 250$ in order to improve the cavity Q-factor. However, by

considering the penetration depth of the electric field into the dielectric half-space, i.e. e^{-1}-decay length of intensity, the cavity wall height needs to be considerably increased then. The penetration depth of the field into the dielectric (δ_d) and the metal (δ_m) can be calculated according to

$$\delta_d(\nu) = \frac{1}{k_0} \left| \frac{\mathrm{Re}[\varepsilon_m(\nu)] + \varepsilon_d(\nu)}{\varepsilon_d(\nu)^2} \right|^{\frac{1}{2}} \tag{A.3}$$

$$\delta_m(\nu) = \frac{1}{k_0} \left| \frac{\mathrm{Re}[\varepsilon_m(\nu)] + \varepsilon_d(\nu)}{\mathrm{Re}[\varepsilon_m(\nu)]^2} \right|^{\frac{1}{2}}. \tag{A.4}$$

The penetration depth into the metal and vacuum half-space are shown by the dashed and solid black lines in Fig. A.1(d), respectively. While δ_m hardly changes across the pictured frequency range δ_d is altered considerably. For ever lower frequencies δ_d approaches, and even exceeds, the corresponding vacuum wavelength since the SPP approaches the light line in the dispersion relation.

Operating the cavities at telecom frequencies hence requires rather high cavity walls to prevent loss by interaction of SPPs with the upper edges. According to equation (A.3) the penetration depth can be reduced by using dielectrics with a high refractive index. However, this will also decrease the propagation length according to (A.2). Hence, all parameters have to be weighed for optimum operation of the desired functionality.

A.2 Retrieving the nanoparticle systems of MIM experiments

The specific nanoparticles which facilitated laser-induced current injection in metal-insulator-metal junctions have been found among 10^6 nanoparticles by comparing the investigated features of the spatially-resolved injected current and back-reflected light to SEM images. Measurements and SEM images are taken at different zoom levels so that the close-up of a nanoparticle can also be related to overview images showing an area of approximately 0.09 mm^2. This procedure has been applied to both MIM systems presented in Chapter 3 and the results for the TaO_x-junction are shown in Fig. A.2 while the results for the AlO_x-junction are presented in Fig. A.3.

It should be noted that comparing the reflectivity of the bare surface to that at the position of the nanoparticle provides no absolute information about the amount of energy that has been absorbed by the particle-electrode system. For instance, the reflectivity measured at the nanoparticle position decreases by 28% in the case of the AlO_x-junction. However, one should take into account that the nanoparticle will inject surface plasmons and the associated energy cannot be monitored in the back-reflection geometry. Furthermore, the Cassegrain objective can only collect reflected light in a limited angular range. The objective also blocks light that is reflected under normal incidence due to the geometry of the two spherical mirrors. As a consequence, an appreciable amount of energy will be blocked especially for dipolar emission.

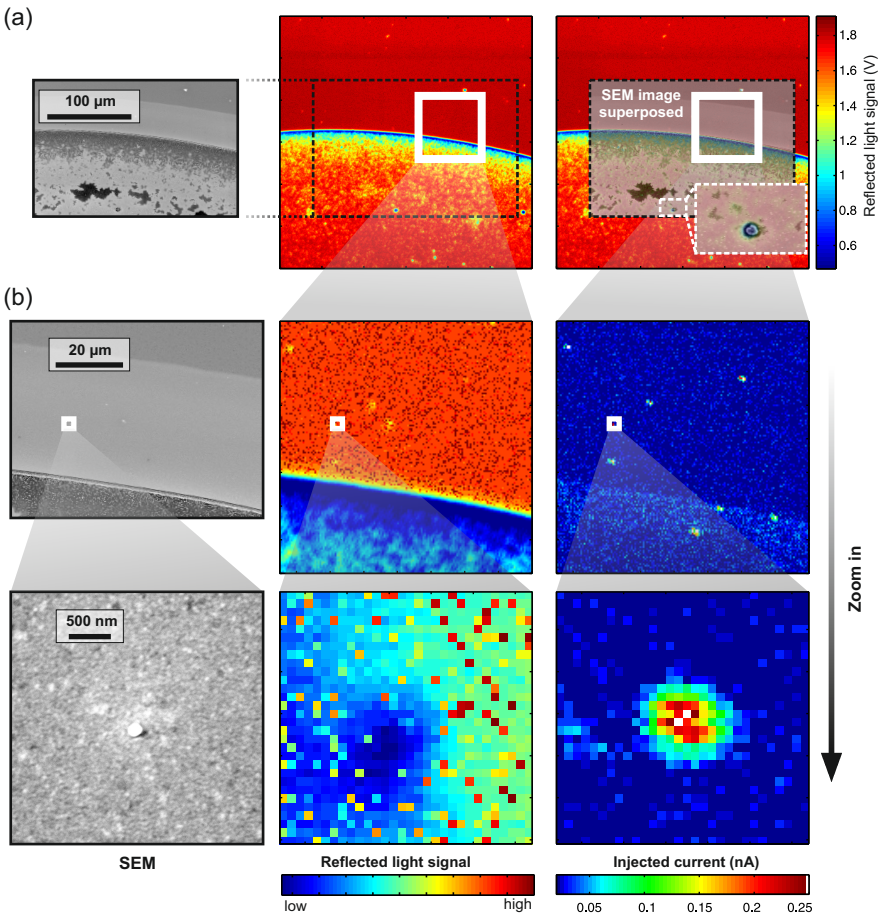

Fig. A.2: Retrieving the nanoparticles used for laser-induced current injection in the TaO_x-junction: SEM images, spatially resolved current injection and the collected reflected light. (a) Overview images. (b) Different zoom levels.

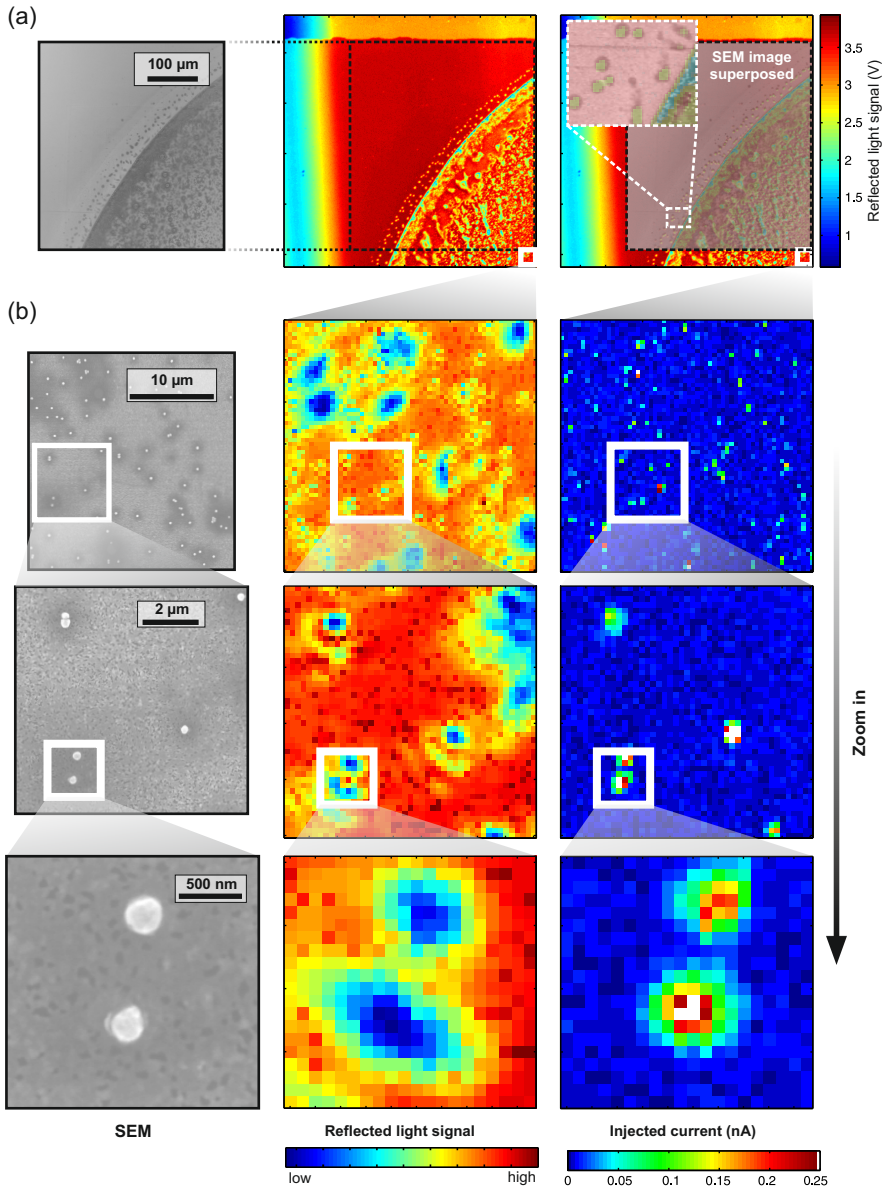

Fig. A.3: Retrieving the nanoparticles used for laser-induced current injection in the AlO_x-junction: SEM images, spatially resolved current injection and the collected reflected light. (a) Overview images. (b) Different zoom levels.

A.3 Derivation of the spatially-resolved energy density for pulsed laser excitation

This section is dedicated to the derivation of the spatially-resolved absorbed energy density

$$e_{abs}(\mathbf{r}) = \int_0^\infty \frac{\omega_0 \varepsilon_0 \, \mathrm{Im}(\varepsilon_r(\mathbf{r}, \omega_0))}{\pi} \left| \mathbf{R}(\mathbf{r}, \omega) \cdot E_{inj}^{(+)}(\omega) \right|^2 \mathrm{d}\omega, \tag{A.5}$$

as it is used in Chapter 3 for the evaluation of FDTD and heat diffusion simulations. In this equation ω_0 is the central angular frequency of the incident laser pulse, ε_0 the vacuum permittivity, ε_r the relative permittivity, $\mathbf{R}(\mathbf{r}, \omega)$ the complex amplitude of the response function obtained from FDTD simulations and $E_{inj}^{(+)}(\omega)$ the positive part of the injected laser spectrum ([86], section 1.1).

Retrieving quantities from simulations in SI units is often cumbersome and the detailed derivation is motivated by the following two issues: First, textbooks often concentrate on continuous wave excitation which restricts the observable to an absorbed power density (see e.g. equation (4.5) in this thesis) that is not suited to describe the time-limited energy deposition of a laser pulse. Second, it may be confusing whether the spectrum at positive frequencies or the spectrum of the entire frequency domain needs to be inserted in equations, especially when the definition of variables and quantities is slovenly. For instance, if the electric field strength of the laser pulse in time-domain is known, the absolute amplitude of the positive frequency spectrum $\left| E^{(+)}(\omega) \right|$ depends on the definition of the applied Fourier transformation. In order to derive measurable quantities in both, time- and frequency-domain, they have to obey Parseval's theorem ([86], section 1.1), which depends on the particular transformation.

First of all Poynting's theorem will be derived for a medium that is homogeneous and linear, but exhibits dispersion and loss. To find an expression of the related energy sink the derivation closely follows the corresponding derivation in Jackson's textbook *Classical Electrodynamics* ([151], section 6.8) and in Orfanidis' script *Electromagnetic Waves and Antennas* ([230], section 1.11). The energy sink is then related to pulsed laser excitation. Finally, a well-defined expression for the absorbed energy density is presented which obeys Parseval's theorem. During the steps an important approximation will be justified that allows to treat the

problem in the small-bandwidth limit although an 8 fs laser pulse is used in the evaluation of FDTD simulations.

The laser pulse is expressed through the real part of the electric field:

$$\mathscr{E}(\mathbf{r},t) = \mathbf{E}_0(\mathbf{r},t)\cos(\omega_0 t), \tag{A.6}$$

in which $\mathbf{E}_0(\mathbf{r},t)$ is the pulse envelope and ω_0 the central angular frequency. The calligraphic notation $\mathscr{E}$ emphasizes that the vectorial quantity is made up of spectral amplitudes at positive and negative frequencies. The representation in time- and frequency-domain is linked by the Fourier transformation:

$$\begin{aligned} \mathscr{E}(\mathbf{r},\omega) &= \int_{-\infty}^{\infty} \mathscr{E}(\mathbf{r},t)\mathrm{e}^{-\mathrm{i}\omega t}dt \\ \mathscr{E}(\mathbf{r},t) &= \frac{1}{2\pi}\int_{-\infty}^{\infty} \mathscr{E}(\mathbf{r},\omega)\mathrm{e}^{\mathrm{i}\omega t}d\omega. \end{aligned} \tag{A.7}$$

Since the electric field $\mathscr{E}(\mathbf{r},t)$ is a real quantity its spectrum $\mathscr{E}(\mathbf{r},\omega)$ can be split into a positive and a negative half-space, which both independently carry the entire information of the laser pulse ([86], section 1.1):

$$\mathscr{E}(\mathbf{r},\omega) = E^{(+)}(\mathbf{r},\omega) + E^{(-)}(\mathbf{r},\omega) \tag{A.8}$$

in which

$$\begin{aligned} E^{(+)}(\mathbf{r},\omega) &= \mathscr{E}(\mathbf{r},\omega) && \text{for } \omega \geq 0 \text{ and} \\ E^{(-)}(\mathbf{r},\omega) &= 0 && \text{for } \omega < 0. \end{aligned}$$

The spectral amplitude $E^{(+)}(\mathbf{r},\omega)$ is a complex quantity. In sophisticated calculations it is recommended to write the temporal electric field as a complex quantity, too:

$$\tilde{\mathbf{E}}(\mathbf{r},t) = \tilde{\mathbf{E}}_0(\mathbf{r},t)\mathrm{e}^{-\mathrm{i}\omega_0 t}, \tag{A.9}$$

The tilde denotes a complex quantity in the following steps. The slowly varying temporal amplitude $\tilde{\mathbf{E}}_0(\mathbf{r},t)$ contains a small residual phase while the oscillating

field is dominated by the central angular frequency ω_0. Taking the real part of (A.9) will directly result in (A.6) if a residual phase is absent.

Light-matter interaction classical electrodynamics is described by Maxwell's equations:

$$\nabla \times \mathscr{E}(\mathbf{r},t) = -\frac{\partial}{\partial t}\mathscr{B}(\mathbf{r},t) \qquad \text{Faraday's law} \qquad (A.10)$$

$$\nabla \times \mathscr{H}(\mathbf{r},t) = \mathscr{J}_i(\mathbf{r},t) + \frac{\partial}{\partial t}\mathscr{D}(\mathbf{r},t) \qquad \text{Ampére's law} \qquad (A.11)$$

$$\nabla \mathscr{D}(\mathbf{r},t) = \rho \qquad \text{Gauss's law} \qquad (A.12)$$

$$\nabla \mathscr{B}(\mathbf{r},t) = 0 \qquad \text{no magnetic monpoles.} \qquad (A.13)$$

Here, it is assumed that the current density $\mathscr{J}_i(\mathbf{r},t)$ is exclusively induced by the applied electric field of the laser pulses and external source currents are absent. The charge density ρ in Gauss's law is the volume charge density. In dielectric materials the interaction of light and matter is commonly described via the polarisation of bound charges induced by the electric field:

$$\mathscr{P}(\mathbf{r},t) = \varepsilon_0 \int_{-\infty}^{t} \chi_e(t-\tau)\mathscr{E}(\mathbf{r},\tau)d\tau = \varepsilon_0 \int_{-\infty}^{\infty} \chi_e(t-\tau)\mathscr{E}(\mathbf{r},\tau)d\tau. \qquad (A.14)$$

Writing $\mathscr{P}(\mathbf{r},t)$ as a convolution indicates the presence of dispersion, i.e. the polarisation at time t is influenced by the non-instantaneous response upon excitation at time $\tau < t$. In this connection it is assumed that the electronic susceptibility $\chi_e(t)$ is homogenous over all space and hence does not depend on a specific position $\mathbf{r}$. The susceptibility of a physical system is causal and obeys the Kramer-Kronig relationship ([151], section 7.10). This allows to extend the upper border of the integral in (A.14) to infinity since the material can only respond subsequently to an excitation and hence $\chi_e(t<0) = 0$.

Another way to express the response of a material to an external field is given by the electric displacement field $\mathscr{D}(\mathbf{r},t)$ which accounts for both, bound and free charge carriers:

$$\mathscr{D}(\mathbf{r},t) = \varepsilon_0 \int_{-\infty}^{t} \varepsilon_r(t-\tau)\mathscr{E}(\mathbf{r},\tau)d\tau = \varepsilon_0 \int_{-\infty}^{\infty} \varepsilon_r(t-\tau)\mathscr{E}(\mathbf{r},\tau)d\tau, \tag{A.15}$$

in which the dielectric function $\varepsilon(t)$ has been separated into the vacuum permittivity ε_0 and the relative permittivity $\varepsilon_r(t)$. By writing the displacement field $\mathscr{D}(\mathbf{r},t)$ as the sum of the electric field $\mathscr{E}(\mathbf{r},t)$ and the polarisation $\mathscr{P}(\mathbf{r},t)$, i.e.

$$\mathscr{D}(\mathbf{r},t) = \varepsilon_0\mathscr{E}(\mathbf{r},t) + \mathscr{P}(\mathbf{r},t), \tag{A.16}$$

the dielectric function can be written as:

$$\varepsilon(t) = \varepsilon_0\delta(t) + \varepsilon_0\chi_e(t) \tag{A.17}$$

The equations (A.14), (A.15) and (A.17) are transformed into frequency-domain by making use of the convolutions theorem:

$$\mathscr{P}(\mathbf{r},\omega) = \varepsilon_0\chi_e(\omega)\mathscr{E}(\mathbf{r},\omega) \tag{A.18}$$

$$\mathscr{D}(\mathbf{r},\omega) = \varepsilon_0\varepsilon_r(\omega)\mathscr{E}(\mathbf{r},\omega) \tag{A.19}$$

$$\varepsilon(\omega) = \varepsilon_0 \underbrace{(1+\chi_e(\omega))}_{\varepsilon_r(\omega)} \tag{A.20}$$

The same procedure can be applied to Ohm's law which connects the induced electric current density $\mathscr{J}_i(\mathbf{r},t)$ with the applied electric field $\mathscr{E}(\mathbf{r},t)$ over the conductivity $\sigma(t)$ ([151], section 7.5):

$$\mathscr{J}_i(\mathbf{r},\omega) = \sigma(\omega)\mathscr{E}(\mathbf{r},\omega) \tag{A.21}$$

The temporal derivative of the electric displacement field in Ampére's law represents a polarisation current of bound electrons. To simplify the derivation the dynamics of conduction electrons is included in the dielectric function in order to obtain a single material parameter. Therefore, the Fourier transformation is applied to both sides of Ampére's law:

$$\nabla \times \mathscr{H}(\mathbf{r},\omega) = \mathscr{J}_i(\mathbf{r},\omega) - \mathrm{i}\omega\mathscr{D}(\mathbf{r},\omega). \tag{A.22}$$

Inserting (A.19) and (A.21) into equation (A.22) gives:

$$\nabla \times \mathscr{H}(\mathbf{r},\omega) = -\mathrm{i}\omega \underbrace{\left(\varepsilon(\omega) - \frac{\sigma(\omega)}{\mathrm{i}\omega}\right)}_{\varepsilon_{dl}} \mathscr{E}(\mathbf{r},\omega). \tag{A.23}$$

The dielectric function $\varepsilon_{dl}(\omega)$ describes the response of the combined system of bound electrons and conduction electrons and it is hence suited to model the response of gold in the visible and NIR spectral range. To keep notation simple the subscript dl is omitted in the following derivation and $\varepsilon(\omega)$ includes the contribution from bound and free charge carriers. The inverse Fourier transformation of (A.23) leads to an alternative version of Ampére's law,

$$\nabla \times \mathscr{H}(\mathbf{r},t) = \frac{\partial}{\partial t}\mathscr{D}(\mathbf{r},t), \tag{A.24}$$

in which $\mathscr{D}(\mathbf{r},t)$ now incorporates the so-called *Drude-Lorentz model*.

In classical electrodynamics energy conservation is described by Poynting's theorem. The power current density flowing through the surface ∂V of an arbitrary volume V can be represented by the divergence of the Poynting vector $\mathscr{S}(\mathbf{r},t) = \mathscr{E}(\mathbf{r},t) \times \mathscr{H}(\mathbf{r},t)$ ([151], section 6.7):

$$\begin{aligned} \nabla\mathscr{S}(\mathbf{r},t) &= \mathscr{H}(\mathbf{r},t)\,(\nabla \times \mathscr{E}(\mathbf{r},t)) - \mathscr{E}(\mathbf{r},t)\,(\nabla \times \mathscr{H}(\mathbf{r},t)) \\ &= -\mathscr{H}(\mathbf{r},t)\left(\frac{\partial}{\partial t}\mathscr{B}(\mathbf{r},t)\right) - \mathscr{E}(\mathbf{r},t)\left(\frac{\partial}{\partial t}\mathscr{D}(\mathbf{r},t)\right). \end{aligned} \tag{A.25}$$

In a non-dispersive medium the right-hand side of (A.25) is usually written as a rate that describes the change of the energy density of the electromagnetic field inside the volume V. Therefore, $-\mathscr{E}\dot{\mathscr{D}}$ is often written as the time derivative of $\mathscr{E}\mathscr{D}/2$. Here, this approach is not allowed since the electric field is incorporated in the convolution of equation (A.15). Due to dispersion, $\varepsilon(t)$ is not an instantaneous response and hence cannot be written in terms of the Dirac delta-function $\delta(t)$.

To give equation (A.25) the form of a continuity equation that explicitly describes the loss of energy, which is transferred to the electronic system of the

material, the term $-\mathscr{E}\dot{\mathscr{D}}$ is further examined. Likewise, all the following steps can be applied to the magnetic field term $-\mathscr{H}\dot{\mathscr{B}}$ in an analogous manner. The temporal derivative of the electric displacement $\mathscr{D}$ field can be written as:

$$\frac{\partial}{\partial t}\mathscr{D}(\mathbf{r},t) = \int_{-\infty}^{\infty} \frac{\partial}{\partial t}\left[\varepsilon(t-\tau)\right]\cdot\mathscr{E}(\mathbf{r},\tau)d\tau. \tag{A.26}$$

By using the Fourier transformation the temporal derivative of the dielectric function reads:

$$\frac{\partial}{\partial t}\varepsilon(t) = -\frac{\mathrm{i}}{2\pi}\int_{-\infty}^{\infty}\omega\varepsilon(\omega)\mathrm{e}^{-\mathrm{i}\omega t}d\omega. \tag{A.27}$$

To further evaluate the integral in (A.27) it is assumed the the envelope of the laser pulse $\tilde{\mathbf{E}}_0(\mathbf{r},t)$ in (A.9) is a slowly varying function in time. More precisely, it varies slowly relative to both, the inverse of the centre frequency ω_0 and the inverse of the frequency range over which $\varepsilon(\omega)$ changes appreciably ([151], section 6.8). The corresponding spectrum $\mathscr{E}(\mathbf{r},\omega)$ located at ω_0 will be narrow, i.e. $\Delta\omega \ll \omega_0$, and hence the term $\omega\varepsilon(\omega)$ in (A.27) is expanded in a Taylor series around ω_0:

$$\omega\varepsilon(\omega) = \omega_0\varepsilon(\omega_0) + \left.\frac{d(\omega\varepsilon(\omega))}{d\omega}\right|_{\omega=\omega_0}(\omega-\omega_0) + O^{(2)} + \ldots \tag{A.28}$$

Terms of order $O^{(2)}$ and higher will be neglected. With this approximation equation (A.27) can be written as:

$$\begin{aligned}\frac{\partial}{\partial t}\varepsilon(t) &= \frac{1}{2\pi}\int_{-\infty}^{\infty}\left[-\mathrm{i}\omega_0\varepsilon(\omega_0) + \left.\frac{d(\omega\varepsilon(\omega))}{d\omega}\right|_{\omega=\omega_0}(-\mathrm{i}\omega+\mathrm{i}\omega_0)\right]\mathrm{e}^{-\mathrm{i}\omega t}d\omega \\ &= -\mathrm{i}\omega_0\varepsilon(\omega_0)\delta(t) + \left.\frac{d(\omega\varepsilon(\omega))}{d\omega}\right|_{\omega=\omega_0}\left(\frac{\partial}{\partial t}+\mathrm{i}\omega_0\right)\delta(t)\end{aligned} \tag{A.29}$$

Using the above approximation for evaluation of the FDTD simulations in Section 3.3.4 is justified by the fact that the dielectric function near $\nu_0 = 375$ THz is dominated its real part which shows a rather linear behaviour in the range of

the 8 fs laser spectrum (see Fig. A.1(a)). Inserting the result of the approximation into equation (A.26) and replacing the real electric field by its complex notation given in (A.9) yields:

$$\begin{aligned}\frac{\partial \tilde{\mathbf{D}}(\mathbf{r},t)}{\partial t} &= \int_{-\infty}^{\infty} \left[-\mathrm{i}\omega_0 \varepsilon(\omega_0)\delta(t-\tau) + \left.\frac{d(\omega\varepsilon(\omega))}{d\omega}\right|_{\omega=\omega_0} \left(\frac{\partial}{\partial t} + \mathrm{i}\omega_0\right)\delta(t-\tau)\right] \cdot \ldots \\ &\quad \ldots \cdot \tilde{\mathbf{E}}_0(\mathbf{r},\tau)\mathrm{e}^{-\mathrm{i}\omega_0\tau} d\tau \\ &= \left(-\mathrm{i}\omega_0 \varepsilon(\omega_0) + \left.\frac{d(\omega\varepsilon(\omega))}{d\omega}\right|_{\omega=\omega_0} \left(\frac{\partial}{\partial t} + \mathrm{i}\omega_0\right)\right) \tilde{\mathbf{E}}_0(\mathbf{r},t)\mathrm{e}^{-\mathrm{i}\omega_0 t} \\ &= \left(-\mathrm{i}\omega_0 \varepsilon(\omega_0)\tilde{\mathbf{E}}_0(\mathbf{r},t) + \left.\frac{d(\omega\varepsilon(\omega))}{d\omega}\right|_{\omega=\omega_0} \left[\frac{\partial}{\partial t}\tilde{\mathbf{E}}_0(\mathbf{r},t)\right]\right) \mathrm{e}^{-\mathrm{i}\omega_0 t}\end{aligned} \tag{A.30}$$

By substituting the dielectric function of the Drude-Lorentz model as $\varepsilon(\omega_0) = \mathrm{Re}[\varepsilon(\omega_0)] + \mathrm{i}\ \mathrm{Im}[\varepsilon(\omega_0)]$ in the previous equation, one obtains:

$$\begin{aligned}\frac{\partial \tilde{\mathbf{D}}(\mathbf{r},t)}{\partial t} = \big(&-\mathrm{i}\omega_0 \mathrm{Re}[\varepsilon(\omega_0)]\tilde{\mathbf{E}}_0(\mathbf{r},t) + \omega_0 \mathrm{Im}[\varepsilon(\omega_0)]\tilde{\mathbf{E}}_0(\mathbf{r},t) + \ldots \\ &\ldots + \left.\frac{d(\omega\varepsilon(\omega))}{d\omega}\right|_{\omega=\omega_0} \left[\frac{\partial}{\partial t}\tilde{\mathbf{E}}_0(\mathbf{r},t)\right]\big)\mathrm{e}^{-\mathrm{i}\omega_0 t}\end{aligned} \tag{A.31}$$

The imaginary part of the dielectric function incorporates the conductance according to (A.25). A similar equation can be derived for the magnetic fields $\mathscr{H}(\mathbf{r},t)$ and $\mathscr{B}(\mathbf{r},t)$. To retrieve measurable quantities time-averaging is applied to the Poynting vector in (A.25):

$$\begin{aligned}\nabla \langle \mathscr{S}(\mathbf{r},t)\rangle &= -\left\langle \mathscr{E}(\mathbf{r},t)\dot{\mathscr{D}}(\mathbf{r},t)\right\rangle - \left\langle \mathscr{H}(\mathbf{r},t)\dot{\mathscr{B}}(\mathbf{r},t)\right\rangle \\ \Leftrightarrow \frac{1}{2}\nabla \mathrm{Re}\left[\tilde{\mathbf{S}}(\mathbf{r},t)\right] &= -\frac{1}{2}\mathrm{Re}\left[\tilde{\mathbf{E}}^*(\mathbf{r},t)\frac{\partial}{\partial t}\tilde{\mathbf{D}}(\mathbf{r},t)\right] - \frac{1}{2}\mathrm{Re}\left[\tilde{\mathbf{H}}^*(\mathbf{r},t)\frac{\partial}{\partial t}\tilde{\mathbf{B}}(\mathbf{r},t)\right],\end{aligned} \tag{A.32}$$

in which $\tilde{\mathbf{S}}(\mathbf{r},t)$, $\tilde{\mathbf{E}}^*(\mathbf{r},t)$, $\tilde{\mathbf{D}}(\mathbf{r},t)$, $\tilde{\mathbf{H}}^*(\mathbf{r},t)$ and $\tilde{\mathbf{B}}(\mathbf{r},t)$ are phasor-like quantities according to (A.9) and the asterisk denotes complex conjugation. The first term on the right hand side is evaluated as follows:

$$-\frac{1}{2}\mathrm{Re}\left[\tilde{\mathbf{E}}^*(\mathbf{r},t)\frac{\partial}{\partial t}\tilde{\mathbf{D}}(\mathbf{r},t)\right] = \ldots$$
$$\ldots\frac{1}{2}\mathrm{Re}\left(\{\omega_0\mathrm{Im}[\varepsilon(\omega_0)] - \mathrm{i}\omega_0\mathrm{Re}[\varepsilon(\omega_0)]\}\,\tilde{\mathbf{E}}_0^*(\mathbf{r},t)\tilde{\mathbf{E}}_0(\mathbf{r},t)\right) + \ldots \qquad \text{(A.33)}$$
$$\ldots + \left.\frac{d(\omega\varepsilon(\omega))}{d\omega}\right|_{\omega=\omega_0}\left[\tilde{\mathbf{E}}_0^*(\mathbf{r},t)\frac{\partial}{\partial t}\tilde{\mathbf{E}}_0(\mathbf{r},t)\right],$$

and hence

$$-\frac{1}{2}\mathrm{Re}\left[\tilde{\mathbf{E}}^*(\mathbf{r},t)\frac{\partial}{\partial t}\tilde{\mathbf{D}}(\mathbf{r},t)\right] = \ldots$$
$$\frac{1}{2}\omega_0\mathrm{Im}[\varepsilon(\omega_0)]\left|\tilde{\mathbf{E}}_0(\mathbf{r},t)\right|^2 + \frac{\partial}{\partial t}\left(\mathrm{Re}\left[\frac{1}{4}\left.\frac{d(\omega\varepsilon(\omega))}{d\omega}\right|_{\omega=\omega_0}\right]\left|\tilde{\mathbf{E}}_0(\mathbf{r},t)\right|^2\right). \qquad \text{(A.34)}$$

Repeating the same steps for the magnetic part leads to Poynting's theorem:

$$\nabla\underbrace{\frac{1}{2}\mathrm{Re}\left[\tilde{\mathbf{S}}(\mathbf{r},t)\right]}_{\mathbf{j}_{en}} + \ldots$$
$$\ldots + \frac{\partial}{\partial t}\left(\underbrace{\mathrm{Re}\left[\frac{1}{4}\left.\frac{d(\omega\varepsilon(\omega))}{d\omega}\right|_{\omega=\omega_0}\right]\left|\tilde{\mathbf{E}}_0(\mathbf{r},t)\right|^2 + \mathrm{Re}\left[\frac{1}{4}\left.\frac{d(\omega\mu(\omega))}{d\omega}\right|_{\omega=\omega_0}\right]\left|\tilde{\mathbf{H}}_0(\mathbf{r},t)\right|^2}_{\rho_{en}}\right)$$
$$\ldots = -\frac{1}{2}\omega_0\mathrm{Im}[\varepsilon(\omega_0)]\left|\tilde{\mathbf{E}}_0(\mathbf{r},t)\right|^2 - \frac{1}{2}\omega_0\mathrm{Im}[\mu(\omega_0)]\left|\tilde{\mathbf{H}}_0(\mathbf{r},t)\right|^2 \qquad \text{(A.35)}$$

According to (A.35), energy conservation is described by the energy current density $\mathbf{j}_{en}$ and the energy density ρ_{en} of the electromagnetic fields, while the terms on the right hand side of the equation are interpreted as energy sinks. Since only non-magnetic materials are considered in the present thesis the total loss is described by the absorbed power density:

$$p_{abs}(\mathbf{r},t) = \frac{1}{2}\omega_0\mathrm{Im}[\varepsilon(\omega_0)]\left|\tilde{\mathbf{E}}_0(\mathbf{r},t)\right|^2, \qquad [p_{abs}] = \frac{\mathrm{W}}{\mathrm{m}^3} \qquad \text{(A.36)}$$

in which $\tilde{\mathbf{E}}_0(\mathbf{r},t)$ is the slowly varying envelope of the electric field. Equation (A.36) is similar to the well-known description of the temporal intensity of a laser pulse $I(\mathbf{r},t)$ given in units of W m^{-2}:

$$I(\mathbf{r},t) = \frac{1}{2}\varepsilon_0 cn \left|\tilde{\mathbf{E}}_0(\mathbf{r},t)\right|^2, \qquad [I(\mathbf{r},t)] = \frac{\mathrm{W}}{\mathrm{m}^2} \tag{A.37}$$

in which n as the refractive index and c as the speed of light. Integrating (A.37) over all times then gives the fluence of the pulse (energy per unit area). The amount energy is a measurable quantity and the associated information should be accessible in both, time- and frequency-domain. This behaviour is formally described by Parseval's theorem which can be written as:

$$\int_{-\infty}^{\infty} I(\mathbf{r},t)dt = \frac{1}{2\pi}\int_{-\infty}^{\infty} I(\mathbf{r},\omega)d\omega \tag{A.38}$$

Parseval's theorem as described in equation (A.38) is linked to the definition of the Fourier transformations given in (A.7). Other definitions of the transformations demand an adapted formulation of Parseval's theorem. $I(\mathbf{r},\omega)$ is the spectral intensity and it is expressed by:

$$I(\mathbf{r},\omega) = \frac{\varepsilon_0 cn}{\pi}\left|\tilde{\mathbf{E}}^{(+)}(\mathbf{r},\omega)\right|^2, \qquad [I(\mathbf{r},\omega)] = \frac{\mathrm{Js}}{\mathrm{m}^2} \tag{A.39}$$

The same formalism holds for the derived absorbed power density in equation (A.36) since it is also a measurable quantity. By considering Parseval's theorem and (A.36) the absorbed energy density in the frequency-domain can be written as:

$$e_{abs} = \int_0^{\infty} \frac{\omega_0\varepsilon_0 \mathrm{Im}[\varepsilon_r(\omega_0)]}{\pi}\left|\tilde{\mathbf{E}}^{(+)}(\mathbf{r},\omega)\right|^2 d\omega, \qquad [e_{abs}] = \frac{\mathrm{J}}{\mathrm{m}^3} \tag{A.40}$$

Finally, it has to be taken into account that the spatially-resolved response function of the FDTD simulation $\mathbf{R}(\mathbf{r},\omega)$ which relates the electric field amplitude $\tilde{\mathbf{E}}^{(+)}(\mathbf{r},\omega)$ at the position $\mathbf{r}$ to the peak amplitude $E_{inj}^{(+)}(\omega)$ injected into the simulation. Hence, the spatially resolved energy density is given by equation (A.5):

$$e_{abs}(\mathbf{r}) = \int_{-\infty}^{\infty} \frac{\omega_0 \varepsilon_0 \, \mathrm{Im}(\varepsilon_r(\mathbf{r}, \omega_0))}{\pi} \left| \mathbf{R}(\mathbf{r}, \omega) \cdot E_{inj}^{(+)}(\omega) \right|^2 \mathrm{d}\omega. \tag{A.41}$$

A.4 Electric near-field distributions supporting the plasmonic Tavis-Cummings model

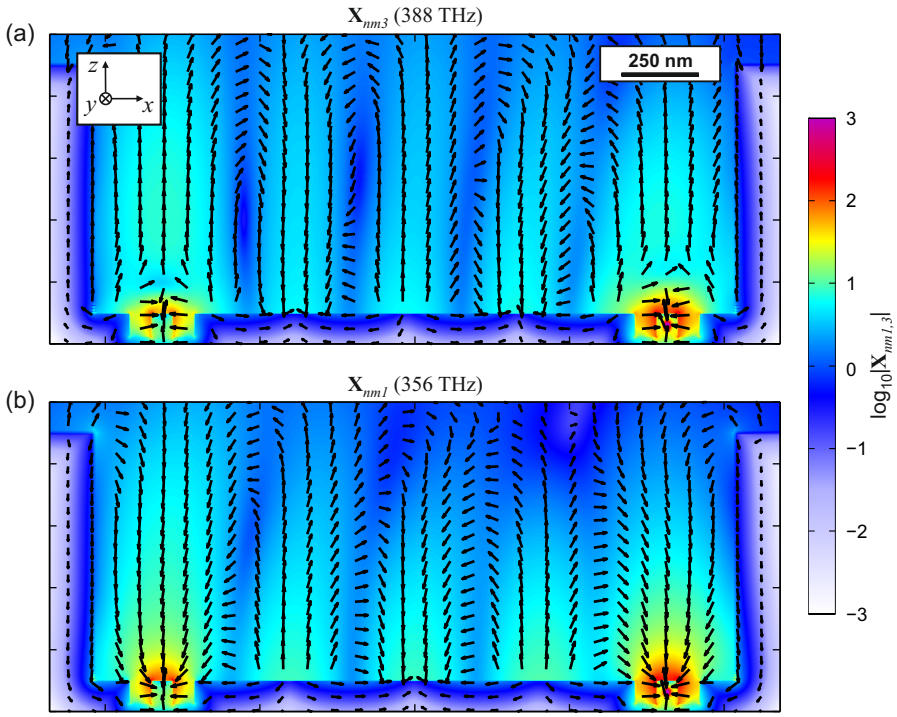

Fig. A.4: Near-field distribution of selected eigenmodes in the coupled antenna-EPAC system. (a) High energy eigenmode $\mathbf{X}_{nm3}$ as retrieved by the imaginary part of the response function $\mathbf{R}(x,z,\nu =$ 388 THz). (b) Low energy eigenmode $\mathbf{X}_{nm1}$ as retrieved by the imaginary part of the response function $\mathbf{R}(x,z,\nu =$ 365 THz). The contour plot in the background represents the overall field amplitudes $\mathbf{X}_{nm3}$ and $\mathbf{X}_{nm1}$. All arrows and the contour plots are scaled according to the decadic logarithm.

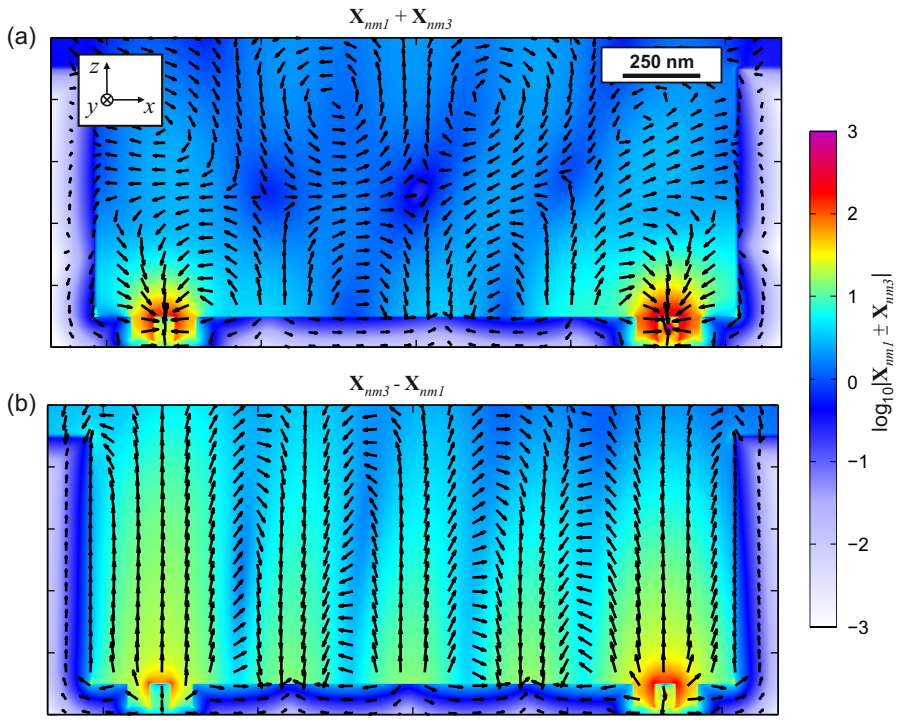

Fig. A.5: Near-field distribution of the superposition of the Tavis-Cummings eigenmodes$\mathbf{X}_{nm3}$ and $\mathbf{X}_{nm1}$ in the coupled antenna-EPAC system. (a) Symmetric superposition $\mathbf{X}_{nm1} + \mathbf{X}_{nm3}$. (b) Anti-symmetric superposition $\mathbf{X}_{nm3} - \mathbf{X}_{nm1}$. All arrows and the contour plots are scaled according to the decadic logarithm.

Bibliography

[1] http://www.independent.co.uk/arts-entertainment/books/features/quantum-theory-via-40-tonne-trucks-how-science-writing-became-popular-1866934.html, Jan. 2010.

[2] http://www.light2015.org/Home.html, Feb. 2016.

[3] M. Aeschlimann, M. Bauer, D. Bayer, T. Brixner, S. Cunovic, F. Dimler, A. Fischer, W. Pfeiffer, M. Rohmer, C. Schneider, F. Steeb, C. Strüber, and D. V. Voronine. Spatiotemporal control of nanooptical excitations. *Proceedings of the National Academy of Sciences*, 107(12):5329–5333, 2010.

[4] M. Aeschlimann, T. Brixner, D. Differt, U. Heinzmann, M. Hensen, C. Kramer, F. Lükermann, P. Melchior, W. Pfeiffer, M. Piecuch, C. Schneider, H. Stiebig, C. Strüber, and P. Thielen. Perfect absorption in nanotextured thin films via Anderson-localized photon modes. *Nature Photonics*, 9(10):663–668, 2015.

[5] M. Aeschlimann, T. Brixner, A. Fischer, M. Hensen, B. Huber, D. Kilbane, C. Kramer, W. Pfeiffer, M. Piecuch, and P. Thielen. Determination of local optical response functions of nanostructures with increasing complexity by using single and coupled Lorentzian oscillator models. *Applied Physics B: Lasers and Optics*, submitted.

[6] M. Aeschlimann, T. Brixner, A. Fischer, C. Kramer, P. Melchior, W. Pfeiffer, C. Schneider, C. Strüber, P. Tuchscherer, and D. V. Voronine. Coherent Two-Dimensional Nanoscopy. *Science*, 333(6050):1723–1726, 2011.

[7] I. Aharonovich, S. Castelletto, D. A. Simpson, C.-H. Su, A. D. Greentree, and S. Prawer. Diamond-based single-photon emitters. *Reports on Progress in Physics*, 74(7):076501, 2011.

[8] J. Aizpurua, G. W. Bryant, L. J. Richter, F. J. García de Abajo, B. K. Kelley, and T. Mallouk. Optical properties of coupled metallic nanorods for field-enhanced spectroscopy. *Physical Review B*, 71(23):235420, 2005.

[9] A. V. Akimov, A. Mukherjee, C. L. Yu, D. E. Chang, A. S. Zibrov, P. R. Hemmer, H. Park, and M. D. Lukin. Generation of single optical plasmons in metallic nanowires coupled to quantum dots. *Nature*, 450(7168):402–406, 2007.

[10] H. Altug, D. Englund, and J. Vučković. Ultrafast photonic crystal nanocavity laser. *Nature Physics*, 2(7):484–488, 2006.

[11] A. Alù and N. Engheta. Input Impedance, Nanocircuit Loading, and Radiation Tuning of Optical Nanoantennas. *Physical Review Letters*, 101(4):043901, 2008.

[12] S. Anders, H. A. Padmore, R. M. Duarte, T. Renner, T. Stammler, A. Scholl, M. R. Scheinfein, J. Stöhr, L. Séve, and B. Sinkovic. Photoemission electron microscope for the study of magnetic materials. *Review of Scientific Instruments*, 70(10):3973–3981, 1999.

[13] M. L. Andersen, S. Stobbe, A. S. Sørensen, and P. Lodahl. Strongly modified plasmon-matter interaction with mesoscopic quantum emitters. *Nature Physics*, 7(3):215–218, 2011.

[14] L. C. Andreani, G. Panzarini, and J.-M. Gérard. Strong-coupling regime for quantum boxes in pillar microcavities: Theory. *Physical Review B*, 60(19):13276–13279, 1999.

[15] P. Andrew and W. L. Barnes. Förster Energy Transfer in an Optical Microcavity. *Science*, 290(5492):785–788, 2000.

[16] P. Andrew and W. L. Barnes. Energy Transfer Across a Metal Film Mediated by Surface Plasmon Polaritons. *Science*, 306(5698):1002–1005, 2004.

[17] S. S. Andrews. Using Rotational Averaging To Calculate the Bulk Response of Isotropic and Anisotropic Samples from Molecular Parameters. *Journal of Chemical Education*, 81(6):877, 2004.

[18] P. Anger, P. Bharadwaj, and L. Novotny. Enhancement and Quenching of Single-Molecule Fluorescence. *Physical Review Letters*, 96(11):113002, 2006.

[19] S. Anisimov, B. Kapeliovich, and T. Perel'man. Electron emission from metal surfaces exposed to ultrashort laser pulses. *Journal of Experimental and Theoretical Physics*, 39(2):375, 1974.

[20] P. K. Aravind, A. Nitzan, and H. Metiu. The interaction between electromagnetic resonances and its role in spectroscopic studies of molecules adsorbed on colloidal particles or metal spheres. *Surface Science*, 110(1):189–204, 1981.

[21] D. K. Armani, T. J. Kippenberg, S. M. Spillane, and K. J. Vahala. Ultra-high-Q toroid microcavity on a chip. *Nature*, 421(6926):925–928, 2003.

[22] F. B. Atar, E. Battal, L. E. Aygun, B. Daglar, M. Bayindir, and A. K. Okyay. Plasmonically enhanced hot electron based photovoltaic device. *Optics Express*, 21(6):7196, 2013.

[23] H. A. Atwater and A. Polman. Plasmonics for improved photovoltaic devices. *Nature Materials*, 9(3):205–213, 2010.

[24] J. S. Avery. Resonance energy transfer and spontaneous photon emission. *Proceedings of the Physical Society*, 88(1):1–8, 1966.

[25] Y. Babayan, J. M. McMahon, S. Li, S. K. Gray, G. C. Schatz, and T. W. Odom. Confining Standing Waves in Optical Corrals. *ACS Nano*, 3(3):615–620, 2009.

[26] G. Baffou and R. Quidant. Thermo-plasmonics: using metallic nanostructures as nano-sources of heat. *Laser & Photonics Reviews*, 7(2):171–187, 2013.

[27] A. Bar-Haim, J. Klafter, and R. Kopelman. Dendrimers as Controlled Artificial Energy Antennae. *Journal of the American Chemical Society*, 119(26):6197–6198, 1997.

[28] W. L. Barnes. Surface plasmon–polariton length scales: a route to sub-wavelength optics. *Journal of Optics A: Pure and Applied Optics*, 8(4):S87, 2006.

[29] E. Bauer. A brief history of PEEM. *Journal of Electron Spectroscopy and Related Phenomena*, 185(10):314–322, 2012.

[30] M. Bayer, P. Hawrylak, K. Hinzer, S. Fafard, M. Korkusinski, Z. R. Wasilewski, O. Stern, and A. Forchel. Coupling and Entangling of Quantum States in Quantum Dot Molecules. *Science*, 291(5503):451–453, 2001.

[31] J. Bellessa, C. Bonnand, J. C. Plenet, and J. Mugnier. Strong Coupling between Surface Plasmons and Excitons in an Organic Semiconductor. *Physical Review Letters*, 93(3):036404, 2004.

[32] J. Bellessa, C. Symonds, K. Vynck, A. Lemaitre, A. Brioude, L. Beaur, J. C. Plenet, P. Viste, D. Felbacq, E. Cambril, and P. Valvin. Giant Rabi splitting between localized mixed plasmon-exciton states in a two-dimensional array of nanosize metallic disks in an organic semiconductor. *Physical Review B*, 80(3):033303, 2009.

[33] P. Bharadwaj, B. Deutsch, and L. Novotny. Optical Antennas. *Advances in Optics and Photonics*, 1(3):438–483, 2009.

[34] P. Biagioni, J.-S. Huang, and B. Hecht. Nanoantennas for visible and infrared radiation. *Reports on Progress in Physics*, 75(2):024402, 2012.

[35] K. M. Birnbaum, A. Boca, R. Miller, A. D. Boozer, T. E. Northup, and H. J. Kimble. Photon blockade in an optical cavity with one trapped atom. *Nature*, 436(7047):87–90, 2005.

[36] R. E. Blankenship. *Molecular Mechanisms of Photosynthesis*. Blackwell Science Ltd, Oxford (UK), 1st edition, 2002.

[37] K. Y. Bliokh, Y. P. Bliokh, V. Freilikher, S. Savel'ev, and F. Nori. Colloquium : Unusual resonators: Plasmonics, metamaterials, and random media. *Reviews of Modern Physics*, 80(4):1201–1213, 2008.

[38] J. G. Bohnet, Z. Chen, J. M. Weiner, D. Meiser, M. J. Holland, and J. K. Thompson. A steady-state superradiant laser with less than one intracavity photon. *Nature*, 484(7392):78–81, 2012.

[39] K.-J. Boller, A. Imamoğlu, and S. E. Harris. Observation of electromagnetically induced transparency. *Physical Review Letters*, 66(20):2593–2596, 1991.

[40] P. Borri, W. Langbein, S. Schneider, U. Woggon, R. L. Sellin, D. Ouyang, and D. Bimberg. Ultralong Dephasing Time in InGaAs Quantum Dots. *Physical Review Letters*, 87(15):157401, 2001.

[41] S. I. Bozhevolnyi, V. S. Volkov, E. Devaux, and T. W. Ebbesen. Channel Plasmon-Polariton Guiding by Subwavelength Metal Grooves. *Physical Review Letters*, 95(4):046802, 2005.

[42] S. I. Bozhevolnyi, V. S. Volkov, E. Devaux, J.-Y. Laluet, and T. W. Ebbesen. Channel plasmon subwavelength waveguide components including interferometers and ring resonators. *Nature*, 440(7083):508–511, 2006.

[43] T. Brabec and F. Krausz. Intense few-cycle laser fields: Frontiers of nonlinear optics. *Reviews of Modern Physics*, 72(2):545–591, 2000.

[44] M. S. Bradley and J. H. Krech. High-pressure Raman spectra of the acetone carbonyl stretch in acetone-methanol mixtures. *The Journal of Physical Chemistry*, 97(3):575–580, 1993.

[45] B. H. Bransden and C. J. Joachain. *Physics of Atoms and Molecules*. Addison-Wesley, 2nd edition, 2003.

[46] H.-P. Breuer and F. Petruccione. *The Theory of Open Quantum Systems*. Oxford University Press, Oxford, 1st edition, 2007.

[47] T. Brixner, J. Stenger, H. M. Vaswani, M. Cho, R. E. Blankenship, and G. R. Fleming. Two-dimensional spectroscopy of electronic couplings in photosynthesis. *Nature*, 434(7033):625–628, 2005.

[48] L. d. Broglie. *Recherches sur la théorie des quanta*. PhD thesis, University of Paris, Paris, 1924.

[49] L. d. Broglie. The reinterpretation of wave mechanics. *Foundations of Physics*, 1(1):5–15, 1970.

[50] M. L. Brongersma, N. J. Halas, and P. Nordlander. Plasmon-induced hot carrier science and technology. *Nature Nanotechnology*, 10(1):25–34, 2015.

[51] W. C. Brown. Optimization of the Efficiency and Other Properties of the Rectenna Element. In *Microwave Symposium, 1976 IEEE-MTT-S International*, pages 142–144, 1976.

[52] W. C. Brown, R. George, N. Heenan, and R. Wonson. Microwave to dc converter, Mar. 1969. US-Klassifikation 244/158.1, 244/1.00R, 307/151, 191/1.00R, 318/16; Internationale Klassifikation H02M11/00, H02J17/00; Unternehmensklassifikation H02M11/00, H02J17/00; Europäische Klassifikation H02M11/00, H02J17/00.

[53] G. W. Bryant, F. J. García de Abajo, and J. Aizpurua. Mapping the Plasmon Resonances of Metallic Nanoantennas. *Nano Letters*, 8(2):631–636, 2008.

[54] D. Budker, D. F. Kimball, S. M. Rochester, and V. V. Yashchuk. Nonlinear Magneto-optics and Reduced Group Velocity of Light in Atomic Vapor with Slow Ground State Relaxation. *Physical Review Letters*, 83(9):1767–1770, 1999.

[55] S. A. Buntin, L. J. Richter, R. R. Cavanagh, and D. S. King. Optically Driven Surface Reactions: Evidence for the Role of Hot Electrons. *Physical Review Letters*, 61(11):1321–1324, 1988.

[56] Z. Burshtein and J. Levinson. Photo-induced tunnel currents in Al-Al_2O_3-Au structures. *Physical Review B*, 12(8):3453–3457, 1975.

[57] J. Y. P. Butter. *Single-molecule nano-optics at low temperature*. PhD thesis, Universität Basel, Basel, 2006.

[58] J. Y. P. Butter, B. Hecht, B. R. Crenshaw, and C. Weder. Absorption and fluorescence of single molecules. *The Journal of Chemical Physics*, 125(15):154710, 2006.

[59] V. Callegari. *Fabrication of photonic elements by focused ion beam (FIB)*. PhD thesis, ETH Zürich, Zürich, 2009.

[60] J. Cesario, R. Quidant, G. Badenes, and S. Enoch. Electromagnetic coupling between a metal nanoparticle grating and a metallic surface. *Optics Letters*, 30(24):3404, 2005.

[61] H. Chalabi, D. Schoen, and M. L. Brongersma. Hot-Electron Photodetection with a Plasmonic Nanostripe Antenna. *Nano Letters*, 14(3):1374–1380, 2014.

[62] D. E. Chang, A. S. Sørensen, P. R. Hemmer, and M. D. Lukin. Quantum Optics with Surface Plasmons. *Physical Review Letters*, 97(5):053002, 2006.

[63] D. E. Chang, V. Vuletić, and M. D. Lukin. Quantum nonlinear optics — photon by photon. *Nature Photonics*, 8(9):685–694, 2014.

[64] K.-P. Chen, V. P. Drachev, J. D. Borneman, A. V. Kildishev, and V. M. Shalaev. Drude Relaxation Rate in Grained Gold Nanoantennas. *Nano Letters*, 10(3):916–922, 2010.

[65] C.-H. Cho, C. O. Aspetti, J. Park, and R. Agarwal. Silicon coupled with plasmon nanocavities generates bright visible hot luminescence. *Nature Photonics*, 7(4):285–289, Apr. 2013.

[66] Y. Chu and K. B. Crozier. Experimental study of the interaction between localized and propagating surface plasmons. *Optics Letters*, 34(3):244, 2009.

[67] M. Cinchetti, A. Gloskovskii, S. A. Nepjiko, G. Schönhense, H. Rochholz, and M. Kreiter. Photoemission Electron Microscopy as a Tool for the Investigation of Optical Near Fields. *Physical Review Letters*, 95(4):047601, 2005.

[68] M. Cinchetti, A. Oelsner, G. H. Fecher, H. J. Elmers, and G. Schönhense. Observation of Cu surface inhomogeneities by multiphoton photoemission spectromicroscopy. *Applied Physics Letters*, 83(8):1503–1505, 2003.

[69] M. Cinchetti, D. A. Valdaitsev, A. Gloskovskii, A. Oelsner, S. A. Nepijko, and G. Schönhense. Photoemission time-of-flight spectromicroscopy of Ag nanoparticle films on Si(1 1 1). *Journal of Electron Spectroscopy and Related Phenomena*, 137–140:249–257, 2004.

[70] J. I. Cirac. Interaction of a two-level atom with a cavity mode in the bad-cavity limit. *Physical Review A*, 46(7):4354–4362, 1992.

[71] C. Clavero. Plasmon-induced hot-electron generation at nanoparticle/metal-oxide interfaces for photovoltaic and photocatalytic devices. *Nature Photonics*, 8(2):95–103, 2014.

[72] R. M. Clegg, M. Sener, and Govindjee. From Förster resonance energy transfer to coherent resonance enrgy transfer and back. In R. R. Alfano, editor, *Optical Biopsy VII*, number 7 in Optical Biopsy, pages 21–41. SPIE Press, Bellingham, USA, 2010.

[73] C. Cohen-Tannoudji, J. Dupont-Roc, and G. Grynberg. *Atom-Photon Interactions: Basic Processes and Applications*. Wiley-VCH, New York, 1st edition, 1998.

[74] D. P. Craig and T. Thirunamachandran. An analysis of models for resonant transer of excitation using quantum electrodynamics. *Chemical Physics*, 167(3):229–240, 1992.

[75] T. Dadosh, Y. Gordin, R. Krahne, I. Khivrich, D. Mahalu, V. Frydman, J. Sperling, A. Yacoby, and I. Bar-Joseph. Measurement of the conductance of single conjugated molecules. *Nature*, 436(7051):677–680, 2005.

[76] T. Dadosh, J. Sperling, G. W. Bryant, R. Breslow, T. Shegai, M. Dyshel, G. Haran, and I. Bar-Joseph. Plasmonic Control of the Shape of the Raman Spectrum of a Single Molecule in a Silver Nanoparticle Dimer. *ACS Nano*, 3(7):1988–1994, 2009.

[77] S. D'Agostino, F. Alpeggiani, and L. C. Andreani. Strong coupling between a dipole emitter and localized plasmons: enhancement by sharp silver tips. *Optics Express*, 21(23):27602, 2013.

[78] N. P. de Leon, B. J. Shields, C. L. Yu, D. E. Englund, A. V. Akimov, M. D. Lukin, and H. Park. Tailoring Light-Matter Interaction with a Nanoscale Plasmon Resonator. *Physical Review Letters*, 108(22):226803, 2012.

[79] R. de Waele, S. P. Burgos, A. Polman, and H. A. Atwater. Plasmon Dispersion in Coaxial Waveguides from Single-Cavity Optical Transmission Measurements. *Nano Letters*, 9(8):2832–2837, 2009.

[80] N. Del Fatti, C. Voisin, M. Achermann, S. Tzortzakis, D. Christofilos, and F. Vallée. Nonequilibrium electron dynamics in noble metals. *Physical Review B*, 61(24):16956–16966, 2000.

[81] G. Della Valle, M. Conforti, S. Longhi, G. Cerullo, and D. Brida. Real-time optical mapping of the dynamics of nonthermal electrons in thin gold films. *Physical Review B*, 86(15):155139, 2012.

[82] R. G. DeVoe and R. G. Brewer. Observation of Superradiant and Subradiant Spontaneous Emission of Two Trapped Ions. *Physical Review Letters*, 76(12):2049–2052, 1996.

[83] D. L. Dexter. A Theory of Sensitized Luminescence in Solids. *Journal of Chemical Physics*, 21(5):836–850, 1953.

[84] R. H. Dicke. Coherence in Spontaneous Radiation Processes. *Physical Review*, 93(1):99–110, 1954.

[85] S. Diehl, A. Micheli, A. Kantian, B. Kraus, H. P. Büchler, and P. Zoller. Quantum states and phases in driven open quantum systems with cold atoms. *Nature Physics*, 4(11):878–883, 2008.

[86] J.-C. Diels and W. Rudolph. *Ultrashort Laser Pulse Phenomena: Fundamentals, Techniques, and Applications on a Femtosecond Time Scale*. Academic Press, USA, 2nd edition, 2006.

[87] D. Diesing, G. Kritzler, M. Stermann, D. Nolting, and A. Otto. Metal/insulator/metal junctions for electrochemical surface science. *Journal of Solid State Electrochemistry*, 7(7):389–415, 2003.

[88] D. Diesing, M. Merschdorf, A. Thon, and W. Pfeiffer. Identification of multiphoton induced photocurrents in metal–insulator–metal junctions. *Applied Physics B*, 78(3-4):443–446, 2004.

[89] D. Differt, W. Pfeiffer, and D. Diesing. Scanning internal photoemission microscopy for the identification of hot carrier transport mechanisms. *Applied Physics Letters*, 101(11):111608, Sept. 2012.

[90] K. H. Drexhage, M. Fleck, F. P. Schäfer, and W. Sperling. Beeinflussung der Fluoreszenz eines Europium-chelates durch einen Spiegel. *Berichte der Bunsengesellschaft für physikalische Chemie*, 70(9-10):1176, 1966.

[91] A. Drezet, A. L. Stepanov, H. Ditlbacher, A. Hohenau, B. Steinberger, F. R. Aussenegg, A. Leitner, and J. R. Krenn. Surface plasmon propagation in an elliptical corral. *Applied Physics Letters*, 86(7):074104, 2005.

[92] H. T. Dung, L. Knöll, and D.-G. Welsch. Intermolecular energy transfer in the presence of dispersing and absorbing media. *Physical Review A*, 65(4):043813, 2002.

[93] H. T. Dung, L. Knöll, and D.-G. Welsch. Resonant dipole-dipole interaction in the presence of dispersing and absorbing surroundings. *Physical Review A*, 66(6):063810, 2002.

[94] D. Dzsotjan, A. S. Sørensen, and M. Fleischhauer. Quantum emitters coupled to surface plasmons of a nanowire: A Green's function approach. *Physical Review B*, 82(7):075427, 2010.

[95] J. H. Eberly and J. Javanainen. Above-threshold ionisation. *European Journal of Physics*, 9(4):265, 1988.

[96] A. Einstein. Über einen die Erzeugung und Verwandlung des Lichtes betreffenden heuristischen Gesichtspunkt. *Annalen der Physik*, 322(6):132–148, 1905.

[97] R. El-Ganainy and S. John. Resonant dipole–dipole interaction in confined and strong-coupling dielectric geometries. *New Journal of Physics*, 15(8):083033, 2013.

[98] J. G. Endriz and W. E. Spicer. Surface-Plasmon-One-Electron Decay and its Observation in Photoemission. *Physical Review Letters*, 24(2):64–68, 1970.

[99] J. A. Fan, C. Wu, K. Bao, J. Bao, R. Bardhan, N. J. Halas, V. N. Manoharan, P. Nordlander, G. Shvets, and F. Capasso. Self-Assembled Plasmonic Nanoparticle Clusters. *Science*, 328(5982):1135–1138, 2010.

[100] W. S. Fann, R. Storz, H. W. K. Tom, and J. Bokor. Electron thermalization in gold. *Physical Review B*, 46(20):13592–13595, 1992.

[101] S. Faris, T. Gustafson, and J. Wiesner. Detection of optical and infrared radiation with DC-biased electron-tunneling metal-barrier-metal diodes. *IEEE Journal of Quantum Electronics*, 9(7):737–745, 1973.

[102] G. H. Fecher, O. Schmidt, Y. Hwu, and G. Schönhense. Multiphoton photoemission electron microscopy using femtosecond laser radiation. *Journal of Electron Spectroscopy and Related Phenomena*, 126(1–3):77–87, 2002.

[103] E. Feigenbaum and M. Orenstein. Ultrasmall Volume Plasmons, yet with Complete Retardation Effects. *Physical Review Letters*, 101(16):163902, 2008.

[104] A. Feist, K. E. Echternkamp, J. Schauss, S. V. Yalunin, S. Schäfer, and C. Ropers. Quantum coherent optical phase modulation in an ultrafast transmission electron microscope. *Nature*, 521(7551):200–203, 2015.

[105] Z. Ficek and R. Tanaś. Entangled states and collective nonclassical effects in two-atom systems. *Physics Reports*, 372(5):369–443, 2002.

[106] J. M. Fink, R. Bianchetti, M. Baur, M. Göppl, L. Steffen, S. Filipp, P. J. Leek, A. Blais, and A. Wallraff. Dressed Collective Qubit States and the Tavis-Cummings Model in Circuit QED. *Physical Review Letters*, 103(8):083601, 2009.

[107] T. Förster. Zwischenmolekulare Energiewanderung und Fluoreszenz. *Annalen der Physik*, 437(1-2):55–75, 1948.

[108] M. Fox. *Quantum Optics: An Introduction*. Number 15 in Oxford Master Series in Physics. Oxford University Press, Oxford, New York, 1st edition, 2006.

[109] B. Frisch. *Untersuchung plasmonischer Kopplungsphänomene an Nanostrukturen*. Master thesis, TU Kaiserslautern, Kaiserslautern, 2016.

[110] C. Frischkorn and M. Wolf. Femtochemistry at Metal Surfaces: Nonadiabatic Reaction Dynamics. *Chemical Reviews*, 106(10):4207–4233, 2006.

[111] F. J. García de Abajo. Optical excitations in electron microscopy. *Reviews of Modern Physics*, 82(1):209–275, 2010.

[112] F. P. García de Arquer, A. Mihi, D. Kufer, and G. Konstantatos. Photoelectric Energy Conversion of Plasmon-Generated Hot Carriers in Metal–Insulator–Semiconductor Structures. *ACS Nano*, 7(4):3581–3588, 2013.

[113] J. M. Gérard, D. Barrier, J. Y. Marzin, R. Kuszelewicz, L. Manin, E. Costard, V. Thierry-Mieg, and T. Rivera. Quantum boxes as active probes for photonic microstructures: The pillar microcavity case. *Applied Physics Letters*, 69(4):449–451, 1996.

[114] J. M. Gérard, B. Sermage, B. Gayral, B. Legrand, E. Costard, and V. Thierry-Mieg. Enhanced Spontaneous Emission by Quantum Boxes in a Monolithic Optical Microcavity. *Physical Review Letters*, 81(5):1110–1113, 1998.

[115] A. Ghoshal and P. G. Kik. Theory and simulation of surface plasmon excitation using resonant metal nanoparticle arrays. *Journal of Applied Physics*, 103(11):113111, 2008.

[116] Y. Gong and J. Vučković. Design of plasmon cavities for solid-state cavity quantum electrodynamics applications. *Applied Physics Letters*, 90(3):033113, 2007.

[117] A. Gonzalez-Tudela, D. Martin-Cano, E. Moreno, L. Martin-Moreno, C. Tejedor, and F. J. Garcia-Vidal. Entanglement of Two Qubits Medi-

ated by One-Dimensional Plasmonic Waveguides. *Physical Review Letters*, 106(2):020501, 2011.

[118] M. Göppert-Mayer. Über Elementarakte mit zwei Quantensprüngen. *Annalen der Physik*, 401(3):273–294, 1931.

[119] M. L. Gorodetsky, A. A. Savchenkov, and V. S. Ilchenko. Ultimate Q of optical microsphere resonators. *Optics Letters*, 21(7):453, 1996.

[120] P. Goy, J. M. Raimond, M. Gross, and S. Haroche. Observation of Cavity-Enhanced Single-Atom Spontaneous Emission. *Physical Review Letters*, 50(24):1903–1906, 1983.

[121] K. C. Grabar, K. J. Allison, B. E. Baker, R. M. Bright, K. R. Brown, R. G. Freeman, A. P. Fox, C. D. Keating, M. D. Musick, and M. J. Natan. Two-Dimensional Arrays of Colloidal Gold Particles: A Flexible Approach to Macroscopic Metal Surfaces. *Langmuir*, 12(10):2353–2361, 1996.

[122] D. K. Gramotnev and D. F. P. Pile. Single-mode subwavelength waveguide with channel plasmon-polaritons in triangular grooves on a metal surface. *Applied Physics Letters*, 85(26):6323–6325, 2004.

[123] W. Greiner, L. Neise, and H. Stöcker. *Thermodynamik und Statistische Mechanik*, volume 9 of *Theoretische Physik*. Verlag Harri Deutsch, Thun und Frankfurt am Main, 2nd edition, 1993.

[124] R. H. M. Groeneveld, R. Sprik, and A. Lagendijk. Femtosecond spectroscopy of electron-electron and electron-phonon energy relaxation in Ag and Au. *Physical Review B*, 51(17):11433–11445, May 1995.

[125] M. Gross and S. Haroche. Superradiance: An essay on the theory of collective spontaneous emission. *Physics Reports*, 93(5):301–396, Dec. 1982.

[126] I. S. Grudinin, V. S. Ilchenko, and L. Maleki. Ultrahigh optical Q factors of crystalline resonators in the linear regime. *Physical Review A*, 74(6):063806, 2006.

[127] Z. Guo, Y. Zhang, Y. DuanMu, L. Xu, S. Xie, and N. Gu. Facile synthesis of micrometer-sized gold nanoplates through an aniline-assisted route in

ethylene glycol solution. *Colloids and Surfaces A: Physicochemical and Engineering Aspects*, 278(1–3):33–38, 2006.

[128] J. C. Gutiérrez-Vega, R. M. Rodríguez-Dagnino, M. A. Meneses-Nava, and S. Chávez-Cerda. Mathieu functions, a visual approach. *American Journal of Physics*, 71(3):233–242, 2003.

[129] H. M. Hachmeister. *Aufbau eines interferometrischen Autokorrelators zur phasensensitiven Charakterisierung ultrakurzer Lichtpulse*. Bachelor thesis, Universität Bielefeld, Bielefeld, 2012.

[130] T. Hanke, J. Cesar, V. Knittel, A. Trügler, U. Hohenester, A. Leitenstorfer, and R. Bratschitsch. Tailoring Spatiotemporal Light Confinement in Single Plasmonic Nanoantennas. *Nano Letters*, 12(2):992–996, 2012.

[131] T. Hanke, G. Krauss, D. Träutlein, B. Wild, R. Bratschitsch, and A. Leitenstorfer. Efficient Nonlinear Light Emission of Single Gold Optical Antennas Driven by Few-Cycle Near-Infrared Pulses. *Physical Review Letters*, 103(25):257404, 2009.

[132] S. Haroche. Nobel Lecture: Controlling photons in a box and exploring the quantum to classical boundary. *Reviews of Modern Physics*, 85(3):1083–1102, 2013.

[133] I. Heesemann. *Kontrollierte Aggregation von Gold- Nanopartikeln (Knäuel-Stäbchen-Knäuel-Blockcopolymere, sternförmige Triknäuel-Blockcopolymere und Acetyl-geschützte Dithiole als strukturgebende Moleküle zur Anordnung von Gold-Nanopartikeln)*. PhD thesis, Universität Bielefeld, Bielefeld, 2014.

[134] M. Heiblum, S. Wang, J. R. Whinnery, and T. Gustafson. Characteristics of integrated MOM junctions at DC and at optical frequencies. *IEEE Journal of Quantum Electronics*, 14(3):159–169, 1970.

[135] P. R. Hemmer and M. G. Prentiss. Coupled-pendulum model of the stimulated resonance Raman effect. *Journal of the Optical Society of America B*, 5(8):1613, 1988.

[136] I. V. Hertel and C.-P. Schulz. *Atome, Moleküle und optische Physik 1*. Springer-Lehrbuch. Springer Berlin Heidelberg, Berlin, Heidelberg, 2008.

[137] T. Hertel and G. Moos. Electron-Phonon Interaction in Single-Wall Carbon Nanotubes: A Time-Domain Study. *Physical Review Letters*, 84(21):5002–5005, 2000.

[138] A. J. Hoffman, S. J. Srinivasan, S. Schmidt, L. Spietz, J. Aumentado, H. E. Türeci, and A. A. Houck. Dispersive Photon Blockade in a Superconducting Circuit. *Physical Review Letters*, 107(5):053602, 2011.

[139] C. E. Hofmann, E. J. R. Vesseur, L. A. Sweatlock, H. J. Lezec, F. J. García de Abajo, A. Polman, and H. A. Atwater. Plasmonic Modes of Annular Nanoresonators Imaged by Spectrally Resolved Cathodoluminescence. *Nano Letters*, 7(12):3612–3617, 2007.

[140] J. Hofmann and W. Steinmann. Plasma Resonance in the Photoemission of Silver. *physica status solidi (b)*, 30(1):K53–K56, 1968.

[141] S. Hong, T. Chen, Y. Zhu, A. Li, Y. Huang, and X. Chen. Live-Cell Stimulated Raman Scattering Imaging of Alkyne-Tagged Biomolecules. *Angewandte Chemie International Edition*, 53(23):5827–5831, 2014.

[142] M. Hopmeier, W. Guss, M. Deussen, E. O. Göbel, and R. F. Mahrt. Enhanced Dipole-Dipole Interaction in a Polymer Microcavity. *Physical Review Letters*, 82(20):4118–4121, 1999.

[143] J.-S. Huang, V. Callegari, P. Geisler, C. Brüning, J. Kern, J. C. Prangsma, X. Wu, T. Feichtner, J. Ziegler, P. Weinmann, M. Kamp, A. Forchel, P. Biagioni, U. Sennhauser, and B. Hecht. Atomically flat single-crystalline gold nanostructures for plasmonic nanocircuitry. *Nature Communications*, 1:150, 2010.

[144] J.-S. Huang, T. Feichtner, P. Biagioni, and B. Hecht. Impedance Matching and Emission Properties of Nanoantennas in an Optical Nanocircuit. *Nano Letters*, 9(5):1897–1902, 2009.

[145] J.-S. Huang, J. Kern, P. Geisler, P. Weinmann, M. Kamp, A. Forchel, P. Biagioni, and B. Hecht. Mode Imaging and Selection in Strongly Coupled Nanoantennas. *Nano Letters*, 10(6):2105–2110, 2010.

[146] M. L. Huang, Y. C. Chang, C. H. Chang, T. D. Lin, J. Kwo, T. B. Wu, and M. Hong. Energy-band parameters of atomic-layer-deposition Al2o3/InGaAs heterostructure. *Applied Physics Letters*, 89(1):012903, 2006.

[147] W. Huang, W. Qian, M. A. El-Sayed, Y. Ding, and Z. L. Wang. Effect of the Lattice Crystallinity on the Electron-Phonon Relaxation Rates in Gold Nanoparticles. *The Journal of Physical Chemistry C*, 111(29):10751–10757, 2007.

[148] T. Hümmer, F. J. García-Vidal, L. Martín-Moreno, and D. Zueco. Weak and strong coupling regimes in plasmonic QED. *Physical Review B*, 87(11):115419, 2013.

[149] B. Huttner and S. M. Barnett. Quantization of the electromagnetic field in dielectrics. *Physical Review A*, 46(7):4306–4322, 1992.

[150] H. Inouye, K. Tanaka, I. Tanahashi, and K. Hirao. Ultrafast dynamics of nonequilibrium electrons in a gold nanoparticle system. *Physical Review B*, 57(18):11334–11340, 1998.

[151] J. D. Jackson. *Classical Electrodynamics*. John Wiley & Sons, New York, 3rd edition, 1998.

[152] K. Jacobs and A. J. Landahl. Engineering Giant Nonlinearities in Quantum Nanosystems. *Physical Review Letters*, 103(6):067201, 2009.

[153] D. L. Jeanmaire and R. P. Van Duyne. Surface raman spectroelectrochemistry. *Journal of Electroanalytical Chemistry and Interfacial Electrochemistry*, 84(1):1–20, 1977.

[154] Y. S. Joe, A. M. Satanin, and C. S. Kim. Classical analogy of Fano resonances. *Physica Scripta*, 74(2):259, 2006.

[155] P. B. Johnson and R. W. Christy. Optical Constants of the Noble Metals. *Physical Review B*, 6(12):4370–4379, 1972.

[156] A. P. Kanavin, I. V. Smetanin, V. A. Isakov, Y. V. Afanasiev, B. N. Chichkov, B. Wellegehausen, S. Nolte, C. Momma, and A. Tünnermann. Heat transport in metals irradiated by ultrashort laser pulses. *Physical Review B*, 57(23):14698–14703, 1998.

[157] L. V. Keldysh. Ionization in the Field of a Strong Electromagnetic Wave. *Journal of Experimental and Theoretical Physics*, 47(5):1945, 1964.

[158] J. Kempe. Quantum random walks: An introductory overview. *Contemporary Physics*, 44(4):307–327, 2003.

[159] A. Kiejna and K. F. Wojciechowski. Chapter 16 - Adsorption of alkali atoms on metal surface. In A. Kiejna and K. F. Wojciechowski, editors, *Metal Surface Electron Physics*, pages 223–243. Pergamon, Oxford, 1996.

[160] H. Kim, D. Sridharan, T. C. Shen, G. S. Solomon, and E. Waks. Strong coupling between two quantum dots and a photonic crystal cavity using magnetic field tuning. *Optics Express*, 19(3):2589, 2011.

[161] S. L. Kleinman, B. Sharma, M. G. Blaber, A.-I. Henry, N. Valley, R. G. Freeman, M. J. Natan, G. C. Schatz, and R. P. Van Duyne. Structure Enhancement Factor Relationships in Single Gold Nanoantennas by Surface-Enhanced Raman Excitation Spectroscopy. *Journal of the American Chemical Society*, 135(1):301–308, 2013.

[162] M. W. Knight, H. Sobhani, P. Nordlander, and N. J. Halas. Photodetection with Active Optical Antennas. *Science*, 332(6030):702–704, 2011.

[163] M. W. Knight, Y. Wang, A. S. Urban, A. Sobhani, B. Y. Zheng, P. Nordlander, and N. J. Halas. Embedding Plasmonic Nanostructure Diodes Enhances Hot Electron Emission. *Nano Letters*, 13(4):1687–1692, 2013.

[164] M. W. Knight, Y. Wu, J. B. Lassiter, P. Nordlander, and N. J. Halas. Substrates Matter: Influence of an Adjacent Dielectric on an Individual Plasmonic Nanoparticle. *Nano Letters*, 9(5):2188–2192, 2009.

[165] J. Kondo. Resistance Minimum in Dilute Magnetic Alloys. *Progress of Theoretical Physics*, 32(1):37–49, 1964.

[166] R. Kopelman, M. Shortreed, Z.-Y. Shi, W. Tan, Z. Xu, J. S. Moore, A. Bar-Haim, and J. Klafter. Spectroscopic Evidence for Excitonic Localization in Fractal Antenna Supermolecules. *Physical Review Letters*, 78(7):1239–1242, 1997.

[167] K. Kopitzki. *Einführung in die Festkörperphysik*. Teubner, Wiesbaden, 5th edition, 2004.

[168] D. A. Kovacs, J. Winter, S. Meyer, A. Wucher, and D. Diesing. Photo and particle induced transport of excited carriers in thin film tunnel junctions. *Physical Review B*, 76(23):235408, 2007.

[169] F. Krausz and M. Y. Ivanov. Attosecond physics. *Reviews of Modern Physics*, 81(1):163–234, 2009.

[170] U. Kreibig and M. Vollmer. *Optical Properties of Metal Clusters*. Number 25 in Springer Series in Materials Science. Springer, 1995.

[171] E. Kretschmann and H. Raether. Radiative Decay of Non Radiative Surface Plasmons Excited by Light. *Z. Naturforsch. A*, 23:2135–2136, 1968.

[172] M. Krüger, M. Schenk, and P. Hommelhoff. Attosecond control of electrons emitted from a nanoscale metal tip. *Nature*, 475(7354):78–81, 2011.

[173] A. Kubo, K. Onda, H. Petek, Z. Sun, Y. S. Jung, and H. K. Kim. Femtosecond Imaging of Surface Plasmon Dynamics in a Nanostructured Silver Film. *Nano Letters*, 5(6):1123–1127, 2005.

[174] W. Kuch, R. Frömter, J. Gilles, D. Hartmann, C. Ziethen, C. M. Schneider, G. Schönhense, W. Swiech, and J. Kirschner. Element-Selective Magnetic Imaging in Exchange-Coupled Systems by Magnetic Photoemission Microscopy. *Surface Review and Letters*, 05(06):1241–1248, 1998.

[175] S. Kumar, N. I. Kristiansen, A. Huck, and U. L. Andersen. Generation and Controlled Routing of Single Plasmons on a Chip. *Nano Letters*, 14(2):663–669, 2014.

[176] M. Kuttge, F. J. García de Abajo, and A. Polman. Ultrasmall Mode Volume Plasmonic Nanodisk Resonators. *Nano Letters*, 10(5):1537–1541, 2010.

[177] M. Kuttge, E. J. R. Vesseur, J. Verhoeven, H. J. Lezec, H. A. Atwater, and A. Polman. Loss mechanisms of surface plasmon polaritons on gold probed by cathodoluminescence imaging spectroscopy. *Applied Physics Letters*, 93(11):113110, 2008.

[178] W. E. Lamb and R. C. Retherford. Fine Structure of the Hydrogen Atom by a Microwave Method. *Physical Review*, 72(3):241–243, 1947.

[179] L. D. Landau and E. M. Lifshitz. *Electrodynamics of Continuous Media*, volume 8 of *Course of Theoretical Physics*. Pergamon Press LTD., 2nd edition, 1963.

[180] I. G. Lang, L. I. Korovin, and S. T. Pavlov. Elastic light scattering by semiconductor quantum dots of arbitrary shape. *Physics of the Solid State*, 49(7):1368–1374, 2007.

[181] I. G. Lang and S. T. Pavlov. Resonant Light Absorption by Semiconductor Quantum Dots. *Advances in Condensed Matter Physics*, 2009:e654190, 2009.

[182] P. Larkin. *Infrared and Raman Spectroscopy*. Elsevier Science Publishing Co Inc, Amsterdam, 2011.

[183] T. A. Laurence, G. Braun, C. Talley, A. Schwartzberg, M. Moskovits, N. Reich, and T. Huser. Rapid, Solution-Based Characterization of Optimized SERS Nanoparticle Substrates. *Journal of the American Chemical Society*, 131(1):162–169, Jan. 2009.

[184] P. Laven. MiePlot, www.philiplaven.com/mieplot.htm, 2015.

[185] F. Le, N. Z. Lwin, J. M. Steele, M. Käll, N. J. Halas, and P. Nordlander. Plasmons in the Metallic Nanoparticle-Film System as a Tunable Impurity Problem. *Nano Letters*, 5(10):2013, 2005.

[186] E. C. Le Ru, E. Blackie, M. Meyer, and P. G. Etchegoin. Surface Enhanced Raman Scattering Enhancement Factors: A Comprehensive Study. *The Journal of Physical Chemistry C*, 111(37):13794–13803, 2007.

[187] E. C. Le Ru and P. G. Etchegoin. *Principles of Surface-Enhanced Raman Spectroscopy*. Elsevier, Amsterdam, 1st edition, 2009.

[188] E. C. Le Ru and P. G. Etchegoin. Quantifying SERS enhancements. *MRS Bulletin*, 38(08):631–640, 2013.

[189] E. C. Le Ru, M. Meyer, and P. G. Etchegoin. Proof of Single-Molecule Sensitivity in Surface Enhanced Raman Scattering (SERS) by Means of a Two-Analyte Technique. *The Journal of Physical Chemistry B*, 110(4):1944–1948, 2006.

[190] X. Li, D. Xiao, and Z. Zhang. Landau damping of quantum plasmons in metal nanostructures. *New Journal of Physics*, 15(2):023011, 2013.

[191] M. Lisowski, P. A. Loukakos, U. Bovensiepen, J. Stähler, C. Gahl, and M. Wolf. Ultra-fast dynamics of electron thermalization, cooling and transport effects in Ru(001). *Applied Physics A*, 78(2):165–176, 2003.

[192] C. Liu, Z. Dutton, C. H. Behroozi, and L. V. Hau. Observation of coherent optical information storage in an atomic medium using halted light pulses. *Nature*, 409(6819):490–493, 2001.

[193] N. Liu, L. Langguth, T. Weiss, J. Kästel, M. Fleischhauer, T. Pfau, and H. Giessen. Plasmonic analogue of electromagnetically induced transparency at the Drude damping limit. *Nature Materials*, 8(9):758–762, 2009.

[194] N. Liu, T. Weiss, M. Mesch, L. Langguth, U. Eigenthaler, M. Hirscher, C. Sönnichsen, and H. Giessen. Planar Metamaterial Analogue of Electromagnetically Induced Transparency for Plasmonic Sensing. *Nano Letters*, 10(4):1103–1107, 2010.

[195] R. Loudon. *The Quantum Theory Of Light*. Oxford University Press, New York, 3rd edition, 1997.

[196] B. Luk'yanchuk, N. I. Zheludev, S. A. Maier, N. J. Halas, P. Nordlander, H. Giessen, and C. T. Chong. The Fano resonance in plasmonic nanostructures and metamaterials. *Nature Materials*, 9(9):707–715, 2010.

[197] S. A. Maier. *Plasmonics: Fundamentals and Applications*. Springer, New York, 1st edition, 2007.

[198] J. Majer, J. M. Chow, J. M. Gambetta, J. Koch, B. R. Johnson, J. A. Schreier, L. Frunzio, D. I. Schuster, A. A. Houck, A. Wallraff, A. Blais, M. H. Devoret, S. M. Girvin, and R. J. Schoelkopf. Coupling superconducting qubits via a cavity bus. *Nature*, 449(7161):443–447, 2007.

[199] L. Mandel and E. Wolf. *Optical Coherence and Quantum Optics*. Cambridge University Press, New York, 1st edition, 1995.

[200] A. Manjavacas, J. G. Liu, V. Kulkarni, and P. Nordlander. Plasmon-Induced Hot Carriers in Metallic Nanoparticles. *ACS Nano*, 8(8):7630–7638, 2014.

[201] H. C. Manoharan, C. P. Lutz, and D. M. Eigler. Quantum mirages formed by coherent projection of electronic structure. *Nature*, 403(6769):512–515, 2000.

[202] M. Mariantoni, H. Wang, T. Yamamoto, M. Neeley, R. C. Bialczak, Y. Chen, M. Lenander, E. Lucero, A. D. O'Connell, D. Sank, M. Weides, J. Wenner, Y. Yin, J. Zhao, A. N. Korotkov, A. N. Cleland, and J. M. Martinis. Implementing the Quantum von Neumann Architecture with Superconducting Circuits. *Science*, 334(6052):61–65, 2011.

[203] D. Marinica, A. Kazansky, P. Nordlander, J. Aizpurua, and A. G. Borisov. Quantum Plasmonics: Nonlinear Effects in the Field Enhancement of a Plasmonic Nanoparticle Dimer. *Nano Letters*, 12(3):1333–1339, 2012.

[204] C. A. Marocico and J. Knoester. Intermolecular resonance energy transfer in the presence of a dielectric cylinder. *Physical Review A*, 79(5):053816, 2009.

[205] D. Martín-Cano, A. González-Tudela, L. Martín-Moreno, F. J. García-Vidal, C. Tejedor, and E. Moreno. Dissipation-driven generation of two-

qubit entanglement mediated by plasmonic waveguides. *Physical Review B*, 84(23):235306, 2011.

[206] D. Martín-Cano, L. Martín-Moreno, F. J. García-Vidal, and E. Moreno. Resonance Energy Transfer and Superradiance Mediated by Plasmonic Nanowaveguides. *Nano Letters*, 10(8):3129–3134, 2010.

[207] J. Y. Marzin, J. M. Gérard, A. Izraël, D. Barrier, and G. Bastard. Photoluminescence of Single InAs Quantum Dots Obtained by Self-Organized Growth on GaAs. *Physical Review Letters*, 73(5):716–719, 1994.

[208] J. C. Maxwell. A Dynamical Theory of the Electromagnetic Field. *Philosophical Transactions of the Royal Society of London*, 155:459–512, 1865.

[209] A. D. McFarland, M. A. Young, J. A. Dieringer, and R. P. Van Duyne. Wavelength-Scanned Surface-Enhanced Raman Excitation Spectroscopy. *The Journal of Physical Chemistry B*, 109(22):11279–11285, 2005.

[210] M. Merschdorf, C. Kennerknecht, and W. Pfeiffer. Collective and single-particle dynamics in time-resolved two-photon photoemission. *Physical Review B*, 70(19):193401, 2004.

[211] M. Merschdorf, W. Pfeiffer, S. Voll, and G. Gerber. Electron gas cooling in Ag nanoparticles on graphite. *Physical Review B*, 68(15):155416, 2003.

[212] F. Merschjohann, S. Neb, P. Bartz, M. Hensen, C. Strüber, S. Fiechter, N. Müller, W. Pfeiffer, and U. Heinzmann. Delayed Core-Level Photoemission from the van der Waals Crystal WSe_2. In K. Yamanouchi, S. Cundiff, R. d. Vivie-Riedle, M. Kuwata-Gonokami, and L. DiMauro, editors, *Ultrafast Phenomena XIX*, number 162 in Springer Proceedings in Physics, pages 68–71. Springer International Publishing, 2015.

[213] B. Metzger, M. Hentschel, M. Lippitz, and H. Giessen. Third-harmonic spectroscopy and modeling of the nonlinear response of plasmonic nanoantennas. *Optics Letters*, 37(22):4741, 2012.

[214] B. Min, E. Ostby, V. Sorger, E. Ulin-Avila, L. Yang, X. Zhang, and K. Vahala. High-Q surface-plasmon-polariton whispering-gallery microcavity. *Nature*, 457(7228):455–458, 2009.

[215] J. J. Mock, R. T. Hill, A. Degiron, S. Zauscher, A. Chilkoti, and D. R. Smith. Distance-Dependent Plasmon Resonant Coupling between a Gold Nanoparticle and Gold Film. *Nano Letters*, 8(8):2245–2252, 2008.

[216] E. Moreno, F. J. Garcia-Vidal, S. G. Rodrigo, L. Martin-Moreno, and S. I. Bozhevolnyi. Channel plasmon-polaritons: modal shape, dispersion, and losses. *Optics Letters*, 31(23):3447–3449, 2006.

[217] E. Moreno, S. G. Rodrigo, S. I. Bozhevolnyi, L. Martín-Moreno, and F. J. García-Vidal. Guiding and Focusing of Electromagnetic Fields with Wedge Plasmon Polaritons. *Physical Review Letters*, 100(2):023901, 2008.

[218] M. Moskovits. Persistent misconceptions regarding SERS. *Physical Chemistry Chemical Physics*, 15(15):5301–5311, 2013.

[219] S. Mubeen, J. Lee, N. Singh, S. Krämer, G. D. Stucky, and M. Moskovits. An autonomous photosynthetic device in which all charge carriers derive from surface plasmons. *Nature Nanotechnology*, 8(4):247–251, 2013.

[220] B. Y. Mueller and B. Rethfeld. Relaxation dynamics in laser-excited metals under nonequilibrium conditions. *Physical Review B*, 87(3):035139, 2013.

[221] C. C. Neacsu, G. A. Reider, and M. B. Raschke. Second-harmonic generation from nanoscopic metal tips: Symmetry selection rules for single asymmetric nanostructures. *Physical Review B*, 71(20):201402, 2005.

[222] N. Nilius, N. Ernst, and H.-J. Freund. Photon Emission Spectroscopy of Individual Oxide-Supported Silver Clusters in a Scanning Tunneling Microscope. *Physical Review Letters*, 84(17):3994–3997, 2000.

[223] A. Nitzan and L. E. Brus. Theoretical model for enhanced photochemistry on rough surfaces. *The Journal of Chemical Physics*, 75(5):2205–2214, 1981.

[224] M. A. Noginov, G. Dewar, M. W. McCall, and N. I. Zheludev, editors. *Tutorials in Complex Photonic Media*. SPIE Publications, Bellingham, Washington (USA), 1st edition, 2009.

[225] P. Nordlander and E. Prodan. Plasmon Hybridization in Nanoparticles near Metallic Surfaces. *Nano Letters*, 4(11):2209–2213, 2004.

[226] J. P. Novak, C. Nickerson, S. Franzen, and D. L. Feldheim. Purification of Molecularly Bridged Metal Nanoparticle Arrays by Centrifugation and Size Exclusion Chromatography. *Analytical Chemistry*, 73(23):5758–5761, 2001.

[227] I. V. Novikov and A. A. Maradudin. Channel polaritons. *Physical Review B*, 66(3):035403, 2002.

[228] L. Novotny. Strong coupling, energy splitting, and level crossings: A classical perspective. *American Journal of Physics*, 78(11):1199–1202, 2010.

[229] L. Novotny and B. Hecht. *Principles of Nano-Optics*. Cambridge University Press, Cambridge, 2nd edition, 2012.

[230] S. J. Orfanidis. Electromagnetic Waves and Antennas (http://www.ece.rutgers.edu/~orfanidi/ewa/), 2008.

[231] S. W. Osborne, P. Blood, P. M. Smowton, Y. C. Xin, A. Stintz, D. Huffaker, and L. F. Lester. Optical absorption cross section of quantum dots. *Journal of Physics: Condensed Matter*, 16(35):S3749, 2004.

[232] R. F. Oulton, D. F. P. Pile, Y. Liu, and X. Zhang. Scattering of surface plasmon polaritons at abrupt surface interfaces: Implications for nanoscale cavities. *Physical Review B*, 76(3):035408, 2007.

[233] N. Papanikolaou. Optical properties of metallic nanoparticle arrays on a thin metallic film. *Physical Review B*, 75(23):235426, 2007.

[234] N. Pazos-Pérez, C. S. Wagner, J. M. Romo-Herrera, L. M. Liz-Marzán, F. J. García de Abajo, A. Wittemann, A. Fery, and R. A. Alvarez-Puebla. Organized Plasmonic Clusters with High Coordination Number and Extraordinary Enhancement in Surface-Enhanced Raman Scattering (SERS). *Angewandte Chemie International Edition*, 51(51):12688–12693, 2012.

[235] A. A. Penzias and R. W. Wilson. A Measurement of Excess Antenna Temperature at 4080 Mc/s. *The Astrophysical Journal*, 142:419, 1965.

[236] J. Peřina, editor. *Coherence and statistics of photons and atoms*. Wiley series in lasers and applications. Wiley, New York, 2001.

[237] S. D. Perrault and W. C. W. Chan. Synthesis and Surface Modification of Highly Monodispersed, Spherical Gold Nanoparticles of 50-200 nm. *Journal of the American Chemical Society*, 131(47):17042–17043, 2009.

[238] W. Pfeiffer, C. Kennerknecht, and M. Merschdorf. Electron dynamics in supported metal nanoparticles: relaxation and charge transfer studied by time-resolved photoemission. *Applied Physics A*, 78(7):1011–1028, 2004.

[239] C. T. Phare, Y.-H. Daniel Lee, J. Cardenas, and M. Lipson. Graphene electro-optic modulator with 30 GHz bandwidth. *Nature Photonics*, 9(8):511–514, 2015.

[240] T. G. Philbin. Canonical quantization of macroscopic electromagnetism. *New Journal of Physics*, 12(12):123008, 2010.

[241] B. Piglosiewicz, S. Schmidt, D. J. Park, J. Vogelsang, P. Groß, C. Manzoni, P. Farinello, G. Cerullo, and C. Lienau. Carrier-envelope phase effects on the strong-field photoemission of electrons from metallic nanostructures. *Nature Photonics*, 8(1):37–42, 2014.

[242] T. Plakhotnik, E. A. Donley, and U. P. Wild. Single-Molecule Spectroscopy. *Annual Review of Physical Chemistry*, 48(1):181–212, 1997.

[243] E. Prodan and P. Nordlander. Structural Tunability of the Plasmon Resonances in Metallic Nanoshells. *Nano Letters*, 3(4):543–547, 2003.

[244] E. Prodan, C. Radloff, N. J. Halas, and P. Nordlander. A Hybridization Model for the Plasmon Response of Complex Nanostructures. *Science*, 302(5644):419–422, 2003.

[245] E. M. Purcell. Spontaneous emission probabilities at radio frequencies. *Physical Review*, 69(11-12):681, 1946.

[246] V. N. Pustovit and T. V. Shahbazyan. Cooperative emission of light by an ensemble of dipoles near a metal nanoparticle: The plasmonic Dicke effect. *Physical Review Letters*, 102(7):077401, 2009.

[247] S. C. Rand. *Lectures on Light: Nonlinear and Quantum Optics Using the Density Matrix*. Oxford University Press, New York, 2010.

[248] J. W. S. Rayleigh. Chapter 14. In *The Theory of Sound*, volume 2 of *The Theory of Sound*, pages 126–129. Macmillan, London, 2nd edition, 1896.

[249] K. K. Rebane. Zero-phonon line as the foundation stone of high-resolution matrix spectroscopy, persistent spectral hole burning, single impurity molecule spectroscopy. *Chemical Physics*, 189(2):139–148, 1994.

[250] J. P. Reithmaier, G. Sęk, A. Löffler, C. Hofmann, S. Kuhn, S. Reitzenstein, L. V. Keldysh, V. D. Kulakovskii, T. L. Reinecke, and A. Forchel. Strong coupling in a single quantum dot–semiconductor microcavity system. *Nature*, 432(7014):197–200, 2004.

[251] G. Rempe, H. Walther, and N. Klein. Observation of quantum collapse and revival in a one-atom maser. *Physical Review Letters*, 58(4):353–356, 1987.

[252] G. F. Rempfer, K. K. Nadakavukaren, and O. H. Griffith. Topographical effects in emission microscopy. *Ultramicroscopy*, 5(4):437–448, 1980.

[253] B. Rethfeld, A. Kaiser, M. Vicanek, and G. Simon. Ultrafast dynamics of nonequilibrium electrons in metals under femtosecond laser irradiation. *Physical Review B*, 65(21):214303, 2002.

[254] C. Rewitz, G. Razinskas, P. Geisler, E. Krauss, S. Goetz, M. Pawłowska, B. Hecht, and T. Brixner. Coherent Control of Plasmon Propagation in a Nanocircuit. *Physical Review Applied*, 1(1):014007, 2014.

[255] J. Rheims, J. Köser, and T. Wriedt. Refractive-index measurements in the near-IR using an Abbe refractometer. *Measurement Science and Technology*, 8(6):601, 1997.

[256] P. R. Rice and H. J. Carmichael. Photon statistics of a cavity-QED laser: A comment on the laser-phase-transition analogy. *Physical Review A*, 50(5):4318–4329, 1994.

[257] B. Richards and E. Wolf. Electromagnetic Diffraction in Optical Systems. II. Structure of the Image Field in an Aplanatic System. *Proceedings of the Royal Society of London A: Mathematical, Physical and Engineering Sciences*, 253(1274):358–379, 1959.

[258] E. C. L. Ru, P. G. Etchegoin, and M. Meyer. Enhancement factor distribution around a single surface-enhanced Raman scattering hot spot and its relation to single molecule detection. *The Journal of Chemical Physics*, 125(20):204701, 2006.

[259] C. Rulliere. *Femtosecond Laser Pulses: Principles and Experiments*. Springer, Berlin, 2nd edition, 2004.

[260] B. E. A. Saleh and M. C. Teich. *Fundamentals of Photonics*. Wiley series in Pure and Applied Optics. John Wiley & Sons, Inc., New Jersey, 2nd edition, 2007.

[261] R. Sapienza, T. Coenen, J. Renger, M. Kuttge, N. F. van Hulst, and A. Polman. Deep-subwavelength imaging of the modal dispersion of light. *Nature Materials*, 11(9):781–787, 2012.

[262] M. Sarovar, A. Ishizaki, G. R. Fleming, and K. B. Whaley. Quantum entanglement in photosynthetic light-harvesting complexes. *Nature Physics*, 6(6):462–467, 2010.

[263] S. Savasta, R. Saija, A. Ridolfo, O. Di Stefano, P. Denti, and F. Borghese. Nanopolaritons: Vacuum Rabi Splitting with a Single Quantum Dot in the Center of a Dimer Nanoantenna. *ACS Nano*, 4(11):6369–6376, 2010.

[264] A. Schiffrin, T. Paasch-Colberg, N. Karpowicz, V. Apalkov, D. Gerster, S. Mühlbrandt, M. Korbman, J. Reichert, M. Schultze, S. Holzner, J. V. Barth, R. Kienberger, R. Ernstorfer, V. S. Yakovlev, M. I. Stockman, and F. Krausz. Optical-field-induced current in dielectrics. *Nature*, 493(7430):70–74, 2013.

[265] O. Schmidt, M. Bauer, C. Wiemann, R. Porath, M. Scharte, O. Andreyev, G. Schönhense, and M. Aeschlimann. Time-resolved two photon photoemission electron microscopy. *Applied Physics B*, 74(3):223–227, 2002.

[266] O. G. Schmidt, editor. *Lateral Alignment of Epitaxial Quantum Dots*. Nanoscience and Technology. Springer, Berlin Heidelberg, 1st edition, 2010.

[267] C. Schneider. *Mapping of surface plasmon polariton fields by time-resolved photoemission electron microscopy: experiments, simulations, and applications*. PhD thesis, TU Kaiserslautern, Kaiserslautern, 2013.

[268] D. T. Schoen, T. Coenen, F. J. García de Abajo, M. L. Brongersma, and A. Polman. The Planar Parabolic Optical Antenna. *Nano Letters*, 13(1):188–193, 2013.

[269] J. A. Schuller, E. S. Barnard, W. Cai, Y. C. Jun, J. S. White, and M. L. Brongersma. Plasmonics for extreme light concentration and manipulation. *Nature Materials*, 9(3):193–204, 2010.

[270] M. P. Seah and W. A. Dench. Quantitative electron spectroscopy of surfaces: A standard data base for electron inelastic mean free paths in solids. *Surface and Interface Analysis*, 1(1):2–11, 1979.

[271] L. Shi, T. K. Hakala, H. T. Rekola, J.-P. Martikainen, R. J. Moerland, and P. Törmä. Spatial Coherence Properties of Organic Molecules Coupled to Plasmonic Surface Lattice Resonances in the Weak and Strong Coupling Regimes. *Physical Review Letters*, 112(15):153002, 2014.

[272] K. Słowik, R. Filter, J. Straubel, F. Lederer, and C. Rockstuhl. Strong coupling of optical nanoantennas and atomic systems. *Physical Review B*, 88(19):195414, 2013.

[273] E. Smith and G. Dent. *Modern Raman Spectroscopy: A Practical Approach*. John Wiley & Sons Ltd, West Sussex, England, 1st edition, 2005.

[274] A. Sobhani, A. Manjavacas, Y. Cao, M. J. McClain, F. J. García de Abajo, P. Nordlander, and N. J. Halas. Pronounced Linewidth Narrowing of an

Aluminum Nanoparticle Plasmon Resonance by Interaction with an Aluminum Metallic Film. *Nano Letters*, 15(10):6946–6951, 2015.

[275] H. Song, M. A. Reed, and T. Lee. Single Molecule Electronic Devices. *Advanced Materials*, 23(14):1583–1608, 2011.

[276] Y. Sonnefraud, N. Verellen, H. Sobhani, G. A. Vandenbosch, V. V. Moshchalkov, P. Van Dorpe, P. Nordlander, and S. A. Maier. Experimental Realization of Subradiant, Superradiant, and Fano Resonances in Ring/Disk Plasmonic Nanocavities. *ACS Nano*, 4(3):1664–1670, 2010.

[277] C. Sönnichsen, T. Franzl, T. Wilk, G. v. Plessen, and J. Feldmann. Plasmon resonances in large noble-metal clusters. *New Journal of Physics*, 4(1):93, 2002.

[278] C. Sönnichsen, T. Franzl, T. Wilk, G. von Plessen, J. Feldmann, O. Wilson, and P. Mulvaney. Drastic Reduction of Plasmon Damping in Gold Nanorods. *Physical Review Letters*, 88(7):077402, 2002.

[279] V. J. Sorger, R. F. Oulton, J. Yao, G. Bartal, and X. Zhang. Plasmonic Fabry-Pérot Nanocavity. *Nano Letters*, 9(10):3489–3493, 2009.

[280] C. Spindler, W. Pfeiffer, and T. Brixner. Field control in the tight focus of polarization-shaped laser pulses. *Applied Physics B*, 89(4):553–558, 2007.

[281] J. M. Steele, N. K. Grady, P. Nordlander, and N. J. Halas. Plasmon Hybridization in Complex Nanostructures. In M. L. Brongersma and P. G. Kik, editors, *Surface Plasmon Nanophotonics*, volume 131 of *Springer Series in Optical Science*, pages 183–197. Springer, Dordrecht, softcover reprint of hardcover 1st ed. 2007 edition, 2010.

[282] K. Stella, D. A. Kovacs, D. Diesing, W. Brezna, and J. Smoliner. Charge Transport Through Thin Amorphous Titanium and Tantalum Oxide Layers. *Journal of The Electrochemical Society*, 158(5):P65–P74, 2011.

[283] P. L. Stiles, J. A. Dieringer, N. C. Shah, and R. P. Van Duyne. Surface-enhanced Raman spectroscopy. *Annu. Rev. Anal. Chem.*, 1:601–626, 2008.

[284] E. A. Stinaff, M. Scheibner, A. S. Bracker, I. V. Ponomarev, V. L. Korenev, M. E. Ware, M. F. Doty, T. L. Reinecke, and D. Gammon. Optical Signatures of Coupled Quantum Dots. *Science*, 311(5761):636–639, 2006.

[285] I. N. Stranski and L. V. Krastanow. *Akad. Wiss. Lit. Mainz Math.-natur. Kl. IIb*, 146:797–810, 1939.

[286] C. Strüber. *Ultrafast Coherent Control and Multidimensional Spectroscopy at the Nanoscale*. PhD thesis, Universität Bielefeld, Bielefeld, 2014.

[287] H. R. Stuart and D. G. Hall. Enhanced Dipole-Dipole Interaction between Elementary Radiators Near a Surface. *Physical Review Letters*, 80(25):5663–5666, 1998.

[288] C. E. Talley, J. B. Jackson, C. Oubre, N. K. Grady, C. W. Hollars, S. M. Lane, T. R. Huser, P. Nordlander, and N. J. Halas. Surface-Enhanced Raman Scattering from Individual Au Nanoparticles and Nanoparticle Dimer Substrates. *Nano Letters*, 5(8):1569–1574, 2005.

[289] M. S. Tame, K. R. McEnery, Ş. K. Özdemir, J. Lee, S. A. Maier, and M. S. Kim. Quantum plasmonics. *Nature Physics*, 9(6):329–340, 2013.

[290] M. Tavis and F. W. Cummings. Exact Solution for an N-Molecule-Radiation-Field Hamiltonian. *Physical Review*, 170(2):379–384, 1968.

[291] V. V. Temnov and U. Woggon. Superradiance and Subradiance in an Inhomogeneously Broadened Ensemble of Two-Level Systems Coupled to a Low-Q Cavity. *Physical Review Letters*, 95(24):243602, 2005.

[292] R. J. Thompson, G. Rempe, and H. J. Kimble. Observation of normal-mode splitting for an atom in an optical cavity. *Physical Review Letters*, 68(8):1132–1135, 1992.

[293] A. Thon, M. Merschdorf, W. Pfeiffer, T. Klamroth, P. Saalfrank, and D. Diesing. Photon-assisted tunneling versus tunneling of excited electrons in metal-insulator-metal junctions. *Applied Physics A: Materials Science & Processing*, 78(2):189–199, 2004.

[294] P. Tian, L. Huang, B. Jiang, S. Fei, and D. Huang. 1.3 μm InAs/GaAs quantum dots with broad emission spectra. *physica status solidi (a)*, 207(8):1930–1933, 2010.

[295] P. Törmä and W. L. Barnes. Strong coupling between surface plasmon polaritons and emitters: a review. *Reports on Progress in Physics*, 78(1):013901, 2015.

[296] R. Trebino. *Frequency-Resolved Optical Gating: The Measurement of Ultrashort Laser Pulses*. Springer Netherlands, 1st edition, 2002.

[297] A. Trügler and U. Hohenester. Strong coupling between a metallic nanoparticle and a single molecule. *Physical Review B*, 77(11):115403, 2008.

[298] J. Turkevich, P. C. Stevenson, and J. Hillier. The Formation of Colloidal Gold. *The Journal of Physical Chemistry*, 57(7):670–673, 1953.

[299] H. Valkenier, E. H. Huisman, P. A. van Hal, D. M. de Leeuw, R. C. Chiechi, and J. C. Hummelen. Formation of High-Quality Self-Assembled Monolayers of Conjugated Dithiols on Gold: Base Matters. *Journal of the American Chemical Society*, 133(13):4930–4939, 2011.

[300] N. Valley, N. Greeneltch, R. P. Van Duyne, and G. C. Schatz. A Look at the Origin and Magnitude of the Chemical Contribution to the Enhancement Mechanism of Surface-Enhanced Raman Spectroscopy (SERS): Theory and Experiment. *The Journal of Physical Chemistry Letters*, 4(16):2599–2604, 2013.

[301] K. C. Vernon, D. K. Gramotnev, and D. F. P. Pile. Channel plasmon-polariton modes in V grooves filled with dielectric. *Journal of Applied Physics*, 103(3):034304, 2008.

[302] F. Verstraete, M. M. Wolf, and J. Ignacio Cirac. Quantum computation and quantum-state engineering driven by dissipation. *Nature Physics*, 5(9):633–636, 2009.

[303] E. J. R. Vesseur. *Electron Beam Imaging And Spectroscopy Of Plasmonic Nanoantenna Resonances*. PhD thesis, Utrecht University, Utrecht, 2011.

[304] E. J. R. Vesseur, F. J. G. de Abajo, and A. Polman. Broadband Purcell enhancement in plasmonic ring cavities. *Physical Review B*, 82(16):165419, 2010.

[305] E. J. R. Vesseur, F. J. García de Abajo, and A. Polman. Modal Decomposition of Surface-Plasmon Whispering Gallery Resonators. *Nano Letters*, 9(9):3147–3150, 2009.

[306] E. J. R. Vesseur and A. Polman. Plasmonic Whispering Gallery Cavities As Optical Nanoantennas. *Nano Letters*, 11(12):5524–5530, Dec. 2011.

[307] W. Vogel and D.-G. Welsch. *Quantum Optics: An Introduction*. Wiley-VCH Verlag GmbH & Co. KGaA, 3rd edition, 2006.

[308] F. Wang and N. A. Melosh. Plasmonic Energy Collection through Hot Carrier Extraction. *Nano Letters*, 11(12):5426–5430, 2011.

[309] F. Wang and Y. R. Shen. General Properties of Local Plasmons in Metal Nanostructures. *Physical Review Letters*, 97(20):206806, 2006.

[310] R. J. Warburton, C. S. Dürr, K. Karrai, J. P. Kotthaus, G. Medeiros-Ribeiro, and P. M. Petroff. Charged Excitons in Self-Assembled Semiconductor Quantum Dots. *Physical Review Letters*, 79(26):5282–5285, 1997.

[311] D. R. Ward, N. J. Halas, J. W. Ciszek, J. M. Tour, Y. Wu, P. Nordlander, and D. Natelson. Simultaneous Measurements of Electronic Conduction and Raman Response in Molecular Junctions. *Nano Letters*, 8(3):919–924, 2008.

[312] G. Wedler. *Lehrbuch der Physikalischen Chemie*. Wiley-VCH Verlag GmbH & Co. KGaA, Weinheim, 5th edition, 2007.

[313] T. Weeks and T. Huser. Raman Spectroscopy of Living Cells. In T. Jue, editor, *Biomedical Applications of Biophysics*, number 3 in Handbook of Modern Biophysics, pages 185–210. Humana Press, 2010.

[314] M. J. Weida, S. Ogawa, H. Nagano, and H. Petek. Parallel excitation pathways in ultrafast interferometric pump-probe correlation measurements

of hot-electron lifetimes in metals. *Applied Physics A*, 71(5):553–559, 2000.

[315] T. Weiland. Eine Methode zur Lösung der Maxwellschen Gleichungen für sechskomponentige Felder auf diskreter Basis. *Electronics and Communication*, 31(3):116–120, 1977.

[316] S.-S. Wellershoff, J. Hohlfeld, J. Güdde, and E. Matthias. The role of electron–phonon coupling in femtosecond laser damage of metals. *Applied Physics A*, 69(1):S99–S107, 1999.

[317] D. D. Whitmore, P. Z. El-Khoury, L. Fabris, P. Chu, G. C. Bazan, E. O. Potma, and V. A. Apkarian. High Sensitivity Surface-Enhanced Raman Scattering in Solution Using Engineered Silver Nanosphere Dimers. *The Journal of Physical Chemistry C*, 115(32):15900–15907, 2011.

[318] X. Wu, P. Geisler, E. Krauss, R. Kullock, and B. Hecht. Silica–gold bilayer-based transfer of focused ion beam-fabricated nanostructures. *Nanoscale*, 7(39):16427–16433, 2015.

[319] X. Wu, R. Kullock, E. Krauss, and B. Hecht. Single-crystalline gold microplates grown on substrates by solution-phase synthesis. *Crystal Research and Technology*, 50(8):595–602, 2015.

[320] H. Xu, E. J. Bjerneld, M. Käll, and L. Börjesson. Spectroscopy of Single Hemoglobin Molecules by Surface Enhanced Raman Scattering. *Physical Review Letters*, 83(21):4357–4360, 1999.

[321] H. Xu, J. Liu, X. Duan, J. Li, J. Xue, X. Sun, Y. Cai, Z.-K. Zhou, and X. Wang. Enhance energy transfer between quantum dots by the surface plasmon of Ag island film. *Optical Materials Express*, 4(12):2586–2594, 2014.

[322] K. Yamada, K. Miyajima, and F. Mafuné. Thermionic Emission of Electrons from Gold Nanoparticles by Nanosecond Pulse-Laser Excitation of Interband. *The Journal of Physical Chemistry C*, 111(30):11246–11251, 2007.

[323] S. Yampolsky, D. A. Fishman, S. Dey, E. Hulkko, M. Banik, E. O. Potma, and V. A. Apkarian. Seeing a single molecule vibrate through time-resolved coherent anti-Stokes Raman scattering. *Nature Photonics*, 8(8):650–656, 2014.

[324] M. Yan and M. Qiu. Guided plasmon polariton at 2d metal corners. *Journal of the Optical Society of America B*, 24(9):2333–2342, 2007.

[325] G. Yang, Y. Qian, C. Engtrakul, L. R. Sita, and G.-y. Liu. Arenethiols Form Ordered and Incommensurate Self-Assembled Monolayers on Au(111) Surfaces. *The Journal of Physical Chemistry B*, 104(39):9059–9062, 2000.

[326] Y. Yin, H. Wang, M. Mariantoni, R. C. Bialczak, R. Barends, Y. Chen, M. Lenander, E. Lucero, M. Neeley, A. D. O'Connell, D. Sank, M. Weides, J. Wenner, T. Yamamoto, J. Zhao, A. N. Cleland, and J. M. Martinis. Dynamic quantum Kerr effect in circuit quantum electrodynamics. *Physical Review A*, 85(2):023826, 2012.

[327] T.-W. Yoo and K. Chang. Theoretical and experimental development of 10 and 35 GHz rectennas. *IEEE Transactions on Microwave Theory and Techniques*, 40(6):1259–1266, 1992.

[328] T. Yoshie, A. Scherer, J. Hendrickson, G. Khitrova, H. M. Gibbs, G. Rupper, C. Ell, O. B. Shchekin, and D. G. Deppe. Vacuum Rabi splitting with a single quantum dot in a photonic crystal nanocavity. *Nature*, 432(7014):200–203, 2004.

[329] Y.-C. Yu, J.-M. Liu, C.-J. Jin, and X.-H. Wang. Plasmon-mediated resonance energy transfer by metallic nanorods. *Nanoscale Research Letters*, 8(1):209, 2013.

[330] H. Yun, S.-Y. Lee, K.-Y. Kim, I.-M. Lee, and B. Lee. Hybrid states of propagating and localized surface plasmons at silver core/silica shell nanocubes on a thin silver layer. *Optics Express*, 22(7):8383, 2014.

[331] S. Zhang, D. A. Genov, Y. Wang, M. Liu, and X. Zhang. Plasmon-Induced Transparency in Metamaterials. *Physical Review Letters*, 101(4):047401, 2008.

[332] L. Zhao, K. L. Kelly, and G. C. Schatz. The Extinction Spectra of Silver Nanoparticle Arrays: Influence of Array Structure on Plasmon Resonance Wavelength and Width. *The Journal of Physical Chemistry B*, 107(30):7343–7350, 2003.

[333] S.-B. Zheng and G.-C. Guo. Efficient Scheme for Two-Atom Entanglement and Quantum Information Processing in Cavity QED. *Physical Review Letters*, 85(11):2392–2395, 2000.

[334] S. Zherebtsov, T. Fennel, J. Plenge, E. Antonsson, I. Znakovskaya, A. Wirth, O. Herrwerth, F. Süßmann, C. Peltz, I. Ahmad, S. A. Trushin, V. Pervak, S. Karsch, M. J. J. Vrakking, B. Langer, C. Graf, M. I. Stockman, F. Krausz, E. Rühl, and M. F. Kling. Controlled near-field enhanced electron acceleration from dielectric nanospheres with intense few-cycle laser fields. *Nature Physics*, 7(8):656–662, 2011.

[335] X. Zhu, J. Zhang, J. Xu, H. Li, X. Wu, Z. Liao, Q. Zhao, and D. Yu. Dispersion Control in Plasmonic Open Nanocavities. *ACS Nano*, 5(8):6546–6552, 2011.

[336] X. Zhu, Y. Zhang, J. Zhang, J. Xu, Y. Ma, Z. Li, and D. Yu. Ultrafine and Smooth Full Metal Nanostructures for Plasmonics. *Advanced Materials*, 22(39):4345–4349, 2010.

[337] X. L. Zhu, Y. Ma, J. S. Zhang, J. Xu, X. F. Wu, Y. Zhang, X. B. Han, Q. Fu, Z. M. Liao, L. Chen, and D. P. Yu. Confined Three-Dimensional Plasmon Modes inside a Ring-Shaped Nanocavity on a Silver Film Imaged by Cathodoluminescence Microscopy. *Physical Review Letters*, 105(12):127402, 2010.

[338] R. Zia, J. A. Schuller, A. Chandran, and M. L. Brongersma. Plasmonics: the next chip-scale technology. *Materials Today*, 9(7–8):20–27, 2006.

[339] D. Zueco, G. M. Reuther, S. Kohler, and P. Hänggi. Qubit-oscillator dynamics in the dispersive regime: Analytical theory beyond the rotating-wave approximation. *Physical Review A*, 80(3):033846, 2009.

Acknowledgements

Die vorliegende Doktorarbeit wurde in der Zeit von Januar 2011 bis März 2016 am *Lehrstuhl für Molekül- und Oberflächenphysik* der Universität Bielefeld angefertigt. In dieser langen Zeit hatte ich die Möglichkeit in zahlreichen thematisch unterschiedlichen und spannenden Projekten mitzuwirken. Auf diesem Weg habe ich viele interessante und nette Menschen kennengelernt und jeder hat auf seine spezielle Art zu der nun vorliegenden Dissertation beigetragen. Deshalb möchte ich mich am Ende dieser Arbeit explizit bei einige Personen bedanken. Falls sich jemand auf diesem Papier vergessen fühlt, so kann er gewiss sein, dass er in meinem Herzen nicht vergessen ist.

- Zunächst möchte ich mich herzlich bei meinem Betreuer Prof. Walter Pfeiffer dafür bedanken, dass er mir zahlreiche spannende Arbeitsthemen und Aufgaben anvertraut hat. Als ich vor acht Jahren meine Masterarbeit in seiner Gruppe begonnen hatte, hatte ich keine Erfahrung auf dem Gebiet der Optik und Ultrakurzzeit-Spektroskopie. Sein didaktisches Talent, seine große Erfahrung in Theorie und Experiment, sein fachübergreifendes Wissen, die vielen Diskussionen und die große Unterstützung, in vielerlei Hinsicht, haben mich in der Wissenschaft am Ende dazu gebracht, auf meinen eigenen Beinen zu stehen und meine Interessen zu verfolgen. Ich freue mich schon auf viele gemeinsame Projekte.

- Ein herzlicher Dank gilt auch Prof. Ulrich Heinzmann für das freundliche Willkommenheißen in der Arbeitsgruppe der *Oberflächen- und Molekülphysik* und für seine stete Sorge um das Wohlergehen der gesamten Gruppe. Die Möglichkeit am Attosekundenpuls-Experiment mitarbeiten zu dürfen, und damit an die derzeitigen Grenzen der experimentellen Zeitauflösung zu gehen, war eine lehrreiche und spannende Erfahrung. In diesem Zuge möchte ich mich auch bei meinen studentischen Mitstreitern Sergej Neb, Fabian Siek, Walter Enns and Christian Oberer im Attosekundenlabor für

die gute Zusammenarbeit, die gegenseitige Unterstützung und das ein oder andere Erfrischungsgetränk bedanken.

- Ebenso gebührt meinem steten Bürokollegen und Mitstreiter Dominik 'MacGyver' Differt ein besonderer Dank. Seine Fingerfertigkeit, sein Improvisationstalent, seine profunden Kentnisse der Physik und seine kritischen Fragen waren enorm hilfreich in zahlreichen Diskussionen und bei gemeinsamen Experimenten. Ich bedanke mich auch bei Felix Becker für die zahlreichen interessanten Diskussionen und für die große Hilfsbereitschaft und gegenseitige Unterstützung.

- An dieser Stelle sei auch meinem alten Mentor Christian Strüber gedankt, der mich während meiner Zeit als Masterstudent betreut hat. Die gemeinsame Arbeit mit Christian im NFC-Projekt und im Attosekundenlabor war äußert motivierend und ermutigend. Sein fachbereichübergreifendes Wissen, und die Fähigkeit dieses Wissen auf das aktuelle Problem umgehend anzuwenden, war immer wieder überraschend. Genauso überraschend wie seine Rückhand im Mini-Tischtennis!

- Ich möchte auch Babak Soleymanzadeh für die gemeinsame Zeit als Doktorrand danken. Nicht nur die Zeit und das Labor haben wir geteilt, sondern auch die gleiche Vorliebe für vergangene und aktuelle Geschehnisse in Physik, Kunst und Musik.

- Einen großen Dank möchte ich Prof. Martin Aeschlimann und seiner gesamten Arbeitsgruppe *Ultrafast Phenomena at Surfaces* an der TU Kaiserslautern für die Gastfreundschaft und das großartige Engagement im NFC-Projekt aussprechen. Hier seien für ihren unermüdlichen Einsatz im Labor und bei der Datenauswertung Philip Thielen, Martin Piecuch und Benjamin Frisch erwähnt. Ohne die zeitaufgelösten Messungen von Benjamin wäre die Demosntration eines kohärenten und langreichweitigen Energietransfers zwischen zwei Nanoantennen in Kapitel 2 nicht so instruktiv gewesen.

- Im Zuge des langreichweitigen Energietransfers zwischen zwei Nanoantennen sei auch Enno Krauss aus der Gruppe von Prof. Bert Hecht (Universität Würzburg) herzlich gedankt. Er hat die plasmonischen Kavitäten in einkristallinen Goldflocken hergestellt.

- Ebenso gebührt Prof. Tobias Brixner (*Physikalische Chemie 1*, Universität Würzburg) ein großer Dank im Rahmen des gesamten NFC-Projekts. Seine Expertise in kohärenter Kontrolle und multi-dimensionaler nichtlinearer Spektroskopie, so wie sein Talent in wissenschaftlicher Kommunikation und in der Formulierung klarer Aussagen, ist essentiel in dieser Kooperation. Besonders möchte ich in seiner Arbeitsgruppe Christian Kramer danken, mit dem ich nun schon einige NFC-Messzeiten absolvieren durfte und der Prof. Brixners Expertisen mit in diese Messzeiten einbringt. Unsere gemeinsamen Diskussionen waren immer sehr interessant und die gegenseitige Unterstützung war so gut, wie man es sich nur wünschen konnte. Das Gleiche gilt auch für Bernhard Huber, dessen umfangreiches Fach- und Literaturwissen, so wie sein Tatendrang, eine große Bereicherung in der gemeinsamen Arbeit sind. Auch bei Sebastian Pres möchte ich mich herzlich für die Unterstützung und gewinnbringenden Diskussionen in den letzten Wochen bedanken.

- Im Projekt der oberflächenverstärkten Raman-Streuung möchte ich Prof. Thomas Huser und Elina Oberländer sehr herzlich für die gute Zusammenarbeit bedanken. Prof. Husers Tür stand jederzeit offen um Einblicke in die Welt der hochauflösenden Mikroskopie und Biophotonik zu bekommen und um Fragen zu klären und Resultate zu besprechen. Ich freue mich auch, dass Prof. Huser als Zweitgutachter dieser Dissertation zugesagt hat und weiß diese Arbeit sehr zu schätzen. Bei Elina möchte ich mich auch noch einmal für die gute Zusammenarbeit über das Projekt hinaus bedanken. Elinas engagierte Arbeitsweise und ihre große Hilfsbereitschaft haben einen wichtigen Teil zu den Ergebnissen dieser Dissertation beigetragen.

- Im Rahmen des Projekts der oberflächenverstärkten Raman-Streuung und der nanolokalisierten Strominjektion möchte ich mich auch bei Prof. Adelheid Godt und Ingo Heesemann für die gute Kooperation und die zur Verfügung gestellten Nanopartikelaggregate bedanken.

- Detlef Diesing möchte im Rahmen des Projekts der nanolokalisierten Strominjektion für die Herstellung der Metall-Isolator-Metall-Kontakte danken.

- Es sei auch allen Mitarbeitern der *Oberflächen- und Molekülphysik* und der

EDV in Bielefeld herzlichst für ihre Unterstützung und Hilfsbereitschaft in technischen sowie wissenschaftlichen Angelegenheiten gedankt. Besonders hervorheben möchte ich hier Kay Lofthouse, die mir unermüdlich in bürokratischen und organisatorischen Angelegenheiten geholfen hat; Christian Meier und Gerd Ahlers, die sich um einen reibunglosen Ablauf der Datenauswertung und Softwarelizenzen gekümmert haben; Wiebke Hachmann für ihre Unterstützung am TEM; und Armin Brechling und Prof. Helmut Stiebig für wissenschaftliche Diskussionen, Ratschläge und Zusammenarbeit, so wie für die Koordination der Übungsgruppen und die Aufrechterhaltung der Kaffeeversorgung.

Zu guter Letzt möchte ich noch meinen Freunden und meiner Familie für all ihre Unterstützung, Geduld, Liebe, Nachsicht, Rückhalt und Verständnis danken, obwohl sie ebenso in ihren Verpflichtungen eingespannt sind. Ihr stetes Interesse hat mich darin bestärkt eine eine gute und sinnvolle Arbeit zu machen.

Der größte Dank gebührt an dieser Stelle meiner Frau, Dana, für ihre beispiellose Unterstützung. Ohne sie hätte diese Arbeit nicht vollendet werden können. Dana hat mir selbstlos den Rücken freigehalten, ohne dabei ihre eigenen Ziele aus den Augen zu verlieren. Ich bin dankbar für jeden Tag, den ich mit ihr erleben darf.

Gedruckt auf alterungsbeständigem Papier nach DIN-ISO 9706